UNIVERSITÉ CÔTE D'AZUR

ÉCOLE DOCTORALE
SCIENCES FONDAMENTALES ET APPLIQUÉES



THÈSE DE DOCTORAT

Dynamique des particules actives dans les superfluides et leur interaction avec les vortex quantiques

Umberto GIURIATO

Laboratoire J.L. Lagrange – Observatoire de la Côte d'Azur

Présentée en vue de l'obtention du grade de docteur en Physique
de l'Université Côte d'Azur
Dirigée par Giorgio Krstulovic, Yannick Ponty
Soutenue le 20/11/2020

Devant le jury composé de:
Carlo Barenghi, Professeur, Newcastle University, Newcastle upon Tyne, UK
Mathieu Gibert, Chercheur CNRS, Institut NÉEL, Grenoble, France
Christophe Josserand, Professeur, École Polytechnique, Paris, France
Giorgio Krstulovic, Chercheur CNRS, Observatoire de la Côte d'Azur, Nice, France
Alessandra Lanotte, Chercheuse CNR, Nanotec, Lecce, Italia
Sergey Nazarenko, Directeur de recherche CNRS, Université Côte d'Azur, Nice, France
Yannick Ponty, Directeur de recherche CNRS, Observatoire de la Côte d'Azur, Nice, France

PROJET FINANCÉ PAR L'ANR – PROJECT FUNDED BY THE ANR

Dynamics of active particles in superfluids and their interaction with quantum vortices

Dynamique des particules active dans les superfluides et leur interaction avec les vortex quantiques

Jury

Président du jury

- Sergey Nazarenko, Directeur de recherche CNRS, Université Côte d'Azur, Nice, France

Rapporteurs

- Carlo Barenghi, Prefesseur, Newcastle University, Newcastle upon Tyne, UK
- Christophe Josserand, Professeur, École Polytechnique, Paris, France

Examinateurs

- Mathieu Gibert, Checheur CNRS, Institut NÉEL, Grenoble, France
- Giorgio Krstulovic, Chercheur CNRS, Observatoire de la Côte d'Azur, Nice, France
- Alessandra Lanotte, Chercheuse CNR, Nanotec, Lecce, Italia
- Sergey Nazarenko, Directeur de recherche CNRS, Université Côte d'Azur, Nice, France
- Yannick Ponty, Directeur de recherche CNRS, Observatoire de la Côte d'Azur, Nice, France

Dynamics of active particles in superfluids and their interaction with quantum vortices

Abstract Superfluids are inviscid flows in which vorticity is supported on filaments with quantized circulation. Such objects, known as quantum vortices, exhibit a hydrodynamical behavior. Experimentally, the dynamics of superfluids has been studied by using particles, which nowadays have become the main tool for visualizing quantum vortices. In this Thesis, we study numerically and analytically the dynamics of active and finite-size particles in superfluids. The superfluid is modeled with the Gross–Pitaevskii equation, while the particles are implemented as moving repulsive potentials coupled with the macroscopic wave function describing the superfluid. Firstly, the model is used to investigate the interaction between particles and quantum vortices at very low temperatures. This part aims to give a theoretical background to the current experiments in which macroscopic particles are used to sample superfluid vortices and quantum turbulence. Specifically, we address the following problems: the capture of a particle by a quantum vortex, the reconnections of vortex filaments and the propagation of Kelvin waves in presence trapped particles and the dynamics of particles in decaying quantum turbulence. In the last part of the manuscript, finite temperature effects are studied in the Fourier-truncated Gross–Pitaevskii model. The goal is to characterize the dynamics of impurities immersed in a thermal bath and how their presence modifies the statistical properties of the fluid. In particular, the random motion of the impurities and the temperature dependence of the friction coefficient are studied. Finally, the clustering of impurities and its effect on the phase transitions of the condensate are investigated.

Keywords Superfluids, Quantum turbulence, Particles, Numerical simulations

---

Dynamique des particules active dans les superfluides et leur interaction avec les vortex quantiques

Résumé Les superfluides sont des fluides non visqueux dans lesquels la vorticité se concentre sur des filaments ayant une circulation quantifiée. Ces objets, appelés vortex quantiques, possèdent un comportement hydrodynamique. Expérimentalement, la dynamique des superfluides est souvent étudiée en utilisant des particules. Les particules sont aujourd'hui devenues l'outil principal pour visualiser les vortex quantiques. Dans cette thèse, nous étudions numériquement et analytiquement la dynamique des particules actives et de taille finie dans les superfluides. Le superfluide est modélisé avec l'équation Gross–Pitaevskii, tandis que les particules sont implémentées comme des potentiels répulsifs mobiles couplés avec la fonction d'onde macroscopique décrivant le superfluide. Le modèle est utilisé pour étudier l'interaction entre les particules et les tourbillons quantiques à très basse température. Cette première partie vise à donner un contexte théorique aux expériences actuelles dans lesquelles des particules macroscopiques sont utilisées pour échantillonner les vortex superfluides et la turbulence quantique. Plus précisément, nous abordons les problèmes suivants : la capture d'une particule par un vortex quantique, les reconnexions des filaments de vortex et la propagation des ondes Kelvin en présence de particules piégées, ainsi que la dynamique des particules dans la turbulence quantique en déclin. Dans la dernière partie du manuscrit, les effets de température finis sont étudiés dans le modèle Gross–Pitaevskii avec une troncature spectrale. L'objectif est de caractériser la dynamique des impuretés immergées dans un bain thermal et comment leur présence modifie les propriétés statistiques du fluide. En particulier, le mouvement aléatoire des impuretés et la dépendance en température du coefficient de frottement sont étudiés. Enfin, le clustering des impuretés et son effet sur les transitions de phase du condensat sont examinés.

Mots-clés Superfluides, Turbulence quantique, Particules, Simulations numeriques

Dinamica di particelle attive nei superfluidi e la loro interazione con i vortici quantistici

Sommario I superfluidi sono fluidi non viscosi nei quali la vorticità è concentrata su strutture unidimensionali aventi circolazione quantizzata. Tali oggetti, chiamati vortici quantistici, mostrano un comportamento idrodinamico su larga scala. Sperimentalmente, la dinamica dei superfluidi viene spesso studiata utilizzando delle particelle come sonde, che attualmente esse sono diventate lo strumento principale per visualizzare i vortici quantistici. In questa Tesi, la dinamica di particelle attive e a taglia finita nei superfluidi viene studiata analiticamente e numericamente. Il superfluido è modellizzato con l'equazione di Gross–Pitaevskii, mentre le particelle sono implementate come potenziali repulsivi mobili, accoppiati con la funzione d'onda macroscopica che descrive il superfluido. Innanzi tutto, tale modello è utilizzato per studiare l'interazione tra le particelle e i vortici quantistici a bassissima temperatura. L'obiettivo di questa prima parte è quello di fornire un contesto teorico agli esperimenti in cui particelle macroscopiche vengono utilizzate per sondare i superfluidi e studiare la turbolenza quantistica. Più precisamente, i seguenti problemi vengono affrontati: la cattura di una particella da parte di un vortice quantistico, le riconnessioni tra filamenti vorticosi e la propagazione di onde di Kelvin in presenza di particelle intrappolate, la dinamica di particelle in regime di turbolenza quantistica. Nell'ultima parte del manoscritto, vengono studiati effetti di temperatura finita nel modello di Gross–Pitaevskii con troncamento spettrale. L'obiettivo è quello di caratterizzare la dinamica di impurità immerse in un bagno termico e come la loro presenza modifichi le proprietà statistiche del fluido quantistico. In particolare, vengono studiati il moto stocastico delle impurità e la dipendenza dalla temperature del coefficiente di frizione. Infine, vengono esaminati il processo di raggruppamento delle impurità e come questo influisca sulle transizioni di fase del condensato.

Parole chiave Superfluidi, Turbulenza quantistica, Particelle, Simulazioni numeriche

Acknowledgements

This Thesis is the end point of the work that I carried on as PhD fellow for the research project ANR GIANTE from October 2017 to November 2020 at the Lagrange laboratory of the "Observatoire de la Côte d'Azur", in Nice, France. I thus thank the director of the Lagrange laboratory **Philippe STEE**, together with the technical and administrative staff of the Observatory, in particular **Christine DELOBELLE** for her help and competence in the mazes of the french burocracy.

The most important acknowledgement goes obviously to my supervisor **Giorgio KRSTULOVIC**, for his guidance, enthusiasm and constant support during these years, without which all the results reported in the present manuscript would have never been achieved. I am very grateful to the two Referees **Carlo BARENGHI** and **Christophe JOSSERAND** for their careful and constructive review of the present manuscript. I thank as well the other members of the jury: **Mathieu GIBERT**, **Alessandra LANOTTE**, **Sergey NAZARENKO** and **Yannick PONTY**. Of course, a big thanks goes to the co-authors that contributed (besides Giorgio) to some of the papers of this project, namely Sergey and **Davide PROMENT**. I thank Davide also for inviting me twice at the University of East Anglia, in the UK. I mention here the other scientists with whom we had fruitful discussions: **Jeremie BEC** (thanks for the insighful lectures on Turbulence!), **Marc BRACHET**, **Gustavo DURING** (with whom I had the pleasure to work during my visit at the Universidad Católica de Chile in the first year), **Luca GALANTUCCI**, **Adam GRIFFIN**, **Marco LA MANTIA**, **Alexei MAILYBAEV**, **Rahul PANDIT**, **Vishwanath SHUKLA**, **Alberto VILLOIS**, **Dario VINCENZI** and my former supervisor for the Master Thesis, **Miguel ONORATO**. A special acknowledgment to the young "superfluidos" that shared with me part of this experience, **Nicolas MULLER** and my office-mate **Juan Ignacio "Nacho" POLANCO**; this last in particular for having patiently listened to my daily speculations (about quantum fluids and more), for his valuable coding advices and for having provided the original version of the template for this manuscript. Thanks also to **Camille GRANIER** for her mothertongue opinion on the french version of the abstract.

I thank all the colleagues and friends that I met in Nice and at the Observatory during these years, which come from all over the world. The possibility to deal, although temporarily, with such a varied, multi-ethnical community has been very enriching for me. Besides the ones already mentioned, a certainly not exhaustive list is the following (in alphabetical order, not to disappoint anyone): **Adrien**, **Andy**, **Annelore**, **Brynna**, **Carlos**, **Christophe**, **Chrysa**, **Clement**, **Edouard**, **Elena**, **Emma**, **Francesco**, **George**, **Gabriele**, **Govind**, **HE!**, **Joao**, **Jun Du**, **Lorenzo**, **Marco**, **Mariachiara**, **Matteo**, **Max**, **Masanori**, **Michael**, **Natalia**, **Nastia**, **Nicola**, **Pablo**, **Pierugo**, **Rafael**, **Rosalba**, **Sebastian**, **Shenxia**, **Sofia**, **Thomas**, **Tobias**, **Vitalii**, **Ximena**.

Comment ne pas mentionner le dream team de la cantine de l'Observatoire, dirigé par **Khaled**? Mon chef, tu es le seul pour qui je réserve des mots en français sur ce document. Tu es vraiment le joker de l'Observatoire, cela ne serait pas pareil sans toi. Merci infiniment pour tes repas pas mal, mais surtout pour tes leçons de vie (ainsi que de bon français). J'ai été honoré d'être ton élu.

***

Questa Tesi e tutto il lavoro che ci sta dietro sono dedicati alla memoria di mio padre **Imer**. Papà, mi hai visto partire ormai più di tre anni fa per andare a fare delle strane simulazioni di superfluidi in Francia, ma purtroppo non potrai mai vedere il risultato di tale lavoro. Sebbene non ne avresti comunque capito molto, so che ti avrei ugualmente reso orgoglioso. Ti ringrazio, perchè senza la tua educazione e il tuo esempio nel conservare sempre la leggerezza non sarei ciò che sono.

Un pensiero va ugualmente a mia madre **Luisa**, la cui caparbietà continua a dimostrarmi come si possa tenere duro e restare dignitosi e fieri, indipendentemente dalle difficoltà che ci si trova di fronte, così nel lavoro come nella vita.

Dulcis in fundo, l'ultimo ringraziamento va alla mia **Angela**, che con il suo affetto onnipresente, la sorprendente ironia e l'infinita dolcezza, è stata per me un'autentica ancora di salvezza in questi ultimi anni.
Oltre a tutti gli altri pezzi di vita che abbiamo condiviso, il periodo di quarantena trascorso a redigere questo manoscritto sotto il tuo sguardo amorevole ha confermato ancora una volta che basti tu per dare un senso a tutto. Grazie, perché sei di gran lunga la "scoperta" più importante di questo dottorato.

List of publications

During the work that has led to the present manuscript, the following articles have been published or submitted. They represent the main results of this Thesis and are integrally reported throughout the manuscript.

P1 – **U. Giuriato, G. Krstulovic**, Interaction between active particles and quantum vortices leading to Kelvin wave generation. *Nature Scientific Reports* **9**, 4839. https://doi.org/10.1038/s41598-019-39877-w [75]

P2 – **U. Giuriato, G. Krstulovic**, Quantum vortex reconnections mediated by trapped particles. *Physical Review B* **102**, 094508. https://doi.org/10.1103/PhysRevB.102.094508 [77]

P3 – **U. Giuriato, G. Krstulovic, S. Nazarenko**, How trapped particles interact with and sample superfluid vortex excitations. *Physical Review Research* **2**, 023149. https://doi.org/10.1103/PhysRevResearch.2.023149 [79]

P4 – **U. Giuriato, G. Krstulovic**, Active and finite-size particles in decaying quantum turbulence at low temperature. *Physical Review Fluids* **5**, 054608. https://doi.org/10.1103/PhysRevFluids.5.054608 [76]

P5 – **U. Giuriato, G. Krstulovic**, Stochastic motion of finite-size immiscible impurities in a dilute quantum fluid at finite temperature. *Physical Review B* **103**, 024509. https://doi.org/10.1103/PhysRevB.103.024509 [78]

P6 – **U. Giuriato, G. Krstulovic, D. Proment**, Clustering and phase transitions in a 2D superfluid with immiscible active impurities. *Journal of Physics A: Mathematical and theoretical* **52**, 305501. https://doi.org/10.1088/1751-8121/ab2607 [80]

Note that the previous list follows the order of appearance in the present manuscript, which is different from the chronological order of publication. In the main body of the manuscript, the articles will be referred to by using the same bibliographic convention adpted for the other references.

Contents

Abstract / Résumé v

Acknowledgements vii

List of publications ix

Contents xi

Introduction 1

1 Superfluidity and Bose–Einstein condensation 9
- 1.1 Superfluid helium . . . 11
  - 1.1.1 Landau two-fluid model . . . 12
- 1.2 Bose–Einstein condensation in an ideal boson gas . . . 15
  - 1.2.1 Statistichal mechanics of a 3D gas of free bosons . . . 16
  - 1.2.2 Condensation in 2D as a finite size effect . . . 22
- 1.3 The Gross–Pitaevskii model . . . 23
  - 1.3.1 Mean field approximation . . . 23
  - 1.3.2 Symmetries and conserved quantities . . . 26
  - 1.3.3 Condensate ground state and Bogoliubov excitations . . . 32
  - 1.3.4 Hydrodynamic picture . . . 35
  - 1.3.5 Quantum vortex solution . . . 38
- 1.4 Dynamics of superfluid vortices . . . 42
  - 1.4.1 The vortex filament model . . . 42
  - 1.4.2 Local induction approximation . . . 45
  - 1.4.3 Mutual friction . . . 46
  - 1.4.4 Vortex reconnections . . . 47
  - 1.4.5 Vortex waves . . . 49

2 Particles in fluids and superfluids 53
- 2.1 Visualization experiments in superfluid helium . . . 54
  - 2.1.1 Ion trapping and electron bubbles . . . 54
  - 2.1.2 PIV with solid particles . . . 56
  - 2.1.3 Vortex imaging and PTV with solidified particles . . . 57
  - 2.1.4 Fluorescence of He_2^* excimers . . . 60
- 2.2 Dynamics of particles in classical hydrodynamics . . . 61
  - 2.2.1 Particle motion in ideal irrotational fluids . . . 62
  - 2.2.2 Rotational effects . . . 65

2.2.3 Magnus effect . . . 66
2.2.4 Viscous effects . . . 67
2.3 Models for particles in quantum fluids . . . 69
2.3.1 One-way coupling . . . 70
2.3.2 Moving spherical boundaries in the vortex filament model . . . 72
2.3.3 Particles coupled with the Gross–Pitaevskii model . . . 75
2.3.4 Bubble fields and multi-component condensates . . . 80

3 Trapping process and long range interaction between particles and quantum vortices 85
3.1 Capture mechanism . . . 85
3.2 *Publication*: Interaction between active particles and quantum vortices leading to Kelvin wave generation . . . 90
3.3 *Publication*: Quantum vortex reconnections mediated by trapped particles 105

4 Superfluid vortex waves sampled and affected by trapped particles 115
4.1 *Publication*: How trapped particles interact with and sample superfluid vortex excitations . . . 115
4.2 The original Kronig–Penney model for a one-dimensional crystal . . . 130
4.3 Comparison between the crystal and the vortex-particles dispersion relations . . . 133

5 Quantum turbulence in presence of particles 137
5.1 Main concepts of classical Kolmogorov turbulence . . . 137
5.2 Turbulence in quantum fluids . . . 139
5.3 *Publication*: Active and finite-size particles in decaying quantum turbulence at low temperature . . . 140

6 Dynamics of impurities in the truncated Gross–Pitaevskii model 163
6.1 The truncated GP equation as a model for finite temperature quantum fluids . . . 163
6.1.1 The stochastic real Ginzburg–Landau model . . . 168
6.1.2 Superfluid and normal fluid decomposition from the momentum correlation . . . 169
6.2 *Publication*: Stochastic motion of finite-size immiscible impurities in a dilute quantum fluid at finite temperature . . . 171
6.3 *Publication*: Clustering and phase transitions in a 2D superfluid with immiscible active impurities . . . 184

Conclusions 197

A Numerical Methods 201
A.1 Time stepping . . . 201
A.2 Pseudo-spectral method for the superfluid field . . . 202

A.3 Projection and dealiasing 203
A.3.1 Dealiasing of the particle interaction term and momentum conservation 204
A.4 Implementation of the particles 206
A.4.1 Particle potential modeling 206
A.4.2 Repulsion potential tuning 207
A.4.3 Interpolation of the superfluid force on the particle 207

Bibliography **211**

Introduction

According to its historical definition, a superfluid (or quantum fluid) is a liquid that flows with zero viscosity. In more general terms, a superfluid can be defined as a many-body system in which quantum coherence appears on a macroscopic scale [140, 176]. Since quantum effects become dominant if thermal fluctuations are low enough, it is not so surprising that the discovery of superfluidy is actually an unexpected outcome of the research in low temperature physics. Almost one century ago, scientists were trying to get closer to the absolute zero [153] and superfluidity was detected by chance in liquid helium ^{4}He, below a critical temperature of about 2.17 K [1, 106]. Nowadays, superfluid helium (or the phase II of liquid helium) is still one of the most studied quantum fluids, although superfluidity has been achieved and is currently investigated in many other systems, from Bose–Einstein condensates of ultracold atoms [174] to quantum fluids of light in non-linear media [38].

A superfluid possesses an intrinsic long-range order, and thus it can be described by a macroscopic complex field which plays the role of order parameter. Perhaps the most fascinating quantum constraint in a superfluid is the restriction of the vorticity to topological defects of such order parameter. These peculiar unidimensional objects are known as quantum vortices. They exhibit a hydrodynamical behaviour at large scales, but they carry the signature of their quantum nature in the discreteness of the circulation around them [55]. A quantum fluid may be a very complex system, in which many scales are involved. In the case of superfluid helium, the core of quantum vortices has a diameter of about ~ 1 Å, while the size of modern experiments can be up to ten orders of magnitude larger [195]. In particular, turbulence can exist in superfluids, despite the lack of viscosity, and it is actually one of the main reasons that currently attract the interest of researchers on quantum fluids [170, 236]. Superfluid turbulence manifests itself in a tangle of quantum vortex filaments, that interact non-linearly redistributing the energy among the different scales. The dynamics of superfluid vortices, which is characterized by peculiar phenomena, is thus crucial for quantum turbulence. One of such phenomena is for instance the reconnection between vortex filaments, a fast event through which two vortex strands are exchanged and the topology of the flow is rearranged [70, 229]. Another feature is the presence of Kelvin waves [192, 220], helicoidal displacements of the vortex filaments that propagate along them and whose mutual non-linear interactions may transfer energy towards smaller and smaller scales, until it is eventually radiated in the form of sound [129, 141, 236]. Moreover, as already realized by Landau in his first phenomenological description of superfluid helium [139, 140], a superfluid always coexists at finite temperature with a normal (viscous) fluid component, in the so-called two-fluid framework. In the most general case, normal fluid, the superfluid and the quantum vortices therein interact

and affect each other's dynamics in an intricate and non-trivial manner.

The experimental investigation of the properties of superfluids and quantum vortices relies mostly on indirect measurements. In particular for superfluid helium, particles are one of the main tools that has been used to sample the flow [91, 208]. Already the early studies in the 1960s used ions and electron bubbles in the framework of rotating superfluid helium [37, 186]. An impressive experimental breakthrough took place in 2006, when quantum vortices were directly visualized thanks to solidified hydrogen particles, combined with the technique of particle tracking velocimetry [30]. Since then, this kind of probes has become a standard technique for studying superfluid vortex dynamics and quantum turbulence in liquid helium. In particular, signatures of reconnections [29, 169] and vortex wave propagation [64] have been observed, as well as statistical measurements of particle velocity and acceleration in turbulent regimes [137, 197]. Such particles have inertia and a size which is more than four orders of magnitude larger than the vortex core. Thus, they certainly affect the flow and may interact with the vortex filaments in a non obvious way. In such context, understanding what drives the actual motion of particles in a superfluid and providing some insights about how they modify the flow are necessary theoretical tasks. This is precisely the main original motivation that inspired the works collected in the present manuscripy. This Thesis is indeed devoted to a systematic study on the dynamics of active and finite-size particles in a superfluid, with a particular focus on their interaction with quantum vortices.

Given the complexity of a superfluid system and the large scale separation involved, a full prime principle theory for superfluid helium or a generic quantum fluid is currently missing. Nowadays, different phenomenological approaches are used, both analytically and numerically, which are valid at different scales. There is not an univocal manner to include the dynamics of particles in these model, and also in this regard different approaches have been proposed [208]. If the typical scales of the flow are much larger than the average separation between the vortex lines, the superfluid vorticity can be treated as a coarse-grained field, so that both the superfluid and the normal fluid are described by two coupled fluid equations. In such approach, known as the Hall-Vinen-Bekarevich-Khalatnikov (HVBK) model [96, 98], there is no notion of quantized circulation and it is of course valid as long as the vortex lines are and not randomly oriented, but rather spatially organized. The dynamics of point particles (i.e. much smaller than the smallest scale resolved by the model) has been recently implemented in the HVBK model [178, 179]. Although suitable for studying the large scale motions of a two-fluid turbulent system, the physics at the scale of the vortex filaments is not accessible by these equations and the particle-vortex interaction is thus absent.

An extremely popular model that is valid at intermediate scales is the vortex filament method. Such model, pioneered by the work of Schwarz [205], describes the dynamics of each isolated vortex filament and the long range interaction between vortices, although the core is not resolved. Moreover, the quantization of circulation is simply assumed, and not derived by prime principles. In particular, the vortex lines evolve following Biot-Savart integrals stemming from basic hydrodynamical assumptions, but a numerical cutoff must be introduced to regularize the model at the scale of

the vortex core. Moreover, the reconnections between the filaments need also to be implemented as *ad hoc* mechanisms. In the beginning of this century, a large amount of articles exploited the vortex filament method coupled with moving spherical boundary conditions in order to study the interaction between finite-size particles and vortex filaments [15, 113–115, 117, 119].

Finally, a microscopic approach valid at the scale of the vortex core is the Gross–Pitaevskii (GP) model, i.e. a non-linear Schrödinger equation that describes directly the dynamics of the superfluid order parameter and in which the topological nature of quantized vortices is naturally contained [174, 176]. The GP equation was originally devised as a mean field model to describe a weakly interacting Bose–Einstein condensate (BEC). It is based on the fundamental idea that at very low temperature a single macroscopic wavefunction can describe a bosonic system in which all the quantum particles belong to the fundamental state. The connection between such system and a compressible, barotropic, irrotational and inviscid superfluid can be shown straightforwardly [164]. Moreover, given that it naturally reproduces the dynamics of quantized vortex filament, the GP model can be considered as an optimal framework to describe a generic quantum fluid at very low temperature. In this sense, it is expected to provide a good qualitative description also for a strongly interacting superfluid, as helium II. The dynamics of particles and impurities can be studied in the GP framework, as already suggested in the seminal work by Gross himself [89]. One possibility is to model each impurity as a field (with infinite degrees of freedom), evolving according to a partial differential equation and coupled with the condensate wavefunction [25, 33, 191, 231]. However, such approach is numerically costly and difficult to handle with if one wants to consider many impurities. A simpler, minimal method consists in modeling the particles with classical degrees of freedom and encoding the coupling with the superfluid in a fixed-shape potential [88, 212, 214, 242, 245].

This last model is specifically the one that I used to achieve the results reported in this manuscript and it has to be intended as complementary to the other methods utilized in the past with a similar purpose [208]. One of the main advantages of this model is the self-consistency: being based on the GP equation, the full superfluid vortex dynamics and the vortex-particles interaction are naturally reproduced, without the need of any numerical cutoff or *ad hoc* mechanism. Moreover, since the particle is described by its classical degrees of freedom (position and momentum of its center mass) the numerical implementation of many particles is relatively cheap and efficient. From the perspective of the superfluid field, a particle is just a dynamical external potential, and thus it has automatically a finite size and an active effect on the flow. We remark that the effective size of the particles that is computationally reasonable to consider in state-of-the-art GP numerical simulations is less than 100 vortex cores, which is still orders of magnitude smaller than the size of solidified hydrogen particles used in superfluid helium experiments. However, as it will be clear throughout the manuscript, there are insights suggesting that some of our main results are likely to remain valid also at the scale of liquid helium experiments.

Note that the GP model is developed for very low temperature quantum fluids, where the thermal excitations play a negligible role and the normal fluid component

is absent. However, the typical range of temperatures at which the experiments with solidified hydrogen particles in liquid helium are conducted is between 1.5 K and 2 K [28, 137, 169]. In this range, the fraction of normal fluid compononent in the system is actually not negligible and finite temperature effects can be important. For this reason, a more accurate study of the vortex-particle interaction should take into account the presence of thermal fluctuations. In the last part of this manuscript, I introduce a truncation procedure that allows to adapt the GP equation to study the dynamics of a bosonic field at finite temperature [51, 52, 128, 131]. In particular, I report two articles in which the dynamics of impurities is implemented for the first time also in the truncated GP system. The specific issue of the vortex-particle interaction at finite temperature is not studied in this Thesis, but it would be a natural follow-up of the results reported here.

During this Thesis, I addressed different specific problems, with several configurations of particles and superfluid field. The principal methods that I exploited to attack different aspects of each problem are the realization of extensive numerical simulations and the development of analytical treatments. The use of parallel computing techniques and well-established pseudo-spectral schemes to solve partial differential equations allowed me to efficiently obtain accurate and trustable results. I also implemented some of the algorithms of the code "FROST" (Full solveR Of Superfluid Turbulence) used by the quantum fluids team of the Observatory of Nice to solve the GP equation, specifically the particles dynamics and the stochastic model to generate GP thermal states. For some of the problems studied, the numerical achievements have been a guidance to develop analytical calculations, containing important insights about the underlying physics. I also gave emphasis to the direct visualization of the dynamics of the systems studied, which is often a powerful tool for grasping an intuitive picture of the observed phenomena.

The present manuscript is structured in six chapters. In the first two, I introduce the fundamental concepts of superfluids and particle dynamics, and the main results found in the literature are reviewed. The main body of the Thesis is then devoted to the presentation of original results, with further discussions and references to the current research context. From chapter 3 to chapter 5, I study the interaction between particles and superfluid vortices at very low temperature (neglecting the finite temperature effects), presenting the achieved results in an increasing order of complexity. In chapter 6, I address the dynamics of impurities in the truncated GP equation, which models a quantum fluid at finite temperature.

An introduction to quantum fluids and superfluidity is provided in chapter 1. I focus mainly on the notion of Bose–Einstein condensation [32, 58], which is a fundamental physical mechanism intimately related to superfluidity. I discuss the formation of a condensate in a gas of free bosons, showing explicitly how the lowest quantum energy level of the system becomes macroscopically populated below a critical temperature. Then, I consider the case of a weakly interacting system and discuss the Gross–Pitaevskii model [176]. My main concern in this chapter is to point out how the presence of non-linear interactions in a dilute bosonic system is naturally linked to a superfluid behaviour [164]. In particular, I introduce the vortex solution of the GP

equation, which is an actual topological defect of the wavefunction with a quantized circulation. Such preliminary discussion is intended to provide satisfactory motivations for the use of the GP model as an optimal framework for the study of a superfluid at very low temperature, although the absence of non-local interactions prevents it to capture all the physics of superfluid helium [23, 187]. In the last part of the chapter the dynamics of quantum vortices is also introduced, in the hydrodynamic framework of the standard vortex filament model [205]. The phenomena of vortex reconnections [70, 229] and propagation of Kelvin waves [97, 192] are also discussed, since they are central in the subsequent parts of the manuscript.

Chapter 2 is dedicated to reviewing the current knowledge about the dynamics of particles in fluids and superfluids. In order to give substance to the motivation of the present Thesis, I briefly list the various experimental techniques implying the use of particles to sample superfluid helium. Then, I retrace the derivation of the equation of motion for a particle in classical hydrodynamics [8, 150]. I focus in particular to the inviscid and irrotational case, which is akin to a low temperature superfluid, and then I discuss the viscous effects for completeness. Eventually, I show the theoretical and numerical models which have been proposed so far to study the dynamics of particles in superfluids. I stress how the presence of quantized vortices, as well as the coexistence of an inviscid superfluid and a normal (viscous) component at finite temperature, are the key differences with respect to a classical fluid. I discuss in particular the one-way coupling, where the particles are just passive points [181] and the vortex filament method with moving spherical boundary conditions [119, 203, 209]. In the last sections I introduce the coupling between the GP wavefunction and the particles, setting the ground for the presentation of the original results of this Thesis.

I start to show my novel results in chapter 3, by studying the long range interaction between a single particle and a single straight vortex filament, reported in the included publication **P1** [75]. In particular, the focus is on the process of particle capture by the vortex. The article contains a derivation of an effective theory, obtained integrating explicitly the GP Hamiltonian coupled with particles. This reduced model explains the observation of the full GP simulations and it is compatible with the dynamics observed in other models describing the same mechanism [15, 24]. This is an important benchmark that proofs the validity of the full GP model coupled with particles, besides confirming that the effects of compressibility are negligible. Moreover, adding weak deformations of the vortex line as degrees of freedom of the effective theory, it is possible to predict a new mechanism for the generation of monochromatic vortex waves along the filament. An interesting property of the effective theory is a scale invariance when both the particle size and the initial vortex-particle distance are multiplied by the same factor λ, while the time is dilated by λ^2. This invariance is respected by the full GP numerical simulations and suggests that the dynamics of particle trapping in real superfluid experiments should be analogous.

Another case in which the long range particle-vortex interaction plays a crucial role is the reconnection between quantum vortices, when particles are already trapped by the filaments. A work addressing this issue is the publication **P2** [77], reported at the end of chapter 3. There, it is shown that reconnections may be triggered by the

presence of particles lying along the filaments and the momentum exchange between reconnecting vortices and particles is characterized. The scaling invariance of the particle trapping [75] can be observed also here, although it is affected by the interaction between the particle and the vortex at which it is attached. This result underlines the similarity between the reconnection and the trapping process, related to the fact that the dimensional parameter controlling the dynamics is just the (quantized) circulation. Eventually, it is observed that the reconnection process is unchanged by the presence of light particles decorating the filaments. This numerical observation supports the superfluid helium experiments in which reconnections have been sampled by solidified hydrogen particles less dense than the fluid [169].

Chapter 4 is dedicated to the interaction between trapped particles and the vortex waves propagating along a straight vortex filament. The article in which this study is reported is **P3** [79]. Also in this case, the main motivation is related to superfluid helium experiments in which Kelvin waves are claimed to have been detected [64]. The first result is that GP simulations can reproduce a precession motion of the particle related to the Magnus force acting on a sphere with a circulating flow about it [19, 109]. Secondly, the motion of trapped particles reflects a rich dynamics, resulting in many branches of the dispersion relation sampled by them. Such surprising result can be explained by means of a mathematical analogy with the standard Kronig–Penney model for the propagation of electrons in a one-dimensional crystal [127]. This effective theory can predict that light particles affect less the vortex motion, compatibly to what observed also for reconnections [77]. Moreover, it shows that the presence of particles has a negligible effect for large Kelvin waves with slow frequencies. At the end of the chapter I dive deeper into the analogy with the crystal, showing explicitly the differences and the similarities with the original Kronig–Penney model.

In chapter 5 I consider the most complex vortex-particle configuration, namely a tangle of vortex filament in decaying turbulence with a number of particles immersed in the system. It is also the last chapter in which the zero temperature GP model is employed. After two introductive sections on classical and quantum turbulence, I report the article **P4** [76], in which the motion of particles in the tangle analyzed. In such setting all the phenomena studied in the previous chapters are present and contribute to the evolution of the system. Also in this case, figuring out how the turbulent superflow and the particles affect each other falls within the research aim of validating the use of particles as probes, besides helping in understanding better quantum turbulence itself. A reassuring result of [76] is that the presence of active and finite-size particles does not modify the building up and decay of the turbulent regime. It is shown that the majority of particles remains trapped inside vortices, with just occasional episodes of detachment and recapture. This result supports the idea that particles may be capable to sample the evolution of the tangle. Accordingly, the predictions of classical Lagrangian turbulence [222, 248] are recovered at scales larger than the inter-vortex distance. At small scales, the presence of a Magnus precession frequency is detected (consistently with the previous article [79]) together with a non-classical particle velocity power spectrum.

Eventually, chapter 6 is dedicated to a supplementary study that I carried out during

this Thesis, in which finite temperature effects are taken into account. In particular, the Galerkin truncation procedure is applied to the Gross–Pitaevskii model [52, 131], together with the coupling with particles. The purpose is to investigate the dynamics of impurities in a finite temperature quantum fluid, having in mind an atomic BEC as physical setting. Indeed, immiscible and finite size impurities can be produced for instance in the strong-repulsive regime of the multi-component BEC [107, 156, 191]. After describing briefly the truncation (or projection) technique to generate thermal states in GP, I present two last articles. In the first one, **P5** [78], the random motion of a spherical impurity is characterized, and in particular the temperature dependence of the friction coefficient is measured. This allows to show that for the typical sizes of impurities implementable numerically, the GP fluid behaves more as a dilute gas of thermal waves rather than as a continuous liquid. Then, in the publication **P6** [80] a (2D) system with many impurities immersed in it is analyzed. It is shown that a phase in which all the impurities are clustered takes place because of the interplay between the impurity-impurity repulsion and the fluid mediated attraction [212]. When such clustering occurs, an increment of the critical temperatures associated with the condensation and the Berezinskii–Kosterlitz–Thouless phase transitions is detected.

At the end of the manuscript, I give some further concluding considerations to all the work done during the Thesis, while in the Appendix A I provide details on the numerical techniques exploited to perform the simulations.

1 Superfluidity and Bose–Einstein condensation

This is an introductory chapter on quantum fluids, in which we give the fundamental notions at the basis of the results presented throughout this Thesis. We introduce the concept of Bose–Einstein condensation and provide the basic hints on how it is deeply linked to superfluidity. First, after shortly reviewing the main phenomenology of superfluid helium, we discuss the phenomenon of Bose–Einstein condensation in the simplest case of a non-interacting boson gas. Then, we derive and characterize the Gross–Pitaevskii model for a weakly interacting bosonic system, that is the framework in which the full work of this Thesis has been carried out. After explaining why the Gross–Pitaevskii model can be considered as the prototype of a superfluid at very low temperature, we discuss the key points of the known physics of quantum vortices, which are one of the most spectacular features of superfluids, as well as the fundamental building blocks of quantum turbulence. In particular, we show how quantum vortices naturally arise in the Gross–Pitaevskii theory and we present the vortex filament method, that is the main phenomenological model to describe their dynamics. Finally, we introduce reconnections and Kelvin wave propagation, two important features of vortex dynamics whose interplay with particles is one of the topics analyzed afterwards.

Superfluidity and Bose–Einstein condensation are two conceptually different physical notions, but they are without doubt intimately interconnected (although in a non trivial and still not completely clear way) [176]. Historically, superfluidity refers to the feature that defines a fluid with zero viscosity, namely which can flow without dissipation of energy. This means that in principle an object moving through a superfluid is not slowed down by any drag. However, a superfluid (or quantum fluid) is not just an ideal fluid. Many spectacular phenomena accompany the occurence of superfluidity in a system, from the propagation of second sound of heat waves to unexpected dynamics of the flow, like the fountain effect [1]. One of the most striking features of superfluids is the emergence of exotic structures known as quantum vortices, unidimensional topological defects with a discrete circulation around them. The first system in which superfluidity was observed is the phase II of liquid helium ^{4}He, below the critical temperature $T_\lambda \simeq 2.17\,K$. Such discovery was reported independently by Kapitza [106] and Allen [1] in 1938. Nowadays, superfluidity has been observed in a wide variety of systems other than liquid helium, like ultracold atomic gases [174] or light in non-linear optical crystals [38], and even hypothized to appear in the core of neutron stars [144].

During the same year in which superfluid helium was experimentally realized, the

first attempts to give a theoretical explanation to the superfluid phenomenology [145, 221] used an idea formulated by Bose and Einstein one decade earlier, related to the fundamental proprieties of quantum mechanical statistics at very low temperature [32, 58]. It was indeed the notion of Bose–Einstein condensation, i.e. the existence of a state of bosonic matter in which, below a certain critical temperature, a macroscopic fraction of particles occupy the same fundamental quantum state.

Bosons and fermions are two cathegories in which quantum particles can be classified. Fermions have semi-integer spin and are constrained to occupy different states due to the Pauli exclusion principle, while bosons are particles with integer spin that are not prevented from coexisting in the same quantum state. Technically, this difference arises from the symmetrization of the bosonic wavefunctions with respect to the exchange of particles and the antisymmetrization of the fermionic ones. Being a consequence of the statistics built on such constraint, Bose–Einstein condensation is a purely quantum mechanical phenomenon, that nevertheless appears on a macroscopic scale.

It should be noticed, however, that BECs can be observed not only in pure bosonic systems, like atomic gases or liquid helium ^{4}He, but also in the fermionic ones. In the latter case, the fermionic condensation is the result of a more complicated rearrangement of fermions into bosonic states. Typical examples are the emergence of bounded states like Cooper pairs in superconductors [12] or in liquid ^{3}He [167].

Einstein's theory of BEC was formulated for an ideal gas, while superfluid helium is a strongly interacting liquid, which makes it a much more complex system. Actually, in the phenomenological theory of superfluidity created by Landau in 1941 [139, 140], which is known as two-fluid hydrodynamics and is still largely used nowadays, Bose–Einstein condensation does not play any direct role. Howsoever, below the temperature at which thermal fluctuations become critically weak and the superfluid phenomenology takes place, the emergence of a Bose-Einstein condensation is an unavoidable occurrence. In particular, superfluid systems are characterized by the emergence of a macroscopic order parameter, resulting in the manifestation of quantum effects on a macroscopic scale. This connection between BECs and superfluidity can be grasped in a somewhat simple way in the framework of the Gross–Pitaevskii model for weakly interacting bosonic systems.

In this chapter, after shortly reviewing the main phenomenology of superfluid helium (section 1.1) and the mechanism of Bose–Einstein condensation in the non-interacting case (section 1.2), we show the derivation of the GP model and discuss its fundamental properties (section 1.3). We present it as a general prototype of a low temperature superfluid in which all the hydrodynamical features coming from quantum-mechanical constraints are naturally included, justifying its use as the fundamental framework in which the original results of this Thesis have been achieved. Finally, in section 1.4 we discuss more in detail the dynamics of quantum vortices.

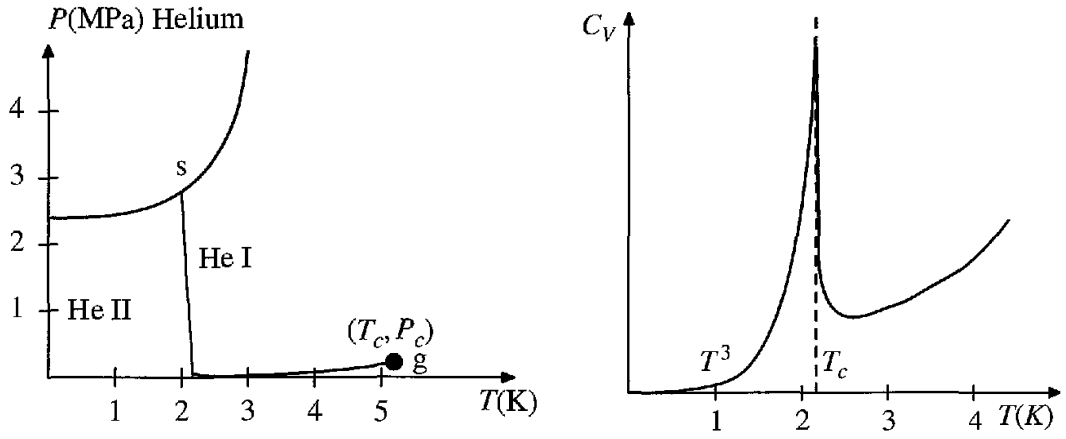


Figure 1.1. (*left*) Phase diagram pressure vs temperature of helium. (*right*) Specific heat of liquid helium as a function of temperature. Figures taken from [225], to which we refer for further details.

1.1 Superfluid helium

The discovery of the superfluid properties of liquid helium is an unexpected result of the research trend developed between the end of the XIX century and beginning of the XX century, which had the broad goal of understanding the behaviour of nature at very low temperature [153]. In a race to reach the absolute zero, many elements which are gaseous at room temperature were systematically liquefied. Helium was the last that resisted, until Onnes was able to generate a sample of liquid ^{4}He in 1908 reaching the temperature of 4 K. Nowadays, helium is still the only known substance which is liquid at the temperature of a few Kelvin and this makes it the most optimal coolant currently available. For instance, it is used to cool down magnets, making possible the engeneering applications of superconductivity, or to refrigerate infrared detectors for astrophysical purposes. Always in Onnes experiments, a critical temperature T_c was then identified at about 2 K, corresponding to a peak in the specific heat of liquid helium, and for this reason named $T_c = T_\lambda$, or "lambda point". It became clear that below such temperature, which is actually a critical line in the pressure-temperature phase diagram, a trasformation in the liquid takes place. The new phase was called phase II of liquid helium ^{4}He, to distinguish it from the standard liquid helium (phase I). One of the peculiarities of liquid helium II is the ability to flow without viscous dissipation and it was discovered in 1938 by Kapitza [106] and Allen [1], who coined the name superfluidity to describe that. The phase diagram of helium is displayed in Fig.1.1 left, while the lambda point in the specific heat is shown in Fig.1.1 right. The power law behavior of the specific heat, including the value of the power (~ 0.012 [143]) and the pre-factors for $T \to T_\lambda^+$ and $T \to T_\lambda^-$ are in good agreement with the theoretical predictions for the three-dimensional XY model universality class (described by the 2-components "$\lambda - \phi^4$" theory), obtained with the renormalization group analysis [100]. This indication suggests indeed the existence of an order parameter that acquires a

non-zero value at the transition to a superfluid state. Such parameter could be thought locally as the macroscopic wavefunction of a Bose–Einstein condensate (see the next sections of this chapter), although it must be stressed that such analogy cannot be exact, given the much stronger interparticle interaction in liquid helium with respect to a dilute bosonic gas.

Subsequent experiments investigated the response of the phase II of liquid helium when subjected to external rotation, which inspired the theories about the quantization of circulation and the existence of quantum vortices by Onsager [166] and Feynman [63], confirmed by the first observation of circulation quanta by Vinen in 1961 [238]. The dynamics of these quantum vortices, largely described throughout this manuscript, is at the basis of the complex phenomenon of quantum turbulence [170, 236]. On the one hand, since quantum vortices break the superfluidity, quantum turbulence is a limitation for the capability of liquid helium to achieve ideal heat transfer in the engeneering applications. On the other hand it is an intriguing complex framework where the universal properties of turbulence can be tested and new non-linear physics can emerge. These are the general motivations for which nowadays superfluid helium is still studied.

Some of the most important facilities in which quantum turbulence in superfluid helium is studied today are the Guo Cryogenics Lab in Florida [94], the Cryogenic Division of the University of Tsukuba in Japan [47] and the Czech Cryogenic Turbulence Facility in Czech Republic [48]. Moreover we mention the Low Temperature Physics department of Lancaster University [146] in UK, where superfluid ^{3}He is produced and studied, and the CEA Grenoble Helium Infrastructures in France [86], where the large Von Karman experiment SHREK is settled [195].

1.1.1 Landau two-fluid model

The first phenomenological theory of superfluid helium at temperatures below the critical point (but still finite), is the so-called two-fluid model and it is due to Landau [139, 140]. In this model, superfluid helium is thought as composed by an immiscible mixture of two components, a normal (viscous) fluid and an inviscid superfluid that does not carry any heat. Each of the two components of the fluid is characterized by its own velocity (v_n and v_s) and density (ρ_s and ρ_n), so that the total density of the fluid is given by $\rho = \rho_s + \rho_n$. The densities of the two components depend non-linearly on the temperature, such that close to the absolute zero only the superfluid survives. The temperature dependence of the superfluid and normal components of liquid ^{4}He II are displayed in Fig.1.2 left. The existence of two different contribution to the fluid density was demonstated experimentally by Andronikashvili in 1946 [66]. He measured the precession frequency of a stack of closely spaced disks immersed inside superfluid helium, which classically is expected to depend on the fluid density via an effective inertia induced by viscous drag. However, he was able to show that only a fraction of the liquid helium did contribute to the inertia, and the other did not. Note that close to the transition temperature, the superfluid component vanishes as $n_s \sim (T_c - T)^{0.67}$, which is again compatible with the universality class of the three-dimensional XY

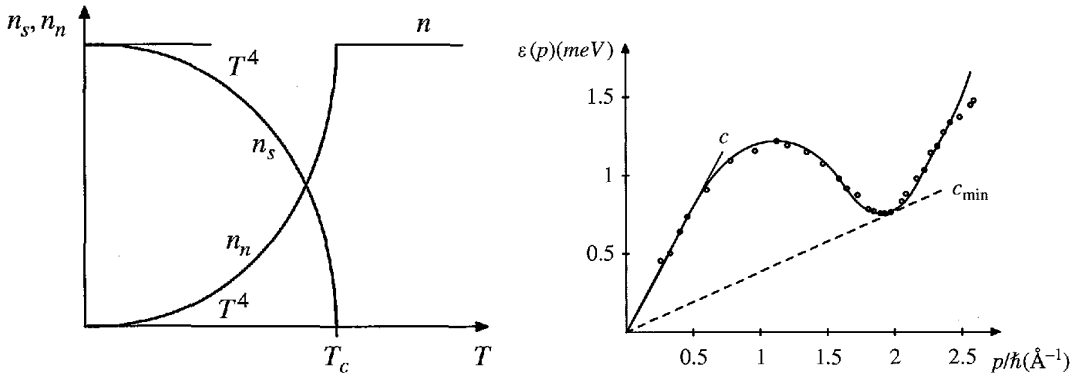


Figure 1.2. (*left*) Temperature dependence of the normal fluid fraction $n_\mathrm{n} = \rho_\mathrm{n}/m_\mathrm{He}$ and the superfluid fraction $n_\mathrm{s} = \rho_\mathrm{s}/m_\mathrm{He}$ in liquid helium II (m_He is the mass of a ^{4}He atom). (*right*) Excitation spectrum in liquid helium II. Figures taken from [225], to which we refer for further details.

model.

The equations of motion of the two-fluid model in the Landau formulation are the following:

$$\frac{\partial \rho}{\partial t} + \nabla \cdot (\rho_\mathrm{s} \boldsymbol{v}_\mathrm{s} + \rho_\mathrm{n} \boldsymbol{v}_\mathrm{n}) = 0 \tag{1.1}$$

$$\frac{\partial (s\rho)}{\partial t} + \nabla \cdot (\rho s \boldsymbol{v}_\mathrm{n}) = 0 \tag{1.2}$$

$$\frac{\partial \boldsymbol{v}_\mathrm{n}}{\partial t} + (\boldsymbol{v}_\mathrm{n} \cdot \nabla)\, \boldsymbol{v}_\mathrm{n} = -\frac{1}{\rho}\nabla p - \frac{\rho_\mathrm{s}}{\rho_\mathrm{n}} s \nabla T + \frac{\eta}{\rho_\mathrm{n}} \nabla^2 \boldsymbol{v}_\mathrm{n} \tag{1.3}$$

$$\frac{\partial \boldsymbol{v}_\mathrm{s}}{\partial t} + (\boldsymbol{v}_\mathrm{s} \cdot \nabla)\, \boldsymbol{v}_\mathrm{s} = -\frac{1}{\rho}\nabla p + s \nabla T, \tag{1.4}$$

where s is the entropy, p is the pressure and η is the normal fluid dynamic viscosity. Equations (1.1) and (1.2) are respectively the conservation of mass and entropy, from which it is explicit that the entropy is transported by the normal fluid. Equations (1.3) and (1.4) are respectively the transport equation of the normal component and of the superfluid component. In absence of a temperature gradient these last are nothing but a Navier–Stokes equation and an Euler (inviscid) equation. Note that the two-fluid model is in principle valid for small velocities and does not account for the presence of quantum vortices [16].

A peculiar consequence which can be easily inferred from the two-fluid model is the existence of a non-dispersive wave equation for temperature perturbationss. The propagation of temperature waves is known as second sound and it is still at the basis of a technique to measure the flow properties in superfluid helium experiments [16, 56]. Another kind of flow, specific of superfluid systems and predicted by the two-fluid model, is the thermal counterflow. Consider a superfluid container with a heat source placed at one closed end. The normal component of the fluid carries the heat away

from the source with an average speed $v_n = q/\rho s T$, where q is the heat flux and T the temperature of the heater. A counterflow arises because , in order to conserve the mass, the superfluid component v_s has to flow in the opposite verse with respect to the normal one, namely towards the source [140]. Turbulence in counterflows can arise because of a mutual friction force between the two fluids (not included in the original version of the two-fluid model), resulting in a complex tangle of quantized vortices, sustained by the counterflow itself [234].

In the Landau picture, superfluidity is the consequence of a gap in the spectrum of the collective excitations of the fluid, with no actual notion of Bose–Einstein condensation. In particular, the normal fluid is constituted by an ensamble of thermal excitations (or quasiparticles) with energy ϵ_p and momentum $\boldsymbol{p}$. If the normal fluid fraction is so low that viscous effects are negligible, an object moving through the fluid would experience no drag, unless its velocity is larger than a critical value. The argument that predicts the existence of such critical velocity, known as Landau criterion, is the following. Consider a superfluid flowing in a pipe with velocity v_s. The superfluidity is broken if an excitation is created as a consequence of the interaction between the fluid and the walls of the pipe: such quasiparticle would be responsible for dissipation, carrying away energy from the fluid. Since $\epsilon_p > 0$ and $\boldsymbol{p}$ are the energy and the momentum of the excitation in the superfluid reference frame, one can simply apply a Galileian transformation to compute the energy of the quasiparticle in the pipe reference frame:

$$\epsilon'_p = \epsilon_p + \boldsymbol{p} \cdot \boldsymbol{v}_s. \tag{1.5}$$

The creation of an excitation happens if it is an energetically favourable process, namely if the quantity (1.5) is negative. This implies a kinematic constraint to the superfluid velocity. In particular, above the critical value

$$v_c \sim \min_{\boldsymbol{p}} (\epsilon_p / |\boldsymbol{p}|), \tag{1.6}$$

the generation of an excitation is possible and the superfluidity is broken, but if the fluid moves with a velocity smaller than (1.6), it does not dissipate energy and in principle can flow forever. From this simple argument it is evident how the functional form of the fluid excitations dispersion relation ϵ_p plays a crucial role for the emergence of a superfluid behaviour. In particular, if one considers a system composed of free particles (with $\epsilon_p \propto p^2$) the critical velocity is zero, meaning that a superfluid state is impossible (although Bose–Einstein condensation can happen, as described in section 1.2). In this sense, the presence of some non-linearity (i.e. interaction among the atoms) is necessary to develop a superfluid state [176]. In the case of liquid helium II the excitations are phonons at low momentum (with a linear dispersion relation) and free particles at high momentum. Between the two behaviours, the excitations spectrum shows a minimum and the quasiparticles in this range are known as rotons. The dispersion relation of helium II excitations, which can be measured using neutron scattering [3], is shown in Fig.1.2 right. One of the main differences between a weakly interacting Bose–Einstein condensate and liquid helium is indeed that in the former case the roton minimum is

absent, and thus the Landau critical velocity is just the speed of sound[1]. Finally, we stress that although the mechanism enlighted by Landau is ultimately correct, the actual critical velocity for breaking the superfluidity is different from the one associated to this roton minimum. Indeed, the superfluidity breaking is often accompanied by the emission of quantized vortices, which are collective topological structures not encoded in the helium quasiparticle spectrum. Instead, they are naturally reproduced by a standard mean field approach for modeling a dilute Bose–Einstein condensate. One of the goals of this chapter is indeed to show that such mean field approach is actually sufficient to catch the fundamental features of a superfluid like liquid helium II and in particular the hydrodynamical behaviour of quantum vortices.

1.2 Bose–Einstein condensation in an ideal boson gas

Starting from this section we focus on the discussion of the phenomenon of Bose–Einstein condensation and the properties of the Gross–Pitaevskii model. In order to understand the mechanism of Bose–Einstein condensation we can consider the simplest case of a homogeneous three-dimensional bosonic gas of particle density n. There is a simple argument which is rather useful to visualize the intuition behind BEC. We assume the statistical mechanical definiton of thermal energy as average kinetic energy

$$\frac{1}{2}m\left\langle v^2\right\rangle = \frac{3}{2}\mathrm{k_B}T, \tag{1.7}$$

where m is the boson mass, v its velocity, T is the temperature and $\mathrm{k_B}$ is the Boltzmann constant. Combining Eq. (1.7) with the usual definition of the de–Broglie wavelength $\lambda_{\mathrm{dB}} = h/p = h/mv$ (i.e. the wavelenght associated with a quantum particle of momentum p), we get

$$\lambda_{\mathrm{dB}}(T) = \frac{h}{\sqrt{3m\mathrm{k_B}T}}, \tag{1.8}$$

which represents the average de Broglie wavelength of the gas at a temperature T and it is related to the distance at which the system shows quantum correlation. When the temperature is low enough, then $\lambda_{\mathrm{dB}}(T)$ becomes of the same order of the average interatomic distance $\ell = n^{-1/3}$, and the quantum collective behaviour of the condensed system becomes evident on a large scale. Indeed, a rough estimate of the critical temperature of the BEC transition can be obtained imposing $\lambda_{\mathrm{dB}}(T_{\mathrm{c}}) = \ell$, which implies

$$T_{\mathrm{c}} = \frac{4\pi\hbar^2}{3m\mathrm{k_B}}n^{\frac{2}{3}}. \tag{1.9}$$

The estimation (1.9) predicts the same dependence on all the physical quantities n, m, $\mathrm{k_B}$, $\hbar$ of the full statistical mechanics treatment (1.28) discussed in detail in the next section, although the numerical prefactor is not accurate. This simple argument is

[1] Note however that the roton minimum can be reproduced in some condensate models with a non-local interaction [23].

also a qualitative justification for describing the condensate by using a macroscopic wavefunction containing all the collective informations of the system. In section 1.3 we will formalize this concept introducing the Gross–Pitaevskii model, which is the main theoretical framework in which the results of this Thesis have been achieved.

1.2.1 Statistichal mechanics of a 3D gas of free bosons

Following a more precise statistical mechanical approach, we consider the gas made of N free bosons with integer spin s, without external confining potential or mutual interaction [176]. It is an idealized picture, not really experimentally achievable, but it is useful to point out the main concepts. We consider the gas in a cubic box of side length L and with periodic boundary conditions. The single-particle energy is the energy of a free particle

$$E_k = \frac{p_k^2}{2m} = \frac{\hbar^2 k^2}{2m}, \tag{1.10}$$

where $\boldsymbol{p}_k = \hbar \boldsymbol{k}$ is the eigenvalue of the momentum in Fourier space and $p_k = \hbar k = \hbar |\boldsymbol{k}|$ its modulus. In the grand-canonical ensemble of statistical mechanics the system is described by the grand-canonical partition function

$$\mathcal{Q}(T, z) = \sum_{N=0}^{\infty} z^N \mathcal{Z}_N(T) \quad \text{with} \quad z = e^{\frac{\mu}{k_B T}}, \tag{1.11}$$

where we have defined the fugacity z as the exponential of the chemical potential μ, namely the energy needed to add a boson to the system. The fugacity weights the canonical partition functions $\mathcal{Z}_N$ for each fixed number of particles N:

$$\mathcal{Z}_N(T) = \left[\sum_{\{n_k\}} e^{-\sum_k \frac{n_k E_k}{k_B T}} \right]^{2s+1}, \tag{1.12}$$

where $2s+1$ is the degeneration related to the spin s, and the sum $\sum_{\{n_k\}}$ runs over all the possible sets of the occupation numbers n_k associated to each energy level E_k (i.e. all configurations), with the constraint of fixed number of particles

$$\sum_k n_k = N. \tag{1.13}$$

The Boltzmann weight depends on the total energy of the system $\sum_k n_k E_k$, for each configuration. Since we are summing also over N in (1.11), we can neglect the constraint (1.13) and just sum, for each k, over a mute index n running from 0 to ∞:

$$\mathcal{Q}(T, z) = \left\{ \prod_k \sum_{n=0}^{\infty} \left(z e^{-\frac{E_k}{k_B T}} \right)^n \right\}^{2s+1}. \tag{1.14}$$

It is easier to work with the logarithm of $\mathcal{Q}$, so that the series inside (1.14) is just a geometrical series:

$$\log \mathcal{Q}(T,z) = (2s+1)\sum_k \log\left[\frac{1}{1-ze^{-\frac{E_k}{k_B T}}}\right]. \tag{1.15}$$

The last expression is all we need to derive the thermodynamical properties of the system. Inside the periodic box, momenta are discretized as

$$\boldsymbol{k} = \frac{2\pi}{L}\boldsymbol{j} \quad \text{with} \quad \boldsymbol{j} = (j_1, j_2, j_3) \in \mathbb{Z}^3, \tag{1.16}$$

so that in 3D the sum over momentum configurations is a sum over integer numbers

$$\sum_k \equiv \sum_{\boldsymbol{j}} = \sum_{j_1=-\infty}^{\infty}\sum_{j_2=-\infty}^{\infty}\sum_{j_3=-\infty}^{\infty} \tag{1.17}$$

and the grand-canonical potential reads

$$\log \mathcal{Q}(T,z) = -(2s+1)\sum_{\boldsymbol{j}} \log\left[1 - ze^{-\frac{1}{2m k_B T}\sum_{i=1}^{3}\left(\frac{2\pi\hbar j_i}{L}\right)^2}\right]. \tag{1.18}$$

The average number of bosons N can be easily computed in this ensemble, just deriving the expression (1.18) with respect to $\log z$

$$N(T,z) = \frac{\partial \log \mathcal{Q}}{\partial \log z} = \sum_{\boldsymbol{j}} n_B(\boldsymbol{k};T,z), \tag{1.19}$$

where $n_B(\boldsymbol{k};T,z)$ is the boson density in momentum space

$$n_B(\boldsymbol{k};T,z) = \frac{(2s+1)}{z^{-1}e^{\frac{E_k}{k_B T}} - 1} = \frac{(2s+1)}{e^{\frac{E_k-\mu}{k_B T}} - 1}. \tag{1.20}$$

We express Eq. (1.19) separating the total number of bosons in the fundamental quantum state (associated to the lowest energy level $E_0 = 0$) from the bosons in the other states, constituting the thermal component N_T of the gas:

$$N = N_0 + N_T. \tag{1.21}$$

Indeed, if we now perform the thermodynamic limit $L \to \infty$, we can convert sums inside (1.19) into integrals and compute them, but only if the boson density (1.20) is a continuous function. In a moment we will see that this is not the case, because the occupation number of the ground state $N_0 = n_B(\boldsymbol{k} = 0;T,z)$ diverges below a critical temperature T_c. Such behaviour is precisely the BEC transition we are looking for. We can see this fact explicitely (fixing the spin $s = 0$ for the sake of simplicity): in the

thermodynamic limit, the occupation number of the zero-mode is still

$$\lim_{L\to\infty} N_0(T,z) = \frac{1}{z^{-1}e^{\frac{E_0}{k_B T}} - 1} = \frac{1}{e^{\frac{E_0-\mu}{k_B T}} - 1}, \tag{1.22}$$

while N_T becomes

$$\lim_{L\to\infty} N_T(T,z) \quad = \left(\tfrac{L}{2\pi}\right)^3 \int n_B(\boldsymbol{k};T,z)\,\mathrm{d}\boldsymbol{k} = \left(\tfrac{L}{\lambda_T}\right)^3 \mathrm{Li}_{\frac{3}{2}}(z), \tag{1.23}$$

where we have introduced the thermal wavelength

$$\lambda_T = \sqrt{\frac{2\pi\hbar^2}{m k_B T}} = \sqrt{\frac{6}{\pi}}\lambda_{\mathrm{dB}}(T), \tag{1.24}$$

and where $\mathrm{Li}_q(z)$ is the polylogarithm function, monothonic and convergent for $\mathrm{Re}[z] < 1$, defined in general by the integral representation

$$\mathrm{Li}_q(z) = \frac{1}{\Gamma(q)} \int \frac{x^{q-1}}{z^{-1}e^x - 1}\,\mathrm{d}x. \tag{1.25}$$

For large temperature, E_0 and all the other levels are populated by an infinitesimal number of particles (with respect to the total number of particles), so that we have $N \sim N_T$. Imposing an infinitesimal boson density for all $\boldsymbol{k}$ we obtain

$$\lim_{T\to\infty} n_B(\boldsymbol{k};T,z) = \frac{1}{z^{-1}-1} \ll 1 \quad \text{iff} \quad z \to 0. \tag{1.26}$$

In this limit, the polylogarithm is asymptotic to a linear function $\lim_{z\to 0} \mathrm{Li}_q(z) = z$, so we can easily invert the expression for the thermal component (1.23) and derive the dipendence of μ on the temperature

$$\mu = -\frac{3}{2} k_B T \log\left[\frac{m k_B T}{2\pi\hbar^2 n^{\frac{2}{3}}}\right], \tag{1.27}$$

which turns out to be monothonic. Decreasing the temperature, there is a critical point T_c in which the chemical potential vanishes. Note that μ cannot become positive, otherwise we would have unphysical levels $E_k < \mu$ with a negative occupation number. Therefore, the critical point corresponds to the saturation $\mu \to E_0 = 0$, namely $z \to 1$. Looking at the dependence of N_0 and N_T with respect to the chemical potential $\mu = k_B T \log z$ (see Fig.1.3) we can see that when the saturation happens, the thermal component remains finite, because $\lim_{z\to 1} \mathrm{Li}_{\frac{3}{2}}(z) = \zeta(3/2) \sim 2.612$, where $\zeta(\cdot)$ is the Riemann Zeta function. In particular, it gets a critical value $N_T = N_c(T, \mu = E_0)$. Conversely, the occupation number of the ground state N_0 diverges. It means that the number of particles in the state with $\boldsymbol{k} = 0$ is macroscopic, which defines the condensation phenomenon for an ideal Bose gas. Note that the function $\mathrm{Li}_{\frac{3}{2}}(z)$ is

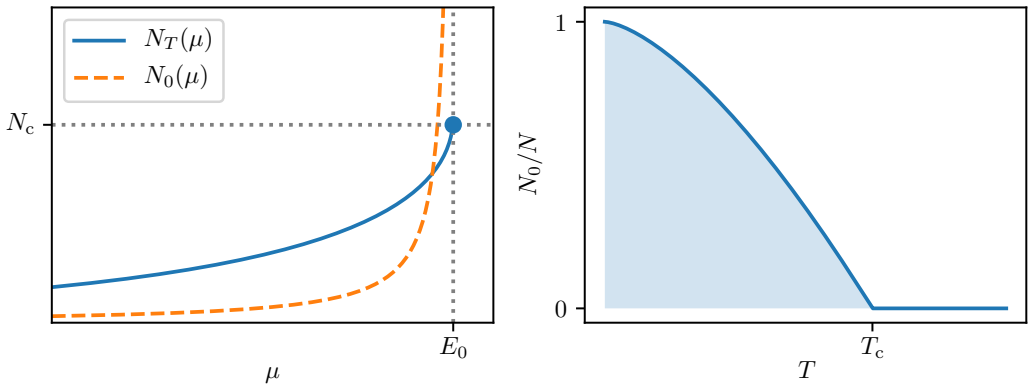


Figure 1.3. Bose–Einstein condensation for an ideal boson gas. (*left*) Occupation number of the thermally excited states (solid blue line) and occupation number of the ground state N_0 (dashed orange line) as a function of the chemical potential. The intersection of the dotted gray lines indicates the critical point, with the saturated chemical potential $\mu = E_0$ and the corresponding finite critical occupation number N_c. (*right*) Condensate fraction as a function of the temperature. We refer to [176] for an exhaustive treatment of the problem.

nothing but the phase-space density $\mathscr{D} = \left(N_T/L^3\right)\lambda_T^3$, which represents the number of particles that occupy a cube of side equal to the thermal wavelength λ_T. The signature of Bose–Einstein condensation is indeed its saturation (at the critical point) to the constant value ~ 2.612. The critical temperature can be obtained imposing $N = N_c(T, \mu = E_0)$ with the saturated chemical potential:

$$T_c = \frac{2\pi\hbar^2}{k_B m}\left(\frac{n}{\zeta\left(\frac{3}{2}\right)}\right)^{\frac{2}{3}}, \tag{1.28}$$

where $n = N/L^3$, the gas density, an intensive parameter which remains finite in the thermodynamic limit. Decreasing the temperature below T_c the fugacity is always 1, but the condition $N = N_T$ is not valid anymore, because an increasing number of particles starts to fill the ground state, populating the condensate. Inverting the Eq. (1.21) below T_c we obtain a simple temperature dependence for the condensed fraction

$$\frac{N_0}{N} = 1 - \left(\frac{T}{T_c}\right)^{\frac{3}{2}}, \tag{1.29}$$

from which we see that when $T = 0$ all the particles are in a condensate state. The formula (1.28) can be inverted and tell what is critical density n_c for which BEC occurs at any fixed temperature[2].

[2]For instance, in neutron stars Bose–Einstein condensation is expected to happen at very high temperature ($T_c \sim 10^7\,K$) compared to atomic BECs or superfluid helium because the density of such system is extremly high [144].

We can characterize further the BEC phase transition cosidering the total energy of the system in the thermodynamic limit:

$$\lim_{L\to\infty} E(T,z) = N_0 E_0 + \left(\frac{L}{2\pi}\right)^3 \int E_k n_B(\boldsymbol{k};T,z)\,\mathrm{d}\boldsymbol{k}. \tag{1.30}$$

For $T \to \infty$ ($\mathrm{Li}_{\frac{3}{2}}(z) \sim z$), quantum effects are negligible and in fact Eq. (1.30) gives the usual equipartition law for an ideal classical gas

$$\lim_{L\to\infty} E = \frac{3}{2}\mathrm{k_B}T\frac{L^3}{\lambda_T^3}\mathrm{Li}_{\frac{5}{2}}(z) \underset{T\gg T_\mathrm{c}}{\longrightarrow} \frac{3}{2}N\mathrm{k_B}T, \tag{1.31}$$

so that the the thermal capacity at fixed volume and number of particles tends to a constant

$$C_V = \left(\frac{\partial E}{\partial T}\right)_{L,N} = \frac{15}{4}\frac{L^3}{\lambda_T^3}\mathrm{k_B}\mathrm{Li}_{\frac{5}{2}}(z) - \frac{9}{2}\frac{\mathrm{Li}_{\frac{3}{2}}(z)}{\mathrm{Li}_{\frac{1}{2}}(z)} \underset{T\gg T_\mathrm{c}}{\longrightarrow} \frac{3}{2}N\mathrm{k_B} = \text{cost.} \tag{1.32}$$

Instead, below the critical temperature $T < T_\mathrm{c}$ ($\mathrm{Li}_q(z=1) = \zeta(q)$) energy decreases more rapidly when the temperature is decreased:

$$\lim_{L\to\infty} E = \frac{3}{2}\mathrm{k_B}T\frac{L^3}{\lambda_T^3}\zeta\left(\frac{5}{2}\right) \tag{1.33}$$

and therefore the thermal capacity is not constant

$$C_V = \left(\frac{\partial E}{\partial T}\right)_{L,N} = \frac{15}{4}\frac{L^3}{\lambda_T^3}\mathrm{k_B}\zeta\left(\frac{5}{2}\right). \tag{1.34}$$

From these limits it is evident that the thermal capacity of the system is a continuous function of the temperature, but its derivative must be discontinuous at the point $T = T_\mathrm{c}$.

In figure 1.4 we have reported a visualization of the peak forming in the momentum distribution across the transition temperature. It refers to one of the first experimental realization of BEC transition in an ultracold atomic gas, which dates back to 1996 [59]. For completeness, we must notice that in the context of cold atoms experiments, the actual systems in which a BEC state is achievable are not free gases but rather confined ones. In the case of trapped gases, the argument followed in this section is still valid, but with some technical differences due to the fact that the eigenstates of the Hamiltonian are affected by the shape of the trap [50]. For instance, a harmonic trap can be realized using lasers or magnetic fields, producing the quantum harmonic oscillator single-particle energy levels

$$E_{n_x n_y n_z} = \left(\frac{1}{2}+n_x\right)\hbar\omega_x + \left(\frac{1}{2}+n_y\right)\hbar\omega_y + \left(\frac{1}{2}+n_z\right)\hbar\omega_z, \qquad n_x, n_y, n_z \in \mathbb{N} \tag{1.35}$$

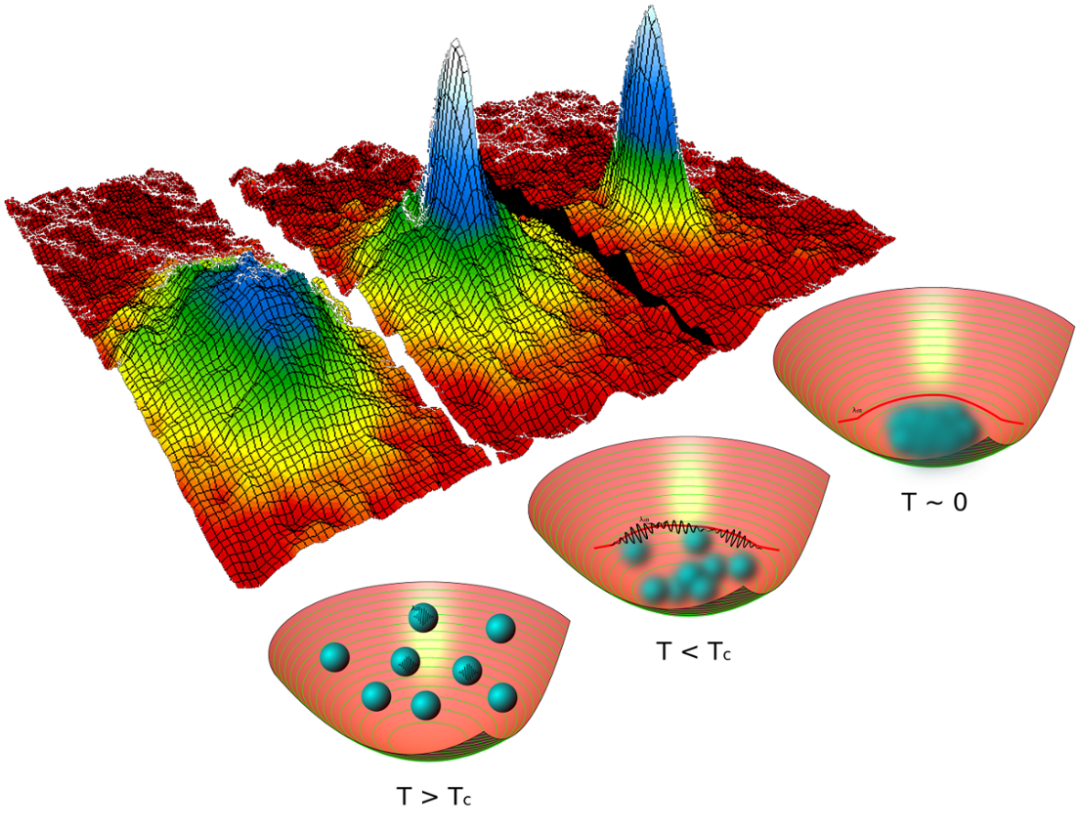


Figure 1.4. Transition to the state of Bose–Einstein condensate as the temperature is decreased. The upper row shows visualization of the momentum distributions, taken in the JILA experiments [59]. The lower row displays schematically the distribution of particles in the trap and the condensation to the lowest particle state. Image taken from [223].

so that the exponent of the temperature dependence of the condensate fraction eventually changes

$$\frac{N_0}{N} = 1 - \left(\frac{T}{T_c}\right)^3, \tag{1.36}$$

and other next order corrections for finite size systems can also arise [50].

1.2.2 Condensation in 2D as a finite size effect

We finally give a short remark on condensation in the two-dimensional case, which in principle is formally prevented bacause of the Mermin–Wagner–Hohenberg theorem [99, 154], although it can be recovered as a finite size effect[3]. We consider the phase-space density of a non-interacting Bose gas in 2D:

$$\mathscr{D} = \frac{N_T}{L^2}\lambda_T^2 = \int_0^\infty \frac{1}{z^{-1}e^x - 1}\,\mathrm{d}x = -\ln(1-z)\,. \tag{1.37}$$

As opposed to the 3D case, we see from Eq. (1.37) that at any non-zero temperature the value of the chemical potential $\mu = \mathrm{k_B}T\ln\left(1-e^{-\mathscr{D}}\right)$ is always strictly negative. This means that arbitrarily small thermal fluctuations are sufficient to prevent the divergence of the occupation number of the fundamental level, i.e. condensation does not occur. The reason of such behaviour is actually a deeper and more general result due to Mermin, Wagner [154] and Hohenberg [99]. Their theorem states that in a system with short-range interactions the emergence of a true long range order (which is the result of a spontaneous breaking of a continuous symmetry) is prevented in dimensions $D \leq 2$. As we will see in the next section, for a weakly interacting bosonic system the order parameter is the macroscopic complex wavefunction of the bosons in the fundamental state and the broken symmetry associated to condensation is the $U(1)$ invariance (multiplication of the wavefunction by a global phase factor). In $2D$, the long range order is destroyed by the long wavelength thermal fluctuations, whose correlator has a logarithmically divergent infrared contribution [172]. Now, the Mermin–Wagner–Hohenberg theorem is valid in the thermodynamic limit, where the system size L is infinite. However, if L is finite, condensation can still occur as a finite size effect. Indeed, one can consider the first order correlation function of an ideal Bose gas, which shows an exponential decay at large scales [95]:

$$g_1(r) \propto \int n_\mathrm{B}(\boldsymbol{k})e^{i\boldsymbol{k}\cdot\boldsymbol{r}}\,\mathrm{d}\boldsymbol{k} \underset{r\gg\lambda_T}{\longrightarrow} e^{-r/\ell}, \tag{1.38}$$

with the correlation length $\ell \sim \lambda_T e^{\mathscr{D}/2}/\sqrt{4\pi}$. Thus, since ℓ increases when the temperature decreases, at a certain temperature it becomes of the same order of the system size: $\ell \sim L$. At this point the system has an effective long-range correlation and a non-zero condensate $n_0 \propto \int_0^L g_1(r)\,\mathrm{d}r > 0$ appears accordingly. Of course, such phase

[3] In this Thesis we deal mainly with 3D systems, except in the publication [80] reported in section 6.3, where the condensation in a 2D weakly interacting bosonic fluid at finite temperature in is investigated numerically in presence of impurities.

transition is not a second-order phase-transition stemming from a symmetry breaking mechanism and thus does not contradict the Mermin–Wagner–Hohenberg theorem.

1.3 The Gross–Pitaevskii model

So far, we have described the condensation mechanism in the simplest case of non-interacting bosons. But the key point for the emergence of superfluidity is actually the presence of non-linear interactions in the system. In this section we will address a system similar to the one described above, but assuming no constraints on homogeneity and including weak non-linear interactions. We will approach the problem with a different strategy, starting from the Hamiltonian dynamics, and performing a mean field approximation in the second quantization framework [31, 50, 176, 193]. Then we will characterize the properties of the model, showing the symmetries and the related conserved quantities. Finally, we will explain the connection with hydrodynamics and the existence of vortex solutions with quantized circulation.

1.3.1 Mean field approximation

We start by considering an inhomogeneous gas of N bosons with mass m, interacting via a 2-body interaction $V_{\text{int}}(\boldsymbol{x}_i, \boldsymbol{x}_j)$ in a D-dimensional space. If the system is further confined by an external potential $V_{\text{ext}}(\boldsymbol{x}, t)$, which in principle may depend on both space and time, its dynamics is governed by the following N-body Schrödinger equation:

$$i\hbar \frac{\partial}{\partial t} \Phi(\boldsymbol{x}_1, \dots, \boldsymbol{x}_N; t) = H_N \Phi(\boldsymbol{x}_1, \dots, \boldsymbol{x}_N; t) \tag{1.39}$$

where $\Phi(\boldsymbol{x}_1, \dots, \boldsymbol{x}_n; t)$ is the symmetric wavefunction of N bosons:

$$\Phi(\boldsymbol{x}_1, \dots, \boldsymbol{x}_i, \dots, \boldsymbol{x}_j, \dots, \boldsymbol{x}_N; t) = \Phi(\boldsymbol{x}_1, \dots, \boldsymbol{x}_j, \dots, \boldsymbol{x}_i, \dots, \boldsymbol{x}_N; t) \qquad \forall i, j \in [1, N], \tag{1.40}$$

and H_N is the N-body Hamiltonian

$$H_N = \sum_{i=1}^{N} \left[-\frac{\hbar^2}{2m} \nabla_i^2 + V_{\text{ext}}(\boldsymbol{x}_i, t) \right] + \sum_{i<j}^{N} V_{\text{int}}(\boldsymbol{x}_i, \boldsymbol{x}_j). \tag{1.41}$$

In general, such equation is impossible to solve for large N and therefore it is necessary to impose some approximations. Adopting the second quantization formalism, we substitute the wavefunction $\Phi(\boldsymbol{x}_1, \dots, \boldsymbol{x}_n; t)$, which depends on ND spatial coordinates, by the boson field operator $\hat{\Psi}(\boldsymbol{x}, t)$ (in the Heisenberg representation) which instead depends only on D spatial coordinates. The field operator $\hat{\Psi}(\boldsymbol{x}, t)$ and its Hermitian conjugate $\hat{\Psi}^\dagger(\boldsymbol{x}, t)$ respectively annihilate and create a particle at the position $\boldsymbol{x}$[4]:

$$\hat{\Psi}^\dagger(\boldsymbol{x}_i, t) \left| \{\boldsymbol{x}\}_{N_B} \right\rangle = \left| \{\boldsymbol{x}\}_{N_B}, \boldsymbol{x}_i \right\rangle, \qquad \hat{\Psi}(\boldsymbol{x}_i, t) \left| \{\boldsymbol{x}\}_{N_B}, \boldsymbol{x}_i \right\rangle = \left| \{\boldsymbol{x}\}_{N_B} \right\rangle, \tag{1.42}$$

[4] Of course $\hat{\Psi}(\boldsymbol{x}, t)|0\rangle = 0$ if $|0\rangle$ is the vacuum state with no particles.

where $\left|\{\boldsymbol{x}\}_M\right\rangle$ is the quantum state populated by N_B bosons labeled by their position. The standard bosonic commutation relations at fixed time hold:

$$\begin{aligned}\left[\hat{\Psi}(\boldsymbol{x},t),\hat{\Psi}^\dagger(\boldsymbol{x}',t)\right] &= \delta(\boldsymbol{x}-\boldsymbol{x}') \\ \left[\hat{\Psi}(\boldsymbol{x},t),\hat{\Psi}(\boldsymbol{x}',t)\right] &= 0 \qquad (1.43)\\ \left[\hat{\Psi}^\dagger(\boldsymbol{x},t),\hat{\Psi}^\dagger(\boldsymbol{x}',t)\right] &= 0\end{aligned}$$

(1.44)

and the Hamiltonian operator is therefore given by

$$\begin{aligned}\hat{H} &= \int \hat{\Psi}^\dagger(\boldsymbol{x},t)\left[-\frac{\hbar^2}{2m}\nabla^2+V_{\text{ext}}(\boldsymbol{x},t)\right]\hat{\Psi}(\boldsymbol{x},t)\,\mathrm{d}\boldsymbol{x}+ \qquad (1.45)\\ &+ \frac{1}{2}\int \hat{\Psi}^\dagger(\boldsymbol{x},t)\hat{\Psi}^\dagger(\boldsymbol{x}',t)V_{\text{int}}(\boldsymbol{x}-\boldsymbol{x}')\hat{\Psi}(\boldsymbol{x},t)\hat{\Psi}(\boldsymbol{x}',t)\,\mathrm{d}\boldsymbol{x}\mathrm{d}\boldsymbol{x}',\end{aligned}$$

where we also assumed translational symmetric interaction, so that V_{int} depends only on $(\boldsymbol{x}-\boldsymbol{x}')$. The corresponding evolution equation for the field $\hat{\Psi}(\boldsymbol{x},t)$ is then the Heisenberg equation

$$\begin{aligned}i\hbar\frac{\partial}{\partial t}\hat{\Psi}(\boldsymbol{x},t) &= \left[\hat{\Psi},\hat{H}\right]= \qquad (1.46)\\ &= \left[-\frac{\hbar^2}{2m}\nabla^2+V_{\text{ext}}(\boldsymbol{x},t)+\int\hat{\Psi}^\dagger(\boldsymbol{x}',t)V_{\text{int}}(\boldsymbol{x}-\boldsymbol{x}')\,\mathrm{d}\boldsymbol{x}'\hat{\Psi}(\boldsymbol{x}',t)\right]\hat{\Psi}(\boldsymbol{x},t).\end{aligned}$$

In general, the field operator can be decomposed as

$$\hat{\Psi}(\boldsymbol{x},t)=\sum_\alpha \Psi_\alpha(\boldsymbol{x},t)\hat{a}_\alpha, \qquad (1.47)$$

where $\Psi_\alpha(\boldsymbol{x},t)$ are the single-particle wavefunctions associated with each bosonic operator $\hat{a}_\alpha$. The action of the operator $\hat{a}_\alpha$ is to annihilate a particle in the α-state. Indeed, $\hat{a}_\alpha$ and its Hermitian conjugate $\hat{a}_\alpha^\dagger$ (the creation operator) are defined in the Hilbert-Fock space through the relations:

$$\begin{aligned}\hat{a}_\alpha^\dagger\left|N_0,\ldots,N_\alpha,\ldots\right\rangle &= \sqrt{N_\alpha+1}\left|N_0,\ldots,N_\alpha+1,\ldots\right\rangle, \qquad (1.48)\\ \hat{a}_\alpha\left|N_0,\ldots,N_\alpha,\ldots\right\rangle &= \sqrt{N_\alpha}\left|N_0,\ldots,N_\alpha-1,\ldots\right\rangle, \qquad (1.49)\end{aligned}$$

where N_α is the number of particle in the α-state, i.e. the eigenvalue of the number operator $\hat{N}_\alpha=\hat{a}_\alpha^\dagger\hat{a}_\alpha$. The commutation relations must be:

$$\left[\hat{a}_\alpha,\hat{a}_\beta^\dagger\right]=\delta_{\alpha,\beta},\qquad \left[\hat{a}_\alpha,\hat{a}_\beta\right]=0,\qquad \left[\hat{a}_\alpha^\dagger,\hat{a}_\beta^\dagger\right]=0. \qquad (1.50)$$

At low temperatures, when the Bose-Einstein condensation occurs, a large number of bosons occupies the fundamental state $|N_0\rangle$, so that $N_0\gg 1$. As a consequence, the action of the creation operator $\hat{a}_0^\dagger$ and the annihilation operator $\hat{a}_0$ is the same and is

negligible, so they can be treated as c-numbers:

$$\hat{a}_0 \simeq \hat{a}_0^\dagger \simeq \sqrt{N_0} \tag{1.51}$$

In other words, since $N_0 \gg 1$, adding a particle to the condensate does not change the physical properties of the system, and the states $|N_0+1\rangle \propto \hat{a}_0^\dagger |N_0\rangle$ and $|N_0-1\rangle \propto \hat{a}_0 |N_0\rangle$ are physically equivalent. If we consider a homogeneous system, namely a bosonic gas of N free particles in a volume $V = L^3$ (exactly the same system studied in the first section), condensation implies that the wavefunction of the single-particle state with zero-momentum is $\Psi_0 = \sqrt{1/V}$. Therefore, the field operator can be written explicitly as

$$\hat{\Psi}(\boldsymbol{x},t) = \Psi_0 \hat{a}_0 + \sum_{\alpha \neq 0} \Psi_\alpha(\boldsymbol{x},t)\hat{a}_\alpha = \sqrt{\frac{N_0}{V}} + \delta\hat{\Psi}(\boldsymbol{x},t) \tag{1.52}$$

where $\delta\hat{\Psi}(\boldsymbol{x},t)$ are small quantum fluctuations over the condensate background. Following a perturbative quantum field theory approach one can show that $\delta\hat{\Psi}(\boldsymbol{x},t)$ is associated, at the first order, to creation and annihilation of excitations known as Bogoliubov pseudoparticles [31].

A more general situation occurs when the configuration $\Psi_0(\boldsymbol{x},t)$ is non-uniform and time-dependent. Then we can write

$$\hat{\Psi}(\boldsymbol{x},t) = \sqrt{N_0}\Psi_0(\boldsymbol{x},t) + \delta\hat{\Psi}(\boldsymbol{x},t), \tag{1.53}$$

because of the approximation (1.51), so that the expectation value $\left\langle \hat{\Psi}(\boldsymbol{x},t) \right\rangle$ is different from zero. Indeed, we can define $\left\langle \hat{\Psi}(\boldsymbol{x},t) \right\rangle = \Psi_0(\boldsymbol{x},t) \equiv \psi(\boldsymbol{x},t)$ and $\left\langle \hat{\Psi}^\dagger(\boldsymbol{x},t) \right\rangle = \Psi_0^*(\boldsymbol{x},t) \equiv \psi^*(\boldsymbol{x},t)$, where $\psi(\boldsymbol{x},t)$ is the complex non-zero order parameter of the BEC transition. If we consider the average $\left\langle \hat{\Psi}(\boldsymbol{x},t) \right\rangle$ over stationary states evolving with the phase factor $e^{-i\frac{E(N_0)t}{\hbar}}$, we get the following time evolution for the order parameter:

$$\psi(\boldsymbol{x},t) = e^{-i\frac{E(N_0)-E(N_0-1)}{\hbar}t}\psi(\boldsymbol{x}) \sim e^{-i\frac{\mu}{\hbar}t}\psi(\boldsymbol{x}) \tag{1.54}$$

since $\mu = \partial E/\partial N_0 \sim E(N_0) - E(N_0-1)$. The fact that the chemical potential replaces the role played by energy in the phase oscillation of quantum steady states is a remarkable evidence of its importance in the physics of Bose-Einstein condensates [176].

The complex function $\psi(\boldsymbol{x},t)$ is usually referred to as the macroscopic wavefunction of the condensate and, if the distance over which its variations are significant is much smaller than the average distance between particles, we can treat it neglecting the quantum fluctuations $\delta\hat{\Psi}(\boldsymbol{x},t)$, namely developing a completely classical mean field theory. Indeed, the main semplification with respect to the many-body theory (1.39) from which we started is that now we have a single function describing the collective properties of the condensed system. Note that the norm of such wavefunction represents the number density of condensed bosons $n = |\psi|^2$. The classical dynamics of the order parameter can be directly inferred from the full quantum equation (1.46) under

the mean field approximation (1.52), and neglecting the small quantum fluctuations:

$$\begin{aligned} i\hbar\frac{\partial}{\partial t}\psi(\boldsymbol{x},t) &= \\ &= \left[-\frac{\hbar^2}{2m}\nabla^2 + V_{\text{ext}}(\boldsymbol{x},t) + \int \psi^*(\boldsymbol{x}',t)V_{\text{int}}(\boldsymbol{x}-\boldsymbol{x}')\psi(\boldsymbol{x}',t)\,\mathrm{d}\boldsymbol{x}'\right]\psi(\boldsymbol{x},t). \end{aligned} \tag{1.55}$$

If the system is dilute enough, only binary collisions at low energy are relevant and the details of the 2-body interaction are negligible. In this regime, an effective delta-potential which depends on the s-wave scattering length a_s of bosons can be used:

$$V_{\text{int}}(\boldsymbol{x}-\boldsymbol{x}') = g\delta^d(\boldsymbol{x}-\boldsymbol{x}'), \qquad g = \frac{4\pi\hbar^2 a_s}{m}. \tag{1.56}$$

This actually means that we are implicitely assuming that the scattering volume $|a_s|^3$ is much smaller than the specific volume V/N of the system. Thus equation (1.56) reduces to:

$$i\hbar\frac{\partial}{\partial t}\psi(\boldsymbol{x},t) = \left[-\frac{\hbar^2}{2m}\nabla^2 + V_{\text{ext}}(\boldsymbol{x},t) + g|\psi(\boldsymbol{x},t)|^2\right]\psi(\boldsymbol{x},t), \tag{1.57}$$

which is a non-linear Schrödinger equation (NLSE) known as Gross–Pitaevskii equation. It is definitely the main tool for studying the evolution of a dilute inhomogeneous BEC from a macroscopic point of view.

In principle the sign of the interaction term can be either positive or negative, depending on whether the interaction between particles is repulsive ($a_s > 0$) or attractive ($a_s < 0$). As it will be clear in section 1.3.3, only the first case is physically allowed for Bose–Einstein condensates. It should be noticed that Eq. (1.57) appears also in other completely different physical situations. For instance in non-linear optics (and also generally in applied mathematics), Eq.(1.57) with repulsive interaction is usually referred to as defocusing NLSE because the non-linear repulsion leads to the spreading of the wavefunction when it is concentrated. The opposite effect arises for attractive interaction, where a modulational instability can develop [219]. In this case Eq. (1.57) is also called focusing NLSE.

In the following section we characterize the properties of the GP model, analyzing the symmetries and conserved quantities of the NLSE.

1.3.2 Symmetries and conserved quantities

The Gross–Pitaevskii model is a classical field theory equipped with a Hamiltonian structure, as well as with symmetries and conserved quantities that can be elegantly related by means of the Noether theorem [72, 164, 219].

In this section we will adopt the notation $\Psi \longrightarrow \Psi_a = (\Psi_1, \Psi_2) = (\psi, \psi^*)$ to indicate the two complex conjugate fields, which are nothing but canonical conjugate variables, $\partial \longrightarrow \partial_\mu = (\partial_t, \nabla)$ to indicate differentiation in both space and time and $\chi \longrightarrow \chi_\mu = (t, \boldsymbol{x})$ as a coordinate over the $(D+1)$ Euclidean spacetime. The Hamiltonian which

describes the system is:

$$H = \int \mathscr{H}[\Psi(\chi), \nabla\Psi(\chi)]\,\mathrm{d}\boldsymbol{x} = \int \left(\frac{\hbar^2}{2m}|\nabla\psi|^2 + \frac{g}{2}|\psi|^4 + V_{\mathrm{ext}}|\psi|^2 \right) \mathrm{d}\boldsymbol{x}, \tag{1.58}$$

while the Lagrangian can be obtained by an usual Legendre transformation:

$$L = \int \mathscr{L}[\Psi(\chi), \partial\Psi(\chi)]\,\mathrm{d}\boldsymbol{x} = \int \frac{i\hbar}{2}\left(\frac{\partial\psi}{\partial t}\psi^* - \frac{\partial\psi^*}{\partial t}\psi \right) \mathrm{d}\boldsymbol{x} - H. \tag{1.59}$$

Integration over time then gives the Gross–Pitaevskii action:

$$\begin{aligned} S[\Psi(\chi), \partial\Psi(\chi)] &= \int L[\Psi(\chi), \partial\Psi(\chi)]\,\mathrm{d}t = \\ &= \int_{\mathscr{D}} \left\{ \frac{i\hbar}{2}\left(\frac{\partial\psi}{\partial t}\psi^* - \frac{\partial\psi^*}{\partial t}\psi \right) - \left(\frac{\hbar^2}{2m}|\nabla\psi|^2 + \frac{g}{2}|\psi|^4 + V_{\mathrm{ext}} \right) \right\} \mathrm{d}\chi, \end{aligned} \tag{1.60}$$

where we have explicitated the spacetime domain of the system $\mathscr{D}$. Thus, the GP equation can be rewritten simply as an Euler–Lagrange equation[5]:

$$\frac{\delta S}{\delta\psi^*} = \frac{\partial\mathscr{L}}{\partial\psi^*} - \partial_\mu \frac{\partial\mathscr{L}}{\partial\partial_\mu\psi^*} = 0 \quad \longrightarrow \quad i\hbar\frac{\partial\psi}{\partial t} = \frac{\delta H}{\delta\psi^*}. \tag{1.61}$$

The functional differentiation of S with respect to ψ instead of ψ^* just leads to the complex-conjugate of Eq. (1.57).

Now, let $\mathscr{G}$ be a generical Lie group with $N_{\mathscr{G}}$ continuous parameters ϵ_k. For small values of the ϵ_k's it transforms coordinates and fields in the following way

$$\tilde{\chi}_\mu = \chi_\mu + \delta\chi_\mu \tag{1.62}$$

$$\tilde{\Psi}_a(\tilde{\chi}) = \Psi_a(\chi) + \bar{\delta}\Psi_a(\tilde{\chi}), \tag{1.63}$$

where $\bar{\delta}$ stands for total variation, not only with respect to fields but also with respect to coordinates

$$\bar{\delta}\Psi_a(\tilde{\chi}) = \delta\Psi_a(\chi) + \left(\partial_\mu\Psi_a\right)\delta\chi^\mu. \tag{1.64}$$

The variation of the coordinates $\delta\chi_\mu$ and the variation of the fields $\delta\Psi_a$ are then defined as

$$\delta\chi_\mu \equiv \sum_{k=1}^{N_{\mathscr{G}}} \epsilon_k \left(\delta_k\chi_\mu\right) \qquad\qquad \delta\Psi_a \equiv \sum_{k=1}^{N_{\mathscr{G}}} \epsilon_k \left(\delta_k\Psi_a\right). \tag{1.65}$$

All the $\delta_k\chi_\mu$ and $\delta_k\Psi_a$ are finite and represent the group generators. Also the domain $\mathscr{D}$ changes into $\tilde{\mathscr{D}}$, and at the first order in ϵ the Jacobian is $\frac{\partial\tilde{\chi}_\mu}{\partial\chi_\nu} = \delta^\nu_\mu + \partial_\mu\delta\chi^\nu$. If the transformations (1.62) and (1.63) leave the GP action unchanged, the group $\mathscr{G}$ is a

[5] from now on, summation is implied by repeated indices.

continuous symmetry of the system. The action S is conserved too, thus we must have[6]:

$$\bar{\delta}S = \int_{\mathscr{D}} \bar{\delta}\mathscr{L}\mathrm{d}\chi + \int_{\mathscr{D}} \mathscr{L}\delta\left(\mathrm{d}\chi\right) = \int_{\mathscr{D}} \left\{\bar{\delta}\mathscr{L} + \left(\partial_\mu \delta\chi^\mu\right)\mathscr{L}\right\}\mathrm{d}\chi = 0 \qquad \forall\,\mathscr{D}. \tag{1.66}$$

Since the total variation of the Lagrangian density can be calculated as

$$\begin{aligned}\bar{\delta}\mathscr{L} &= \frac{\partial\mathscr{L}}{\partial\Psi_a}\delta\Psi_a + \frac{\partial\mathscr{L}}{\partial\partial_\mu\Psi_a}\delta\left(\partial_\mu\Psi_a\right) + \left(\partial_\mu\mathscr{L}\right)\delta\chi^\mu = \\ &= \left(\frac{\partial\mathscr{L}}{\partial\Psi_a} - \partial_\mu\frac{\partial\mathscr{L}}{\partial\partial_\mu\Psi_a}\right)\delta\Psi_a + \partial_\mu\left(\frac{\partial\mathscr{L}}{\partial\partial_\mu\Psi_a}\delta\Psi_a\right) + \left(\partial_\mu\mathscr{L}\right)\delta\chi^\mu,\end{aligned} \tag{1.67}$$

Eq. (1.66) becomes

$$\bar{\delta}S = \int_{\mathscr{D}}\left\{\left(\frac{\partial\mathscr{L}}{\partial\Psi_a} - \partial_\mu\frac{\partial\mathscr{L}}{\partial\partial_\mu\Psi_a}\right)\delta\Psi_a + \partial_\mu\left(\frac{\partial\mathscr{L}}{\partial\partial_\mu\Psi_a}\delta\Psi_a + \mathscr{L}\delta\chi^\mu\right)\right\}\mathrm{d}\chi = 0. \tag{1.68}$$

This must hold for all the domains $\mathscr{D}$, thus the integrand itself vanishes. The first term is proportional to the Euler–Lagrange equation, therefore it is zero by definition if ψ solves the GP equation. Then, the condition that an invariance group must satisfy is:

$$\partial_\mu\left(\frac{\partial\mathscr{L}}{\partial\partial_\mu\Psi_a}\delta\Psi_a + \mathscr{L}\delta\chi^\mu\right) = 0. \tag{1.69}$$

As it is valid for each of the group parameters, Eq. (1.69) eventually leads to the conservation of $N_{\mathscr{G}}$ Noether currents:

$$\partial_\mu j_k^\mu = 0, \qquad j_k^\mu = \left(\frac{\partial\mathscr{L}}{\partial\partial_\mu\Psi_a}\delta_k\Psi_a + \mathscr{L}\delta_k\chi^\mu\right), \tag{1.70}$$

while the associated Noether charges are the following quantities Q_k, which turn out to be constant in time:

$$\frac{dQ_k}{dt} = 0, \qquad Q_k(t) = \int j_k^0(\boldsymbol{x},t)\,\mathrm{d}\boldsymbol{x} = \int\left(\frac{\partial\mathscr{L}}{\partial\partial_t\Psi_a}\delta_k\Psi_a + \mathscr{L}\delta_k t\right)\mathrm{d}\boldsymbol{x}. \tag{1.71}$$

This general result allows us to find out conserved quantities associated to the symmetries of the GP equation.

1.3.2.1 Global gauge invariance and wave action conservation

Since the only non-linear term of the Gross–Pitaevskii model is $\propto |\psi|^2 = \psi\psi^*$ an evident internal symmetry of the system is the unitary group $U(1)$. Indeed, if we tranform the

[6] We have used that $\delta\left(d\chi\right) = d\tilde{\chi} - \mathrm{d}\chi$, and the differential tranforms as $\mathrm{d}\tilde{\chi} = \det\left[\frac{\partial\tilde{\chi}_\mu}{\partial\chi_\nu}\right]\mathrm{d}\chi = \exp\left[\mathrm{Tr}(\ln(\partial_\nu\chi^\mu))\right]\mathrm{d}\chi \simeq (1+\partial_\mu\delta\chi^\mu)\mathrm{d}\chi$ [18].

wavefunction as

$$\tilde{\psi}(\tilde{\boldsymbol{x}}, \tilde{t}) = e^{-\frac{i}{\hbar}\varphi}\psi(\boldsymbol{x}, t), \tag{1.72}$$

namely a global phase shift independent of spacetime coordinates, then the GP equation is invariant. Since the infinitesimal transformation is

$$\tilde{\psi}(\boldsymbol{x}, t) = \psi(\boldsymbol{x}, t) - \varphi\frac{i}{\hbar}\psi(\boldsymbol{x}, t) \tag{1.73}$$

with space and time unchanged ($\delta x = \delta t = 0$), the charge associated to this symmetry is

$$Q = \frac{i\hbar}{2}\int\left(-\frac{i}{\hbar}\psi^*\psi - \frac{i}{\hbar}\psi\psi^*\right)\mathrm{d}\boldsymbol{x}, \tag{1.74}$$

which is nothing but the conserved normalization of the wavefunction:

$$N_0 = \int|\psi|^2\,\mathrm{d}\boldsymbol{x} = \int n\,\mathrm{d}\boldsymbol{x} = \text{cost.} \tag{1.75}$$

It represents the total number of condensed bosons, and it is usually referred to as wave action. From now on, we will omit the subscript "0" and we will indicate it just with N. As it will be clear in section 1.3.4, the wave action is related to the total mass of the condensate $M = mN$ in the hydrodynamic interpretation of the GP model. The spatial component of the Noether current associated to the $U(1)$ symmetry is the gauge current

$$\boldsymbol{j} = -\frac{i\hbar}{2m}\left(\psi^*\nabla\psi - \psi\nabla\psi^*\right), \tag{1.76}$$

which leads to the continuity equation

$$\frac{\partial n}{\partial t} + \nabla\cdot\boldsymbol{j} = 0. \tag{1.77}$$

1.3.2.2 Time translation invariance and Hamiltonian conservation

If the external potential V_{ext} is constant in time, there is no explicit time dependence in the action (1.60) and an infinitesimal time shift

$$\tilde{t} = t + \delta t \tag{1.78}$$

with $\tilde{\boldsymbol{x}} = \boldsymbol{x}$ and $\tilde{\psi}(\tilde{\boldsymbol{x}}, \tilde{t}) = \psi(\boldsymbol{x}, t)$ is an external symmetry of the system. In this case the total variation of the field vanishes, and therefore:

$$\bar{\delta}\Psi_a(\boldsymbol{x}, \tilde{t}) = \delta\Psi_a(\boldsymbol{x}, t) + \partial_t\Psi_a(\boldsymbol{x}, t)\delta t = 0 \quad \longrightarrow \quad \delta\Psi_a = -\frac{\partial\Psi_a}{\partial t}\delta t. \tag{1.79}$$

The direct application of Eq. (1.71) leads to the conservation of the Hamiltonian:

$$\begin{aligned} H &= \int \left\{ \frac{i\hbar}{2}\left(\frac{\partial \psi}{\partial t}\psi^* - \frac{\partial \psi^*}{\partial t}\psi \right) - \mathscr{L} \right\} \mathrm{d}\boldsymbol{x} = \int \mathscr{H}(\boldsymbol{x},t)\,\mathrm{d}\boldsymbol{x} = \\ &= \int \left(\frac{\hbar^2}{2m}|\nabla\psi|^2 + \frac{g}{2}|\psi|^4 + V_{\mathrm{ext}}(\boldsymbol{x})|\psi|^2 \right) \mathrm{d}\boldsymbol{x} = \mathrm{cost}, \end{aligned} \tag{1.80}$$

and the spatial Noether current associated to it, sometimes simply called energy flux density, is

$$\boldsymbol{q}_H = -\frac{\hbar^2}{2m}\left(\frac{\partial \psi}{\partial t}\nabla\psi^* + \frac{\partial \psi^*}{\partial t}\nabla\psi \right), \tag{1.81}$$

so that the continuity equation for the Hamiltonian density is[7]

$$\frac{\partial \mathscr{H}}{\partial t} + \nabla \cdot \boldsymbol{q}_H = 0. \tag{1.82}$$

1.3.2.3 Space translation invariance and momentum conservation

Another external symmetry of the system is the translation of the space coordinates

$$\tilde{\boldsymbol{x}} = \boldsymbol{x} + \delta\boldsymbol{x}, \tag{1.83}$$

with $\tilde{t} = t$ and $\tilde{\psi}(\tilde{\boldsymbol{x}},\tilde{t}) = \psi(\boldsymbol{x},t)$. Of course, this transformation leaves the action (1.60) unchanged only if the external potential V_{ext} is homogeneous in space. As in the case of time translation invariance, the total variation of the fields vanishes:

$$\bar{\delta}\Psi_a(\tilde{\boldsymbol{x}},t) = \delta\Psi_a(\boldsymbol{x},t) + \nabla\Psi_a(\boldsymbol{x},t)\cdot\delta\boldsymbol{x} = 0 \quad \longrightarrow \quad \delta\Psi_a = -\nabla\Psi_a\cdot\delta\boldsymbol{x} \tag{1.84}$$

The associated conserved charge is the total linear momentum of the GP equation:

$$\boldsymbol{P} = \frac{i\hbar}{2}\int (\psi\nabla\psi^* - \psi^*\nabla\psi)\,\mathrm{d}\boldsymbol{x}. \tag{1.85}$$

Now, if we define the center of mass of the system as

$$\boldsymbol{X}_M = \frac{1}{N}\int m|\psi|^2\boldsymbol{x}\,\mathrm{d}\boldsymbol{x} \tag{1.86}$$

and recall the continuity equation (1.77), we get

$$\begin{aligned} N\frac{\mathrm{d}\boldsymbol{X}_M}{\mathrm{d}t} &= -\int \frac{i\hbar}{2}\left[\nabla\cdot(\psi\nabla\psi^* - \psi^*\nabla\psi)\right]\boldsymbol{x}\,\mathrm{d}\boldsymbol{x} = \\ &= -\int (\nabla\cdot\boldsymbol{P})\boldsymbol{x}\,\mathrm{d}\boldsymbol{x} = \boldsymbol{P} \end{aligned} \tag{1.87}$$

[7] In Eqs. (1.80) and (1.81) we are implicitly applying a global minus sign in order to get a positive defined Hamiltonian.

where last equality follows from integration by part, under the assumption that all the fields and their derivatives are periodic or vanish at the boundary of the spatial domain. Thus, Eq. (1.87) tells us that the center of mass of the condensate moves with constant velocity. It is also interesting that the gauge current associated to the mass conservation (1.76) is directly linked to the total momentum (1.85):

$$\boldsymbol{P} = m \int \boldsymbol{j} \, \mathrm{d}\boldsymbol{x}, \tag{1.88}$$

even though these quantities are associated to different symmetries. From Eq. (1.88) we also see explicitly that the momentum density is simply proportional to the gauge current

$$\boldsymbol{p}(\boldsymbol{x}) = m\boldsymbol{j}(\boldsymbol{x}). \tag{1.89}$$

Finally, the spatial components of the Noether currents of the space translation invariance (1.83) constitute the stress tensor Π_{jk} which represents the flux density of the j-th component of momentum in direction k:

$$\begin{aligned} \Pi_{jk} &= \frac{\hbar^2}{2m}\left(\frac{\partial\psi}{\partial x_j}\frac{\partial\psi^*}{\partial x_k} + \frac{\partial\psi^*}{\partial x_j}\frac{\partial\psi}{\partial x_k}\right) + \mathscr{L}\delta_{jk} = \\ &= \frac{\hbar^2}{2m}\left(\frac{\partial\psi}{\partial x_j}\frac{\partial\psi^*}{\partial x_k} + \frac{\partial\psi^*}{\partial x_j}\frac{\partial\psi}{\partial x_k}\right) + \left(\frac{3}{2}g|\psi|^4 - \frac{\hbar^2}{2m}\left(|\nabla\psi|^2 + \nabla^2|\psi|^2\right) + V_{\mathrm{ext}}(t)|\psi|^2\right)\delta_{jk}, \end{aligned} \tag{1.90}$$

where δ_{jk} is the $D-$dimensional Kronecker delta. The momentum conservation equation eventually reads:

$$\partial_t P_k + \partial_j \Pi_{jk} = 0. \tag{1.91}$$

If the external potential depends on some spatial coordinate x_k, only the components $P_{i\neq k}$ of the linear momentum are conserved. Note that the only possibility for having both the Hamiltonian and the linear momentum conserved is homogeneous and constant external potential.

1.3.2.4 Galileian invariance and center of mass conservation

The last important symmetry of the GP model that we analyze here is the invariance with respect to a Galileian transformation, defined as

$$\begin{aligned} \tilde{\boldsymbol{x}} &= \boldsymbol{x} - \boldsymbol{v}t \\ \tilde{t} &= t \\ \tilde{\psi}(\tilde{\boldsymbol{x}}, \tilde{t}) &= \psi(\tilde{\boldsymbol{x}}, \tilde{t}) e^{-i\frac{m}{\hbar}\left(\boldsymbol{v}\cdot\tilde{\boldsymbol{x}} + \frac{1}{2}v^2\tilde{t}\right)} \end{aligned} \tag{1.92}$$

where $\boldsymbol{v}$ is a constant velocity which plays the role of group parameter. We set $V_{\mathrm{ext}} = 0$ for the sake of simplicity. For small values of $\boldsymbol{v}$ the field transforms at the leading order as $\tilde{\psi}(\tilde{\boldsymbol{x}}, \tilde{t}) = \psi(\boldsymbol{x}, t) - i\frac{m}{\hbar}\boldsymbol{v}\cdot\boldsymbol{x}$. Therefore, applying the formula (1.71), we see the the conserved Noether charge associated to the Galileian invariance is the center of mass (1.86) and the conservation of the Noether current (1.70) implies the relation between

center of mass and linear momentum Eq. (1.87).

1.3.3 Condensate ground state and Bogoliubov excitations

The ground state of the GP system is the stationary field configuration ψ_0 that minimizes the free energy $F[\psi, \psi^*] = H[\psi, \psi^*] - \mu N[\psi, \psi^*]$, i.e.:

$$\frac{\delta F}{\delta \psi^*} = \frac{\delta F}{\delta \psi} = 0. \tag{1.93}$$

For the sake of simplicity, we first consider the external potential V_{ext} switched off. The free energy is defined as a linear combination of two of the invariants found in the previous section, the Hamiltonian H (1.80) and the wave action N (1.75). In this way the chemical potential μ assumes the role of a Lagrange multiplier, taking into account the fact that the number of bosons in the condensate state is generally not fixed. In particular, it quantifies the energy needed to add a particle to the condensate. In general, the minimization condition (1.93) implies the stationary Gross–Pitaevskii equation:

$$\mu\psi = -\frac{\hbar^2}{2m}\nabla^2\psi + g|\psi|^2\psi, \tag{1.94}$$

but clearly the global minimum is reached when the kinetic term is zero, namely when the solution is homogeneous. The ground state ψ_0 is therefore a minimum of the Higgs-like potential

$$\int \left\{\frac{g}{2}|\psi|^4 - \mu|\psi|^2\right\} \mathrm{d}\boldsymbol{x}. \tag{1.95}$$

It means that there is a continuum of degenerate ground states, all with the same modulus $|\psi_0|$, but with different phases. This is a natural consequence of the $U(1)$ gauge invariance of the system. When the system falls into a ground state configuration the phase is fixed and takes a constant value. In this sense, it is ususally said that the choice of the minimum state spontaneously breaks the symmetry. Indeed, each specific ground state is not invariant under the $U(1)$ gauge transformation, as a phase shift will trasform it into a different ground state. Thus, except such fixed but arbitrary phase, the ground state is a flat condensate described by the homogeneous wavefunction

$$\psi_0(t) = |\psi_0|e^{-i\frac{\mu}{\hbar}t} \tag{1.96}$$

and the chemical potential which determines its temporal evolution depends on the (homogeneous) density and on the self interaction:

$$\mu = g|\psi_0|^2 = gn_0. \tag{1.97}$$

Note that in presence of an external constant potential $V_{\text{ext}}(\boldsymbol{x})$, the actual ground state has a non-zero kinetic term and in general cannot be found analitically. However, if $V_{\text{ext}}(\boldsymbol{x})$ varies slowly in space, one can still neglect the kinetic term and obtain the

solution in the Thomas–Fermi approximation

$$|\psi_{\mathrm{TF}}(\boldsymbol{x},t)|^2 = \frac{1}{g}\left(\mu - V_{\mathrm{ext}}(\boldsymbol{x})\right)\theta_{\mathrm{H}}\left[1 - \frac{V_{\mathrm{ext}}(\boldsymbol{x})}{\mu}\right], \tag{1.98}$$

where θ_{H} is the Heaviside Theta function. The actual ground state in this case (and in general) can be found numerically by using the gradient descent method. In practice, the GP equation with imaginary time evolution, also known as real Ginzburg Landau equation, is evolved until the stationary state is reached. The same method can be used to find other solutions of the steady GP equation (1.94) which correspond to local minima of the free energy. An example of these solutions is the stationary vortex state, described in section 1.3.5.

Coming back to the homogeneous case with $V_{\mathrm{ext}} = 0$, we see that the energy associated to the flat condensate ground state is

$$E_0 = \frac{g}{2}\int |\psi_0|^4 \,\mathrm{d}\boldsymbol{x} = \frac{gNn_0}{2} \tag{1.99}$$

Therefore, unlike in a non-interacting condensate, the pressure does not vanish

$$p = -\frac{\partial E_0}{\partial V} = \frac{gn_0^2}{2}, \tag{1.100}$$

so that the compressibility is finite, too:

$$\frac{\partial n_0}{\partial p} = \frac{1}{gn_0}. \tag{1.101}$$

Since stable thermodynamic systems must have a positive compressibility, from last equation we learn that only positive couplings g are allowed. Namely, as announced in section 1.3.1, only bosons with repulsive interactions can form a condensate[8] . From compressibility we can also compute the speed of sound c inside the system, using the hydrodynamic relation

$$\frac{\partial n_0}{\partial p} = \frac{1}{mc^2} \quad \rightarrow \quad c = \sqrt{\frac{gn_0}{m}}. \tag{1.102}$$

Another important physical quantity which characterize the condensate is the healing length ξ, that estimates the correlation of the system. We can determine it as the distance at which the density passes from zero to the homogeneous value n_0. Since the flat condensate has no kinetic energy, its total energy is entirely contained in the interaction term. Thus, in the region where the density is depleted, the same happens to the interaction term, and it must be compensed by the kinetic term:

$$-\frac{\hbar^2}{2m}\nabla^2 \sim \frac{\hbar^2}{2m\xi^2} = g|\psi|^2. \tag{1.103}$$

[8] Actually, if the scattering length is negative, the presence of an external trapping allows Bose-Einstein condensation in a metastable configuration [176].

The healing length is determined inverting this relation:

$$\xi = \frac{\hbar}{\sqrt{2mn_0 g}} = \frac{1}{\sqrt{8\pi\rho_0 a_s}}. \tag{1.104}$$

Speed of sound c and healing length ξ are the main parameters that characterize the GP system, together with the condensate density n_0. They also control the propagation of the elementary linear excitations of the condensate, known as Bogoliubov modes [31, 135, 176]. The dispersion relation of the Bogoliubov modes can be found directly in the classical mean field theory. Indeed, we can consider a solution consisting of a small perturbation of the flat condensate (always keeping $V_{\text{ext}} = 0$ for simplicity) (1.96):

$$\psi(\boldsymbol{x}, t) = (|\psi_0| + \delta\psi(\boldsymbol{x}, t))\, e^{-i\frac{\mu}{\hbar}t}, \quad \text{with} \quad |\delta\psi| \ll |\psi_0|, \tag{1.105}$$

plug it into the GP equation (1.57), and obtain the linearized equation

$$\mu\delta\psi + i\hbar\frac{\partial\delta\psi}{\partial t} = -\frac{\hbar^2}{2m}\nabla^2\delta\psi + g|\psi_0|^2\delta\psi^2 + 2g|\psi_0|^2\delta_\psi, \tag{1.106}$$

where we kept only the terms linear in $\delta\psi$. In particular, we consider as perturbation $\delta\psi$ a planar wave of wavenumber $\boldsymbol{k}$ and frequency ω:

$$\delta\psi(\boldsymbol{x}, t) = \sum_{\boldsymbol{k}} u_{\boldsymbol{k}} e^{i(\boldsymbol{k}\cdot\boldsymbol{x}-\omega t)} + v^*_{\boldsymbol{k}} e^{-i(\boldsymbol{k}\cdot\boldsymbol{x}+\omega t)}. \tag{1.107}$$

Comparing the terms which multiply the same exponential in (1.106), we obtain the condition on the chemical potential (1.97) and the linear system

$$\begin{pmatrix} \frac{\hbar k^2}{2m} + \mu & \mu \\ -\mu & -\frac{\hbar k^2}{2m} - \mu \end{pmatrix} \begin{pmatrix} u_{\boldsymbol{k}} \\ v^*_{\boldsymbol{k}} \end{pmatrix} = \omega \begin{pmatrix} u_{\boldsymbol{k}} \\ v^*_{\boldsymbol{k}} \end{pmatrix}. \tag{1.108}$$

The linear operator in the left hand side of Eq. (1.108) can be diagonalized to find the eigenfrequencies of the system. The result is the Bogoliubov spectrum

$$\omega^{\pm}_{\text{B}}(\boldsymbol{k}) = \pm\sqrt{\frac{\hbar k^2}{2m}\left(\frac{\hbar k^2}{2m} + 2\mu\right)}, \tag{1.109}$$

that can be rewritten in terms of speed of sound c and healing length ξ as

$$\omega^{\pm}_{\text{B}}(\boldsymbol{k}) = \pm ck\sqrt{1 + \frac{\xi^2 k^2}{2}}. \tag{1.110}$$

It is clear from Eq. (1.110) that at large scales the Bogoliubov excitations are not dispersive and propagate with speed c. This is the reason why we generally refer to Bogoliubov excitations as sound waves. The healing length ξ is the scale at which dispersive ef-

fects become important and at smaller scales $k\xi \gg 1$ the excitations propagate as free particles with a quadratic dispersion relation. We can finally note that for each solution $(u_{\boldsymbol{k}}, v^*_{\boldsymbol{k}})$ that propagates with frequency $\omega_{\mathrm{B}}(\boldsymbol{k})$ there exists another solution $(v_{\boldsymbol{k}}, u^*_{\boldsymbol{k}})$ that propagate with frequency $-\omega_{\mathrm{B}}(\boldsymbol{k})$. In the diagonalized Bogoliubov basis this does not happen and indeed the two solutions represent the same physical oscillation, being associated one to $\delta\psi$ and the other to $\delta\psi^*$ [176]. Finally note that for the excitation spectrum (1.110), the critical velocity for the breaking of superfluidity (1.6) should be the speed of sound, according to the Landau criterion. However, a drag force acting on a finite size object moving in the GP system appears already at smaller velocities and it is related to the emission of quantum vortices [67, 101, 245], not included in the Landau picture.

1.3.4 Hydrodynamic picture

In this section we show the hydrodynamic interpretation of the GP model, clarifying why it is a suitable theory for the description of a superfluid. Actually, the connection with hydrodynamics is rather straightforward. It lies in the Madelung transformation applied to the the macroscopic wavefunction:

$$\psi(\boldsymbol{x},t) = \sqrt{\frac{\rho(\boldsymbol{x},t)}{m}}e^{i\frac{m}{\hbar}\phi(\boldsymbol{x},t)} = \sqrt{\frac{\rho(\boldsymbol{x},t)}{m}}e^{i\frac{\sqrt{2}}{2c\xi}\phi(\boldsymbol{x},t)}, \tag{1.111}$$

where the complex degree of freedom ψ is splitted into 2 real degrees of freedom, the mass density $\rho = mn$ and the phase ϕ. The field ρ will play the role of superfluid density, while the superfluid velocity field $\boldsymbol{v}_{\mathrm{s}}$ can be derived writing the momentum density (1.89) as

$$\boldsymbol{p} = m\boldsymbol{j} = -\frac{i\hbar}{2}\left(\psi^*\nabla\psi - \psi\nabla\psi^*\right) = \hbar\,\mathrm{Im}\left[\psi^*\nabla\psi\right] = \rho\boldsymbol{v}_{\mathrm{s}}, \tag{1.112}$$

from which we see that $\boldsymbol{v}_{\mathrm{s}}$ is related to the gradient of the phase

$$\boldsymbol{v}_{\mathrm{s}} = \nabla\phi. \tag{1.113}$$

The first important property that we can infer is that the flow described by Gross–Pitaevskii theory is potential and therefore intrinsically irrotational:

$$\nabla\times\boldsymbol{v}_{\mathrm{s}} = \nabla\times\nabla\phi = 0. \tag{1.114}$$

The next step consists in applying the definitions (1.111) and (1.113) to the GP equation (1.57). Separating real and imaginary part we get the following set of hydrodynamic

equations (neglecting the external potential V_{ext}):

$$\frac{\partial \rho}{\partial t} + \nabla \cdot (\rho \boldsymbol{v}_{\text{s}}) = 0, \tag{1.115}$$

$$\frac{\partial \phi}{\partial t} + \frac{1}{2}(\nabla \phi)^2 = -c^2 \frac{\rho}{\rho_0} + c^2 \xi^2 \left(\frac{\nabla^2 \sqrt{\rho}}{\sqrt{\rho}} \right), \tag{1.116}$$

where $\rho_0 = m n_0$ and we used the definitions of the speed of sound c (1.102) and the healing length ξ (1.104). The first equation is just the continuity equation (1.77) associated with the conservation of the Noether charge of the global gauge symmetry. In the hydrodynamic picture it expresses the conservation of the fluid mass. The second equation is a Bernoulli equation which in turn is related to the conservation of energy. Since dissipation terms are absent, the fluid described by the GP model is effectively inviscid. We can recognize two contributions to the pressure field in the right hand side of Eq. (1.116) $p = p_{\text{cl}} + p_{\text{q}}$:

$$\frac{p_{\text{cl}}}{\rho} = \frac{g\rho}{m} = c^2 \frac{\rho}{\rho_0}, \qquad \frac{p_{\text{q}}}{\rho} = -\frac{\hbar^2}{2m^2} \left(\frac{\nabla^2 \sqrt{\rho}}{\sqrt{\rho}} \right) = -c^2 \xi^2 \left(\frac{\nabla^2 \sqrt{\rho}}{\sqrt{\rho}} \right). \tag{1.117}$$

The term p_{cl} is the classical pressure of a barotropic fluid, while p_{q} is the so called quantum pressure. This contribution arises when inhomogeneities are present in the system and embodies the difference between an inviscid irrotational ideal fluid and an actual superfluid. As we will explain in the next section, it is responsible for the regularization of the flow close to the core of quantum vortices and drives their small scale dynamics, allowing phenomena like vortex reconnections [162, 229]. Indeed, as we will show in the next section, the GP model contains naturally the full non-linear dynamics of superfluid vortices. This is maybe the most important reason why it can be considered as an optimal model for a low temperature superfluid.

It is useful to express also the energy in the context of the hydrodynamic picture [164]. In this framework, it is more suitable to redefine the Hamiltonian (1.58) as $H \to H - \mu N + \frac{\mu^2}{2g} V$, namely:

$$H = \int \left(\frac{\hbar^2}{2m} |\nabla \psi|^2 + \frac{g}{2} \left(|\psi|^2 - \frac{\mu}{g} \right)^2 + V_{\text{ext}} |\psi|^2 \right) \mathrm{d}\boldsymbol{x}. \tag{1.118}$$

In this way we remove the contribution of the flat condensate ground state, where the largest amount of energy is contained. From the dynamical point of view, the equation of motion associated to the Hamiltonian (1.118) is the following equation:

$$i\hbar \frac{\partial}{\partial t} \psi(\boldsymbol{x}, t) = \left[-\frac{\hbar^2}{2m} \nabla^2 + V_{\text{ext}}(\boldsymbol{x}, t) + g|\psi(\boldsymbol{x}, t)|^2 - \mu \right] \psi(\boldsymbol{x}, t), \tag{1.119}$$

which has the same solution of Eq. (1.57) multiplied by $e^{i\frac{\mu}{\hbar}t}$, that compensates the

global phase oscillation of the condensate. The two solutions have the same physical content, in particular they provide the same density and velocity fields. Expressing the Hamiltonian density H/V in terms of the hydrodynamic variables ρ and v_s, we can split it into three contributions $H/V = e_{kin} + e_{int} + e_{qnt}$ [140, 164]:

$$e_{kin} = \frac{E_{kin}}{V} = \frac{1}{V}\int \frac{1}{2}\left(\sqrt{\rho}v_s\right)^2 \mathrm{d}\boldsymbol{x}, \tag{1.120}$$

$$e_{int} = \frac{E_{int}}{V} = \frac{1}{V}\int \frac{c^2}{2\rho_0}\left(\rho - \frac{\mu m}{g}\right)^2 \mathrm{d}\boldsymbol{x}, \tag{1.121}$$

$$e_{qnt} = \frac{E_{qnt}}{V} = \frac{1}{V}\int c^2\xi^2\left(\nabla\sqrt{\rho}\right)^2 \mathrm{d}\boldsymbol{x}. \tag{1.122}$$

The terms (1.120) and (1.121) are respectively the kinetic energy and the interaction energy, while Eq. (1.122) is a term which is absent in classical fluid, and it is directly related to quantum pressure. Since all the integrands inside (1.120,1.121,1.122) are quadratic, the energies can be expressed in Fourier space using the Parseval theorem[9]. If the system is isotropic we can integrate over angles and define the 1D energy spectra, which depends only on the modulus of the wavenumber $k = |\boldsymbol{k}|$:

$$e^{1D}_{kin}(k) = \frac{1}{(2\pi)^D}\int \frac{1}{2}\left|\int \sqrt{\rho}v_s e^{-i\boldsymbol{k}\cdot\boldsymbol{x}}\,\mathrm{d}\boldsymbol{x}\right|^2 k^{D-1}\mathrm{d}\Omega_k, \tag{1.123}$$

$$e^{1D}_{int}(k) = \frac{1}{(2\pi)^D}\int \frac{g}{2m^2}\left|\int\left(\rho - \frac{\mu m}{g}\right)e^{-i\boldsymbol{k}\cdot\boldsymbol{x}}\,\mathrm{d}\boldsymbol{x}\right|^2 k^{D-1}\,\mathrm{d}\Omega_k, \tag{1.124}$$

$$e^{1D}_{qnt}(k) = \frac{1}{(2\pi)^D}\int c^2\xi^2\left|\int \nabla\sqrt{\rho}e^{-i\boldsymbol{k}\cdot\boldsymbol{x}}\,\mathrm{d}\boldsymbol{x}\right|^2 k^{D-1}\,\mathrm{d}\Omega_k, \tag{1.125}$$

so that $E_{kin} = \int e_{kin}(k)\,\mathrm{d}k$, $E_{int} = \int e_{int}(k)\,\mathrm{d}k$, $E_{qnt} = \int e_{qnt}(k)\,\mathrm{d}k$, and where $\mathrm{d}\Omega_k$ is the surface measure of the sphere in the wavenumber space. The spectra describe the distribution of the energy components over different lenghtscales. Of course, if an external potential $V_{ext}(\boldsymbol{x}, t)$ is present, the sum of these three energies is not conserved. If V_{ext} does not depend on time, the Hamiltonian $H = E_{kin} + E_{int} + E_{qnt} + E_{ext}$, with the extra energy term

$$E_{ext} = \int \frac{1}{m}V_{ext}(\boldsymbol{x})\rho(\boldsymbol{x})\,\mathrm{d}\boldsymbol{x} \tag{1.126}$$

is conserved, otherwise it will vary with time. Finally, note that the kinetic energy can be further separated into compressible and incompressible part, by splitting the integrand as

$$\sqrt{\rho}v_s = \left(\sqrt{\rho}v_s\right)^{\mathrm{I}} + \left(\sqrt{\rho}v_s\right)^{\mathrm{C}}, \tag{1.127}$$

where $\nabla\cdot\left(\sqrt{\rho}v_s\right)^{\mathrm{I}} = 0$. In practice, the decomposition is made in Fourier space, applying the projector $P^{\mathrm{I}}_{ij} = \delta_{ij} - \frac{k_i k_j}{k^2}$ to the Fourier transform of $\sqrt{\rho}v_s$. The compressible part of

[9] Defining the Fourier transform of a function $f(\boldsymbol{x})$ as $\hat{f}(\boldsymbol{k}) = (2\pi)^{-D}\int f(\boldsymbol{x})e^{-i\boldsymbol{k}\cdot\boldsymbol{x}}\,\mathrm{d}\boldsymbol{x}$, the Parseval theorem is stated as $\int |f(\boldsymbol{x})|^2\,\mathrm{d}\boldsymbol{x} = (2\pi)^D\int |\hat{f}(\boldsymbol{k})|^2\,\mathrm{d}\boldsymbol{k}$.

the kinetic energy is associated to the Bogoliubov excitations (sound waves) described in the previous section, while the incompressible one is supported by vortices, as it will be clear in the following.

1.3.5 Quantum vortex solution

As already mentioned more than once, vortices in quantum fluids may exist, despite the irrotationality of the superfluid flow. Superfluid vortices (or quantum vortices) are topological defects with quantized circulation. In 3D they appear like unidimesional filaments where the density is depleted and the phase is not defined, while in $2D$ they are just points. The quantization of circulation is a natural consequence of the quantum mechanical nature of the macroscopic wavefunction ψ and it was already postulated by Feynman in 1955 in the context of superfluid helium [63]. If we consider a bidimensional region $\mathscr{A}$ (a disc for instance), we could think to calculate the circulation of the superfluid around the contour of $\mathscr{A}$ applying the Stokes theorem:

$$\Gamma = \oint_{\partial\mathscr{A}} \boldsymbol{v}_\mathrm{s} \cdot \mathrm{d}\boldsymbol{\delta} = \int_{\mathscr{A}} (\nabla \times \boldsymbol{v}_\mathrm{s}) \cdot \mathrm{d}\boldsymbol{\Sigma} = 0, \tag{1.128}$$

where the last equality comes from irrotationality. It is evident that we can have non zero circulation only if the domain $\mathscr{A}$ is not simply connected, namely if there are regions in which the velocity field $\boldsymbol{v}_\mathrm{s}$ diverges and the condensate phase ϕ. In fact, if this is the case, the second equality of Eq. (1.128) does not hold. The aforementioned regions are lines along which the wavefunction vanishes ($\mathrm{Re}\psi = \mathrm{Im}\psi = 0$), and which indeed identify vortices. Along the vortex lines the velocity field is virtually infinite and the vorticity $\boldsymbol{\omega} = \nabla \times \boldsymbol{v}_\mathrm{s}$ is proportional to a Dirac delta, so that $\Gamma \neq 0$. If the contour of $\mathscr{A}$ encircles one or more singularities of the velocity field, Γ can be directly computed as

$$\Gamma = \oint_{\partial\mathscr{A}} \nabla\phi \cdot \mathrm{d}\boldsymbol{\ell} = \phi(\boldsymbol{x}_\mathrm{end}) - \phi(\boldsymbol{x}_\mathrm{start}), \tag{1.129}$$

where $\boldsymbol{x}_\mathrm{end}$ and $\boldsymbol{x}_\mathrm{start}$ are respectively the ending point and the starting point of the loop $\partial\mathscr{A}$. Clearly, since these two points coincide $\boldsymbol{x}_\mathrm{end} \equiv \boldsymbol{x}_\mathrm{start}$, the phase difference can be only a descrete multiple of the constant

$$\kappa = \frac{2\pi\hbar}{m} = 2\pi\sqrt{2}c\xi, \tag{1.130}$$

otherwise the wavefunction ψ would have non physical polidromy points in which it can take multiple values. The parameter κ (1.130) is called quantum of circulation, and the circulation of superfluid vortices can be simply written as

$$\Gamma = n\kappa, \quad \text{with} \quad n \in \mathbb{N}, \tag{1.131}$$

where n is called the charge of the vortex. The velocity v_v of the superfluid flow rotating around the vortex is therefore diverging as

$$v_\mathrm{v} = \frac{\Gamma}{2\pi r} = \frac{\hbar}{m}\frac{n}{r}, \tag{1.132}$$

where r is the distance to the singular line (or point, in 2D) that defines the vortex core.

Although such singular behaviour of the velocity field, the superfluid field remains by definition regular on the nodal lines, because the density $\rho = m|\psi|^2$ vanishes along the vortex filaments. The beauty of the GP model is that such regularization is achieved automatically, making it a robust theory for superfluid dynamics. To see this, we note that the GP model admits a steady solution that correspond to a straight quantum vortex [74, 177]. This solution has cylindrical symmetry, therefore it can be written in cylindrical coordinates (r, φ, z) as

$$\psi_\mathrm{v}(r, \varphi, t) = \sqrt{\frac{\rho_\mathrm{v}(r)}{m}} e^{-i\frac{\mu}{\hbar}t} e^{in\varphi}, \quad \text{with} \quad n \in \mathbb{N}, \tag{1.133}$$

where z is the axis of symmetry (taken along the axis of the filament), φ is the azimuthal angle around the filament and r is the radial distance. The (incompressible) velocity field generated by this solution is indeed the one associated to the singularity (1.132):

$$\mathrm{v}_\mathrm{v}(r) = \frac{\Gamma}{2\pi r}\hat{\boldsymbol{\varphi}}, \tag{1.134}$$

where $\hat{\boldsymbol{\varphi}}$ is the unit vector oriented along the azimuthal direction. The phase and the velocity streamlines of the quantum vortex with winding number $n = 1$ (corresponding to one quantum of circulation) are displayed in Fig.1.5 right.

We define the vortex profile as $R(r) = \sqrt{\rho_\mathrm{v}(r)/\rho_0}$, where ρ_0 is the homogeneous density of the superfluid far from the vortex. Plugging the solution (1.133) into the stationary GP equation (1.94), we get the following equation for R:

$$\tilde{r}^2 \frac{\mathrm{d}^2 R}{\mathrm{d}\tilde{r}^2} + \tilde{r}\frac{\mathrm{d}R}{\mathrm{d}\tilde{r}} + \left(\tilde{r}^2 - n^2\right) R - \tilde{r}^2 R^3 = 0, \tag{1.135}$$

where the radial coordinate has been rescaled with the healing length $\tilde{r} = r/\xi$. From this equation we can derive the two asymptotics for the vortex profile, close and far from the core:

$$\lim_{\tilde{r}\to 0} R(\tilde{r}) \sim c_1 \tilde{r}^n, \qquad \lim_{\tilde{r}\to\infty} R(\tilde{r}) \sim 1 - \frac{n^2}{\tilde{r}^2}, \tag{1.136}$$

where the prefactor $c_1 = 0.5827811878$ can be determined numerically [22]. We can see that the density is actually depleted in the vortex core, where the velocity is diverging. Note that the kinetic energy of the GP model (1.120) is then always finite, because the velocity appears in the product $\sqrt{\rho}v_\mathrm{s}$, sometimes also called regularized velocity. For the same reason, the incompressible projector in the decomposition (1.127) must be applied to $\sqrt{\rho}v_\mathrm{s}$, and not to the bare velocity. We point out that the scale of the vortex

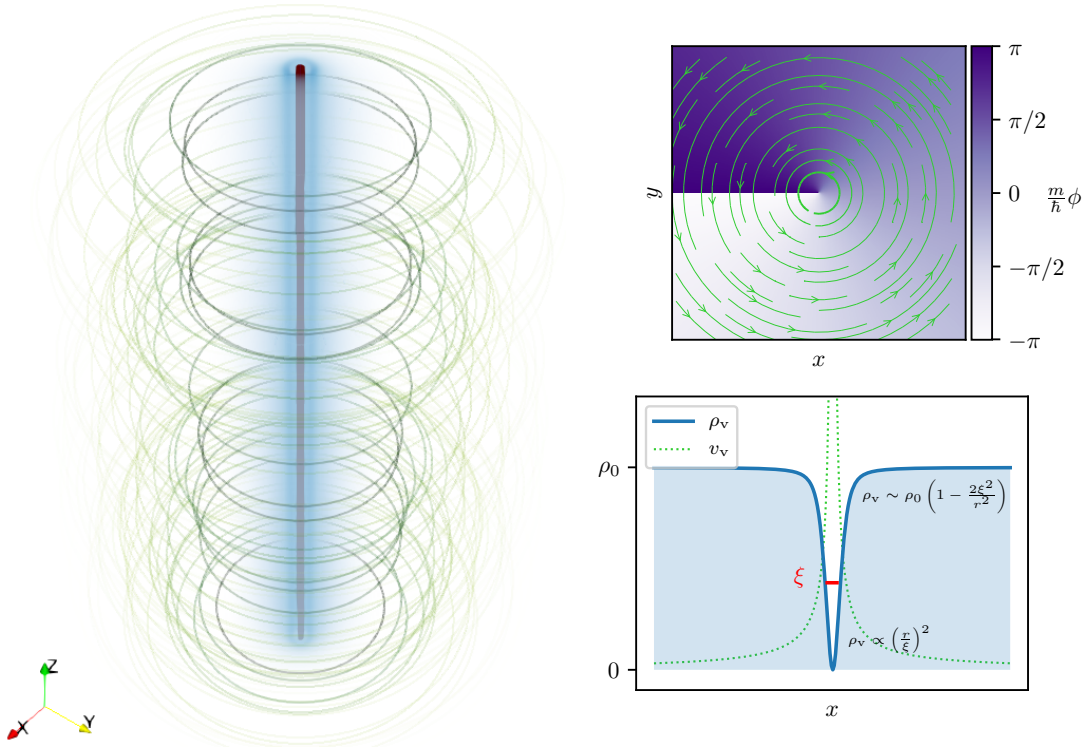


Figure 1.5. The Gross–Pitaevskii quantum vortex. (*left*) 3D visualization of the quantum vortex steady solution (1.133) of the GP model, obtained numerically. The vortex is represented as a red isosurface at low density ($\rho = 0.12\rho_0$). The volume rendering of the density is displayed in shaded blue and the streamlines of the velocity are in green. (*top right*) Phase of the straight vortex solution (1.133) in the plane orthogonal to the filament. In green the streamlines of the vortex velocity field (1.134), with linewidth proportional to its modulus. (*bottom right*) Vortex density profile (blue solid line) in the plane parallel to the filament and vortex velocity profile (1.132) (dotted green line).

core is defined by the healing length, since the vortex density goes to zero for distances shorter than ξ and approaches the bulk value ρ_0 at distances larger than ξ. This is not a surprise, given that the healing length is the fundamental length scale in the GP model. In atomic Bose–Einstein condensates the size of ξ can be manipulated, and typically is around $\sim 1\,\mu m = 10\,000$ Å. Instead, in superfluid helium the vortex core has a much smaller size ~ 1 Å.

The exact shape of the vortex profile $R(r)$ cannot be found analytically, even though pretty accurate approximations can be found in the literature. One of these is the Padé approximation derived by Pismen [175] and studied by Berloff [22], which for a vortex with charge $n = 1$ reads:

$$\frac{\rho_{\mathrm{Pade}_1}(\tilde{r})}{\rho_0} = R^2_{\mathrm{Pade}_1}(\tilde{r}) = \frac{\tilde{r}^2\left(a_1 + a_2\tilde{r}^2\right)}{1 + b_1\tilde{r}^2 + b_2\tilde{r}^4}, \tag{1.137}$$

where $a_1 = 11/32$, $b_1 = (5 - 32a_1)/(48 - 192a_1)$, $a_2 = a_1(b_1 - 1/4)$, and $b_2 = a_2$. The constants are fixed by imposing the match of Eq. (1.137) with the two known asymptotics of the vortex profile (1.136). Another more precise Padé approximation is the following:

$$\frac{\rho_{\mathrm{Pade}_2}(\tilde{r})}{\rho_0} = R^2_{\mathrm{Pade}_2}(\tilde{r}) = \frac{\tilde{r}^2\left(a_1 + a_2\tilde{r}^2 + a_3\tilde{r}^4\right)}{1 + b_1\tilde{r}^2 + b_2\tilde{r}^4 + a_3\tilde{r}^6}, \tag{1.138}$$

with the coefficients $a_1 = 0.340038$, $a_2 = 0.0360207$, $a_3 = 0.000985125$, $b_1 = 0.355931$, $b_2 = 0.037502$, which has been used for instance in our paper [75]. The actual vortex profile can be found numerically starting from an approximated initial condition like (1.137) and applying the gradient descent method to the GP model. Indeed, the straight vortex solution is a steady state which correspond to a local minimum of the Hamiltonian (1.118). An example of the vortex density profile obtained numerically in this way is displayed in Fig.1.5 right, together with the corresponding velocity profile, for a winding number $n = 1$. In Fig.1.5 left, the full 3D visualization of the GP vortex is also displayed. The filament is indicated as a red isosurface at low temperature, the velocity streamlines are in green and the density depletion is rendered in blue. In Fig.1.6 we compare the vortex density profile obtained numerically with the asyptotics and the Padé approximations. Note in particular the lost of monothony of the approximation (1.137) close to the bulk density.

We point out that since the energy associated to the vortex solution (1.133) is roughly proportional to n^2, vortices with a charge $n > 1$ are energetically disadvantaged. For this reason, a single vortex of charge $n > 1$ is not stable and would rather split into n singly charged vortex filaments.

As a final remark, we stress once again that the fundamental parameters of the GP model are the healing length ξ (which coincides with the vortex core size), the speed of sound c and the bulk density ρ_0. The GP equation expressed expliciting these parameters reads

$$\frac{\partial\psi}{\partial t} = -i\frac{c}{\sqrt{2}\xi}\left(-\xi^2\nabla^2\psi - \psi + \frac{1}{\rho_0}|\psi|^2\psi\right). \tag{1.139}$$

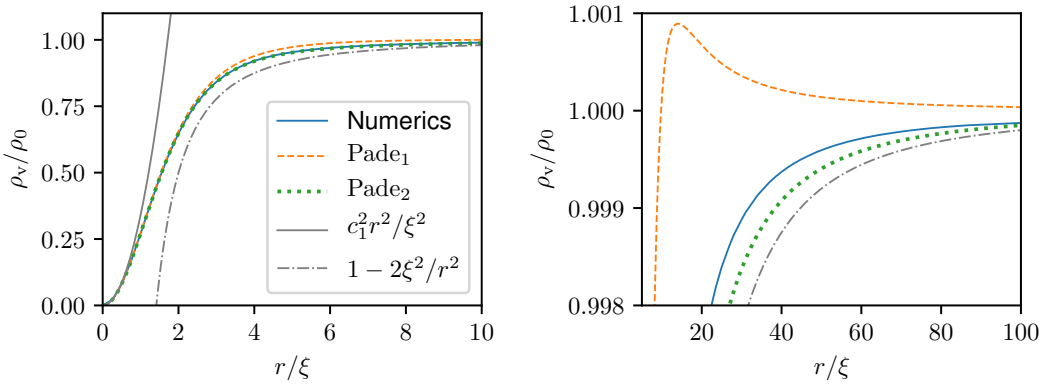


Figure 1.6. Comparison between approximations of the vortex density profile. Blue solid line is obtained numerically applying the gradient descent method to the GP model, dashed orange line is the Padé approximation (1.137) and dotted green line is the Padé approximation (1.138). The small distance and far field asymptotics (1.136) are displayed respectively as grey solid line and grey dash-dotted line. On the left a zoom close to the bulk density.

Moreover, the GP equation can be fully adimensionalized if written in terms of the adimensional spatial variable $\tilde{x} = x/\xi$ and the adimensional time $\tilde{t} = t/\tau$ (with $\tau = \xi/c$), besides normalizing the wave function as $\tilde{\psi} = \psi\sqrt{m/\rho_o}$. Thus, the results provided by the GP model can be directly compared with experiments (for instance with superfluid helium) if distances are expressed in units of ξ, times in units of τ, densities in units of ρ_0, and velocities in units of the speed of sound c. If not explicitly mentioned, in all the results reported in this Thesis we express variables in the aforementioned units.

1.4 Dynamics of superfluid vortices

In the previous section we showed the existence of quantized vortices in the GP model, which arise as a direct consequence of the monodromy of the macroscopic wavefunction. The full non-linear dynamics of superfluid vortices, as well as the interaction between different vortices, are self-consistently reproduced by the GP model. In this section we briefly review the dynamics of superfluid vortex filaments, using the phenomenological hydrodynamical approach known as vortex filament method [49, 55, 199, 204]. The main dynamical features of quantum vortices, i.e. vortex reconnections and propagation of Kelvin waves are then discussed, and the corrections due to finite temperature are mentioned. We already anticipate that the dynamics of quantum vortices plays a fundamental role in superfluid turbulence, that we will discuss in chapter 5.

1.4.1 The vortex filament model

A vortex filament can be thought as a thin core of radius a_0 passing through a fluid with zero vorticity outside it [204], but with non-zero circulation around it. Quantum

effects are relevant in the region of the core, but outside it the dynamics of the vortex can be described by classical hydrodynamics. In general, the velocity $\boldsymbol{v}(\boldsymbol{x})$ in a point $\boldsymbol{x}$ generated by a vorticity field $\boldsymbol{\omega}(\boldsymbol{y})$ can be computed by applying the Green function of the curl [199]:

$$\boldsymbol{v}(\boldsymbol{x}) = \frac{1}{4\pi}\int_{\mathbb{R}^3} \frac{\boldsymbol{\omega}(\boldsymbol{y})\times(\boldsymbol{x}-\boldsymbol{y})}{|\boldsymbol{x}-\boldsymbol{y}|^3}\,\mathrm{d}\boldsymbol{y}. \tag{1.140}$$

In the case of a vortex filament, the vorticity is concentrated in a tube with infinitesimal cross-section σ. Specifically, when $\sigma \to 0$, the vorticity goes to infinity in such a way that the circulation $\Gamma = \omega\sigma$ is kept constant. Therefore, we can formally write the vorticity as

$$\boldsymbol{\omega}(\boldsymbol{y}) = \Gamma\int_{\mathscr{C}} \delta(\boldsymbol{y}-\boldsymbol{s})\,\mathrm{d}\boldsymbol{s}, \tag{1.141}$$

where the integral extends over the filament $\mathscr{C}$. The velocity field (1.140) generated by such vorticity distribution is thus given by the Biot–Savart law:

$$\boldsymbol{v}_{\mathrm{BS}}(\boldsymbol{x}) = \frac{\Gamma}{4\pi}\int_{\mathscr{C}} \frac{(\boldsymbol{s}-\boldsymbol{x})\times\mathrm{d}\boldsymbol{s}}{|\boldsymbol{s}-\boldsymbol{x}|^3}. \tag{1.142}$$

Note that the integral in (1.142) is independent of the parametrization of the filament. The idea behind the vortex filament method is to apply this equation to describe the dynamics of the vortex filament itself, namely taking $\boldsymbol{x} = \boldsymbol{s}$. However, Eq. (1.142) is asymptotically valid in the region where $|\boldsymbol{x}-\boldsymbol{s}| \gg a_0$ and the vortex can be effectively considered as a one-dimensional curve. In fact, if we try to apply directly the Biot–Savart integral for $\boldsymbol{x} = \boldsymbol{s}$, we see immediately that it diverges. The way in which the divergence is regularized depends on the structure of the vortex core, which is precisely what we discussed in section 1.3.5 in the specific case of a GP quantum vortex. In order to describe the self-induced motion of the vortex filament with the equation

$$\dot{\boldsymbol{s}} = \boldsymbol{v}_{\mathrm{BS}}(\boldsymbol{s}), \tag{1.143}$$

it is necessary to introduce a cutoff length l, where the small scale physics of the core is hidden. In particular, the velocity of the filament is splitted into a local and a non-local contribution $\dot{\boldsymbol{s}} = \dot{\boldsymbol{s}}_{\mathrm{loc}} + \dot{\boldsymbol{s}}_{\mathrm{nonloc}}$. The non-local contribution is given by the Biot–Savart integral computed along the filament $\mathscr{C}'$ in which a portion δ of size $2l$ centered in the point $\boldsymbol{s}$ has been removed:

$$\dot{\boldsymbol{s}}_{\mathrm{nonloc}} = \frac{\Gamma}{4\pi}\int_{\mathscr{C}'} \frac{(\boldsymbol{s}_1-\boldsymbol{s})\times\mathrm{d}\boldsymbol{s}_1}{|\boldsymbol{s}_1-\boldsymbol{s}|^3}. \tag{1.144}$$

The local contribution is computed assuming that the portion δ of the filament close to the point $\boldsymbol{s}$ can be approximated with a segment of a ring having a radius equal to the curvature radius $R(\boldsymbol{s}) = |\boldsymbol{s}'|^3/|\boldsymbol{s}'\times\boldsymbol{s}''|$ of the filament at the point $\boldsymbol{s}$[10]. Such

[10] If not explicitly specified, primes denote differentiation with respect to a generic parametrization of the curve.

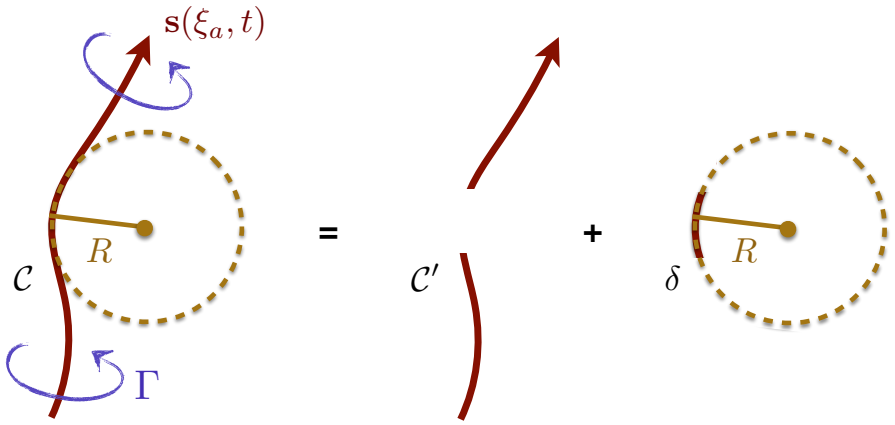


Figure 1.7. Sketch of the regularization procedure of the vortex filament method. See main text and [204] for further details.

approximation is valid if the cutoff is sufficiently small, i.e. $l \ll R(\boldsymbol{s})$. Its usefulness lies in the fact that an expression for the constant speed of an inviscid vortex ring can be evaluated independently using Euler equations [138]:

$$\dot{\boldsymbol{s}}_{\text{ring}} = \frac{\Gamma}{4\pi R}\boldsymbol{b}\left[\log\left(\frac{8R}{e^{\Delta}a_0}\right) + \mathcal{O}\left(\frac{a_0}{R}\right)\right], \tag{1.145}$$

where $\boldsymbol{b} = \boldsymbol{s}' \times \boldsymbol{s}''/|\boldsymbol{s}' \times \boldsymbol{s}''|$ is the binormal unit vector (orthogonal to the plane of the ring), a_0 is the vortex core size and Δ is a constant that depends on the structure of the core ($\Delta = 1/4$ if the vorticity in the core is uniform, or $\Delta = 1/2$ if it is confined to the surface of the ring [97]). In the case of vortex filaments in superfluid helium, the exact value of the core size parameter a_0 has been measured experimentally. Taking $\Delta = 1/2$ in Eq. (1.145) it turns out to be about 1.3 Å at $T = 0.3\,K$ and it slightly increases with temperature [81]. In the GP model, the speed of vortex rings is well reproduced in numerical simulations with $a_0 \sim 1.12\,\xi$ and $\Delta = 1/2$ [130]. Therefore, the local contribution to the filament velocity (1.143) is

$$\dot{\boldsymbol{s}}_{\text{loc}} = \frac{\Gamma}{4\pi R(\boldsymbol{s})}\boldsymbol{b}\log\left(\frac{2l}{e^{\Delta}a_0}\right), \tag{1.146}$$

where we removed from the total ring velocity (1.145) the non-local contribution coming from the portion of the ring outside the region δ close to the point $\boldsymbol{s}$. Thus, the regularized velocity of a vortex filament reads:

$$\dot{\boldsymbol{s}} = \frac{\Gamma}{4\pi R(\boldsymbol{s})}\boldsymbol{b}\log\left(\frac{2l}{e^{\Delta}a_0}\right) + \frac{\Gamma}{4\pi}\int_{\mathcal{C}'}\frac{(\boldsymbol{s}_1 - \boldsymbol{s}) \times \mathrm{d}\boldsymbol{s}_1}{|\boldsymbol{s}_1 - \boldsymbol{s}|^3}. \tag{1.147}$$

The regularization procedure of the vortex filament method is sketched in Fig.1.7.

We point out that the equation of motion of the vortex (1.143) can be deduced

identifying the Magnus effect as the only force acting on the line [14]. Indeed, when an object with circulation moves in a fluid, it is subjected to a transverse lift force which is the consequence of the pressure imbalance due to the different velocities on its sides. We will deepen the notion of Magnus effect in section 2.2.3 discussing the dynamics of particles in a fluid, but applying this concept to the vortex line we can write the following force per unit length:

$$\boldsymbol{f}_{\text{Magnus}} = \rho \Gamma \boldsymbol{s}' \times (\dot{\boldsymbol{s}} - \boldsymbol{v}_{\text{tot}}(\boldsymbol{s}))\,. \tag{1.148}$$

The term $\boldsymbol{v}_{\text{tot}}$ is given by the sum of the self-induced velocity of the vortex on itself and the bulk fluid velocity far from the vortex: $\boldsymbol{v}_{\text{tot}}(\boldsymbol{s}) = \boldsymbol{v}_{\text{BS}}(\boldsymbol{s}) + \boldsymbol{v}_0$. Then, we make use of the fact that the inertia of the filament is negligible, so that the second Newton law reads

$$\boldsymbol{f}_{\text{Magnus}} = 0, \tag{1.149}$$

and the resulting equation of motion of the filament is

$$\dot{\boldsymbol{s}} = \boldsymbol{v}_{\text{BS}}(\boldsymbol{s}) + \boldsymbol{v}_0, \tag{1.150}$$

which coincides with Eq. (1.143) if $\boldsymbol{v}_0 = 0$.

When a number N_{v} of vortices is present in the system, the velocity field generated by a filament will also induce a motion of the other lines, in addition to the self-induced velocity. This is not an issue, since the Biot–Savart integral (1.142) is not singular when evaluated on points $\boldsymbol{x}$ which not lie on the integration curve. Adding the contribution due to the other vortices to the regularized velocity (1.147), the equation of motion of the vortex filament $\boldsymbol{s}_i$ reads:

$$\dot{\boldsymbol{s}}_i = \frac{\Gamma}{4\pi}\left[\frac{\boldsymbol{b}_i}{R(\boldsymbol{s}_i)}\log\left(\frac{2l}{e^{\Delta}a_0}\right) + \int_{\mathscr{C}_i'}\frac{(\boldsymbol{s}_1 - \boldsymbol{s}_i)\times \mathrm{d}\boldsymbol{s}_1}{|\boldsymbol{s}_1 - \boldsymbol{s}_i|^3} + \sum_{j\neq i}^{N_{\text{v}}}\int_{\mathscr{C}_j}\frac{(\boldsymbol{s}_j - \boldsymbol{s}_i)\times \mathrm{d}\boldsymbol{s}_j}{|\boldsymbol{s}_j - \boldsymbol{s}_i|^3}\right]. \tag{1.151}$$

We point out that this equation is formally valid if the scale separation $a_0 \ll l \ll R(\boldsymbol{s})$ holds for every point $\boldsymbol{s}$ on the line. Furthermore it is derived considering an unbounded fluid and neglecting the friction due to the interaction with thermal excitations, which will be briefly introduced in section 1.4.3. We finally stress again that the hydrodynamics of the vortex filament described by Eq. (1.143) is reproduced by the GP model. Although this fact can be intuitive, given that the vortex filament is a solution of the GP equation and at large scales the GP fluid behaves as a perfect fluid, it has been formally demonstrated only recently [35].

1.4.2 Local induction approximation

One of the simplest and most used approximations that can be applied to the equation of motion of a vortex filament is the local induction approximation (LIA) [4, 49, 54, 199]. As the name suggests, this simplification consists in neglecting the non-local contribution to the self-induced vortex speed, assuming that the motion of the filament

is basically determined by the local curvature at each point $\boldsymbol{s}$. More precisely, let us consider the natural parametrization of the filament $\boldsymbol{s}(\xi_a)$, where the parameter ξ_a is the arclenght. One can take the Taylor expansion of the Biot–Savart integrand in Eq. (1.142), for points $\boldsymbol{x} = \boldsymbol{s}_1(\xi_a + \epsilon_a)$ on the vortex line close to the point $\boldsymbol{s}_1(\xi_a)$. The resulting integral

$$\dot{\boldsymbol{s}} \sim \frac{\Gamma}{4\pi} \int_{a_0}^{L} \frac{\partial \boldsymbol{s}}{\partial \xi_a} \times \frac{\partial^2 \boldsymbol{s}}{\partial \xi_a^2} \frac{1}{|\epsilon_a|} \, \mathrm{d}|\epsilon_a| \tag{1.152}$$

must be evaluated between the physical small scale cutoff a_0 and some length L, which denotes the scale above which the non-local contributions are negligible. The integration leads to the velocity

$$\dot{\boldsymbol{s}} \sim \frac{\Gamma}{4\pi} \Lambda \frac{\partial \boldsymbol{s}}{\partial \xi_a} \times \frac{\partial^2 \boldsymbol{s}}{\partial \xi_a^2}, \tag{1.153}$$

where $\Lambda = \log L/a_0$. The parameter L is a large lenght scale which depends on the specific vortex configuration and should be chosen in order to give a good approximation to the actual Biot–Savart dynamics [54]. Typically, a good choice is to take $L \sim R$, and in general the LIA approximation remains accurate as long as this parameter is large. In the case of small displacements of a straight filament oriented along the z-axis, the LIA self-induced velocity can be written parametrizing the vortex in complex variables as $s(z,t) = s_x(z,t) + i s_y(z,t)$ and neglecting the variation of the vortex length, $\zeta(z) \sim z$. It becomes

$$\dot{s}(z,t) \sim i \frac{\Gamma}{4\pi} \Lambda \frac{\partial^2}{\partial z^2} s(z,t), \tag{1.154}$$

which is just a linear Schrödinger equation. We used the local induction approximation in the form (1.154) to study analytically the interaction between particles and slightly perturbed straight vortices. These calculations have been devoloped in the publication [75] in the case of particles outside the vortex cores and in [79] for trapped particles, both reported in this Thesis, respectively in sections 3.2 and 4.1.

1.4.3 Mutual friction

If the temperature in a quantum fluid is different from zero, a normal fluid component with density ρ_n and velocity $\boldsymbol{v}_\mathrm{n}$ is present in the system, while the superfluid component has density ρ_s and velocity $\boldsymbol{v}_\mathrm{s}$. The interaction between the vortex lines and the thermal excitations of the normal fluid generates a mutual friction, encoded in a drag force per unit length acting on the filament [13, 14, 96, 204]:

$$\boldsymbol{f}_\mathrm{mf} = -\alpha(T)\rho_\mathrm{s}\Gamma \boldsymbol{s}' \times \left[\boldsymbol{s}' \times \left(\boldsymbol{v}_\mathrm{n} - \boldsymbol{v}_\mathrm{s,tot}\right)\right] - \alpha'(T)\rho_\mathrm{s}\Gamma \boldsymbol{s}' \times \left(\boldsymbol{v}_\mathrm{n} - \boldsymbol{v}_\mathrm{s,tot}\right), \tag{1.155}$$

where $\boldsymbol{v}_\mathrm{s,tot} = \boldsymbol{v}_\mathrm{BS}(\boldsymbol{s}) + \boldsymbol{v}_{\mathrm{s},0}$, exactly as in (1.148). The dimensionless parameters $\alpha(T)$ and $\alpha'(T)$ are related respectively to the fundamental longitudinal and transverse scattering lengths of the interaction with the thermal excitations. They contain all the temperature dependence and can be measured experimentally [96].

Taking into account such effect together with the Magnus effect (1.148), the balance of the forces acting on the filament is

$$f_{\text{Magnus}} + f_{\text{mf}} = 0, \tag{1.156}$$

given that the vortex inertia is negligible. The resulting equation of motion for a superfluid vortex at finite temperature is

$$\dot{s} = v_{\text{s},0} + v_{\text{BS}}(s) + v_{\text{mf}}, \tag{1.157}$$

where the velocity component induced by the mutual friction is

$$v_{\text{mf}} = \alpha(T)s' \times \left(v_{\text{n}} - v_{\text{s},0} - v_{\text{BS}}(s)\right) - \alpha'(T)s' \times \left[s' \times \left(v_{\text{n}} - v_{\text{s},0} - v_{\text{BS}}(s)\right)\right]. \tag{1.158}$$

Note that in writing (1.157) we are considering the normal fluid velocity v_{n} as the average drift velocity of the thermal excitation gas [204]. A more comprehensive analysis can be performed, which takes into account a local normal fluid velocity induced by the presence of the filament and which is far from the scope of the present manuscript. It can be found in [103], whose main result is indeed a new formula for the mutual fricition velocity:

$$v_{\text{mf}} = h_{**}\left(v_{\text{s},0} + v_{\text{BS}}\right) + h_{*}s' \times \left(v_{\text{n}} - v_{\text{s},0} - v_{\text{BS}}\right) + h_{**}s' \times \left(s' \times v_{\text{n}}\right), \tag{1.159}$$

coupled via a mutual friction forcing with a Navier–Stokes equation for the normal fluid velocity v_{n}, and where the friction coefficients $h_{**}(T)$ and $h_{*}(T)$ are a combination of $\alpha(T)$ and $\alpha'(T)$. In the remainder of this chapter, as well as in the novel results exposed later, we will ignore finite temperature effects on the vortex dynamics.

1.4.4 Vortex reconnections

One of the most interesting phenomena that occur in superfluids is the reconnection of vortex filaments. In general, in fluid mechanics a vortex reconnection is an event in which the topology of the vorticity field is rearranged [108]. Similarly, reconnections also occur in plasma physics as a rearrangement of the magnetic field [34]. In classical viscous fluids, where the vorticity is not confined in one-dimensional objects, the reconnection of vortex tubes is a complex phenomenon, [102], while the case of vortex filaments is a limiting and to some extent simpler situation. Two reconnecting vortex filaments approach each other, touch in a point and separate, after exchanging their strands. According to the Kelvin circulation theorem, reconnections in a barotropic inviscid fluid (as a superfluid is) should be prevented, since the circulation around a closed curve moving with the fluid is constant [133]. However, as it happens for the healing of the singularity of the vortex velocity field, superfluid vortex reconnections are possible because of the vanishing density at the core of the vortices [123]. Note that in classical Navier–Stokes fluids, the Kelvin circulation theorem is broken by the viscous dissipation, which is absent in superfluids.

Vortex reconnections have been already predicted in the seminal works by Feynman [63] and Schwarz [205], and nowadays it is known that they play a fundamental dissipative role in superfluid turbulence. Specifically, they provide a channel through which the kinetic energy is redistributed. In fact, after the reconnection, helicoidal waves propagating along the filaments are produced (see section 1.4.5) and the incompressible energy contained inside the vortex lines cascades towards the scale of the core, where it is radiated into sound [170]. Recently, vortex reconnections have been directly observed in atomic BECs, by using destructive absorption imaging [206] and in superfluid helium experiments by means of the PTV technique with solidified hydrogen particles as probes [29, 169] (see section 2.1.3). From the numerical side, it should be noted that even if the route to reconnection is reproduced by the vortex filament model, the reconnection event (intended as the exchange of strands) must be added by *ad hoc* mechanisms. This is not the case for the GP model, in which reconnections are self-consistently reproduced because the regularization due to the vanishing density is naturally included. For this reason, the GP equation is the optimal framework for the study and characterization of quantum vortex reconnections. Indeed, in order to validate and support the last experimental observations [29, 169], in the publication [77] reported in section 3.3 of this Thesis we used precisely the Gross–Piteaveskii model to study the reconnections of quantum vortices mediated by particles.

The simplest observable that characterizes a superfluid vortex reconnection is the separation $\delta(t)$ between the two reconnecting points. In the limits where $\delta \ll \xi$ and $\delta \gg \xi$ (assuming that other vortices or boundaries are not present in the system), the only relevant parameter is the circulation Γ, and from a simple dimensional analysis argument it follows that the separation rate should scale as:

$$\delta(t) \propto (\Gamma t)^{1/2}. \tag{1.160}$$

Such scaling was derived analytically in the context of the Gross–Pitaevskii model in [162], where it was also shown that locally the reconnecting vortices are always antiparallel and closely to reconnection they are arranged in hyperbola branches. The calculation reported in [162] neglects the non-linearity of the GP equation, since it is subdominant close to the core where $\psi \sim 0$. This fact suggests the universality of the scaling law (1.160), outlining its purely kinetic origin. Moreover, scaling laws different from Eq. (1.160) can be justified only by the introduction of other lenght scales. Nevertheless, many contradictory numerical results appeared in the literature (see for instance [194] and [253]), which showed different scaling before and after the reconnection. The controversy was ended by the systematic study reported in [229], in which the $t^{1/2}$ law was confirmed for a number of initial GP vortex configurations (included filaments in a turbulent tangle) for separations up to $\sim 10\xi$. In the same work, the non-universality of the prefactors in Eq. (1.160) before and after the reconnection was pointed out. However, it seems that vortices always separate faster than they approach, and this dynamics has been related to the irreversible emission of a sound pulse after the reconnection [230]. Visualizations of GP vortex reconnections from [229] are reported in Fig.1.8. In a recent publication, it was shown that the $t^{1/2}$

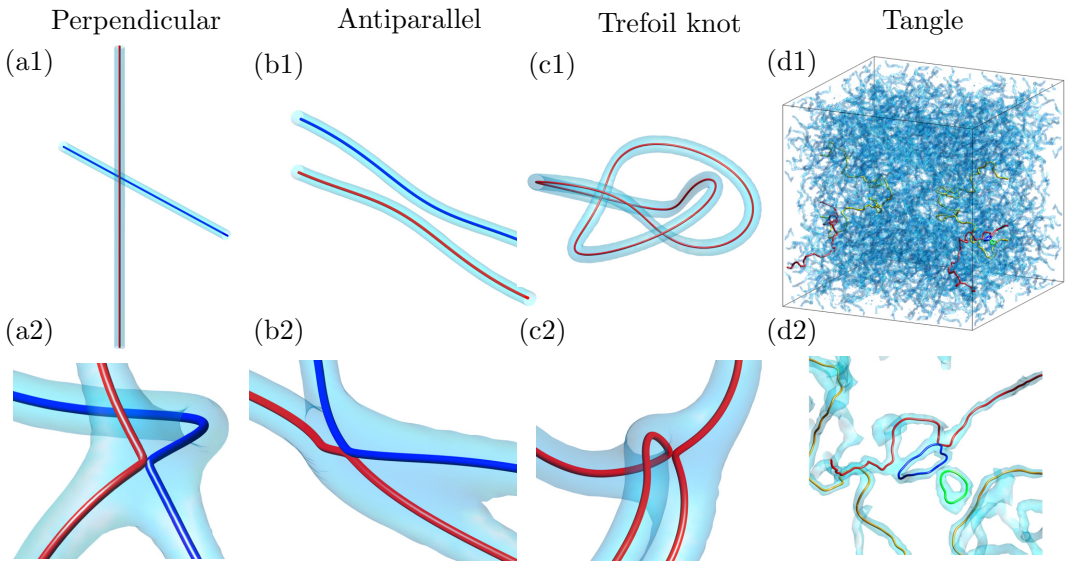


Figure 1.8. Visualization of reconnection events in GP simulations. The initial configuration is displayed for (**a1**) perpendicular vortex lines, (**b1**) antiparallel lines, (**c1**) trefoil knot and (**d1**) turbulent tangle. Red and blue correspond to the reconnecting vortex filaments; the light blue isosurfaces render the density field at low values. The bottom row shows a zoom at the reconnection time of the correspondig event in the upper row. Image taken from [229] to which we refer for further details.

scaling can sussist even for large times far from the reconnection event and in presence of an external trapping, provided that the vortex-vortex mutual interaction keeps on governing the dynamics [70]. However, at distances larger than 10ξ from the reconnection event, steeper scalings of the separation rate can be observed, depending on the presence of extrinsic factors like the presence of other vortices, density gradients and interaction with the boundaries. In particular, in the fully driven regime the separation rate is ballistic, scaling as $\delta(t) \propto t$.

1.4.5 Vortex waves

When thermal, quantum or turbulent fluctuations are present in a superfluid, or violent events like reconnections happen, excitations of quantum vortices are induced. These excitations are helicoidal waves propagating along the filaments, known as vortex waves. In the case of a slightly perturbed straight vortex filament, vortex waves propagate with a dispersion relation $\Omega_{\mathrm{v}}(k)$, where k is the wavenumber associated to the vortex direction. At scales much larger than the vortex core size ξ, the frequency of vortex waves matches asymptotically the classical dispersion relation derived by Sir William Thomson (better known as Lord Kelvin) in 1880 in the case of a hollow vortex

in an ideal fluid [220]. Such dispersion relation reads:

$$\Omega_{\mathrm{KW}}(k) = \frac{\Gamma}{2\pi a_0^2}\left[1 - \sqrt{1 + a_0|k|\frac{K_0(a_0|k|)}{K_1(a_0|k|)}}\right], \tag{1.161}$$

where $K_n(x)$ is the modified Bessel function of order n and a_0 identifies the size of the vortex core. The long wavelength limit of Eq. (1.161) is quadratic, with a logarithmic correction:

$$\lim_{ka_0\to 0}\Omega_{\mathrm{KW}}(k) = -\frac{\Gamma}{4\pi}k^2\left(\ln\frac{2}{a_0|k|} - \gamma_{\mathrm{E}}\right), \tag{1.162}$$

where $\gamma_{\mathrm{E}} \sim 0.5772$ is the Euler–Mascheroni constant. The explicit formal demonstration that long vortex waves in the Gross–Pitaevskii model propagate asymptotically as Eq. (1.162) is already contained in the original work of Pitaevskii himself [177], and has been refined and extended later by Roberts [192]. In his analysis, Roberts writes the perturbed vortex filament (in cylindrical coordinates) as the solution $\psi_{\mathrm{v}} + \delta\psi_{\mathrm{v}}$ of the GP equation, where ψ_{v} is the straight vortex state (1.133) and $\delta\psi_{\mathrm{v}}$ a small amplitude linear fluctuation:

$$\delta\psi_{\mathrm{v}} = \left[u_1(r)e^{-i(kz+m_\varphi\varphi-\Omega_{\mathrm{v}}t)} + u_2^*(r)e^{i(kz+m_\varphi\varphi+\Omega_{\mathrm{v}}t)}\right]e^{i\varphi}, \tag{1.163}$$

where m_φ is the (integer) mode of the vortex excitation and $u_1(r)$ and $u_2(r)$ are complex radial functions. The solutions for which the angular velocity Ω_{v} is real are called "bound modes", while if Ω_{v} has a non vanishing imaginary part the solutions are "free modes", which lose energy through sound radiation as time passes. The main result reported in [192] is that almost all the modes are free for all k and the only mode which is bound for all k is the slow mode with $m_\varphi = 1$. In the long wavelength limit, this mode is exactly the one which propagates with the dispersion relation (1.162):

$$\lim_{k\xi\to 0}\Omega_{\mathrm{v}}(k) = \lim_{ka_0\to 0}\Omega_{\mathrm{KW}}(k), \tag{1.164}$$

with the vortex core parameter $a_0 \sim 1.12\xi$. For this reason, superfluid vortex waves are usually called Kelvin waves at these scales, as their classical analog. It is interesting to notice that the angular velocity (1.161) has an opposite sign with respect to the vortex velocity field (1.132), meaning that the helicoidal Kelvin waves rotate in the opposite verse with respect to the superflow around the vortex. An example of Kelvin wave obtained tracking a vortex filament in a GP simulation is displayed in Fig.1.9. In the small scale limit, vortex excitations behave as Bogoliubov free particles with a quadratic dispersion relation, namely

$$\lim_{k\xi\to\infty}\Omega_{\mathrm{v}}(k) = \lim_{k\xi\to\infty}\omega_{\mathrm{B}}^-(k), \tag{1.165}$$

where $\omega_{\mathrm{B}}^-(k)$ is given by Eq. (1.110). A complete analytical formula that matches the two asymptotics of the GP vortex wave dispersion relation has been given in the publication [79], in which the propagation of Kelvin waves in presence of particles

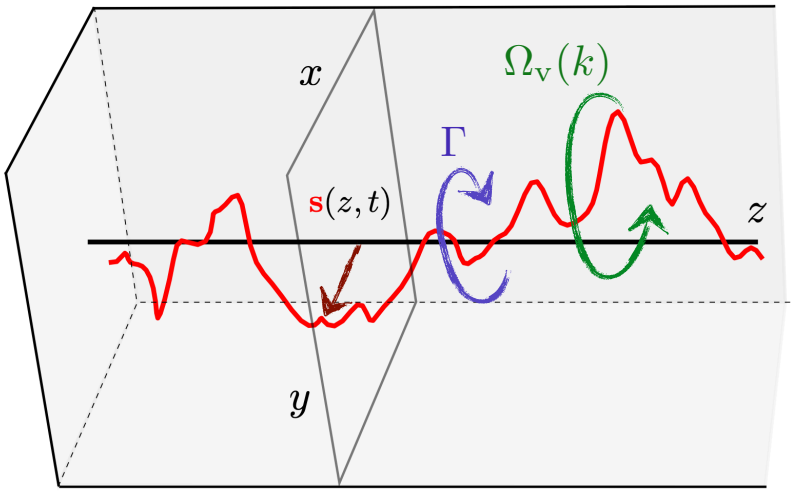


Figure 1.9. Example of Kelvin wave obtained tracking a vortex filament in a GP simulation. See text for further details.

trapped inside the vortex filaments is investigated. Such work constitutes one of the major findings of this Thesis and it is reported in chapter 4.

From the experimental side, Kelvin waves have been visualized directly in superfluid helium only recently, by using solidified hydrogen particles [64] (see section 2.1.3). On the other hand, the theoretical achievements are further ahead and the non-linear interactions of vortex waves have been deeply investigated, producing intense debates during the last two decades in the framework of the weak wave turbulence theory [126, 136, 141]. The non-linear interactions among waves produce a direct energy cascade towards small scales, which is believed to be one of the fundamental dissipation mechanisms in quantum turbulence [236]. Indeed, at scales smaller than the inter-vortex distance, the Kelvin wave cascade transfers the hydrodynamics energy of the vortex lines towards smaller scales along the filaments, until it is radiated in the form of sound waves at the scale of the vortex core size. Two predictions for the energy spectrum associated to such cascade have been derived. The first one, by Kozik and Svistunov, invoked a symmetry argument which saves the locality of the energy transfer in a six-wave non-linear interaction theory and leads to an energy spectrum $E_{\rm KS} \propto k^{-7/5}$ [126]. The second one, by L'vov and Nazarenko, showed the actual non-locality of the Kozik–Svistunov theory and derived an energy spectrum $E_{\rm LN} \propto k^{-5/3}$ as a result of an effective four-wave interaction theory [136]. Numerical evidences in the Gross–Pitaevskii framework support this last prediction [129]. Recently, the actual presence of Kelvin waves in a GP quantum turbulent regime has been detected [43] and a spectrum compatible with the cascade in the four-wave interaction theory has been measured [228].

2 Particles in fluids and superfluids

In this second introductory chapter, we give a motivational background to the study of particle dynamics in superfluids and present the model that has been used to achieve the results reported in this manuscript. We first provide a general overview of the main techniques involving the use of particle as probes in superfluid helium experiments. Then we review the physics that governs the motion of spherical particles in a classical fluid, highlighting the concepts which apply for quantum fluids as well. In the last part, we discuss the theoretical and numerical models developed in the past and current years for the description of particle dynamics in a superfluid. These models include the one-way coupling, which is a generalization of the classical dynamics to the two-fluid model and the vortex filament method with moving spherical boundary conditions. Finally we introduce the coupling between the Gross–Pitaevskii model and moving repulsive potentials, which is the principal investigation tool used in this Thesis, besides mentioning the bubble fields and multi-component condensate models.

How an object moves when it is immersed in a fluid is one of the most natural questions that can be asked in hydrodynamics. In the case of quantum fluids, the fact that an object can move without experiencing any drag is the natural consequence of superfluidity, or it can be even considered as the feature which defines superfluidity. As already predicted by Landau, superfluidity is broken if the velocity of the object is larger than a critical value [139, 176] (see section 1.1). Nowadays, experimental evidence in liquid helium and numerical studies agree that the appearance of a drag is accompanied by the emission of quantum vortices [54, 67, 101, 180, 245]. Moreover, the temperature of a quantum fluid can never be strictly zero, and therefore a normal fluid component is always present. Besides interacting with the superfluid component, the normal flow always couples to any particle or impurity immersed in it, necessarily affecting its motion. Thus, in the most general case the behaviour of a particle in a quantum fluid is determined by the combined action of superfluid, the quantized vortices therein, and normal fluid. At the same time, particles modify actively the flow, making their dynamics rather far from obvious and in need of being studied.

In the case of superfluid helium, the main interest in understanding the motion of particles relies on the experimental implementation of particles as probes for visualizing the flow [91, 208]. In general, the two most successful techniques for flow visualization are the Particle Image Velocimetry (PIV) and the Particle Tracking Velocimetry (PTV) [185]. The first one requires the use of a dense distribution of particles and consists in the local average of their velocities, resulting in a smooth velocity field. The second one involves the tracking of each individual particle trajectory, providing a tool for

the investigation of Lagrangian properties of the flow. Practically, in both techniques particles are suspended in the flow and reflect the light of a laser sheet, making possible to capture their time dependent position. Whilst in experiments with classical fluids the visualization techniques are currently employed with a high level of precision, for superfluid helium such development is yet to be achieved, given the intrinsic complexity of quantum fluids, as well as the practical issue of reaching and maintaining very low temperatures. Several methods which involve the use of particles have been developed for the visualization of superfluid and quantum vortex dynamics in liquid helium. The early efforts date back to the late 50's, when ions were implemented to study the properties of liquid helium and to detect the motion of vortex filaments [37, 83, 186, 241]. During the last 20 years, PIV and PTV techniques have been adopted in superfluid helium experiments using different categories of particles, from solidified hydrogen and deuterium to He_2 excimers [28–30, 91].

We give an overview of such techniques in the next section 2.1, enlighting some of the most important results obtained with their use. Afterwards, in section 2.2 we will discuss the theory behind the motion of spherical particles in a classical fluid, starting from the inviscid case and then considering the effects of viscosity. The specific models used to describe the dynamics of particles in quantum fluids are examinated in the last section 2.3, emphasizing the analogies with the classical theory. Note that a prime principle theory for superfluid helium is missing, so that the use of phenomenological methods is required. In this regard, the main difficulty is caused by the large extent of scales involved in the problem, which makes currently impossible to have a single model able to capture at once all the physical properties. In this chapter we will give a major focus on the modeling of particles at very low temperature, where viscous thermal excitations are absent, which is the setting in which the largest part of the findings exposed in this manuscript is concerned. In particular, in section 2.3.3, the model based on the coupling between moving repulsive potentials and the Gross–Pitaevskii model is described, which is central for the follow-up of the Thesis. Indeed, starting from the next chapters, specific problems related to the interaction between particles and superfluid will be addressed using this model.

2.1 Visualization experiments in superfluid helium

2.1.1 Ion trapping and electron bubbles

When a single negative charge carried by an electron is injected in liquid helium, it self-localizes in a spherical void region from which ^{4}He atoms are excluded. This is the phenomenon that leads to the formation of the so-called electron bubbles, charged particles of size between 12 Å and 20 Å, that can be used as detectors of quantum vortices [37, 83, 186]. The idea is that negative ion bubbles are attracted to the vortices because of Bernoulli force and eventually get captured. Such mechanism is actually the same at the basis of the use of positive ions and even large solid particles, given that in general the energy of the system is lower when an object is trapped in the core

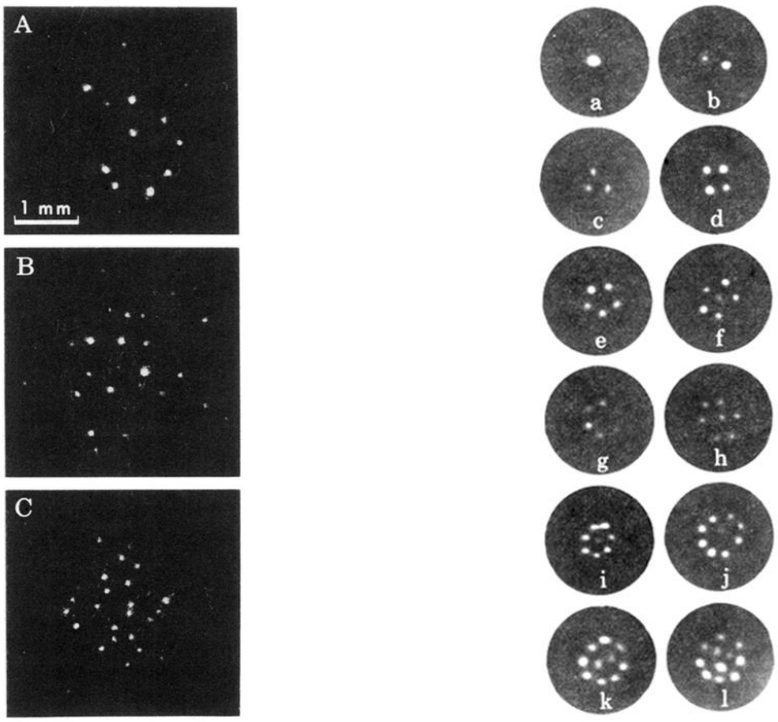


Figure 2.1. Photographs of discrete quantized vortex lines (*left*) and stable vortex arrays (*right*) in rotating ^{4}He experiments with trapped ion bubbles. Different labels correspond to different angular velocities. Images taken respectively from [240] and [247], to which we refer for further details.

than far from it [55, 173]. We will give more details on this mechanism in chapter 3. In the case of a positive ion, the particle attracts the surrounding fluid, triggering a liquid-solid transition and generating a "snowball" of solid helium [6]. However, given the extremely small size of such objects (~ 8 Å) and therefore of the cross-section of the snowball-vortex interaction, their practical use in experiments is limited.

Being the electron bubbles charged, the application of an external electric field can be used to manipulate them. In the early experiments, the technique consisted in generating straight vortices by rotating a bucket of liquid helium, loading them with ions injected orthogonally to the filaments and applying an electric field parallel to them. As a consequence, the electron bubbles slided along the vortices and reached a detector, where they were revealed. In this way it was eventually possible to detect individual vortex lines [168], and an improvement of such method led to the measurement of vortex line density in a turbulent tangle [215]. Later, a photographic technique combined with the negative ion detection allowed for the first direct visualization of individual quantized vortices and symmetric arrays of vortices in rotating ^{4}He [240, 247]. These first photographs of quantum vortices are reported Fig. 2.1.

In conclusion, the advantages of the standard bubble ion trapping technique is

that the smallness of the particles prevent them from disturbying the flow and can be implemented in very low temperature regimes. On the other hand, the actual visualization of the full three dimensional dynamics of superfluid vortices is hardly possible and when the temperature is too high ($> 1.7\,K$) they do not remain trapped inside the vortex filaments [208].

We mention here that a further technique based on the acoustic cavitation imaging of electron bubbles is being developed. The basic principle behind this method is that if a negative pressure is applied to liquid helium, the size of the bubbles increases from the typical radius of ~ 12 Å up to several microns. After a critical value of the negative pressure there is no longer an energy minimum, thus a bubble becomes unstable and eventually explodes [44, 73, 93, 104]. Recently, bubble expansions of 1 mm have been observed [246]. In these experiments, the variation of pressure is generated by an acoustic forcing and the large bubbles can be visualized using standard optical methods. Unlike the traditional ion trapping technique, the cavitating electrons are those already present in the system (by natural or induced ionization), and no external electron beam is used. As a consequence, they are supposed to trace the normal fluid component, unless they get captured by quantized vortices and slide along them, which could explain the observation of snakelike paths [93]. Finally note that since the pressure around particles trapped inside quantum vortices is reduced (see section 3.1), the explosion can be triggered at a lower critical pressure, providing thereby a way to distinguish the trapped bubbles from the free ones [73].

2.1.2 PIV with solid particles

Micron-size polymer micro-spheres have been used in combination with the PIV method to study average properties of liquid helium below the critical temperature [249–251]. This technique has been implemented particularly in the specific setting of turbulent thermal counterflow.

One of the most relevant early experiments with counterflow sampled with PIV is the one reported in [250] by Zhang and Van Sciver, where the sedimentation of heavy solid particles is studied. A heat source is applied at the bottom of the helium container, so that the normal fluid component flows upwards and the superfluid component flows downwards. Heavy particles (with a mass density 9 times higher than the liquid helium one) are immersed in the system in a temperature range between $1.62\,K$ and $2.0\,K$ and with heat fluxes between $q = 110\,\mathrm{mW/cm^2}$ and $q = 1370\,\mathrm{mW/cm^2}$. In these conditions, one could have expected the viscous Stokes drag due to the normal fluid to balance the gravitational body force, so that the particle velocity is given by $v_\mathrm{p} = v_\mathrm{n} - v_\mathrm{slip}$, namley the difference between the normal fluid velocity v_n and the terminal velocity of particle sedimentation v_slip. Instead, the instructive result of [250] is that the actual particle velocity has an extra contribution v_add in the direction opposite to the normal fluid. This deviation, which produced an average particle velocity $v_\mathrm{p} \sim 0.5\, v_\mathrm{n}$ for all the temperatures analyzed, can be indeed explained with the presence of a tangle of superfluid vortices strongly interacting with the particles.

The same authors used similar particles in the same range of temperatures to study

thermal counterflow past a macroscopic cylinder [251]. The striking result of the PIV measurements was the emergence of large eddies at the scale of the cylinder both downstream and upstream. Also in this case, Zhang and Van Sciver explained these unclassical structures as the consequence of mutual friction between quantized vortex lines and the normal fluid. However, in this case an alternative explanation has been proposed, based on the existence of stationary locations in the point vortex model in a setting analogous to the experiment [207].

In general, the interpretation of PIV measurements in finite temperature superfluids is much harder than in classical hydrodynamics, given the intrinsic bifluid nature of the flow. In particular, particles interact with both the superfluid and the normal fluid component, and they are affected by the presence of quantized vortices. Therefore, although the use of this technique gave important results in the description of the mean flow properties, it is not suitable for the investigation of the detailed structure of quantum turbulence and the dynamics of superfluid vortices. For this reason, other techniques and innovative kind of particles have been recently implemented, which are described in the following.

2.1.3 Vortex imaging and PTV with solidified particles

The PTV technique, which consists in the tracking of each single particle trajectory, is a powerful method that provides more insights about the details of the flow than PIV. Since the solid particles usually used in PIV experiments turned out to be generally too dense to allow for a detailed description of superfluid turbulence, solidified hydrogen (or deuterium) particles have been introduced for the PTV measurements [28, 30, 91, 208]. These new probes are produced via injection of a gaseous mixture of hydrogen and helium directly in the liquid helium sample at a temperature slightly above the transition point. The solidification of hydrogen then leads to "ice" particles with a diameter of few microns and a density slightly less than the liquid helium one ($\rho_H = 0.7\rho_{He}$) [30]. After the generation of solidified particles inside the liquid helium sample, the temperature is slowly decreased below the critical value, so that turbulent vortex filaments appear. In 2006, the groundbreaking experiment [28] by the Lathrop's group in Maryland used this new technique to directly visualize quantum vortex filaments in superfluid helium for the first time. The already famous images of this experiment are reported in Fig. 2.2.

Subsequent studies used the same procedure to characterize the dynamics of superfluid vortices, especially the process of vortex reconnection [29, 169] and the propagation of Kelvin waves [64], introduced in the first chapter of this Thesis. In particular, the experiments strongly suggest that the reconnections between vortex filaments effectively take place [29] (see Fig. 2.3) and the measured vortex approaching rate before and after the reconnection is compatible with the scaling $(|t - t_0|)^{1/2}$ predicted in theory [70, 162, 229], with some deviation that may be due to the local properties of the environment [169]. The reconnection scaling, which is ultimately determined by the presence of the quantum of circulation as the only significant parameter at small scales, has been proposed to be the physical origin of the power law tails observed in

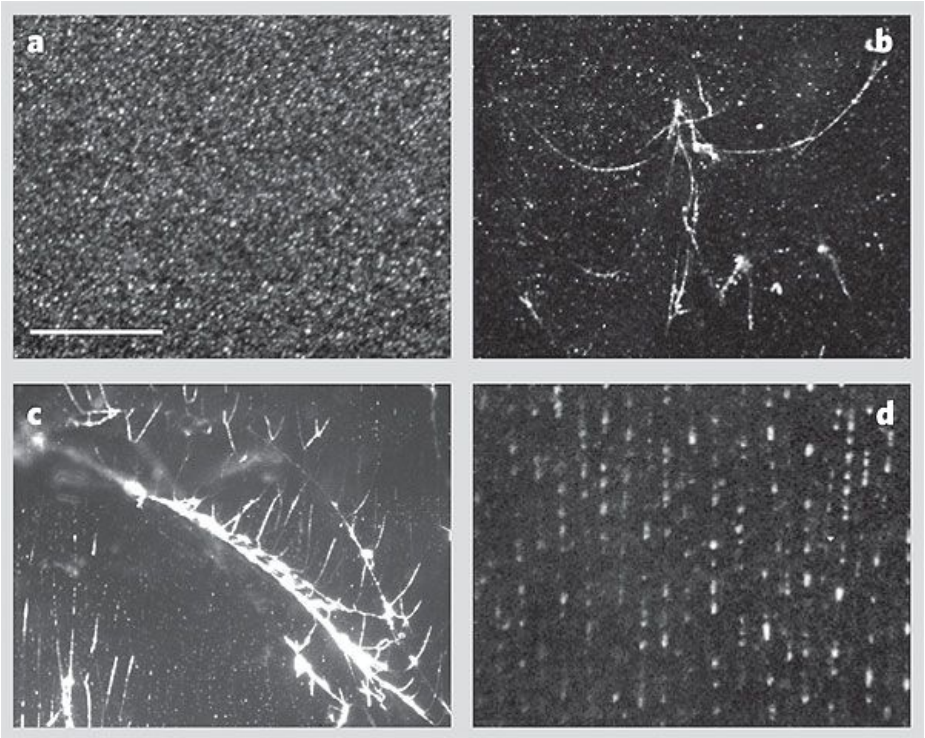


Figure 2.2. Visualization of quantum vortices with solidified hydrogen particles in the experiment [28]. (**a**) Slightly above the superfluid transition temperature. (**b,c**) Tens of mK below the transition temperature, regrouped in branching filaments and (**d**) along vertical lines for stationary rotation about the vertical axis. Images taken from [28] to which we refer for further details.

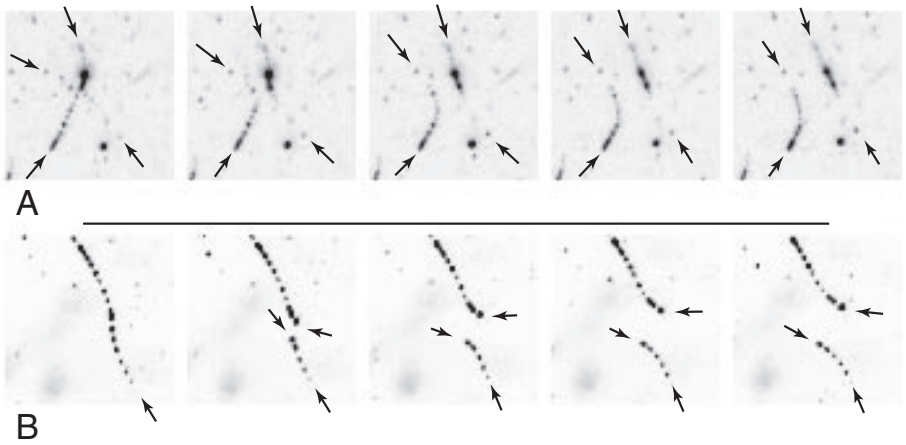


Figure 2.3. Visualization of individual pairs of reconnecting vortices decorated with hydrogen particles in superfluid helium. Different labels refer to different events with different visual perspectives. Subsequent snapshots in each row are taken at intervals of 50 ms. Images taken from [29] to which we refer for further details.

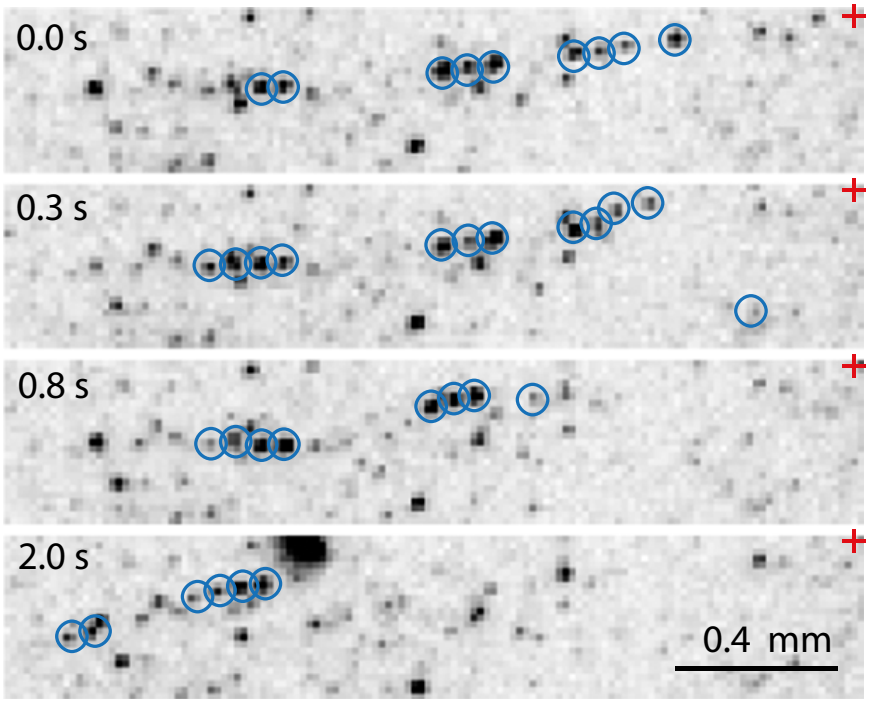


Figure 2.4. Visualization of Kelvin waves propagating after a reconnection event in superfluid helium. The circles indicate hydrogen particles decorating the vortex. Images taken from [64] to which we refer for further details.

the velocity distribution of particles in quantum turbulence experiments [137, 170]. Such issue will be discussed in more detail in chapter 5.

The first observation of Kelvin waves in superfluid helium sampled with hydrogen ice particles [64] is reported in Fig. 2.4. The helicoidal perturbation observed in the experiment is generated after a reconnection event and it is compatible with LIA and Biot-Savart self-similar solutions, adjusted with a damping term that takes into account finite temperature mutual friction effects.

Solidifed particles have been adopted in combination to PTV to study thermal counterflow as well. An important counterflow experiment was performed by Paoletti et al. [197] in the same range of temperatures of [250] but at lower values of the heat flux (between $q = 13\,\mathrm{mW/cm^2}$ and $q = 91\,\mathrm{mW/cm^2}$). Thanks to the PTV method, a bimodal probability distribution for the particle velocity along the counterflow was observed, with one peak associated with smooth trajectories following the normal fluid component and another associated with irregular trajectories moving in the opposite direction. These results partially confirmed the scenario arised in the PIV experiment [250] in which a fraction of particles moves in the direction opposite to the normal fluid component, being trapped in a tangle of quantum vortices carried by the superflow. However, the peak associated to the particles trapped in the tangle drops when the temperature is increased (which means lower vortex line density) or the heat flux is

increased (which means higher normal fluid velocity). Therefore, an apparent paradox emerged, since in the PIV experiment [250] the average particle velocity was always proportional to v_n and independent of temperature. This contradition was solved by further theoretical studies in the vortex filament framework [114, 115] and a subsequent PTV experiments over a wider range of heat fluxes and normal fluid velocities [39, 148]. It was shown that the bimodal behaviour is present only for sufficiently low counterflow velocities. Conversely, above a critical velocity the particles get untrapped from the vortices and the distribution becomes monovalued, with the tangle causing a friction slowdown as in the original PIV experiment [250].

In conclusion, the PTV technique with solidified ice particles as probes is a powerful and promising method for the investigation of superfluid physics, provided that a strong theoretical backgroung is able to support them. This is indeed the main motivation that led to the work exposed in the following chapters of this Thesis, which has been inspired precisely by the avant-garde experiments described in this section.

2.1.4 Fluorescence of He_2^* excimers

Finally, we mention a recent visualization technique using excited He_2^* molecules as probes, which are claimed to be sensitive only to the normal fluid [71, 90, 147, 151]. In particular the triplet state $He_2(a^3\Sigma_u^+)$ is metastable but with a long decay time ($\sim 13\,s$), and can be produced easily and in large amount by excitating helium ground state atoms. Excimers immersed in liquid helium form very small bubbles of radius 6 Å, which can be detected using a laser-induced fluorescence technique [91]. Given their small size, the binding energy of the He_2^* molecules to quantum vortices at temperatures larger than 1 K is not sufficient to get them trapped and Stokes drag is expected to be the dominating force [235]. Therefore these excimers are perfect candidates for sampling the normal fluid component, even at the Kolmogorov scale. In the experiments [71, 90, 147] a tracer line of excimers is produced with a laser-field ionization and then probed using a laser in a counterflow setting of superfluid helium. The presence of a turbulent regime in the normal fluid is shown, in which the dissipation acts at all scales due to the mutual friction with the superfluid component. Such turbulence is achieved when the heat flux generating the counterflow is large (see Fig. 2.5) and the local velocity can be measured by dividing the displacement of a small line segment along the counterflow direction by the drift time (i.e. the time gap between the creation and the imaging of the tracer line). One limitation is thus that only the velocity component perpendicular to the tracer line can be measured, but some expedients are being studied to overcome this issue [92].

The imaging of helium excimers is an interesting technique because it allows for the estimation of useful quantities in turbulence like structure functions, and thus helps in characterizing the normal fluid component in thermal counterflow. Moreover, at sufficiently low temperature, triplet molecules could become trapped in quantized vortex cores, allowing for the imaging of superfluid vortices [235] and tracing a turbulent quantum vortex tangle [252]. As we will stress in the publications [76, 79], having small particles as probes for quantum vortices is theoretically the best solution,

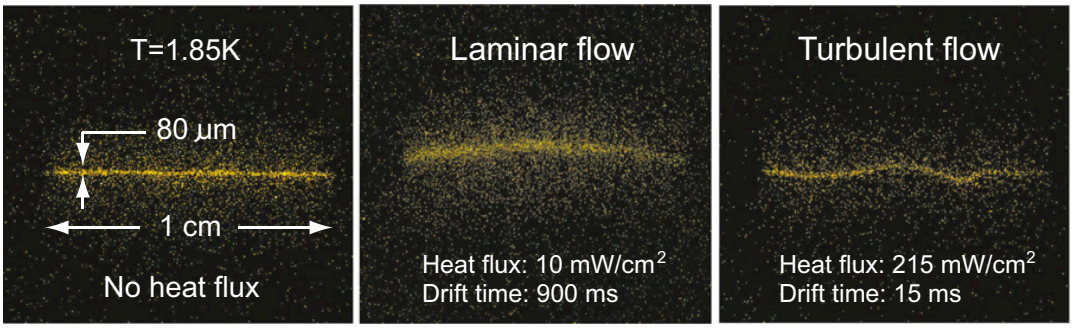


Figure 2.5. Fluorescence imaging of a thin line of He_2^* excimers in thermal counterflow. Images taken from [91], to which we refer for further details.

therefore excimers could be a promising option also for vortex tracking at very low temperature, if succesfully developed.

2.2 Dynamics of particles in classical hydrodynamics

In this section we review the key steps for the derivation of the equation of motion for a body immersed in a classical fluid. Some of the concepts introduced here will be recovered in the following section describing the models for particles in superfluids, as well as in the results presented in the publications included later in this Thesis. In particular, we focus on the case of an incompressible fluid described by the velocity field $\boldsymbol{v}(\boldsymbol{x}, t)$, which obeys the Navier–Stokes equation:

$$\frac{D\boldsymbol{v}}{Dt} = -\frac{1}{\rho}\nabla p + \nu\nabla^2\boldsymbol{v} + \tilde{\boldsymbol{g}}, \tag{2.1}$$

with the incompressibility condition

$$\nabla \cdot \boldsymbol{v} = 0, \tag{2.2}$$

and where $D/Dt = \partial/\partial t + (\boldsymbol{v}\cdot\nabla)$ is the material derivative, ρ is the constant homogenous density, $p(\boldsymbol{x}, t)$ is the pressure field, ν is the kinematic viscosity and $\tilde{\boldsymbol{g}}$ is the gravitational acceleration. We start by defining a tracer, also called Lagrangian particle or fluid particle, which is a point $\boldsymbol{q}(t)$ following the streamlines of the flow. Its equation of motion is thus

$$\dot{\boldsymbol{q}}(t) = \boldsymbol{v}(\boldsymbol{q}(t), t), \tag{2.3}$$

with the initial condition $\dot{\boldsymbol{q}}(t_0) = \boldsymbol{v}(\boldsymbol{q}(t_0), t_0)$. By definition a tracer is a passive and buoyant point particle. The trajectories of tracers are fundamental objects, since all the Lagrangian description of fluid dynamics is based on them. However, the dynamics of real finite size and inertial particles is more complex than the one of an ideal fluid particle. We will show at the end of this section some limits in which the tracer behaviour can be recovered.

In general, we assume that a particle immersed in a fluid is a rigid body of mass M_p described by the position of its center of mass $\boldsymbol{q}(t)$, which moves with a velocity $\dot{\boldsymbol{q}}(t)$. Note that the incompressibility approximation (2.2) is valid as long as the velocity of the particle remains smaller compared to the speed of sound in the liquid. The equation of motion for such particle is given by

$$M_\mathrm{p}\ddot{q}_i = M_\mathrm{p}\tilde{g}_i + F_i \qquad \text{with} \quad F_i = \oint_{\partial\mathbb{B}} \sigma_{ij} n_j \,\mathrm{d}\Sigma, \tag{2.4}$$

where $\mathbb{B}[\boldsymbol{q}(t)]$ is the volume occupied by the particle and the integral is extended over the full particle surface $\partial\mathbb{B}[\boldsymbol{q}(t)]$. The unit vector $\hat{\boldsymbol{n}}$ is the outward normal to the particle surface and σ_{ij} in the stress tensor of the fluid

$$\sigma_{ij} = -p\delta_{ij} + \nu\rho\left(\frac{\partial v_i}{\partial x_j} + \frac{\partial v_j}{\partial x_i}\right). \tag{2.5}$$

In this Thesis we deal with spherical particles but many of the conclusions can be in principle generalized to the case of rigid particles with an arbitrary shape. The problem consists in giving an explicit expression for the force F_i in Eq. (2.4) that only depends on the particle degrees of freedom, or in other words evaluating the stress tensor on the particle surface. In the following, we first consider the case of an inviscid irrotational fluid, adding later the contribution due to rotational and viscous effects.

2.2.1 Particle motion in ideal irrotational fluids

We indicate with $\boldsymbol{v}_0(\boldsymbol{x},t)$ the undisturbed fluid velocity field when the particle is absent, while $\boldsymbol{v}(\boldsymbol{x},t)$ is the velocity field in presence of the particle, both in the laboratory reference frame. In the following we will consider the coordinate system moving with the particle $\boldsymbol{x}'(t) = \boldsymbol{x} - \boldsymbol{q}(t)$, in which the relative velocity field is denoted by $\boldsymbol{w}(\boldsymbol{x}',t) = \boldsymbol{v}(\boldsymbol{x}'+\boldsymbol{q}(t),t) - \dot{\boldsymbol{q}}$. Analytical calculations can be performed if the length scale at which the flow varies is much larger than the particle size a_p, namely if the following parameter remains small:

$$\epsilon_\mathrm{p} = a_\mathrm{p}\frac{\|\nabla\boldsymbol{v}_0(\boldsymbol{q})\|}{|\boldsymbol{v}_0(\boldsymbol{q}) - \dot{\boldsymbol{q}}|} = a_\mathrm{p}\frac{\|\nabla\boldsymbol{v}_0(\boldsymbol{q})\|}{|\boldsymbol{w}_0(\boldsymbol{0})|} \ll 1. \tag{2.6}$$

In the case of an ideal (inviscid) fluid the viscous term proportional to ν in Eq. (2.1) is absent, and the stress tensor (2.5) is just given by the diagonal terms proportional to the pressure $\sigma_{ij} = -p\delta_{ij}$. The presence of the particle imposes the free slip boundary condition for the flow around it

$$\boldsymbol{w}(\boldsymbol{x}')\cdot\hat{\boldsymbol{n}} = 0, \qquad \forall\boldsymbol{x}' \text{ s.t. } |\boldsymbol{x}'| = |\boldsymbol{x}-\boldsymbol{q}| = a_\mathrm{p}, \tag{2.7}$$

while far from the particle the flow tends to the undisturbed field

$$\boldsymbol{w}(\boldsymbol{x}') \to \boldsymbol{w}_0(\boldsymbol{x}'), \qquad \forall\boldsymbol{x}' \text{ s.t. } |\boldsymbol{x}'| = |\boldsymbol{x}-\boldsymbol{q}| \gg a_\mathrm{p}. \tag{2.8}$$

In the standard treatment of the problem, the fluid velocity field is splitted into the far field component plus corrections due to the presence of the particle [8, 150, 181]:

$$\boldsymbol{w} = \boldsymbol{w}_0 + \boldsymbol{w}_\mathrm{p} + \boldsymbol{w}_\mathrm{BC}, \tag{2.9}$$

where we are assuming that the flow is also irrotational. In this case, Eq. (2.9) can be written also in terms of the corresponding velocity potentials:

$$\phi = \phi_0 + \phi_\mathrm{p} + \phi_\mathrm{BC}, \tag{2.10}$$

so that $\boldsymbol{w} = \nabla\phi$, $\boldsymbol{w}_0 = \nabla\phi_0$, $\boldsymbol{w}_\mathrm{p} = \nabla\phi_\mathrm{p}$ and $\boldsymbol{w}_\mathrm{BC} = \nabla\phi_\mathrm{BC}$. The contribution $\boldsymbol{w}_\mathrm{p}$ is of the order of magnitude of $\boldsymbol{w}_0$, and it represents the perturbation of a homogeneous flow due to the presence of a sphere. Its potential reads [19]

$$\phi_\mathrm{p} = \frac{a_\mathrm{p}^3}{2|\boldsymbol{x}'|^3}\boldsymbol{x}' \cdot \boldsymbol{w}_0(\boldsymbol{0}, t) = \frac{a_\mathrm{p}^3}{2|\boldsymbol{x}-\boldsymbol{q}|^3}\,(\boldsymbol{x}-\boldsymbol{q}) \cdot (\boldsymbol{v}_0(\boldsymbol{q}, t) - \dot{\boldsymbol{q}})\,, \tag{2.11}$$

so that at the boundary of the particle

$$\boldsymbol{w}_\mathrm{p}(a_\mathrm{p}\hat{\boldsymbol{n}}) \cdot \hat{\boldsymbol{n}} = -\boldsymbol{w}_0(\boldsymbol{0}) \cdot \hat{\boldsymbol{n}} = (\dot{\boldsymbol{q}} - \boldsymbol{v}_0(\boldsymbol{q})) \cdot \hat{\boldsymbol{n}} \tag{2.12}$$

In the case of a homogenous flow this correction would be sufficient to satisfy the boundary condition (2.7) by construction, while the general case of an inhomogenous flow it is necessary to add the contribution $\boldsymbol{w}_\mathrm{BC}$. This is indeed fixed by the condition

$$\boldsymbol{w}_\mathrm{BC}(a_\mathrm{p}\hat{\boldsymbol{n}}) \cdot \hat{\boldsymbol{n}} = \Big(\boldsymbol{w}_0(a_\mathrm{p}\hat{\boldsymbol{n}}) - \boldsymbol{w}_0(\boldsymbol{0})\Big) \cdot \hat{\boldsymbol{n}} = \Big(\boldsymbol{v}_0(\boldsymbol{q} + a_\mathrm{p}\hat{\boldsymbol{n}}) - \boldsymbol{v}_0(\boldsymbol{q})\Big) \cdot \hat{\boldsymbol{n}}, \tag{2.13}$$

which is satisfied at the order $\mathcal{O}(\epsilon_\mathrm{p})$ if the potential ϕ_BC reads

$$\phi_\mathrm{BC} = \frac{1}{2}e_{ij}x_i'x_j' = \frac{1}{2}\left(\left.\frac{\partial v_i}{\partial x_j}\right|_{\boldsymbol{q}} + \left.\frac{\partial v_j}{\partial x_i}\right|_{\boldsymbol{q}}\right)(x_i - q_i)(x_j - q_j), \tag{2.14}$$

where e_{ij} is a shortcut for the strain rate tensor evaluated at the particle position. The pressure field $p'(\boldsymbol{x}', t)$ in the coordinates system of the particle can be evaluated writing the momentum equation (2.1) for an inviscid irrotational fluid

$$\frac{\partial \boldsymbol{w}}{\partial t} + \ddot{\boldsymbol{q}} + \frac{1}{2}\nabla|\boldsymbol{w}|^2 = -\frac{1}{\rho}\nabla p' + \tilde{\boldsymbol{g}}, \tag{2.15}$$

which implies the Bernoulli equation

$$p' = -\rho\left(\frac{\partial\phi}{\partial t} + \frac{1}{2}|\nabla\phi|^2 + \ddot{\boldsymbol{q}} \cdot \boldsymbol{x}' - \tilde{\boldsymbol{g}} \cdot \boldsymbol{x}'\right) + C_p(t), \tag{2.16}$$

where $C_p(t)$ is a homogenous term which is fixed by the far field boundary condition

(2.8). Therefore, the force term in Eq. (2.4) can be computed as

$$\boldsymbol{F} = -\oint_{\partial\mathbb{B}} p'\hat{\boldsymbol{n}}\,\mathrm{d}\Sigma = \rho\oint_{\partial\mathbb{B}}\left(\frac{\partial\phi}{\partial t}+\frac{1}{2}|\nabla\phi|^2\right)\hat{\boldsymbol{n}}\,\mathrm{d}\Sigma + M_0\left(\ddot{\boldsymbol{q}}-\tilde{\boldsymbol{g}}\right), \tag{2.17}$$

where in the last term we have used the divergence theorem and defined the fluid mass displaced by the particle as

$$M_0 = \rho\int_{\mathbb{B}}\mathrm{d}\boldsymbol{x}' = \frac{4}{3}\pi\rho a_\mathrm{p}^3. \tag{2.18}$$

Using the definition (2.10) with (2.11) and (2.14) and applying again the divergence theorem we get the formula for the hydrodynamic force [8]

$$\boldsymbol{F} = (C_\mathrm{a}+1)\,M_0\left.\frac{D\boldsymbol{v}_0}{Dt}\right|_{\boldsymbol{q}} - M_0\tilde{\boldsymbol{g}} - C_\mathrm{a}M_0\ddot{\boldsymbol{q}}, \tag{2.19}$$

where the value of the coefficient $C_\mathrm{a} = 1/2$ is due to the spherical shape of the particle. Considering particles of different shapes would give a different value, for instance for a cylinder $C_\mathrm{a} = 1$ [19]. The equation of motion (2.4) can be rearranged in the following way:

$$M_\mathrm{eff}\ddot{\boldsymbol{q}} = \left(M_\mathrm{p}-M_0\right)\tilde{\boldsymbol{g}} + (C_\mathrm{a}+1)\,M_0\left.\frac{D\boldsymbol{v}_0}{Dt}\right|_{\boldsymbol{q}}, \tag{2.20}$$

where we have defined an effective mass

$$M_\mathrm{eff} = M_\mathrm{p} + C_\mathrm{a}M_0, \tag{2.21}$$

in which we have collected the actual mass of the particle M_p and the so called added mass $C_\mathrm{a}M_0$. The physical origin of such increment of the inertia lies in the finite size of the particle, which has to displace the same amount of fluid occupied by its volume while it moves. The force term related to the fluid acceleration is

$$\boldsymbol{F}_\mathrm{acc} = (C_\mathrm{a}+1)\,M_0\left.\frac{D\boldsymbol{v}_0}{Dt}\right|_{\boldsymbol{q}}, \tag{2.22}$$

and in Eq. (2.20) we also recognize the familiar body force term

$$\boldsymbol{F}_\mathrm{g} = (M_\mathrm{p}-M_0)\tilde{\boldsymbol{g}}, \tag{2.23}$$

which is gravitational force minus buoyancy. It arises for a reason similar to the added mass effect and its consequence is that particles with the same mass density of the fluid (i.e. with unitary mass ratio $\mathscr{M} = M_\mathrm{p}/M_0 = 1$) do not feel the effect of gravity. These kind of particles are usually called neutrally buoyant particles, while they are called heavy if $\mathscr{M} > 1$ and light if $\mathscr{M} < 1$. It is interesting to notice that in the case of neutral particles any dependence on the mass disappears in (2.20), which becomes

simply

$$\ddot{\boldsymbol{q}} = \left.\frac{D\boldsymbol{v}_0}{Dt}\right|_{\boldsymbol{q}}, \tag{2.24}$$

meaning that particle and fluid feel exactly the same acceleration, given by the pressure gradient.

At this point we should stress that a quantum fluid like liquid helium close to zero temperature can be modeled at sufficiently large scales as an inviscid, incompressible and irrotational classical fluid. The same is true for a fluid described by the GP model at scales larger that the healing length and if sound waves are weak. As a consequence, Eq. (2.20) can be used to describe the motion of a large spherical particle in a low temperature superfluid, in the case in which the flow does not circulate around the sphere, namely if there are no vortex filaments piercing the particle. This situation is indeed the one studied in [15] in the framework of the vortex filament method and in [75] using the GP theory. This latter case is reported in chapter 3 of this manuscript, where Eq. (2.20) is derived in the GP framework (in absence of gravity), taking as undisturbed flow $\boldsymbol{v}_0$ the one generated by a straight vortex line (1.132) far from the particle.

2.2.2 Rotational effects

We briefly mention what changes in the case of a rotational ambient flow, in which the vorticity $\boldsymbol{\omega}_0 = \nabla \times \boldsymbol{v}_0$ is different from zero. At order $\mathcal{O}(\epsilon_\mathrm{p})$, namely for a uniform straining flow, the vorticity is also uniform. Then, since the rate of change of vorticity is of order $|\partial\boldsymbol{\omega}_0/\partial t| \sim \|\nabla \boldsymbol{v}_0\|^2$, in the time interval needed for the flow to go past the sphere $\delta t = a_\mathrm{p}/|\boldsymbol{w}_0(\boldsymbol{0})|$ the change in the vorticity is small $|\delta\boldsymbol{\omega}_0| = a_\mathrm{p}\|\nabla \boldsymbol{v}_0\|^2/|\boldsymbol{w}_0(\boldsymbol{0})| \ll \boldsymbol{\omega}_0$. Therefore the rate of change of the vorticity can be also neglected at the order $\mathcal{O}(\epsilon_\mathrm{p})$ and the decomposition (2.9) is still valid with the addition of an extra rotational term $\boldsymbol{w}_\omega$. The rotational correction must satisfy the usual boundary condition $\boldsymbol{w}_\omega \cdot \hat{\boldsymbol{n}} = 0$ at the surface of the particle and leads to the following force [7, 8]:

$$\boldsymbol{F}_\omega = C_\omega M_0 \left(\boldsymbol{v}_0(\boldsymbol{q}) - \dot{\boldsymbol{q}}\right) \times \boldsymbol{\omega}_0(\boldsymbol{q}), \tag{2.25}$$

with $C_\omega = 1/2$ for a spherical particle. Such force, which must be added in the right hand side of Eq. (2.20), represents a lift force orthogonal to the relative velocity between the ambient flow and the particle, that arises because of the stretching of the vorticity lines in the vicinity of the particle surface. We write for completeness the full equation of motion of the particle in an incompressible ideal fluid:

$$M_\mathrm{eff}\ddot{\boldsymbol{q}} = \left(M_\mathrm{p} - M_0\right)\tilde{\boldsymbol{g}} + \left(C_\mathrm{a} + 1\right) M_0 \left.\frac{D\boldsymbol{v}_0}{Dt}\right|_{\boldsymbol{q}} + C_\omega M_0 \left(\boldsymbol{v}_0(\boldsymbol{q}) - \dot{\boldsymbol{q}}\right) \times \boldsymbol{\omega}_0(\boldsymbol{q}). \tag{2.26}$$

The rotational term requires the existence of a continous non-zero vorticity field. The limiting case in which the vorticity is always zero apart where the particle is gives rise to the Kutta-Jukovskii lift force (also called Magnus effect), which can be completely

solved using just the potential flow.

2.2.3 Magnus effect

If the flow is inviscid, incompressible and irrotational but it has a non-zero circulation Γ around the particle another term arises in its equation of motion. This limiting situation in which irrotationality and circulation coexist in the same flow is possible only if a line of singular vorticity runs through the particle. Although such picture is rather unnatural in a classical perfect fluid, it corresponds exactly to what happens in superfluid helium experiments, where particles used as probes are trapped by quantum vortex filaments [54]. However, such exotic object is still a solution that can be treated in classical fluid mechanics, and gives rise to the lift force known as Magnus effect [109, 138]. The velocity field v_v generated by the vortex is the same given in Eq. (1.132). We choose the system of reference with the particle center as origin, the vortex line that lies on the z axis and the relative velocity between the particle and the ambient fluid aligned to the y axis. In this configuration, the potential associated to the vortex is

$$\phi_\mathrm{v} = \frac{\Gamma}{2\pi} \arctan \frac{y}{x}, \tag{2.27}$$

which has to be added to the decomposition (2.10). The Magnus effect arises from the coupling $\nabla\phi_\mathrm{p} \cdot \nabla\phi_\mathrm{v}$ inside the pressure term integrated in (2.19). In the chosen coordinates system the only non-zero contribution to the force is along the x axis, orthogonal to both the vortex filament and the particle relative velocity:

$$F_x^{\mathrm{Magnus}} = \rho \oint_{\partial\mathbb{B}} \rho \left(\nabla\phi_\mathrm{v} \cdot \nabla\phi_\mathrm{p}\right) \hat{\boldsymbol{n}} \, \mathrm{d}\Sigma = \frac{3}{2}\rho\Gamma a_\mathrm{p} w_{0x}(\boldsymbol{q}). \tag{2.28}$$

Generalizing to the laboratory reference frame, the Magnus force eventually reads

$$\boldsymbol{F}_{\mathrm{Magnus}} = -\frac{3}{2}\rho a_\mathrm{p} \boldsymbol{\Gamma} \times \left(\boldsymbol{v}_0(\boldsymbol{q}) - \dot{\boldsymbol{q}}\right), \tag{2.29}$$

where the modulus of the vector $\boldsymbol{\Gamma}$ is the circulation and it is oriented along the vortex filament. It is evident that such effect is present only if the particle inside the vortex and the ambient flow have a non-zero relative velocity. Magnus force causes a precession of the particle around the vortex filament. This dynamics is present in quantum fluids and studied in detail in the article [79], reported in chapter 4.

It is worthwile to point out a subtle difference between the Magnus effect described here and the one present in viscous fluids. In fact, the usual Magnus force is a lift force that arises when an object rotates and at the same time moves with a translational velocity in a viscous fluid [19, 196]. In this case the presence of viscosity produces a boundary layer close to the particle surface that rotates together with the particle. When the rotating particle also moves with a translational velocity, an asymmetry in the flow is produced. In particular, on one side of the particle the velocity coming from rotation is added to the one coming from translation, while on the opposite side the

two contributions are subtracted. The velocity difference is converted into a pressure difference via Bernoulli principle, producing as a consequence a lift force (see [196] and next section). Therefore, both in the inviscid and the viscous case the Magnus effect is induced by Bernoulli pressure. The difference is that in a viscous fluid the circulation results from the rotation of the particle which carries the fluid close to its boundary, and could not be possible in absence of viscosity. Conversely, in a perfect fluid the rotation of an object does not have any effect on the sourrunding flow and the circulation around it must be triggered by another independent mechanism, which is indeed the presence of a vortex filament.

2.2.4 Viscous effects

When the viscous dissipation is present in a classical fluid described by the incompressible Navier–Stokes equations (2.1) and (2.2), the derivation of the equation of motion for the particle becomes much more complex, requiring further approximations besides the smallness of the flow inhomogeneity at the particle scale[1] (2.6) [150, 152]. Firstly, the no-slip boundary condition must be satisfied at the particle boundary:

$$\boldsymbol{w}(\boldsymbol{x}') = \boldsymbol{\Omega} \times \boldsymbol{x}', \qquad \forall \boldsymbol{x}' \text{ s.t. } |\boldsymbol{x}'| = |\boldsymbol{x} - \boldsymbol{q}| = a_\mathrm{p}, \tag{2.30}$$

where $\boldsymbol{\Omega}$ is the angular velocity of the sphere and the usual notation $\boldsymbol{w} = \boldsymbol{v} - \dot{\boldsymbol{q}}$ for the flow in the coordinate system comoving with the particle is used. An anlytical treatment of the problem has been performed in [150] in the case of a creeping flow. In particular, we can decompose the velocity field as

$$\boldsymbol{w} = \boldsymbol{w}_0 + \boldsymbol{w}_1, \tag{2.31}$$

where $\boldsymbol{w}_0$ is the undisturbed flow and $\boldsymbol{w}_1$ is the term arising because of the presence of the particle. Then, the advective terms in the equation for $\boldsymbol{w}_1$ can be neglected if the particle Reynolds number tends to zero:

$$\mathrm{Re}_\mathrm{p} = \frac{a_\mathrm{p} \boldsymbol{w}_0(\boldsymbol{0})}{\nu} \ll 1. \tag{2.32}$$

Note that the condition (2.32) is generally satisfied in the typical particle tracking experiments, in both classical and quantum fluids [208]. The equation of motion obtained in [150] is

$$M_\mathrm{eff} \ddot{\boldsymbol{q}} = \left(M_\mathrm{p} - M_0\right) \tilde{\boldsymbol{g}} + M_0 \left.\frac{D\boldsymbol{v}_0}{Dt}\right|_{\boldsymbol{q}} + C_\mathrm{a} M_0 \left.\frac{\mathrm{d}\boldsymbol{v}_0}{\mathrm{d}t}\right|_{\boldsymbol{q}} + \boldsymbol{F}_\mathrm{drag} + \boldsymbol{F}_\text{Faxén} + \boldsymbol{F}_\text{Basset}. \tag{2.33}$$

The immediate consequence of the creeping flow condition (2.32) is that the fluid acceleration term $C_\mathrm{a} \left.(D\boldsymbol{v}_0/Dt)\right|_{\boldsymbol{q}}$ in the inviscid case (2.20) has been substituted with

[1] Note that in turbulent flows, this condition implies that the particle size must be smaller than the Kolmogorov length scale $\eta = (\nu^3/\epsilon_\mathrm{d})^{1/4}$, where ϵ_d is the dissipation rate.

$C_a\ (\mathrm{d}\boldsymbol{v}_0/\mathrm{d}t)|_{\boldsymbol{q}}$, where now the total derivative follows the particle trajectory $\mathrm{d}/\mathrm{d}t = \partial/\partial t + (\dot{\boldsymbol{q}}\cdot\nabla)$. However, the added mass coefficient C_a remains the same, only depending on the geometry of the particle. It has been proposed that in the case of an arbitrary viscous inhomogenoeus flow, the generalization of Eq. (2.33) should contain the material derivative D/Dt, in analogy with the inviscid case (2.20) [152].

Several new forces emerge in the dynamics of a sphere in a viscous fluid. At low particle Reynolds number, the dominant one is the Stokes drag

$$\boldsymbol{F}_{\mathrm{drag}} = 6\pi\rho a_p \nu\,(\boldsymbol{v}_0(\boldsymbol{q}) - \dot{\boldsymbol{q}})\,, \tag{2.34}$$

whose effect is to align the particle velocity to the flow velocity.

The Faxén corrections arise because of the local inhomogeneities of the undisturbed flow:

$$\boldsymbol{F}_{\mathrm{Faxén}} = \frac{C_a}{10} M_0 a_p^2 \frac{\mathrm{d}}{\mathrm{d}t}\,\nabla^2\boldsymbol{v}\big|_{\boldsymbol{q}} + \pi\rho a_p \nu\,\nabla^2\boldsymbol{v}\big|_{\boldsymbol{q}}\,, \tag{2.35}$$

and it is of order $\mathcal{O}(a_p^2/\ell_f^2 \boldsymbol{F}_{\mathrm{drag}})$, where ℓ_f is the length scale of the fluid motion. In turbulent flow it is equal to the Kolmogorov dissipative scale η, so that the Faxén correction is generally neglected if $a_p < \eta$.

The Basset history term takes into account the time lag in the development of the viscous boundary layer as the relative particle-fluid velocity varies with time:

$$\boldsymbol{F}_{\mathrm{Basset}} = 6\pi\rho a_p \nu \int_{-\infty}^{t} K(t-t',t')\,\frac{\mathrm{d}}{\mathrm{d}t'}\left[\boldsymbol{v}_0(\boldsymbol{q}(t'),t') - \dot{\boldsymbol{q}}(t') + \frac{1}{6}a_p^2\,\nabla^2\boldsymbol{v}\big|_{\boldsymbol{q}}\right]\mathrm{d}t', \tag{2.36}$$

with the kernel $K(t-t',t') = a_p/\sqrt{\pi\nu(t-t')}$ for short times. The analysis of these terms at larger times has been developed in [110]. If the viscous relaxation time

$$\tau_p = \frac{a_p^2(2\mathscr{M}+1)}{9\nu}, \tag{2.37}$$

is shorter than the timescale of the fluid motion τ_f, then the Basset hystory term can be neglected. In turbulent flows, this means that the viscous relaxation time must be smaller than the Kolmogorov dissipative timescale $\tau_p < \tau_f = \tau_\eta = (\nu/\epsilon_d)^{1/2}$.

When Stokes drag is the only non negligible viscous effect, the equation of motion of the particle can be written in the compact form

$$\ddot{\boldsymbol{q}} = \gamma_p\tilde{\boldsymbol{g}} + \beta_p\,\frac{D\boldsymbol{v}_0}{Dt}\bigg|_{\boldsymbol{q}} + \frac{1}{\tau_p}\,(\boldsymbol{v}_n(\boldsymbol{q}) - \dot{\boldsymbol{q}})\,, \tag{2.38}$$

where the parameters

$$\gamma_p = \frac{2\mathscr{M}-2}{2\mathscr{M}+1} \qquad \text{and} \qquad \beta_p = \frac{3}{2\mathscr{M}+1} \tag{2.39}$$

account for the inertial effects. If $\tau_p/\tau_f \ll 1/\beta_p$ and $\tau_p/\tau_f \ll 1/\gamma_p$ then the drag force (2.34) is dominant with respect to all the other terms and we obtain the equation of

motion for a heavy particle

$$\ddot{\boldsymbol{q}} = \frac{1}{\tau_\mathrm{p}} \left(\boldsymbol{v}_0(\boldsymbol{q}) - \dot{\boldsymbol{q}} \right) , \tag{2.40}$$

which gets aligned to the fluid velocity exponentially fast, with a characteristic time τ_p. Eventually, when the relaxation time τ_p is so short to be negligible compared with the shortest timescale of the flow, then the left hand side of Eq. (2.40) can be set to zero and one recovers the equation for a tracer (2.24).

Note that other subleading terms have been neglected in (2.33), like the Saffman lift in presence of high shear [198], which become more important when the particle Reynolds number is larger and are out of the scope of this Thesis. We just mention that among these extra terms we find also the viscous Magnus force, mentioned in the end of the previous section, which arises because of the asymmetry in the flow close to the surface of a rotating particle. If both the particle Reynolds number (2.32) and the rotational Reynolds number $4|\boldsymbol{\Omega}|a_\mathrm{p}^2/\nu$ are small, such lift force reads [196]:

$$\boldsymbol{F}_{\boldsymbol{\Omega}} = -\rho\pi a_\mathrm{p}^3 \boldsymbol{\Omega} \times \left(\boldsymbol{v}(\boldsymbol{q}) - \dot{\boldsymbol{q}} \right) , \tag{2.41}$$

and must not be confused with the Magnus force in absence of viscosity (2.29), which is independent of the particle spin $\boldsymbol{\Omega}$.

We finally mention that the use of particles to study the Lagrangian properties of (classical) turbulent flows has seen an important development during the last 30 years, thanks to the introduction of fast cameras and particle tracking techniques [222]. From the theoretical side, the behaviour of particles in turbulent flows has been thoroughly investigated as well [61]. In particular, many studies focused on the transition from the ballistic regime of particle pairs dispersion (in which the squared separation scales as t^2) to the Richardson regime (in which the squared separation scales as t^3, accordingly to the Kolmogorov theory) [21, 200, 202]. Moreover, the preferential concentration of particles in turbulent flows has been extensively studied [36]: for instance, in the case of heavy particles it was observed that they form fractal clusters in the dissipative range [20]. In general, the amount of results for classical Lagrangian turbulence is huge compared to the quantum case. In the next section we will present the main theoretical and numerical models developed to understand the dynamics of particles in superfluids and quantum turbulence.

2.3 Models for particles in quantum fluids

Now we outline the models which have been used to describe theoretically and numerically the motion of particles in superfluids. The analytical treatment of the classical hydrodynamical problem prompted in the previous section will serve as a guidance for comparison and analogies, both here and in the results presented later.

2.3.1 One-way coupling

The equations for the dynamics of spherical particles in a classical fluid can be straightforwardly generalized to superfluids in the case in which the particles are passive (they do not modify the flow properties), they are small compared to the scale of the flow variation, and do not interact strongly with quantized vortices. The last condition in particular implies that particles are not trapped into vortex lines and do not interfere with their dynamics. Such assumptions are rather constraining, being satisfied for those flows in which both the Kolmogorov length scale and the mean inter-vortex distance are much larger than the particle size [181, 208]. If this is the case, the equation of motion of the particle at finite temperature can be written collecting the force terms coming from both the superfluid and the normal fluid component, which have respectively densities ρ_s and ρ_n, and velocities $\boldsymbol{v}_\mathrm{s}$ and $\boldsymbol{v}_\mathrm{n}$. The two components contribute equally to the body force $\boldsymbol{F}_\mathrm{g}$ (2.23) and the effective inertia M_eff (2.21). Being the superfluid irrotational and assuming no vortex trapping, the contribution of the superflow alone is only a Bernoulli fluid acceleration $\boldsymbol{F}^{(\mathrm{s})}_\mathrm{acc}$ (2.22). The normal fluid also contributes with a term in the form $\boldsymbol{F}^{(\mathrm{n})}_\mathrm{acc}$ (2.22), besides the viscous effects. Among the latter, at small particle Reynolds number only the Stokes drag $\boldsymbol{F}^{(\mathrm{n})}_\mathrm{drag}$ (2.34) is taken into account. Eventually the equation of motion for the particle in this one-way coupling model reads [181, 208]:

$$
\begin{aligned}
M_\mathrm{eff}\ddot{\boldsymbol{q}} \;&=\; \boldsymbol{F}_\mathrm{g} + \boldsymbol{F}^{(\mathrm{s})}_\mathrm{acc} + \boldsymbol{F}^{(\mathrm{n})}_\mathrm{acc} + \boldsymbol{F}^{(\mathrm{n})}_\mathrm{drag} = \\
&\qquad (M_\mathrm{p} - M_0)\tilde{\boldsymbol{g}} + (C_\mathrm{a}+1)\,\Theta_\mathrm{p}\left[\rho_\mathrm{s}\left.\frac{D\boldsymbol{v}_\mathrm{s}}{Dt}\right|_{\boldsymbol{q}} + \rho_\mathrm{n}\left.\frac{D\boldsymbol{v}_\mathrm{n}}{Dt}\right|_{\boldsymbol{q}}\right] + 6\pi\rho_\mathrm{n}a_\mathrm{p}\nu\,(\boldsymbol{v}_\mathrm{n}(\boldsymbol{q}) - \dot{\boldsymbol{q}})\,,
\end{aligned}
\tag{2.42}
$$

where $\Theta_\mathrm{p} = \frac{4}{3}\pi a_\mathrm{p}^3$ is the volume of the particle and the displaced mass is computed with the total fluid density $M_0 = \Theta_\mathrm{p}\rho$ with $\rho = \rho_\mathrm{s} + \rho_\mathrm{n}$. Note that Eq. (2.42) implicitly assumes incompressibility, which is a good approximation for superfluid helium. An even more compact way of writing Eq. (2.42) is the following:

$$
\ddot{\boldsymbol{q}} = \gamma_\mathrm{p}\tilde{\boldsymbol{g}} + \beta_\mathrm{p}\left[\frac{\rho_\mathrm{s}}{\rho}\left.\frac{D\boldsymbol{v}_\mathrm{s}}{Dt}\right|_{\boldsymbol{q}} + \frac{\rho_\mathrm{n}}{\rho}\left.\frac{D\boldsymbol{v}_\mathrm{n}}{Dt}\right|_{\boldsymbol{q}}\right] + \frac{1}{\tau_\mathrm{p}}\,(\boldsymbol{v}_\mathrm{n}(\boldsymbol{q}) - \dot{\boldsymbol{q}})\,,
\tag{2.43}
$$

where the parameters γ_p and β_p are the same defined in the previous section in Eq. (2.39) and the viscous relaxation time τ_p (2.37) represents how fast the particle adjusts its motion to the normal flow. It is evident that the effect of superfluidity is the lack of a relaxation force aligning the particle velocity to the superflow. This fact was checked in the case of neutrally buoyant particles [181]. For these particles, with relative mass $\mathscr{M} = 1$, the effect of gravity is absent $\gamma_\mathrm{p} = 0$, as well as the added mass effect $\beta_\mathrm{p} = 1$:

$$
\ddot{\boldsymbol{q}} = \frac{\rho_\mathrm{s}}{\rho}\left.\frac{D\boldsymbol{v}_\mathrm{s}}{Dt}\right|_{\boldsymbol{q}} + \frac{\rho_\mathrm{n}}{\rho}\left.\frac{D\boldsymbol{v}_\mathrm{n}}{Dt}\right|_{\boldsymbol{q}} + \frac{1}{\tau_\mathrm{p}}\,(\boldsymbol{v}_\mathrm{n}(\boldsymbol{q}) - \dot{\boldsymbol{q}})\,.
\tag{2.44}
$$

Therefore, if the particle relaxation time τ_p is much shorter than the timescale of the fluid motion τ_f, particles behave as tracers of the normal fluid [181]. If $\tau_p \gtrsim \tau_f$, the force term coming from the fluid acceleration becomes important. Considering for example the simplest case in which the two fluids are locked $v_s = v_n = v$ (which is true if the mutual friction is high) , we get the equation

$$\ddot{\boldsymbol{q}} = \left.\frac{D\boldsymbol{v}}{Dt}\right|_{\boldsymbol{q}} + \frac{1}{\tau_p}\left(\boldsymbol{v}(\boldsymbol{q}) - \dot{\boldsymbol{q}}\right). \tag{2.45}$$

Such equation admits the formal solution $\dot{\boldsymbol{q}}(t) = \boldsymbol{v}(\boldsymbol{q}, t)$ with the initial condition $\dot{\boldsymbol{q}}(t_0) = \boldsymbol{v}(\boldsymbol{q}(t_0), t_0)$, meaning that in principle neutral particles could follow the flow. However it has been shown that this is not the case, since the particle trajectories are unstable and separate from the streamlines [181]. A similar situation occurs at zero temperature, when the normal fluid is absent. In particular, for neutral particles the equation of motion becomes the Eq. (2.24) already recovered for an incompressible, inviscid and irrotational fluid in which the particle acceleration equals the fluid acceleration. In such case, although in principle imposing the initial condition $\dot{\boldsymbol{q}}(t_0) = \boldsymbol{v}(\boldsymbol{q}(t_0), t_0)$ would allow the particles to trace the superflow, this is nevertheless impossible for finite-size particles. Indeed, when the particle velocity is aligned to the superfluid velocity, next orders in the parameter ϵ_p (2.6) become important and Eq. (2.24) is not a good description anymore. Such consideration applies perfectly to the setting of a particle placed far from a vortex line at very low temperature. The trajectories instability in this particular scenario has been pointed out by the Newcastle group [15] and recovered in the GP model in the publication [75], presented later in this manuscript.

As we will show later, particle trapping into quantum vortices seems to be the dominating mechanism at very low temperature. As a consequence, the one-way coupling is a suitable model if the temperature is sufficiently high and the inter-vortex distance is sufficiently large, so that the trapping of particles into quantized vortices is prevented. It has been shown, indeed, that the presence of a normal fluid can generate a viscous dipolar disturbance in the vicinity of a quantized vortex [103], which deflects the particle trajectory and avoid the capture [210]. Other numerical works showed that in specific settings, the use of a one-way coupling can be appropriate. In [116] a single vortex ring modeled with the Biot-Savart equation (1.143) with finite temperature correction collides with a plane sheet of neutrally buoyant particles. It is shown that less than the 5% of the particles is likely to get trapped, and the particle velocity is similar to the normal fluid one. An anologus result is shown in [112], where a counterflow with laminar normal fluid and a vortex tangle is simulated for temperatures larger than $T = 1.3\,\mathrm{K}$.

Recently, the equation of motion for inertial particles (2.44) has been simulated coupled with the Hall-Vinen-Bekarevich-Khalatnikov (HVBK) model [54], which is a coarse-grained set of equations, suitable to describe the large-scale motion of a turbulent superfluid at finite temperature. It consists of two coupled incompressible

Navier–Stokes equations for the velocity fields $\boldsymbol{v}_\mathrm{n}$ and $\boldsymbol{v}_\mathrm{s}$:

$$\frac{\partial \boldsymbol{v}_\mathrm{n}}{\partial t} + (\boldsymbol{v}_\mathrm{n}\cdot\nabla)\boldsymbol{v}_\mathrm{n} = -\frac{1}{\rho_\mathrm{n}}\nabla p_\mathrm{n} + \nu_\mathrm{n}\nabla^2\boldsymbol{v}_\mathrm{n} - \frac{\rho_\mathrm{s}}{\rho_\mathrm{n}}\boldsymbol{f}_\mathrm{ns} + \boldsymbol{\phi}_\mathrm{n} \tag{2.46}$$

$$\frac{\partial \boldsymbol{v}_\mathrm{s}}{\partial t} + (\boldsymbol{v}_\mathrm{s}\cdot\nabla)\boldsymbol{v}_\mathrm{s} = -\frac{1}{\rho_\mathrm{s}}\nabla p_\mathrm{s} + \nu_\mathrm{s}\nabla^2\boldsymbol{v}_\mathrm{s} + \boldsymbol{f}_\mathrm{ns} + \boldsymbol{\phi}_\mathrm{s} \tag{2.47}$$

$$\nabla\cdot\boldsymbol{v}_\mathrm{n} = \nabla\cdot\boldsymbol{v}_\mathrm{n} = 0, \tag{2.48}$$

where ν_n is the viscous dissipation of the normal fluid component and the effective superfluid viscosity ν_s accounts for energy dissipation at scales smaller than those resolved by the HVBK model, originating from quantum vortex reconnections and Kelvin wave excitation. The velocity fields are coupled by the mutual friction force $\boldsymbol{f}_\mathrm{ns} = \alpha\Omega_0(\boldsymbol{v}_\mathrm{n}-\boldsymbol{v}_\mathrm{s})$, where α is a temperature-dependent parameter, and Ω_0 is associated to the density of quantum vortices in the flow. The forcing terms $\boldsymbol{\phi}_\mathrm{n}$ and $\boldsymbol{f}_\mathrm{s}$ represent the stirring of the flow by an external mechanism. Studying such framework in a coflow turbulence regime, it was found that at sufficiently low temperature (small normal fluid fraction) particles cluster along vorticity filaments regardless their physical properties [179]. Instead, when the normal component is significant the distribution of particles is comparable to the case of heavy particles in classical turbulence [20]. A mean counterflow may be also imposed in the HVBK model by setting the average of the external forces to different values for each of the two fluids. In a strong counterflow regime, the particle distribution is compatible with a quasi-two-dimensionalization of the flow, consistent with the arising of an inverse cascade [178].

It is important to stress that a possible bias of all these numerical works is the absence of an active effect of the particles on the two fluids and on the quantum vortices, which could in principle modify the scenario. The model discussed in the following section does not present such issue, given that it is based precisely on the vortex-particle interaction.

2.3.2 Moving spherical boundaries in the vortex filament model

At low temperature, the chance that particles get captured by quantum vortices seems to be rather high, as we will see many times in the course of this Thesis and given the experimental signatures mentioned in section 2.1 . Therefore, the development of models which take into account the mutual interaction between particles and superfluid vortices is needed. The most straightforward approach to challenge this issue is probably the one devised by the Newcastle group, which implemented particles as moving boundary conditions of the vortex filament model [15, 113–115, 117, 119], developing theoretically and numerically the seminal calculations by Schwarz [203]. This model consists of two coupled equations of motion, one for the particle and one for the vortex. The latter is the standard equation of a vortex filament described as a parametrized curve $\boldsymbol{s}(\xi_\mathrm{a}, t)$ (1.143) (see section 1.4.1), modified for taking into account

the presence of a sphere, together with finite temperature effects:

$$\dot{\boldsymbol{s}} = \boldsymbol{v}_{\mathrm{BS}}(\boldsymbol{s}) + \boldsymbol{v}_{\mathrm{b}}(\boldsymbol{s}, \boldsymbol{q}) + \boldsymbol{v}_{\mathrm{p}}(\boldsymbol{s}, \boldsymbol{q}, \dot{\boldsymbol{q}}) + \boldsymbol{v}_{\mathrm{mf}}(\boldsymbol{s}, \boldsymbol{q}, \dot{\boldsymbol{q}}). \tag{2.49}$$

The component $\boldsymbol{v}_{\mathrm{b}}$ represents the effect of the presence of a static sphere at the boundary of the filament, and it is determined by the free slip boundary condition at the surface of the particle:

$$(\boldsymbol{v}_{\mathrm{BS}}(\boldsymbol{x}) + \boldsymbol{v}_{\mathrm{b}}(\boldsymbol{x}, \boldsymbol{q})) \cdot \hat{\boldsymbol{n}} = 0, \qquad \forall \boldsymbol{x} \text{ s.t. } |\boldsymbol{x} - \boldsymbol{q}| = a_{\mathrm{p}}. \tag{2.50}$$

The component $\boldsymbol{v}_{\mathrm{p}} = \nabla \phi_{\mathrm{p}}$ is the standard potential flow induced by a moving sphere in a homogeneous fluid (2.11) evaluated along the filament. Finally, the term $\boldsymbol{v}_{\mathrm{mf}}$ accounts for the mutual friction of the the filament with the thermal excitations of the normal fluid component. It is given by the the formula (1.159) where the bulk superflow $\boldsymbol{v}_{s,0}$ includes now the boundary conditions due to the particle: $\boldsymbol{v}_{s,0} = \boldsymbol{v}_{\mathrm{b}} + \boldsymbol{v}_{\mathrm{p}}$. The corresponding equation of motion for the spherical particle results from the integration of the fluid stress stensor (2.5) in the particular case of the flow generated by vortex - sphere system just described:

$$M_{\mathrm{eff}} \ddot{\boldsymbol{q}} = (C_{\mathrm{a}} + 1)\, \Theta_{\mathrm{p}} \rho_{\mathrm{s}} \left. \frac{\partial \boldsymbol{v}_{\mathrm{BS}}}{\partial t} \right|_{q} + 6\pi \rho_{\mathrm{n}} a_{\mathrm{p}} \nu\, (\boldsymbol{v}_{\mathrm{n}}(\boldsymbol{q}) - \dot{\boldsymbol{q}}) + \frac{1}{2} \int_{\partial \mathbb{B}} |\boldsymbol{v}_{BS} + \boldsymbol{v}_{\mathrm{b}}|^2\, \hat{\boldsymbol{n}}\, \mathrm{d}\Sigma. \tag{2.51}$$

Note that in this model gravity forces are neglected and Stokes drag is assumed to be the only normal fluid force which affects directly the particle dynamics. The last term of Eq. (2.51) is a novel contribution to the particle dynamics, which is the direct expression of the vortex-particle interaction.

One of the main applications in which the vortex filament method has been adopted is the numerical study of the collision between a finite size neutral particle and a quantum vortex at finite temperature[2] [15, 113, 118–120]. Although the coupled equations (2.49) and (2.51) describe self-consistently the interaction between a particle and a vortex when they are well separated, the process of capture needs to be implemented with an ad-hoc numerical mechanism. Indeed, given the singular nature of the Biot–Savart integral, the reconnection between the filament and the sphere is not reproduced by the model. The algorithm developed in [113] for this purpose entails that, if the particle-vortex distance is smaller than the mesh-size on the filament, extra vortex points need to be added on the particle surface as well as inside the sphere. Then, the system composed by the vortex and the trapped particle is treated as a single filament and also the particle detachement is mimicked with an analogous scheme.

A typical simulation of the vortex filament model for the collision problem is displayed in Fig. 2.6, in which the particle is shot towards the vortex at high velocity [119]. When the particle gets trapped by the vortex, the generation of Kelvin waves along the filament can be observed. Subsequently, the particle drags the vortex, producing a

[2] We refer to chapter 3 for a treatment in greater detail of the fundamental problem of particle capture by a superfluid vortex, where we present analytical calculations supported by GP simulations.

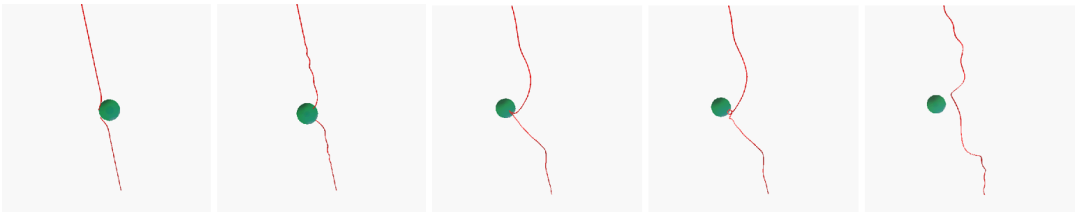


Figure 2.6. Collision between a neutral particle and a vortex in the vortex filament method coupled with hard spheres. The temperature is $T = 1.3\,K$, the particle size is $1\,\mu m$ and the initial velocity of the particle is $25\,cm/s$. Images taken from [119] to which we refer for further details.

stretching of the strands attached to it. These become closer until a self-reconnection of the filament is produced and the particle is finally released with the generation of a small ring. In other simulations of the same setting but with a smaller initial particle velocity, it has been observed that the particle does not escape but remains attached to the filament [119]. The authors suggested the existence of a critical initial particle velocity (proportional to temperature and inversely proportional to the sphere radius) above which the particles always escapes from the vortex. It has been noticed, however, that such velocities are pretty high and therefore constitute extreme events in typical flows [208]. Moreover, in [113] it is prompted that the occurrence of capture events depends strongly on the damping force exerted by the fluid on the particles, that is basically viscous drag present at finite temperature. As a consequence, at very low temperature capture events should be prevented. However, in the publication [76], to which chapter 5 is dedicated, we observed that in a zero temperature quantum turbulence regime modeled by the GP equation, the majority of particles remains trapped, with just sporadic episodes of particle detachement and recapture.

The motion of a single particle in a thermal counterflow and in presence of a vortex tangle has been also investigated using the vortex filament model [115], in support of the PIV experiment [250] discussed in section 2.1. Such situation has been mimicked by considering v_n in Eq. (2.49) and (2.51) as a prescribed normal fluid counterflow velocity. The result of the computation in [115] is that for low counterflow velocities and a dilute tangle, the particle can sample the normal fluid. Some deviations due to the interactions with the filaments are detected, but never larger than the 4% of the normal fluid velocity. At the same time, it has been shown that if the number of particles is too large (as it is the case in PIV experiments) the properties of the tangle can be drastically modified [227]. In particular, the vortex line density can increase and the polarization of the tangle can be affected. Indeed, counterflow tangles are typically partially polarized, because of the mutual friction that tends to organize them orthogonally to the stream-wise direction. The presence of particles reduces the anysotropy between the vortex line density in the transverse and in the stream-wise direction [16]. The reason of such behaviour can be traced back to the effect of Stokes drag, that aligning the particle velocities to the normal flow, allows them to strech the vortex lines in the stream-wise direction.

We finally mention that another effect observed in simulations of the vortex filament

model is a drift of particles along a vortex, once they get stably trapped by the filament [118]. For a neutrally buoyant, micron-sized particle the drift velocity is $\sim 0.5 cm/s$, and it has been associated with a momentum transfer between the Kelvin waves present along the vortex and the particle. Of course, this is the case if an asymmetry of Kelvin waves with respect to the particle is present. Otherwise the net drift is expected to be zero, as it has been observed for instance in GP simulations [79].

In conclusion, the vortex filament model has been certainly the main tool for the investigation of the particle dynamics in (finite temperature) superfluids during the last two decades. Although such method enables for the use of particles having a size comparable with the current liquid helium experiments, obvious limitations are the intrinsic presence of a numerical cutoff in the system and the fact that both reconnections and particle trapping must be added with ad-hoc numerical mechanisms. For these reasons, other models based on the GP equation have been recently adopted, in which quantized vortices, reconnections and interaction with the particle are self-consistently included. We will discuss these models in the remainder of this chapter.

2.3.3 Particles coupled with the Gross–Pitaevskii model

In this pivotal section of the manuscript, we introduce the model that has been used to achieve the results reported in the following chapters. The first appearance of a model based on the Gross–Pitaevskii equation, in which particles are described as repulsive potentials dates back to the 1958 milestone work by Gross himself [89]. The physical intuition behind such method is actually very simple and therefore powerful. It lies in the observation that from the perspective of the superfluid, a finite-size particle is nothing but an extended region of space where the fluid is fully depleted. In the language of the GP framework this is equivalent to ask that the macroscopic wavefunction ψ must vanish inside the particle (we refer to section 1.3 for more details on the GP model). Instead of imposing by hand such constraint as a boundary condition, the same result can be achieved considering as external potential of the GP model (1.57) a highly repulsive potential $V_{\text{ext}}(\boldsymbol{x}, t) = V_{\text{p}}(\boldsymbol{x}, \boldsymbol{q}(t))$, localized around the position $\boldsymbol{q}(t)$. The effect of this potential is indeed to deplete the wavefunction in all the regions where $V_{\text{p}} > \mu$, so that if its functional form has a compact support, it can actually mimic a localized object. The point $\boldsymbol{q}(t)$ plays the role of the particle position and if the potential is isotropic, it coincides with its center. Note that the precise functional shape of the potential is in general not crucial, provided that it extends for a distance larger than the healing length (where its strength must be larger than the chemical potential), and that it drops rapidly to zero at the particle boundaries (say in a distance of the order of ξ). A typical particle potential that has been used in the results reported in the next chapters is the isotropic smoothed hat function:

$$V_{\text{p}}(r) = \frac{V_0}{2}\left(1 - \tanh\left[\frac{r^2 - \zeta_{\text{p}}^2}{4\Delta_{\text{p}}^2}\right]\right), \tag{2.52}$$

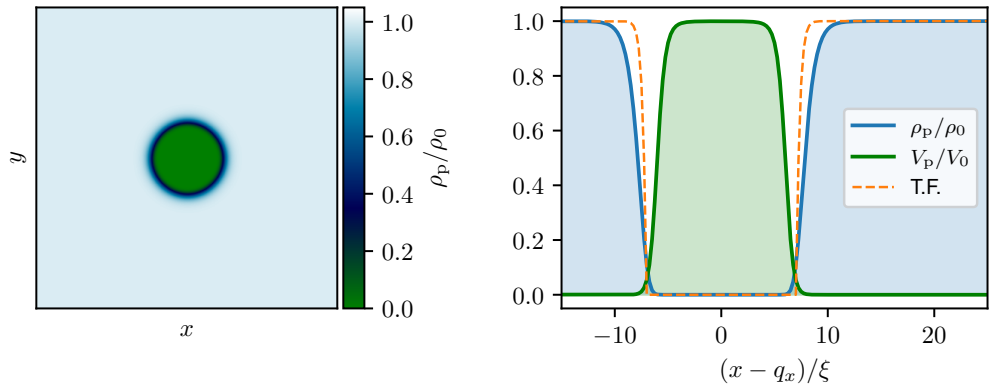


Figure 2.7. Ground state of the GP equation with a particle modeled as a repulsive potential. (*left*) 2D slice of the GP density passing through the particle center. (*right*) Corresponding density profile along the x direction (solid blue), and Thomas–Fermi approximation (dashed orange). In green the particle potential (2.52), with the parameters $V_0 = 20\mu$, $\zeta_p = 6\xi$ and $\Delta_p = 1.5\xi$. The other parameters of the calculation are $N_c = 256$ collocation points per side, box size $L = 2\pi$ and healing length $\xi = 4L/N_c$.

where the parameters ζ_p and Δ_p are related respectively to the boundary size and the core size of the particle. We refer to the Appendix for further details on the parameters and the numerical implementation of the particles. In the left side of Fig. 2.7 we see a bidimensional slice of the GP density $\rho_p = m|\psi_p|^2$, corresponding to the ground state ψ_p containing one particle modeled in this way. The ground state is obtained as usual using the gradient descent method. In the right side, the corresponding density profile in the x direction (solid blue line) is compared with the Thomas–Fermi approximation (1.98), computed taking $V_{ext} = V_p$ (dashed orange line). The potential (2.52), which repels the fluid density inside the particle is displayed in green. Note how the density profile passes smoothly from zero (in the region occupied by the particle) to the bulk value ρ_0 in a distance of approximately one healing length. This behaviour does not depend on the particle potential but it is an unavoidable occurrence in the GP model, given the intrinsic dispersion of the system. We stress that particles modeled in this way are by definition active particles, since they emerge from an interaction potential coupled with the fluid.

The GP model with hard localized potentials has been initally used without giving any degree of freedom to the potential center (i.e. fixing $\boldsymbol{q}(t) = \boldsymbol{q} = \text{cost}$) to study the vortex nucleation or the acceleration of an object immersed in a quantum fluid [67, 101, 165, 243–245]. It allowed to measure the critical velocity for which the superfluidity is broken and a non-zero drag appears, as well as to show that it is related to the emission of vortex dipoles (for a circle in 2D) and vortex rings (for a sphere in 3D). In this last case, three possible stationary solutions have been found for a given sub-critical relative velocity between the condensate and the obstacle [244]. The lowest energy state is the laminar flow, the middle energy state consists in a vortex ring pinned by

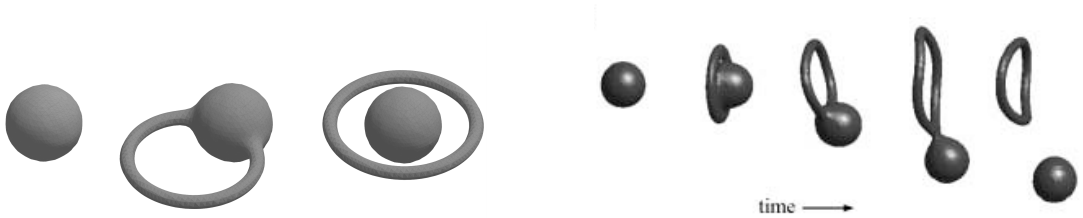


Figure 2.8. (*left*) The three stationary solutions (laminar flow, pinned ring and encircling ring) of the GP model with highly repulsive isotropic obstacle. Figure taken from [244] to which we refer for further details. (*right*) Dynamical evolution of the GP model coupled with a repulsive particle (2.53). The particle is subjected to a constant force towards the horizontal direction, slightly tilted to break the symmetry. Figure taken from [242] to which we refer for further details.

the particle, and the highest level is a particle encircled by a ring (see Fig. 2.8 left). For high velocities the pinned ring and the encircling ring solution are indistinguishable and a bifurcation between the two appears at a certain (sub-critical) speed, whose value depends on the obstacle size.

The effective dynamics of a finite size particle within this GP approach was first investigated 20 years ago in a seminal work by Winiecki and Adams [242], where the GP fluid back-action on the particle was included. The Hamiltonian of such system, including the chemical potential as in (1.118), is

$$H = \frac{\boldsymbol{p}^2}{2M_{\rm p}} + \int \left(\frac{\hbar^2}{2m}|\boldsymbol{\nabla}\psi|^2 + \frac{g}{2}|\psi|^4 - \mu|\psi|^2 + V_{\rm p}\left(|\boldsymbol{x}-\boldsymbol{q}(t)|\right)|\psi|^2 \right) \mathrm{d}\boldsymbol{x}, \tag{2.53}$$

where the position $\boldsymbol{q}(t)$ of the particle is now a time dependent degree of freedom and where the first term is its kinetic energy, quadratic in the particle momentum $\boldsymbol{p} = M_{\rm p}\dot{\boldsymbol{q}}(\boldsymbol{t})$. The associated Hamilton equations can be derived straightforwardly, variating with respect to the degrees of freedom:

$$i\hbar\frac{\partial}{\partial t}\psi(\boldsymbol{x},t) = \left[-\frac{\hbar^2}{2m}\nabla^2 + g|\psi(\boldsymbol{x},t)|^2 - \mu + V_{\rm p}\left(|\boldsymbol{x}-\boldsymbol{q}(t)|\right)\right]\psi(\boldsymbol{x},t) \tag{2.54}$$

$$M_{\rm p}\ddot{\boldsymbol{q}} = -\int V_{\rm p}\left(\boldsymbol{x}-\boldsymbol{q}(t)\right)\nabla|\psi(\boldsymbol{x},t)|^2\,\mathrm{d}\boldsymbol{x}. \tag{2.55}$$

The first equation is the standard GP equation, while the second one is a Newton equation for the particle position, for which the force term is given by the convolution between the particle potential and the gradient of the superfluid density. The physical meaning of Eq. (2.55) can be somehow appreciated considering the limit of a point-particle, namely substituting the particle potential with a Dirac delta $V_{\rm p} = g_{\rm p}\delta(\boldsymbol{x}-\boldsymbol{q}(t))$, where $g_{\rm p}$ is a coupling constant. In this case the equation for the particle becomes

$$M_{\rm p}\ddot{\boldsymbol{q}} = -\mu\frac{g_{\rm p}}{g}\nabla\left(\frac{\rho}{\rho_0}\right)\Big|_{\boldsymbol{q}} = -m\frac{g_{\rm p}}{g}\nabla\left(\frac{p_{\rm cl}}{\rho}\right)\Big|_{\boldsymbol{q}} \tag{2.56}$$

where $p_{\rm cl}$ is the classical pressure of a barotropic fluid (1.117). Therefore, it is clear that also the force in the right hand side of Eq. (2.55) is a hydrodynamical force related to the classical pressure gradient, and the convolution with the particle potential just takes into account the finite size effects. The equation (2.56) coupled with GP has been studied by Pitaevskii and Astrakharchik, who found that even point particles feel a drag when they travel at supersonic speed because of the Cherenkov radiation of phonons [5].

Getting back to the case of finite-size particles, in their pioneering article [242] Winiecki and Adams observed that the time-dependent evolution of the particle velocity is indeed consistent with the steady states classified in [244]. Their procedure consisted in adding an extra constant force $\boldsymbol{F}_{\rm ext}$ in the right-hand-side of the equation for the particle (2.55), in order to dynamically variates its momentum as time passes. As displayed in Fig. 2.8 right the transition between laminar and pinned state was detected at the critical speed. Moreover, it was observed that the interaction between the particle and the generated ring induces perturbations on the vortex itself, which in turn affect the motion of the sphere. This was one of the first numerical evidences of the back-action of the quantum fluid on the sphere, which is entirely due to the interaction between the particle and the superfluid and it is encoded in the coupling between the condensate wavefunction and the particle potential.

In recent years, other works explored further the phenomenology of such interactions, in particular in the case where many particles are present in the system. In [212] the existence of an attractive interaction between particles immersed in the GP fluid was investigated. The attraction is mediated by the presence of the superfluid and it is a consequence of the density gradients originated by the particle potential. A downside of such effect is that adding more particles to the model (2.53) would in principle lead to the collapse of all the them. The state in which the potentials overlap with each other is indeed an optimal configuration for the energy of the system. A technique to avoid such unphysical occurrence has been implented already in [212] and consists in the introduction of an interaction potential between the particles, which mimics a hard sphere repulsion. In the case of $N_{\rm p}$ particles immersed in the system, the modified GP Hamiltonian reads:

$$\begin{aligned} H &= \int \left(\frac{\hbar^2}{2m} |\nabla \psi|^2 + \frac{g}{2} \left(|\psi|^2 - \frac{\mu}{g} \right)^2 + \sum_{i=1}^{N_{\rm p}} V_{\rm p}(|\boldsymbol{x} - \boldsymbol{q}_i|) |\psi|^2 \right) \mathrm{d}\boldsymbol{x} \\ &+ \sum_{i=1}^{N_{\rm p}} \frac{\boldsymbol{p}_i^2}{2M_{\rm p}} + \sum_{i<j}^{N_{\rm p}} V_{\rm rep}^{ij}, \end{aligned} \tag{2.57}$$

where the new potential $V_{\rm rep}^{ij}$ is indeed a repulsive interaction between each couple of particles (labelled by i and j). Also in this case, its exact functional shape is not crucial, provided that it is highly repulsive and short range, so that its only effect is to avoid the particle overlap. Typically, a good choice is the repulsive part of the Lennard–Jones

potential used in molecular physics [105]:

$$V_{\rm rep}^{ij} = \gamma_{\rm rep}\mu\left(\frac{2r_{\rm rep}}{|\boldsymbol{q}_i - \boldsymbol{q}_j|}\right)^{12}, \tag{2.58}$$

where $2r_{\rm rep}$ is the range at which the repulsion starts to act and $\gamma_{\rm rep}$ is an adjusting numerical pre-factor (see the Appendix A) for further details). Typically the length $2r_{\rm rep}$ is set equal to the particle diameter. In this way the overlap is prevented but particles can still collide. In some other cases it is interesting to study specific effects due to larger or smaller repulsion (as in the publications [80] and [79] reported in sections 4.1 and 6.3). In particular, if the repulsion range is sufficiently short, particles can form compact clusters even at finite temperature **??**.

We report here for completeness the equations associated with the Hamiltonian (2.57) with many particles, which are a straightforward generalization of Eqs. (2.54) and (2.55):

$$i\hbar\frac{\partial}{\partial t}\psi(\boldsymbol{x},t) = \left[-\frac{\hbar^2}{2m}\nabla^2 + g|\psi(\boldsymbol{x},t)|^2 - \mu + \sum_{i=1}^{N_{\rm p}} V_{\rm p}\left(|\boldsymbol{x}-\boldsymbol{q}_i(t)|\right)\right]\psi(\boldsymbol{x},t) \tag{2.59}$$

$$M_{\rm p}\ddot{\boldsymbol{q}}_i = -\int V_{\rm p}\left(\boldsymbol{x}-\boldsymbol{q}_i(t)\right)\nabla|\psi(\boldsymbol{x},t)|^2\,{\rm d}\boldsymbol{x} - \sum_{j\neq i}^{N_{\rm p}}\frac{\partial}{\partial \boldsymbol{q}_i}V_{\rm rep}^{ij}. \tag{2.60}$$

The full model (2.57) has been further used to study the interaction between particles and vortices in 2D [214], extending a previous work with static obstacles [87]. In particular, it was elighted how the dynamics of particles can easily become chaotic, as well as the tendency of particles to be captured by vortices, even when the system is highly perturbed. Always in the bidimensional case of the model (2.57), it was recently shown that a dynamics based on Magnus force (2.29) drives vortex dipoles loaded with massive particles [88]. For what concerns the dynamics described by the model (2.57) in three dimension, we refer to the original results reported in the chapters 3,4 and 5 of the present manuscript. Finally, in chapter 6, we use the same model combined with the truncation technique in order to study the motion of impurities in a quantum fluid at finite temperature.

We specify that in all the works presented in this Thesis we considered a spherical particle and without any rotational degree of freedom. This choice allows us to keep the model minimal. Of course, a generalization of the model discussed here could take into account an arbitrary shape for the particle. Studies in this direction may be justified by the actual suspect of some anysotropy existing in the particles used in liquid helium experiments. For instance, some angular momentum exchanged when an elongated particle is trapped by a vortex may be identified. Here we propose the simplest generalization of a spherical particle, which consists in an axisymmetric ellipsoid. Calling $\hat{\boldsymbol{n}} = (\sin\theta\cos\phi, \sin\theta\sin\phi, \cos\theta)$ the orientation unit vector of the

ellipsoid symmetry axis, a Gaussian potential for the particle would read

$$V_{\mathrm{p}}(\boldsymbol{x}-\boldsymbol{q},\hat{\boldsymbol{n}}) = V_0 \exp\left\{\left(-\frac{(\boldsymbol{r}\cdot\hat{\boldsymbol{n}})^2}{2a_{\parallel}^2} - \frac{|\boldsymbol{r}-(\boldsymbol{r}\cdot\hat{\boldsymbol{n}})\hat{\boldsymbol{n}}|^2}{2a_{\perp}^2}\right)\right\}, \tag{2.61}$$

where $\boldsymbol{r} = \boldsymbol{x}-\boldsymbol{q}$ (with $\boldsymbol{q}$ the centroid of the ellipsoid) and where $a_{\parallel}$ and $a_{\perp}$ are the lengths of the principal axis (parallel and orthogonal to the symmetry axis, respectively). The new rotational degrees of freedom are $\theta(t)$ (which is the angle between the z axis and $\hat{\boldsymbol{n}}$) and $\phi(t)$ (which is the angle between the x axis and the plane where $\boldsymbol{n}$ lies). Thus, a rotational kinetic energy term must be added to the Lagrangian of the system [82]:

$$E_{\mathrm{kin}}^{\mathrm{rot}}(\theta,\phi) = \frac{I_{\perp}}{2}\left(\dot{\phi}^2\sin^2\theta + \dot{\theta}^2\right) + I_{\parallel}\left(\dot{\phi}\cos\theta\right)^2, \tag{2.62}$$

where $I_{\parallel} = \frac{1}{10}M_{\mathrm{p}}\left(a_{\perp}^2 + a_{\parallel}^2\right)$ and $I_{\perp} = \frac{1}{5}M_{\mathrm{p}}\left(a_{\perp}^2\right)$ are the moments of inertia respectively along the axis $\hat{\boldsymbol{n}}$ and orthogonal to it. Note that these are also the only parameters that would change if an axisymmetric particle with an arbitrary shape is considered. Then, the Hamiltonian of the system is the same as (2.53) with the additional term (2.62), where $\dot{\theta}$ and $\dot{\phi}$ must be expressed in terms of the canonical moments associated to the variables θ and ϕ.

2.3.4 Bubble fields and multi-component condensates

In this last section, we mention another technique that has been used to model particles and impurities in the Gross–Pitaevskii framework. It appeared for the first time in the 1958 article by Gross mentioned in the previous section [89], and was shortly after resumed by Clark [41] as a theoretical support of the electron bubble technique for probing superfluid helium (see section 2.1.1). In this Gross–Clark model a particle is not simply described as a single classical degree of freedom, but instead as a full field driven by a partial differential equation. In particular, the motion of an electron in a quantum fluid can be described by a linear Schrödinger equation for the electron wavefunction ϕ coupled with the mean field equation for the condensate wavefunction ψ. Explicitly, the Hamiltonian of the system is

$$H = \int\left(\frac{\hbar^2}{2m_1}|\nabla\psi|^2 + \frac{g_1}{2}|\psi|^4 - \mu_1|\psi|^2 + \frac{\hbar^2}{2m_2}|\nabla\phi|^2 - \mu_2|\phi|^2 + g_{12}|\phi|^2|\psi|^2\right)\mathrm{d}\boldsymbol{x}, \tag{2.63}$$

where m_1 is the mass of the condensed bosons, m_2 is the mass of the impurity atom (the electron), μ_1 is the energy (per atom) of the condensate and μ_2 the energy of the impurity. The coupling constant of the repulsive interaction between the condensate and the impurity is denoted by $g_{12} < 0$, assuming a local interaction. The corresponing

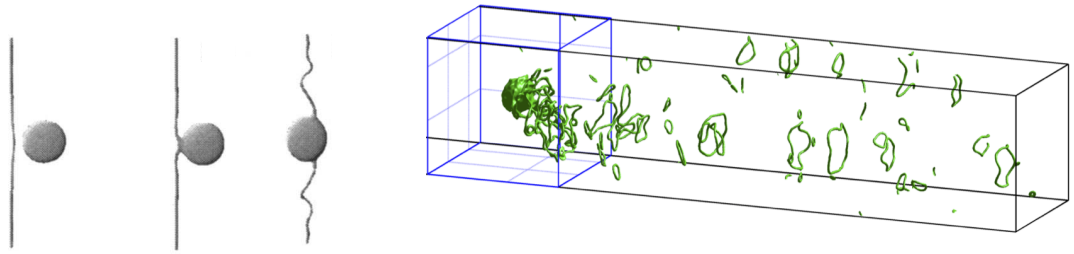


Figure 2.9. (*left*) Trapping process of a bubble by a quantum vortex in the Gross–Clark model. Figure taken from [24] to which we refer for further details. (*right*) Vortex wake generated by a bubble in its ground state driven by a strong external force. Figure taken from [231] to which we refer for futher details.

system of equations of motion is then:

$$i\hbar\frac{\partial}{\partial t}\psi(\boldsymbol{x},t) = \left[-\frac{\hbar^2}{2m_1}\nabla^2 + g_1|\psi(\boldsymbol{x},t)|^2 - \mu_1 + g_{12}|\phi(\boldsymbol{x},t)|^2\right]\psi(\boldsymbol{x},t), \quad (2.64)$$

$$i\hbar\frac{\partial}{\partial t}\phi(\boldsymbol{x},t) = \left[-\frac{\hbar^2}{2m_2}\nabla^2 - \mu_2 + g_{12}|\psi(\boldsymbol{x},t)|^2\right]\phi(\boldsymbol{x},t). \quad (2.65)$$

In the same spirit of the repulsive potential (2.53), the repulsion between the condensate and the bubble field generates a depletion in the superfluid which is filled by the impurity. The main difference between and the model described in the previous section (2.53) and this one (2.63) is that in the latter case the bubble can deform its shape, giving rise potentially to a much higher degree of complexity. In particular, an oblate shape of a bubble moving through a condensate has been observed, which has been related to a reduction of the critical velocity [25]. As the vortex filament method (see section 2.3.2), also the bubble model has been used to study the capture process of a particle by a quantum vortex [24]. Despite the complexity of the model, the deformation of the bubble appears to be negligible and it keeps an almost spherical shape (see Fig.2.9 left). The observed dynamics is thus consistent with the general hydrodynamic picture of the trapping mechanism, that we will describe in the next chapter.

When parameters compatible with superfluid helium are used, the Gross–Clark equations become costly to be simulated. Indeed the ratio between the masses of ^{4}He atoms and the electrons is large, which is translated into a large time scale separation of the respective dynamics. To overcome this issue, in [231] an adiabatic approximation (already developed in [25]) has been used, constraining the electronic wavefunction to remain in its ground state. Such semplification allowed the numerical study of the transport of negative ions in a superfluid when an external electric field is applied to the particle. The typical dynamics of the system when a large electric field is applied is shown in Fig.2.9 right, where a complex wake of vortex rings is visible behind the impurity. The authors of [231] measured the mobility of the electron, which is the proportionality between the drift velocity of the particle and the applied electric field,

and found that the vortex emission is indeed a key contribution to the superfluid drag force acting on the particle.

In the Gross–Clark model, the bubble field dynamics is not affected by any self-interaction as it would be in a BEC mixture. Such effect can be implemented adding an extra non-linear term to Eq. (2.65), making it effectively a Gross–Pitaevskii equation:

$$i\hbar\frac{\partial}{\partial t}\phi(\boldsymbol{x},t) = \left[-\frac{\hbar^2}{2m}\nabla^2 + g_2|\phi(\boldsymbol{x},t)|^2 - \mu_{\mathrm{I}} + g_{12}|\psi\,(\boldsymbol{x},t)\,|^2\right]\phi(\boldsymbol{x},t), \tag{2.66}$$

with g_2 a new coupling constant. The new set of equations (2.64) - (2.66) models a system composed of a mixture of two different condensates [107], which have been observed in experiments with cold atomic gases [156, 160, 171]. In a certain domain of the parameter space (g_1, g_2, g_{12}), one of the two condensates exists in a localized region and can be effectively thought as an impurity. Such immiscibility condition can be simply derived for a homogeneous system [155]. Denoting by $N_1 = \int |\psi|^2\,\mathrm{d}\boldsymbol{x}$ and $N_2 = \int |\phi^2|\,\mathrm{d}\boldsymbol{x}$ the number of bosons in the two components, the energies of the uniform configuration and the separated configuration are respectively:

$$E_{\mathrm{unif}} = \frac{g_1}{2}\frac{N_1^2}{V} + \frac{g_2}{2}\frac{N_2^2}{V}, \qquad E_{\mathrm{sep}} = \frac{g_1}{2}\frac{N_1^2}{V_1} + \frac{g_2}{2}\frac{N_2^2}{V_2} + g_{12}\frac{N_1 N_2}{V}. \tag{2.67}$$

The volumes occupied by each component in the separated configuration are indicated by V_1 and V_2, while the total volume is $V = V_1 + V_2$. Imposing the mechanical equilibrium between the two separated condensates $\partial E_{\mathrm{sep}}/\partial V_1 = \partial E_{\mathrm{sep}}/\partial V_2$ and requiring that such configuration is energetically favourable $E_{\mathrm{sep}} > E_{\mathrm{unif}}$, one obtains the immiscibility condition

$$g_{12} > \sqrt{g_1 g_2}. \tag{2.68}$$

It means that the mutual repulsion between the components must dominate over the self-interactions, as intuitively expected. An application of the two-components model in the immiscible regime is the study of the dynamics of localized impurites inside the core of quantum vortices. It was indeed observed that if vortices are present in one of the condensate, the other component gets trapped inside their cores (as in the other models analyzed so far), providing them with an effective inertia [190]. The dynamics of such system is rich and still largely unknown, including for instance the possible decoupling of the two components during a vortex reconnection [184] or the multiple splitting of composed vortices [134]. Being the two-components condensate feasible with current experimental techniques for the manipulation of cold atoms, it constitutes a promising background for the investigation of non-linear physics.

In this perspective, an even more complex system constituted by a large condensate with a multitude of impurity fields has been recently studied [188, 191]. Different phases of the system have been identified, depending on the ratios between the different coupling parameters. In particular, two crystallization mechanisms are possible when the mutual repulsion among the impurities is larger than their self-interaction. In one case, if their interaction with the bulk condensate is low, the crystal of separated

impurities remains immersed in the bulk condensate. In a second case, if the impurities highly repel also the bulk condensate, a large cluster of separated impurities is formed. In the publication [80], presented in chapter 6 of this manuscript, we show that the particle model (2.57) in the finite temperature regime reproduces a similar steady state with clusters of impurites immersed in a bath of thermal excitations. This supports that idea that the model (2.57) can be also intended as an approximation of the multi-condensate system in the strong repulsion limit.

3 Trapping process and long range interaction between particles and quantum vortices

In this chapter we analyze the long range interaction between particles and quantum vortices. We discuss the process of particle capture, which is the fundamental mechanism that allows particles to get trapped and thus provide information on the vortex dynamics. After giving some general intuitions behind the trapping dynamics, we present the original publication "Interaction between active particles and quantum vortices leading to Kelvin wave generation" [75]. Therein, an effective model for the particle dynamics is derived from the Gross–Pitaevskii Hamiltonian and confirmed by numerical simulations. In the same article we show that the vortex deformations can be included in the effective model, predicting the generation of a cusp on the filament during the particle approach. In addition, the generation of Kelvin waves due to the long range particle-vortex interaction is also observed and explained by a resonance mechanism. Then, we report the article "Quantum vortex reconnections mediated by trapped particles" [77], in which we study how the vortex-particle long range interaction affects the reconnection process. We focus on two different configurations: a dipole of two vortices with a particle trapped in one of them and a Hopf link of two vortex rings decorated by particles. In the first case the reconnection is triggered by the symmetry breaking induced the particle, which is then detached after exchanging momentum with the filaments. In the second case we observe that light and neutral particles do not affect the time scaling of the vortex separation.

3.1 Capture mechanism

As an introduction to the the work in which the long range particle-vortex interaction is investigated in the Gross–Pitaevskii framework, we give the essential intuitions on the dynamics through which particles get captured by quantum vortices. The following basic physical insights about the trapping mechanism can be formulated with a classical hydrodynamic approach for an irrotational ideal fluid.

As one might expect, the mechanism of particle trapping when the particle is far from the vortex, is triggered simply by Bernoulli pressure. Indeed, as we discussed in section 2.2, this is the only force that drives the particle in an inviscid and irrotational fluid. Since the velocity field generated by a superfluid vortex rotates about the vortex filament and scales as the inverse of the distance to the core (1.132), the corresponding pressure gradient scales as the cube of the distance and it is aligned along the radial

direction. Therefore, the corresponding attracting force on the particle coming from (2.22) is simply:

$$\boldsymbol{F} = -M_0 \left(1 + C_a\right) \frac{\Gamma^2}{4\pi^2 r^3} \hat{\boldsymbol{r}}, \tag{3.1}$$

where r is the particle-vortex distance. Clearly, if this is the only force that acts on a particle it will be eventually trapped.

From the perspective of the filament, when the particle is close to it, the vortex starts to feel its own images inside the region occupied by the particle, which are an unavoidable consequence of the boundary condition at the particle surface. As a result, the vortex moves according to its interaction with the images, adding complexity to the actual vortex-particle dynamics. It is worth it to see this fact more in detail in the bidimensional case, where explicit calculations can be performed thanks to conformal mapping. Let us consider a bidimensional flow described by the complex potential $W(z,t) = \Phi(x,y,t) + i\Psi(x,y,t)$, where $z = x + iy = re^{i\varphi}$ and Φ and Ψ are respectively the velocity potential and the stream function, so that $\boldsymbol{v} = \nabla\Phi = \nabla \times (\Psi\hat{\boldsymbol{k}})$. If a circular particle of radius a_p is placed at the origin of the domain, the flow potential is modified according to the Milne–Thomson theorem [19]:

$$\tilde{W}(z,t) = W(z,t) + \left[W\left(\frac{a_p^2}{z^*}, t\right)\right]^* = W(z,t) + W^*\left(\frac{a_p^2}{z}, t\right), \tag{3.2}$$

which maps every complex point outside the particle into a point inside the circle, in such a way that at the particle boundary $|z|^2 = z^* z = a_p^2$ it reads $\tilde{W}(z) = W(z) + W^*(z^*)$. As a consequence the particle boundary is always a streamline with $\tilde{\Psi} = \mathrm{Im}\left[\tilde{W}\right] = 0$ and the free slip condition is automatically satisfied. In the case of the flow generated by a (point) vortex placed at the position $z_v(t)$ outside the particle, the complex potential is $W(z,t) = i\frac{\Gamma}{2\pi}\log\left[z - z_v(t)\right]$ and the presence of the particle transforms it as

$$\tilde{W}(z,t) = i\frac{\Gamma}{2\pi}\left(\log\left[z - z_v(t)\right] - \log\left[\frac{a_p^2}{z} - z_v^*(t)\right]\right). \tag{3.3}$$

It is easy to check that a consequence of Eq. (3.3) is the emergence of two new singularities inside the particle, that together constitute an image vortex dipole, which keeps the total circulation constant (and equal to zero around the particle). The first image vortex is placed at the inverse of the physical vortex position a_p^2/z_v^* and it has opposite charge with respect it. The second one is placed at the origin, i.e. at the particle center, and it has the same charge of the physical vortex. A picture of the flow is displayed in Fig.3.1 left, where both the velocity potential $\Phi = \mathrm{Re}\left[\tilde{W}\right]$ (3.3) and the streamlines are shown. Of course, in 3D the situation is more complex and such an immediate analytical treatment is impossible, but qualitatively the physical picture is analogous. In particular, the presence of images inside the approaching spherical particle drives the motion of the vortex, so that the resulting dynamics of the particle itself is affected.

When the particle capture eventually happens, the new system constituted by the

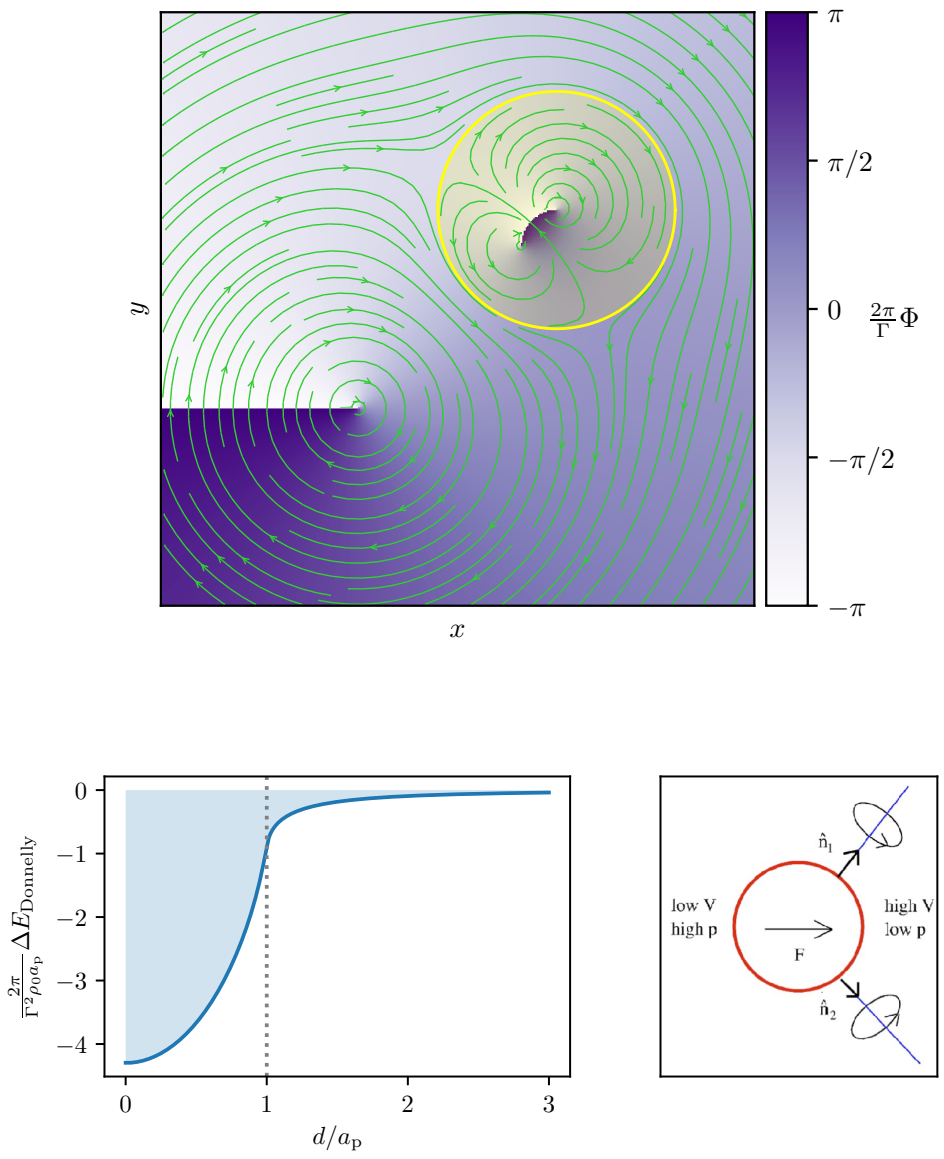


Figure 3.1. (*top*) Two-dimensional flow generated by a point vortex and a (static) circular particle. The colormap is the velocity potential $\Phi = \mathrm{Re}\left[\tilde{W}\right]$ (3.3), while the corresponding streamlines are in green. The particle boundary is indicated by the yellow solid line. Note the presence of an image dipole inside the particle, aligned with the external real point vortex. (*bottom left*) Substitution energy $\Delta E_{\text{Donnelly}}$ (3.5) numerically integrated as a function of the distance between the spherical particle and the straight vortex line [173]. The vortex core radius is set to $a_0 = 0.01 a_p$. (*bottom right*) Sketch of the origin of restoring force for non symmetrical trapped particle-vortex configurations (taken from [209]).

trapped particle and the vortex turns out to be energetically favourable with respect to the case when the vortex and the particle are well separated. In 1966, Donnelly and Parks computed explicitly this "substitution energy", which is the kinetic energy of the fluid excluded by the presence of the particle [173]

$$\Delta E_{\text{Donnelly}} = \frac{1}{2}\int_{\mathbb{B}[q]} \rho_{\text{v}} v_{\text{v}}^2 \, \mathrm{d}\boldsymbol{x}, \tag{3.4}$$

where ρ_{v} and v_{v} are the density profile and the velocity field of a straight vortex line. The cited calculation has been performed having in mind the ions which were being used extensively in that period, but generalizes to every finite size particle. Choosing a system of reference centered at the particle position, so that a straight vortex is placed at a distance d and aligned with the z axis, we call r and φ the radial and the azimuthal coordinates. Approximating the vortex density profile as $\rho_{\text{v}} = \rho_0 r'^2 \left(r'^2 + a_0^2\right)^{-1}$ [62], where $r' = \sqrt{r^2 + d^2 + 2rd\cos\varphi}$ is the radial coordinate in the vortex reference frame and a_0 is the vortex core size, the substitution energy reads:

$$\Delta E_{\text{Donnelly}}(d) = -\frac{\Gamma^2\rho_0}{2\pi}\int_0^{a_{\text{p}}} \sqrt{\frac{a_{\text{p}}^2 - r^2}{\left(r^2 + d^2 + a_0^2\right)^2 - 4d^2r^2}}\, r \, \mathrm{d}r. \tag{3.5}$$

In the two limiting cases of the particle symmetrically trapped by the straight vortex ($d = 0$), or far away from it ($d/a_0 \to \infty$), the expression (3.5) can be fully evaluated:

$$d = 0 \quad \longrightarrow \quad \Delta E_{\text{Donnelly}} = -\frac{\Gamma^2\rho_0}{2\pi} a_{\text{p}} \left[1 - \sqrt{1 + \frac{a_0^2}{a_{\text{p}}^2}}\,\operatorname{arcsinh}\left(\frac{a_{\text{p}}}{a_0}\right)\right], \tag{3.6}$$

$$d/a_0 \to \infty \quad \longrightarrow \quad \Delta E_{\text{Donnelly}} = -\frac{\Gamma^2\rho_0}{2\pi} a_{\text{p}} \left[1 - \sqrt{\frac{d^2}{a_{\text{p}}^2} - 1}\,\arcsin\left(\frac{a_{\text{p}}}{d}\right)\right]. \tag{3.7}$$

The numerical integration of the substitution energy as a function of the particle-vortex distance is displayed in Fig.3.1 bottom left, where it is clear that the trapped configuration is the stable one. More than that, for distances $d < a_{\text{p}}$ the energy $\Delta E_{\text{Donnelly}}$ is steeply monothonically increasing. This means that there is an attractive force $-\nabla\Delta E_{\text{Donnelly}}$, stronger than the long range force (3.1), which tends to keep trapped a particle when it is displaced from the symmetric configuration. Another qualitative way to see this attraction is sketched in Fig.3.1 bottom right, originally reported in [209]. If we consider a non symmetric vortex-particle configuration, the velocity is larger on the side of the particle surface where the two vortex strands are closer. As a consequence of Bernoulli principle, the pressure is larger on the opposite side, generating a net restoring force that tends to establish a symmetric configuration.

In the next section, we present the work [75] in which the capture process is thoroughly investigated in the GP framework. Before that, we give a qualitative glimpse of the complexity of the system when the actual particle-vortex mutual interaction

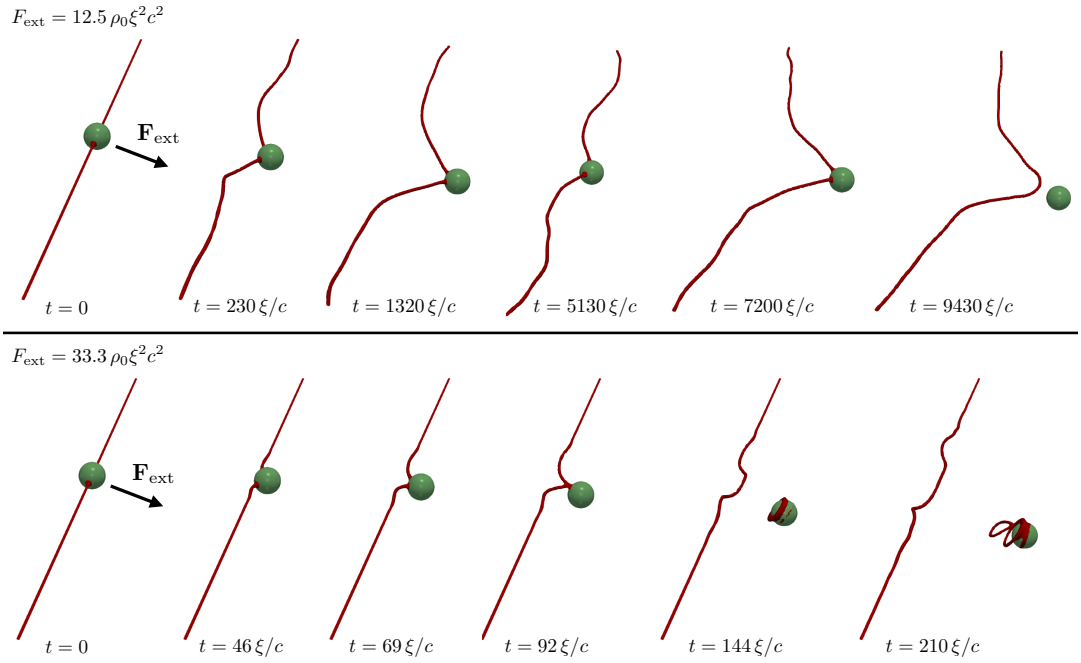


Figure 3.2. Time evolution of a straight vortex and a trapped particle of radius 7.6ξ and relative mass $\mathscr{M} = 1$ subject to a transverse external constant force $F_{\text{ext}} = 12.5\,\rho_0\xi^2c^2$ (*top panel*) and $F_{\text{ext}} = 33.3\,\rho_0\xi^2c^2$ (*bottom panel*) , according to the GP model. The vortex is rendered as a red isosurface at low density $\rho = 0.15\rho_0$ and the particle as a green sphere. The parameters of the particle potential are $V_0 = 20\mu, \zeta_{\text{p}} = 2.5\xi, \Delta_{\text{p}} = 2.5\xi$ and the other parameters of the simulation are $L = 2\pi, N_{\text{c}} = 256$ and $\xi = L/N_{\text{c}}$.

(provided by such model) is taken into account. It should be noticed, indeed, that the substitution energy (3.4) is not necessarily the energy needed to pull out a particle from a vortex. For instance, consider an external force suddenly applied to a steadily trapped particle. It may happen that the energy injected in the system thereby is redistributed among the degrees of freedom of the vortex, instead of allowing the particle to escape. Specifically, it can induce a deformation or a stretching of the filament, keeping the particle captured. An example of such phenomenology is displayed in Fig.3.2, where a particle trapped by a straight vortex is indeed pulled by an external constant force, transverse to the filament. The time evolution is given by a simulation of the equations (2.54) and (2.55), with an extra force $\boldsymbol{F}_{\text{ext}}$ added to the right hand side of Eq. (2.55). Clearly, the vortex and the particle affect each other. In particular, if the force acting on the trapped particle is sufficiently low (top panel of Fig.3.2) its effect is to pump energy into the vortex. The filament is stretched and when the particle eventually gets detached, the vortex is longer (and thus more energetic) than in the intial condition. Conversely, if the forcing is high enough (bottom panel of Fig.3.2), the vortex does not react sufficiently fast and the particle can escape without inducing a large stretching of the filament. Therefore, the particle trapping process is certainly not a reversible mechanism[1] and the stability of the vortex-captured particle system may be more robust than what expected from static energetic considerations.

3.2 *Publication*: Interaction between active particles and quantum vortices leading to Kelvin wave generation

The trapping mechanism discussed in the previous section is somehow simplified, essentially because it does not take into account the relative interactions between the vortex and the particle. For this reason, the use of more elaborated models is necessary, which could give better insights on the actual forces that dominate the dynamics. One of these model is indeed the GP equation coupled with repulsive potentials presented in section 2.3.3, which in the article attached below [75] has been used to study the vortex-particle interaction at large distance. Therein, we derive an effective Hamiltonian for the attractive interaction between a particle and a straight vortex, which depends only on the particle degrees of freedom. The procedure consists in guessing an ansatz for the solution of the GP equation in such setting and imposing the proper boundary conditions for the phase of the wavefunction about the surface of the sphere. The effective Hamiltonian follows then from a perturbative analysis in the same small parameter (2.6) introduced in section 2.2 for the dynamics of a particle in a classical fluid. Indeed, at the leading order we recover exactly the equation of motion (3.1). Such prediction and the next-to-leading-order correction are well reproduced by the direct numerical simulations of the GP model.

Since the effective Hamiltonian describes a central force problem, particularly interesting is the studying of the orbits predicted by it. At the leading order, a critical

[1] Another direct signature of irreversibility is the pulse of sound emitted at the trapping time [75].

angular momentum exists below which the particle is always trapped and above which it always escapes from the vortex. At the critical angular momentum, the leading order of the attracting force vanishes and a close circular orbit is predicted. The critical angular momentum is reached for a neutral particle if it initially moves with the same velocity of the vortex flow (1.132). However, in this case the corrections to the leading order become crucial: numerics and analytics agree that the actual particle trajectory is a spiral that eventually collapses to the vortex core. Such fact is perfectly consistent with the fact that a tracer of the superfluid velocity field cannot exist at zero temperature because of the lack of Stokes drag.

Another interesting property of the effective Hamiltonian discussed in [75] is a scaling invariance valid at all the orders. It applies when the particle size and its distance to the vortex are multiplied by a factor λ and the time is scaled by a factor λ^2:

$$\mathrm{q} \to \lambda \mathrm{q}, \quad a_\mathrm{p} \to \lambda a_\mathrm{p}, \quad t \to \lambda^2 t \qquad \forall \lambda \in \mathbb{R}^+. \tag{3.8}$$

Such scaling invariance indicates that the main dimensional parameter that actually controls the dynamics of the system is just the circulation of the vortex. It is indeed reminiscent of the scaling invariance of the Biot–Savart integral (1.142), which is also conserved if distances are rescaled by λ and times by λ^2. The symmetry (3.8) is important because allows us to generalize our results to the case of much larger particles, in principle similar to the one used in superfluid helium experiments.

In a second part of the publication, we introduce the vortex dynamics in the effective Hamiltonian. In particular we provide degrees of freedom to the filament, allowing it to deform according to the Local Induction Approximation (see section 1.4.2). As a result, we can predict the formation of a cusp along the filament (observed in the GP simulations) as a consequence of the vortex-particle long range mutual interaction. Furthermore, such interaction is able to induce the generation of a monochromatic Kelvin wave along the filament. Indeed, we find that for a given combination of the particle angular frequency about the vortex and linear velocity along the vortex, a specific frequency can be excited on the vortex, as a consequence of a linear resonance mechanism. The far reaching hope associated to this observation is that a similar mechanism could be used to excite Kelvin waves in a controlled manner[2].

[2] An atomic Bose–Einstein condensate (more than superfluid helium) is probably a better setting for a possible implementation of a similar mechanism.

SCIENTIFIC REPORTS

OPEN

Interaction between active particles and quantum vortices leading to Kelvin wave generation

Received: 13 November 2018
Accepted: 4 February 2019
Published online: 18 March 2019

Umberto Giuriato & Giorgio Krstulovic

One of the main features of superfluids is the presence of topological defects with quantised circulation. These objects are known as quantum vortices and exhibit a hydrodynamic behaviour. Nowadays, particles are the main experimental tool used to visualise quantum vortices and to study their dynamics. We use a self-consistent model based on the three-dimensional Gross-Pitaevskii (GP) equation to explore theoretically and numerically the attractive interaction between particles and quantized vortices at very low temperature. Particles are described as localised potentials depleting the superfluid and following Newtonian dynamics. We are able to derive analytically a reduced central-force model that only depends on the classical degrees of freedom of the particle. Such model is found to be consistent with the GP simulations. We then generalised the model to include deformations of the vortex filament. The resulting long-range mutual interaction qualitatively reproduces the observed generation of a cusp on the vortex filament during the particle approach. Moreover, we show that particles can excite Kelvin waves on the vortex filament through a resonance mechanism even if they are still far from it.

Quantum vortices have a long history in physics of superfluids and superconductors. Already in the 40's Onsager had suggested the existence of quantised flows. This idea was further developed by Feynman by introducing the concept of quantum vortices[1]. What makes these vortices fascinating is that they appear as topological defects of the order parameter describing the system. As a consequence their charge or circulation is quantised, making them topological protected objects. Their core size varies form a few Angstroms in superfluid ^{4}He to micrometers in Bose-Einstein condensates (BECs). In systems such as ^{4}He, ^{3}He and atomic BECs, quantum vortices behave as hydrodynamic vortices, reconnecting and rearranging their topology, forming in this way complex vortex tangles. Such out-of-equilibrium state is today known as quantum turbulence[2]. In rotating BECs, quantised vortices naturally appear and they have been studied since the early 2000s[3,4]. In superfluid helium, ions and impurities have been extensively used since long time to investigate the properties of quantum vortices[1]. However, an important experimental breakthrough occurred in 2006[5], when quantum vortices were directly visualised by using micrometer-sized hydrogen particles. These impurities are trapped inside the vortex core and they can be directly visualised by using standard particle-tracking techniques, that are commonly exploited in classical hydrodynamic turbulence. Thanks to this method, quantum vortex reconnections[6] and Kelvin waves propagating along the vortex filaments[7] have been observed. In addition, the employment of particles has been helpful to enlighten similarities and differences between classical hydrodynamic and quantum turbulence[8,9]. For superfluid helium, the typical size of hydrogen particles is several orders of magnitude larger than the vortex core, whereas recent experiments have used He_2^* excimers that are slightly larger than the vortex core[10]. Therefore, understanding the interaction between particles and vortices has become crucial for current experiments.

In general, utilising particles to unveil the properties of a fluid is a common technique in classical hydrodynamics. For instance, air bubbles are used to visualise classical vortices in water since the pioneering work of Couder *et al.* in 1991[11] and tracers (very small and neutrally-buoyant particles) are followed by using ultra-fast-cameras to determine the statistics of turbulent flows[12]. When particles are not tracers, they manifest inertia with respect to the fluid flow, deviating from its stream lines. Although complex, their dynamics is well understood in classical fluids if their size is small enough[13,14].

Université Côte d'Azur, Observatoire de la Côte d'Azur, CNRS, Laboratoire Lagrange, Bd de l'Observatoire, CS 34229, 06304 Cedex 4, Nice, France. Correspondence and requests for materials should be addressed to U.G. (email: umberto.giuriato@oca.eu) or G.K. (email: krstulovic@oca.eu)

Superfluids differ in several aspects to classical fluids. Firstly, at very low temperature, an object moving at low velocity experiences no drag. Secondly, the quantum nature of vortices makes the vorticity field (the curl of the velocity) a Dirac-δ distribution supported on the vortex filaments. Finally, at finite temperature, they are modelled by an immiscible mixture of two components: the actual superfluid and a *normal* fluid. The latter is described by the (viscous) Navier-Stokes equations. Such mixture of fluids is responsible for some quantum effects with no classical analogous such as the fountain effect and second sound[1]. The dynamics of a particle moving in a finite temperature superfluid happens to be richer than in an ordinary fluid. Its equations of motion have been generalised to the case where the flow is prescribed by the two-fluid model[15,16]. This model provides a large-scale description of a finite temperature superfluid where vortices are described with a coarse-grained field, therefore the quantised nature of superfluid vortices is missing. A different model that does account for the quantised nature of superfluid vortices, was introduced by Schwartz and it is known as the vortex filament method[17]. Also in this case, the dynamics of particles has been addressed both theoretically and numerically[18,19]. Eventually, in the limit of very low temperature, superfluids can be described by another important model, the Gross-Pitaevskii (GP) equation. This model derives from a mean field approximation of a quantum system and directly applies to weakly-interacting BECs, but it is also expected to qualitatively apply to other types of superfluids. The GP equation governs the dynamics of the macroscopic wave function of the system, hence quantum vortices are naturally included. In the GP framework, impurities and particles are often described in terms of classical fields[20–23]. In particular, it was shown by Roberts and Rica[22] that, depending on the coupling constants, the impurity field separates from the condensate and the two fields become immiscible. In this regime, an impurity can be seen as a hard-core particle described with classical (Newtonian) degrees of freedom[24–26]. Such approach is numerically much cheaper than the classical field description, and thus allow for simulations of a large number of particles[27]. It also suitable for developing analytical predictions.

In this Report we study numerically and analytically the interaction of quantum vortices and particles by using the Gross-Pitaevskii model coupled with a particle having classical degrees of freedom. We take advantage of the Hamiltonian structure of the system to derive a simplified model for the particle motion that it is then directly confronted with numerical simulations of the full GP model. In particular, we study the trapping of particles by a straight vortex, where an explicit analogy of a Newtonian central force problem can be established. The model is then generalised to describe the deformation of the vortex filament. The consequences of the long-range interaction between the particle and the filament are analytically studied and a prediction for the generation of Kelvin wave is obtained.

Results

Model for particles in a superfluid. We consider a superfluid at very low temperature with one spherical particle of radius a_p and mass M_p immersed in it. The superfluid is described by a complex field $\psi(\mathbf{x}, t)$ and the particle classical degrees of freedom are its position $\mathbf{q}=(q_x, q_y, q_z)$ and momentum $\mathbf{p} = M_\mathrm{p}\dot{\mathbf{q}} = (p_x, p_y, p_z)$. The dynamics of the system is governed by the following Hamiltonian:

$$H = \frac{\mathbf{p}^2}{2M_\mathrm{p}} + \int\left(\frac{\hbar^2}{2m}|\nabla\psi|^2 + \frac{g}{2}|\psi|^4 - \mu|\psi|^2 + V_\mathrm{p}(|\mathbf{x}-\mathbf{q}|)|\psi|^2\right)\mathrm{d}\mathbf{x}, \tag{1}$$

where m is the mass of the fundamental bosons constituting the superfluid, μ is the chemical potential and the coupling constant $g = 4\pi a_\mathrm{s}\hbar^2/m$ depends on the s-wave scattering length a_s. The potential $V_\mathrm{p}(|\mathbf{x}-\mathbf{q}|) \gg \mu > 0$ is localised around $\mathbf{q}$ and it determines the shape of the particle. Its presence induces a full depletion of the superfluid around the position $\mathbf{q}$ up to a distance a_p. The equations of motion for the field and the particle position are directly obtained by varying (1) and read

$$\begin{aligned} i\hbar\frac{\partial\psi}{\partial t} &= -\frac{\hbar^2}{2m}\nabla^2\psi + (g|\psi|^2 - \mu)\psi + V_\mathrm{p}(|\mathbf{x}-\mathbf{q}|)\psi, \\ M_\mathrm{p}\ddot{\mathbf{q}} &= -\int V_\mathrm{p}(|\mathbf{x}-\mathbf{q}|)\nabla|\psi|^2\,\mathrm{d}\mathbf{x}. \end{aligned} \tag{2}$$

The Hamiltonian (1), the total superfluid mass $M = m\int|\psi|^2\,\mathrm{d}\mathbf{x}$ and the total momentum $\mathbf{P} = \frac{i\hbar}{2}\int(\psi\nabla\psi^* - \psi^*\nabla\psi)\,\mathrm{d}\mathbf{x} + \mathbf{p}$ are conserved quantities. The connection of Eq. (2) with hydrodynamics is made through the Madelung transformation $\psi(\mathbf{x}) = \sqrt{\rho(x)/m}\,e^{i\frac{m}{\hbar}\phi(\mathbf{x})}$ that maps the GP model into the continuity and Bernoulli equations of a fluid of density ρ and velocity $\mathbf{v}_\mathrm{s}=\Delta\phi$.

In absence of the particle, the GP equation has a simple steady solution corresponding to a constant flat condensate $\psi_\infty = \sqrt{\rho_\infty/m} = \sqrt{\mu/g}$. If (2) is linearised about ψ_∞, large wavelength waves propagate with the phonon (sound) velocity $c = \sqrt{g\rho_\infty/m^2}$ and dispersive effects take place at length scales smaller than the healing length $\xi = \sqrt{\hbar^2/2g\rho_\infty}$.

Another important steady solution corresponds to a straight quantum vortex

$$\psi_\mathrm{v}(x, y, z) = \sqrt{\rho_\mathrm{v}(x, y)/m}\,e^{i\frac{m}{\hbar}\phi_\mathrm{v}(x,y)}. \tag{3}$$

The vortex density ρ_v vanishes at $(0, 0, z)$ and the phase is given by $\phi_\mathrm{v} = \frac{\hbar}{m}\kappa\varphi$, with φ the angle in the (x, y) plane and κ a non-zero integer. The corresponding velocity field $\mathbf{v}_\mathrm{v}$ satisfies

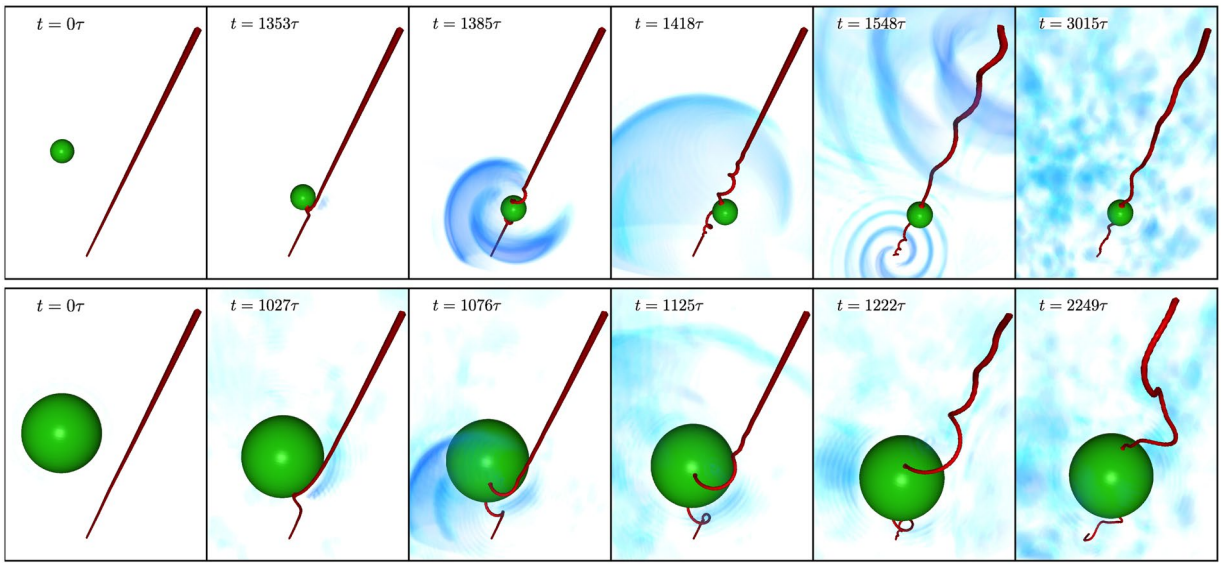


Figure 1. Snapshots of the superfluid density and a neutral-mass particle during the trapping (times varies from left to to right). Vortices are displayed in red, particles in green and sound waves are rendered in blue. *Top*: small particle ($a_p = 7.6\xi$). *Bottom*: large particle ($a_p = 23.5\xi$). Images were produced with VAPOR rendering software.

$$\mathbf{v}_v = \frac{\kappa\hbar}{m}\frac{\hat{\varphi}}{|\mathbf{x}_\perp|} \text{ and } \Gamma = \frac{1}{\kappa}\oint_{\mathcal{C}} \mathbf{v}_v \cdot d\mathbf{l} = \frac{h}{m} = 2\pi\sqrt{2}\,c\xi, \tag{4}$$

where $\hat{\varphi}$ is the azimuthal versor and $\boldsymbol{x}_\perp = (x, y, 0)$. Similarly, in the following we will denote $q_\perp = (q_x, q_y, 0)$ and $q_\perp = |\mathbf{q}_\perp|$. The close path $\mathcal{C}$ surrounds the vortex, whose circulation is thus given by $\kappa\Gamma$. We will consider $\kappa = \pm 1$ because it is the only stable solution. Note that the vortex core size is given by the healing length ξ, ρ_v and $\mathbf{v}_v$ are radial functions and $\rho_v \to \rho_\infty$ away from the vortex[28].

When a particle is present, the ground state (without vortices) corresponds to a flat condensate with a strong density depletion at places where $V_p(|\mathbf{x} - \mathbf{q}|) > \mu$. A good approximation when $a_p \gg \xi$ is given by the Thomas-Fermi ground state that is obtained neglecting the kinetic term. It reads

$$\rho_p(\mathbf{x}; \mathbf{q}) = \rho_p(|\mathbf{x} - \mathbf{q}|) = \rho_\infty\left(1 - \frac{V_p(|\mathbf{x} - \mathbf{q}|)}{\mu}\right)\theta\left[1 - \frac{V_p(|\mathbf{x} - \mathbf{q}|)}{\mu}\right], \tag{5}$$

with θ the Heaviside function. The size of the particles is thus roughly determined by the relation $V_p(a_p) \approx \mu$. The results presented in this work are independent of the functional shape of V_p, provided that it is isotropic.

In numerics, we express the particle mass as $M_p = \mathcal{M}M_0$, where M_0 is the mass of the displaced superfluid. Therefore, neutral-mass particles have $\mathcal{M} = 1$, heavy particles have $\mathcal{M} > 1$ and light particles have $\mathcal{L} < 1$. Lengths are expressed in units of ξ, times in units of $\tau = \xi/c$, velocities in units of c and energies are normalised by M_0c^2. Details on the numerical implementation and the particular choice of V_p are given in Methods.

Interaction between particles and quantum vortices. We begin by presenting some numerical experiments where a particle is attracted and captured by a vortex. We integrate the model (2) in a 3D periodic domain of size $L = 256\xi$ with an initial condition consisting of one particle at rest and one straight vortex initially separated by a distance $q_\perp = q_0 \gg \xi$. The domain contains image vortices in order to preserve periodicity that are not displayed in figures. Their effect on the particle has been checked to be negligible. Snapshots of the superfluid density field with the particle at different times are displayed in Fig. 1. The top row refers to a relatively small particle ($a_p = 7.6\xi$), while the bottom row to a large one ($a_p = 23.5\xi$). Both particles have a neutral relative mass $\mathcal{M} = 1$. Note that hydrogen particles used for visualization of quantum vortices in superfluid helium have a relative mass $\mathcal{M} \sim 0.7$ and a typical size of $a_p \sim 10^3\xi$. Simulating such particle size is not achievable numerically, however a clear difference is already observed for our large particle. In both cases, the particle is attracted by the vortex. Before the merging, while the particle is moving closer to the vortex, a deformation of the vortex line is observed. Such deformation is a cusp regularised at the scale of the healing length by the dispersion of the GP equation. Initially, the cusp develops perpendicularly to the particle velocity. Later, it curves towards the particle, until the contact point the vortex separates into two branches. The two contact points then slide on the particle surface towards opposite directions. The oscillation of the trapped particle excites helicoidal waves on the filament. Such waves, that propagate along the vortex line, are known as Kelvin waves. We note that the vortex deformation is less marked for smaller particles and the amplitude of Kelvin waves increases with the particle size. A similar behaviour has been already observed in the hydrodynamical model adopted in refs[15,29,30], as well as in the

classical field impurity model studied by Berloff and Roberts[21]. The trapping process was then interpreted as a reconnection of the straight vortex with its images inside the particle, whose presence is necessary to set the boundary conditions for the flow around the particle.

The model (2) also allow us to observe the sound emitted by the particle-vortex pair during the trapping process. In a first stage, a big pulse is emitted at the moment of the trapping due to the strong acceleration experienced by the particle. In a later time, for the smaller particle a clear quadrupolar radiative pulse is observed ($t = 1548\tau$, top row of Fig. 1). Remarkably, this kind of pattern is expected in superfluids when some symmetry cancels the first order of the multipolar radiative expansion. For instance, this is the case in 2D counter-rotating vortices[31,32]. Here, the symmetry could be related to the two antisymmetric traveling waves emerging from the particle and meeting at the boundary of the periodic domain. This issue will be investigated further in a future work. Finally, the particle remains trapped inside the vortex and coexists with a bath of sound waves. For the big particle, all the phenomena are amplified. Movies of the numerical simulations can be found as a Supplementary Information.

From these simulations it is manifest that the trapping of a particle by a quantum vortex is accompanied by a myriad of complex physical phenomena. In the next sections, we take advantage of the simplicity of the model to derive effective equations for the particle and the vortex Filament dynamics.

Reduced theoretical model for the particle-vortex interaction. In the following we set the origin of the reference frame at the intersection between the unperturbed vortex line and its orthogonal plane where the particle lies. At $t = 0$, the vortex line coincides then with the z axis. To derive a simplified theory, we consider the following ansatz for the superfluid field:

$$\psi(\mathbf{x};\,\mathbf{q},\,\mathbf{q}) = \sqrt{\frac{\rho_\infty}{m}}\sqrt{\widetilde{\rho}_{\rm v}(\mathbf{x})}\sqrt{\widetilde{\rho}_{\rm p}(|\mathbf{x}-\mathbf{q}|)}\,e^{i\frac{m}{\hbar}\phi(\mathbf{x};\mathbf{q},\mathbf{q})}, \tag{6}$$

where $\widetilde{\rho}_{\rm v} = \sqrt{\rho_{\rm v}/\rho_\infty}$ and $\widetilde{\rho}_{\rm p} = \sqrt{\rho_{\rm p}/\rho_\infty}$ are the normalised ground states of an isolated vortex and an isolated particle given in (3) and (5) respectively. At first approximation, we neglect the deformation of the vortex. This last assumption is valid at the stages where the particle is attracted by the vortex, but still far from it. We will consider the vortex deformation in the last section. The ansatz (6) also neglects small density variations due to sound emission and might not be valid at the exact moment of the trapping, but it gives a good description elsewhere. The phase ϕ leads to the superfluid velocity field $\boldsymbol{v}_{\rm s} = \nabla\phi$ and it is determined by imposing the boundary conditions around the particle and at infinity:

$$\dot{\mathbf{q}}\cdot\mathbf{n} = \mathbf{v}_{\rm s}\cdot\mathbf{n} \quad \forall\,\mathbf{x}\ \text{s. t.}|\mathbf{x}-\mathbf{q}| = a_{\rm p} \quad \text{and} \quad \mathbf{v}_{\rm s} \xrightarrow[|\mathbf{x}-\mathbf{q}|\to\infty]{} \mathbf{v}_{\rm v}. \tag{7}$$

where $\mathbf{n} = (\mathbf{x}-\mathbf{q})/|\mathbf{x}-q|$ and $\mathbf{v}_{\rm v}$ the vortex velocity field (4). Since $\mathbf{v}_{\rm v}$ describes a non-uniform irrotational flow, we have to take into account how the superfluid velocity field is modified when the particle accelerates in it. As it is done in classical fluid mechanics[13–15], we include in the superfluid velocity the corrections to the pure vortex flow $\mathbf{v}_{\rm v}$ that are generated by the moving particle. We set $\mathbf{v}_{\rm s} = \mathbf{v}_{\rm v} + \mathbf{v}_{\rm p} + \mathbf{v}_{\rm BC}$, or in terms of the phase $\phi = \phi_{\rm v} + \phi_{\rm p} + \phi_{\rm BC}$.

The potential $\phi_{\rm p}$ describes the flow of a sphere of radius $a_{\rm p}$ moving in a uniform flow given by the relative velocity $\dot{\mathbf{q}} - \mathbf{v}_{\rm v}(\mathbf{q})$. It reads[33]

$$\phi_{\rm p}(\mathbf{x};\,\mathbf{q},\,\dot{\mathbf{q}}) = -\frac{a_{\rm p}^3}{2|\mathbf{x}-\mathbf{q}|^3}(\mathbf{x}-\mathbf{q})\cdot(\dot{\mathbf{q}}-\mathbf{v}_{\rm v}(\mathbf{q})). \tag{8}$$

The potential $\phi_{\rm BC}$ is in principle determined by the condition at the particle boundary $\nabla\phi_{\rm BC}\cdot\mathbf{n} = [\mathbf{v}_{\rm v}(\mathbf{q} + a_{\rm p}\mathbf{n}) - \mathbf{v}_{\rm v}(\mathbf{q})]\cdot\mathbf{n}$. In practice, it is obtained by a Taylor expansion of the vortex velocity flow around the particle and hence $\phi_{\rm BC}$ is expressed in terms of its gradients[13–15]. This flow gives a contribution of order

$$\varepsilon = a_{\rm p}\frac{|\nabla\mathbf{v}_{\rm v}(\mathbf{q})|}{|\mathbf{v}_{\rm v}(\mathbf{q})|} = \frac{a_{\rm p}}{q_\perp} \ll 1, \tag{9}$$

where we have used $|\mathbf{v}_{\rm v}(\mathbf{q})| \sim 1/q_\perp$. We include in our calculations $\phi_{\rm BC}$ up to $\mathcal{O}(\varepsilon^2)$.

In order to express the Hamiltonian (1) only in terms of q and q we split it as $H = K + H^{\rm GP}_{\rm hydro} + H^{\rm GP}_{\rm int} + H^{\rm GP}_{\rm p} + H^{\rm GP}_{\rm qnt}$, where

$$\begin{aligned} K &= \frac{1}{2}M_{\rm p}\dot{\mathbf{q}}^2, \quad H^{\rm GP}_{\rm hydro} = \frac{1}{2}\int\rho\mathbf{v}_{\rm s}^2{\rm d}\mathbf{x}, \quad H^{\rm GP}_{\rm int} = \frac{g}{2m^2}\int\rho^2{\rm d}\mathbf{x}, \\ H^{\rm GP}_{\rm p} &= \frac{1}{m}\int(V_{\rm p}-\mu)\rho\ {\rm d}\mathbf{x}, \quad H^{\rm GP}_{\rm qnt} = \frac{\Gamma^2}{8\pi^2}\int(\nabla\sqrt{\rho})^2{\rm d}\mathbf{x}. \end{aligned} \tag{10}$$

We use the ansatz (6) to explicitly perform the space integrals. From (5), we observe that for a strong localised potential $V_{\rm p} \gg \mu$ the field $1 - \widetilde{\rho}_{\rm p}(x)$ is supported on a ball of center q and radius $a_{\rm p}$, up to a layer of size ξ. We use this fact to reduce the domain of integration. Inside this ball and if $\varepsilon \ll 1$, we can assume that $\widetilde{\rho}_{\rm v}(\mathbf{x}) \approx \widetilde{\rho}_{\rm v}(q_\perp)$ and $\mathbf{v}_{\rm v}(\mathbf{x}) \approx \mathbf{v}_{\rm v}(q_\perp)$. All the integrations can be then carried out. Details on these computations are given in Methods. The Hamiltonian components (10) eventually read

$$H^{\rm GP}_{\rm hydro} \approx \overline{H}^{GP}_{\rm hydro} - \frac{(1+C)M_0\Gamma^2}{8\pi^2 q_\perp^2}\widetilde{\rho}_{\rm v}(q_\perp) - \frac{\Gamma^2 a_{\rm p}^{\,2}}{20\pi^2 c^2 q_\perp^4}\widetilde{\rho}_{\rm v}(q_\perp) + E_{\rm add},$$

with

$$E_{\rm add} = \frac{1}{2}C\widetilde{\rho}_{\rm v}(q_\perp)M_0\dot{\mathbf{q}}^2, \tag{11}$$

$$H^{\rm GP}_{\rm int} \approx \overline{H}^{\rm GP}_{\rm int} - \frac{1}{2}M_0c^2\widetilde{\rho}^2_{\rm v}(q_\perp),\ H^{\rm GP}_{\rm p} \approx \overline{H}^{\rm GP}_{\rm p} + M_0c^2\widetilde{\rho}_{\rm v}(q_\perp),\ H^{\rm GP}_{\rm qnt} \approx \overline{H}^{\rm GP}_{\rm qnt} \tag{12}$$

where $C=1/2$ and overbars denote constants at the leading order. $E_{\rm add}$ is the classical added mass energy in three dimensions[33] modified by the density profile. Gathering all the terms, we obtain the reduced Hamiltonian (RH)

$$H_{\rm red}[\mathbf{q},\mathbf{p}] = \overline{H}^{\rm GP} + \frac{\mathbf{p}^2}{2M_{\rm eff}} + M_0c^2\Big[-\frac{1}{2}\widetilde{\rho}^2_{\rm v}(q_\perp) + \widetilde{\rho}_{\rm v}(q_\perp) - \frac{(1+C)\Gamma^2}{8\pi^2c^2q_\perp^2}\widetilde{\rho}_{\rm v}(q_\perp) - \frac{\Gamma^2a_{\rm p}^{\,2}}{20\pi^2c^2q_\perp^4}\widetilde{\rho}_{\rm v}(q_\perp)\Big]. \tag{13}$$

In (13) the added mass has been absorbed in the effective particle mass $M_{\rm eff} = M_{\rm p} + C\widetilde{\rho}_{\rm v}M_0 = (\mathcal{M} + C\widetilde{\rho}_{\rm v})M_0$ and the particle momentum has been redefined as $\mathbf{p} = M_{\rm eff}\dot{\mathbf{q}}$. Note that, as $\widetilde{\rho}_{\rm v}$ only depends on $q_\perp$, the coordinate q_z of the particle is cyclic and can be trivially integrated. The dynamics thus simplifies to a motion in the plane perpendicular to the vortex. The reduced model (13), therefore describes a classical central force problem in two dimensions with a potential given by its last term. Note that the same calculations can be performed in two dimensions, by redefining the phase (8) which leads to the constant $C=1$.

The reduced Hamiltonian (13) can be further simplified using the asymptotic behaviour of $\widetilde{\rho}_{\rm v}$. At large distances, $\widetilde{\rho}_{\rm v} \sim 1 - \xi^2/q_\perp^2 - 2\xi^4/q_\perp^4 + O(\xi^6/q_\perp^6)$, hence at the leading order $H^{\rm GP}_{\rm p} \approx -H^{\rm GP}_{\rm int}$ and the main contribution comes only from $H^{\rm GP}_{\rm hydro}$. Finally, at lowest order, we obtain the effective Hamiltonian (EH) for the particle dynamics

$$H_{\rm eff}[\mathbf{q},\mathbf{p}] = \frac{\mathbf{p}^2}{2M_{\rm eff}} + U(q_\perp),\ U(q_\perp) = -\frac{(1+C)M_0\Gamma^2}{8\pi^2q_\perp^2},\ \text{and}$$
$$M_{\rm eff} = M_{\rm p} + CM_0 = (\mathcal{M}+C)M_0. \tag{14}$$

The equations of motion for the particle position are then:

$$(\mathcal{M}+C)\ddot{\mathbf{q}}_\perp = -\frac{(1+C)\Gamma^2}{4\pi^2q_\perp^4}\mathbf{q}_\perp, \qquad \ddot{q}_z = 0, \tag{15}$$

Note that the added mass effect is suppressed for neutral-mass particles having $\mathcal{M}=1$ and the particle size explicitly appears only at high order terms. The attractive force scaling as $q_\perp^{-3}$ was first proposed by Donnelly[34] as the result of a pressure gradient. Equation (15) has been also studied for neutral-mass particles in the framework of pure hydrodynamical models[15,16].

Finally, note that if we replace in (13) the density by its leading order $\widetilde{\rho}_{\rm v}=1$, then the associated equations of motion are invariant under the following scaling transformation:

$$\mathbf{q} \to \lambda\mathbf{q}, \quad a_{\rm p} \to \lambda a_{\rm p}, \quad t \to \lambda^2 t \qquad \forall\ \lambda \in \mathbb{R}^+ \tag{16}$$

Such invariance will be also preserved in terms coming from higher orders in ε.

Numerical measurements and comparison with theory. We compare now our reduced model to the numerical experiment presented in Fig. 1. We first consider a small neutral-mass particle of size $a_{\rm p}=2.7\xi$. For this particle, the condition (9) is valid for a wide range of separations and the deformation of the vortex during the particle approach is negligible. We measured the variation of the different components of the Hamiltonian (10) as a function of distance between the particle and the vortex. Figure 2a displays such energies (markers) compared to the respective theoretical predictions (lines).

The striped region identifies the particle radius $a_{\rm p}/\xi$ where the particle and the vortex overlap. Since the added mass energy $E_{\rm add}$ (11) only modifies the particle inertia but has no effect in determining the force in the r.h.s. of (15), we subtract it from the hydrodynamic component $H^{\rm GP}_{\rm hydro}$ and the total GP energy $H^{\rm GP}=H-K$. We have used the Padé approximation given in Methods as an analytical expression for the vortex density profile $\widetilde{\rho}_{\rm v}$, so that both asymptotics (large and short vortex-particle separations) are reproduced. Even if our model is not supposed to be quantitatively accurate for $q_\perp \sim a_{\rm p}$, we can still observe a quite good agreement. Remarkably, the hypothesis that leads to neglect $H^{\rm GP}_{\rm q}$ is perfectly valid up to a distance about twice of the particle radius. Moreover, $H^{\rm GP}_{\rm p} \approx -H^{\rm GP}_{\rm int}$ and thus during the particle approach $H^{\rm GP} \approx H^{\rm GP}_{\rm hydro}$. Figure 2b shows in a log−log plot the absolute value of the measured energies for large distances. Clearly, all the energy contributions follow the predicted $q_\perp^{-2}$ scaling, as long as the vortex-particle separation is large. We have checked that the data in Fig. 2 are almost independent of

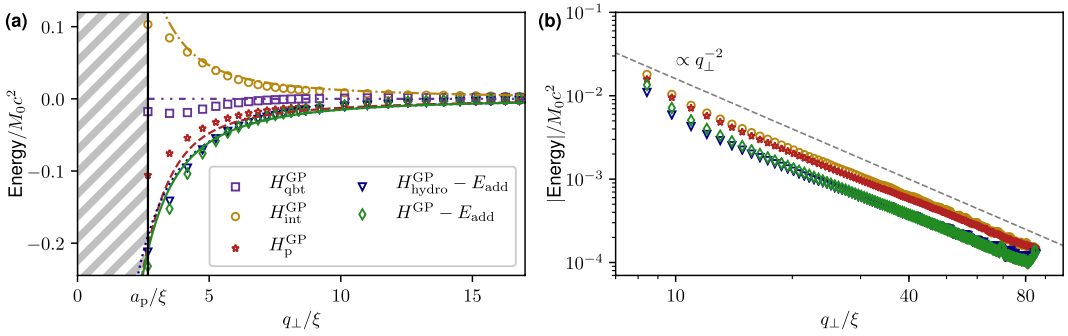


Figure 2. (**a**) Different energies as a function of the vortex-particle distance $q_\perp/\xi$ during the approach of a particle with size $a_p = 2.7\xi$. The initial separation is $q_\perp = 45.3\xi$ and the particle has zero velocity. Markers are numerical data and lines theoretical curves of corresponding colours. **(b)** Same energies as in **(a)** in ($log-log$ scale). Initial $q_\perp = 85.1\xi$ and initial velocity $\dot{q}_\perp = -0.04c$.

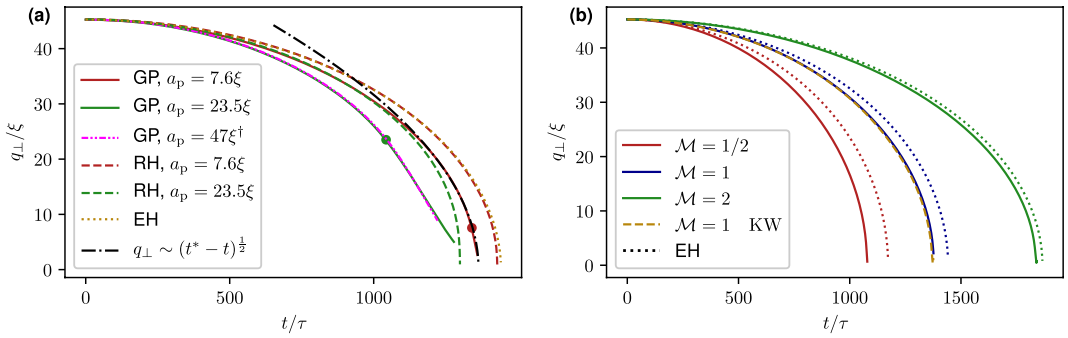


Figure 3. (**a**) Measured vortex-particle separation as a function of time for neutral-mass ($\mathcal{M} = 1$) particles of different sizes moving towards a straight vortex (solid lines). The initial condition is $q_\perp = 45.3\xi$ and $\dot{q} = 0$. Round markers indicate the corresponding trapping times. †The pink dash-dot-dotted line refers to a big particle initially at $q_\perp = 90.6\xi$ rescaled using Eq. (16) with $\lambda = 2$. The figure also displays the predictions RH (13) in dashed lines of the corresponding colours, the theoretical prediction (17) of the effective model EH (dotted golden line) and the scaling $q \sim (t^* - t)^{\frac{1}{2}}$, obtained by fitting the numerical data (dash-dotted black line). **(b)** The same as **(a)** but for particles with $a_p = 2.7\xi$ and different masses. Data from GP simulation are displayed in solid lines whereas the predictions (17) are in dotted lines. The dashed golden line refers to a GP simulation with a vortex containing Kelvin waves of *rms* amplitude 0.5ξ.

the particle mass. Discrepancies between data and theory might be due to sound radiation or to sub-leading terms in the boundary conditions of the superfluid velocity. We conclude that the effective potential energy is relatively well described by $U(q_\perp)$ in Eqs (14) and(15) gives a good approximation for the motion of the particle.

Equation (15) can be straightforwardly integrated and the solution for the particle-vortex distance reads

$$q_\perp(t) = \sqrt{\frac{2E_\perp}{M_{\text{eff}}}t^2 + q_0^2 + q_0\dot{q}_0 t}, \tag{17}$$

where $q_0 = q_\perp(t=0)$, $\dot{q}_0 = \dot{q}_\perp(t=0)$ and $E_\perp = H_{\text{eff}}[\mathbf{q}(t=0), \mathbf{p}(t=0)] - p_z^2/2M_{\text{eff}}$ is the conserved energy in the effective model. In the case of a neutral-mass particle with zero initial velocity Eq. (17) reduces to the one derived by Barenghi *et al.*[30]. In Fig. 3 the prediction (17) and the one obtained numerically from RH (13) are compared with numerical data.

Figure 3a shows the particle-vortex distance for neutral-mass particles of different sizes initially located at a distance $q_0 = 45.3\xi$. The markers denote the capture times, after which particles keep moving inside the vortex. The assumption (9) is ideally satisfied for point-like particles but it reasonably applies as long as the particle radius is sufficiently small compared to its distance to the vortex. Indeed, for the particle $a_p = 7.6\xi$ the accordance with theory is good, while for the one having $a_p = 23.5\xi$ is just qualitative. For such particle, the full reduced Hamiltonian gives a better description. In addition, the motion curve of a particle of radius $a_p = 2 \times 23.5\xi$, initially located at $2q_0$ is in good agreement (pink dashed-dot-dotted curve) with the scaling relation (16). It is interesting to note that close to the capture time the particle-vortex separation scales as

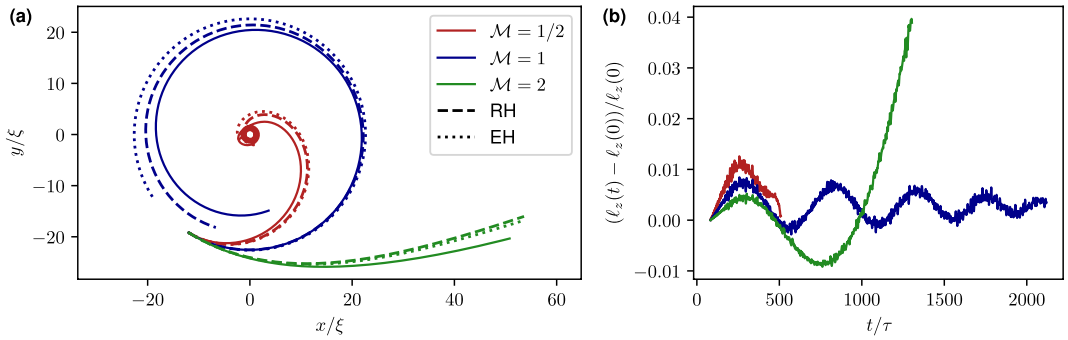


Figure 4. (**a**) Trajectories of small particles ($a_p = 2.7\xi$) with $\dot{\mathbf{q}}_\perp(t=0) = \mathbf{v}_v(q_\perp)$ and $q_\perp(t=0) = 22.6\xi$. GP data are displayed in solid lines, predictions of EH (14) in dotted lines and the predictions of RH (13) in dashed lines of the corresponding colours. (**b**) Relative variation of angular momentum as a function of time for the same simulations of (**a**).

$$q(t) \xrightarrow[t\to t^{*-}]{} \left(\frac{1+C}{\pi^2(\mathcal{M}+C)}\right)^{1/4} \sqrt{\Gamma(t^*-t)}, \qquad \text{with} \quad t^* = \frac{q_0^2}{\Gamma}\sqrt{\frac{4\pi^2(\mathcal{M}+C)}{1+C}}, \tag{18}$$

where we have set $\dot{\mathbf{q}}(t=0) = 0$ for sake of simplicity. In Fig. 3a such scaling is also apparent up to a separation of $q \sim 30\xi$ for the particle with $a_p = 7.6\xi$ (dotted-dashed line). The capture time t^* predicted by the effective model is compatible with the one observed in the GP simulation with a relative error of 5%. The scaling (18), that is also observed in vortex reconnections[35], suggests the idea that the trapping process could be seen as reconnection of the vortex with its images inside the particle. Finally, in Fig. 3b the vortex-particle separation has been measured for a small particle ($a_p = 2.7\xi$) with the same initial condition but with different masses. Remarkably, the heavier the particle, the better the agreement with theory. This could due to the fact that light particles are more sensitive to sound waves and compressible effects not taken into account in the theory. For completeness, we also show the case of a vortex filament perturbed with small-amplitude Kelvin waves (dashed golden line). As expected, the effect of Kelvin waves is sub-leading and no difference is appreciable with respect to the unperturbed case.

It is well known in classical hydrodynamics that light particles go into vortices whereas the heavy ones escape from them[11]. The same situation takes place for a particle in a superfluid, even if there is no Stokes drag at zero temperature. Indeed, as a central force problem, the effective Hamiltonian (14) conserves the angular momentum $\ell_z = M_{\text{eff}}(\mathbf{q}_\perp \times \dot{\mathbf{q}}_\perp)\cdot\hat{z}$. This conserved quantity leads to the emergence of a repulsive potential $\ell_z^2/2M_{\text{eff}}q_\perp^2$ in the effective Hamiltonian for $q_\perp$. Therefore there exists a critical angular momentum $\ell_{\text{crit}} = \sqrt{(1+C)(\mathcal{M}+C)}\,M_0\Gamma/2\pi$ such that for $\ell_z < \ell_{\text{crit}}$ particles collapse into the vortex and escape from it for $\ell_z > \ell_{\text{crit}}$. Now, if the particle is initially at rest in the reference frame moving with vortex flow, i.e. $\dot{\mathbf{q}}_\perp = \mathbf{v}_v(q_\perp)$, the condition on the critical value of ℓ_z is expressed in terms of the mass, as $\mathcal{M} < 1$ for trapping and $\mathcal{M} > 1$ for escaping. At $\mathcal{M} = 1$ the model (14) predicts a closed circular orbit, i.e. a particle tracing the flow. However, this orbit is unstable and modified by high order terms (see Methods) that lead to a collapse also in this case. The three situations $\mathcal{M} = 1$ and $\mathcal{M} > 1$ are manifest in Fig. 4a, where we display the trajectories of a small particle ($a_p = 2.7\xi$) with initial velocity $\dot{\mathbf{q}}_\perp = \mathbf{v}_v(q_\perp)$ but different masses. For the $\mathcal{M} = 1$ case the prediction given by (13) works better than the leading order solution. This is consistent with the fact that the terms proportional to $q_\perp^{-2}$ cancel for $\ell_z = \ell_{\text{crit}}$, so that the next-to-leading order becomes predominant.

Figure 4b shows that the angular momentum is conserved up to 4%. Note that the escaping particle feels the attraction of image vortices in the periodic box that break down the conservation of ℓ_z.

Generation of cusps and Kelvin waves on the vortex filament. We now address the effect of the particle on the vortex filament. As the vortex remains almost straight, it can be parametrised as $\mathbf{R}(z) = (\mathbf{s}(z), z)$, where $\mathbf{s}(z)$ is a bi-dimensional vector. The ansatz (6) can be generalised by replacing $\mathbf{x}_\perp$ in ρ_v and ϕ_v by $\mathbf{x}_\perp - \mathbf{R}(z)$. Assuming $|\mathbf{s}(z)| \ll q_\perp$ and small deflections $|\partial_z \mathbf{s}| \ll 1$, all the calculations made in the previous section to reduce the Hamiltonian can be performed in the same way if we keep only contributions at the first order in $\mathbf{s}(z)$. The vortex deformation appears in the term $\overline{H}^{\text{GP}}$ in (13) and simply corresponds to the Local Induced Approximation (LIA) Hamiltonian[28] (see Methods). The effective vortex-particle Hamiltonian (14) becomes

$$H_{v-p}[\mathbf{q},\mathbf{p},\mathbf{s}] = \frac{\mathbf{p}_{\text{eff}}^2}{2M_{\text{eff}}} + \frac{\Gamma^2\rho_\infty}{8\pi}\int_0^L \left[-\mathbf{s}\cdot\Lambda\frac{\partial^2\mathbf{s}}{\partial z^2} - \frac{(1+C)M_0}{\rho_\infty\pi|\mathbf{q}_\perp - \mathbf{s}(z)|^2}\delta(z-q_z)\right]\mathrm{d}z, \tag{19}$$

where from now on $q_\perp = (q_x, q_y)$. In principle Λ is a non-local operator yielding the correct Kelvin wave dispersion relation[28]. For the moment, we treat it as a constant. Up to a logarithmic correction, this is equivalent to consider the limit of large-scale vortex deformations. Although rough, such approximation provides a qualitatively

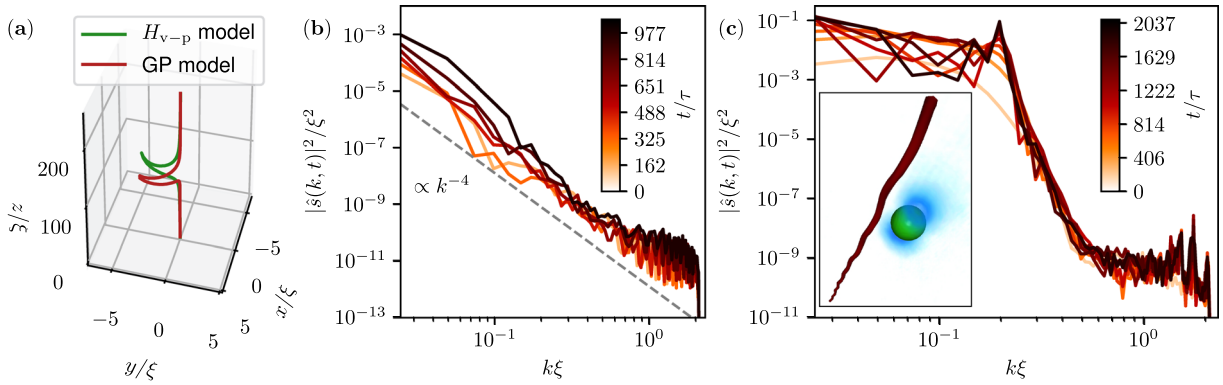


Figure 5. (**a**) Cusp generated during the trapping of a neutral-mass particle of size $a_p = 7.6\xi$ at the capture time t^*. The initial particle condition is $q_\perp = 45.3\xi$ and $q = 0$. Red solid line is the vortex line tracked during GP simulation, whereas green solid line is $\mathbf{s}(z, t^*)$ computed with the dynamics (20, 21). **(b)** Spectrum of vortex displacement measured from GP simulation at different times during the trapping of a particle. The parameters are the same as in **(a)**. **(c)** Spectrum of vortex displacement measured from GP simulation during the motion of a particle. The parameters for the particle are $a_p = 7.6\xi$, $q_\perp(t=0) = 22.6\xi$, $q_\perp(t=0) = \mathbf{v}_v(q_\perp)$ and $\dot{q}_z = 0.27c$ (see Methods). The inset shows the superfluid density and the particle where Kelvin waves are clearly present on the vortex filament.

good description of the vortex dynamics. The equations of motion coupling the vortex filament and the particle are thus found to be:

$$\begin{aligned}(\mathcal{M}+C)\ddot{\mathbf{q}}_\perp &= -\frac{(1+C)\Gamma^2}{4\pi^2|\mathbf{q}_\perp - \mathbf{s}(q_z)|^4}(\mathbf{q}_\perp - \mathbf{s}(q_z)),\\ (\mathcal{M}+C)\ddot{q}_z &= \frac{(1+C)\Gamma^2}{4\pi^2|\mathbf{q}_\perp - \mathbf{s}(q_z)|^4}(\mathbf{q}_\perp - \mathbf{s}(q_z))\cdot\frac{\partial s}{\partial z}|_{z=q_z}\end{aligned} \tag{20}$$

$$\kappa\frac{\partial \mathbf{s}}{\partial t} = \hat{z}\times\left[\frac{\Lambda\Gamma}{4\pi}\frac{\partial^2\mathbf{s}}{\partial z^2} + \frac{(1+C)M_0\Gamma}{\rho_\infty 4\pi^2|\mathbf{q}_\perp - \mathbf{s}(z)|^4}(\mathbf{q}_\perp - \mathbf{s}(z))\delta(z-q_z)\right],\ \text{with } \kappa = \pm 1, \tag{21}$$

where $(\hat{z}\times\mathbf{A})_i = \varepsilon_{ij}A_j$, with ε_{ij} the Levi-Civita symbol. The l.h.s of Eq. (21) can be straightforwardly derived following the calculations performed in refs[36,37]. Note that the r.h.s. of equation for $\ddot{q}_z$ is negligible in the limit $|\partial_z\mathbf{s}| \ll 1$ and $|\mathbf{q}| \gg |\mathbf{s}|$. In Eq. (21) a point force is exerted by the particle giving rise to the deformation of the vortex line, while the dispersive term leads to Kelvin wave propagation. This simplified model reproduces the generation of a cusp similar to the one observed in the numerical simulations of the full GP model, as apparent in Fig. 5a.

In previous works, such cusp-shaped deformations have been interpreted as the result of the vortex reconnection with the images inside the particle[21]. Such effect is not taken into account in our model and the formation of a cusp is the result of a simple action-reaction mechanism between the particle and the vortex. In addition, the curvature of the vortex filament during the trapping is not well described by the universal theoretical prediction for pure vortex reconnections obtained by Villois *et al.*[35] (data not shown).

From the particle-vortex model (20,21) we can extract further analytical predictions. Since $|\mathbf{s}| \ll \mathbf{q}_\perp$, we can set $\mathbf{q}_\perp - \mathbf{s} \approx \mathbf{q}_\perp$ in the model. The particle thus decouples from the vortex and just drives the forcing acting on it. We write $\mathbf{s}(z, t)$ and $\mathbf{q}(t)$ in complex variables as $s(z) = s_x(z, t) + is_y(z, t)$ and $q(t) = |q(t)|e^{i\Omega_q(t)t}$, and linearise (21) for small s. The equation now reads

$$\frac{\partial \hat{s}_k}{\partial t} = -i\kappa\frac{\Gamma\Lambda_k}{4\pi}k^2\hat{s}_k + i\frac{F_0}{|q(t)|^3}e^{-i(\Omega_q(t)+k\dot{q}_z)t}\ \text{with } F_0 = \kappa\frac{(1+C)M_0\Gamma}{4\pi^2\rho_\infty}, \tag{22}$$

where $\hat{s}_k$ is the Fourier transform of $s(z)$ and k a wave-vector. We have now phenomenologically included the non-local operator Λ_k that in Fourier space reads $\Lambda_k = 2(1 - \sqrt{1 - ka_0K_0(ka_0)/K_1(ka_0)})/(a_0k)^2$, with K_n the modified Bessel function of order n and $a_0 = 1.1265\xi$. The operator Λ_k has been defined in order to obtain the correct Kelvin wave relation dispersion $\omega_k^{KW} = \kappa\Gamma\Lambda_k k^2/4\pi$ computed in refs[28,38] and the cut-off a_0 has been fixed to satisfy the known GP small-k asymptotic expansion[38]. First, let us consider the case of radial approach ($\Omega_q = 0$) with vertical velocity $\dot{q}_z = 0$. Integrating Eq. (22), it follows that the spectrum of the vortex displacement obeys the scaling $|\hat{s}_k|^2 \sim k^{-4}$ at large scales, up to a logarithmic correction. Such scaling corresponds to the deformation of the vortex line which starts to develop already at the early times of the trapping process. We compute the spectra using the tracked vortex lines obtained from GP simulations by using the method explained in refs[39,40]. They present a good agreement with theory (see Fig. 5b). Finally, if $\dot{q}_z \neq 0$ or $\Omega_q \neq 0$, the particle-vortex model predicts the generation of Kelvin waves when the particle is still distant. Indeed, when the particle is far from the vortex,

the time dependence of $|q(t)|$ and the one of $\Omega_q(t)$ are much slower than the one of $s(t)$ and they can be treated as constants in Eq. (22). Therefore, the model (22) predicts a linear resonance if $\omega_k^{KW} = \Omega_q + k\dot{q}_z$. As a consequence, any motion of the particle not purely radial generates waves on the filament. In order to check this claim, we performed a GP simulation with a particle orbiting around the vortex while moving parallel to it. A movie of the simulation is available as Supplementary Information. The corresponding vortex displacement spectrum is presented in Fig. 5c, where the development of a resonance is clearly visible. The resonant mode predicted by the model (22) is $k\xi = 0.24$, compatible with the position of the observed peak. In the inset a snapshot of the superfluid density shows the corresponding Kelvin waves generated on the filament. Actually, all the small-k modes of the filament are growing during the first stages of particle motion. Indeed, the forcing driven by the particle produces an oscillation in time of such modes, with low frequency and high amplitude. Note that the considerations made from Eq. (22) could be in principle formalised using a multi-time asymptotic expansion.

Discussion

We have studied the interaction of a particle and a quantum vortex in a self-consistent framework given by the particle-superfluid Hamiltonian (1). The superfluid is described by the Gross-Pitaevskii equation and the particle through classical degrees of freedom. This minimal system is able to extend results obtained in more complex models[21,30] with a much lower numerical cost. The simplicity of the model allowed us to derive the reduced Hamiltonian (13) for the particle dynamics, that also includes corrections due to the vortex density profile. Similar theoretical computations can be straightforwardly performed in the case of non-local models of superfluids, that are more adequate for describing superfluid helium. In such models, the vortex density profile shows oscillations as a function of the distance to the core[41,42], which could have some impact on the dynamics of small and light particles. In our derivation, we have neglected acoustic radiation and interaction of vortices with with sound waves. Compressibility effects of this kind might be also important for light particles and they could be included, in principle, generalising the ansatz (6). The Gross-Pitaevskii model used in this work has a very simple equation of state valid in the weak coupling limit. When the coupling is not so weak, like in superfluid helium, the equation of state can be easily modified changing the type of non-linearity of the model to account for the effect of beyond-mean-field quantum fluctuations[43,44]. It would be interesting to study how these fluctuations modify the particle dynamics. In the same spirit, at extremely low temperatures, quantum fluctuations could excite low-amplitude Kelvin waves[45]. However, we expect this effect to be negligible as it was shown in Fig. 3b.

The vortex-particle interaction leads to the trapping of the particle by the vortex. The bounded state with a particle trapped inside a vortex line possesses an energy lower that the state in which the vortex and the particle are far apart. This energy gap, known as substitution energy, was first computed by Parks and Donelly[46]. It simply corresponds to the vortex kinetic energy contained in the volume occupied by the particle. We have checked that this estimate gives the good order of magnitude for the incompressible kinetic energy difference. However, it overestimates it as it does not account for dynamical processes like the generation of Kelvin waves after the capture. The substitution energy was then used in ref.[46] to assess the life time of a Brownian ion inside a vortex in presence of an electric field. The model used in this Report can be trivially extended to describe a charged particle by adding an external potential, and similar considerations could be easily rephrased. We have observed that the vortex considerably stretches while the particle is pulled out from it by an external force (data not shown). Therefore, even at zero temperature, the energy needed to remove a particle can be much larger than the substitution energy. The release of a particle from a vortex is an interesting problem for traditional and modern experiments with superfluids. We plan to use the model studied here to study this issue in a future work.

We have observed a non-trivial dynamics of vortex filament if a particle moves around it. The vortex dynamics has been included in the effective model (19), and we explained the motion of the vortex as the result of a mutual long-range interaction between the particle and the vortex itself. Moreover, we highlighted that long-range particle-vortex interaction is sufficient to generate Kelvin waves on the filament even if the particle never touches the vortex. It would be interesting to include such a simple interaction term in the vortex filament model, to study the effect of a large number of particles. In this regard, note that the model (2) can be trivially extended to include many particles, both at zero and finite temperature[27]. It is then natural to use it for studying the effect of particles in a quantum turbulent regime. Indeed, it is still not clear how the dynamics of active particles modify the evolution and decay of complex tangle of quantised vortex lines. Addressing such issues is fundamental for current experiments, since particles are nowadays the main tool for tracking and visualising vortices in superfluid helium.

Methods

Numerical methods and parameters. Equations (2) are solved with a standard pseudo-spectral code and a 4^{th} order Runge-Kutta scheme for the time stepping in a domain of size L with N_p mesh points per dimension. We set $c = \rho_\infty = 1$. The steady states for the particle and the vortex are prepared separately by performing imaginary time evolution of the GP equation and then they are multiplied to obtain the wished initial condition. To impose the initial flow around the particle, the initial condition is evolved for a short time ($\sim 40\tau$) using GP without the particle dynamics. In Fig. 5c, the target velocity in the z component is reached by adding an external force $\mathbf{F} = (0,\, 0{,}2 \times 10^{-3} M_0 c^2/\xi)$ that then is switched off.

The particle potential is a smoothed hat-function $V_p(r) = \frac{V_0}{2}\left(1 - \tanh\left[\frac{r^2-\eta^2}{4\Delta l^2}\right]\right)$ and the mass displaced by the particle is measured as $M_0 = \rho_\infty L^3 (1 - \int |\psi_p|^2 \, d\mathbf{x} / \int |\psi_\infty|^2 \, d\mathbf{x})$, where ψ_p is the steady state with just one particle. Since the particle boundaries are not sharp, we measure the particle radius as $a_p = (3M_0/4\pi\rho_\infty)^{\frac{1}{3}}$ for given values of the numerical parameters η and Δl. For all the particles $V_0 = 20$. The parameters used are the following. For $a_p = 2.7\xi$: $N_p = 512$, $\eta = \xi$ and $\Delta l = 0.75\xi$. For $a_p = 7.6\xi$: $N_p = 256$, $\eta = 2\xi$ and $\Delta l = 2.5\xi$. For $a_p = 23.5\xi$: $N_p = 256$,

$\eta = 20\xi$ and $\Delta l = 4\xi$. Finally, for $a_p = 47\xi$: $N_p = 512$, $\eta = 43\xi$ and $\Delta l = 5\xi$. Only for the last case $L = 512\xi$, while for all the others $L = 256\xi$.

In theoretical predictions we have used the Padé approximation $\tilde{\rho}_v = \bar{r}^2(a_1 + a_2\bar{r}^2 + a_3\bar{r}^4)/(1 + b_1\bar{r}^2 + b_2\bar{r}^4 + a_3\bar{r}^6)$ where $\bar{r} = |\mathbf{x}|/\xi$. The coefficients are: $a_1 = 0.340038$, $a_2 = 0.0360207$, $a_3 = 0.000985125$, $b_1 = 0.355931$, $b_2 = 0.037502$.

Derivation of the reduced model for the particle trapping. We report here the calculations leading to the reduced Hamiltonian (13). We denote by an overbar some constants that at the leading order are independent of $\mathbf{q}$. The quantum energy term H^{GP}_{qnt} contains gradients of the density and it is sub-leading when $|\mathbf{q}| \gg a_p > \xi$. We thus we set $H^{GP}_{qnt} \approx \overline{H}^{GP}_{qnt}$. As discussed in the text, $1 - \tilde{\rho}_p(x)$ is supported on a ball of center q and radius a_p denoted by $\mathbb{B}(\mathbf{q}, a_p)$. At the leading order we also have $\tilde{\rho}_p^2 \approx \tilde{\rho}_p$, and H^{GP}_{int} can be computed as

$$\begin{aligned} H^{GP}_{int} &\approx \frac{g\rho_\infty}{2m^2}\int (1 - (1 - \tilde{\rho}_p))\tilde{\rho}_v^2 \, d\mathbf{x} \\ &= \overline{H}^{GP}_{int} - \frac{g\rho_\infty^2}{2m^2}\int (1 - \tilde{\rho}_p)\tilde{\rho}_v^2 \, d\mathbf{x} \\ &\approx \overline{H}^{GP}_{int} - \frac{g\rho_\infty^2}{2m^2}\int_{\mathbb{B}(\mathbf{q},a_p)} \tilde{\rho}_v^2 \, d\mathbf{x} \\ &\approx \overline{H}^{GP}_{int} - \frac{1}{2}M_0 c^2 \tilde{\rho}_v^2(q_\perp). \end{aligned} \tag{23}$$

where we have treated $\tilde{\rho}_v$ as constant inside $\mathbb{B}(\mathbf{q}, a_p)$, recognised the displaced superfluid mass $M_0 = \rho_\infty \int_{\mathbb{B}} d\mathbf{x}$ and used the definition of the speed of sound. A similar calculation can be performed for the the term H^{GP}_p:

$$\begin{aligned} H^{GP}_p &\approx \overline{H}^{GP}_p - \frac{\mu\rho_\infty}{m}\int (1 - \tilde{\rho}_p)\tilde{\rho}_v \, d\mathbf{x} \\ &\approx \overline{H}^{GP}_p - \frac{\mu\rho_\infty}{m}\int_{\mathbb{B}_{\mathbf{q},a_p)}} \tilde{\rho}_v \, d\mathbf{x} \approx \overline{H}^{GP}_p + M_0 c^2 \tilde{\rho}_v(q_\perp). \end{aligned} \tag{24}$$

In the first equality we used the Thomas-Fermi approximation (5) and again $\tilde{\rho}_p^2 \approx \tilde{\rho}_p$.

To compute the hydrodynamic term H^{GP}_{hydro} we write $\mathbf{v}_s^2 = \mathbf{v}_v^2 + \mathbf{v}_p \cdot (2\mathbf{v}_v + \mathbf{v}_p) + \mathbf{v}_{BC} \cdot (2\mathbf{v}_v + 2\mathbf{v}_p + \mathbf{v}_{BC})$ and consider the contribution of the three addends differently. Firstly we have

$$\begin{aligned} H^{GP(v)}_{hydro} &= \frac{1}{2}\int \rho \mathbf{v}_v^2 \, d\mathbf{x} = \overline{H}^{GP}_{hydro} - \frac{\rho_\infty}{2}\int (1 - \tilde{\rho}_p)\tilde{\rho}_v \mathbf{v}_v^2 d \\ &\approx \overline{H}^{GP}_{hydro} - \frac{M_0\tilde{\rho}_v(q_\perp)}{2}\mathbf{v}_v(q_\perp)^2 = \overline{H}^{GP}_{hydro} - \frac{\Gamma^2 M_0 \tilde{\rho}_v(q_\perp)}{8\pi^2 q_\perp^2}. \end{aligned} \tag{25}$$

The second term is computed integrating by parts, using the incompressibility of the flows and neglecting the gradients of ρ_v:

$$\begin{aligned} H^{GP(p)}_{hydro} &= \frac{\rho_\infty}{2}\int \tilde{\rho}_p\tilde{\rho}_v \nabla\phi_p \cdot (2\mathbf{v}_v + \mathbf{v}_p) \, d\mathbf{x} \\ &\approx \frac{\rho_\infty}{2}\int_{\mathbb{B}^c(\mathbf{q},a_p)} \tilde{\rho}_v \nabla\phi_p \cdot (2\mathbf{v}_v + \mathbf{v}_p) d\mathbf{x} \\ &\approx -\frac{\rho_\infty a_p^2}{2}\oint_{\partial\mathbb{B}(\mathbf{q},a_p)} \tilde{\rho}_v\phi_p(2\mathbf{v}_v + \mathbf{v}_p) \cdot \hat{n} d\Omega, \end{aligned} \tag{26}$$

where $\mathbb{B}^c(\mathbf{q}, a_p)$ is the complement of $\mathbb{B}(\mathbf{q}, a_p)$ and $\partial\mathbb{B}(\mathbf{q}, a_p)$ its boundary. For $\varepsilon \ll 1$ (see Eq. (9)), in the last integral ρ_v and $\mathbf{v}_v$ can be evaluated at q. The angular integral is then computed exactly and it gives $H^{GP(vp)}_{hydro} = \frac{M_0\tilde{\rho}_v(\mathbf{q})}{2}C(\dot{\mathbf{q}}^2 - \mathbf{v}_v^2)$, with $C = 1/2$.

The velocity $\mathbf{v}_{BC}$ is obtained at order ε^2 from the potential $\phi_{BC} = \frac{1}{2}e_{ij}x'_i x'_j$, where $e_{ij}(q) = (\partial_i v_v^j + \partial_j v_v^i)/2$ is the strain rate tensor evaluated at the particle position. Following the same procedure of (26), we see that the only non-zero contribution is given by

$$\begin{aligned} H^{GP(BC)}_{hydro} &= -\frac{\rho_\infty a_p^2}{2}\oint_{\partial\mathbb{B}(\mathbf{q},a_p)} \tilde{\rho}_v\varphi_{BC}\mathbf{v}_{BC} \cdot \hat{n} d\Omega \\ &= -\frac{\rho_\infty a_p^5}{4}\tilde{\rho}_v \, e_{ij}e_{rs}\oint \hat{n}_i\hat{n}_j\hat{n}_r\hat{n}_s d\Omega \\ &= -\frac{M_0\tilde{\rho}_v a_p^2}{10}(e_{ij})^2 = -\frac{M_0\Gamma^2\tilde{\rho}_v a_p^2}{20\pi^2 q_\perp^4}. \end{aligned} \tag{27}$$

We have used $\oint \hat{n}_i\hat{n}_j\hat{n}_r\hat{n}_s d\Omega = (\delta_{ij}\delta_{rs} + \delta_{ir}\delta_{js} + \delta_{is}\delta_{ir})\Omega_d/d(d+2)$, where Ω_d is the surface of the unit sphere in d dimensions. The total hydrodynamic kinetic term is the just given by $H^{\rm GP}_{\rm hydro} = H^{{\rm GP}(v)}_{\rm hydro} + H^{{\rm GP}(p)}_{\rm hydro} + H^{{\rm GP(BC)}}_{\rm hydro}$.

Note that at the order $\xi^4/q_\perp^4$ for large vortex-particle separations, the reduced Hamilonian (13) becomes

$$H_{\rm red}[\mathbf{q},\mathbf{p}] = \overline{H}^{\rm GP} + \frac{\mathbf{p}^2}{2M_{\rm eff}} + M_0c^2\left[\frac{1}{2} - \frac{(1+C)\xi^2}{q_\perp^2} + \frac{(10C+5-4(a_{\rm p}/\xi)^2)}{10}\frac{\xi^4}{q_\perp^4}\right], \tag{28}$$

where the term proportional to $\xi^4/q_\perp^4$ turns out to be repulsive if $a_{\rm p}^2 < \frac{5}{4}(1+2C)\xi^2$.

Vortex deformation. We can give a rough derivation of the effective vortex-particle Hamiltonian (19) by assuming a small deformation of the vortex line. Similarly to the previous calculations, we neglect the gradients of $\widetilde{\rho}_{\rm p}$. At the leading order, the terms $H^{\rm GP}_{\rm hydro}$ and $H^{\rm GP}_{\rm qnt}$ are the only contributing to $H_{\rm v-p}$. For distant particles, the only component of the superfluid velocity modified by the vortex displacement is $\mathbf{v}_{\rm v}$. The new contributions to the energy coming from the products of $\mathbf{v}_{\rm v}$ and the other velocity fields vanish after angular integration. We thus need to compute the term $\mathbf{v}_{\rm v}(|\mathbf{x}-\mathbf{R}(z)|)^2 = \nabla_\perp\phi_{\rm v}(\mathbf{x}_\perp - \mathbf{s}(z))^2 + (\nabla_\perp\phi_{\rm v}(|\mathbf{x}_\perp - \mathbf{s}(z)|)\cdot\partial_z\mathbf{s}(z))^2$ where now $\mathbf{x}_\perp = (x,y)$ and $\nabla_\perp = (\partial_x,\partial_y)$. The first term leads directly to the potential (11) evaluated at $\mathbf{q}_\perp - \mathbf{s}(q_z)$. The second term is treated by using the fact that $1-\widetilde{\rho}_{\rm p}$ is practically supported on $\mathbb{B}(\mathbf{q},a_{\rm p})$ and $\widetilde{\rho}_{\rm p} = 1-(1-\widetilde{\rho}_{\rm p})$. We need to compute

$$\begin{aligned} H^{\rm GP}_{\rm LIA} &\approx \frac{\rho_\infty}{2}\int \widetilde{\rho}_{\rm v}(|\mathbf{x}_\perp - \mathbf{s}(z)|)(\nabla_\perp\phi_{\rm v}(|\mathbf{x}_\perp - \mathbf{s}(z)|)\cdot\partial_z s(z))^2\,\mathrm{d}\mathbf{x} \\ &\quad - \frac{\rho_\infty}{2}\int_{\mathbb{B}(\mathbf{q},a_{\rm p})} \widetilde{\rho}_{\rm v}(|\mathbf{x}_\perp - \mathbf{s}(z)|)(\nabla_\perp\phi_{\rm v}(|\mathbf{x}_\perp - \mathbf{s}(z)|)\cdot\partial_z\mathbf{s}(z))^2\,\mathrm{d}\mathbf{x} \\ &\approx \frac{\rho_\infty}{2}\int_0^L \partial_z s_i(z)\partial_z s_j(z)\left(\int\widetilde{\rho}_{\rm v}(x_\perp)v_{\rm v}^i(x_\perp)v_{\rm v}^j\mathrm{d}\mathbf{x}_\perp\right)\mathrm{d}z \\ &\quad + \frac{M_0}{2}\widetilde{\rho}_{\rm v}(q_\perp)(\mathbf{v}_{\rm v}(q_\perp)\cdot\partial_z\mathbf{R}(z))^2 \end{aligned} \tag{29}$$

$$\approx \frac{\rho_\infty}{4}\int_0^L(\partial_z\mathbf{s}(z))^2\left(\int\widetilde{\rho}_{\rm v}(x_\perp)\mathbf{v}_{\rm v}(x_\perp)^2\mathrm{d}\mathbf{x}_\perp\right)\mathrm{d}z = \frac{\rho_\infty\Gamma^2\Lambda_{\rm hydro}}{8\pi}\int_0^L(\partial_z\mathbf{s}(z))^2\mathrm{d}z, \tag{30}$$

where we have neglected the second term in (29) as it subdominant. The constant $\Lambda_{\rm hydro}$ is given by the radial integral

$$\begin{aligned} \Lambda_{\rm hydro} &= \int_0^{L_{\rm d}}\frac{\widetilde{\rho}_{\rm v}(r)}{r}\mathrm{d}r = \int_0^{\xi}\frac{\widetilde{\rho}_{\rm v}(r)}{r}\mathrm{d}r \\ &\quad + \int_\xi^\infty\frac{\widetilde{\rho}_{\rm v}(r)-1}{r}\mathrm{d}r + \log\frac{L_{\rm d}}{\xi} + O((L_{\rm d}/\xi)^2) \\ &= \log\frac{L_{\rm d}}{\xi} - 0.3978 + O((L_{\rm d}/\xi)^2), \end{aligned} \tag{31}$$

where $L_{\rm d}$ is a cut-off of the order of the inter-vortex distance. The last integral has been performed numerically using $\widetilde{\rho}_{\rm v}$ obtained by imaginary time evolution of the GP equation in a infinite domain. The quantum energy term $H^{\rm GP}_{\rm qnt}$ gives a contribution equal to (30) but with the constant $\Lambda_{\rm hydro}$ replaced by $\Lambda_{\rm qnt} = \frac{1}{4}\int_0^\infty\left(\frac{\mathrm{d}\widetilde{\rho}_{\rm v}}{\mathrm{d}r}\right)^2\frac{r}{\widetilde{\rho}_{\rm v}}\mathrm{d}r = 0.2854$. Finally, in Eq. (19) the constant is $\Lambda = \Lambda_{\rm hydro} + \Lambda_{\rm qnt}$. This oversimplified derivation does not recover the full dispersion relation of Kelvin waves as it neglects non-linear interactions and the 3D modifications of $v_{\rm v}$ due to vortex deformations. For a more accurate discussion see refs[28,38,47].

Data Availability

The datasets generated and analysed during the current study are available from the corresponding authors on request.

References

1. Donnelly, R. J. *Quantized vortices in helium II*, vol. 2 (Cambridge University Press, 1991).
2. Barenghi, C. F., Skrbek, L. & Sreenivasan, K. R. Introduction to quantum turbulence. *Proceedings of the National Academy of Sciences* **111**, 4647–4652, https://doi.org/10.1073/pnas.1400033111 (2014).
3. Madison, K. W., Chevy, F., Wohlleben, W. & Dalibard, J. Vortex formation in a stirred bose-einstein condensate. *Phys. Rev. Lett.* **84**, 806–809, https://doi.org/10.1103/PhysRevLett.84.806 (2000).
4. Abo-Shaeer, J. R., Raman, C., Vogels, J. M. & Ketterle, W. Observation of vortex lattices in bose-einstein condensates. *Science* **292**, 476–479, https://doi.org/10.1126/science.1060182 (2001).
5. Bewley, G. P., Lathrop, D. P. & Sreenivasan, K. R. Superfluid helium: Visualization of quantized vortices. *Nature* **441**, 588 (2006).
6. Bewley, G. P., Paoletti, M. S., Sreenivasan, K. R. & Lathrop, D. P. Characterization of reconnecting vortices in superfluid helium. *Proceedings of the National Academy of Sciences* **105**, 13707–13710, https://doi.org/10.1073/pnas.0806002105 (2008).
7. Fonda, E., Meichle, D. P., Ouellette, N. T., Hormoz, S. & Lathrop, D. P. Direct observation of kelvin waves excited by quantized vortex reconnection. *Proceedings of the National Academy of Sciences* **111**, 4707–4710, https://doi.org/10.1073/pnas.1312536110 (2014).

8. Paoletti, M. S., Fisher, M. E., Sreenivasan, K. R. & Lathrop, D. P. Velocity statistics distinguish quantum turbulence from classical turbulence. *Phys. Rev. Lett.* **101**, 154501, https://doi.org/10.1103/PhysRevLett.101.154501 (2008).
9. La Mantia, M. & Skrbek, L. Quantum turbulence visualized by particle dynamics. *Phys. Rev. B* **90**, 014519, https://doi.org/10.1103/PhysRevB.90.014519 (2014).
10. Zmeev, D. E. *et al*. Excimers he^*_2 as tracers of quantum turbulence in ^{4}He in the $t = 0$ limit. *Phys. Rev. Lett.* **110**, 175303, https://doi.org/10.1103/PhysRevLett.110.175303 (2013).
11. Douady, S., Couder, Y. & Brachet, M. E. Direct observation of the intermittency of intense vorticity filaments in turbulence. *Phys. Rev. Lett.* **67**, 983–986, https://doi.org/10.1103/PhysRevLett.67.983 (1991).
12. Toschi, F. & Bodenschatz, E. Lagrangian properties of particles in turbulence. *Annual review of fluid mechanics* **41**, 375–404 (2009).
13. Maxey, M. R. & Riley, J. J. Equation of motion for a small rigid sphere in a nonuniform flow. *The Physics of Fluids* **26**, 883–889, https://doi.org/10.1063/1.864230 (1983).
14. Auton, T. R., Hunt, J. C. R. & Prud'Homme, M. The force exerted on a body in inviscid unsteady non-uniform rotational flow. *Journal of Fluid Mechanics* **197**, 241–257, https://doi.org/10.1017/S0022112088003246 (1988).
15. Poole, D. R., Barenghi, C. F., Sergeev, Y. A. & Vinen, W. F. Motion of tracer particles in he ii. *Phys. Rev. B* **71**, 064514, https://doi.org/10.1103/PhysRevB.71.064514 (2005).
16. Sergeev, Y. A. & Barenghi, C. F. Particles-vortex interactions and flow visualization in 4he. *Journal of Low Temperature Physics* **157**, 429, https://doi.org/10.1007/s10909-009-9994-8 (2009).
17. Schwarz, K. W. Three-dimensional vortex dynamics in superfluid ^{4}He: Homogeneous superfluid turbulence. *Phys. Rev. B* **38**, 2398–2417, https://doi.org/10.1103/PhysRevB.38.2398 (1988).
18. Schwarz, K. W. Spherical probes and quantized vortices: Hydrodynamic formalism and simple applications. *Phys. Rev. A* **10**, 2306–2317, https://doi.org/10.1103/PhysRevA.10.2306 (1974).
19. Kivotides, D., Barenghi, C. F. & Sergeev, Y. A. Collision of a tracer particle and a quantized vortex in superfluid helium: Self-consistent calculations. *Phys. Rev. B* **75**, 212502, https://doi.org/10.1103/PhysRevB.75.212502 (2007).
20. Astrakharchik, G. E. & Pitaevskii, L. P. Motion of a heavy impurity through a bose-einstein condensate. *Phys. Rev. A* **70**, 013608, https://doi.org/10.1103/PhysRevA.70.013608 (2004).
21. Berloff, N. G. & Roberts, P. H. Capture of an impurity by a vortex line in a bose condensate. *Phys. Rev. B* **63**, 024510, https://doi.org/10.1103/PhysRevB.63.024510 (2000).
22. Rica, S. & Roberts, D. C. Induced interaction and crystallization of self-localized impurity fields in a bose-einstein condensate. *Phys. Rev. A* **80**, 013609, https://doi.org/10.1103/PhysRevA.80.013609 (2009).
23. Villois, A. & Salman, H. Vortex nucleation limited mobility of free electron bubbles in the gross-pitaevskii model of a superfluid. *Phys. Rev. B* **97**, 094507, https://doi.org/10.1103/PhysRevB.97.094507 (2018).
24. Winiecki, T. & Adams, C. S. Motion of an object through a quantum fluid. *EPL (Europhysics Letters)* **52**, 257 (2000).
25. Shukla, V., Brachet, M. & Pandit, R. Sticking transition in a minimal model for the collisions of active particles in quantum fluids. *Phys. Rev. A* **94**, 041602, https://doi.org/10.1103/PhysRevA.94.041602 (2016).
26. Shukla, V., Pandit, R. & Brachet, M. Particles and fields in superfluids: Insights from the two-dimensional gross-pitaevskii equation. *Phys. Rev. A* **97**, 013627, https://doi.org/10.1103/PhysRevA.97.013627 (2018).
27. Giuriato, U., Krstulovic, G. & Proment, D. Clustering and phase transitions in a 2d quantum fluid with impurities. *arXiv preprint arXiv:1807.08721* (2018).
28. Pismen, L. M. *Vortices in nonlinear fields: from liquid crystals to superfluids, from non-equilibrium patterns to cosmic strings*, vol. 100 (Oxford University Press, 1999).
29. Kivotides, D., Barenghi, C. F. & Sergeev, Y. A. Numerical calculation of the interaction of superfluid vortices and a rigid sphere. *Journal of Low Temperature Physics* **144**, 121–134, https://doi.org/10.1007/s10909-006-9253-1 (2006).
30. Barenghi, C. F., Kivotides, D. & Sergeev, Y. A. Close approach of a spherical particle and a quantised vortex in helium ii. *Journal of Low Temperature Physics* **148**, 293–297, https://doi.org/10.1007/s10909-007-9387-9 (2007).
31. Barenghi, C. F., Parker, N., Proukakis, N. & Adams, C. Decay of quantised vorticity by sound emission. *Journal of Low Temperature Physics* **138**, 629–634, https://doi.org/10.1007/s10909-005-2272-5 (2005).
32. Krstulovic, G., Brachet, M. & Tirapegui, E. Radiation and vortex dynamics in the nonlinear schrödinger equation. *Phys. Rev. E* **78**, 026601, https://doi.org/10.1103/PhysRevE.78.026601 (2008).
33. Batchelor, G. K. *An Introduction to Fluid Dynamics*. Cambridge Mathematical Library (Cambridge University Press, 2000).
34. Donnelly, R. J. Theory of the interaction of ions and quantized vortices in rotating helium ii. *Phys. Rev. Lett.* **14**, 39–41, https://doi.org/10.1103/PhysRevLett.14.39 (1965).
35. Villois, A., Proment, D. & Krstulovic, G. Universal and nonuniversal aspects of vortex reconnections in superfluids. *Phys. Rev. Fluids* **2**, 044701, https://doi.org/10.1103/PhysRevFluids.2.044701 (2017).
36. Nemirovskii, S. K. Thermodynamic equilibrium in the system of chaotic quantized vortices in a weakly imperfect bose gas. *Theoretical and Mathematical Physics* **141**, 1452–1460, https://doi.org/10.1023/B:TAMP.0000043860.52270.0c (2004).
37. Bustamante, M. D. & Nazarenko, S. Derivation of the biot-savart equation from the nonlinear schrödinger equation. *Phys. Rev. E* **92**, 053019, https://doi.org/10.1103/PhysRevE.92.053019 (2015).
38. Roberts, P. H. On vortex waves in compressible fluids. ii. the condensate vortex. *Proceedings of the Royal Society of London A: Mathematical, Physical and Engineering Sciences* **459**, 597–607, https://doi.org/10.1098/rspa.2002.1033 (2003).
39. Krstulovic, G. Kelvin-wave cascade and dissipation in low-temperature superfluid vortices. *Phys. Rev. E* **86**, 055301, https://doi.org/10.1103/PhysRevE.86.055301 (2012).
40. Villois, A., Krstulovic, G., Proment, D. & Salman, H. A vortex filament tracking method for the gross–pitaevskii model of a superfluid. *Journal of Physics A: Mathematical and Theoretical* **49**, 415502 (2016).
41. Berloff, N. G. & Roberts, P. H. Motions in a bose condensate: Vi. vortices in a nonlocal model. *Journal of Physics A: Mathematical and General* **32**, 5611 (1999).
42. Reneuve, J., Salort, J. & Chevillard, L. Structure, dynamics, and reconnection of vortices in a nonlocal model of superfluids. *Phys. Rev. Fluids* **3**, 114602, https://doi.org/10.1103/PhysRevFluids.3.114602 (2018).
43. Berloff, N. G., Brachet, M. & Proukakis, N. P. Modeling quantum fluid dynamics at nonzero temperatures. *Proceedings of the National Academy of Sciences*, https://doi.org/10.1073/pnas.1312549111 (2014).
44. Adhikari, S. & Salasnich, L. Vortex lattice in the crossover of a bose gas from weak coupling to unitarity. *Scientific reports* **8**, 8825 (2018).
45. Krstulovic, G. & Brachet, M. Anomalous vortex-ring velocities induced by thermally excited kelvin waves and counterflow effects in superfluids. *Phys. Rev. B* **83**, 132506, https://doi.org/10.1103/PhysRevB.83.132506 (2011).
46. Parks, P. E. & Donnelly, R. J. Radii of positive and negative ions in helium ii. *Phys. Rev. Lett.* **16**, 45–48, https://doi.org/10.1103/PhysRevLett.16.45 (1966).
47. Laurie, J., L'vov, V. S., Nazarenko, S. & Rudenko, O. Interaction of kelvin waves and nonlocality of energy transfer in superfluids. *Phys. Rev. B* **81**, 104526, https://doi.org/10.1103/PhysRevB.81.104526 (2010).

Acknowledgements

We acknowledge useful scientific discussions with Marc Brachet, Gustavo During, Davide Proment, Vishwanath Shukla and Sergey Nazarenko. The authors were supported by Agence Nationale de la Recherche through the project GIANTE ANR-18-CE30-0020-01. Computations were carried out on the Mésocentre SIGAMM hosted at the Observatoire de la Côte d'Azur and the French HPC Cluster OCCIGEN through the GENCI allocation A0042A10385.

Author Contributions

U.G. performed the numerical simulations and analysed the data. U.G. and G.K. developed the theory and wrote the manuscript.

Additional Information

Supplementary information accompanies this paper at https://doi.org/10.1038/s41598-019-39877-w.

Competing Interests: The authors declare no competing interests.

Publisher's note: Springer Nature remains neutral with regard to jurisdictional claims in published maps and institutional affiliations.

Open Access This article is licensed under a Creative Commons Attribution 4.0 International License, which permits use, sharing, adaptation, distribution and reproduction in any medium or format, as long as you give appropriate credit to the original author(s) and the source, provide a link to the Creative Commons license, and indicate if changes were made. The images or other third party material in this article are included in the article's Creative Commons license, unless indicated otherwise in a credit line to the material. If material is not included in the article's Creative Commons license and your intended use is not permitted by statutory regulation or exceeds the permitted use, you will need to obtain permission directly from the copyright holder. To view a copy of this license, visit http://creativecommons.org/licenses/by/4.0/.

© The Author(s) 2019

3.3 *Publication*: Quantum vortex reconnections mediated by trapped particles

As we discussed in section 3.1 and in the publication [75] just reported, the long range interaction that leads to the particle trapping can be interpreted as a reconnection dynamics between the vortex and its images inside the particle. Such long range interaction plays a key role also in the actual reconnection between two real vortex filaments in the case in which particles are trapped inside them. How the presence of particles affect a vortex reconnection is indeed the topic addressed in the article [77], presented below[3]. The findings of this work are intended to give some theoretical support to the superfluid helium experiments in which reconnections have been observed by means of trapped solidified particles [29, 169].

Firstly, we study the reconnection of a vortex dipole, with a single particle initially trapped in one of the filaments. Note that a vortex dipole moving with constant speed is a steady solution of the GP equation (in the co-moving frame) and thus a spontaneous self-reconnection does not happen unless some instability is induced [26]. However, the presence of a particle breaks the symmetry of the system, triggering in this way the reconnection dynamics. The reconnecting point of the bare vortex lies on the plane orthogonal to the dipole and containing the particle center. As the system evolves, the separation $\delta(t)$ between such point and the particle surface scales accordingly to the $t^{1/2}$ scaling (1.160). Unlike what observed for the particle trapping [75], the vortex-particle separation is independent of the particle mass. This means that, although the reconnection is triggered by the simmetry breaking induced by the particle, the vortex dynamics is effectively fully governed only by the circulation. After the reconnection, the particle is detatched with a higher velocity because of an abrupt momentum exchange with the vortex. In the paper, we characterize such momentum exchange, which also determines a mass-dependent deflection of the transverse particle trajectory. Moreover, we observe that in the direction parallel to the initial dipole velocity the vortex and the particle momenta do not compensate exactly each other. This is compatible with the expected momentum transfer to a sound pulse orthogonally to the reconnection plane, which is a signature of the irreversibility of the reconnection process [230]. In order to check if the scaling invariance (3.8) still holds in this case, we perform another set of simulations doubling the particle size and the vortex distance. We indeed observe a good agreement, although the invariance is polluted by the precession of the trapped particle due to Magnus effect (2.29) (see the publication [79] in the next chapter for an analysis on such precession motion).

In the last part of the paper, we consider the reconnection of two linked rings decorated with randomly distributed particles. Unlike the case of the dipole, in such system a reconnection is known to happen spontaneosly without particles. Thus, the effect of the presence of the particles can be directly compared with the bare case. Also here we observe that the reconnection is likely to happen at the particle position. The main finding is that light particles do not modify the evolution of the separation rate

[3] We refer to the introductory section 1.4.4 for a review of superfluid vortex reconnections.

at large scales, apart from a speed-up taking place close to the reconnection event. Conversely, if the particles are too heavy, the reconnection dynamics is driven by their ballistic motion.

Quantum vortex reconnections mediated by trapped particles

Umberto Giuriato and Giorgio Krstulovic
Université Côte d'Azur, Observatoire de la Côte d'Azur, Laboratoire Lagrange, CNRS, Nice, France

(Received 20 July 2020; accepted 18 August 2020; published 8 September 2020)

Reconnections between quantum vortex filaments in the presence of trapped particles are investigated using numerical simulations of the Gross-Pitaevskii equation. Particles are described with classical degrees of freedom and modeled as highly repulsive potentials which deplete the superfluid. First, the case of a vortex dipole with a single particle trapped inside one of the vortices is studied. It is shown that the reconnection takes place at the position of the particle as a consequence of the symmetry breaking induced by it. The separation rate between the reconnecting points is compatible with the known dynamics of quantum vortex reconnections, and it is independent of the particle mass and size. After the reconnection, the particle is pushed away with a constant velocity, and its trajectory is deflected because of the transverse momentum exchange with the vortex filaments. The momentum exchanges between the particle, the vortex, and a density pulse are characterized. Finally, the reconnection of two linked rings, each of them with several initially randomly distributed particles, is studied. It is observed that generically, reconnections take place at the location of trapped particles. It is shown that reconnection dynamics is unaffected for light particles.

DOI: 10.1103/PhysRevB.102.094508

I. INTRODUCTION

One of the most striking features of superfluids is the presence of quantum vortices, thin tornadoes which arise as topological defects and nodal lines of the complex order parameter describing the system [1]. Quantum vortices have been observed in different kinds of superfluids, from atomic Bose-Einstein condensates (BECs), where their core is micrometer sized, to superfluid ^{4}He, where the core size is a few angstroms. The topological nature of quantum vortices constrains their circulation to be a discrete multiple of the quantum of circulation $\Gamma = h/m$, where h is the Planck constant and m is the mass of the bosons constituting the superfluid.

The dynamics of such vortex filaments is rich and still not fully comprehended. In particular, a fundamental phenomenon is the occurrence of reconnection events. In general, in fluid mechanics a vortex reconnection is an event in which the topology of the vorticity field is rearranged [2]. In the case of classical fluids, the presence of viscosity breaks the Kelvin circulation theorem, allowing the reconnection between vortex tubes [3]. In the case of inviscid superfluids, the vorticity is supported exclusively along the unidimensional vortex filaments, and the reconnection between them is made possible because of the vanishing density at the core of the vortices [4]. Specifically, the process of superfluid vortex reconnection consists in the local exchange of two strands of different filaments after a fast approach, allowing the topology to vary. In quantum turbulence, reconnections are also thought to be a fundamental mechanism for the redistribution of energy at scales smaller than the intervortex distance [5].

The separation $\delta(t)$ between the two reconnecting points is the simplest observable that characterizes a vortex reconnection. Given that a reconnection is an event localized in space and time, sufficiently close to the reconnection event it is expected to be fully driven by the interaction between two filaments. Assuming that at this scale the only parameter that determines the dynamics is the circulation Γ about each filament, a simple dimensional analysis suggests the following scaling for the separation rate:

$$\delta(t) = A^{\pm}(\Gamma|t - t_{\rm rec}|)^{1/2}, \tag{1}$$

where $A^{\pm}$ are dimensionless prefactors, $t_{\rm rec}$ is the reconnection time, and the labels $-$ and $+$ refer, respectively, to the times before and after the reconnection event. Such scaling has been demonstrated analytically in the context of the Gross-Pitaevskii (GP) model for $\delta \to 0$ [6–8], and it has been observed to be valid even at distances that go beyond several healing lengths [7,9]. Note that previous studies reported disparate exponents that still need to be explained [10–12]. The scaling (1) has also been observed in Biot-Savart simulations [9,13,14] and superfluid helium experiments [15]. If an external driving mechanism is absent, the scaling (1) is considered a universal feature of vortex reconnections, and the filaments always approach slower than they separate, i.e., $A^+/A^- > 1$. This last observation has been explained by a novel matching theory as the consequence of an irreversible mechanism related to the sound radiated during the event [8,16].

In recent years, vortex reconnections have been directly observed in atomic BECs by means of destructive absorption imaging [17] and in superfluid helium experiments by using solidified hydrogen particles as probes [15,18]. This latter technique has become a standard tool for the investigation of the properties of superfluid helium and quantum vortices, following its first utilization in 2006 [19]. Indeed, such particles get captured by quantum vortices thanks to pressure gradients and are carried by them, unveiling in this way the dynamics of the filaments. Besides the reconnections between vortices and Kelvin waves (helicoidal displacements

 ©2020 American Physical Society

that propagate along the vortex filaments), solidified hydrogen particles succeeded in revealing important differences between the statistics of classical and quantum turbulent states [20,21]. However, given that the typical size of such particles is four orders of magnitude larger than the vortex core size, it is far from trivial that they actually behave as tracers. For this reason, understanding the actual vortex-particle interactions and how particles and fluids affect each other's motions is a crucial theoretical task.

Many models have been developed and studied in this regard. The main difficulty is caused by the large extent of the scales involved in the problem, so that different phenomenological approaches need to be used. For what concerns large scales, the dynamics of particles in classical fluids has been phenomenologically adapted to the two-fluid description of a superfluid [22], and the distribution of inertial passive particles has been studied in the Hall-Vinen-Bekarevich-Khalatnikov (HVBK) model [23]. In this macroscopic approach, the vorticity is a coarse-grained field, and there is no notion of quantized vortices. Instead, in the vortex-filament model, the superfluid is modeled as a collection of filaments that evolve according to Biot-Savart integrals [1]. This method involves nonlocal contributions and a singular integral for the computation of the vortex self-induced velocity that needs to be regularized [24]. In this framework, hard spherical particles can be modeled as moving boundary conditions [25,26], although the reconnections both between vortices and between a vortex and a particle surface need to be implemented with an *ad hoc* procedure. These issues are absent in the GP model, in which the evolution of the order parameter of the superfluid is described with a nonlinear Schrödinger equation. Indeed, although the GP equation is formally derived for dilute Bose–Einstein condensates, it can be considered as a general model for low temperature superfluids, including superfluid helium. Unlike the vortex-filament method or the HVBK model, the full dynamics of vortices emerges naturally, including the reconnection events. Particles modeled as highly repulsive potentials have been successfully implemented in the GP framework, allowing for an extensive study of the capture process [27], the interaction between trapped particles and Kelvin waves [28], and the Lagrangian properties of quantum turbulence [29]. Recently, the dynamics of particles trapped inside GP vortices was also addressed in two dimensions [30].

Because the GP equation is a microscopic model, regular at the vortex core, it is the natural setting in which quantum vortex reconnections can be studied. In this work, we combine such suitability with the simplicity of modeling particles in the GP framework to study vortex reconnections in the presence of particles trapped by the filaments. We focus on two different configurations. In Sec. III we study the evolution of a dipole of two counterrotating straight vortices with a particle trapped in one of them. In Sec. IV we characterize the reconnection of two linked rings loaded with a number of particles. In the first case the reconnection is induced by the presence of the particle, and its simplicity allows for a systematic investigation of the mutual interaction between vortices and particles during the process of the reconnection. In the second case, the reconnection happens even in the absence of particles, so that how the presence of particles effectively affects the reconnection process can be addressed.

II. MODEL FOR PARTICLES AND QUANTUM VORTICES

We consider a quantum fluid with N_p spherical particles of mass M_p and radius a_p immersed in it. We describe the system by a self-consistent model based on the three-dimensional Gross-Pitaevskii equation. The particles are modeled by strong localized potentials V_p that completely deplete the superfluid up to a distance a_p from the position of their center $\mathbf{q}_i$. The dynamics of the system is governed by the following Hamiltonian:

$$H = \int \left(\frac{\hbar^2}{2m} |\nabla \psi|^2 - \mu |\psi|^2 + \frac{g}{2} |\psi|^4 + \sum_{i=1}^{N_\mathrm{p}} V_\mathrm{p}(\mathbf{r} - \mathbf{q}_i) |\psi|^2 \right) d\mathbf{r} + \sum_{i=1}^{N_\mathrm{p}} \frac{\left(\mathbf{p}_i^{\mathrm{part}}\right)^2}{2M_\mathrm{p}} + \sum_{i<j}^{N_\mathrm{p}} V_{\mathrm{rep}}^{ij}, \tag{2}$$

where ψ is the order parameter of the quantum and $\mathbf{p}_i^{\mathrm{part}} = M_\mathrm{p}\dot{\mathbf{q}}_i$ are the particles linear momenta. The chemical potential is denoted by μ. The nonlinear self-interaction coupling constant of the fluid is denoted by g, and m is the mass of the condensed bosons. The potential V_{rep}^{ij} is a repulsive potential between particles, needed to avoid an unphysical overlap, due to a short-range fluid-mediated interaction [31,32]. The equations of motion for the superfluid field ψ and the particle positions $\mathbf{q}_i = (q_{i,x}, q_{i,y}, q_{i,z})$ are

$$i\hbar \frac{\partial \psi}{\partial t} = -\frac{\hbar^2}{2m} \nabla^2 \psi + g|\psi|^2 \psi - \mu \psi + \sum_{i=1}^{N_\mathrm{p}} V_\mathrm{p}(|\mathbf{x} - \mathbf{q}_i|)\psi, \tag{3}$$

$$M_\mathrm{p} \ddot{\mathbf{q}}_i = -\int V_\mathrm{p}(|\mathbf{x} - \mathbf{q}_i|) \nabla |\psi|^2 \, d\mathbf{x} + \sum_{j \neq i}^{N_\mathrm{p}} \frac{\partial}{\partial \mathbf{q}_i} V_{\mathrm{rep}}^{ij}. \tag{4}$$

We refer to [27–29,33] for further details about the model, which was recently adopted to study extensively the interaction between particles and quantum vortices.

In the absence of particles, the ground state of the system is a homogeneous flat condensate $\psi_\infty = \sqrt{\mu/g} \equiv \sqrt{\rho_\infty/m}$, with a constant mass density ρ_∞. Linearizing around this value, dispersive effects take place at scales smaller than the healing length $\xi = \sqrt{\hbar^2/2g\rho_\infty}$, while large-wavelength excitations propagate with the phonon (sound) velocity $c = \sqrt{g\rho_\infty/m^2}$. The close relation between the GP model and hydrodynamics comes from the Madelung transformation $\psi(\mathbf{x}) = \sqrt{\rho(\mathbf{x})/m}\, e^{i\frac{m}{\hbar}\phi(\mathbf{x})}$, which maps the GP (3) into the continuity and Bernoulli equations of a superfluid of density ρ and velocity $\mathbf{v}_\mathrm{s} = \nabla\phi$. Although the superfluid velocity is described by a potential flow, vortices may appear as topological defects because the phase is not defined at the nodal lines of $\psi(\mathbf{x})$, and thus, vortices may appear to be topological defects. Each superfluid vortex carries a quantum of circulation $\Gamma = h/m = 2\pi\sqrt{2}c\xi$, and vortices are characterized by a vanishing density core size of the order of ξ.

In this work, we perform numerical simulations of the coupled differential equations (3) and (4) in a periodic cubic

box with sides $L = 128\xi$ with $N_c = 256^3$ collocation points. We use a standard pseudospectral method with a fourth-order Runge-Kutta scheme for the time step. In numerics, we measure distances in units of ξ, velocities in units of c, and times in units of $\tau = \xi/c$. As described in the Appendix and in Ref. [34], dealiasing is applied to equations (3) and (4), in such a way that they conserve the total energy H (2), the total fluid mass $N = \int |\psi|^2 \, d\mathbf{x}$, and the total momentum

$$\mathbf{p}^{\rm tot} = \mathbf{p}^{\rm GP} + \sum_{i=1}^{N_p} \mathbf{p}^{\rm part}, \tag{5}$$

where $\mathbf{p}^{\rm GP} = i\hbar/2 \int (\psi \nabla \psi^* - \psi^* \nabla \psi) \, d\mathbf{x}$ is the momentum of the quantum fluid. If dealiasing is not carefully performed, the discrete system does not conserve momentum. In the simulations presented here the total momentum is conserved up to eight decimal digits.

We use two different particle potentials to model the particles. For the simulations with the dipole, a smoothed hat function $V_p^1(r) = \frac{V_0}{2}(1 - \tanh[\frac{r^2-\zeta^2}{4\Delta_a^2}])$ is used. The parameters ζ and Δ_a are set to model the particle attributes. In particular, ζ fixes the width of the potential, and it is related to the particle size, while Δ_a controls the steepness of the smoothed hat function. The latter needs to be adjusted in order to avoid the Gibbs effect in the Fourier transform of V_p^1. For the simulations of the Hopf link, we use a Gaussian potential $V_p^2(r) = V_0 \exp(-r^2/2d_{\rm eff}^2)$, where the width is fixed using the Thomas-Fermi approximation to set an approximate radius ζ of the particle as $d_{\rm eff} = \zeta/\sqrt{2\ln(V_0/\mu)}$. Since the particle boundaries are not sharp, the effective particle radius is measured as $a_p = (3M_0/4\pi\rho_\infty)^{\frac{1}{3}}$, where $M_0 = \rho_\infty L^3(1 - \int |\psi_p|^2 \, d\mathbf{x}/\int |\psi_\infty|^2 \, d\mathbf{x})$ is the fluid mass displaced by the particle and ψ_p is the steady state with just one particle. Practically, given the set of numerical parameters ζ and Δ_a, the state ψ_p is obtained numerically with imaginary time evolution and the excluded mass M_0 is measured directly. We use the repulsive potential $V_{\rm rep}^{ij} = \gamma_{\rm rep}(2a_p/|\mathbf{q}_i - \mathbf{q}_j|)^{12}$ in order to avoid an overlap between them. The functional form of $V_{\rm rep}^{ij}$ is inspired by the repulsive term of the Lennard-Jones potential and the prefactor $\gamma_{\rm rep}$ is adjusted numerically so that the interparticle distance $2a_p$ minimizes the sum of $V_{\rm rep}^{ij}$ with the fluid mediated attractive potential [31,32].

The initial conditions for the dipole and a single ring (without particles) are obtained using the Newton-Raphson method and a biconjugate-gradient technique in order to minimize the sound emission [35]. The Hopf link of two rings is obtained by multiplying two states containing a ring each.

III. RECONNECTION OF A VORTEX DIPOLE

We start by presenting a series of numerical simulations of a dipole of two counterrotating superfluid vortices, with a single particle initially trapped inside one of them. Such a setting is useful to illustrate how a superfluid vortex reconnection can be triggered by the symmetry breaking produced by the presence of particles. Indeed, in the absence of trapped particles, the vortex dipole is a steady configuration, in which a spontaneous self-reconnection does not happen unless a Crow instability is induced [36]. At the same time, the simplicity of the initial configuration allows for the systematic study of the mutual effects between the particle and the reconnecting filaments.

TABLE I. Simulation parameters for the vortex dipole reconnection experiment.

λ	d/ξ	a_p/ξ	ζ/ξ	Δ_a/ξ	V_0/μ
1	10	4.3	3.0	0.75	20
2	20	8.6	7.4	0.75	20

In the initial time of each simulation, the vortices are straight and aligned along the z direction. The initial velocity of the particle is set equal to the translational speed of the dipole $\mathbf{v}_d \sim (\Gamma/2\pi d)\hat{\mathbf{y}}$, where d is the distance between the two filaments and $\hat{\mathbf{y}}$ is the unit vector along the y direction [30,37]. We performed the same experiment using particles of two different sizes and for a wide range of mass densities.

It has been observed in Ref. [27] that the effective Hamiltonian describing the process of particle capture by a vortex induces a dynamics which is invariant under the following scaling transformation:

$$d \to \lambda d, \quad a_p \to \lambda a_p, \quad t \to \lambda^2 t \qquad \forall\, \lambda \in \mathbb{R}^+, \tag{6}$$

where d is the vortex-particle distance. In order to check if the scaling invariance (6) is valid also in the present simulations, we set the radius of the large particle exactly $\lambda = 2$ times larger than the radius of the small one. Analogously, in the case of the large particle, the vortex filaments are initially placed $\lambda = 2$ times more distant than for the small particle. If such invariance subsists, it would be an indication of the analogy between the reconnection process and the trapping mechanism. In addition, it would naturally extend the validity of the results reported below in the case of particles with larger sizes, comparable to the ones used in current experiments. Note, however, that the scaling invariance (6) neglects the density profile of the vortex core, as well as other more complex particle-vortex interactions which can become relevant when a particle is trapped, like the Magnus effect.

The parameters used for these sets of simulations are summarized in Table I [note that the repulsive potential $V_{\rm rep}^{ij}$ in Eq. (4) is absent because only one particle is present].

Snapshots of the typical evolution of the dipole configuration under the GP dynamics (3) and (4) are displayed in Fig. 1 for a neutral particle of size $a_p = 4.3\xi$ and initial vortex separation $d = 10\xi$. During the motion of the dipole, the particle starts to precede about the filament because of the Magnus effect [28,30,38]. At the same time, the two vortices start to bend, until the filament without a particle reconnects with the surface of the sphere at time $t_{\rm rec}^-$. After the reconnection, the contact point of the free vortex separates into two branches, which then slide on the particle surface toward opposite directions. For a time window of about $\sim 20\tau$ the particle is pierced by both vortices, until the couple of pinning points above and below the particles merge and the vortices detach symmetrically. The reconnection changes the topology of the flow, so that the dipole is eventually converted into a single vortex ring (which in Fig. 1 appears to be folded on the vertical direction because of spatial periodicity). At the time

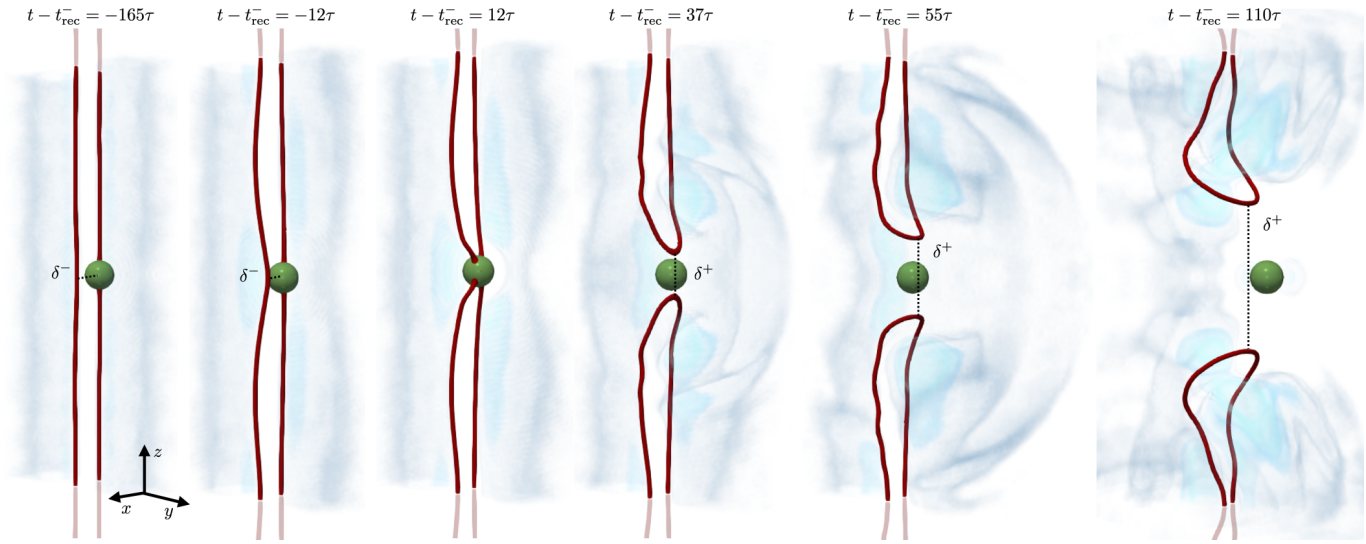


FIG. 1. Snapshots of the superfluid density and a neutral-mass particle of size $a_{\rm p} = 4.3\xi$ during the dipole reconnection (time varies from left to right). The initial distance between the vortices is $d = 10\xi$. Vortices are displayed as red isosurfaces at low density; particles are the green spheres, and sound is rendered in blue.

of the detachment, a clear spherical sound pulse is generated at the reconnection point. It expands and propagates along the y direction, which is the dipole propagation direction and coincides with the normal to the reconnection plane, in agreement with Refs. [8,16]. Simultaneously, the particle is released and abruptly accelerated. Eventually, it keeps on moving forward with a constant speed larger than the dipole velocity.

Before exploring in more detail the origin of the particle dynamics, we address the question of whether the observed reconnections induced by the particle are compatible with the standard picture of GP reconnections. In order to do so, we compute the separation $\delta(t)$ between the reconnecting points as a function of time. When the circulation Γ is the only relevant parameter driving the reconnection dynamics, $\delta(t)$ is expected to scale as Eq. (1). We operatively define the separation before the reconnection δ^- as the distance between the reconnecting point on the free vortex and the particle surface. After reconnection time $t_{\rm rec}^-$ between the free vortex and the sphere surface, the separation is not well defined until the particle detachment, after which δ^+ becomes simply the distance between the two extremal points of the outgoing vortex ring (see Fig. 1). The vortex filaments have been tracked using the method based on the pseudovorticity developed in [39]. Since the initial measurable value of δ^+ is of the order of the particle diameter $2a_{\rm p}$, we extrapolate the virtual original time $t_{\rm rec}^+$ at which $\delta^+(t_{\rm rec}^+) = 0$, performing a linear fit of $[\delta^+(t)]^2$ and evaluating the point where it vanishes. The same protocol was used with $\delta^-(t)$ to refine the value of $t_{\rm rec}^-$. The evolution of $\delta(t)$ is displayed in Fig. 2(a) for all the types of particles analyzed. In Fig. 2(b), $\delta^+(t)$ and $\delta^-(t)$ are plotted in a logarithmic scale, after rescaling the distances by a factor of λ and times by a factor of λ^2 ($\lambda = 1$ for the small particle, and $\lambda = 2$ for the large one), according to Eq. (6). It is apparent that the separation rate is independent of the particle mass and always shows a scaling compatible with $t^{1/2}$. This evidence confirms that, although the reconnection is triggered by the presence of the particle, the vortex dynamics is effectively fully governed only by the circulation. Moreover, the scaling invariance (6) seems to be respected for the separation rate. Finally, note that the observed positive ratio between the prefactors of the separation rate (1) after and before the reconnection ($A^+/A^- \sim 5.5$) is consistent with the irreversibility of the reconnection dynamics, which is related to the conversion of energy into sound [7,8,16].

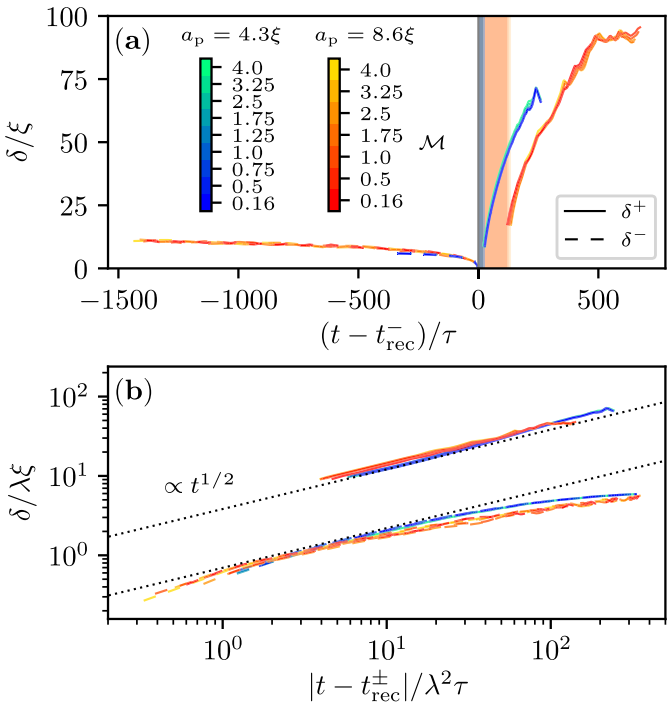


FIG. 2. (a) Distance $\delta(t)$ between reconnecting points for particles of size $a_{\rm p} = 4.3\xi$ and $a_{\rm p} = 8.6\xi$. Dashed lines correspond to δ^- before reconnection, and solid lines correspond to δ^+ after reconnection. (b) Log-Log plot of $\delta(t)$, with the rescaling (6). $\lambda = 1$ for the particle of size $a_{\rm p} = 4.3\xi$, and $\lambda = 2$ for the particle of size $a_{\rm p} = 8.6\xi$. Dotted lines indicate the scaling $t^{1/2}$.

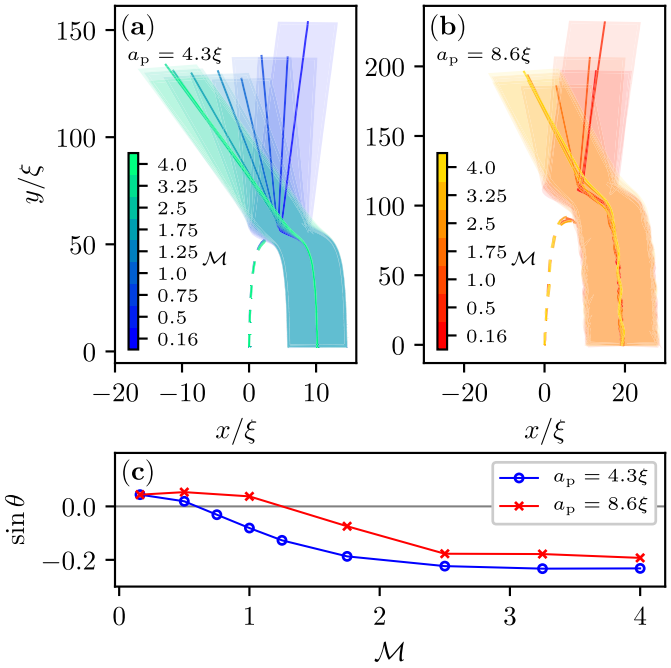


FIG. 3. Trajectories of particles of size (a) $a_p = 4.3\xi$ and (b) $a_p = 8.6\xi$ during the dipole reconnection. Different colors correspond to different masses, and the shaded regions indicate the area spanned by each particle. The dashed lines in corresponding colors are the trajectories of the reconnecting point of the vortex without particles at times $t < t_{rec}^-$. (c) Angle of deflection of the particle trajectory after the reconnection as a function of the particle mass for both particle sizes (blue circles correspond to $a_p = 4.3\xi$, and red crosses correspond to $a_p = 8.6\xi$). The angle considered is with respect to the dipole propagation direction.

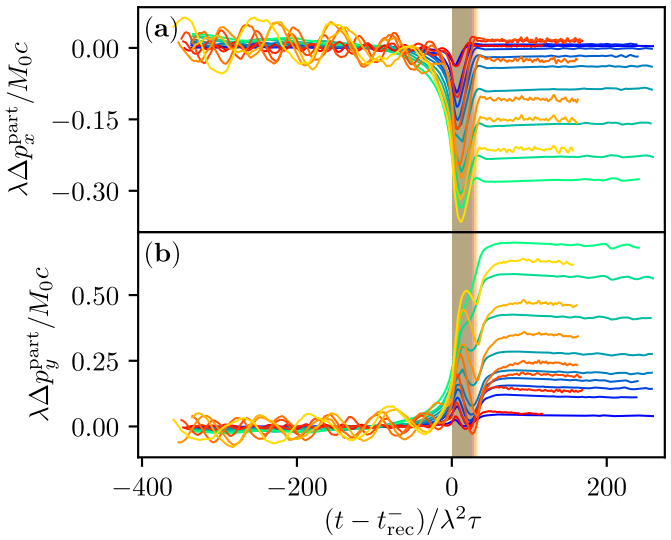


FIG. 4. (a) x component and (b) y component of the particle momentum increment with the rescaling (6) as a function of time. Different colors correspond to different particle species, with the same convention as in Fig. 2.

In Figs. 3(a) and 3(b) we show the trajectories of the particles on the plane orthogonal to the dipole for the small and large particles, respectively, and for all the different masses used. The shaded regions indicate the actual area spanned by each particle. In Figs. 3(a) and 3(b), the dashed lines show the trajectories of the reconnecting point on the vortex without the particle (initially placed at $x = 0$, $y = 0$) until it touches the particle surface at time t_{rec}^-. For the large particle one can appreciate the different Magnus precession frequencies, which are inversely proportional to the mass. We observe that the ballistic motion of the particle after the reconnection is deflected with respect to the propagation direction of the dipole, and a correlation between the particle mass and the deflection angle is apparent. In particular, the heaviest particles show a smooth trajectory and a deflection concordant with the velocity orientation at the reconnection point. Conversely, light particles slightly bounce back in the opposite direction. In Fig. 3(c) the deflection angle θ of the particle trajectory with respect to the dipole propagation direction is displayed as a function of the particle mass. As already qualitatively observed in Figs. 3(a) and 3(b), both the small and large particles (indicated, respectively, by blue circles and red crosses) deviate in a similar manner, with a deflection angle that saturates at $\sin\theta \sim -0.2$ for the largest masses. The origin of such behavior can be understood as the consequence of a transverse momentum transfer between the vortices and the particle, which we analyze in the remainder of this section.

The x component and y component particle momentum increments $\Delta\mathbf{p}^{\rm part}(t) = \mathbf{p}^{\rm part}(t) - \mathbf{p}^{\rm part}(t = 0)$ are plotted as a function of the rescaled time, respectively, in Figs. 4(a) and 4(b). The data associated with all the species of particles analyzed are displayed using the same convention as in Fig. 3, and also the particle momentum has been rescaled as $\mathbf{p}^{\rm part} \to \mathbf{p}^{\rm part}/\lambda$, according to the transformation (6). Note that at the initial time of the simulations the particle is placed in the reference frame comoving with the dipole, so that its momentum is aligned with the propagation direction of the dipole (the y direction) and reads $\mathbf{p}^{\rm part}(t = 0) = M_p\mathbf{v}_d = (M_p\Gamma/2\pi d)\hat{\mathbf{y}}$. We can clearly observe the abrupt acceleration felt by the particle in both the transverse and longitudinal directions during the reconnection event, followed after the detachment by a relaxation to a ballistic motion with constant speed. The ballistic motion is due to the absence of Stokes drag in the superfluid, and a negligible interaction with sound or with the outgoing vortex ring. The shaded area represents the time window after t_{rec}^- in which the particle is pierced by both the filaments and the vortex separation δ is undefined. Remarkably, such a window turns out to be the same in the rescaled units regardless of the particle size. Note how before the reconnection the momentum of the trapped particle oscillates weakly about a constant average because of the Magnus precession induced by the vortex [28]. If the invariance (6) really holds, the net particle momentum increment after the detachment in the rescaled units is expected to coincide for particles of different radii but the same relative mass $\mathcal{M}$. However, a small mismatch can be observed, which is probably due to the interaction between the particle and the vortex by which it is trapped before the reconnection. Such interaction indeed produces Magnus oscillations of greater amplitude for the large particle, as well as the generation of Kelvin waves along

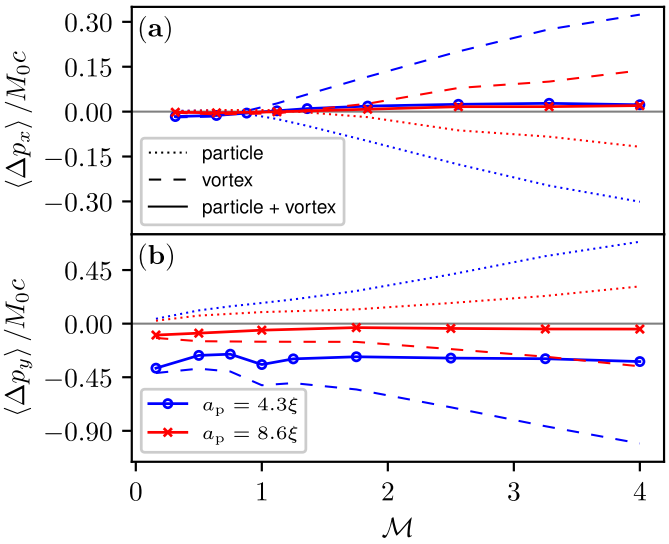


FIG. 5. (a) x component and (b) y component of the net momentum increment as a function of the particle mass for different particle sizes. Dotted lines are the particle momentum, dashed lines are the vortex ring momentum, and solid lines show the sum of the two. Blue lines refer to the small particle ($a_p = 4.3\xi$), and red lines refer to the large one ($a_p = 8.6\xi$).

the filament and sound radiation, which certainly corrupt the scaling invariance (6).

We eventually analyze the momentum exchange between the vortices and particle. Parametrizing the vortex ring after the reconnection as $\mathbf{R}(s,t)$, where s is a spatial parametrization variable, the linear momentum of the vortex can be expressed within the Biot-Savart framework as [40]

$$\mathbf{p}^{\text{vort}} = \frac{\rho_0 \Gamma}{2} \oint \mathbf{R}(s,t) \times \mathrm{d}\mathbf{R}(s,t), \tag{7}$$

where the contour integral is evaluated along the ring. Note that the vortex linear momentum (7) is *de facto* a purely geometrical quantity, determined by the spatial configuration of the ring. In fact, each component of the vortex momentum can be related to the projection of the oriented area enclosed by the filament onto the corresponding direction [41]. The momentum contribution of the superfluid $\mathbf{p}_{\text{GP}}$ to the total momentum in Eq. (5) contains the vortex momentum (7) and compressible waves.

The net momentum increment for the vortex is defined as $\langle \Delta \mathbf{p}^{\text{vort}} \rangle = \langle \mathbf{p}^{\text{vort}}(t > t_{\text{rec}}) \rangle - \mathbf{p}^{\text{vort}}(t = 0)$, which is analogous to the net momentum increment for the particle. In practice, the vortex momentum is computed from the filaments tracked during the GP simulation. Then it is averaged over a time window of $\sim 20\tau$ after the particle detachment, during which it remains steady. The x and y components of the net momentum increments as a function of the mass are displayed Fig. 5. The dotted lines are the particle net momentum increments, the dashed lines are the corresponding vortex net momentum increments, and the solid lines are the sum of the two. Blue lines refer to the small particle, and red lines refer to the large one.

In the x direction (perpendicular to the dipole velocity) the momentum acquired by the particle compensates almost exactly the momentum increment of the vortex, and thus, the transfer to sound modes is negligible. On the contrary, in the y direction and, in particular, for the small particle (solid blue line with circles), we observe a net momentum transfer from the particle and the vortices to other degrees of freedom. This transfer is independent of the particle mass, and it is consistent with the observation of a sound pulse after the reconnection in Fig. 1.

IV. RECONNECTION OF TWO LINKED RINGS

In this section we study a different setting in which vortices reconnect regardless of the presence of particles. In particular, we consider as the initial configuration a Hopf link consisting of two vortex rings with radius $R = 18\xi$, which is known to spontaneously undergo reconnection. We place $N_p = 8$ particles of size $a_p = 3.7\xi$ randomly distributed along each ring. The initial condition is shown in the first snapshot on the left in Fig. 6. The numerical parameters for the particle potential are $V_0 = 20\mu$ and $\zeta = 3\xi$.

We set as the initial velocity of each particle the velocity of the ring by which it is trapped $\mathbf{v}_{\text{ring}}$. In order to study how the presence of particles modifies the reconnection we consider three different particle masses, light ($\mathcal{M} = 0.51$), neutral ($\mathcal{M} = 1$), and heavy ($\mathcal{M} = 3.14$ and $\mathcal{M} = 12.56$). The evolution of the system for light particles ($\mathcal{M} = 0.51$) according to the GP dynamics is displayed in Fig. 6. Analogous to what was observed for the dipole, as a result of the particle-vortex interaction [27], the reconnection takes place between one trapped particle and the other filament. In the particular case of light particles, two unlinked vortex rings emerge after the reconnection: a large ring which contains the majority of the particles and a small ring with two particles still attached. Moreover, because of the violence of the event, a couple of particles get detached from the vortices.

In order to give a quantitative description, we measured the separation rate $\delta(t)$ for the different masses. They are reported in Fig. 7(a) as solid lines with markers. For comparison, Fig. 7(a) also includes the distance δ for the vortices without particles (dashed red line). Overall, if the particles are not too heavy, the reconnection remains almost unaffected by their presence. However, at very close distances a speedup takes place due to particle-vortex interactions. Conversely, in the case of heavy particles, their inertia is so large that vortices are driven by them. To illustrate this fact, we consider the fictitious case in which free heavy particles (without vortices) are set in the same positions as and with the initial velocity of the trapped ones. The distance in this case is computed as the minimal distance between the two groups of particles. Comparing this separation with that of heavy trapped particles $\mathcal{M} = 12.56$ (light green triangles), it is clear that in the latter case the ballistic motion of particles governs the dynamics.

Finally, in Figs. 7(b) and 7(c) a reconstruction of the event displayed in Fig. 6 using the tracked vortex filaments (rendered as blue solid lines) is also shown from a different perspective. For comparison, the tracked vortices corresponding to a simulation with the same initial configuration but without particles are shown as red lines. It is evident that the dynamics in the two cases are rather similar, especially before the reconnection. However, in the moments immediately prior to the reconnection one of the vortices decorated with particles shows a clear bending toward a particle set on the other

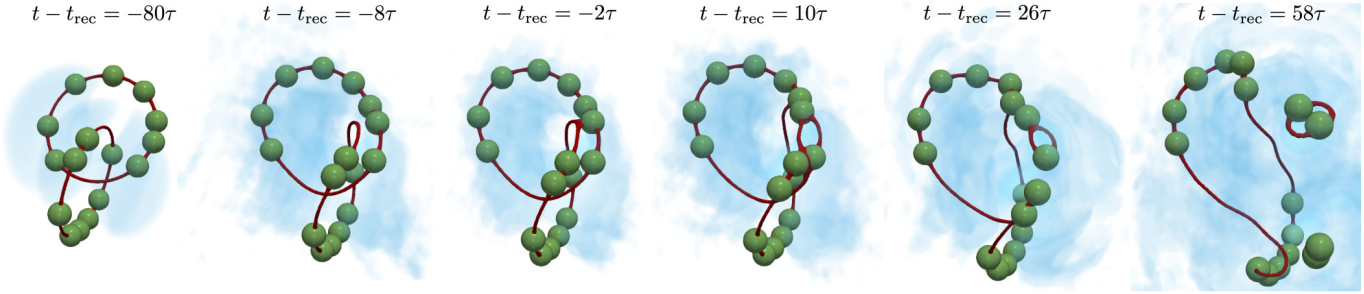


FIG. 6. Snapshots of the superfluid density and light particles ($\mathcal{M} = 0.51$) during the Hopf link reconnection (time varies from left to right). Vortices are displayed as red isosurfaces at low density; particles are the green spheres, and sound is rendered in blue.

filament. This is a clear indication of a fast acceleration, which is induced by the fluid depletion generated by the presence of the particle.

V. DISCUSSION

In this work we studied how particles trapped inside quantum vortices modify the process of vortex reconnections. We have investigated two different settings: a vortex dipole with one trapped particle and a Hopf link with a number of particles randomly positioned within the vortex. Whereas in the first case the reconnection is triggered by the symmetry breaking induced by the particle, in the second one vortices reconnect regardless of the presence of particles. In the case of the dipoles, we observed that the $t^{1/2}$ temporal reconnection scaling is preserved independently of the particle mass and size. During the reconnection process, we observe a net momentum transfer from vortices to particles in both directions perpendicular to the axis of the vortex dipole. In the transverse direction with respect to the dipole initial velocity, the transfer is proportional to the mass of the particles, and it is almost exactly compensated by an equal change in the vortex momentum. In the direction of the dipole displacement, the particle speedup after reconnection is not fully compensated by the vortices. The net momentum difference is roughly independent of the mass, and it could be associated with the emission of a sound pulse, such as the one studied in [16]. In the case of the Hopf link vortex, it was observed that the reconnection process at large distances is almost unaffected by neutral or light particles. On the contrary, if particles are heavy, it is driven by the particle ballistic motion. At very close distances, the reconnection is speeded up because of the interaction between the particles and the reconnecting vortex. In general, it was also observed that reconnection takes place generically between a trapped particle and an approaching filament.

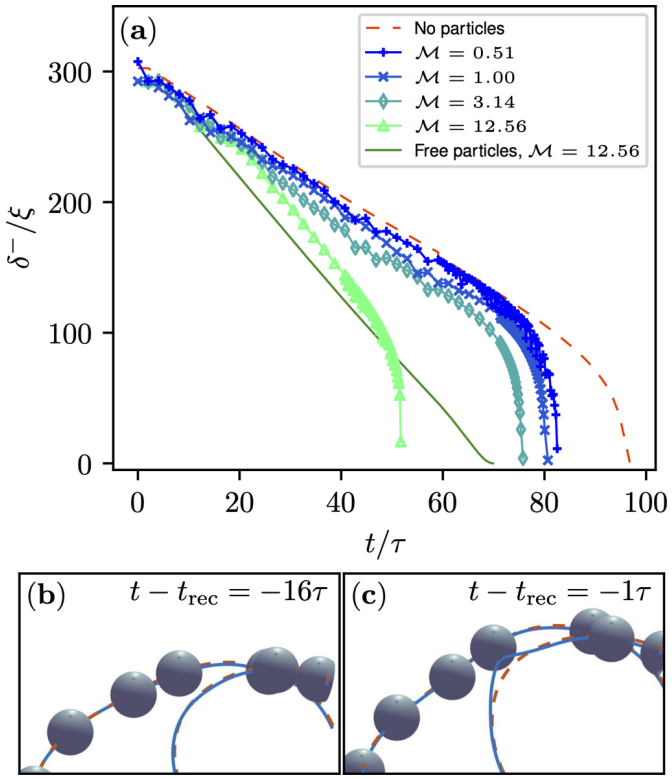


FIG. 7. (a) Separation between the reconnecting rings for different masses of the trapped particles (solid lines with markers). The red dashed line is the vortex separation in the absence of particles, and the green solid line is the separation between ballistic particles without vortices. A reconstruction of the event for light particles ($\mathcal{M} = 0.51$) using the tracked filaments (b) before and (c) at the reconnection. The filaments of the simulation with particles are displayed as blue solid lines. The filaments corresponding to a simulation with the same initial conditions but without particles are shown as red dashed lines.

In conclusion, besides providing further insights into the current knowledge of the vortex reconnection process, our findings constitute theoretical support and a benchmark for the superfluid ^{4}He experiments at very low temperature, in which the vortices are sampled by solid particles [15,18]. In particular, as has been proved in the case of Kelvin wave tracking [28], we stress that the use of light particles is recommended for reproducing the bare vortex dynamics, provided, of course, that buoyancy effects remain negligible.

ACKNOWLEDGMENTS

The authors were supported by Agence Nationale de la Recherche through the project GIANTE ANR-18-CE30-0020-01. Computations were carried out on the Mésocentre SIGAMM hosted at the Observatoire de la Côte d'Azur and the French HPC Cluster OCCIGEN through GENCI Allocation No. A0042A10385.

APPENDIX: DEALIASING OF THE EQUATIONS OF MOTIONS AND CONSERVATION OF THE INVARIANTS

The set of equations of motion (3) and (4) needs to be dealiased in order to conserve the total momentum (5). The equations are dealiased by performing a Galerkin truncation, which consists in keeping only the Fourier modes with wave numbers smaller than a UV cutoff $k_{\max}$. The truncated equations of motion are

$$i\hbar\frac{\partial\psi}{\partial t} = \mathcal{P}_G\left[-\frac{\hbar^2}{2m}\nabla^2\psi - \mu\psi + g\mathcal{P}_G\left[|\psi|^2\right]\psi + \sum_{i=1}^{N_p} V_p^i\psi\right], \tag{A1}$$

$$M_p\ddot{\mathbf{q}}_i = -\int V_p^i\mathcal{P}_G\left[\nabla|\psi|^2\right]d\mathbf{x} + \sum_{j\neq i}^{N_p}\frac{\partial}{\partial\mathbf{q}_i}V_{\text{rep}}^{ij}, \tag{A2}$$

where $V_p^i = V_p(|\mathbf{x}-\mathbf{q}_i|)$ and $\mathcal{P}_G$ is a Galerkin truncation operator. $\mathcal{P}_G$ acts on the function $f(\mathbf{x})$ as $\mathcal{P}_G[f(\mathbf{x})] = \sum_{\mathbf{k}}\hat{f}(\mathbf{k})e^{i\mathbf{k}\cdot\mathbf{x}}\theta_H(k_{\max}-|\mathbf{k}|)$, where $\hat{f}(\mathbf{k})$ is the Fourier transform of $f(\mathbf{x})$ and θ_H is a Heaviside theta function. It is also assumed that the particle potential is always truncated: $V_p^i = \mathcal{P}_G[V_p^i]$. Equations (A1) and (A2) exactly conserve all the invariants (Hamiltonian, fluid mass, and total momentum) if the 2/3 rule is used, namely, if $k_{\max} = \frac{2}{3}\frac{N_{\text{res}}}{2}$, with N_{res} being the number of uniform grid points per direction [34]. For a pseudospectral code, this technique implies an extra computational cost of one extra back and forth fast Fourier transform.

[1] R. J. Donnelly, *Quantized Vortices in Helium II* (Cambridge University Press, Cambridge, 1991).
[2] S. Kida and M. Takaoka, Annu. Rev. Fluid Mech. **26**, 169 (1994).
[3] F. Hussain and K. Duraisamy, Phys. Fluids **23**, 021701 (2011).
[4] J. Koplik and H. Levine, Phys. Rev. Lett. **71**, 1375 (1993).
[5] W. F. Vinen and J. J. Niemela, J. Low Temp. Phys. **128**, 167 (2002).
[6] S. Nazarenko and R. West, J. Low Temp. Phys. **132**, 1 (2003).
[7] A. Villois, D. Proment, and G. Krstulovic, Phys. Rev. Fluids **2**, 044701 (2017).
[8] D. Proment and G. Krstulovic, arXiv:2005.02047.
[9] L. Galantucci, A. W. Baggaley, N. G. Parker, and C. F. Barenghi, Proc. Natl. Acad. Sci. USA **116**, 12204 (2019).
[10] S. Zuccher, M. Caliari, A. W. Baggaley, and C. F. Barenghi, Phys. Fluids **24**, 125108 (2012).
[11] A. J. Allen, S. Zuccher, M. Caliari, N. P. Proukakis, N. G. Parker, and C. F. Barenghi, Phys. Rev. A **90**, 013601 (2014).
[12] C. Rorai, J. Skipper, R. M. Kerr, and K. R. Sreenivasan, J. Fluid Mech. **808**, 641 (2016).
[13] M. Tsubota and H. Adachi, J. Low Temp. Phys. **162**, 367 (2011).
[14] A. W. Baggaley, L. K. Sherwin, C. F. Barenghi, and Y. A. Sergeev, Phys. Rev. B **86**, 104501 (2012).
[15] M. S. Paoletti, M. E. Fisher, and D. P. Lathrop, Phys. D (Amsterdam, Neth.), **239**, 1367 (2010).
[16] A. Villois, D. Proment, and G. Krstulovic, arXiv:2005.02048.
[17] S. Serafini, M. Barbiero, M. Debortoli, S. Donadello, F. Larcher, F. Dalfovo, G. Lamporesi, and G. Ferrari, Phys. Rev. Lett. **115**, 170402 (2015).
[18] G. P. Bewley, M. S. Paoletti, K. R. Sreenivasan, and D. P. Lathrop, Proc. Natl. Acad. Sci. USA **105**, 13707 (2008).
[19] G. P. Bewley, D. P. Lathrop, and K. R. Sreenivasan, Nature (London) **441**, 588 (2006).
[20] M. L. Mantia and L. Skrbek, Europhys. Lett. **105**, 46002 (2014).
[21] M. La Mantia and L. Skrbek, Phys. Rev. B **90**, 014519 (2014).
[22] D. R. Poole, C. F. Barenghi, Y. A. Sergeev, and W. F. Vinen, Phys. Rev. B **71**, 064514 (2005).
[23] J. I. Polanco and G. Krstulovic, Phys. Rev. Fluids **5**, 032601 (2020).
[24] K. W. Schwarz, Phys. Rev. B **38**, 2398 (1988).
[25] D. Kivotides, C. F. Barenghi, and Y. A. Sergeev, Phys. Rev. B **77**, 014527 (2008).
[26] Y. A. Sergeev and C. F. Barenghi, J. Low Temp. Phys. **157**, 429 (2009).
[27] U. Giuriato and G. Krstulovic, Sci. Rep. **9**, 4839 (2019).
[28] U. Giuriato, G. Krstulovic, and S. Nazarenko, Phys. Rev. Res. **2**, 023149 (2020).
[29] U. Giuriato and G. Krstulovic, Phys. Rev. Fluids **5**, 054608 (2020).
[30] A. Griffin, V. Shukla, M.-E. Brachet, and S. Nazarenko, Phys. Rev. A **101**, 053601 (2020).
[31] V. Shukla, M. Brachet, and R. Pandit, Phys. Rev. A **94**, 041602(R) (2016).
[32] U. Giuriato, G. Krstulovic, and D. Proment, J. Phys. A **52**, 305501 (2019).
[33] V. Shukla, R. Pandit, and M. Brachet, Phys. Rev. A **97**, 013627 (2018).
[34] G. Krstulovic and M. Brachet, Phys. Rev. E **83**, 066311 (2011).
[35] M. Abid, C. Huepe, S. Metens, C. Nore, C. T. Pham, L. S. Tuckerman, and M. E. Brachet, Fluid Dyn. Res. **33**, 509 (2003).
[36] N. G. Berloff and P. H. Roberts, J. Phys. A **34**, 10057 (2001).
[37] P. G. Saffman, *Vortex Dynamics* (Cambridge University Press, Cambridge, 1992).
[38] L. Kiknadze and Y. Mamaladze, arXiv:cond-mat/0604436.
[39] A. Villois, G. Krstulovic, D. Proment, and H. Salman, J. Phys. A **49**, 415502 (2016).
[40] L. M. Pismen, *Vortices in Nonlinear Fields: From Liquid Crystals to Superfluids, from Non-Equilibrium Patterns to Cosmic Strings*, International Series of Monographs on Physics (Oxford University Press, Oxford, 1999).
[41] S. Zuccher and R. L. Ricca, Phys. Rev. E **100**, 011101(R) (2019).

4 Superfluid vortex waves sampled and affected by trapped particles

This chapter is devoted to the presentation of the publication "How trapped particles interact with and sample superfluid vortex excitations", [79], in which we study the interaction between an array of trapped particles and wave excitations that propagate along almost straight vortex filaments. We predict and measure a natural precession frequency due to Magnus force, which is proportional to the number of vortices attached to each particle. Then we build an effective theory based on the Bloch decomposition, thanks to which we can explain the emergence of frequency gaps in the spectrum of vortex waves and show that large scale Kelvin waves can be efficiently tracked by trapped particles. The effective model, which agrees well with GP numerical simulations, can be thought as an analogy with the motion of electrons in an unidimensional periodic crystal. The original quantum model of the crystal is described after the paper, and the analogy with the vortex-particles system is further commented with a direct comparison of the dispersion relations predicted by the two models.

4.1 *Publication*: How trapped particles interact with and sample superfluid vortex excitations

In the last chapter we analyzed the long range interaction between a particles and vortices using the model described in section 2.3.3. Here we use the same model to provide some insights about the interaction of particles trapped inside the vortex core and the excitations of a straight vortex. In particular, we ask to what extent particles can detect the presence of Kelvin waves on the filaments and simultaneously how the propagation of Kelvin waves is affected by the presence of particles. Such work is inspired by the experimental result [64]. We consider first one single particle placed along a straight vortex filament, and then an array of equally separated particles. We slightly perturb the filament, in order to excite linear vortex waves (described in section 1.4.5) and look at the motion of the particles.

As it can be derived from classical hydrodynamic arguments (see section 2.2.3), the dynamics of a particle pierced by a vortex (namely with a circulation Γ about it) is driven by the Magnus force (2.29). Such force induces a particle precession of a given frequency

$$\Omega_{\mathrm{p}} = \frac{3}{2}\frac{\rho\Gamma a_{\mathrm{p}}}{M_{\mathrm{p}}^{\mathrm{eff}}}, \tag{4.1}$$

which can be detected as a peak in the power spectrum of the particle position in the plane orthogonal to the filament. The particle precedes in the same direction of the circulating flow around the vortex and opposite to the Kelvin waves. We recognize such oscillation in GP simulations, even in the case where a bundle of many polarized vortices are attached to the same particle. A possible experimental implication of our measurement is that, since the value of $\Omega_{\rm p}$ is proportional to the circulation about the sphere, it gives an indirect estimation of the number of vortices that are piercing the particle.

In order to investigate the dynamics of the system in the case when a collection of particles is placed along an excited straight vortex, we build a spatio-temporal spectrum of the particle transverse displacement $q_j(t) = q_{x,j}(t) + iq_{y,j}(t)$, with j the particle label. In particular, we use the positions of the particles along the filament $q_{z,j}$ as spatial mesh points. Note that since by construction there is not a preferential propagation direction of the vortex waves, the net particle translation along the direction of the filament is negligible. We first consider an artificial case, with overlapping particles that mimic a continuous massive wire. This allows us to determine the role of inertia in the propagation of vortex wave excitations. Using the vortex self-induced velocity as flow velocity in the Magnus force, we can predict a flattening of the vortex wave dispersion relation at small scales, which is proportional to the mass and is confirmed by the numerical measurements.

Then we address the more realistic case of equally separated particles. Note that in superfluid helium experiments, solidified hydrogen particles are effectively found to be homogeneously distributed along the vortices (see section 2.1 and references therein). A possible explanation of this behaviour is the presence of a residual electric charge on the particles, when they are injected in the system. Indeed this would lead to a homogeneous distribution as a consequence of Coulomb repulsion[1]. Both in the spatio-temporal spectrum computed from the particle positions, as well as in the one extracted directly from the GP field, we observe striking and unexpected patterns. Besides the excited frequencies associated with sound waves (1.110) and a constant frequency at all the wavenumbers compatible with the Magnus precession (4.1), we observe a deformed vortex wave dispersion relation together with a completely new branch at high frequency. The effective theory that we develop to successfully explain such rich dynamics is inspired by the standard Kronig–Penney (KP) model, used in solid state physics to describe the quantum mechanics of electrons in a crystal lattice [111, 127]. In our analogy, the vortex waves play the role of the electronic wavefunction and the particles are akin to the potential barriers that in the KP model represent the atoms of a 1D solid. We provide more details on the original KP model in section 4.2, after the article and a further comparison with the vortex-particles system in section 4.3.

The main difference between the KP model and the vortex-particles system is that in the first one the potential barriers have a fixed amplitude, while in our case they are also proportional to the frequency squared of the incoming (vortex) waves. The

[1]Such simple mechanism is however just a hypothesis, devoid of any experimental evidence.

fortunate consequence of this fact is that long wavelength Kelvin waves, which have small frequencies, do not feel high potential barriers and can propagate almost freely. In other terms, the transverse motion of particles can efficiently follow such slow modes and thus sample the long Kelvin wave dispersion relation. The other important result that can be extracted from the effective theory (always confirmed by GP simulations) is that lighter particles are more suitable for the tracking of vortex waves. This observation trivially follows from the inverse proportionality with the particle mass of the effective KP potential.

After the paper, in section 4.2, we will describe the original KP model in order to deepen the analogy reported in the publication. A direct comparison of the dispersion relation in the two cases is finally commented in section 4.3.

How trapped particles interact with and sample superfluid vortex excitations

Umberto Giuriato* and Giorgio Krstulovic
Université Côte d'Azur, CNRS, OCA, Laboratoire Lagrange, Boulevard de l'Observatoire CS 34229 - F 06304 NICE Cedex 4, France

Sergey Nazarenko
Université Côte d'Azur, Institut de Physique de Nice (INPHYNI), CNRS UMR 7010, Parc Valrose, 06108 Nice Cedex 2, France

(Received 11 July 2019; revised manuscript received 23 March 2020; accepted 25 March 2020; published 11 May 2020)

Particles have been used for more than a decade to visualize and study the dynamics of quantum vortices in superfluid helium. In this work we study how the dynamics of a collection of particles set inside a vortex reflects the motion of the vortex. We use a self-consistent model based on the Gross-Pitaevskii equation coupled with classical particle dynamics. We find that each particle oscillates with a natural frequency proportional to the number of vortices attached to it. We then study the dynamics of an array of particles trapped in a quantum vortex and use particle trajectories to measure the frequency spectrum of the vortex excitations. Surprisingly, due to the discreetness of the array, the vortex excitations measured by the particles exhibit bands, gaps, and Brillouin zones, analogous to the ones of electrons moving in crystals. We then establish a mathematical analogy where vortex excitations play the role of electrons and particles that of the potential barriers constituting the crystal. We find that the height of the effective potential barriers is proportional to the particle mass and the frequency of the incoming waves. We conclude that large-scale vortex excitations could be in principle directly measured by particles and novel physics could emerge from particle-vortex interaction.

DOI: 10.1103/PhysRevResearch.2.023149

I. INTRODUCTION

When a fluid composed of bosons is cooled down, a spectacular phase transition takes place. The system becomes superfluid and exhibits exotic physical properties. Unlike any classical fluid, a superfluid flows with no viscosity. This is an intriguing example of the manifestation of pure quantum-mechanical effects on a macroscopic level. The first discovered superfluid is liquid helium ^{4}He in its so-called phase II, below the critical temperature $T_\lambda \simeq 2.17$ K. In one of the first attempts of describing the behavior of superfluid helium, London suggested that superfluidity is intimately linked to the phenomenon of Bose-Einstein condensation (BEC) [1]. In the same years, Landau and Tisza independently put forward a phenomenological two-fluid model, wherein superfluid helium can be regarded as a physically inseparable mixture of two components: a normal viscous component that carries the entire entropy and an inviscid component with zero entropy [2,3].

Because of its intrinsic long-range order, a superfluid can be described by a macroscopic complex wave function. A stunning quantum-mechanical constraint is that vortices appear as topological defects of such order parameter. In three dimensions, such defects are unidimensional structures, usually referred to as quantum vortices. Indeed, the circulation (contour integral) of the flow around a vortex must be a multiple of the Feynman-Onsager quantum of circulation h/m, where h is the Planck constant and m is the mass of the Bosons constituting the fluid [4]. Such peculiarity is necessary to ensure the monodromy of the wave function. In superfluid helium, quantum vortices have a core size on the order of an angstrom. At low temperatures, below 1 K, the normal component is negligible and vortices are stable and do not decay by any diffusion process, unlike their classical counterparts. The understanding of superfluid vortex dynamics has a direct impact on many interesting, complex nonequilibrium multiscale phenomena, such as turbulence [5–7].

Most of the experimental knowledge on superfluid vortices is based on indirect measurement of their properties. The early efforts in the observation of quantized vortices were made in the framework of rotating superfluid helium, by using electron bubbles (ions) as probes [8]. Since then, impurities have been extensively used to unveil the dynamics of superfluid vortices. An important breakthrough occurred in 2006, when micrometer-sized hydrogen ice particles were used to directly visualize superfluid helium vortices [9]. Thanks to pressure gradients, particles get trapped inside quantum vortices and are subsequently carried by them. Hence, it has been possible to observe vortex reconnections and Kelvin waves (helicoidal displacements that propagate along the vortex line) by means of standard particle-tracking techniques [10]. Furthermore, the particle dynamics unveiled important differences between

*Corresponding author: umberto.giuriato@oca.eu

Published by the American Physical Society under the terms of the Creative Commons Attribution 4.0 International license. Further distribution of this work must maintain attribution to the author(s) and the published article's title, journal citation, and DOI.

velocity statistics of quantum and classical turbulent states [11,12]. In experiments, such particles are used as tracers, despite their very large size compared to the vortex core. Therefore, it is of the utmost importance that the mechanisms driving their dynamics are fully comprehended. Specifically, how well is vortex dynamics reflected by the motion of the particles trapped in it? How much does their presence in the core modify the propagation of Kelvin waves? Would they affect the reconnection rates?

Describing the interaction of particles with isolated vortex lines or complex quantum vortex tangles is not an easy task. Depending on the scale of interest, there are different theoretical and numerical models that can be adopted. A big effort has been made in adapting the standard dynamics of particles in classical fluids to the case of superfluids described by two-fluid models [13,14]. This is a macroscopic model in which vorticity is a coarse-grained field and therefore there is no notion of quantized vortices. A medium-scale description is given by the vortex filament model, where the superfluid is modeled as a collection of lines that evolve following Biot-Savart integrals. In this approximation, circulation of vortices is by construction quantized but reconnections are absent and have to be implemented via some *ad hoc* mechanism. Finite-size particles can be studied in the vortex filament framework but the resulting equations are numerically costly and limited [15]. A microscopic approach consists in describing each impurity by a classical field in the framework of the Gross-Pitaevskii model [16–18]. In principle, such method is valid for weakly interacting BECs, and is numerically and theoretically difficult to handle if one wants to consider more than just a few particles. In the same context, an alternative possibility is to assume classical degrees of freedom for the particles, while the superfluid is still a complex field obeying the Gross-Pitaevskii equation. This idea of modeling particles as simple classical hard spheres has been shown to be both numerically and analytically very powerful [19–22]. In particular, such minimal and self-consistent model allows for simulating a relatively large number of particles, and describes well the particle-vortex interaction [22]. Although formally valid for weakly interacting BECs, it is expected to give a good qualitative description of superfluid helium.

In this paper we investigate how particles trapped in quantum vortices interact with vortex excitations and in particular how well they can be used to infer properties of superfluid vortices. We use the Gross-Pitaevskii equation coupled with inertial and active particles obeying classical dynamics to answer this question. We first address how the Magnus force acting on trapped particles induces oscillations at a certain natural frequency. This quantity may be experimentally measured to determine the number of vortices composing a polarized bundle (see a discussion later in this paper). Second, in order to understand the effect of particle inertia, we analyze the spectrum of vortex excitations in the case when a continuous distribution of mass is contained inside the vortex core. Then, we study an array of particles trapped inside a vortex, in a setting similar to the one observed in experiments. Surprisingly, the dispersion relation of vortex waves measured by the particles is found to contain band gaps and the periodicity typically observed in the energy spectra of solids. We explain the numerical observation applying the concepts used in the standard Kronig-Penney model [23,24], which describes the motion of electrons in a unidimensional crystal. Finally, based on our results, we discuss in which regimes particles could be reliably used to sample vortex excitations.

II. THEORETICAL BACKGROUND

A. Model for superfluid vortices and active particles

We consider a superfluid at very low temperature containing N_p spherical particles of mass M_p and radius a_p. We describe the system by a self-consistent model based on the three-dimensional Gross-Pitaevskii equation. The particles are modeled by strong localized potentials V_p, which completely deplete the superfluid up to a distance a_p from their center position $\mathbf{q}_i$. Particles have inertia and obey a Newtonian dynamics. The Hamiltonian of the system is

$$H = \int \left(\frac{\hbar^2}{2m}|\nabla\psi|^2 + \frac{g}{2}|\psi|^4 + \sum_{i=1}^{N_\mathrm{p}} V_\mathrm{p}(\mathbf{r}-\mathbf{q}_i)|\psi|^2 \right) d\mathbf{r} + \sum_{i=1}^{N_\mathrm{p}} \frac{\mathbf{p}_i^2}{2M_\mathrm{p}} + \sum_{i<j}^{N_\mathrm{p}} V_\mathrm{rep}^{ij}, \tag{1}$$

where ψ is the wave function that describes the superfluid and m is the mass of the condensed bosons interacting with an s-wave scattering length a_s, so that the coupling constant is $g = 4\pi a_\mathrm{s}\hbar^2/m$. The potential $V_\mathrm{rep}^{ij} = \varepsilon(r_0/|\mathbf{q}_i - \mathbf{q}_j|)^{12}$ is a repulsive potential of radius r_0 between particles. See Refs. [20,22] and the next section for further details about the model. The equations of motion for the superfluid field ψ and the particle positions $\mathbf{q}_i = (q_{i,x}, q_{i,y}, q_{i,z})$ are

$$i\hbar\frac{\partial\psi}{\partial t} = -\frac{\hbar^2}{2m}\nabla^2\psi + (g|\psi|^2 - \mu)\psi + \sum_{i=1}^{N_\mathrm{p}} V_\mathrm{p}(|\mathbf{x}-\mathbf{q}_i|)\psi, \tag{2}$$

$$M_\mathrm{p}\ddot{\mathbf{q}}_i = -\int V_\mathrm{p}(|\mathbf{x}-\mathbf{q}_i|)\nabla|\psi|^2\, d\mathbf{x} + \sum_{j\neq i}^{N_\mathrm{p}} \frac{\partial}{\partial\mathbf{q}_i} V_\mathrm{rep}^{ij}. \tag{3}$$

This model has been successfully used to study vortex nucleation [19] and trapping of particles by quantum vortices [22]. We denote by GP the Gross-Pitaevskii model without particles and by GP-P the full coupled system (2) and (3).

In the absence of particles, the chemical potential μ fixes the value of the condensate ground state $\psi_\infty = \sqrt{\rho_\infty/m} = \sqrt{\mu/g}$. Linearizing around this value, wave excitations are described by the Bogoliubov dispersion relation

$$\Omega_\mathrm{B}(k) = c|\mathbf{k}|\sqrt{1 + \frac{\xi^2|\mathbf{k}|^2}{2}}, \tag{4}$$

where $\mathbf{k}$ is the wave number of the excitation. Large-wavelength excitations propagate with the phonon (sound) velocity $c = \sqrt{g\rho_\infty/m^2}$, while at length scales smaller than the healing length $\xi = \sqrt{\hbar^2/2g\rho_\infty}$ excitations behave as free particles.

The close relation between the GP model and hydrodynamics comes from the Madelung transformation $\psi(\mathbf{x}) = \sqrt{\rho(\mathbf{x})/m}\, e^{i\frac{m}{\hbar}\phi(\mathbf{x})}$, which maps the GP (2) into the continuity

and Bernoulli equations of a superfluid of density ρ and velocity $\mathbf{v}_s = \nabla\phi$. Although the superfluid velocity is potential, the phase is not defined at the nodal lines of $\psi(\mathbf{x})$ and thus vortices may appear as topological defects. The simplest case corresponds to a straight quantum vortex given by

$$\psi_v(x, y, z) = \sqrt{\rho_v(x, y)/m}\, e^{i\frac{m}{\hbar}\phi_v(x,y)}, \tag{5}$$

where $\rho_v(x, y)$ vanishes at the vortex core line $(0, 0, z)$. The core size of a vortex is on the order of the healing length ξ and the phase $\phi_v = \frac{n_v\hbar}{m}\varphi$, with φ the angle in the (x, y) plane, ensures the monodromy of the solution (5) only if n_v is an integer number. The corresponding velocity field is $\mathbf{v}_v = \frac{n_v\hbar}{m}\frac{\hat{\varphi}}{|\mathbf{x}_\perp|}$, where $\hat{\varphi}$ is the azimuthal unit vector and $\mathbf{x}_\perp = (x, y, 0)$. The circulation along a closed path $\mathcal{C}$ surrounding the vortex is therefore quantized:

$$\Gamma = \oint_{\mathcal{C}} \mathbf{v}_v \cdot d\mathbf{l} = n_v \frac{h}{m} = 2\pi n_v \sqrt{2} c\xi. \tag{6}$$

Actually, for $|n_v| > 1$ vortices are structurally unstable and split into single-charged vortices. We shall consider only $n_v = \pm 1$ vortices. Note that the Bogoliubov spectrum (3) obtained in the GP framework describes well the excitations of atomic BECs, but does not match the one observed in superfluid helium. In particular, the dispersion relation never changes convexity and the roton minimum is absent. Nevertheless, the hydrodynamic description of vortices and of their large-scale excitations (summarized in the following section) is similar both in helium and in the GP model.

B. Frequency spectrum of superfluid vortex excitations

Excitations are present in quantum vortices because of thermal, quantum, or turbulent fluctuations. They are waves propagating along the vortex line with a certain frequency $\Omega_v(k)$, where k is the (one-dimensional) wave number of the excitation. At scales larger than the vortex core size ($k\xi \ll 1$), such excitations are known as Kelvin waves (KWs) and they play the important role of carrying energy toward the smallest scales of a superfluid [25]. At such scales, the dynamics of a vortex line can be described by the vortex filament model, according to which the motion of the filament is determined by the self-induced velocity $\mathbf{v}_{si}$ of the line on itself [8]. This model involves nonlocal contributions and a singular integral that needs to be regularized [26]. Note that this model has also been derived at large scales also in the framework of the GP equation [27]. The simplest approximation that can be done is the well-known local-induction approximation (LIA), where only the contribution to $\mathbf{v}_{si}$ due to the local curvature at each point of the filament is considered. Such approximation is valid when the curvature is much larger than the vortex core size. The LIA model reads [28]

$$\dot{\mathbf{s}}(\zeta, t) = \mathbf{v}_{si}(\zeta, t), \quad \mathbf{v}_{si}(\zeta, t) = \frac{\Gamma}{4\pi}\Lambda \frac{\partial \mathbf{s}}{\partial \zeta} \times \frac{\partial^2 \mathbf{s}}{\partial \zeta^2}, \tag{7}$$

where $\mathbf{s}(\zeta, t)$ is the curve that parametrizes the filament, and ζ is the arclength. The parameter $\Lambda > 0$ is in principle a nonlocal operator yielding the correct Kelvin wave dispersion relation. At a first approximation and for the sake of simplicity in analytical treatments, it can be considered as a constant. In the case of small displacements of a straight filament oriented along the z axis, the vortex line can be parametrized as $s(z, t) = s_x(z, t) + is_y(z, t)$. At the leading order (7) reduces to

$$\dot{s}(z, t) = v_{si}(z, t), \quad v_{si}(z, t) = i\frac{\Gamma}{4\pi}\Lambda \frac{\partial^2}{\partial z^2} s(z, t). \tag{8}$$

The LIA equation (8) admits solutions in the form of helicoidal waves propagating along the vortex line with a dispersion relation

$$\Omega_{LIA}(k) = -\frac{\Gamma\Lambda}{4\pi}k^2. \tag{9}$$

A better description of vortex waves was formally derived from the Euler equations for an ideal incompressible fluid by Sir W. Thomson (Lord Kelvin) [29] in the case of a hollow vortex, namely if the vorticity is concentrated in a thin tube of radius a_0. In this case the frequency of propagation is given by the well-known Kelvin wave dispersion relation

$$\Omega_{KW}(k) = \frac{\Gamma}{2\pi a_0^2}\left[1 - \sqrt{1 + a_0|k|\frac{K_0(a_0|k|)}{K_1(a_0|k|)}}\right], \tag{10}$$

where $K_n(x)$ is the modified Bessel function of order n and a_0 depends on the model of the vortex core. It has been shown by Roberts [30] that the small wave number limit of expression (10) is valid also for large-scale waves propagating along the superfluid vortex described by the GP equation:

$$\Omega_v(k) \underset{k\xi\ll 1}{\longrightarrow} \Omega_{KW}(ka_0 \to 0) = -\frac{\Gamma}{4\pi}k^2\left(\ln\frac{2}{a_0|k|} - \gamma_E\right), \tag{11}$$

where $a_0 = 1.1265\xi$ and $\gamma_E \sim 0.5772$ is the Euler-Mascheroni constant. On the other hand, at small scales the excitations of a quantum vortex behave as (GP) free particles and the dispersion relation is simply given by [30]

$$\Omega_v(k) \underset{k\xi\gg 1}{\longrightarrow} -\Omega_B(k\xi \to \infty) = -\frac{\Gamma}{4\pi}k^2. \tag{12}$$

Note that all the frequencies (9)–(12) have an opposite sign with respect to the circulation Γ; namely KWs rotate opposite to the vortex flow $\mathbf{v}_v$. Since there is not an analytic expression for the full dispersion relation of vortex excitations of the GP model, in the numerics presented in this work we use a fit of the dispersion relation that matches both asymptotic (10) and (12). It reads

$$\Omega_v^{\text{fit}}(k) = \Omega_{KW}(k)\left[1 + \epsilon_{\frac{1}{2}}(a_0|k|)^{\frac{1}{2}} + \epsilon_1(a_0|k|) + \tfrac{1}{2}(a_0|k|)^{\frac{3}{2}}\right]. \tag{13}$$

The dimensionless parameters $\epsilon_{\frac{1}{2}} = -0.20$ and $\epsilon_1 = 0.64$ are obtained from the measured dispersion relation of a bare vortex tracked in a GP simulation without particles. In Fig. 1 the spatiotemporal spectrum of a bare GP vortex is compared with the result of the fit (solid green line), together with the asymptotics. Note that in Eq. (13) we used the full Kelvin wave frequency relation (10) (dashed cyan line) instead of the asymptotic (11) (dotted yellow line). This is because its large-k limit $\Omega_{KW}(k) \sim \frac{\Gamma}{2\pi a_0^2}(a_0|k|)^{\frac{1}{2}}$ can be straightforwardly adjusted to obtain the free particle dispersion relation (12) (dash-dotted magenta line).

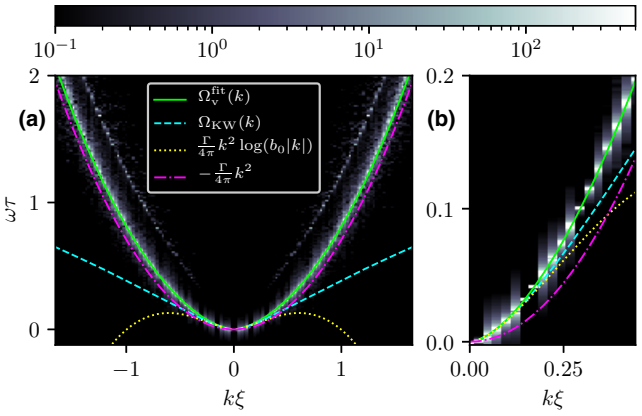


FIG. 1. (a) Spatiotemporal spectrum of a GP bare vortex loaded with small-amplitude Kelvin waves. Solid green line is the fit (13). Dashed cyan line is KW dispersion relation (10). Dotted yellow line is the small-k asymptotic (11), with $b_0 = a_0 e^{\gamma_E}/2$. Magenta dash-dotted line is the large-k asymptotic (12). The resolution of the simulation is $N_\perp = N_\parallel = 256$ in a computational domain of size $L_\perp = L_\parallel = 256\xi$. (b) A zoom close to small wave numbers.

III. MOTION OF PARTICLES TRAPPED BY QUANTUM VORTEX

We are interested in the behavior of particles captured by quantum vortices. Since hydrogen and deuterium particles used to visualize vortices in superfluid helium experiments are considerably larger than the vortex core (typically $a_p \sim 10^4\xi$) they could be captured not by an isolated vortex but by bundles of many polarized vortices. In such complex system, the large particle size and inertia might affect the vortex dynamics. It is then natural to try to understand how the dynamics of vortices is modified by the presence of the particles, or in other terms, how well particles track superfluid vortices.

An amazing piece of experimental evidence is that trapped particles distribute themselves at an almost equal spacing (see for instance Ref. [10]). In this work we do not address the physical origins of this distribution, but we adopt it as a hypothesis for setting the initial condition of our simulations.

We start our discussion by presenting the settings of the GP-P model in our simulations. The GP-P equations are integrated in a 3D periodic domain of dimensions $L_\perp \times L_\perp \times L_\parallel$. The initial conditions consist of a perturbed straight vortex containing small-amplitude vortex excitations. The vortex is loaded with a number of particles and then evolved under GP-P dynamics. The computational domain contains three other image vortices in order to preserve periodicity. Only one vortex contains particles whereas the three others are bare. We have used resolutions up to $256 \times 256 \times 1024$ and 512^3 collocation points. We express the particle mass as $M_p = \mathcal{M}M_p^0$, where M_p^0 is the mass of the displaced superfluid. Therefore, light, neutral, and heavy particles have $\mathcal{M} < 1$, $\mathcal{M} = 1$, and $\mathcal{M} > 1$, respectively. Lengths are expressed in units of ξ, times in units of $\tau = \xi/c$, and velocities in units of c. Further details on the numerical implementation are given in Appendix A.

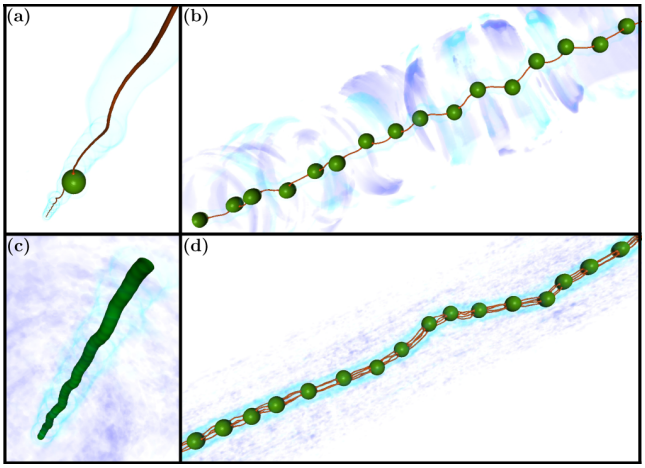


FIG. 2. Visualization of particles trapped by superfluid vortices from GP simulations. Vortices are displayed in red, particles in green, and sound waves are rendered in blue. (a) A single particle of size $a_p = 13.1\xi$ trapped in a vortex filament. (b) An array of particles of size $a_p = 13.1\xi$ and relative distance $d = 51.2\xi$. (c) A wire made of 50 overlapping particles of size 2.7ξ trapped in a vortex filament. (d) An array of particles of size $a_p = 13.1\xi$ trapped in a bundle of 4 vortex filaments. Movies of the simulations are available in the Supplemental Material [34].

Figure 2 displays the four different configurations studied in this work. Figure 2(a) shows one particle moving in a quantum vortex which clearly induces KWs on the filament. Figure 2(b) displays an array of particles initially set at equal distances. We have checked that provided that particles are distant enough, they remain equally distributed along the vortex, with very small fluctuations along its axis. Figure 2(c) displays a snapshot in the case where particles strongly overlap creating an almost continuous distribution of mass inside the vortex. Producing this state is possible by properly adjusting the repulsive potential $V_{\rm rep}^{ij}$ in Eq. (3). The purpose of studying this configuration is twofold. First, from the theoretical point of view it will provide an easier way to describe the role of the particle mass in the vortex dynamics and its effect on vortex excitations. On the other hand, such setting is similar to recent experiments that study the nanowire formation by the coalescence of gold nanofragments on quantum vortices [31] or experiments with vibrating wires inside quantum vortices in superfluid ^{3}He and ^{4}He [32,33]. Finally, Fig. 2(d) displays a bundle of four equally charged vortices loaded with an array of particles. In all cases, we clearly see the interaction between particles and vortices producing sound (phonon) and Kelvin waves. Movies of the simulations are available in the Supplemental Material [34].

A. Natural frequency of particles trapped by superfluid vortices

We first consider the dynamics of a particle trapped by an almost straight superfluid vortex. At the leading order this is the classical hydrodynamical problem of a moving sphere with nonzero circulation in an ideal fluid. The main force acting on the particle is the Magnus force, which arises from the pressure distribution generated at the boundary of the particle in such configuration [35,36]. We introduce the

complex variable $q(t) = q_x(t) + iq_y(t)$ for the center of the particle in the plane orthogonal to the vortex filament, and $v = v_x + iv_y$ for the velocity of the ambient superfluid flow. In these variables, the equation of motion for the particle in the absence of any external force is [36]

$$\ddot{q}(t) = i\Omega_{\rm p}[\dot{q}(t) - v], \quad \Omega_{\rm p} = \frac{3}{2}\frac{\rho\Gamma a_{\rm p}}{M_{\rm p}^{\rm eff}}, \tag{14}$$

where $M_{\rm p}^{\rm eff} = M_{\rm p} + \frac{1}{2}M_{\rm p}^0 = (\mathcal{M} + \frac{1}{2})M_{\rm p}^0$ is the effective mass of the particle and $M_{\rm p}^0 = \frac{4}{3}\pi\rho a_{\rm p}^3$ is the displaced mass of the fluid. In Eq. (14), the fluid is assumed to be incompressible with density $\rho \sim \rho_\infty$, which is a good approximation when the particle size is larger than the healing length. From (14) we can derive the temporal spectrum of the particle position

$$|\hat{q}(\omega)|^2 = \frac{\Omega_{\rm p}^2|\hat{v}(\omega)|^2}{\omega^2(\omega - \Omega_{\rm p})^2}, \tag{15}$$

where $\hat{q}(\omega) = \int q(t)e^{-i\omega t}\,dt$ and $\hat{v}(\omega) = \int v(t)e^{-i\omega t}\,dt$. The vortex line tension, which is responsible for the propagation of Kelvin waves [37], is implicitly contained in the superfluid flow v in Eq. (14). It generates particle oscillations in the rotation direction opposite to the flow generated by the vortex. However, from Eq. (15) we see that the particle motion is dominated by a precession with frequency $\Omega_{\rm p}$, which has the same sign of Γ and therefore has the same direction of the vortex flow. Such frequency is the natural frequency of the particle: expressing it as a function of $\mathcal{M}$ we get

$$\Omega_{\rm p} = \frac{9}{4\pi}\frac{\Gamma}{a_{\rm p}^2(2\mathcal{M}+1)}. \tag{16}$$

For current experiments using particles as probes, such characteristic frequency is of order 10–100 Hz, which is actually measurable [38].

We have performed a series of numerical experiments with particles trapped in a superfluid vortex excited with small-amplitude Kelvin waves. Measurements of temporal spectra (15) for particles characterized by different values of $\Omega_{\rm p}$ are reported in Fig. 3. In the x axis of the plot we have the angular frequencies with the same sign of Γ. The different natural frequencies have been obtained varying the mass and the size of the particles. The observed peak at $\Omega_{\rm p}$ is well predicted by Eq. (15). The natural frequency is also observed for particles in the particle-array configuration. In particular, if particles are attached to a bundle of $N_{\rm v}$ quantum vortices instead of a single filament, the corresponding characteristic frequency is $N_{\rm v}$ times larger. The case of a bundle of $N_{\rm v} = 4$ is also reported in Fig. 3, in a remarkable agreement with theory. This has an important experimental implication. Measuring the natural frequency $\Omega_{\rm p}$ could give an independent estimate of the circulation (and therefore of the number of vortices) in the bundles visualized by the particles in superfluid helium experiments.

Note that in general the vortex line tension could have a nontrivial coupling with the particles and lead to a modification of the precession frequency $\Omega_{\rm p}$. Indeed, in the idealized derivation of Eq. (14), it is assumed that the particle center coincides with the center of a straight vortex line. In principle, one should solve Eq. (14) together with the equation of motion of the vortex, taking into account the proper boundary

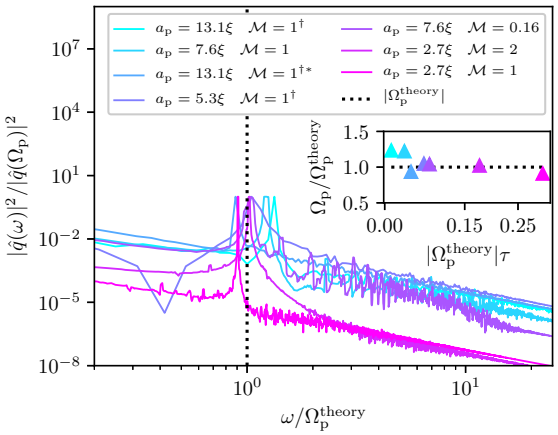


FIG. 3. Temporal spectra of the particle positions for different values of the natural frequency $\Omega_{\rm p}$, obtained varying mass and size of the particles. The expected natural frequency $|\Omega_{\rm p}^{\rm theory}|$ (16) is the dotted vertical line. Inset: Comparison of the measured natural particle frequency with the theory. A dagger (†) indicates that the particle considered belongs to a particle array. An asterisk (∗) indicates that the particle considered is trapped in a bundle of 4 vortices.

conditions between a sphere and a vortex filament [26], which will include restoring forces maintaining the particle trapped. Accounting for such phenomena might lead to a more accurate prediction of the precession frequency. However, the GP system naturally contains all these effects. Therefore, given the agreement between the prediction (16) and GP numerical simulations, we conclude that the modification of the particle natural frequency $\Omega_{\rm p}$ due to the coupling at the particle-vortex boundary is a negligible effect. The simple formula (16) can be thus safely used as a first estimate in current experiments.

B. Dispersion relation of a massive quantum vortex

As already mentioned above, in order to study the dynamics of an array of particles and their interaction with vortex waves in a setting like Figs. 2(b) or 2(d), it is instructive to first analyze the case of a massive quantum vortex, as the one in Fig. 2(c). Our considerations are necessary to give a picture of the role of inertia in the propagation of vortex wave excitations. They are not meant to model a real wire, for which some results are well known in literature [39,40] and which has been used to measure the quantized circulation in superfluid helium [41,42]. We consider a wire of length $L_{\rm w}$, radius $a_{\rm w}$, and mass $M_{\rm w}$, filling a superfluid vortex. The effective mass is $M_{\rm w}^{\rm eff} = M_{\rm w} + M_{\rm w}^0$ and the displaced mass is now $M_{\rm w}^0 = \rho L_{\rm w}\pi a_{\rm w}^2$. Since such wire possesses a circulation, each mass element is driven by the Magnus force as in Eq. (14), but with a different prefactor [35]

$$\Omega_{\rm w} = \frac{\rho\Gamma L_{\rm w}}{M_{\rm w}^{\rm eff}}, \tag{17}$$

which arises because of the geometrical difference between a spherical particle and a cylinder. We allow the wire to deform, which means that the complex variable q is now a function of the z component too. Such physical system is analogous to a massive quantum vortex with a finite size core, which is already well known in literature [39,40], and it has

been used to measure the quantized circulation in superfluid helium [41,42]. If the curvature radius is much greater than the wire radius and the healing length, the flow velocity v can be approximated by the self-induced velocity of the vortex filament on itself. In the LIA approximation, the self-induced velocity is simply given by $v_{\rm si}$ in Eq. (8). The dynamics of the wire is therefore driven by the equation

$$\ddot{q}(z,t) = i\Omega_{\rm w}\left[\dot{q}(z,t) - i\frac{\Gamma}{4\pi}\Lambda\frac{\partial^2}{\partial z^2}q(z,t)\right]. \tag{18}$$

In this simplified model, we are neglecting modes propagating along the wire due to elastic tension and the wave number dependence of the added mass. This choice is done because we want to focus on the inertial effects that will be relevant in the case of a particle array, developed in the following section. Equation (18) allows as a solution linear circularly polarized waves in the form $q(z,t) = q_0 e^{i(\Omega_{\rm M}^{\pm}t - kz)}$, where the frequency is given by

$$\Omega_{\rm M}^{\pm}(k) = \frac{\Omega_{\rm w}}{2} \pm \frac{1}{2}\sqrt{\Omega_{\rm w}^2 + \frac{\Omega_{\rm w}\Gamma\Lambda}{\pi}k^2}. \tag{19}$$

More generally, one can consider a phenomenological extrapolation based on a more realistic model for the self-induced velocity of the vortex in Eq. (18), so that the dispersion relation of waves propagating along the wire is generalized as

$$\Omega_{\rm M}^{\pm}(k) = \frac{1}{2}\left[\Omega_{\rm w} \pm \sqrt{\Omega_{\rm w}^2 - 4\Omega_{\rm w}\Omega_{\rm v}(k)}\right], \tag{20}$$

where $\Omega_{\rm v}(k)$ is the *bare* vortex wave frequency and depends on the model chosen for the self-induced velocity. We will refer to (20) as the "massive vortex wave" dispersion relation. In the LIA approximation we have $\Omega_{\rm v}(k) = \Omega_{\rm LIA}(k)$ (9) and we recover Eq. (19), but a more accurate result is expected if the wave propagation is instead described by $\Omega_{\rm KW}(k)$ or by the measured dispersion relation $\Omega_{\rm v}^{\rm fit}(k)$ (13). Note that the zero mode of the branch $\Omega_{\rm M}^{+}$ coincides with $\Omega_{\rm w}$ and does not vanish even if $M_{\rm w} = 0$ because of the added mass $M_{\rm p}^0$. This is related to the fact that the wire possesses an effective inertia because during its motion it has to displace some fluid [39,43]. In the limit $k\xi \ll 1$, the result (20) can be obtained from the one derived in Ref. [40] using fluid dynamic equations to study ions in superfluid helium.

We build numerically a massive vortex placing a large number of small overlapping particles along a vortex filament. We set the repulsion between particles at a radius $r_0 = 2L_{\rm w}/(N_{\rm p}a_{\rm p})$ (see Appendix A), so that they are kept at constant distance $r_0/2$. Such system mimics a continuum of matter with total mass given by the sum of all particle masses $M_{\rm w} = N_{\rm p}M_{\rm p} = N_{\rm p}M_{\rm p}^0\mathcal{M}$. We have checked that the repulsion among particles leads to matter sound waves with frequencies that are subleading with respect to other terms present in Eq. (18). We initially excite the system with small-amplitude Kelvin waves and we let it evolve under GP-P dynamics. Figure 2(c) shows a typical snapshot of the system but in the case of a larger initial perturbation (in order to enhance visibility). We then use the particle positions to construct the spatiotemporal spectrum $S_q(k,\omega) \sim |\hat{q}(k,\omega)|^2$, with $\hat{q}(k,\omega)$ the time and space Fourier transform of $q(z,t)$ (see Appendix B for further details). Density plots of $S_q(k,\omega)$ are displayed in Fig. 4 for different values of the particle mass. For a better presentation, we have chosen $\Gamma < 0$ so that vortex wave frequencies lie in the upper plane. This convention will be adopted also in the following section.

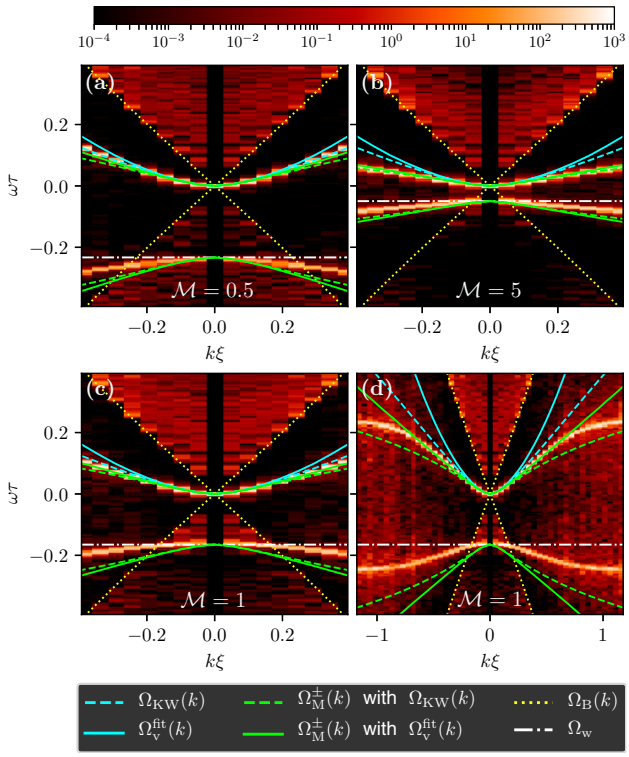


FIG. 4. Spatiotemporal spectra of massive vortices for different masses. The vortex length is $L_{\rm w} = 128\xi$ and there are $N_{\rm p} = 50$ particles of radius $a_{\rm p} = 2.7\xi$, with repulsion radius $r_0 = 2L_{\rm w}/(N_{\rm p}a_{\rm p})$. Dotted yellow line is the Bogoliubov dispersion relation $\Omega_{\rm B}(k)$ (4). Dashed cyan line is low-k KW dispersion relation $\Omega_{\rm KW}(k)$ (10). Solid cyan line is full fitted vortex wave dispersion relation $\Omega_{\rm v}^{\rm fit}(k)$ (13). Dash-dotted green lines are massive vortex wave dispersion relation $\Omega_{\rm M}(k)$ (20) computed using low-k KW dispersion relation. Solid green lines are massive vortex wave dispersion relation computed using full fitted vortex wave dispersion relation. Dotted horizontal white line is the natural frequency $\Omega_{\rm w}$ (17). The other parameters of the simulations are $L_\perp = L_\parallel = 128\xi$ and $N_\perp = N_\parallel = 256$. (a) $\mathcal{M} = 0.5$; (b) $\mathcal{M} = 5$; (c) $\mathcal{M} = 1$; (d) same as (c), but displaying the full range.

We first observe that the massive vortex is able to capture the Bogoliubov dispersion relation $\Omega_{\rm B}(\mathbf{k})$ (4) due to the presence of excitations in the superfluid, as displayed by yellow dotted lines in Fig. 4. The bare Kelvin wave dispersion relation $\Omega_{\rm KW}(k)$ and the measured bare vortex frequency spectrum $\Omega_{\rm v}^{\rm fit}(k)$ are displayed by the cyan dashed and solid lines, respectively. They coincide in the limit $k\xi \ll 1$, as expected. The corresponding massive vortex wave predictions (20) are also displayed in green dashed and solid lines. For low masses, the effect of inertia is negligible, so that massive vortex wave (20) and bare vortex wave (13) predictions are similar. As the mass increases, the wire inertia becomes important and the measured frequencies of the wire excitations decrease at small scales, in good agreement with the massive vortex wave

prediction. The model (20) is not expected to give a good explanation for the negative branches, as it neglects the details of the internal structure of the wire, as well as the dependence on the wave number of the effective mass. Such features, which are out of the scope of the present work, are taken into account in Ref. [40] in the case of an elastic and massive hollow vortex (with no notion of the free-particle behavior of vortex excitations at small scales). The predicted natural frequency of the wire $\Omega_{\rm W} = |\Omega_{\rm M}^{+}(0)|$ is clearly reproduced by the numerical measurements and it does not become infinite when $\mathcal{M} \to 0$ because of the added mass effect. For completeness, Fig. 4(d) displays the dispersion relation over the full accessible range of wave numbers. The dispersion curves are bent due to the discreteness of the wire at scales of order $k\xi \sim 0.8$. Note that the KW dispersion relation (dashed cyan line) seems to be very similar to the fitted one (solid cyan line). However, the difference between the two is apparent in Fig. 4(d). Moreover, it is clear how the massive vortex wave dispersion relation computed using $\Omega_{\rm v}(k) = \Omega_{\rm v}^{\rm fit}(k)$ (solid green line) fits the data for all the masses analyzed. In particular, in Fig. 4(d), it is shown that it can predict the dispersion relation of a massive vortex wire with relative mass $\mathcal{M} = 1$ up to a wave number $k\xi \sim 0.7$. This is not the case for the massive vortex wave dispersion relation computed using $\Omega_{\rm v}(k) = \Omega_{\rm KW}(k)$ (dashed green line). We thus conclude that the main effect of the inertia of the particles constituting the wire is to modify the frequency spectrum of vortex waves, as follows from simple hydrodynamical considerations.

C. Frequency gaps and Brillouin zones for an array of trapped particles

Now we shall address the main question of this work. How well do particles, seating in a quantum vortex, track vortex waves? In order to study this problem, we consider an array of particles as the one displayed in Fig. 2(b). Particles are placed in a quantum vortex, initially separated by a distance d. The system is excited by superimposing small-amplitude KWs. We can build a discrete spatiotemporal spectrum $S_q(k, \omega)$ of the measured vortex excitations by using the displacement of particles in the plane perpendicular to the vortex. In Figs. 5(a) and 5(c) we display the particle spatiotemporal spectra for an array of $N_{\rm p} = 20$ particles of size $a_{\rm p} = 2.7\xi$ with masses $\mathcal{M} = 5$ and $\mathcal{M} = 1$, respectively, placed at a distance $d = 12.8\xi$. The Bogoliubov waves are still weakly sampled by the particles, as displayed by yellow dotted lines. Surprisingly, a higher-frequency branch appears. Such pattern is similar to those observed in the typical energy spectra of crystals [24]. Particles are actually able to sample the vortex excitations only in the first Brillouin zone; namely they cannot see wave numbers larger than π/d. However, spatiotemporal spectra can be also computed by directly using the superfluid wave function. Performing the time and space Fourier transform of ψ we define the spectrum $S_\psi(k, \omega) = |\hat{\psi}(k_x = 0, k_y = 0, k, \omega)|^2$. The corresponding spectra S_ψ are shown in Figs. 5(b) and 5(d) where wave numbers go now up to $kd \sim 10$, giving access to all the small scales solved by the numerical simulations. Several Brillouin zones are clearly appreciated, as well as the opening of band gaps in the dispersion relation. At the same time, Bogoliubov modes

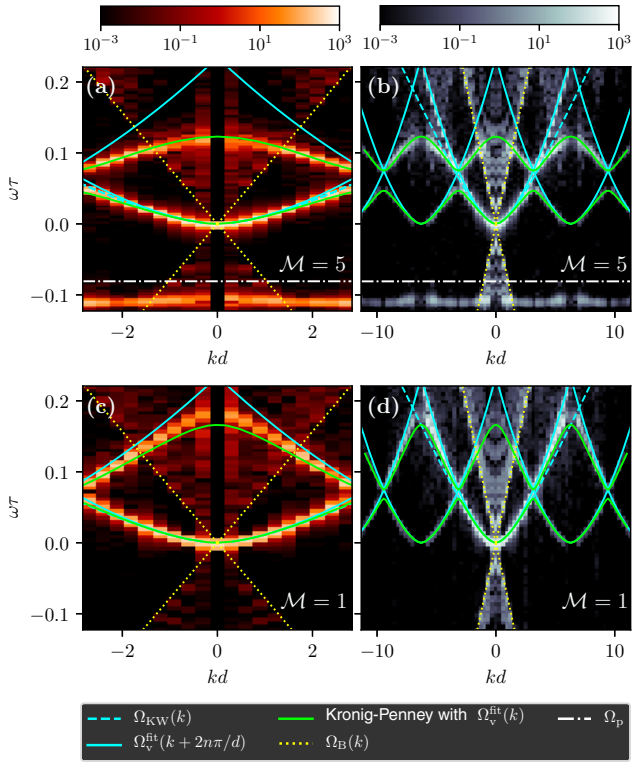


FIG. 5. Spatiotemporal spectra computed from the particle positions (left) and from the wave function ψ (right) for an array of particles with mass $\mathcal{M} = 5$ (top) and $\mathcal{M} = 1$ (bottom). Solid green lines are the contour plot of the dispersion relation (22) computed with $\Omega_{\rm v}^{\rm fit}$ (13). Dashed cyan line is low-k KW dispersion relation $\Omega_{\rm KW}(k)$ (10). Solid cyan line is the fitted vortex wave dispersion relation (13). Dotted yellow line is Bogoliubov dispersion relation $\Omega_{\rm B}(k)$ (4). Dash-dotted horizontal white line is the predicted natural frequency $\Omega_{\rm p}$. The other parameters of the particles are $d = 12.8\xi$, $a_{\rm p} = 2.7\xi$, $r_0 = 4a_{\rm p}$. The size of the computational box is $L_\perp = L_\parallel = 256\xi$, with $N_\perp = N_\parallel = 512$ collocation points.

can be observed and also bare vortex waves. The latter belong to the image vortices in the computational domain, where no particles have been attached.

The presence of particles clearly affects the propagation of waves along the vortex line inducing high-frequency excitations not only for small but also for large wavelengths. The intuitive idea is that when a vortex wave reaches a particle, it is partially reflected or transmitted, depending on the mass and the size of the particles, and eventually on its own frequency. This reminds us of the standard quantum-mechanical problem of an electron described by the (linear) Schrödinger equation hitting a potential barrier. Furthermore, if particles are set at almost equal distances, the system is similar to an electron propagating in a periodic array of potential barriers, as in the Kronig-Penney model [23,24]. In order to apply quantitatively this intuition and explain the opening of band gaps in the dispersion relation of vortex wave excitations, we start by considering an artificial system made of segments of bare quantum vortex of length $(d - L_{\rm w})$, alternated with massive vortex wires of length $L_{\rm w}$. A sketch of the problem is given in Fig. 6(a). To recover the excitations in the case of the

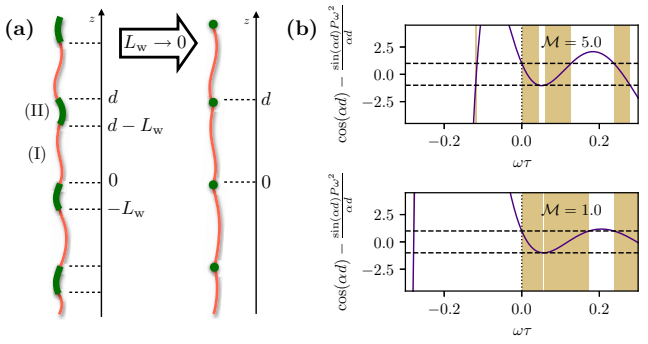


FIG. 6. (a) Sketch of the lattice vortex wave model. Bare vortex segments are in red and massive vortex segments are in green. (b) Right-hand side of Eq. (22) computed with LIA as a function of $\omega\tau$ for an array of particles with radius $a_p = 2.7\xi$ and mass $\mathcal{M} = 5$. Bands of allowed frequencies are displayed in gold. (c) The same as (b) but for particles with mass $\mathcal{M} = 1$.

particle array, we will later take the limit $L_w \to 0$, keeping the mass of the wires equal to the effective mass of the particles. The resulting effective theory must be intended as an asymptotic limit of the actual system for long waves $ka_p \ll 1$, in which the nonlinear interactions of the vortex excitations are neglected and the complexity of the vortex-particle boundary is ignored. The accuracy of such model has to be checked by comparing its predictions with the results of the GP simulations. The motion of the bare vortices is driven by the self-induced velocity that leads to the propagation of vortex waves, while the wires are driven by the Magnus force. For the sake of simplicity, we first consider the LIA approximations (8) and (18), respectively. The dynamics is thus given in each zone by

$$\dot{q}(z,t) = i\frac{\Gamma}{4\pi}\Lambda\frac{\partial^2}{\partial z^2}q(z,t) \quad \text{(I)},$$
$$\ddot{q}(z,t) = i\Omega_w\left[\dot{q}(z,t) - i\frac{\Gamma}{4\pi}\Lambda\frac{\partial^2}{\partial z^2}q(z,t)\right] \quad \text{(II)}, \quad (21)$$

where (I) is the region $0 < z < d - L_w$ and (II) is the region $d - L_w < z < d$. Note that the use of LIA in the system (21) is rather qualitative, given the high level of complexity of the problem. In particular it ignores the nonlocal dynamics of the vortex, does not reproduce the good dispersion relation of vortex excitations, and may not be able to take into account the exact boundary condition between the particles and the vortex. However, it allows us to introduce some general physical concepts and perform a fully analytical treatment of the problem. The effective model will be then generalized in order to take into account a more realistic description of vortex waves and provide quantitative predictions. The dispersion relation can be found borrowing standard techniques from solid state physics, in particular by adapting the solution of the Kronig-Penny model [23,24]. We look for a wave solution $q(z,t) = \Phi(z)e^{i\omega t}$, where the spatial function $\Phi(z)$ can be written in the form $\Phi(z) = e^{ikz}u(z)$ according to the Bloch theorem, where $u(z)$ is a periodic function of period d [44]. The key point is the imposition of continuity and smoothness of the function $\Phi(z)$ as well as periodicity of $u(z)$ and its derivative. These constraints lead to an implicit equation relating the frequency of the excitations ω, the wave number k, and all the physical parameters. The full derivation is explained in Appendix C. The last step in order to describe the excitations of the particle array is to take the limit $L_w \to 0$ at constant M_{eff}. The dispersion relation is finally determined by the implicit equation

$$\cos(kd) = \cos(\alpha_\omega d) - \frac{\sin(\alpha_\omega d)}{\alpha_\omega d}P\omega^2, \quad (22)$$

where $P = 3\pi d a_p/\Lambda\Gamma\Omega_p$ and α_ω satisfies the equation $\Omega_{\text{LIA}}(\alpha_\omega) = \omega$:

$$\alpha_\omega = \sqrt{-\frac{4\pi\omega}{\Gamma\Lambda}}. \quad (23)$$

In Figs. 6(b) and 6(c) the right-hand side of Eq. (22) is plotted as a function of $\omega\tau$ for heavy and light small particles (that is, low and high Ω_p). The curve must be equal to $\cos(kd)$ and this selects the only allowed frequencies (displayed in gold). It is exactly the same mechanism that leads to the formation of energy bands in crystals [24].

The previous calculations can be directly generalized for more realistic wave propagators (see Appendix C). In particular, if we consider a dispersion relation $\Omega_v(k)$ for the vortex excitations, the only change in the result (22) is the functional dependence of α_ω (23), which must satisfy $\Omega_v(\alpha_\omega) = \omega$. Furthermore, the constant P becomes independent of any adjustable parameter: $P = 3\pi d a_p/\Gamma\Omega_p$. We consider the dispersion relation $\Omega_v^{\text{fit}}(\omega)$ (13) that matches large- and small-scale excitations and we invert it numerically to find α_ω.

In Fig. 5 the contour plot of the theoretical prediction (22) obtained this way is compared with the numerical data (solid green lines), exhibiting a remarkable agreement with the observed excited frequencies. From Fig. 6(b), we remark that the only allowed negative frequencies lie in a thin band around Ω_p. This is also in qualitative agreement with the data. Note that the bare Kelvin wave dispersion relation (10) (dashed cyan line) and the fitted bare vortex wave dispersion relation (13) (solid cyan line) are very similar in Fig. 5. The reason is that the smallest scale that can be solved by the considered array of particles is $k\xi = 0.25$ (i.e., $kd = \pi$), and for wave numbers smaller than this value $\Omega_v^{\text{fit}}(k)$ tends to $\Omega_{\text{KW}}(k)$ by construction.

In order to make a closer connection with experiments, we now describe an array of larger particles of size $a_p = 13.1\xi$ and relative mass $\mathcal{M} = 1$ set in a single quantum vortex and in a bundle composed of four vortices. The corresponding spatiotemporal spectra $S_p(k,\omega)$ are displayed in Fig. 7. In principle such setting should not be well described by our theoretical approach. However, the excitation curves can be reproduced by using the model before the limit $L_w \to 0$ (C6) and phenomenologically replacing $L_w = 2a_p$ while keeping $\Omega_w^{\text{eff}} = \Omega_p^{\text{eff}}$. The agreement is remarkably good, considering the rough modeling that has been done. The case of a bundle in Fig. 7(b) is even more striking. At large scales, we could expect that such system is analogous to a hollow vortex with four quanta of circulation and some effective core size. We have estimated the effective core size by measuring the mean

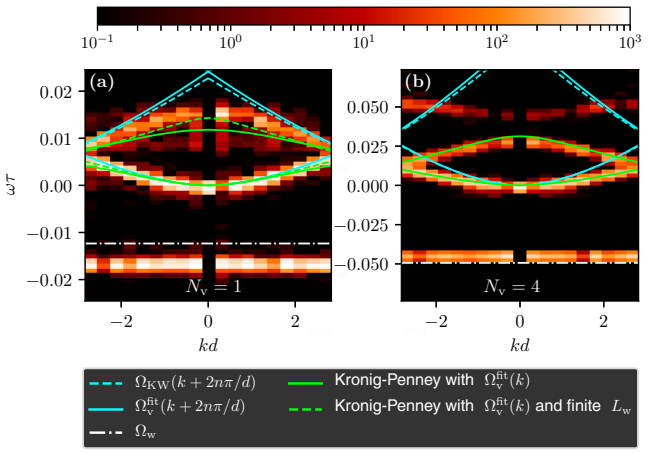


FIG. 7. Spatiotemporal spectra computed from the particle positions for an array of large particles of radius $a_p = 13.1\xi$ and mass $\mathcal{M} = 1$ placed at a distance $d = 51.2\xi$. The repulsion radius is $r_0 = 2a_p$. Solid green lines are the contour plot of the dispersion relation (22) computed with Ω_v^{fit}. Dashed cyan line is low-k KW dispersion relation $\Omega_{KW}(k)$. Solid cyan line is the fitted vortex wave dispersion relation. Dash-dotted horizontal white line is the predicted natural frequency Ω_p. (a) Particles set in a single vortex. Dashed greed line is the dispersion relation (C6) before the limit computed using a finite $L_w = 2a_p$. For the LIA calculations $\Lambda = 2.6$. (b) Particles set in a bundle of 4 vortices. The dispersion relation (22) has been computed using Ω_v^{fit} with an effective core size of $a_0 = 12\xi$ (see text). The other parameters of the simulations are $L_\perp = 1024\xi$, $L_\parallel = 256\xi$, and $N_\perp = 1024$, $N_\parallel = 256$.

distance between the vortices. The theoretical prediction (22) combined with this phenomenological approach still impressively matches the numerical data.

IV. DISCUSSION

In this work we have presented a theoretical and numerical study of the interaction between quantum vortices and a number of particles trapped in them. We have first pointed out that a trapped particle oscillates with a well-defined natural frequency that depends on its mass and the circulation of the flow surrounding it. Because of the typical values of particle parameters used in current superfluid helium experiments, such frequency should be measurable. This measurement can thus provide an independent way of estimating the number of vortices constituting the bundles at which particles are attached.

Based on the experimental evidence that particles spread along quantum vortices keeping a relatively constant interparticle distance, we have studied how the particles modify the vortex excitations. The most exciting result of this work is the strong analogy with solid state physics. Here, particles play the role of ions in the periodic structure of a crystal and vortex excitations that of the electrons. When an electron propagates, it feels the ions as the presence of a periodic array of potential barriers. One of the simplest and idealized descriptions of this physical phenomenon is the Kronig-Penney model, where the barriers have a constant height U_0. Similarly, vortex waves propagate and interact with particles and we have shown that a similar theoretical approach can be used. The main difference is that the constant height of the barriers in the standard Kronig-Penney model induces constant shift of the energy (frequency here). As a consequence, the lowest energy level in a crystal is different from zero (unlike the case of free electrons). Instead, in the vortex case, the interaction potential is due to the Magnus force and depends on the frequency. Comparing the models, we can then establish a mathematical analogy (see Eq. (22) and Refs. [23,24]) by noticing that the effective potential in the case of vortex excitations is given by

$$U_0 \sim \omega^2/\Omega_p \propto \omega^2 M_p^{eff}. \tag{24}$$

The height of the potential is thus proportional to the squared frequency of the incoming wave and to the particle mass. In particular, for very low frequencies the presence of particles does not perturb much the vortices and large-scale Kelvin waves could be tracked by directly measuring the particle dynamics. Moreover, we observe that for particles with a higher natural frequency Ω_p (namely lighter and smaller particles), the value of U_0 and of P in Eq. (22) decrease. As a consequence, the bands of allowed frequencies are broadened. Ideally, in the limiting case of particles with zero mass, the natural frequency is infinite and P and U_0 vanish. Therefore Eq. (22) gets simplified dramatically and becomes $\cos(kd) = \cos(\alpha_\omega d)$. This implies

$$\omega(k) = \Omega_v\left(k + \frac{2n\pi}{d}\right), \quad n \in \mathbb{Z}, \tag{25}$$

which is just the vortex wave dispersion relation, but repeated with period $k_d = 2\pi/d$. In other words, light and small particles can follow the filament without modifying the vortex waves. On the contrary, particle inertia reduces the excited frequencies (in absolute value) of vortex excitations. This fact (actually coming from simple linear physics) should be taken into account when one tries to measure the Kelvin waves experimentally.

In this work we did not take into account the relevance of buoyancy effects for light and heavy particles. We can estimate it by comparing the buoyancy force $F_b = (M_p - M_0)\tilde{g}$, where $\tilde{g} \sim 9.8\ \mathrm{m/s^2}$ is the gravitational acceleration, with the Magnus force that drives the particles $F_M = \frac{3}{2}\rho\Gamma a_p u$, where u is the typical particle velocity estimated as $u \sim \Omega_p a_p$. It turns out that $F_b/F_M = C(\mathcal{M} - 1)(2\mathcal{M} + 1)$, where $C = \frac{32}{81}\pi^2\frac{\tilde{g}a_p^3}{\Gamma^2}$. This expression strongly depends on the particle size. For instance, given that the quantum of circulation in superfluid helium is $\Gamma \sim 10^{-7}\ \mathrm{m^2/s}$, we get that $C \sim 4 \times 10^{-3}$ for a particle of size $a_p = 1\ \mu\mathrm{m}$ and therefore the buoyancy is negligible. However C becomes of order 1 for a particle of size $a_p = 7\ \mu\mathrm{m}$. We conclude that small and light particles would be the most suitable for tracking the vortex excitations.

Several questions can be immediately raised. If particles are not actually equally distributed along the vortex but instead they present some randomness, vortex waves will then propagate in a disordered medium. It will be natural then to study the possibility of Anderson localization in such a system [45,46]. Such situation could perhaps appear if the vortex lines are excited by external means, for instance close to the onset of the Donnelly-Glaberson instability [47,48].

The physical system studied in this work is a first idealized picture of what happens in real superfluid helium experiments. The most evident difference is that the size of particles is typically orders of magnitude larger than the vortex core size ($a_p \sim 10^4\xi$). However, the prediction (22) comes from an asymptotic theory in which $ka_p \ll 1$ and particles can be considered pointlike, independently of the functional form of $\Omega_v(k)$. Therefore, we expect that our result should still apply for wavelengths larger than the particle size. Such long waves are indeed observed in experiments [10]. In particular, the fact that particle inertia does not affect the (low) frequency Kelvin waves should be still valid. A more quantitative prediction for vortices in He II would be always Eq. (22), but with α_ω such that $\omega = \Omega_{He}(\alpha_\omega)$, where $\Omega_{He}(k)$ is the true vortex excitation dispersion relation in superfluid helium. In any case all the main conclusions remain valid, since the analogy with a crystal is independent of $\Omega_v(k)$. Moreover, the behavior at large scales is expected to work quantitatively also for superfluid helium vortices because $\Omega_{He}(ka_0 \to 0) \sim \Omega_{KW}(ka_0)$.

Furthermore, we have used arrays of particles with all identical masses. Instead, in actual experiments there is not a perfect control on the mass and size of particles. In particular, the mass distribution of particles could be polydispersed. In this case, new gaps in the dispersion relation are opened revealing much more complex configurations. A preliminary numerical study confirms this behavior and it will be reported in a future work. In any case, the basic interaction between one particle and vortex waves remains the same regardless of the presence of some disorder. Therefore, large-scale Kelvin waves are not disturbed by the particles. Studying in detail the effects of different species of particles trapped in a vortex can be done systematically in the same spirit of the effective theory developed in the present work, for example adapting tight-binding models [24] to the vortex-particles system. We think that this is a worthy research direction that could establish new and deeper connections with concepts already known in solid state physics, introducing a plethora of novel phenomena in the framework of quantum fluids.

Last but not least, note that the basic equations considered in this work to build up the effective model are based on classical hydrodynamics. Therefore, one could expect that most of the phenomenology remains valid in a classical fluid provided that a mechanism to sustain a vortex exists. Such mechanism could be for instance provided by two corotating propellers at moderate speeds. Since these systems are achievable in much less extreme conditions than in cold superfluid helium and because the manipulation of particle parameters is much simpler, it could be possible to build analogs of solid state physics phenomena by using classical fluid experiments.

ACKNOWLEDGMENTS

We acknowledge useful scientific discussions with Davide Proment and Vishwanath Shukla. U.G. and G.K. were supported by Agence Nationale de la Recherche through the project GIANTE ANR-18-CE30-0020-01. Computations were carried out on the Mésocentre SIGAMM hosted at the Observatoire de la Côte d'Azur and the French HPC Cluster OCCIGEN through the GENCI allocation A0042A10385. S.N. is supported by the Chaire d'Excellence IDEX, UCA. G.K. and S.N. are supported by the EU Horizon 2020 research and innovation programme under the Grant Agreement No. 823937 in the framework of Marie Skodowska-Curie HALT project and the Simons Foundation Collaboration grant Wave Turbulence (Award ID 651471).

APPENDIX A: NUMERICAL SCHEME AND PARAMETERS

Equations (2) and (3) are solved with a standard pseudospectral code and a fourth-order Runge-Kutta scheme for the time stepping in a 3D periodic domain of dimensions $L_\perp \times L_\perp \times L_\parallel$ with $N_\perp \times N_\perp \times N_\parallel$ collocation points. We set $c = \rho_\infty = 1$.

The ground states with particles and straight vortices are prepared separately by performing imaginary-time evolution of the GP equation. In order to have an initial state with zero global circulation (and therefore ensure periodic boundary conditions) we need to add in the computational box three image vortices with alternating charges. The state with bundles of $N_v = 4$ vortices [Fig. 2(d)] is prepared imposing a phase jump of $2N_v\pi$ around a vortex (including its images). Then, imaginary-time evolution of the GP equation is performed for a time $\sim 150\tau$, so that the vortex filaments separate and the bundles form. KWs are generated from the state with straight vortices slightly shifting each xy plane of the computational domain. Then the states with KWs and particles are multiplied to obtain the desired initial condition. Just one vortex filament is loaded with particles, while the three other images remain bare. The initial condition is evolved for a short time ($\sim 40\tau$) using GP without the particle dynamics in order to adapt the system.

The particle potential is a smoothed hat function $V_p(r) = \frac{V_0}{2}(1 - \tanh[\frac{r^2-\eta^2}{4\Delta l^2}])$ and the mass displaced by the particle is measured as $M_w^0 = \rho_\infty L_\perp L_\parallel^2 (1 - \int |\psi_p|^2\, d\mathbf{x} / \int |\psi_\infty|^2\, d\mathbf{x})$, where ψ_p is the steady state with just one particle. Since the particle boundaries are not sharp, we measure the particle radius as $a_p = (3M_p^0/4\pi\rho_\infty)^{\frac{1}{3}}$ for given values of the numerical parameters η and Δl. For all the particles $V_0 = 20$. The parameters used are the following: for $a_p = 2.7\xi$, $\eta = \xi$ and $\Delta l = 0.75\xi$; for $a_p = 7.6\xi$, $\eta = 2\xi$ and $\Delta l = 2.5\xi$; and for $a_p = 13.1\xi$, $\eta = 10\xi$ and $\Delta l = 2.8\xi$.

The parameter r_0 of the potential $V_{rep}^{ij} = \varepsilon(r_0/|\mathbf{q}_i - \mathbf{q}_j|^{12})$ is the radius of the repulsion between particles. The parameter ε is fixed numerically in order to impose an exact balance between the repulsive force and the GP force $-\int V_p(|\mathbf{x} - \mathbf{q}_i|)\nabla|\psi|^2\, d\mathbf{x}$ in the ground state with two particles placed at distance $2a_p$ when $r_0 = 2a_p$. The parameters used for the repulsion are the following: for the wires in Fig. 4, $r_0 = 2L_w/(N_p a_p)$ and $\varepsilon = 4.4 \times 10^{-5}$; for the array of particles in Fig. 5, $r_0 = 4a_p$ and $\varepsilon = 4.4 \times 10^{-5}$; and for the array of particles in Fig. 7, $r_0 = 2a_p$ and $\varepsilon = 1.7 \times 10^{-3}$.

APPENDIX B: SPATIOTEMPORAL SPECTRA

We use the particle positions to define the spatiotemporal spectra of vortex excitations by computing

$$S_q(k,\omega) = C_q \left| \int \sum_{j=1}^{N_p} q(z_j,t) e^{-i(kz_j+\omega t)} dt \right|^2, \qquad \text{(B1)}$$

where z_j is the z component of the particle j. Similarly, the spatiotemporal spectrum of the superfluid wave function is defined as

$$S_\psi(k,\omega) = C_\psi \left| \int \psi(x,y,z,t) e^{-i(kz+\omega t)}\, dx\, dy\, dz\, dt \right|^2. \quad \text{(B2)}$$

Note that in Eq. (B2) an average of ψ in the x and y directions is implicit. The normalization constants C_q and C_ψ are set such that the full (k,ω) integrals of the spatiotemporal spectra are 1. In order to enhance the small-scale excitations, in the density plots shown in the present work, both the spectra (B1) and (B2) are further normalized with the frequency-averaged spectra, respectively $\int S_q(k,\omega)\, d\omega$ and $\int S_\psi(k,\omega)\, d\omega$. All the color maps shown in the present work are in log scale.

APPENDIX C: DERIVATION OF THE KRONIG-PENNEY DISPERSION RELATION FOR VORTEX WAVES

We look for a linear wave solution $q(z,t) = \Phi(z)e^{i\omega t}$ of the system (21) and in particular we want to know which frequencies ω are excited. The function $\Phi(z)$ must satisfy the system

$$\begin{aligned} &\frac{\partial^2}{\partial z^2}\Phi(z) + \alpha_\omega^2 \Phi(z) = 0 \quad \text{(I)}, \\ &\frac{\partial^2}{\partial z^2}\Phi(z) + \beta_\omega^2 \Phi(z) = 0 \quad \text{(II)}, \end{aligned} \quad \text{(C1)}$$

where α_ω and β_ω are such that

$$\Omega_{\rm LIA}(\alpha_\omega) = \omega, \quad \Omega_{\rm LIA}(\beta_\omega) = \omega - \frac{\omega^2}{\Omega_{\rm w}}, \quad \text{(C2)}$$

which means

$$\alpha_\omega = \sqrt{-\frac{4\pi\omega}{\Gamma\Lambda}}, \quad \beta_\omega = \sqrt{\frac{4\pi}{\Gamma\Lambda}\left(\frac{\omega^2}{\Omega_{\rm w}} - \omega\right)}. \quad \text{(C3)}$$

Since the system (C1) is a linear and homogeneous differential equation with periodic coefficients of period d, it admits a solution in the form $\Phi(z) = e^{ikz}u(z)$, where $u(z)$ is a periodic function of period d. The solutions of (C1) in the two regions (I) and (II) are

$$\begin{aligned} \Phi_{\rm I}(z) &= e^{ikz}u_{\rm I}(z) = e^{ikz}[Ae^{i(\alpha_\omega - k)z} + Be^{-i(\alpha_\omega + k)z}], \\ \Phi_{\rm II}(z) &= e^{ikz}u_{\rm II}(z) = e^{ikz}[Ce^{i(\beta_\omega - k)z} + De^{-i(\beta_\omega + k)z}]. \end{aligned} \quad \text{(C4)}$$

The coefficients A, B, C, D are fixed by imposing continuity and smoothness of the function $\Phi(z)$ and periodicity of $u(z)$ and its derivative:

$$\begin{aligned} \Phi_{\rm I}(0) &= \Phi_{\rm II}(0), \\ \Phi'_{\rm I}(0) &= \Phi'_{\rm II}(0), \\ u_{\rm I}(d - L_{\rm w}) &= u_{\rm II}(-L_{\rm w}), \\ u'_{\rm I}(d - L_{\rm w}) &= u'_{\rm II}(-L_{\rm w}). \end{aligned} \quad \text{(C5)}$$

The system (C5) is a homogeneous linear system for the variables A, B, C, D. It admits nontrivial solutions only if the determinant of the coefficients is equal to zero. This implies the following condition:

$$\begin{aligned} \cos(kd) = \cos(\beta_\omega L_{\rm w})\cos[\alpha_\omega(d - L_{\rm w})] \\ -\frac{\alpha_\omega^2 + \beta_\omega^2}{2\alpha_\omega\beta_\omega}\sin(\beta_\omega L_{\rm w})\sin[\alpha_\omega(d - L_{\rm w})], \end{aligned} \quad \text{(C6)}$$

which determines implicitly the dispersion relation $\omega(k)$. Such expression is structurally identical to the standard Kronig-Penney condition but the functions α_ω and β_ω are different. The limit $L_{\rm w} \to 0$ is applied to Eq. (C6), substituting at the same time the mass of the massive vortex segment $M_{\rm w}^{\rm eff}$ with the mass of the particle $M_{\rm p}^{\rm eff}$. In this way the system becomes a vortex filament loaded with massive point particles (see Fig. 6). The limit implies $\beta_\omega \to \infty$, $\beta_\omega L_{\rm w} \to 0$, $\sin(\beta_\omega L_{\rm w}) \sim \beta_\omega L_{\rm w}$, $\alpha_\omega \ll \beta_\omega$, and $\beta_\omega^2 L_{\rm w} \sim 6\pi a_{\rm p}\omega^2/\Lambda\Gamma\Omega_{\rm p}$, so that Eq. (C6) becomes Eq. (22).

The previous result can be extended to the case of more realistic vortex waves with some caveat. We can formally rewrite the model (21) as

$$\begin{aligned} &\dot q(z,t) = i\hat{\mathcal{L}}_{\rm v}[q(z,t)] \quad \text{(I)}, \\ &\ddot q(z,t) = i\Omega_{\rm w}\{\dot q(z,t) - i\hat{\mathcal{L}}_{\rm v}[q(z,t)]\} \quad \text{(II)}, \end{aligned} \quad \text{(C7)}$$

where $\hat{\mathcal{L}}_{\rm v}$ is the linear nonlocal differential operator that generates the vortex wave dispersion relation $\Omega_{\rm v}(k)$. Namely, calling $s(z,t) = \sum_k s_k(t)e^{ikz}$ the wave operator simply reads

$$\hat{\mathcal{L}}_{\rm v}[s(z,t)] = \sum_k \Omega_{\rm v}(k)s_k(t)e^{ikz}. \quad \text{(C8)}$$

The system (C1) thus becomes

$$\begin{aligned} &\hat{\mathcal{L}}_{\rm V}[\Phi(z)] - \omega\Phi(z) = 0 \quad \text{(I)}, \\ &\hat{\mathcal{L}}_{\rm V}[\Phi(z)] - \left(\omega - \frac{\omega^2}{\Omega_{\rm v}}\right)\Phi(z) = 0 \quad \text{(II)}. \end{aligned} \quad \text{(C9)}$$

The functions (C4) are still a solution of (C9), but now α_ω and β_ω are defined as

$$\Omega_{\rm v}(\alpha_\omega) = \omega, \quad \Omega_{\rm v}(\beta_\omega) = \left(\omega - \frac{\omega^2}{\Omega_{\rm w}}\right). \quad \text{(C10)}$$

In general such equations cannot be inverted explicitly, but α_ω and β_ω can be found numerically. In particular the inversion is intended with respect to $\Omega_{\rm v}(k > 0)$. The functions α_ω and β_ω are well defined (at least for $\omega/\Gamma > 0$) because any model for the self-induced velocity of a vortex generates a dispersion relation $\Omega_{\rm v}(k)$ that is monotonically increasing for positive k. For evaluating the limit $L_{\rm w} \to 0$, $M_{\rm w}^{\rm eff} \to M_{\rm p}^{\rm eff}$, we note that $\lim_{L_{\rm w}\to 0}\Omega_{\rm v}(\beta_\omega) = \infty$. Therefore, we can explicitly use the asymptotics of $\Omega_{\rm v}(k)$ for large k, which is just the free particle dispersion relation (12) and can be inverted explicitly:

$$\beta_\omega \underset{L_{\rm w}\to 0}{\longrightarrow} \sqrt{\frac{4\pi\omega^2}{\Gamma\Omega_{\rm w}}}, \quad \text{(C11)}$$

so that $\beta_\omega^2 L_{\rm w} \sim 6\pi a_{\rm p}/\Gamma\Omega_{\rm p}$. In this way we recover Eq. (22), with α_ω defined as in (C10) and the amplification factor P is now independent of any free parameter:

$$P = \frac{3\pi d a_{\rm p}}{\Gamma\Omega_{\rm p}}. \quad \text{(C12)}$$

[1] F. London, Nature (London) **141**, 643 (1938).
[2] L. Landau, Phys. Rev. **60**, 356 (1941).
[3] L. Tisza, Nature (London) **141**, 913 (1938).
[4] R. Feynman, Prog. Low Temp. Phys. **1**, 17 (1955).
[5] W. Vinen and J. Niemela, J. Low Temp. Phys. **128**, 167 (2002).
[6] M. S. Paoletti and D. P. Lathrop, Annu. Rev. Condens. Matter Phys. **2**, 213 (2011).
[7] C. F. Barenghi, L. Skrbek, and K. R. Sreenivasan, Proc. Natl. Acad. Sci. USA **111**, 4647 (2014).
[8] R. J. Donnelly, *Quantized Vortices in Helium II*, Vol. 2 (Cambridge University Press, Cambridge, 1991).
[9] G. P. Bewley, D. P. Lathrop, and K. R. Sreenivasan, Nature (London) **441**, 588 (2006).
[10] E. Fonda, D. P. Meichle, N. T. Ouellette, S. Hormoz, and D. P. Lathrop, Proc. Natl. Acad. Sci. USA **111**, 4707 (2014).
[11] M. S. Paoletti, M. E. Fisher, K. R. Sreenivasan, and D. P. Lathrop, Phys. Rev. Lett. **101**, 154501 (2008).
[12] M. La Mantia and L. Skrbek, Phys. Rev. B **90**, 014519 (2014).
[13] D. R. Poole, C. F. Barenghi, Y. A. Sergeev, and W. F. Vinen, Phys. Rev. B **71**, 064514 (2005).
[14] Y. A. Sergeev and C. F. Barenghi, J. Low Temp. Phys. **157**, 429 (2009).
[15] C. F. Barenghi, D. Kivotides, and Y. A. Sergeev, J. Low Temp. Phys. **148**, 293 (2007).
[16] G. E. Astrakharchik and L. P. Pitaevskii, Phys. Rev. A **70**, 013608 (2004).
[17] S. Rica and D. C. Roberts, Phys. Rev. A **80**, 013609 (2009).
[18] A. Villois and H. Salman, Phys. Rev. B **97**, 094507 (2018).
[19] T. Winiecki and C. S. Adams, Europhys. Lett. **52**, 257 (2000).
[20] V. Shukla, M. Brachet, and R. Pandit, Phys. Rev. A **94**, 041602(R) (2016).
[21] U. Giuriato, G. Krstulovic, and D. Proment, J. Phys. A: Math. Theor. **52**, 305501 (2019).
[22] U. Giuriato and G. Krstulovic, Sci. Rep. **9**, 4839 (2019).
[23] R. D. L. Kronig, W. G. Penney, and R. H. Fowler, Proc. R. Soc. London, Ser. A **130**, 499 (1931).
[24] C. Kittel, P. McEuen, and P. McEuen, *Introduction to Solid State Physics*, Vol. 8 (Wiley, New York, 1976).
[25] W. F. Vinen, Phys. Rev. B **64**, 134520 (2001).
[26] K. W. Schwarz, Phys. Rev. B **38**, 2398 (1988).
[27] M. D. Bustamante and S. Nazarenko, Phys. Rev. E **92**, 053019 (2015).
[28] R. J. Arms and F. R. Hama, Phys. Fluids **8**, 553 (1965).
[29] S. W. Thomson, The London, Edinburgh, and Dublin Philosophical Magazine and Journal of Science **10**, 155 (1880).
[30] P. H. Roberts, Proc. R. Soc. London, Ser. A **459**, 597 (2003).
[31] E. B. Gordon, M. E. Stepanov, M. I. Kulish, A. V. Karabulin, V. I. Matyushenko, and I. I. Khodos, Laser Phys. Lett. **16**, 026002 (2018).
[32] R. J. Zieve, Y. Mukharsky, J. D. Close, J. C. Davis, and R. E. Packard, Phys. Rev. Lett. **68**, 1327 (1992).
[33] L. Hough, L. A. K. Donev, and R. J. Zieve, Phys. Rev. B **65**, 024511 (2001).
[34] See Supplemental Material at http://link.aps.org/supplemental/10.1103/PhysRevResearch.2.023149 for movies of the simulations.
[35] G. K. Batchelor, *An Introduction to Fluid Dynamics*, Cambridge Mathematical Library (Cambridge University Press, Cambridge, 2000).
[36] L. Kiknadze and Y. Mamaladze, arXiv:cond-mat/0604436.
[37] E. B. Sonin, *Dynamics of Quantised Vortices in Superfluids* (Cambridge University Press, Cambridge, 2016).
[38] M. Gibert (private communication, 2019).
[39] H. E. Hall, W. F. Vinen, and D. Shoenberg, Proc. R. Soc. Lond. A **238**, 215 (1997).
[40] A. L. Fetter and K. Harvey, Phys. Rev. A **4**, 2305 (1971).
[41] P. W. Karn, D. R. Starks, and W. Zimmermann, Phys. Rev. B **21**, 1797 (1980).
[42] J. C. Davis, J. D. Close, R. Zieve, and R. E. Packard, Phys. Rev. Lett. **66**, 329 (1991).
[43] T. Simula, Phys. Rev. A **97**, 023609 (2018).
[44] G. Floquet, Annales scientifiques de l'école Normale Supérieure **12**, 47 (1883).
[45] P. W. Anderson, Phys. Rev. **109**, 1492 (1958).
[46] B. Kramer and A. MacKinnon, Rep. Prog. Phys. **56**, 1469 (1993).
[47] D. K. Cheng, M. W. Cromar, and R. J. Donnelly, Phys. Rev. Lett. **31**, 433 (1973).
[48] W. I. Glaberson, W. W. Johnson, and R. M. Ostermeier, Phys. Rev. Lett. **33**, 1197 (1974).

4.2 The original Kronig–Penney model for a one-dimensional crystal

In this section we report the explicit derivation of the Kronig–Penney model, which describes the quantum mechanics of an electronic wavefunction in a periodic unidimensional crystal [111, 127]. In this way, the reader not familiar with these solid state concepts can appreciate better the analogy with the vortex-particle system reported in the publication [79].

Let us consider a quantum wavefunction ψ_e (which has nothing to do with with the superfluid field ψ), describing an electron of mass m_e in a one dimensional space. Such wavefunction evolves accordingly to the (linear) Schrödinger equation

$$i\hbar\frac{\partial}{\partial t}\psi_e(x,t) = -\frac{\hbar^2}{2m_e}\frac{\partial^2}{\partial x^2}\psi_e(x,t) + V(x)\psi_e(x,t), \tag{4.2}$$

where $V(x)$ is an external potential field. The simplest way of modeling a crystal lattice consists in choosing $V(x)$ as a periodic series of potential barriers, as sketched in Fig.4.1. The fundamental cell of the potential field is thus defined as

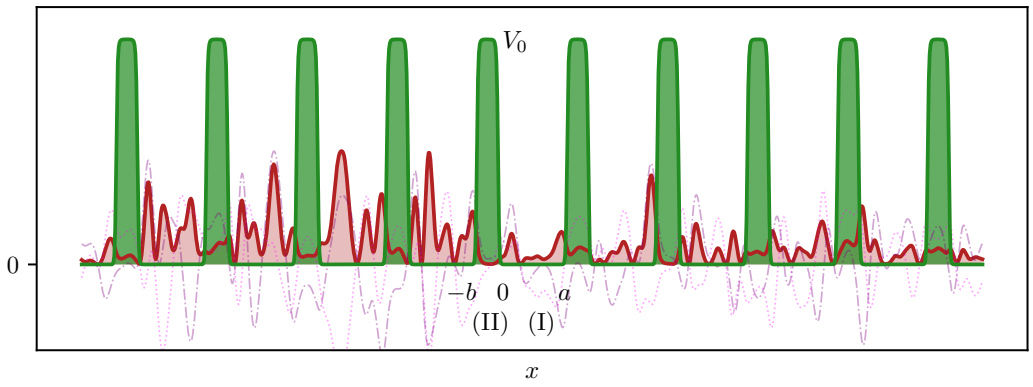


Figure 4.1. Sketch of the original Kronig–Penney model. The potential barriers are displayed in green and the electronic wavefunction ψ_e is in red. The dotted and dash-dotted lines are the real and the imaginary part of ψ_e.

$$V(x) = \begin{cases} 0, & \text{for} \quad 0 < x < a \qquad \text{(I)} \\ V_0, & \text{for} \quad -b < x < 0 \qquad \text{(II)} \end{cases} \tag{4.3}$$

where V_0 is the height of the barrier, b its width and $d = a + b$ the distance between two consecutive barriers. In each of the two zones of the fundamental cell, the equation of

motion for the quantum wavefunction reads

$$i\hbar\frac{\partial}{\partial t}\psi_{\mathrm{e}}(x,t) = -\frac{\hbar^2}{2m_{\mathrm{e}}}\frac{\partial^2}{\partial x^2}\psi_{\mathrm{e}}(x,t), \qquad \text{(I)} \tag{4.4}$$

$$i\hbar\frac{\partial}{\partial t}\psi_{\mathrm{e}}(x,t) = -\frac{\hbar^2}{2m_{\mathrm{e}}}\frac{\partial^2}{\partial x^2}\psi_{\mathrm{e}}(x,t) + V_0\psi_{\mathrm{e}}(x,t). \qquad \text{(II)} \tag{4.5}$$

Such system admits as solution a stationary quantum state of energy $E > 0$ given by $\psi(x,t) = \Phi(x)e^{-\frac{i}{\hbar}Et}$, where $\Phi(x)$ is a spatial function that satisfies the system

$$\frac{\partial^2}{\partial x^2}\Phi(x) = \alpha^2\Phi(x), \qquad \text{(I)} \tag{4.6}$$

$$\frac{\partial^2}{\partial x^2}\Phi(x) = \beta^2\Phi(x), \qquad \text{(II)} \tag{4.7}$$

where we have defined

$$\alpha = \sqrt{\frac{2mE}{\hbar^2}}, \qquad \beta = \sqrt{\frac{2m_{\mathrm{e}}}{\hbar^2}(V_0 - E)}. \tag{4.8}$$

The problem consists in finding the energy levels of such system, i.e. the energy spectrum of an electron immersed in a periodic lattice of potential barriers. The analogous of the energy E in [79] is the frequency of Kelvin waves when an array of particles is trapped by the vortex filament. Note that the definition of β is valid both for $E < V_0$ and $E > V_0$, being purely real in the first case and purely imaginary in the latter.

From now on, the derivation is formally equivalent to the one showed in the appendix of Ref. [79], although the physical meaning of the various terms is rather different. Since Eqs. (4.6) and (4.7) constitute together a linear and homogeneous differential equation with periodic coefficients of period $d = a + b$, one can appeal to the Bloch theorem [111] and look for a solution

$$\Phi(x) = e^{ikx}u(x), \tag{4.9}$$

where $u(x)$ is a periodic function of period $d = a + b$ (usually called Bloch function) and k the wavenumber. In the two regions (I) and (II) the Bloch function reads

$$u_{\mathrm{I}}(x) = Ae^{i(\alpha-k)x} + Be^{-i(\alpha+k)x},$$
$$u_{\mathrm{II}}(x) = Ce^{i(\beta-k)x} + De^{-i(\beta+k)x}.$$

The conditions that one need to impose to determine the coefficients A, B, C, D are the continuity of the Bloch function and its derivative at the interfaces between the two

region of the fundamental cell:

$$\begin{cases} u_{\mathrm{I}}(0^+) = u_{\mathrm{II}}(0^-) \\ u'_{\mathrm{I}}(0^+) = u'_{\mathrm{II}}(0^-) \\ u_{\mathrm{I}}(a^-) = u_{\mathrm{II}}(-b^+) \\ u'_{\mathrm{I}}(a^-) = u'_{\mathrm{II}}(-b^+) \end{cases} \tag{4.10}$$

where the primes indicate spatial differentiation. As usual, nontrivial solutions A, B, C, D of the system (4.10) exist if the determinant of the corresponding coefficients vanishes. This imply the condition

$$\cos(kd) = \cosh(\beta b)\cos(\alpha(d-a)) - \frac{\alpha^2-\beta^2}{2\alpha\beta}\sinh(\beta b)\sin(\alpha(d-a)) \tag{4.11}$$

which determines implicitly the energy spectrum $E(k)$ as a function of the wavenumber k (the energy is hidden in the variables α and β). The equation holds both for $E < V_0$ and $E > V_0$, but in the latter case β is purely imaginary. Thus, in such case it is convenient to redefine it as $\beta = \sqrt{\frac{2m_{\mathrm{e}}}{\hbar^2}(E-V_0)}$ so that the the implicit dispersion relation reads

$$\cos(kd) = \cos(\beta b)\cos(\alpha(d-b)) + \frac{\beta^2-\alpha^2}{2\alpha\beta}\sin(\beta b)\sin(\alpha(d-b)), \tag{4.12}$$

which is structurally identical to Eq. (C6) of [79], but with different α and β. Note that Eq. (4.11) can be derived in the same way also in the case of attractive potentials $V_0 < 0$, i.e. for potential wells instead of potential barriers. The equation for the energy spectrum can be further simplified performing simultaneously the limit of infinite potential height $V_0 \to \infty$ and infinitesimal potential width $b \to 0$, but keeping the product $V_0 b$ constant. In this situation $\beta^2 b$ remains also constant, βb and $\alpha^2 b$ vanish and one can substitute $\sinh(\beta b) \sim \beta b$ and $\cosh(\beta b) \sim 1$, so that Eq. (4.11) becomes

$$\cos(kd) = \cos(\alpha d) + \frac{\sin(\alpha d)}{\alpha d}P, \tag{4.13}$$

with the parameter

$$P = \frac{ma}{\hbar^2}V_0 b, \tag{4.14}$$

that quantifies the energy barrier. In particular, the free particle dispersion relation is recovered for $P \to 0$, although replicated with period d. The limit leading to Eq.(4.13) is also analogous to the one performed to pass from the system made of bare vortex segments alternated by massive vortex segments to a vortex filament with inertial point particles placed on it. In the latter case, the length of the massive vortices is sent to zero, while the inertia is kept fixed.

4.3 Comparison between the crystal and the vortex-particles dispersion relations

The energy spectrum in the limit of delta-supported potential barriers (4.13) can be compared directly with the dispersion relation (22) of [79], that we report also here:

$$\cos(kd) = \cos(\alpha_\omega d) + \frac{\sin(\alpha_\omega d)}{\alpha_\omega d} P\omega^2, \tag{4.15}$$

where d is now the distance between the inertial point particles, α_ω is defined implicitly in Eq. (C9) of [79] as the inverse of the vortex wave dispersion relation and $P = 3\pi d a_p/\Gamma\Omega_p$. In Fig.4.2 the contourplot of Eq. (4.13) in the plane E-k is compared with the contourplot of Eq. (4.15) in the plane ω-k for different values of the parameter P.

There are basically three main differences between the two spectra (4.13) and (4.15). The first one is of course the definition of the constant P, that in the vortex-particles system contains the parameters of the particle (size and mass) and the circulation, while in the standard KP model P is controlled by the product between the potential barrier and the potential width. Apart from that, its role is exactly the same, namely tuning the strenght of the energy barrier due to the impurities (potentials/particles). When the value of P is larger, the gaps between the allowed energies/frequencies are larger and the allowed bands thinner.

The second difference is the functional form of α_ω, i.e. the "bare" wave dispersion relation. If one considers a realistic vortex wave dispersion relation it basically implies a logarithmic correction for the slow modes. Instead, if one consider the LIA approximation, the functional form is actually the same for a vortex wave and for an electron, being $\alpha_\omega \propto \sqrt{\omega}$ in the first case and $\alpha \propto \sqrt{E}$ ((4.8)) in the latter. As a consequence, when $P = 0$ (upper row of Fig.4.2) the two models reproduce the same continuous spectrum, which is just the free wave dispersion relation, replicated with period $kd = 2\pi$. Such result trivially follows from the fact that both the vortex waves in the LIA approximation and free electrons are described by a linear Schrödinger equation with quadratic dispersion.

The last and crucial difference is the presence of an ω^2 in the second term of the right hand side of Eq. (4.15). Such term stems directly from the Newton acceleration term in the equation for the particles before the limit of zero length, which acts as an effective potential barrier for the wave propagation. Indeed, substituting the wave solution $q(z,t) = \Phi(z)e^{i\omega t}$ into Eq. (21-II) of [79] one gets

$$\frac{\partial^2}{\partial z^2}\Phi(z) = \frac{4\pi}{\Gamma\Lambda}\left(\omega - \frac{\omega^2}{\Omega_w}\right)\Phi(z). \tag{4.16}$$

Comparing Eq. (4.16) with (4.7), it is evident that the role of the inertial term ω^2/Ω_w is the same of the potential height V_0. Note that in the limit $L_w \to 0$ with $M_w^{eff} = M_p^{eff}$,

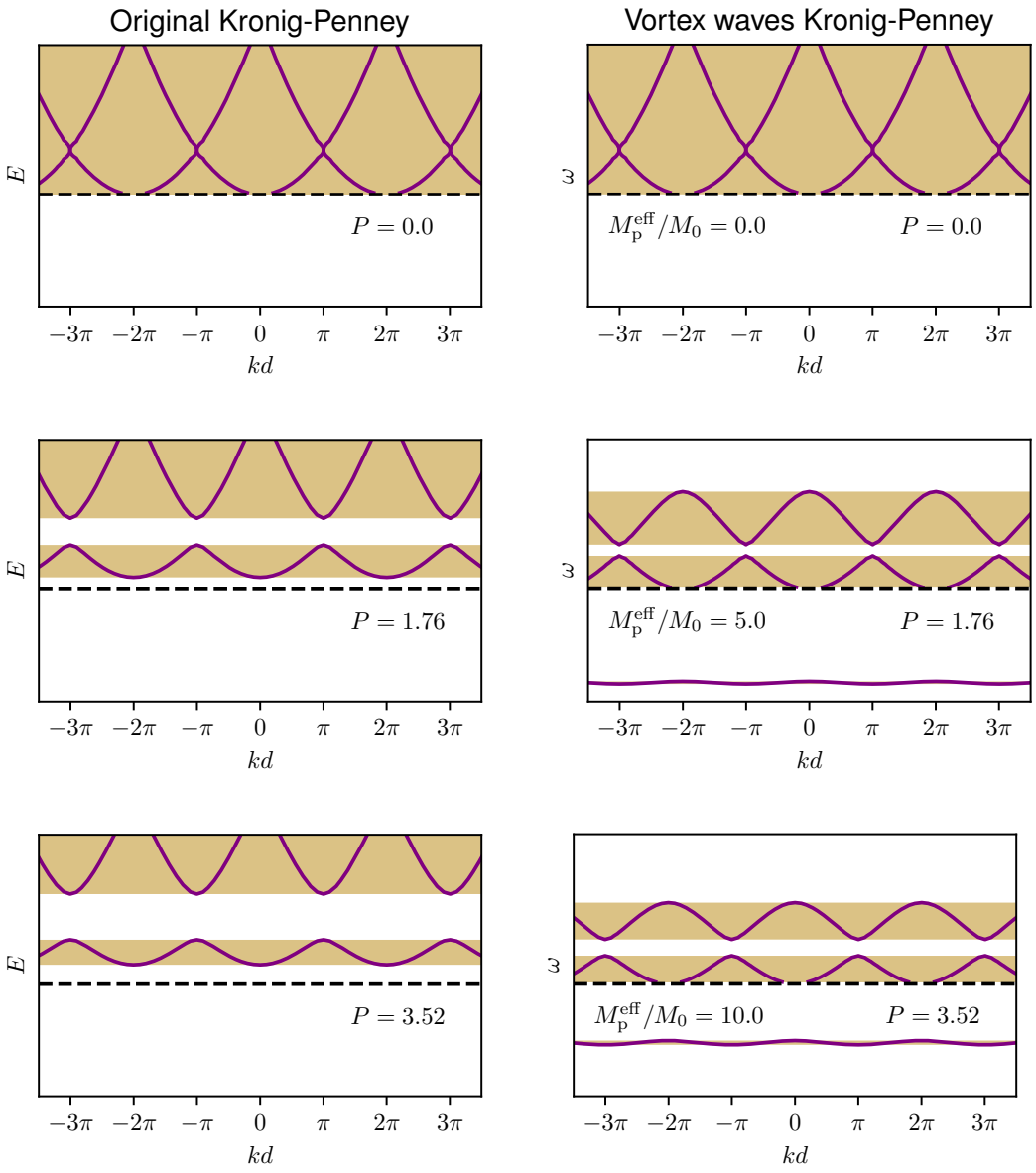


Figure 4.2. Comparison between the original KP energy spectrum (4.13) (*left*) and the vortex waves KP dispersion relation (4.15) (*right*) for different values of the parameter P. The LIA dispersion relation has been used to model the bare vortex wave dispersion relation and energies (frequencies) are normalized to match in the free wave regime ($P = 0$, upper row).

Eq. (21) of [79] becomes:

$$\frac{\partial^2}{\partial z^2}\Phi(z) = \frac{4\pi}{\Gamma\Lambda}\left(\omega - \frac{3}{2}a_p\delta(z - z_j)\frac{\omega^2}{\Omega_p}\right)\Phi(z), \tag{4.17}$$

where the Dirac deltas are peaked at the position z_j of the particles. As already mentioned in the discussion of the paper, the dependence on ω^2 of the potential implies that slow modes with low ω feel a less intense barrier and can propagate freely. A consequence of this fact is that the dispersion relation is always pinned at the point $(k = 0, \omega = 0)$, regardless the value of P or the particle mass. As it is clear in Fig.4.2 this is not the case for the original KP model, where the lowest modes are found to be at a higher energy when the potential barriers of the crystal lattice are different from zero. We conclude by remarking once again that having these unperturbed slow modes is an indication that large Kelvin waves could be efficiently tracked by particles in superfluid helium experiments, which is the fundamental question addressed in the article.

5 Quantum turbulence in presence of particles

In this chapter we present the publication "Active and finite-size particles in decaying quantum turbulence at low temperature" [76], in which a zero temperature quantum turbulence regime with particles immersed in it is investigated. As an introduction, we first provide the general concepts behind the standard Kolmogorov theory of turbulence in classical fluids, followed by a summary of the phenomenology of turbulence in quantum fluids. The results exposed later try to answer the questions whether the presence of finite-size particles affects the development of a turbulent vortex tangle and how the actual dynamics of particles reflects the superfluid turbulent motions.

5.1 Main concepts of classical Kolmogorov turbulence

Kolmogorov developed the foundations of the theory of turbulence in 1941 [68, 121, 122], for a classical fluid described by the incompressible Navier–Stokes equations (2.1), (2.2). The onset of a turbulent regime in classical fluids is controlled by the Reynolds number Re, a dimensionless parameter which controls the relative magnitude of the inertial terms $(\boldsymbol{v}\cdot\nabla)\boldsymbol{v}$ with respect to the dissipative one $\nu\nabla^2\boldsymbol{v}$. Calling L the characteristic length of the system, ν the kinematic viscosity and v_L the characteristic velocity of the flow, the Reynolds number reads:

$$\mathrm{Re} = \frac{L v_L}{\nu}. \tag{5.1}$$

A necessary condition for the onset of fluid turbulence in the classical sense is that the Reynolds number must be large. If this is the case, the viscous dissipation is efficient in dissipating the flow at small scales, while the high non-linearity leads to complex and chaotic motion at intermediate scales between the dissipative scale and large scale of the system.

Two scalar quantities which are important in turbulence are the total energy $E = \left\langle \frac{1}{2}|\boldsymbol{v}|^2 \right\rangle$ and the total enstrophy $\Omega = \left\langle \frac{1}{2}|\boldsymbol{\omega}|^2 \right\rangle$, where $\boldsymbol{\omega} = \nabla\times\boldsymbol{v}$ is the vorticity and $\langle\cdot\rangle$ stands for spatial average. These global quantities satisfy the balance equation

$$\epsilon = -\frac{\mathrm{d}E}{\mathrm{d}t} = 2\nu\Omega, \tag{5.2}$$

which comes directly from the Navier–Stokes equations and where we have defined the dissipation ϵ as the negative rate of energy variation in time. An important assumption in classical turbulence is the existence of a dissipative anomaly [68]. It means that

the dissipation (5.2) remains finite when $\nu \to 0$, which in turn implies a divergent behaviour of the velocity gradients.

One of the cornerstone ideas of turbulence is the energy cascade, already suggested by Richardson twenty years before the work of Kolmogorov [189]. Imagine that energy is suddenly injected at large scale in a fluid at rest. Initially such energy will excite structures at the scale of the forcing and (if the Reynolds number is high enough) the dissipation ϵ will be small, since the right hand side of Eq.(5.2) is sensitive only to variation of the flow at small scales. The non-linearity of the Navier–Stokes equations will start to excite smaller and smaller structures, carrying the energy (in a cascade process, indeed) down to the scale where the dissipation is strong enough to remove it definitively from the fluid system.

In his famous 1941 theory [121, 122], Kolmogorov extracted quantitative estimations from this idea, using simple dimensional arguments. He assumed homogeneity and isotropy, together with the hypothesis of the existence of an inertial range of scales in which the transfer of energy is independent of the forcing mechanism and of the viscosity. Then, if the typical velocity variation[1] at the scale ℓ in the inertial range only depends on the dissipation rate ϵ and on ℓ itself, by dimensional analysis it must scale as $\delta u_\ell \sim (\epsilon\ell)^{1/3}$. Such scaling law leads immediately to the historical expression for the 1D energy spectrum in Fourier space:

$$E(k) = C_K \epsilon^{2/3} k^{-5/3}, \tag{5.3}$$

where the dimensionless Kolmogorov constant C_K is not predicted. Its measured value is about 1.5 and it was believed to be an universal constant [217]. The Reynolds number at the scale ℓ can be also estimated as $\mathrm{Re}_\ell = \delta v_\ell \ell/\nu \sim \epsilon^{1/3}\ell^{4/3}/\nu$. Thus, the dissipative scale $\ell = \eta$ is defined as the scale at which the viscous dissipation balances the inertial forces, which means $\mathrm{Re}_\eta \sim 1$. Such scale is also called Kolmogorov length and it reads

$$\eta \sim \left(\frac{\nu^3}{\epsilon}\right)^{1/4}. \tag{5.4}$$

For completeness, we mention another historical result achieved by Kolomogorov, the so-called 4/5 law. It is a prediction for the third order longitudinal structure function of the homogeneous and isotropic turbulent velocity field, in the limit of infinite Reynolds number:

$$\left\langle \left(\delta v_\parallel(\boldsymbol{r},\ell)\right)^3 \right\rangle = \left\langle \left([\boldsymbol{v}(\boldsymbol{r}+\ell) - \boldsymbol{v}(\boldsymbol{r})]\cdot\hat{\ell}\right)^3 \right\rangle = \frac{4}{5}\epsilon\ell. \tag{5.5}$$

Equation (5.5) is actually one of the few exact results (both scaling and pre-factor) in the turbulence theory that can be derived directly from the Navier–Stokes equations.

A fundamental role in turbulence is played by strong fluctuations, that can be characterized by looking at the higher order moments of the structure functions. These should follow power-laws in the inertial range $\left\langle \left(\delta v_\parallel(\ell)\right)^p \right\rangle \sim (\epsilon\ell)^{\zeta_p}$, as suggested by

[1] Note that the relevant quantity is the velocity variation because of the Galileian invariance of the Navier–Stokes equations.

experimental measurements [68, 69]. Assuming a full self-similar behaviour (according to the Kolmogorov scenario) one would expect $\zeta_p = p/3$. However, experiments and numerical simulations show consistent deviations from such prediction (except for $p = 3$, i.e. Eq. (5.5)) meaning that corrections to the self-similar Kolmogorov picture due to intermittency shall be present [68]. Nevertheless, the prediction for the energy spectrum (5.3) remains accurate despite intermittency. Indeed, the scaling of the energy spectrum is related to the exponent of the second order structure function ζ_2, whose deviation from the Kolmogorov prediction ($\zeta_2 = 2/3$) due to intermittency is small.

5.2 Turbulence in quantum fluids

Since a superfluid is characterized by the absence of viscous dissipation, the classical picture sketched in the previous section should not apply directly. Nevertheless, different regimes of turbulent flows have been observed in superfluids, which together constitute the research branch known as quantum turbulence (intended as the study and the characterization of turbulence in quantum fluids) [17].

We are particularly concerned with superfluid turbulence at very low temperature, when the effect of the thermal fluctuations can be neglected. This is the setting studied in the publication [76], presented later in this chapter. In this extreme case, vortex filaments organized in a complex tangle are the main actors of the turbulent motions and the typical picture of quantum turbulence still involves an energy cascade process from large to small scales. At scales much larger than the typical inter-vortex distance ℓ_v, the discrete nature of the quantum vortex filaments is irrelevant. The total vortex line density can be splitted in a part composed of metastable bundles of polarized vortices and another made of randomly oriented filaments [10]. The bundles move in a way reminiscent of the motion of the large-scale eddies in classical turbulent flows [158]. The non-linear interactions between them generates smaller structures, in a cascade fashion compatible with the Kolmogorov picture. Indeed, the (incompressible) energy spectrum has been found to be consistent with Eq. (5.3), both in numerical simulations [10, 164, 213] and in experiments with superfluid helium [149, 201]. Once the scale of the inter-vortex distance is reached, the isolated filaments become distinguishable and their quantum origin starts to play a key role in the redistribution of the energy. In particular, vortices undergo fast and spatially localized reconnection events, which are followed by the emission of a sound pulse [230]. Moreover, reconnections trigger the propagation of polychromatic Kelvin waves along the filaments. The non-linear interactions between Kelvin waves excite modes of larger and larger wavenumbers, building another cascade of energy down to the scale of the vortex core ξ [136, 228, 233]. Here, at the the bottom of the Kelvin wave cascade, the kinetic energy of the filaments is eventually radiated away in the form of sound waves (see sections 1.4.4 and 1.4.5 of this manuscript and references therein for details on reconnections and Kelvin waves). Therefore, unless the turbulence is sustained by a continuous forcing mechanism at large scales, the vortex line density L_v decays in time until all the energy has been converted into sound. A decay law $L_v \sim t^{-3/2}$ has been observed for the

vortex line density [84, 239], which has been argued to be consistent with a classical Kolmogorov picture [216].

However, another kind of decaying superfluid turbulence may exist, whose signature is indeed a less steep scaling law for the vortex line density decay: $L_v \sim t^{-1}$. This regime is sometimes called "ultraquantum" turbulence in order to distinguish it from the semiclassical quantum turbulence and consists in a random vortex tangle, with the inter-vortex distance ℓ_v as single dominant scale [17]. It has been produced experimentally injecting negative ions in superfluid helium below $T = 0.5\,K$ [239]. Also numerical measurements are consistent with the outlined picture, both in simulations of the vortex filament model [9] and in the Gross–Pitaevskii framework [228]. The vortex line density decay of ultraquantum turbulence can be explained by a phenomenological argument due to Vinen (originally formulated in the context of counterflow turbulence) [237], so that such regime is also known simply as Vinen turbulence.

For completeness, we mention one last cathegory of superfluid turbulence, which arises when the temperature is high enough to have a relevant density of normal fluid, besides the inviscid superfluid component. This regime can be achieved in ^{4}He below the lambda point for instance by a standard mechanical forcing (e.g. towed grids [218]). It is definitely the most complex kind of quantum turbulence, since both the two fluid components can be turbulent. In the superfluid component, turbulence has the features just outlined above due to the quantum constraints on the vorticity, while in the normal component it develops as a standard classical (viscous) turbulence. What adds complexity is that the two fluids can interact by means of the mutual friction between the thermal excitations of the normal fluid and the quantum vortices in the inviscid superfluid. This constitutes a new channel for the energy transfer, so that each of the two fluids acts both as forcing and dissipation for the other [17]. Moreover, at finite temperature a counterflow regime can be established, in which the velocity field of the two components is different. We refer to section 1.1 and references therein for a brief description of the phenomenon. Some of the phenomenology associated to this regime has also been mentioned in section 2.1. It is particularly interesting because the emergence of a turbulent superfluid vortex tangle in the superfluid component is easily triggered, and depending on a tunable parameter (the heat flux applied to the system), the normal fluid can be set as just laminar, rather than turbulent as well. Note that in the publication shown below we are not concerned with these finite temperature effects. Indeed, we study a quantum turbulence regime modeled with the GP equation, which is suitable to describe a very low temperature superfluid system.

5.3 *Publication*: Active and finite-size particles in decaying quantum turbulence at low temperature

In the article reported below we consider the decay of a quantum turbulence regime at very low temperature. Particles are immersed in the superfluid, modeled as usual with the Gross–Pitaevskii equation coupled with repulsive potentials (see section 2.3.3). The degree of complexity of the system studied here is much higher than in the

works discussed in the previous chapters. A (relatively) large number of particles is considered and all the phenomena studied previously in a controlled manner (capture mechanism, dynamics of trapped objects, reconnections) are present and contribute to the evolution of the system.

The first part of the publication is dedicated to the characterization of the average properties of the flow. The time evolution of the energy components and of the incompressible dissipation rate are confronted in the case of different particles species. Fortunately no important differences are detected. This means that, although active, particles do not prevent the development and the decay of the quantum vortex tangle and thus they are good candidates to be used as probes for the superflow properties. Also the evolution of the inter-vortex distance and the incompressible energy spectrum are the same with and without particles, and the emergence of a Kolmogorov regime at large scales is confirmed.

Three-dimensional visualizations of the flow show that helicoidal excitations on the filaments develop earlier if particles are present (as a consequence of the trapping process). Although this affects the details of the vortex configurations when the turbulent stage is achieved, the statistical features of the flow remain unchanged.

In a second part of the paper, the actual motion of the particles is investigated. An important measurement is the evolution of the fraction of particles trapped inside the vortices. Almost the totality of the particles is found to be pierced by the filaments during the turbulent regime and even later, when the vortex line density decays. Moreover, each particle spends long times inside a vortex, with just occasional episodes of detachment and fast recapture. We note that in current superfluid helium experiment with solidified hydrogen particles (see section 2.1.3) there is not a clear measurement of the fraction of particles trapped and whether this number remains constant.

Our observations suggest that (at least for large scales) particles can behave as tracers of the vortex motions, which is confirmed by a measurement of the particle velocity power spectrum. Indeed, at slow frequencies the velocity spectrum is consistent with a classical Lagrangian picture [248], meaning that particles are effectively able to sample the Kolmogorov turbulence behaviour of a vortex tangle. At small scales, we recover a signature of the Magnus precession due to the particle-vortex interaction, already detected in [79] (see chapter 4). The particle natural frequency is observed as a peak in the velocity power spectrum and it also identifies the time scale at which the particle acceleration decorrelates.

Finally, we explore the particle velocity and the acceleration statistics. In experiments, power law tails in the probability distributions have been observed more than once [137, 197]. However, in our numerical experiment only Gaussian distributions are detected. We remark that the origin of the power law behaviour has a two-fold explanation. From the one hand, given that at scales smaller than the inter-vortex distance the relevant parameter is the quantum of circulation Γ, the time scaling of the vortex velocities is $v \sim (\Gamma/t)$, consistently with the reconnection dynamics. On the other hand, the velocity field of each filament scales in space as $v \sim \Gamma/2\pi r$ (1.132). Both these considerations lead to a velocity probability distribution $\mathbb{P}[v] \sim v^{-3}$ [170], but at zero temperature only the first one could be sampled by the (trapped) particles. Indeed, in order to be

sensitive to the superfluid velocity field (and not just the vortex one), the particles must be driven by Stokes drag, which is possible only if a normal component is present and locked with the superflow. This argument could explain the absence of power law tails in our simulations, although the lack of sufficient statistics is also a possible cause.

As a final note, we mention that deviations from Gaussian statistics are unexpectedly detected in our simulations as numerical artifacts if the interpolation method used for the force exerted by the superfluid on the particles does not have spectral accuracy (see the section A.4.3 of the Appendix to the present manuscript for further details on the interpolation methods).

Active and finite-size particles in decaying quantum turbulence at low temperature

Umberto Giuriato* and Giorgio Krstulovic
Université Côte d'Azur, Observatoire de la Côte d'Azur, CNRS, Laboratoire Lagrange, Nice, France

(Received 26 February 2020; accepted 21 April 2020; published 29 May 2020)

The evolution of a turbulent tangle of quantum vortices in the presence of finite-size active particles is studied by means of numerical simulations of the Gross-Pitaevskii equation. Particles are modeled as potentials depleting the superfluid and described with classical degrees of freedom following a Newtonian dynamics. It is shown that particles do not modify the building-up and the decay of the superfluid Kolmogorov turbulent regime. It is observed that almost the totality of particles remains trapped inside quantum vortices, although they are occasionally detached and recaptured. The statistics of this process is presented and discussed. The particle Lagrangian dynamics is also studied. At large timescales, the velocity spectrum of particles is reminiscent of a classical Lagrangian turbulent behavior. At timescales faster than the turnover time associated with the mean intervortex distance, the particle motion is dominated by oscillations due to the Magnus effect. For light particles, a nonclassical scaling of the spectrum arises. The particle velocity and acceleration probability distribution functions are then studied. The decorrelation time of the particle acceleration is found to be shorter than in classical fluids, and related to the Magnus force experienced by the trapped particles.

DOI: 10.1103/PhysRevFluids.5.054608

I. INTRODUCTION

When a fluid is stirred, energy is injected into the system exciting structures at different scales. In particular, in three-dimensional classical flows, the energy supplied at large scales is transferred toward small scales in a cascade process. Eventually, it reaches the smallest scales of the system, where dissipation acts efficiently. In the presence of a very large separation between the injection and dissipation scale, this cascade scenario proposed by Richardson leads to a fully developed turbulent state that can be described by the Kolmogorov phenomenology [1]. Kolmogorov turbulence is expected to be universal, and it is in fact commonly observed in nature, industrial applications, and in more exotic flows such as superfluids.

A superfluid is a peculiar flow, whose origin is a consequence of quantum mechanics. At finite temperature, a superfluid is considered to be a mixture of two components: the normal fluid, which can be described by the Navier-Stokes equations, and the superfluid component with zero viscosity [2]. At very low temperatures, the normal component can be neglected and the fluid becomes completely inviscid. As a consequence, an object moving at low velocities does not experience any drag from the fluid. However, when the object exceeds a critical velocity, quantum vortices are

*Corresponding author: umberto.giuriato@oca.eu

Published by the American Physical Society under the terms of the Creative Commons Attribution 4.0 International license. Further distribution of this work must maintain attribution to the author(s) and the published article's title, journal citation, and DOI.

nucleated [3,4]. Quantum vortices (or superfluid vortices) are the most fundamental hydrodynamical excitations of a superfluid. They are topological defects (and nodal lines) of the macroscopic wave function describing the system, and as a consequence their circulation is quantized. In superfluid helium, the core size of quantum vortices is of the order of 1 Å. Despite the lack of viscosity, quantum vortices can reconnect and change their topology (see, for instance, [5–8]), unlike classical (prefect) fluids.

When energy is injected in a low-temperature superfluid at scales much larger than the mean intervortex distance ℓ, a classical Kolmogorov regime is expected. Such a behavior has been observed numerically [9–11] and experimentally [12,13]. Indeed, at such scales the quantum nature of vortices is not important and the superfluid behaves like a classical fluid. At the scales of the order of ℓ and smaller, the isolated nature of quantized vortices becomes relevant. The system keeps transferring energy toward small scales but through different nonclassical mechanisms [14]. An example of such mechanisms is the turbulent Kelvin wave cascade. Kelvin waves are helical oscillations propagating along quantum vortices, and the energy can be carried toward small scales thanks to nonlinear wave interactions. This energy cascade has been successfully described in the framework of weak-wave turbulence theory [15,16]. The resulting theoretical predictions have been observed numerically in vortex-filament and Gross-Pitaevskii numerical simulations [17–19].

Flow visualization is certainly a fundamental issue in every fluid dynamics experiment. Among the techniques that have been developed to sample a fluid, particle image velocimetry (PIV) and particle tracking velocimetry (PTV) are two of the most common methods [20]. The use of particles as probes has also been adapted to the study of cryogenic flows, in particular in superfluid helium ^{4}He experiments [21], where micrometer-sized hydrogen and deuterium particles have been used. For instance, hydrogen ice particles have been successfully employed to visualize isolated or reconnecting vortex lines [22], as well as the propagation of Kelvin waves [23]. Moreover, the observation of power-law tails in the probability density of the particle velocity is an important difference with respect to classical turbulent states [24–26]. Similar deviations from classical behaviors have recently been reported also for the acceleration statistics [26,27]. Particles in such experiments typically have a size that can rise up to several microns, which is many orders of magnitude larger than the size of the vortex core in superfluid helium. For instance, the solidified hydrogen particles produced in the experiments [22,23] are slightly smaller than 2.7 μm, while in [25,26] their size is between 5 and 10 μm. Although it has been seen that particles unveil the dynamics of quantum vortices, it is not yet clear how much they affect the dynamics of quantum turbulent flows.

Several theoretical efforts have been made in the past decade in order to clarify what is the dynamics of particles in a superfluid and how particles interact with quantum vortices. For example, the vortex-filament (VF) method can be coupled with the classical hydrodynamical equations of a sphere, allowing us to study different specific problems. The interaction between one particle and one vortex has been addressed [28,29], as well the backreaction of tracers in a thermal counterflow [30,31]. In the context of finite-temperature superfluids, the spatial statistics of particles have been recently addressed in simulations of the Hall-Vinen-Bekarevich-Khalatnikov (HVBK) model [32].

Finally, since the work of Winiecki and Adams [4], particles described by classical degrees of freedom have been implemented self-consistently in the framework of the Gross-Pitaevskii (GP) equation [33–37]. Although the GP model is formally derived for dilute Bose-Einstein condensates, it is considered a general tool for the study of superfluid dynamics at very low temperature. Indeed, unlike the VF method or the HVBK model, it naturally contains quantum vortices as topological defects of the order parameter. It was found analytically and confirmed numerically that the GP model can reproduce the process of trapping of large active inertial particles by straight vortex lines [34], in accordance with hydrodynamical calculations [28,29]. In this framework, the interplay between many trapped particles and Kelvin waves has also been investigated [36].

In the present work, we study the influence of particles on quantum turbulent flows at very low temperature by using the GP model coupled with classical particles. In particular, we study the evolution of a free decaying superfluid turbulent vortex tangle loaded with finite-size active

particles. We consider spherical particles of different masses and having a diameter up to 20 core sizes. Such a size is about 1000 times smaller than that of solidified particles used in superfluid helium experiments. Nevertheless, it is slightly smaller than or comparable to the mean intervortex distance in our simulations, similar to current experiments. We also study the different regimes of the turbulent evolution from the Lagrangian point of view. The paper is organized as follows. In Sec. II we describe the Gross-Pitaevskii model coupled with classical particles. We also review the standard properties of the model and give the basic definitions used later to analyze the flow. We also describe the numerical method used in this work. Then, in Sec. III, we present our main results. In particular, in Sec. III A we address whether the presence of particles affects the scales of the flow at which Kolmogorov turbulence takes place. Section III B is devoted to a study of the particle dynamics inside the vortex tangle, their trapping by vortices, and their dynamics at scales larger and smaller than the intervortex distance. Particle velocity and acceleration statistics are then presented in Sec. III C. Finally, Sec. IV contains our conclusions.

II. MODEL FOR PARTICLES IN A LOW-TEMPERATURE SUPERFLUID

A. Gross-Pitaevskii equation coupled with particles

We describe a superfluid of volume V at low temperature by using the complex field ψ, which obeys the GP dynamics. We consider N_p particles in the system. Each particle is characterized by the position of its center of mass $\mathbf{q}_i$ and its classical momentum $\mathbf{p}_i$. The presence of a particle of size a_p generates a superfluid depletion in a spherical region of radius a_p. This effect is reproduced by coupling the superfluid field with a strong localized potential V_p, which has a fixed shape and is centered at the position $\mathbf{q}_j(t)$.

All the particles considered have the same size, as well as the same mass M_p. The Hamiltonian of the system is given by

$$H = \int \left(\frac{\hbar^2}{2m}|\nabla\psi|^2 + \frac{g}{2}\left(|\psi|^2 - \frac{\mu}{g}\right)^2 + \sum_{i=1}^{N_\mathrm{p}} V_\mathrm{p}(|\mathbf{x}-\mathbf{q}_i|)|\psi|^2 \right) d\mathbf{x} + \sum_{i=1}^{N_\mathrm{p}} \frac{\mathbf{p}_i^2}{2M_\mathrm{p}}, + \sum_{i<j}^{N_\mathrm{p}} V_\mathrm{rep}^{ij}, \quad (1)$$

where m is the mass of the bosons constituting the superfluid, and g is the nonlinear coupling constant between the bosons, related to the s-wave scattering length a_s so that $g = 4\pi a_\mathrm{s}\hbar^2/m$. The chemical potential is denoted by μ. The particle interaction potential V_rep^{ij} is responsible for short-range repulsion between particles, so that they behave as hard spheres and do not overlap. A detailed discussion on the inclusion of this short-range repulsion and the effect on the particle collisions in the model (1) can be found in [33]. The equations of motion that govern the superfluid field and the particle positions are obtained varying the Hamiltonian (1):

$$i\hbar\frac{\partial\psi}{\partial t} = -\frac{\hbar^2}{2m}\nabla^2\psi + (g|\psi|^2 - \mu)\psi + \sum_{i=1}^{N_\mathrm{p}} V_\mathrm{p}(|\mathbf{x}-\mathbf{q}_i|)\psi, \quad (2)$$

$$M_\mathrm{p}\ddot{\mathbf{q}}_i = -\int V_\mathrm{p}(|\mathbf{x}-\mathbf{q}_i|)\nabla|\psi|^2\, d\mathbf{x} + \sum_{j\neq i}^{N_\mathrm{p}} \frac{\partial}{\partial\mathbf{q}_i} V_\mathrm{rep}^{ij}. \quad (3)$$

This model has been successfully used to study vortex nucleation [4], trapping of particles by quantum vortices [34], and the interaction between particles trapped inside quantum vortices and Kelvin waves [36]. We denote by GP the Gross-Pitaevskii model without particles, and by GP-P the full coupled system (2) and (3).

In the case in which particles are absent, the chemical potential μ fixes the value of the ground state of the system $\psi_\infty = \sqrt{\rho_\infty/m} = \sqrt{\mu/g}$. Large-wavelength perturbations around this state are sound waves that propagate with the speed of sound $c = \sqrt{g\rho_\infty/m^2}$, while they become dispersive at length scales smaller than the healing length $\xi = \sqrt{\hbar^2/2g\rho_\infty}$.

The GP model describes a superfluid with zero viscosity. Using the Madelung transformation $\psi(\mathbf{x}) = \sqrt{\rho(\mathbf{x})/m}\, e^{i\frac{m}{\hbar}\phi(\mathbf{x})}$, the GP equation (2) is mapped into the continuity and Bernoulli equations of a superfluid of density ρ and velocity $\mathbf{v}_s = \nabla\phi$. A superfluid flow is potential, but the phase is not defined at the nodal lines of $\psi(\mathbf{x})$. Therefore, the vorticity is concentrated along these filaments, which are the topological defects usually called quantum vortices. The effective size of the quantum vortex core coincides with the healing length ξ, and the contour integral of the superfluid velocity around a single vortex filament is the Feynman-Onsager quantum of circulation $\kappa = h/m = 2\pi\sqrt{2}c\xi$.

Using the Madelung transformation and the Helmholtz decomposition, the kinetic term of the superfluid energy density is decomposed into incompressible, compressible, and quantum energy [9]:

$$E_{\rm kin}^{\rm GP} = \frac{\hbar^2}{2mV}\int |\nabla\psi|^2\,{\rm d}\mathbf{x} = E_{\rm kin}^{\rm I} + E_{\rm kin}^{\rm C} + E^{\rm Q}$$
$$= \frac{1}{2V}\int\left([(\sqrt{\rho}\mathbf{v}_s)^{\rm I}]^2 + [(\sqrt{\rho}\mathbf{v}_s)^{\rm C}]^2 + \frac{\kappa^2}{4\pi^2}[\nabla\sqrt{\rho}]^2\right){\rm d}\mathbf{x}, \tag{4}$$

where $(\sqrt{\rho}\mathbf{v}_s)^{\rm I} = \mathcal{P}_{\rm I}[\sqrt{\rho}\mathbf{v}_s]$ and $(\sqrt{\rho}\mathbf{v}_s)^{\rm C} = \mathbf{v}_s - (\sqrt{\rho}\mathbf{v}_s)^{\rm I}$, the operator $\mathcal{P}_{\rm I}[\cdot]$ being the projector onto the space of divergence-free fields. The other energies of the superfluid are the internal energy $E_{\rm int} = (2V)^{-1}\int g(\rho/m - \mu/g)^2\,d\mathbf{x}$, where the energy of the ground state is subtracted, and the interaction energy with the particles $E_{\rm P}^{\rm GP} = V^{-1}\int\sum_i^{N_{\rm p}} V_{\rm p}(|\mathbf{x}-\mathbf{q}_i|)\rho\,d\mathbf{x}$, so that the total energy is given by $E_{\rm tot} = E_{\rm kin}^{\rm GP} + E_{\rm int} + E_{\rm P}^{\rm GP}$. From these definitions follow the corresponding energy spectra defined in terms of the Fourier transform of the fields [9].

B. Numerical methods and parameters

In the simulations presented in this work, we solve the system (2) and (3) in a cubic periodic box of side $L = 341\xi$ with $N_{\rm c} = 512^3$ collocation points by using a standard pseudospectral method. We use a fourth-order Runge-Kutta scheme for the time-stepping and the standard 2/3 rule for the dealiasing. In numerics, we fix $c = 1$ and $\psi_\infty = 1$.

To produce a homogeneous and isotropic tangle of quantized vortex lines, we impose an initial Arnold-Beltrami-Childress (ABC) flow, following the procedure described in [38]. In particular, we use a superposition of $k = 1\times 2\pi/L$ and $k = 2\times 2\pi/L$ basic ABC flows: $\mathbf{v}_{\rm ABC} = \mathbf{v}_{\rm ABC}^{(1)} + \mathbf{v}_{\rm ABC}^{(2)}$, with

$$\mathbf{v}_{\rm ABC}^{(k)} = [B\cos(ky) + C\sin(kz)]\hat{x} + [C\cos(kz) + A\sin(kx)]\hat{y} + [A\cos(kx) + B\sin(ky)]\hat{z}, \tag{5}$$

and the parameters $A = 0.5196$, $B = 0.5774$, and $C = 0.6351$. The basic ABC flow is a stationary (periodic) solution of the Euler equation with maximal helicity. The resulting wave function contains a tangle whose nodal lines follow the ABC vortex lines. The initial mean intervortex distance is $\ell(t=0) \sim 25\xi$. As the flow is prepared by minimizing the energy, most of the energy of the system is in the incompressible part of the energy and resulting from the vortex configuration.

The ground state for the particles consists in a number of particles (we use $N_{\rm p} = 200$ and 80) of the same size and mass, randomly distributed in the computational box. Particles are initially at rest. This state is prepared using the imaginary-time evolution of Eq. (2). Then, the initial condition for the simulations is obtained by multiplying the wave function associated with the ABC flow and the wave function associated with the particle ground state. An example of an initial field containing particles is displayed in Fig. 1(d).

Because of the presence of a healing layer, the particle boundary is never sharp, independently of the functional form of the potential $V_{\rm p}$. The superfluid field vanishes in the region where $V_{\rm p} > \mu$, and at the particle boundary the fluid density passes from zero to the bulk value ρ_∞ in approximately one healing length. The potential used to model each particle is a smoothed hat-function $V_{\rm p}(r) = \frac{V_0}{2}(1 - \tanh[\frac{r^2-\zeta^2}{4\Delta_a^2}])$, where the parameters ζ and Δ_a are set to model the

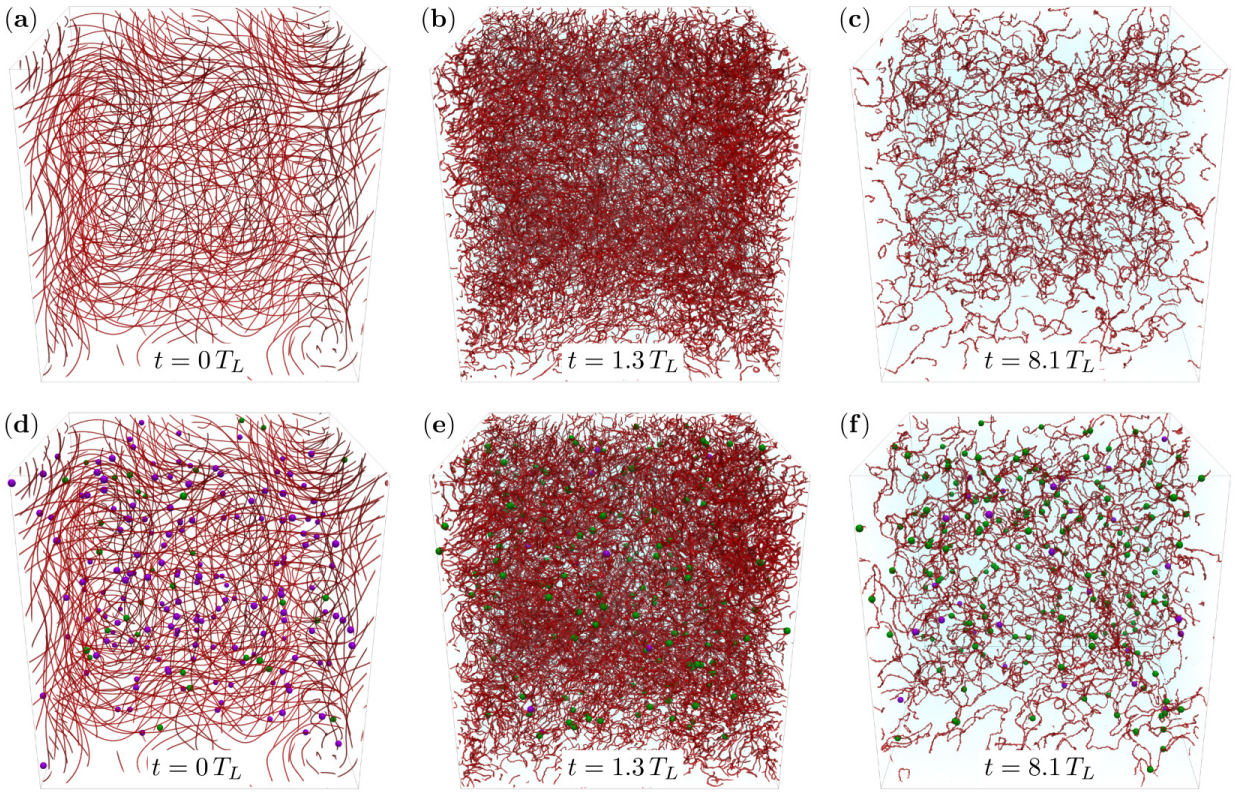


FIG. 1. Visualizations of the superfluid vortex tangle. Vortices are represented as isosurfaces in red of the density field ($\rho = 0.15\rho_\infty$), sound is rendered in blue, trapped particles in green, and free particles in purple. The upper row is without particles, the lower row is with 200 neutrally buoyant particles of radius $a_\mathrm{p} = 4\xi$. (a,d) The ABC initial states. (b,e) The most turbulent regime ($t = 1.3T_L$). (c,f) A late time ($t = 8.1T_L$). T_L denotes the large-eddy-turnover time (see the text).

particle. Their values are listed in Table I. In particular, ζ fixes the width of the potential and it is related to the particle size, while Δ_a controls the steepness of the smoothed hat-function. The latter needs to be adjusted in order to avoid the Gibbs effect in the Fourier transform of V_p. Since the particle boundaries are not sharp, the effective particle radius is defined as $a_\mathrm{p} = (3M_0/4\pi\rho_\infty)^{\frac{1}{3}}$, where $M_0 = \rho_\infty L^3(1 - \int |\psi_\mathrm{p}|^2\, d\mathbf{x}/\int |\psi_\infty|^2\, d\mathbf{x})$ is the fluid mass displaced by the particle and ψ_p is the steady state with just one particle. Practically, given the set of numerical parameters ζ and Δ_a, the state ψ_p is obtained numerically with imaginary-time evolution and the excluded mass M_0 is measured directly. Particles attract each other by a short-range fluid mediated interaction

TABLE I. Simulation parameters.

Run	N_p	a_p	$\mathcal{M}$	ζ	Δ_a	V_0/μ	γ/μ
I	0						
II	200	4.0ξ	0.125	1.5ξ	1.2ξ	20.0	1.4×10^{-4}
III	200	4.0ξ	0.25	1.5ξ	1.2ξ	20.0	1.4×10^{-4}
IV	200	4.0ξ	1.0	1.5ξ	1.2ξ	20.0	1.4×10^{-4}
V	200	4.0ξ	2.0	1.5ξ	1.2ξ	20.0	1.4×10^{-4}
VI	80	10.0ξ	1.0	8.0ξ	2.0ξ	20.0	5.8×10^{-4}
VII	200	10.0ξ	0.125	8.0ξ	2.0ξ	20.0	5.8×10^{-4}
VIII	200	10.0ξ	0.25	8.0ξ	2.0ξ	20.0	5.8×10^{-4}
IX	200	10.0ξ	1.0	8.0ξ	2.0ξ	20.0	5.8×10^{-4}

[33,35], thus we use the repulsive potential $V_{\rm rep}^{ij} = \gamma(2a_{\rm p}/|\mathbf{q}_i - \mathbf{q}_j|)^{12}$ in order to avoid an overlap between them. The functional form of $V_{\rm rep}^{ij}$ is inspired by the repulsive term of the Lennard-Jones potential, and the prefactor γ is adjusted numerically so that the interparticle distance $2a_{\rm p}$ minimizes the sum of $V_{\rm rep}^{ij}$ with the fluid-mediated attractive potential [33,35]. We express the particle mass as $M_{\rm p} = \mathcal{M}M_0$, where M_0 is the mass of the superfluid displaced by the particle. Namely, heavy particles have $\mathcal{M} > 1$ and light particles have $\mathcal{M} < 1$. In Table I all the parameters for the particles used in the simulations presented in this work are reported. In the following, we will refer to each simulation specifying the size and the mass of the particles used.

Note that although the model (1) is a minimal model for implementing particles in the GP framework, we cannot add to the system an arbitrary number of particles. Indeed, since particles have a finite size, they occupy a volume at the expense of the superfluid field, and packing effects could become important if the filling fraction is too high. Moreover, the potential $V_{\rm p}$ must be updated at each time step, which is numerically costly. Finally, note that the the evaluation of the force term (3) acting on particles requires us to know the value of the fields at intermesh points. When the number of particles in the simulation is not large, the force $\mathbf{f}_i^{\rm GP}(\mathbf{q}_i) = -(V_{\rm p} * \boldsymbol{\nabla}\rho)[\mathbf{q}_i]$ (3) can be computed with spectral accuracy using a Fourier interpolation. Such a method has been used in [34–36], where the particle dynamics is extremely sensitive. In this work, the use of a Fourier interpolation for each particle is numerically unaffordable, due to the large number of particles involved and the resolutions used. Instead, we use a fourth-order B-spline interpolation method, which has been shown to be highly accurate with a reduced computational cost [39] and particularly well adapted for pseudospectral codes. Indeed, the use of a Fourier interpolation to evaluate the three-dimensional force for $N_{\rm p}$ particles requires $\sim 3N_{\rm p}N_{\rm c}$ operations and evaluations of complex exponentials ($N_{\rm c} = 512^3$ in the present work). Such a cost quickly becomes too expensive at high resolutions and/or a large number of particles. On the contrary, B-spline interpolation requires just one fast Fourier transform of a field per component, and an interpolation using only four neighboring grid points per dimension [39]. Such a scheme saves a factor $\sim N_{\rm p}$ of computational cost compared to Fourier interpolation. Note that in the previous discussion, we have not taken into consideration parallelization issues, where local schemes (B-splines) are much more advantageous than global ones (Fourier transforms). Nevertheless, some issues with physical quantities at small scales arising from the B-spline interpolation are discussed in the Appendix.

III. PARTICLES IMMERSED IN A TANGLE OF SUPERFLUID VORTICES

Superfluid turbulence in the context of the GP model has been studied extensively [9,11,38,40,41]. In general, quantum turbulence develops from an initial state with a vortex configuration where the incompressible kinetic energy is mainly contained at large scale. During the evolution, vortex lines move, interact among themselves, and reconnect, creating complex vortex tangles. Through this process, sound is produced and incompressible kinetic energy is irreversibly converted into quantum, internal, and compressible kinetic energy. Eventually, the compressible energy produced in the form of acoustic fluctuations starts to dominate, thermalizes, and acts as a thermal bath providing an effective dissipation acting on the vortices. As a consequence, vortices shrink and eventually disappear through mutual friction effects following Vinen's decay law [19,42]. In particular, it has been shown that the decrease of the incompressible kinetic energy behaves in a similar manner to decaying classical turbulence [9]. To make a connection with decaying classical Kolmogorov turbulence, the incompressible energy dissipation or dissipation rate is usually defined in the context of GP turbulence as

$$\epsilon = -\frac{dE_{\rm kin}^{\rm I}}{dt}. \tag{6}$$

As in decaying Navier-Stokes turbulence, in GP the most turbulent stage is achieved around the time when this quantity is maximal. About this time, the classical picture holds and the incompressible

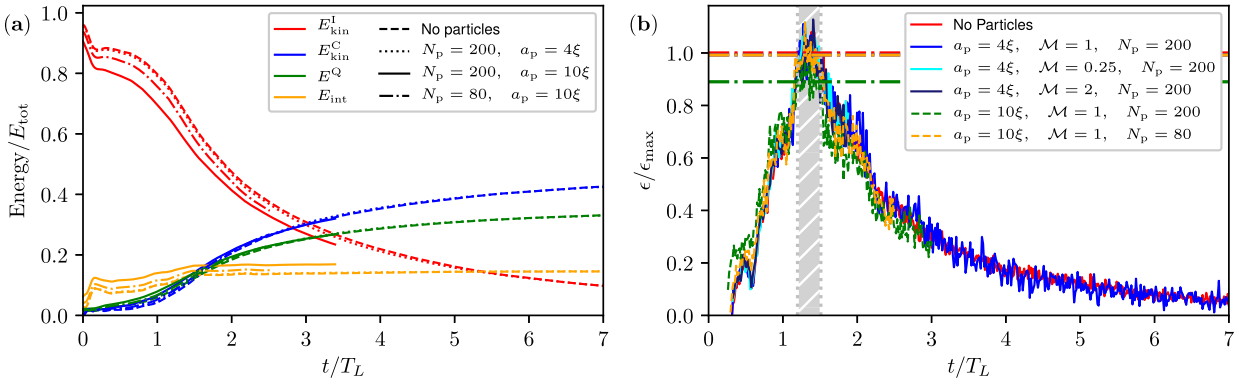


FIG. 2. (a) Time evolution of the superfluid energy components in the cases with no particles (dashed line), 200 small particles (dotted line), 200 large particles (solid line), and 80 large particles (dash-dotted line). (b) Incompressible energy dissipation rate for different numbers of particles with different sizes and different masses (solid lines). Dash-dotted horizontal lines of the corresponding colors indicate the value of the maximum of dissipation, obtained averaging over the shaded region. The dissipation is expressed in units of its maximum $\epsilon_{\rm max}$ in the case without particles.

energy spectrum satisfies the Kolmogorov prediction

$$E^{\rm I}_{\rm kin} = C\epsilon^{2/3}k^{-5/3},$$

where C is the Kolmogorov constant, the value of which has been found to be close to 1 in GP turbulence [11,38,41].

The first purpose of this work is to check whether and to what extent the presence of particles in the system modifies Kolmogorov turbulence. We add to the ABC initial condition a number of randomly distributed particles and let the system evolve under the dynamics (2) and (3). In Figs. 1(a), 1(b) and 1(c), the three stages of the evolution (initial condition, turbulent vortex tangle, and residual filaments in a bath of sound, respectively) are visualized in the case of 200 neutrally buoyant particles of radius 4ξ. See the supplemental material [43] for movies of this simulation and others with particles of a different size. Trapped particles by vortices are displayed in green, whereas free ones are displayed in purple. The algorithm to distinguish a trapped particle from a free one is based on the circulation around it and it is discussed in Sec. III B.

In Fig. 1 we observe that the building up and decay of the turbulent tangle is not strongly modified by the presence of particles. Moreover, it can be noticed how during the first stages of the evolution of the system the majority of particles gets trapped into the vortices. At zero temperature, as there is no normal component in the flow, no drag is experienced by the particles and their motion is completely driven by the pressure gradients. As a consequence, they are attracted by quantum vortices [28,34,44]. During the turbulent regime, violent and strongly nonlinear events like reconnections dominate the vortex dynamics and the flow evolution. A fundamental question is whether and how much the hydrodynamical attraction between vortices and particles is sufficient to keep them attached to the filaments. Indeed, since quantum vortices are actually the main actors of turbulence in superfluid, if particles are really able to follow them in this regime, it is a good indication that they are suitable for use as probes.

In the following subsection, we will quantitatively study the effect of particles on quantum turbulent flows. We will first focus on the large scales of the flow, where Kolmogorov turbulence takes place. Then the particle dynamics and their statistics will be addressed.

A. The effect of particles on Kolmogorov superfluid turbulence

We shall start our analysis by comparing the temporal evolution of global quantities. In Fig. 2(a) the time evolution of the different components of the energy is displayed. Times are expressed in

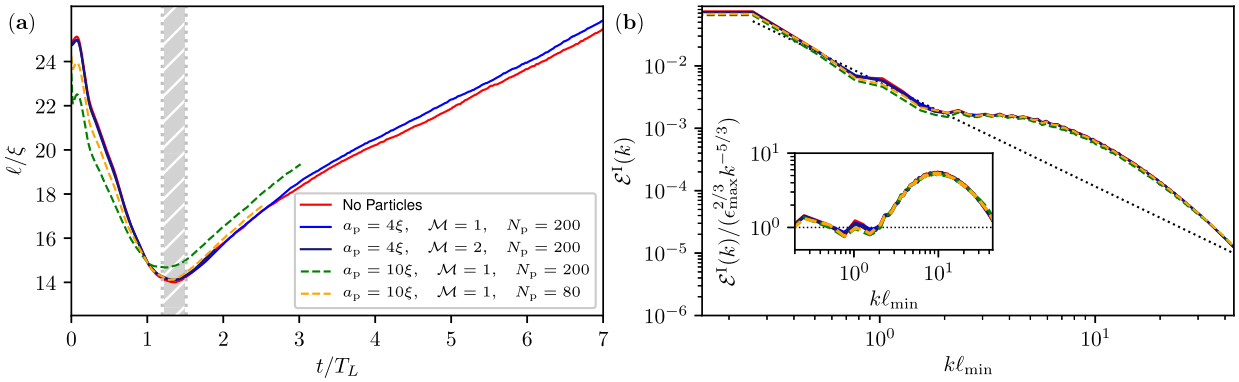


FIG. 3. (a) Time evolution of the mean intervortex distance for different numbers of particles of different sizes and different masses. (b) Incompressible energy spectrum for different numbers of particles of different sizes and different masses. Inset: Compensated incompressible energy spectrum. Solid lines refer to particles of size $a_p = 4\xi$, dashed lines refer to particles of size $a_p = 10\xi$. The dotted line is the classical scaling $\epsilon_{max} k^{-5/3}$. The spectrum is computed averaging over times in the shaded region.

units of the large-eddy-turnover time defined as $T_L = L/2v_{rms}$, where $v_{rms} = \sqrt{2E_{kin}^I(t=0)/3}$ is the root-mean-square velocity associated with the initial vortex tangle, and $L/2$ is its characteristic length scale. We compare the case in which no particles are present in the flow to the cases having particles of different sizes and of relative mass $\mathcal{M} = 1$. The net transfer of incompressible energy toward compressible, quantum, and internal energy is qualitatively unchanged in the various cases. The only difference is a slightly lower value of the incompressible energy in the case of large particles, in favor of the internal energy of the superfluid. Such an effect is more evident if the number of large particles is increased, and could be related to an increment of the filling fraction Φ, namely the fraction of the total volume occupied by the particles. In fact, for $N_p = 200$ particles of radius $a_p = 4\xi$ the filling fraction is $\Phi = 0.1\%$, for $N_p = 80$ particles of radius $a_p = 10\xi$ it is $\Phi = 0.8\%$, and for $N_p = 200$ particles of radius $a_p = 10\xi$ we have $\Phi = 2.1\%$. The kinetic and repulsion energies of the particles, as well as the particle-vortex interaction E_P^{GP}, are negligible compared with the other energies throughout the duration of the simulations (data not shown).

The dissipation rate of the incompressible kinetic energy is reported in Fig. 2(b) for particles of different masses and different sizes. The dissipation increases in the early stages when the energy begins to be transferred to the smaller scales, it reaches a maximum when all the scales are excited, and then it starts to decay since no forcing is sustaining the turbulence. We observe that the evolution of the dissipation is clearly not significantly modified by the presence of particles. In particular, the value of the maximum of dissipation, which is the signature of the most turbulent state reached by the tangle, is slightly lower only in the case in which many large particles are moving in the system. In particular for this case, it is about 90% of ϵ_{max}, the value measured in the case with no particles. The shaded region in Fig. 2(b) represents the most turbulent time of the simulations. We consider that in this short stage the system is in a quasisteady state, and we perform the temporal average of certain physical quantities in order to improve statistical convergence.

Another important quantity that is not affected much by the interplay between tangle and particles is the mean intervortex distance ℓ, whose time evolution is reported in Fig. 3(a). The mean intervortex distance is then estimated as $\ell = \sqrt{V/L_v}$, where L_v is the total vortex length in the system. This latter is estimated using the method introduced in [9], where L_v is shown to be related to the proportionality constant between the incompressible momentum density $J^I(k)$ of the flow and the spectrum of a two-dimensional point-vortex $J_{vort}^{2D}(k)$:

$$\frac{L_v}{2\pi} = \frac{\sum_k J^I(k)}{\int J_{vort}^{2D}(k)\, dk}. \tag{7}$$

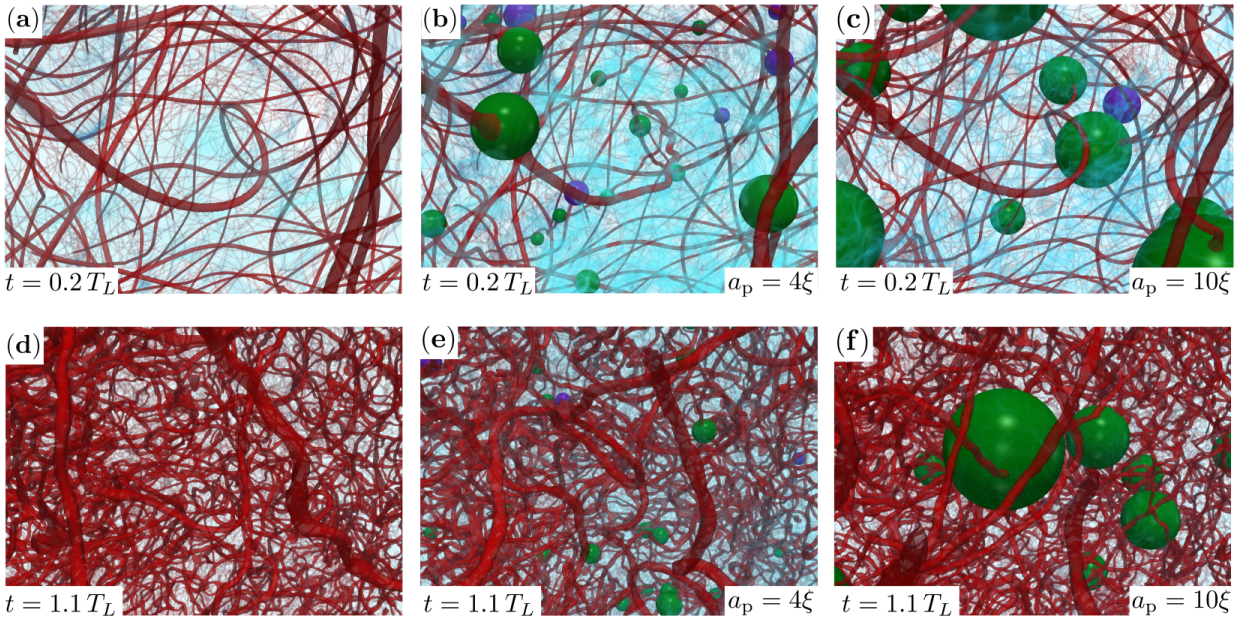


FIG. 4. Closeup of the superfluid vortex tangle at the early stage of the simulation (upper row: $t = 0.27T_L$) and during the turbulent regime (lower row: $t = 1.1T_L$) for the cases with no particles [left column (a),(d)], small particles [central column (b),(e): $a_p = 4\xi$], and large particles [right column (c),(f): $a_p = 10\xi$]. Vortices are represented as isosurfaces of the density field ($\rho = 0.15\rho_\infty$) and rendered in red, sound is rendered in blue, trapped particles in green, and free particles in purple.

The spectra of momentum densities are the angle average of the norm in Fourier space of the momentum density $\mathbf{J} = \rho\mathbf{v}_s$, and the incompressible part is obtained projecting onto the space of divergence-free fields. We have checked the validity of this formula by using the vortex filament tracking method described in [45] at some checkpoints.

In the turbulent regime, where the dissipation gets its maximum, the total length of the entangled vortices is also larger by a factor 4 compared to the initial condition, and the distance between the filaments is minimum. The value $\ell_{\rm min} \sim 14\xi$ of the intervortex distance in this regime will be used as a characteristic small length scale of the Kolmogorov turbulent regime. Such length is smaller than the diameter of the largest particles considered ($2a_p = 20\xi$), but nevertheless this has no appreciable repercussions on the behavior of the observables studied. Furthermore, as shown in Fig. 3(c), the scaling of the incompressible energy spectrum $\mathcal{E}^{\rm I}(k)$ averaged around the maximum of dissipation is unaltered by particles in the system. Figure 3(b) displays the incompressible energy spectrum. It is apparent that the scaling of the spectrum is always compatible with classical turbulence at scales larger than the intervortex distance, and the way in which the energy is accumulated at smaller scales is not modified by the particles. In the inset of Fig. 3(b), the spectrum is compensated by the Kolmogorov prediction $\mathcal{E}^{\rm I}(k) = C\epsilon_{\rm max}^{2/3}k^{-5/3}$ for classical hydrodynamic turbulence. The dotted horizontal black line shows that the value of the constant C in the Kolmogorov law is a number of order 1 for superfluid turbulence.

The only appreciable difference observed between the case with and without particles is that in the early stages of the evolution, the trapping of particles perturbs the vortex filaments and excites Kelvin waves. A comparison between the volume renderings can be seen in the upper row of Fig. 4. Such perturbations propagate during the evolution of the tangle. At the times when turbulence is developed, the details of the vortex configurations are completely different (see the lower row of Fig. 4). Nevertheless, the statistical properties of the system in this regime remain unchanged. We stress that the intervortex distance in quantum turbulence experiments lies typically in the range 10–100 μm, which is equal to or slightly larger than the particle size [24,25,27]. In this sense, the simulations presented here are compatible with the experimental parameters. They thus support

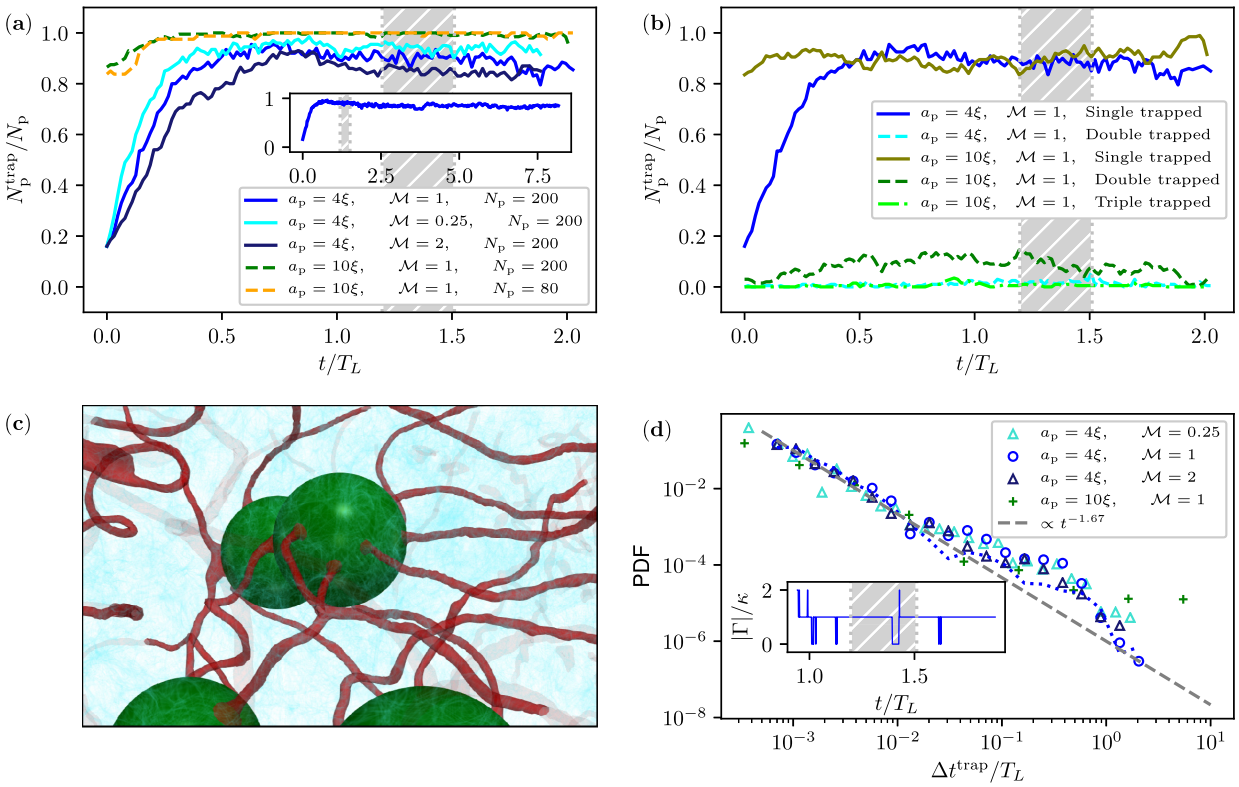


FIG. 5. (a) Fraction of trapped particles as a function of time for different numbers of particles of different sizes and different masses. Inset: The same for longer time in the case of 200 neutrally buoyant particles of size $a_p = 4\xi$. (b) Comparison between the fraction of multiply trapped particles as a function of time for neutrally buoyant particles. (c) Volume rendering of large particles ($a_p = 10\xi$) multiply trapped by quantum vortices. Vortices are rendered in red, sound in blue, particles in green. (d) Probability density function of the continuous time spent by particles inside vortices for different species of particles. The dotted blue line corresponds to the same simulation of blue circles (particles with size a_p and mass $\mathcal{M} = 1$) but averaged over the full simulation times). Inset: Absolute value of the circulation around a single particle of size $a_p = 4\xi$ and mass $\mathcal{M} = 1$ as a function of time. The PDF is computed averaging over times in the shaded region.

the belief that active particles have effectively no influence on the typical development and decay of quantum turbulence. This numerical fact helps to validate past and future experiments that use particles as probes of superfluids.

On the other hand, because of the lack of a Stokes drag in the system, particles cannot be treated as simple tracers of the superfluid velocity $\mathbf{v}_s$. Nevertheless, if they remain trapped inside the vortices they can track the evolution of the vortex filaments, which are the structures that effectively become turbulent. With the purpose of characterizing this scenario, in the next subsection we investigate the motion of particles once they are immersed in a tangle of quantum vortices.

B. Motion of particles in the superfluid vortex tangle

Looking at the time evolution of the vortex tangle (see Fig. 1 and movies in the supplemental material), the first thing that is apparent is how particles quickly get trapped into vortex filaments. This dynamics is expected and it has been studied in the case in which vortices move slowly [34]. It is a consequence of the pressure gradients. However, it is less obvious if such behavior remains dominant when turbulence take place and reconnections become frequent.

We study the evolution of particles and compute whether they are free or trapped by vortices. The temporal evolution of the fraction of trapped particles is displayed in Fig. 5(a) for all runs. This measurement is made by computing the circulation $\Gamma = \oint_{\mathcal{C}} \mathbf{v}_s \cdot d\mathbf{x}$ of the superfluid velocity $\mathbf{v}_s$

along contours $\mathcal{C}$ encircling each particle, and counting for which particles it is different from zero. Specifically, we compute the circulation along many parallel square contours of side $2(a_\mathrm{p} + \Delta_x)$ around each particle, where Δ_x is the grid spacing. If the circulation around at least one of these contours is different from zero, the particle is considered as trapped [46]. For practical reasons, due to the parallelization of the numerical code, we consider only contours perpendicular to the z axis of the computational box. As a consequence, the protocol is not able to grasp vortices that are crossing the particles exactly on a plane perpendicular to the z axis. This means that our estimation of the fraction of trapped particles is effectively a lower bound. However, it should be noticed that this pathological situation is an extremely rare situation that does not change the conclusions of our analysis.

In the initial condition the particles are placed randomly in the computational box. It happens then that some of them are already positioned inside a vortex. In the case of particles with a size comparable to the intervortex distance, the majority of particles are in this situation. In the first stages of the evolution of the flow, the number of trapped particles increases rapidly until it becomes stationary always at times much smaller than one T_L. The time needed to reach a stationary state depends slightly on the mass of the particles, as well as the fraction of trapped particles once a steady regime is reached. The steady value of $N_\mathrm{p}^\mathrm{trap}/N_\mathrm{p}$ is between 80% and 90% for small particles ($2a_\mathrm{p} < \ell$), while on average the totality of particles of size $2a_\mathrm{p} \sim \ell$ is found to be trapped by vortices, independently of the filling fraction. When the system reaches the most turbulent regime (indicated by the shaded region), the fraction of trapped particles does not undergo any appreciable changing. In the inset of Fig. 5(a), $N_\mathrm{p}^\mathrm{trap}/N_\mathrm{p}$ is also shown for late times in the case of small particles of relative mass $\mathcal{M} = 1$. It manifestly remains stable. This means that even when the density of vortex lines is decaying (along with the intensity of turbulence), the particles stay trapped inside vortices. Note that in this work we are dealing with homogeneous and isotropic decaying quantum turbulence at low temperature. We mention that the fraction of trapped particles measured in thermal counterflow simulated by means of the VF method is lower that the one observed here [31].

The circulation around each superfluid vortex filament is equal to a single quantum of circulation κ. As a consequence, measuring the circulation along a closed line $\mathcal{C}$ allows us to count the number of filaments in the region delimited by the line, provided that the quanta of circulation around every filament have the same sign. This is true also if the vortices are trapping particles, because their topological nature does not change. In Fig. 5(b) we show again the fraction of trapped particles, but now separating the number of particles trapped by multiple vortices. It turns out that at least the 5–10 % of the particles with size $2a_\mathrm{p} \sim \ell$ are always attached to at least two different filaments. Sometimes even more vortices pass simultaneously through the same particle, as can be visualized in the volume plot of Fig. 5(c).

Once a particle is trapped by a vortex, it can experience violent events, for instance during vortex reconnections. In such circumstances, such a particle could be detached and expelled from the vortex until it will eventually get trapped by another vortex of the tangle. We compute the probability density function (PDF) of the continuous time intervals Δt_trap spent by the particles inside the vortices regime. The PDFs for particles of different sizes and masses are displayed in Fig. 5(d). For all the species of particles examined, the probability distribution seems to follow roughly a power-law scaling in time $\sim(\Delta t_\mathrm{trap})^{-\alpha}$, with $\alpha \sim 1.67$. The PDF certainly vanishes much slower than an exponential decay at large Δt^trap, which would typically result from a standard escape problem over energy barriers. We checked that the intermittency of the circulation and the shape of the trapping time PDF are not characteristic of the most turbulent regime, since they persist also at the late times of the simulations [see the dotted blue line in Fig. 5(d)]. Therefore, many particles spend a time at least of the order of the simulation time ($\sim 10T_L$) inside a vortex filament, i.e., the typical escape time from the vortices is virtually infinite. This observation is exemplified in the inset of Fig. 5(d), where the evolution of the circulation around a single-small neutral particle is reported (the qualitative behavior is the same for the other particles). It is also clear that the time spent by the particles with zero circulation around them (namely free from vortices) is short. Since

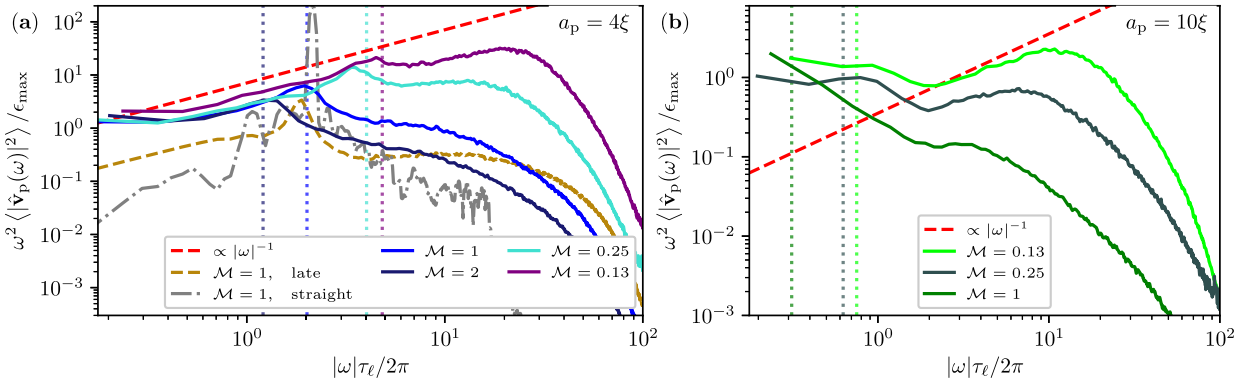


FIG. 6. Frequency spectrum of the particle velocity for particles of different masses and different sizes, compensated with the prediction for the Lagrangian spectrum in classical turbulence $\propto \epsilon/\omega^2$: (a) small particles with $a_p = 4\xi$; (b) large particles with $a_p = 10\xi$. The dash-dotted gray line is the frequency spectrum of a single small particle trapped in a straight vortex slightly perturbed. Dotted lines of corresponding colors are the prediction for the particle natural frequency Ω_p. The dashed red line is the scaling due to vortex reconnection or Kelvin waves $\propto |\omega|^{-1}$. The dashed golden line is the spectrum evaluated at late times in the simulation ($6T_L < \tau < 7T_L$).

we established that particles immersed in a tangle spend most of the time inside vortex filaments, in the following we study their motion once they get trapped.

At large scales, the vortex tangle seems to behave as a classical hydrodynamic turbulent system. Therefore, the first natural question is whether the particles can trace such large-scale fluctuations. In classical turbulence, it is well known that the Lagrangian velocity spectrum scales as

$$\langle |\hat{\mathbf{v}}_p(\omega)|^2 \rangle = B\epsilon\omega^{-2}, \tag{8}$$

where B is a constant of order unity and $\hat{\mathbf{v}}_p(\omega)$ is the Fourier transform of the Lagrangian particle velocity $\mathbf{v}_p(t)$ [47,48]. Such scaling is valid in the inertial range $2\pi/T_L \ll \omega \ll 2\pi/\tau_\eta$, where τ_η is the Kolmogorov timescale. In our case, we build an analog of the Kolmogorov time scale under the assumptions that the dissipation rate ϵ_{max} is the only important physical parameter in the classical turbulence regime and that the Kolmogorov turbulent cascade ends at the intervortex distance ℓ_{min}. Therefore, we define the smallest timescale of the classical turbulence regime as $\tau_\ell = (\ell_{min}^2/\epsilon_{max})^{1/3}$, and we expect classical turbulent phenomenology to hold for times $\tau_\ell \ll t \ll T_L$. In Fig. 6, the measurement of the frequency spectrum of the particle velocity $\langle |\hat{\mathbf{v}}_p(\omega)|^2 \rangle = \langle | \int \dot{\mathbf{q}}(t) e^{-i\omega t}\, dt|^2 \rangle$ during the turbulent regime is shown for different species of particles, compensated with the classical scaling $\epsilon_{max}\omega^{-2}$. Note that the average that defines the spectrum is meant over different realizations. In numerics we average over all the particle trajectories during the turbulent regime. At frequencies $\omega < \tau_\ell/2\pi$, the spectra approach a plateau of value 1, confirming that particles sample well the flow and their behavior is described by the standard classical turbulence picture at large scales. Note that the classical temporal inertial range of our simulations is pretty small, since $T_L \sim 5\tau_\ell$. For comparison, we also present the velocity spectrum of a particle of size $a_p = 4\xi$ and mass $\mathcal{M} = 1$, computed in a temporal window at much later times, when Kolmogorov turbulence has decayed and only a few vortices are left. Note that a ω^{-2} scaling of the Lagrangian velocity spectrum has also been observed in numerical simulations of the vortex filament model [49], although not in the Kolmogorov inertial range and not related to the energy dissipation rate nor to Kolmogorov turbulence.

As expected, in our simulations no Kolmogorov scaling is observed at small timescales. Indeed, one of the most striking features of quantum turbulence is the crossover between the classical Kolmogorov regime and the physics taking place at scales smaller than the mean intervortex distance. Unlike classical turbulence (see, for instance, [47]), there is still a nontrivial scaling at

timescales shorter than τ_ℓ. Such a difference is a consequence of the quantum nature of the system, here manifested by the presence of quantized vortices.

When a particle is trapped by a vortex, the superfluid flow turns around it. As a consequence, while the particle moves, it experience a Magnus force. This lift force is simply expressed as $\mathbf{F}_{\text{Magnus}} = \frac{3}{2}\rho_\infty a_\text{p}\boldsymbol{\Gamma}\times(\dot{\mathbf{q}}-\mathbf{v}_\text{s})$, where the circulation vector $\boldsymbol{\Gamma}$ is oriented along the vortex filament, and the superfluid velocity $\mathbf{v}_\text{s}$ contains the contributions of the mean flow and the vortex motion [36,50]. The Magnus effect induces a precession of the particle about the filament with the characteristic angular velocity

$$\Omega_\text{p} = \frac{3}{2}\frac{\rho_\infty a_\text{p}}{M_\text{p}^\text{eff}}\Gamma, \tag{9}$$

where the particle effective mass $M_\text{p}^\text{eff} = M_\text{p} + \frac{1}{2}M_0 = (\mathcal{M}+\frac{1}{2})M_0$ takes into account the added mass effect due to the mass of the superfluid displaced by the particle M_0. As mentioned in [36], for current experiments with hydrogen particles in superfluid helium, this frequency is of order 10–100 Hz. If the Magnus force is the main force acting on a trapped particle, the Newton equation $M_\text{p}^\text{eff}\ddot{\mathbf{q}} = \mathbf{F}_{\text{Magnus}}$ implies the following expression for the frequency spectrum of the particle velocity:

$$\langle|\hat{\mathbf{v}}_\text{p}(\omega)|^2\rangle = \frac{\Omega_\text{p}^2}{\Gamma^2(\omega-\Omega_\text{p})^2}\langle|\boldsymbol{\Gamma}\times\hat{\mathbf{v}}_\text{s}(\omega)|^2\rangle. \tag{10}$$

Independently of the external superfluid velocity, the expression (11) predicts that the spectrum $\langle|\hat{\mathbf{v}}_\text{p}(\omega)|^2\rangle$ must be peaked around the natural frequency of trapped particles $\omega = \Omega_\text{p}$. Such behavior has been studied in detail in the case of particles trapped inside slightly perturbed straight vortex filaments [36]. The spectrum of this simple configuration is also reported for comparison in Fig. 6(a) for a small particle of relative unit mass. A clear bump in the frequency spectrum, corresponding to Ω_p, is still visible when particles are immersed in a complex quantum vortex tangle. For the large particles, the presence of a peak is less evident because the natural frequency is lower, and therefore a longer sampling (in time) would be necessary to resolve it properly ($2\pi/\Omega_\text{p} = 0.7T_L$ for the particles of size $a_\text{p} = 10\xi$ and mass $\mathcal{M} = 1$). Moreover, as large particles are multiply trapped by many vortices, the resulting motion is certainly more complex than a precession with a single characteristic angular frequency of one single vortex. The broadness of the peak around the Magnus frequency for the small particles in Fig. 10(a) could also be related to this fact.

At small timescales, a different scaling of the velocity spectrum is observed for the light particles, now in agreement with $\langle|\hat{\mathbf{v}}_\text{p}(\omega)|^2\rangle \propto |\omega|^{-1}$. This behavior is consistent with the fact that at scales smaller than the intervortex distance, the typical velocities of a superfluid turbulent tangle are supposed to scale as $v_\text{fast}(t) \propto \sqrt{\kappa/|t-t_0|}$, because the circulation becomes the only relevant physical parameter, and the motion of vortices is dominated by their mutual advection and reconnections. In this scenario, if particles are sufficiently light to be able to follow the fast vortex dynamics, we can substitute $\langle|\hat{\mathbf{v}}_\text{p}(\omega)|^2\rangle \sim \hat{v}^2_\text{fast}(\omega) \propto \kappa|\omega|^{-1}$. Another effect that could contribute to the same result is the attraction of particles by the vortices, since the scaling in time of the particle-vortex distance is the same as that of vortex reconnection [34]. Note that for the heaviest particles, such fast scaling is absent since their reaction is probably too slow to be sensible to the fast fluctuations of the tangle.

C. Particle velocity and acceleration statistics

Unlike classical turbulence, where the statistics of the one-point particle velocity v is known to be Gaussian [1], experiments in superfluid helium using hydrogen and deuterium particles as tracers have reported long tails, with a v^{-3} power-law scaling in their velocity distribution [24–26]. Such scaling has been related to the singular velocity field of quantized vortices [51,52]. At low temperatures, as Stokes drag is negligible, particles should not move with the superfluid flow

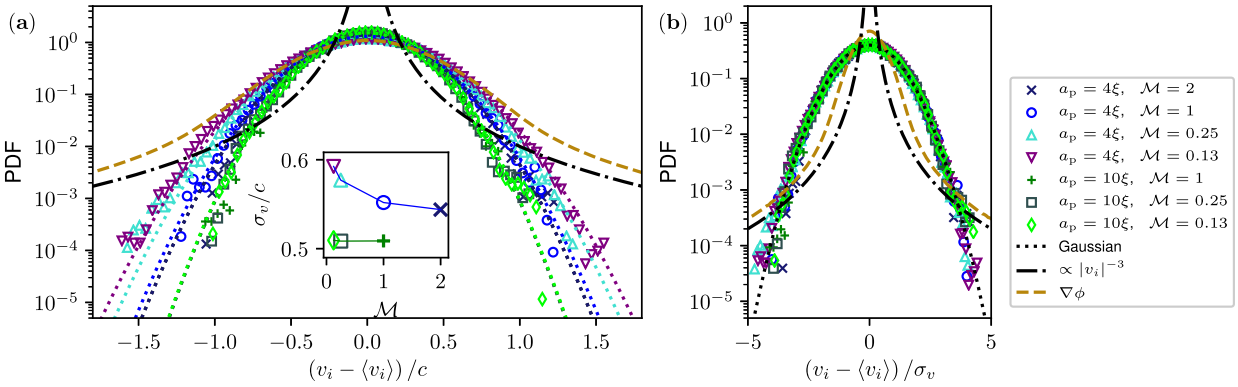


FIG. 7. (a) Probability density function of the single-component particle velocity, for different species of particles. The dotted golden line is the Eulerian velocity field $\nabla\phi$, corresponding to the simulation without particles at the time $1.4\,T_L$. The data for the particles are averaged in time between $t = 1.2T_L$ and $1.6T_L$. Inset: Standard deviation of the particle velocity as a function of the particle mass. (b) The same as (a) but with the velocities normalized by the standard deviation σ_v. Dotted lines are Gaussian, dash-dotted line is a power-law scaling $|v_i|^{-3}$.

and such scaling can be understood as a consequence of quantum vortex reconnections sampled by trapped particles [7,24]. Furthermore, in Ref. [25], by using particle tracking velocimetry in counterflow turbulence, it was shown that while varying the sampling scale, the velocity PDFs continuously change from Gaussian statistics to power-law tails, the crossover taking place at scales of the order of the intervortex distance. In this final subsection we present measurements of particle velocity and acceleration statistics within the GP-P model.

We start the discussion by presenting the Eulerian velocity field. Formally, the velocity of the superfluid is simply given by $\nabla\phi$. This field contains the density fluctuations, as well as the divergence of the vortex velocity flow close to its core. This divergence leads to the well-observed v^{-3} scaling of velocity PDF [51,53,54]. The PDF of $\nabla\phi$ is displayed in Fig. 7. We turn now to analyze the particle velocity PDFs. We compute the velocity PDFs for all runs in the turbulent regime. Data are filtered with a Gaussian convolution in order to smooth out the noisy oscillations at frequencies $\omega < \omega_{\text{noise}} = 50\,(2\pi/\tau_\ell)$ (see Appendix). In Fig. 7 the PDF of the single-component velocity is plotted for all the species of analyzed particles. In Fig. 7(a), velocities are expressed in terms of the speed of sound c, whereas in Fig. 7(b) they are normalized by their root-mean-squared values. The root-mean-squared values are displayed in the inset of Fig. 7(a) as a function of the mass for the two particle sizes. It is apparent from Fig. 7(b) that the particle statistics exhibits a Gaussian distribution. Note that Gaussian velocity statistics was also observed in thermal counterflow simulations of the vortex filament method with tracers particles [30]. The absence of power-law tails could be a consequence of weak statistical sampling of large velocity fluctuations due to the low number of particles present in the system and/or by compressible effects of the GP model. We will comment more about this in Sec. IV.

We would like to remark here that high-frequency fluctuations are strongly sensitive to numerical artifacts. In the Appendix, inspired by the experimental results of Ref. [25], we have computed the velocity PDFs of the velocity fluctuations filtered at a given frequency ω_c. The frequency was varied from values lower to larger than $2\pi/\tau_\ell$. For one simulation we have compared two different interpolation methods to evaluate the force term in Eq. (3) needed to drive the particles. It turns out that for the fourth-order B-spline method, the velocity PDFs start to develop tails while the filtering scale is varied, eventually leading to a v^{-3} scaling. However, when using Fourier interpolation, which is an exact evaluation (up to spectral convergence of the pseudospectral code) of the force term, the PDFs do not develop any tail and remain Gaussian. We have decided to keep this example with spurious numerical effects in the Appendix, as it might be useful for future numerical studies

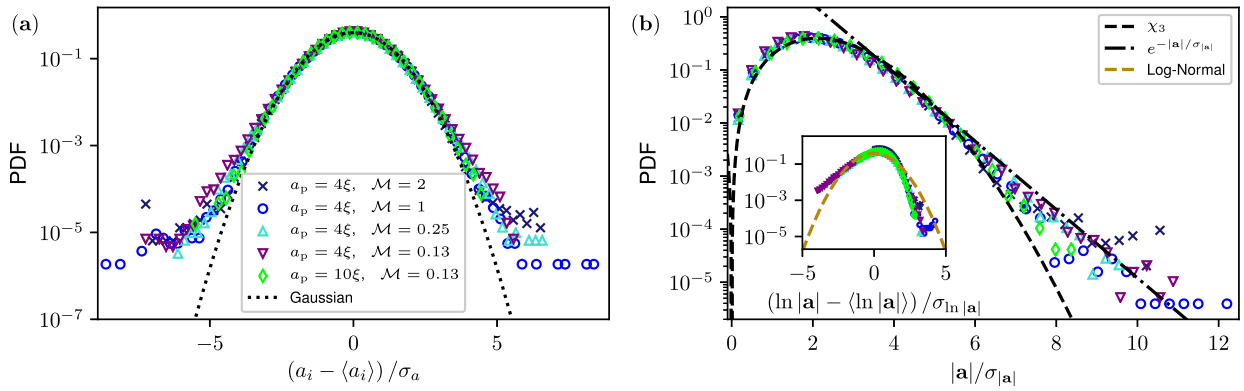


FIG. 8. (a) Probability density functions of the single-component particle acceleration. (b) Probability density functions of the norm of the particle acceleration. The dotted line is a Gaussian, the dashed line is a χ_3 distribution, and the dash-dotted line is an exponential tail $e^{-|\mathbf{a}|/\sigma_{|\mathbf{a}|}}$. Inset: Probability density functions of the natural logarithm of the norm of the particle acceleration. The dashed golden line is a log-normal distribution.

and data analysis of similar problems. We have checked that the results presented in the paper are independent of the interpolation scheme.

We turn now to study the acceleration statistics. As displayed in Fig. 8(a), the PDF of the acceleration presents some deviations from a Gaussian distribution at large values. The norm of the acceleration has also an exponential tail for $|\mathbf{a}| > \sigma_{|\mathbf{a}|}$, as displayed in Fig. 8(b). The core of the PDF in this case is a χ_3 distribution, which is expected for the norm of a vector with Gaussian components. In classical Lagrangian turbulence, the norm of the particle acceleration is observed to obey a log-normal distribution [55]. In the inset of Fig. 8(b), we compare our data with such distribution. For the lightest and smallest particle, the small accelerations appear to be more probable than in the classical case. Note that, as pointed out in [55], small values of the acceleration are very sensible to experimental (numerical) errors. By contrast, the large accelerations are less probable than a log-normal distribution. This observation is compatible with classical numerical calculations in the framework of the viscous vortex filament model, in which it has been shown that, because of inertia, solid particles undergo less rapid changes of velocity than fluid particles [56].

Finally, in Fig. 9, we show the two-point correlator of the particle acceleration, defined as

$$\rho^a(t) = \frac{\langle a_i(t_0) a_i(t_0 + t)\rangle - \langle a_i(t_0)\rangle \langle a_i(t_0 + t)\rangle}{\sigma_a(t_0)\sigma_a(t_0 + t)}. \tag{11}$$

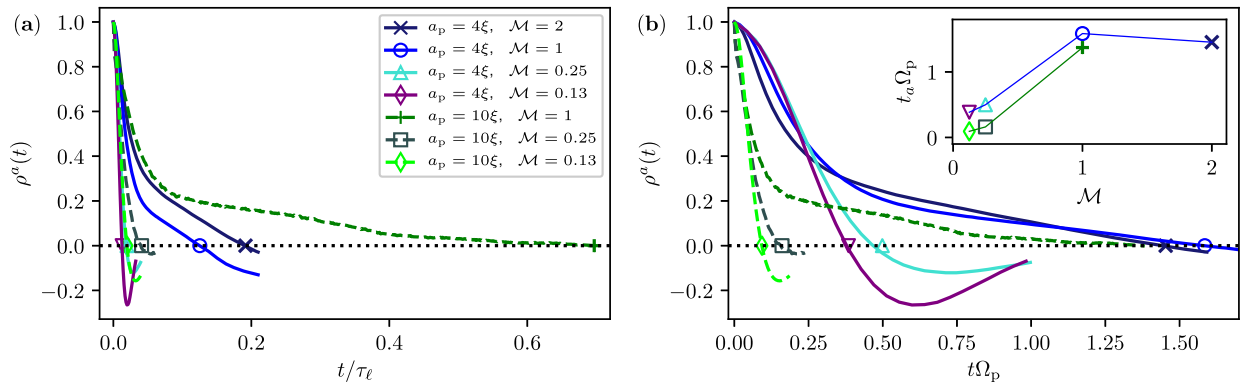


FIG. 9. Acceleration two-point correlator, plotted vs time normalized by the dissipation timescale τ_ℓ (a), and by the Magnus natural frequency $1/\Omega_p$. (b) Markers indicate the time of acceleration decorrelation t_a. Inset: t_a normalized by $1/\Omega_p$ as a function of the particle relative mass.

In classical Lagrangian turbulence, the decorrelation time t_a [such that $\rho^a(t_a) = 0$] is related to the Kolmogorov timescale $t_a = 2\tau_\eta$ [57]. This is not the case in quantum turbulence. Figure 9(a) displays the autocorrelation $\rho^a(t)$ for all the simulations. It is apparent that the acceleration decorrelates much faster than τ_ℓ, the equivalent of the Kolmogorov timescale in our system. This fact is a consequence of the myriad of physical phenomena taking place at smaller scales. As most particles are trapped by vortices, they oscillate at the Magnus frequency Ω_p in Eq. (9). If time is normalized by Ω_p (9), then $t_a\Omega_\mathrm{p}$ becomes of order 1, at least for the heaviest particles [see Fig. 9(b) and the inset therein]. For the lightest particles, the decorrelation time is even lower, meaning that they are sensible to other mechanisms, such as reconnection events between vortex filaments and Kelvin wave excitations at even smaller scales.

IV. DISCUSSION

In this work, we used the Gross-Pitaevskii model to study free decaying quantum turbulence at zero temperature in the presence of finite-size active particles. We considered different families of spherical particles having sizes smaller than and of the order of the mean intervortex distance. We first performed a standard analysis of the observables commonly used for studying Kolmogorov turbulence, such as the energy decomposition, the temporal evolution of mean energy, the rate of incompressible kinetic energy, and the mean intervortex distance. Although particles are active and get captured by vortices generating Kelvin waves, there is not a significant impact at scales larger than the intervortex distance, where Kolmogorov turbulence takes place. Monitoring the motion of the particles in the system, we confirmed their tendency to remain trapped into vortex filaments during the evolution of the tangle, with intermittent episodes of detachment and recapture. This behavior is independent of the vortex line density. We also found that particles can be easily captured simultaneously by several quantum vortices.

We also studied turbulence from the Lagrangian point of view. In particular, we computed the power spectra of the particle velocities. At large scales the particle dynamics is compatible with that of Lagrangian tracers in classical turbulence, while at short timescales the Magnus precession around the filaments caused by the vortex circulation is dominating the motion. Such information can be extracted consistently both in the frequency spectrum of the velocity and in the decay time of the correlation of the acceleration. Furthermore, if particles are light enough, faster frequencies are also excited. This suggests (as intuitively expected) that light particles can be more sensitive to the small-scale fluctuations of the flow.

Finally, we investigated the particle velocity statistics. The distribution of the particle velocity is Gaussian, in contrast with the power-law scaling $|v_i|^{-3}$ recently observed in superfluid helium experiments [24,25]. There are several reasons why power-law tails are absent in our simulations. First, since the simulation of each particle has an important numerical cost, the number of particles is restricted only to a couple of hundred. Due to this issue, vortex reconnections might be unlikely sampled by the sparse distribution of particles. Note also that, as particles have a finite size, increasing their number keeping the size of the system constant will increase substantially the filling fraction. In this case, turbulence could even be prevented by the presence of particles. Although interesting, this limit is beyond the scope of this work. Secondly, the GP model is compressible, and particles moving at large velocities are slowed down by vortex nucleations. This certainly reduces large velocity fluctuations, perhaps limiting the development of power-law tails. It would be interesting to address such issues in generalized GP models, including a roton minimum and high-order nonlinearities. Moreover, our simulations are by definition at zero temperature, and particles do not follow the singular superfluid velocity field because of the lack of viscosity in the system. Indeed, in the GP model the pressure gradients that drive the particle dynamics are always regular because of the vanishing density at the vortex cores, unlike other models such as the vortex filament method. As a consequence, the divergence of the superfluid velocity along the vortex lines cannot be experienced by the particles. Conversely, at finite temperature the superfluid and the normal component can be locked thanks to mutual friction. In this case, since particles

would sample the normal fluid velocity because of Stokes drag, they might be able to sample the $1/r$ flow around a quantum vortex. Finally, we observed that fast velocity fluctuations are highly sensitive to interpolation and filtering methods that could even lead to power-law tails. These tails are completely spurious, and special care is needed while analyzing numerical or experimental data.

ACKNOWLEDGMENTS

U.G. acknowledges J. I. Polanco for fruitful discussions. The authors were supported by Agence Nationale de la Recherche through the project GIANTE ANR-18-CE30-0020-01. Computations were carried out on the Mésocentre SIGAMM hosted at the Observatoire de la Côte d'Azur and the French HPC Cluster OCCIGEN through the GENCI allocation A0042A10385.

APPENDIX: NUMERICAL ARTIFACTS ON THE PARTICLE VELOCITY STATISTICS: COMPARISON BETWEEN B-SPLINE AND SPECTRAL INTERPOLATION METHODS

As explained in the main text, we evaluate the force $\mathbf{f}_i^{\mathrm{GP}} = -(V_{\mathrm{p}} * \nabla\rho)[\mathbf{q}_i]$ (3) at the particle position $\mathbf{q}_i$ using a B-spline interpolation method [39] at each time step. Such a method is precise and computationally cheap, but it turns out to present some issues that we have to take care of. To check the reliability of the method, we rerun a simulation using Fourier interpolation for one species of particles in the time window corresponding to the turbulent regime. Fourier interpolation is exact in the sense that it uses the information of the full three-dimensional field, which is resolved with spectral accuracy (i.e., discretization errors are at most exponentially small with the number of discretization points). The numerical cost of this method is that of one Fourier transform (per particle). In Fig. 10 the velocity and acceleration spectra computed using B-spline and Fourier interpolation methods are compared. Clearly, the B-spline interpolation introduces nonphysical fast oscillations, but at the frequencies $\omega < \omega_{\mathrm{noise}} = 50(2\pi/\tau_\ell)$ the behavior of the spectra is unchanged. Nevertheless, some differences in the features of particle statistics are still visible at fast timescales once the noise is filtered out.

We use a Gaussian convolution to perform a filtering of the velocity time series for each particle in the frequency window $\omega_c < \omega < \omega_{\mathrm{noise}}$, where ω_{c} is a variable infrared cutoff frequency. Then we compute the PDF of the filtered velocity for different values of ω_c. Such PDFs are shown in Fig. 11 comparing the simulations in which Fourier and B-spline interpolation are used for the same species of particle. Surprisingly, only in the latter case do we observe power-law tails for the fast oscillation distributions. Such PDFs are similar to the ones observed experimentally [24,25], but in the present case they are just a consequence of numerical artifacts.

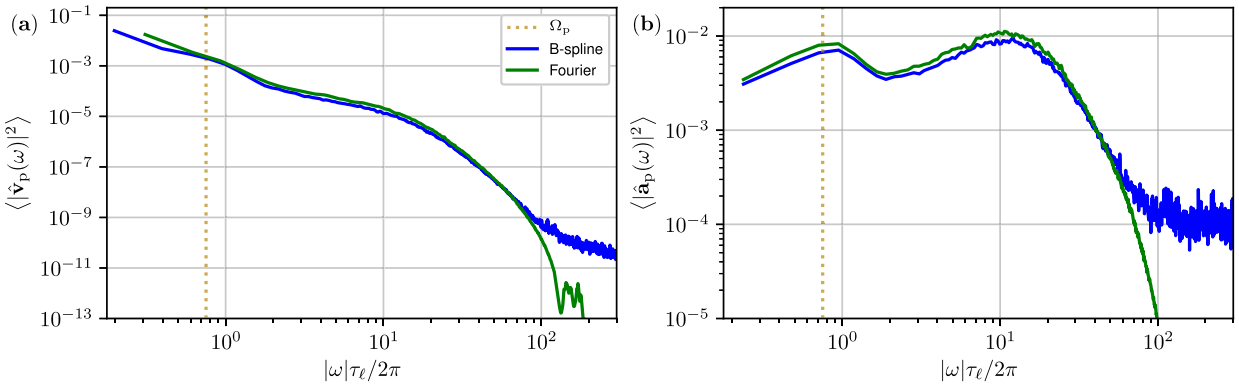


FIG. 10. Velocity spectra (a) and the acceleration spectra (b) for particles of size $a_{\mathrm{p}} = 10\xi$ and mass $\mathcal{M} = 0.13$, evolved using B-spline interpolation (blue lines) and spectral Fourier interpolation (green lines). The spectra are averaged over particles and over the times $1.3T_L < t < 1.5T_L$.

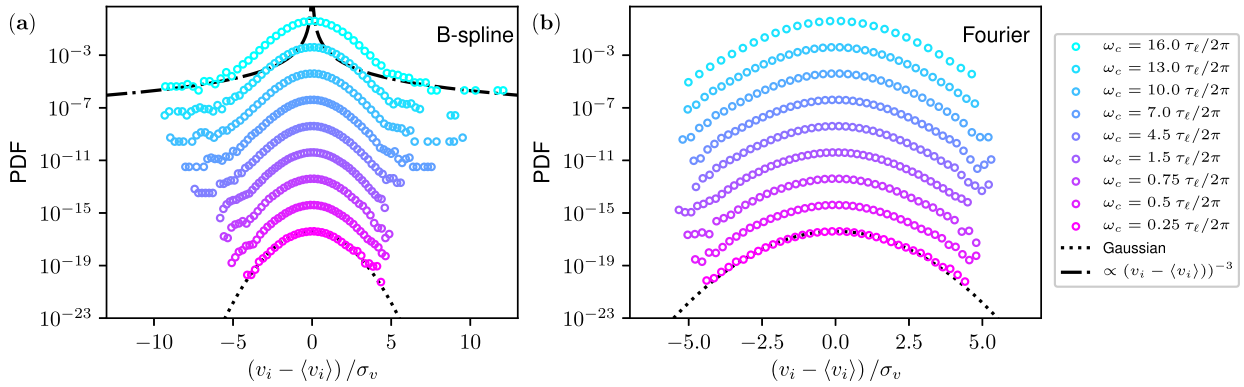


FIG. 11. Probability density function of the velocity filtered in the frequency window $\omega_c < \omega < \omega_{\text{noise}}$ for different values of ω_c. Data refer to particles of size $a_p = 10\xi$ and mass $\mathcal{M} = 0.13$. The dotted line is a Gaussian distribution, and the dash-dotted line is a power-law scaling $0.002(v_i - \langle v_i \rangle)^{-3}$. The data are averaged over particles and over the times $1.3T_L < t < 1.5T_L$. Different PDFs are shifted for visualization. (a) Particle force interpolated with the B-spline method. (b) Particle force interpolated with the Fourier method.

[1] U. Frisch and A. N. Kolmogorov, *Turbulence: The Legacy of AN Kolmogorov* (Cambridge University Press, Cambridge, 1995).

[2] R. J. Donnelly, *Quantized Vortices in Helium II* (Cambridge University Press, Cambridge, 1991), Vol. 2.

[3] T. Frisch, Y. Pomeau, and S. Rica, Transition to Dissipation in a Model of Superflow, Phys. Rev. Lett. **69**, 1644 (1992).

[4] T. Winiecki and C. S. Adams, Motion of an object through a quantum fluid, Europhys. Lett. **52**, 257 (2000).

[5] J. Koplik and H. Levine, Vortex Reconnection in Superfluid Helium, Phys. Rev. Lett. **71**, 1375 (1993).

[6] G. P. Bewley, M. S. Paoletti, K. R. Sreenivasan, and D. P. Lathrop, Characterization of reconnecting vortices in superfluid helium, Proc. Natl. Acad. Sci. USA **105**, 13707 (2008).

[7] A. Villois, D. Proment, and G. Krstulovic, Universal and nonuniversal aspects of vortex reconnections in superfluids, Phys. Rev. Fluids **2**, 044701 (2017).

[8] L. Galantucci, A. W. Baggaley, N. G. Parker, and C. F. Barenghi, Crossover from interaction to driven regimes in quantum vortex reconnections, Proc. Natl. Acad. Sci. USA **116**, 12204 (2019).

[9] C. Nore, M. Abid, and M. E. Brachet, Decaying Kolmogorov turbulence in a model of superflow, Phys. Fluids **9**, 2644 (1997).

[10] A. W. Baggaley, J. Laurie, and C. F. Barenghi, Vortex-Density Fluctuations, Energy Spectra, and Vortical Regions in Superfluid Turbulence, Phys. Rev. Lett. **109**, 205304 (2012).

[11] V. Shukla, P. D. Mininni, G. Krstulovic, P. C. di Leoni, and M. E. Brachet, Quantitative estimation of effective viscosity in quantum turbulence, Phys. Rev. A **99**, 043605 (2019).

[12] J. Maurer and P. Tabeling, Local investigation of superfluid turbulence, Europhys. Lett. **43**, 29 (1998).

[13] J. Salort, C. Baudet, B. Castaing, B. Chabaud, F. Daviaud, T. Didelot, P. Diribarne, B. Dubrulle, Y. Gagne, F. Gauthier, A. Girard, B. Hébral, B. Rousset, P. Thibault, and P.-E. Roche, Turbulent velocity spectra in superfluid flows, Phys. Fluids **22**, 125102 (2010).

[14] W. F. Vinen, Decay of superfluid turbulence at a very low temperature: The radiation of sound from a kelvin wave on a quantized vortex, Phys. Rev. B **64**, 134520 (2001).

[15] V. S. L'vov and S. Nazarenko, Weak turbulence of kelvin waves in superfluid he, Low Temp. Phys. **36**, 785 (2010).

[16] J. Laurie, V. S. L'vov, S. Nazarenko, and O. Rudenko, Interaction of kelvin waves and nonlocality of energy transfer in superfluids, Phys. Rev. B **81**, 104526 (2010).

[17] G. Krstulovic, Kelvin-wave cascade and dissipation in low-temperature superfluid vortices, Phys. Rev. E **86**, 055301(R) (2012).

[18] A. W. Baggaley and J. Laurie, Kelvin-wave cascade in the vortex filament model, Phys. Rev. B **89**, 014504 (2014).
[19] A. Villois, D. Proment, and G. Krstulovic, Evolution of a superfluid vortex filament tangle driven by the Gross-Pitaevskii equation, Phys. Rev. E **93**, 061103(R) (2016).
[20] F. Toschi and E. Bodenschatz, Lagrangian properties of particles in turbulence, Annu. Rev. Fluid Mech. **41**, 375 (2009).
[21] W. Guo, M. La Mantia, D. P. Lathrop, and S. W. Van Sciver, Visualization of two-fluid flows of superfluid helium-4, Proc. Natl. Acad. Sci. USA **111**, 4653 (2014).
[22] G. P. Bewley, D. P. Lathrop, and K. R. Sreenivasan, Superfluid helium: Visualization of quantized vortices, Nature (London) **441**, 588 (2006).
[23] E. Fonda, D. P. Meichle, N. T. Ouellette, S. Hormoz, and D. P. Lathrop, Direct observation of kelvin waves excited by quantized vortex reconnection, Proc. Natl. Acad. Sci. USA **111**, 4707 (2014).
[24] M. S. Paoletti, M. E. Fisher, K. R. Sreenivasan, and D. P. Lathrop, Velocity Statistics Distinguish Quantum Turbulence from Classical Turbulence, Phys. Rev. Lett. **101**, 154501 (2008).
[25] M. L. Mantia and L. Skrbek, Quantum, or classical turbulence?, Europhys. Lett. **105**, 46002 (2014).
[26] M. La Mantia and L. Skrbek, Quantum turbulence visualized by particle dynamics, Phys. Rev. B **90**, 014519 (2014).
[27] M. La Mantia, D. Duda, M. Rotter, and L. Skrbek, Lagrangian accelerations of particles in superfluid turbulence, J. Fluid Mech. **717**, R9 (2013).
[28] Y. A. Sergeev and C. F. Barenghi, Particles-vortex interactions and flow visualization in 4he, J. Low Temp. Phys. **157**, 429 (2009).
[29] C. F. Barenghi, D. Kivotides, and Y. A. Sergeev, Close approach of a spherical particle and a quantised vortex in helium II, J. Low Temp. Phys. **148**, 293 (2007).
[30] Y. Mineda, M. Tsubota, Y. A. Sergeev, C. F. Barenghi, and W. F. Vinen, Velocity distributions of tracer particles in thermal counterflow in superfluid ^{4}He, Phys. Rev. B **87**, 174508 (2013).
[31] E. Varga, C. F. Barenghi, Y. A. Sergeev, and L. Skrbek, Backreaction of tracer particles on vortex tangle in helium ii counterflow, J. Low Temp. Phys. **183**, 215 (2016).
[32] J. I. Polanco and G. Krstulovic, Inhomogeneous distribution of particles in coflow and counterflow quantum turbulence, Phys. Rev. Fluids **5**, 032601 (2020).
[33] V. Shukla, M. Brachet, and R. Pandit, Sticking transition in a minimal model for the collisions of active particles in quantum fluids, Phys. Rev. A **94**, 041602(R) (2016).
[34] U. Giuriato and G. Krstulovic, Interaction between active particles and quantum vortices leading to kelvin wave generation, Sci. Rep. **9**, 4839 (2019).
[35] U. Giuriato, G. Krstulovic, and D. Proment, Clustering and phase transitions in a 2d superfluid with immiscible active impurities, J. Phys. A **52**, 305501 (2019).
[36] U. Giuriato, G. Krstulovic, and S. Nazarenko, How trapped particles interact with and sample superfluid vortex excitations, Phys. Rev. Research **2**, 023149 (2020).
[37] A. Griffin, S. Nazarenko, V. Shukla, and M.-E. Brachet, The vortex-particle magnus effect, arXiv:1909.11010.
[38] P. Clark di Leoni, P. D. Mininni, and M. E. Brachet, Dual cascade and dissipation mechanisms in helical quantum turbulence, Phys. Rev. A **95**, 053636 (2017).
[39] M. A. T. van Hinsberg, J. H. M. Thije Boonkkamp, F. Toschi, and H. J. H. Clercx, On the efficiency and accuracy of interpolation methods for spectral codes, SIAM J. Sci. Comput. **34**, B479 (2012).
[40] N. Sasa, T. Kano, M. Machida, V. S. L'vov, O. Rudenko, and M. Tsubota, Energy spectra of quantum turbulence: Large-scale simulation and modeling, Phys. Rev. B **84**, 054525 (2011).
[41] G. Krstulovic, Grid superfluid turbulence and intermittency at very low temperature, Phys. Rev. E **93**, 063104 (2016).
[42] W. F. Vinen, Mutual friction in a heat current in liquid helium ii iii. theory of the mutual friction, Proc. R. Soc. London, Ser. A **242**, 493 (1957).
[43] See Supplemental Material at http://link.aps.org/supplemental/10.1103/PhysRevFluids.5.054608 for movies of the simulations.

[44] N. G. Berloff and P. H. Roberts, Capture of an impurity by a vortex line in a Bose condensate, Phys. Rev. B **63**, 024510 (2000).
[45] A. Villois, G. Krstulovic, D. Proment, and H. Salman, A vortex filament tracking method for the gross-pitaevskii model of a superfluid, J. Phys. A **49**, 415502 (2016).
[46] The circulation measured with this method is subjected to a numerical error coming from the grid spacing. Such error is removed in postprocessing, knowing that Γ can only be an integer multiple of κ. Furthermore, extremely high values of Γ have been removed since they are related to the ill-defined situation in which a topological defect is placed at the boundary $\mathcal{C}$.
[47] P. K. Yeung, Lagrangian characteristics of turbulence and scalar transport in direct numerical simulations, J. Fluid Mech. **427**, 241 (2001).
[48] H. Tennekes, J. L. Lumley, J. Lumley *et al.*, *A First Course in Turbulence* (MIT Press, Cambridge, 1972).
[49] D. Kivotides, Y. A. Sergeev, and C. F. Barenghi, Dynamics of solid particles in a tangle of superfluid vortices at low temperatures, Phys. Fluids **20**, 055105 (2008).
[50] L. Kiknadze and Y. Mamaladze, The magnus (kutta-jukovskii) force acting on a sphere, arXiv:cond-mat/0604436.
[51] A. C. White, C. F. Barenghi, N. P. Proukakis, A. J. Youd, and D. H. Wacks, Nonclassical Velocity Statistics in a Turbulent Atomic Bose-Einstein Condensate, Phys. Rev. Lett. **104**, 075301 (2010).
[52] M. S. Paoletti and D. P. Lathrop, Quantum turbulence, Annu. Rev. Condens. Matter Phys. **2**, 213 (2011).
[53] A. W. Baggaley and C. F. Barenghi, Quantum turbulent velocity statistics and quasiclassical limit, Phys. Rev. E **84**, 067301 (2011).
[54] V. Shukla, M. Brachet, and R. Pandit, Turbulence in the two-dimensional fourier-truncated gross-pitaevskii equation, New J. Phys. **15**, 113025 (2013).
[55] N. Mordant, A. M. Crawford, and E. Bodenschatz, Three-Dimensional Structure of the Lagrangian Acceleration in Turbulent Flows, Phys. Rev. Lett. **93**, 214501 (2004).
[56] D. Kivotides, C. F. Barenghi, A. J. Mee, and Y. A. Sergeev, Interaction of Solid Particles with a Tangle of Vortex Filaments in a Viscous Fluid, Phys. Rev. Lett. **99**, 074501 (2007).
[57] P. K. Yeung and S. B. Pope, Lagrangian statistics from direct numerical simulations of isotropic turbulence, J. Fluid Mech. **207**, 531 (1989).

6 Dynamics of impurities in the truncated Gross–Pitaevskii model

In this chapter we report a supplementary study on the dynamics of immiscible active impurities coupled with a quantum fluid at finite temperature. First, we give a short introduction to the truncation procedure for the Gross–Pitaevskii equation, which is a method to implement finite temperature effects in the system. This allows us to provide the minimal theoretical background to understand the two subsequent original papers. The first of them, "Stochastic motion of finite-size immiscible impurities in a dilute quantum fluid at finite temperature" [78], is related to the random dynamics of a single impurity in a thermal bath. In particular, we characterize the friction coefficient and its temperature dependence. In the second publication, "Clustering and phase transitions in a 2D superfluid with immiscible active impurities" [80], we consider the dynamics of many impurities in two dimensions. The random motion of the impurities induced by the thermal bath combined with their mutual interaction leads to the formation of clusters. We characterize the critical temperature of such clustering transition and its dependence on the particle repulsion. Eventually, we observe a shift of the condensation and Berezinskii-Kosterlitz–Thouless critical temperatures, which is proportional to the filling fraction of the impurity clusters.

6.1 The truncated GP equation as a model for finite temperature quantum fluids

Until now, we have considered the Gross–Pitaevskii equation to model a superfluid at very low temperature, namely when the number of non-condensed atoms is negligible and a the use of a single collective mean field wavefunction to describe the system is justified. As shown in the first chapter, the GP equation can be derived from the more general dynamics of a bosonic system, given by the quantum Heisenberg equation (1.46) for the Bose operator $\hat{\Psi}$, under the assumption that the fundamental mode, the condensate, is largely populated. However, if the other modes of the system are also highly occupied ($n_{\boldsymbol{k}} \gg 1$) the classical fluctuations are dominating over the quantum fluctuations and therefore also these states may be described by a (classical) coherent wavefunction. This is the fundamental intuition behind the use of the truncated (or projected) GP equation to model a bosonic system at nonzero temperature, developed in the early 2000s by Davis et al [52].

One issue which is immediately evident when one tries to use the GP equation to

model a system in thermal equilibrium is the arising of an ultraviolet catastrophe. Indeed, being GP a classical equation, the equipartition theorem holds at low temperature, meaning that each mode would carry a thermal energy $n_{\boldsymbol{k}} E_{\boldsymbol{k}} = \mathrm{k_B} T$ at temperature T, where $E_{\boldsymbol{k}}$ is the single-particle energy. This implies that the total energy $\int n_{\boldsymbol{k}} E_{\boldsymbol{k}} \, \mathrm{d}\boldsymbol{k}$ diverges at infinitely small scales, as in the historical problem of the black body radiation [132]. Another consequence of equipartition is that at small scales, where the single-particle energy scales as $E_{\boldsymbol{k}} \sim k^2$ (1.10), the occupation number $n_{\boldsymbol{k}} = \mathrm{k_B} T / E_{\boldsymbol{k}}$ becomes smaller and smaller and at a certain scale the classical limit $n_{\boldsymbol{k}} \gg 1$ is no longer valid. In this perspective, the ultraviolet divergence is nothing but an unphysical occurrence due to the fact that a classical theory is being extrapolated in a region where the dynamics is fully quantum.

The technique of truncating the system imposing an ultraviolet cutoff scale k_{max} is an approximation which solves this problem. The idea is to set the cutoff such that the modes with energies higher than the value $\hbar\omega(k_{\mathrm{max}}) = \mathrm{k_B} T$ are simply ignored, and thus the region where a classical description is not valid is just not considered. The justification is that in the full quantum statistics (1.20) the small scale (high energy) modes with $\hbar\omega(k) \gg \mathrm{k_B} T$ are indeed weakly populated in comparison to the classical ones. Note that in practice the same cutoff is used for every temperature, which is a further approximation. Formally, one can define a projection operator $\hat{\mathscr{P}}$ that acts on the boson operator (1.47) as [51, 52]

$$\hat{\mathscr{P}} \hat{\Psi}(\boldsymbol{x}) = \sum_{k \in C} \Psi_{\boldsymbol{k}}(\boldsymbol{x}) \hat{a}_{\boldsymbol{k}} \sim \sum_{k \in C} \Psi_{\boldsymbol{k}}(\boldsymbol{x}) c_{\boldsymbol{k}} = \psi(\boldsymbol{x}), \tag{6.1}$$

where C is a "classical" region with highly populated modes $n_{\boldsymbol{k}} = \left\langle \hat{a}^\dagger_{\boldsymbol{k}} \hat{a}_{\boldsymbol{k}} \right\rangle \gg 1$. In this region it is safe to treat the annihilation and creation operators $\hat{a}_{\boldsymbol{k}}$ and $\hat{a}^\dagger_{\boldsymbol{k}}$ as c-numbers $c_{\boldsymbol{k}}$ (namely neglecting the quantum fluctuations $\hat{\delta}_{\boldsymbol{k}}$ in the expansion $\hat{a}_{\boldsymbol{k}} = c_{\boldsymbol{k}} + \hat{\delta}_{\boldsymbol{k}}$) and describe the system with a coherent field $\psi(\boldsymbol{x}) = \left\langle \hat{\Psi}(\boldsymbol{x}) \right\rangle$. Analogously, the orthogonal projector $\hat{\mathscr{Q}} = 1 - \hat{\mathscr{P}}$ acts on the Bose operator projecting it to the "incoherent" region I, which is the complement of C. The resulting field $\hat{\eta}(\boldsymbol{x}) = \sum_{k \in I} \hat{\mathscr{Q}} \hat{\Psi}(\boldsymbol{x})$ describes an effective heat bath coupled with the field $\psi(\boldsymbol{x})$ and that in principle evolves according to some quantum kinetic theory. Applying the decomposition of the Bose operator $\hat{\Psi} = \left[\hat{\mathscr{P}} + \hat{\mathscr{Q}}\right] \Psi$ to the quantum equation (1.46), taking the expectation values of the operators and neglecting the quantum fluctuations in the coherent region (6.1), one obtains the finite temperature Gross–Pitaevskii equation

$$i\hbar \frac{\partial \psi}{\partial t} = \hat{\mathscr{P}} \left[-\frac{\hbar^2}{2m} \nabla^2 \psi + g|\psi^2|\psi + V_{\mathrm{ext}} \psi \right] \tag{6.2}$$

$$+ \hat{\mathscr{P}} \left[2g|\psi|^2 \left\langle \hat{\eta} \right\rangle + g\psi^2 \left\langle \hat{\eta}^\dagger \right\rangle + g\psi^* \left\langle \hat{\eta}\hat{\eta} \right\rangle + 2g\psi \left\langle \hat{\eta}^\dagger \hat{\eta} \right\rangle + \left\langle \hat{\eta}^\dagger \hat{\eta}\hat{\eta} \right\rangle \right]. \tag{6.3}$$

Several sophisticated techniques to deal with the thermal cloud exist [183]. For the sake of simplicity and conciseness, only the truncation procedure is described here, which basically consists in neglecting all the terms that contain the heat bath $\hat{\eta}$ in Eq. (6.3). The resulting equation is therefore microcanonical and conserves the energy.

However, if the classical region is large ($n_k \gg 1$), the fluctuations of energy in the full equation (6.3) are small. As a consequence, the truncated equation and the full equation (6.3) would relax to a similar equilibrium state.

Operatively, in numerical simulations the truncation operation is performed in Fourier space introducing a Galerkin operator $\mathcal{P}_G$, which acts on the field $\psi(\boldsymbol{x})$ as[1]:

$$\mathcal{P}_G\left[f(\boldsymbol{r})\right] = \sum_{\boldsymbol{k}} \hat{f}(\boldsymbol{k}) e^{i\boldsymbol{k}\cdot\boldsymbol{x}} \theta_H(k_{max} - |\boldsymbol{k}|) \tag{6.4}$$

where $\hat{\psi}(\boldsymbol{k})$ is the Fourier transform of $\psi(\boldsymbol{x})$ and $\theta_H(k_{max} - |\boldsymbol{k}|) \equiv \theta_{\boldsymbol{k}}$ is the Heaviside theta. The resulting truncated Gross–Pitaevskii (TGP) equation reads

$$i\hbar \frac{\partial \psi}{\partial t} = \mathcal{P}_G\left[-\frac{\hbar^2}{2m}\nabla^2\psi + g\mathcal{P}_G\left[|\psi^2|\right]\psi + V_{ext}\psi \right], \tag{6.5}$$

which conserves exactly energy, mass and, if properly dealiased using the 2/3 rule, also the momentum (see [128, 131] and the Appendix A). The fundamental dimensionless parameter of such system is ξk_{max} (where ξ is the standard healing length at zero temperature (1.104)), that controls the amount of dispersion at the cutoff scale and which is inversely proportional to the intensity of the non-linear interactions [131, 213]. Indeed, for a larger value of ξk_{max}, more modes with a free particle dispersion relation are present in the system (as it can be seen from the Bogoliubov spectrum (1.110)) and thus the non-linearity is weaker. This fact can be also appreciated considering the magnitude of the non-linear broadening $\Delta\omega(k)$ of the dispersion relation, which provides a measure of the non-linear interaction time. As it is observed in the spatio-temporal spectra measured in [213] and reported in Fig.6.1, $\Delta\omega(k)$ significantly decreases when ξk_{max} is increased, confirming that the strength of the non-linearity is indeed weaker.

Given a finite size system of volume V, so that it contains a number of modes $\mathcal{N} = k_{max}^3 V$, the thermodynamic limit must be performed by setting $\mathcal{N} \to \infty$ and keeping $\xi k_{max} = const$, in order to obtain equivalent systems. In this limit, the relevant thermodynamic variables are the intensive quantities H/V, N/V (and $\boldsymbol{P}/V$ if the average momentum if different from zero).

The truncated GP equation possesses absolute equilibrium solutions, distributed with the probability

$$\mathbb{P}\left[\hat{\psi}_{\boldsymbol{k}}\right] \propto e^{-\beta(H-\mu N)}, \tag{6.6}$$

which is a solution of the Liouville equation associated to Eq. (6.5). The argument of the exponent in Eq. (6.6) is a linear combination of the invariants of the TGP equation, namely energy and mass[2] [128]. The parameters β and μ are Lagrange multipliers that play the roles of inverse temperature and chemical potential, respectively. At the

[1] Note that actually every system simulated numerically is always implicitly truncated, since the existence of a numerical cutoff (which defines the resolution of the numerical approximation) is an unavoidable occurrence of the descrete calculations performed by a machine.

[2] Considering for simplicity only the zero momentum states.

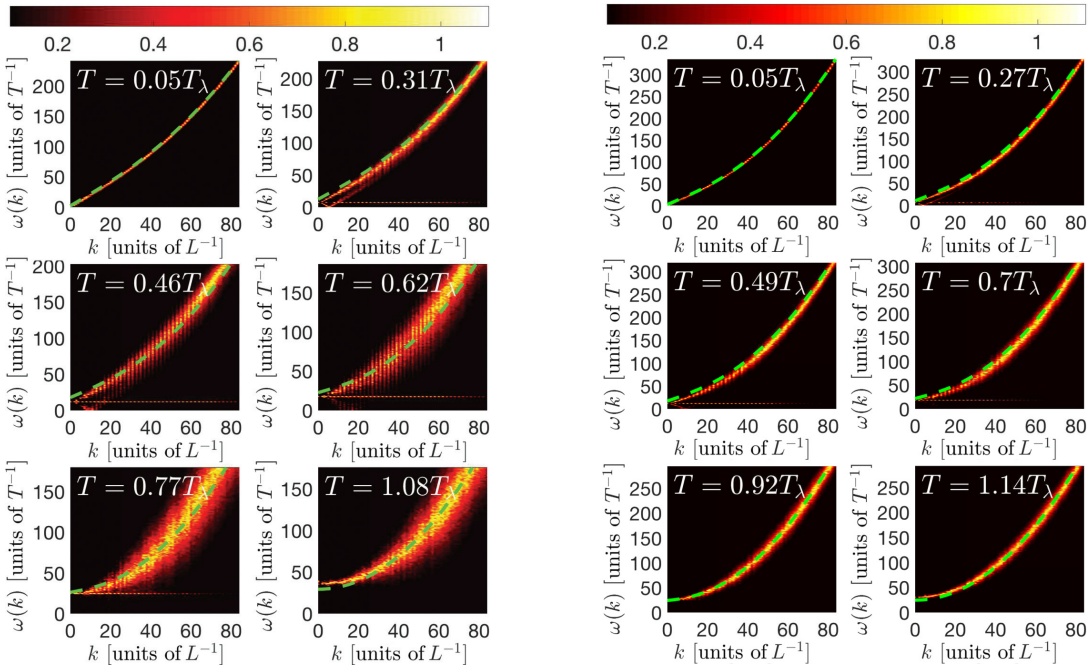


Figure 6.1. Spatio-temporal spectra of the superfluid field ψ in three-dimensional truncated GP simulations with $\xi k_{\mathrm{max}} = 1.5$ (*left*) and $\xi k_{\mathrm{max}} = 2.5$ (*right*), for different values of the temperature. Simulations are perfomed with $N_{\mathrm{c}} = 256^3$ collocation points. The linear Bogoliubov dispersion relation is reported as dashed green line. At fixed temperature, the non-linear broadening of the spectrum decreases when ξk_{max} increases. Note also that it increases when the temperature increases as a consequence of the larger amplitude of the density fluctuations (and thus of the non-linearity). Image taken from [213] to which we refer for further details.

equilibrium, the mean occupation of the mode $\boldsymbol{k}$ is the Reyleigh-Jeans distribution

$$\langle n_{\boldsymbol{k}} \rangle = \left\langle |\psi_{\boldsymbol{k}}|^2 \right\rangle = \frac{\mathrm{k_B} T}{E_k - \mu}, \tag{6.7}$$

which is the classical limit of the Bose-Einstein distribution (1.20) and where the temperature and the chemical potential depend on the energy and waveaction of the initial condition (conserved over time). This fact is expected, since the TGP is the high occupation limit of the full equation for the Bose field operator [52]. Indeed, the spectrum (6.7) is different from the standard Bose distribution (1.20) only close to the boundary of the coherent region: the Bose distribution goes smoothly to zero for $k > k_{\mathrm{max}}$, while in the truncated system the Reyleigh-Jeans distribution is abruptly set to zero at the UV cutoff k_{max}.

We remark that for a field ψ which is a regular solution of the (zero temperature) GP equation, the spectrum vanishes in the limit $k \to \infty$. The standard GP equation and the TGP model coincide for these solutions (if k_{max} is large enough), and the presence of a cutoff in Fourier space does not play an important role. On the contrary, the truncation is crucial for the states (6.7), since the small scale modes are highly populated. Note that in such regime the gradients do not exist, and the TGP equation (6.5) shall be considered as a large set of ordinary differential equations (one for each mode), rather than a single partial differential equation. In physical terms, one can consider the thermal states of the TGP model as a gas constituted by a finite number of classical modes in thermal equilibrium.

The TGP equation is also expected to describe the BEC phase transition, as long as the condition $n_{\boldsymbol{k}} \gg 1$ is satisfied for the coherent region. In fact the energy functional of the GP model corresponds exactly to that of the two-components "$\lambda - \phi^4$" theory used to study second order phase transitions with the renormalization group approach [100].

In [52] Davis et al. showed that the condensation transition can be reproduced by the truncated GP equation. In particular, they simulated the evolution of initial states with a flat distribution of momentum (up to a maximum wavenumber) and random phases. The maximum wavenumber was determined by the prescribed energy, increasing which the system reached microcanonical equilibrium states with less average condensed fractions. Above a critical value of the energy (and therefore of the temperature, which is its conjugate variable in the canonical ensable) the condensate was observed to vanish, compatibly with the BEC phase transition. This condensation transition was later interpreted as a condensation process of classical waves due to non-linear interactions [46, 57]. More recently, the out-of-equilibrium thermalization process in the TGP equation has been associated to a direct energy cascade, with a partial thermalization at small scales accompanied by vortex annihilation [131].

The TGP equation has been also a successful tool for studying quantum vortex dynamics at finite temperature. In [27] Berloff and Youd observed the dissipation of a vortex ring, measuring a linear decay in time of its length, which is in accordance with the HVBK model of superfluid helium [96]. On the contrary, if a thermal counterflow

is imposed to the system (setting $\boldsymbol{P} \neq 0$ [131]) a dilatation of vortex rings has been observed, as well as their slowdown due to the presence of thermally excited Kelvin waves [130].

Finally, in the articles [78] and [80], introduced at the end of this chapter, we considered for the first time the truncated GP equation coupled with highly repulsive impurities, adapting the model introduced in section 2.3.3.

6.1.1 The stochastic real Ginzburg–Landau model

The TGP equation (6.5) provides a microcanonical description of the thermal states. However, achieving the thermal equilibrium with such dynamical process is in general numerically costly. Moreover, it does not provide a direct access to the conjugate thermodynamical variables, like temperature and chemical potential (and counterflow velocity, if the average momentum is not zero [131]). The stochastic real Ginzburg–Landau model is an algorithm that has been developed to overcome these issues [131]. It is a grand-canonical approach leading to the same thermal states of the (microcanonical) truncated GP model, but much faster and with the temperature as an explicit tunable parameter. Given the free energy of the truncated system

$$F = \int \left(\frac{\hbar^2}{2m} |\nabla \psi|^2 + \frac{g}{2} \mathcal{P}_{\mathrm{G}} \left[|\psi|^2 \right]^2 + V_{\mathrm{ext}} \mathcal{P}_{\mathrm{G}} \left[|\psi|^2 \right] - \mu |\psi|^2 \right) \mathrm{d}\boldsymbol{x}, \tag{6.8}$$

we consider the following stochastic equation (in Fourier space)

$$\hbar \frac{\partial \hat{\psi}_{\boldsymbol{k}}}{\partial t} = -\frac{\partial F}{\partial \hat{\psi}_{\boldsymbol{k}}} + \sqrt{\frac{2\hbar}{\beta}} \hat{\xi}_{\boldsymbol{k}}, \tag{6.9}$$

where β is a real parameter corresponding to the inverse temperature and $\hat{\xi}_{\boldsymbol{k}}$ are independent Gaussian white noises of unit variance. Equation (6.9) is nothing but the gradient descent equation used in the imaginary time evolution to reach the steady state associated with the minimum of F, with the addition of the stochastic noise. The role of the noise is indeed to generate fluctuations around the ground state, whose amplitude is related to the temperature. More precisely, the stationary probability distribution, which solves the Fokker–Planck equation associated to the stochastic process (6.9), is given by the Gibbs grand-canonical distribution $\mathbb{P}\left[\hat{\psi}_{\boldsymbol{k}}\right] \propto e^{-\beta F}$. Note that such distribution is also the stationary solution (6.6) of the Liouville equation that describes the evolution of the phase-space in the microcanonical ensemble. The stochastic real Ginzburg–Landau model (6.9) has been adapted to the case when impurities are present in the system in the publication [80], reported in section 6.3.

Finally, we mention another model which can be used to study a finite temperature BEC. The stochastic Gross–Pitaevskii equation [45, 183] describes the (real time) evolution of cold bosons in contact with a thermal cloud. It reads:

$$i\hbar \frac{\partial \psi}{\partial t} = \left(1 - i\hbar \frac{\beta}{4} \gamma \right) \left[-\frac{\hbar^2}{2m} \nabla^2 \psi + g|\psi^2|\psi + V_{\mathrm{ext}} \psi \right] + \eta, \tag{6.10}$$

where $\eta(\boldsymbol{x},t)$ is a Gaussian noise such that $\langle \eta^*(\boldsymbol{x},t)\eta(\boldsymbol{x}',t')\rangle = i(\hbar^2/2)\gamma(\boldsymbol{x},t)\delta(\boldsymbol{x}'-\boldsymbol{x})\delta(t-t')$. The function $\gamma(\boldsymbol{x},t)$ describes the interaction with the thermal cloud and it is usually set to a phenomenological damping constant [40, 183]. In practice, the model (6.10) is a combination of the microcanonical dynamics of the GP equation (6.5) with the fluctuations-dissipation dynamics of the stochastic real Ginzburg–Landau model (6.9).

6.1.2 Superfluid and normal fluid decomposition from the momentum correlation

In this section we briefly recall the theoretical justification behind a useful method that allows to extract the superfluid and the normal fluid components from the decomposition of the momentum correlation matrix. Such tecnique, based on a linear response approach, is thoroughly explained for instance in [42], [176] or in the Appendix of [65] and can be applied to a mean field theory as the TGP model. We used it in the article [78], discussed below.

Consider a superfluid at finite temperature confined in a pipe. The superfluid component of the system flows with an average velocity v_s inside the pipe. The system is in equilibrium, meaning that the normal component is at rest and in equilibrium with the walls of the pipe, i.e. $v_n = 0$. In the two-fluid framework, the momentum (density) is thus carried entirely by the superfluid and reads $\boldsymbol{p} = \rho_s v_s$. Performing a Galileian transformation to the reference frame of the superfluid, moving with speed $\boldsymbol{u} = -v_s$ with respect to the pipe, the momentum density becomes

$$\boldsymbol{p} = \rho_s v_s - \rho v_s = \rho_n \boldsymbol{u}. \tag{6.11}$$

The idea is to compare Eq. (6.11) with the microscopic calculation of the momentum density, evaluated averaging over states comoving with the superfluid (with $v_s = 0$). In general, the expectation value of $\boldsymbol{p}(\boldsymbol{x}) = \frac{i\hbar}{2}(\psi\nabla\psi^* - \psi^*\nabla\psi)$ in a reference frame moving with velocity $\boldsymbol{u}$ is

$$\langle \boldsymbol{p}(\boldsymbol{x})\rangle_{\boldsymbol{u}} = \frac{\int e^{-\beta\left(H-\mu N-\boldsymbol{P}\cdot\boldsymbol{u}+\frac{1}{2}Mu^2\right)}\boldsymbol{p}(\boldsymbol{x})\mathcal{D}\psi\mathcal{D}\psi^*}{\int e^{-\beta\left(H-\mu N-\boldsymbol{P}\cdot\boldsymbol{u}+\frac{1}{2}Mu^2\right)}\mathcal{D}\psi\mathcal{D}\psi^*}, \tag{6.12}$$

where P, M and N are the total momentum, mass and wave action in the reference frame at rest. Choosing the coordinates so that the velocity $\boldsymbol{u}$ is aligned to the z direction, the normal fluid density is formally defined as [131, 140]

$$\rho_n = \left.\frac{\partial \langle p_z\rangle_u}{\partial u}\right|_{u=0}. \tag{6.13}$$

Expanding the expectation value (6.12) for small $\boldsymbol{u}$ one gets

$$\langle \boldsymbol{p}(\boldsymbol{x})\rangle_{\boldsymbol{u}} = \langle \boldsymbol{p}(\boldsymbol{x})\rangle_0 + \beta\left(\langle \boldsymbol{p}(\boldsymbol{x})\boldsymbol{P}\cdot\boldsymbol{u}\rangle_0 - \langle \boldsymbol{p}(\boldsymbol{x})\rangle_0\langle \boldsymbol{P}\cdot\boldsymbol{u}\rangle_0\right), \tag{6.14}$$

where $\langle\cdot\rangle_0$ is the expectation values in the equilibrium system at rest, in which $\boldsymbol{v}_\mathrm{s} = \boldsymbol{u} = 0$ and thus $\langle \boldsymbol{p}(\boldsymbol{x})\rangle_0 = 0$. In the infinite domain limit, where homogeneity and isotropy hold, the component of (6.14) along the direction of $\boldsymbol{u}$ (chosen to coincide with the z axis) can be rewritten as [42, 65]

$$\langle p_z(\boldsymbol{x})\rangle_{\boldsymbol{u}} = \lim_{\boldsymbol{k}\to 0} \beta \chi_{zz}(\boldsymbol{k}) u, \tag{6.15}$$

where $\chi_{ij}(\boldsymbol{k}) \propto \int \langle p_i(\boldsymbol{0}) p_j(\boldsymbol{r})\rangle_0 e^{-i\boldsymbol{k}\cdot\boldsymbol{r}}\, \mathrm{d}\boldsymbol{r}$ is the momentum correlation matrix. The subtle point is that in order to match Eq. (6.15) with the momentum density (6.11), we need to consider in the expectation value (6.12) only states with zero superfluid velocity. This is equivalent to ask that the pipe has open ends, namely it extends infinitely in the z direction. In other words, one has to perform the limit ($k_z \to 0$) before performing the infinite domain limit in the transverse direction ($\boldsymbol{k}_\perp \to 0$). On the other end, inverting the order of the limits (performing $\boldsymbol{k}_\perp \to 0$ before $k_z \to 0$) is equivalent to consider a box with closed ends. In this case all the states contributing to the expectation value (6.12) have nonzero superfluid velocity, since both the superfluid component and the normal fluid component move, together with the box, with the speed of the Galileian transformation $\boldsymbol{u}$. As a consequence, the momentum density (6.15) should be set equal to ρu instead of $\rho_\mathrm{n} u$. This argument can be generalized for an arbitrary direction of $\boldsymbol{u}$ considering the decomposition of the momentum correlation matrix in its transverse and longitudinal components:

$$\chi_{ij}(\boldsymbol{k}) = \chi_\mathrm{C}(k)\frac{k_i k_j}{k^2} + \chi_\mathrm{I}(k)\left(\delta_{ij} - \frac{k_i k_j}{k^2}\right), \tag{6.16}$$

where $\chi_\mathrm{C}(k)$ and $\chi_\mathrm{I}(k)$ are respectively the longitudinal (compressible) and transverse (incompressible) coefficients, and $k = |\boldsymbol{k}|$. Indeed, observing that

$$\lim_{\boldsymbol{k}_\perp\to 0}\lim_{k_z\to 0}\frac{k_z k_z}{k^2} = 0 \qquad \text{and} \qquad \lim_{k_z\to 0}\lim_{\boldsymbol{k}_\perp\to 0}\frac{k_z k_z}{k^2} = 1 \tag{6.17}$$

we can provide the microscopic expressions for ρ_n and ρ, confronting Eq. (6.15) respectively with $\rho_\mathrm{n} u$ (6.11) and with ρu:

$$\rho_\mathrm{n} = \beta \lim_{k\to 0}\chi_\mathrm{I}(k), \qquad \rho = \beta \lim_{k\to 0}\chi_\mathrm{C}(k). \tag{6.18}$$

Practically, the superfluid fraction and the normal fluid fraction are thus computed as

$$\frac{\rho_\mathrm{n}}{\rho} = \frac{\lim_{k\to 0}\chi_\mathrm{I}(k)}{\lim_{k\to 0}\chi_\mathrm{C}(k)}, \qquad \frac{\rho_\mathrm{s}}{\rho} = 1 - \frac{\rho_\mathrm{n}}{\rho}. \tag{6.19}$$

We stress that the analytical argument just summarized, in which boundaries and Galileian velocity have been introduced, must be intended just as a thought experiment to apply the linear response method. As it is clear from the result (6.19), the knowledge of the coefficients of the momentum correlator decomposition is actually sufficient to

estimate the superfluid and the normal fluid fractions. Indeed, such technique can be succesfully used in isotropic numerical simulations with periodic boundary conditions [65].

For completeness, we mention another method that can be used to compute the normal fluid density in the truncated GP framework. It consists in the direct evaluation of Eq. (6.13) by performing several simulations with different counterflow velocities imposed to the system, and then extrapolating the value of the momentum derivative when $u \to 0$ [130, 131]. However, besides requiring to perform many simulations, this method turns out not to be very robust because of the metastability of the truncated GP counterflow states [131].

6.2 *Publication*: Stochastic motion of finite-size immiscible impurities in a dilute quantum fluid at finite temperature

In this article we introduce the coupling between the truncated GP model (6.5) and the dynamics of immiscible and finite-size 3D impurities. The impurities are modeled with the method described in section 2.3.3 and thus they are effectively analogous to the particles described in the zero temperature works, presented in the previous chapters. We stress that both in this case and in [80] the particles are modeled with a spherical symmetry potential. Moreover, no rotational degrees of freedom are added to the particles. The roughness observed about the sphere (see Fig.1 of [78]) is due to the density fluctuations on the particle surface and it does not induce any rotation.

In the framework of dilute Bose–Einstein condensates, these kind of impurities could mimic an additional condensate satisfying the immiscibility condition in the highly repulsive regime [107, 191]. We are interested in characterizing the dynamics of such objects when they are immersed in a bosonic thermal bath. Our first observation is that an impurity thermalizes fast, respecting the classical equipartition theorem, regardless of its mass and size. Then we measure an exponential decay of the impurity velocity correlation function, suggesting that its dynamics is compatible with a standard Ornstein–Uhlenbeck process. This picture is confirmed by the transition of the mean squared displacement from a ballistic behaviour at short times to a diffusive one at large time.

The final result is the measurement of the temperature dependence of the friction coefficient, derived from the dynamical relaxation time of the impurity. We observe a linear proportionality with the temperature, which can be explained phenomenologically by a momentum exchange between the impurity and the thermal waves, in the same spirit of the Epstein drag exerted on a sphere by a classical gas [60]. Indeed, in the range of temperatures studied, the mean free path of the GP excitations (λ_{mfp} between 10ξ and 50ξ, see Fig.6.2 bottom left) is larger than the particle sizes considered ($a_{\mathrm{p}} \lesssim 10\xi$). Thus, the corresponding Knudsen number $\mathrm{Kn} = \lambda_{\mathrm{mfp}}/a_{\mathrm{p}}$ is typically larger than 1, meaning that the quantum fluid behaves more like a dilute gas of thermal waves than a continuous medium. For this reason, the Stokes drag proportional to the viscosity of the normal component of a quantum fluid is not observed by using the TGP

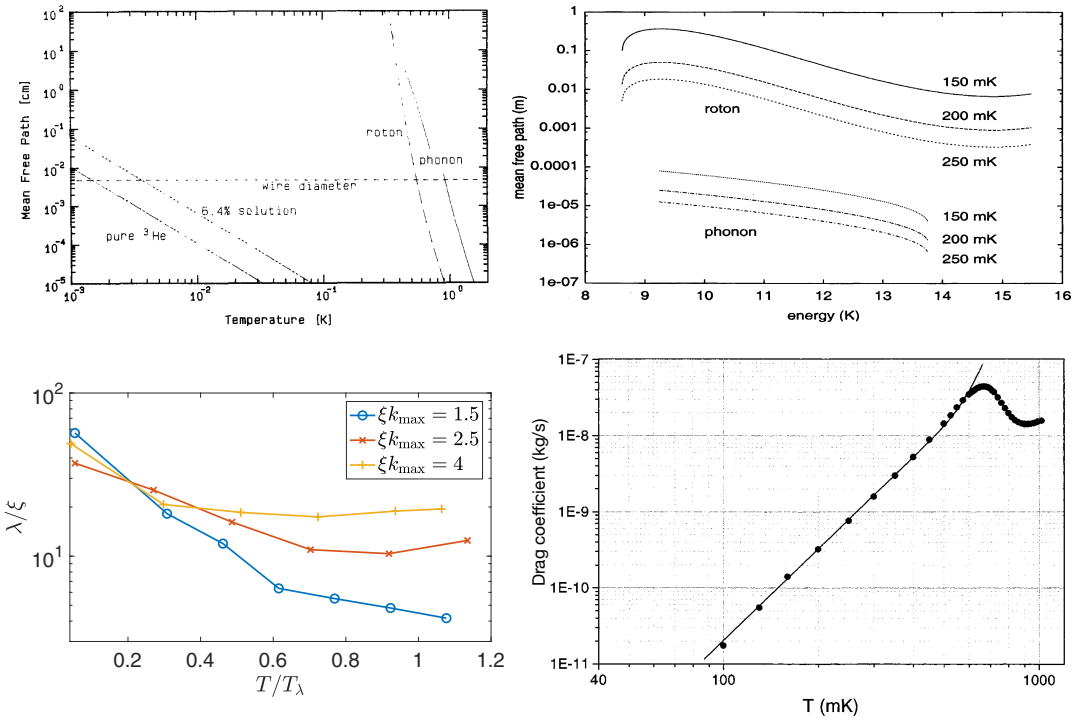


Figure 6.2. (*top left*) Temperature dependence of the mean free path of phonons and rotons in He II and that of ^{3}He-quasiparticles in ^{3}He and ^{3}He-^{4}He mixture. Figure taken from [157]. (*top right*) Mean free paths of phonons and rotons in the superfluid as a function of quasiparticle energy and superfluid temperature. Figure taken from [142]. (*bottom left*) Mean free path computed in the truncated GP system as a function of temperature for different values of $\xi k_{\max}$. Figure taken from [213]. (*bottom right*) Drag coefficient measured in the experiment discussed in [163], from which the plot is taken. The solid line is computed assuming ballistic phonon scattering.

model in the regime studied. If one wants to recover such effect, much larger particles need to be considered, which however require too expensive numerical resources and are not achievable in the current atomic BEC experimental facilities.

For what concernes liquid helium, we briefly comment here on the values of the mean free path λ_{mfp} estimated from the phonons or rotons scattering theory (see for instance [224]). Such estimations are reported in Fig.6.2 top as a function of temperature. It is evident how the mean free path strongly depends on temperature. In particular, for temperatures larger than $0.8\,K$ it is smaller than $1\,\mu m$, which is the typical size of the solidified hydrogen particles used in PTV experiments (see section 2.1.3 and references therein). Since the typical temperature of such experiments is larger than $1.5\,K$, the Knudsen number in this regime is certainly smaller than 1, implying that the drag force experienced by the particle is of the Stokes type. However, at temperatures smaller than $0.5\,K$ one can reach $\text{Kn} > 1$ for particles of a size $a_{\text{p}} > 100\,\mu m$. This is precisely the regime investigated in the experiments by Niemetz and Schoepe [163],

in which a megnetically levitated microsphere is placed in superfluid helium at very low temperature. In Fig. 6.2 bottom right the drag coefficient measured in [157] is displayed as a function of temperature. For low temperature it is dominated by the ballistic scattering of phonons and its temperature dependence is thus controled by the phonon density $\rho_{\mathrm{ph}} \propto T^4$. The physics behind such behavior is thus consistent with what we observe in the truncated GP system (see Fig.7 of [78]), although in the latter the temperature dependence of the non-condensed modes density is linear rather than quartic.

As a final note, the article presented below contains already references to the publication [80] (presented in the next section) because the latter has been completed before. However, since the stochastic motion of a single impurity is essential to trigger the clustering transition discussed in [80], it is smoother to present the work [78] first.

Stochastic motion of finite-size immiscible impurities in a dilute quantum fluid at finite temperature

Umberto Giuriato * and Giorgio Krstulovic

Université Côte d'Azur, Observatoire de la Côte d'Azur, CNRS, Laboratoire Lagrange, Boulevard de l'Observatoire CS 34229 - F 06304 NICE Cedex 4, France

(Received 22 September 2020; revised 11 December 2020; accepted 16 December 2020; published 12 January 2021)

The dynamics of an active, finite-size, and immiscible impurity in a dilute quantum fluid at finite temperature is characterized by means of numerical simulations of the Fourier truncated Gross-Pitaevskii equation. The impurity is modeled as a localized repulsive potential and described with classical degrees of freedom. It is shown that impurities of different sizes thermalize with the fluid and undergo a stochastic dynamics compatible with an Ornstein-Uhlenbeck process at sufficiently large time lags. The velocity correlation function and the displacement of the impurity are measured and an increment of the friction with temperature is observed. Such behavior is phenomenologically explained in a scenario where the impurity exchanges momentum with a dilute gas of thermal excitations, experiencing an Epstein drag.

DOI: 10.1103/PhysRevB.103.024509

I. INTRODUCTION

A Bose-Einstein condensate (BEC) is an exotic state of matter, which takes place in bosonic systems below a critical temperature, when a macroscopic fraction of particles occupy the same fundamental quantum state [1]. Almost three decades ago, Bose-Einstein condensation was observed for the first time by Anderson *et al.* in a dilute ultracold atomic gas [2]. Since then, BECs have been realized in a wide range of different systems, from solid-state quasiparticles [3,4] to light in optical microcavities [5].

Bose-Einstein condensation is intimately related to the notion of superfluidity, which is the capability of a system to flow without viscous dissipation [1]. Superfluidity was first detected almost one century ago in liquid helium ^{4}He [6,7] below 2.17 K, and it is a known feature also of atomic BECs and light in nonlinear optical systems [8]. Both superfluidity and Bose-Einstein condensation are a manifestation of quantum effects on a macroscopic scale, which is why these systems are usually called quantum fluids. Theoretically, a quantum fluid can be described by a macroscopic complex wave function. This represents the order parameter of the Bose-Einstein condensation phase transition and it is directly related to the density and the inviscid velocity of the superflow via a Madelung transformation [9].

As a consequence of superfluidity, an impurity immersed in a quantum fluid does not experience any drag and can move without resistance. However, if the speed of the impurity is too large, superfluidity is broken because of the emission of topological defects of the order parameter, known as quantum vortices [10–13]. Moreover, at finite temperature the thermal excitations in the system may interact with the impurities and drive their motion [14]. The behavior of particles and impurities immersed in a superfluid has been a central subject of study since long time [10]. The interest has been recently renewed by the experimental implementation of solidified hydrogen particles to visualize quantum vortices in superfluid helium [15,16], the study of polarons in atomic gases [17,18], and the use of impurities to investigate the properties of superfluids of light [19,20]. A particularly interesting kind of impurity arises in the immiscible regime of the multicomponent BEC. It has been shown that when two condensates of different species highly repel each other, one of the two components exists in a localized region and can be thought as a finite-size impurity [21,22]. If many components are present simultaneously, different phases can be identified, depending on the ratios between the coupling constants [22]. In particular, for positive scattering lengths between the impurity fields, the components separate from the main condensate and show a hard-sphere repulsion between each other. Experimentally, mixtures of different condensates have been realized with cold atomic gases [23,24], and the immiscibility properties have been studied [25].

In this work we aim at studying numerically the dynamics of an immiscible and finite-size impurity in a quantum fluid at finite temperature. There are several models which have been proposed to take into account finite-temperature effects in a quantum fluid, although at the moment there is no uniform consensus on which is the best one [26]. A successful example is the Zaremba-Nikuni-Griffin framework, in which a modified-dissipative Gross-Piteaevskii equation for the condensate wave function is coupled with a Boltzmann equation for the thermal cloud [27]. A simpler model is the Fourier truncated Gross-Pitaevskii (FTGP) equation, in which thermal fluctuations of the bosonic field are naturally taken into account without the coupling with an external thermal bath [28]. The main idea behind the FTGP model is that imposing an ultraviolet cutoff $k_{\max}$, and truncating the system in Fourier space, allows for the regularization of the classical ultraviolet divergence and states at thermal equilibrium can be generated. The FTGP model has been successfully used to reproduce the condensation transition [28–31], to study finite-temperature effects on quantum vortex dynam-

*umberto.giuriato7@gmail.com

 ©2021 American Physical Society

ics [32–34], and to investigate the effective viscosity in the system [35].

In this paper, we couple the FTGP equation with a minimal model for impurities, which are described as localized repulsive potentials with classical degrees of freedom [13,36]. It has been recently utilized systematically to investigate the interaction between particles and quantum vortices at very low temperature [37–40]. We stress that this minimal model is suitable for extensive numerical simulations and Monte Carlo sampling. Indeed, its simplicity makes it computationally much cheaper than more complex approaches in which the impurities have many (infinite) degrees of freedom, like the Gross-Clark model [41,42] or the multicomponent BEC model [22].

Recently, a drag force acting on an impurity in the weak coupling regime has been detected using a damped GP equation at finite temperature [43], extending an analytical work in which the resistance of the GP fluid on a point particle was studied at zero temperature [44]. In the case of immiscible active impurities, it has been shown that a multitude of them coupled with the FTGP model can form clusters, depending on the temperature and the ratio between the fluid-mediated attraction and the impurity-impurity repulsion [14]. Moreover, the presence of such clusters turned out to be responsible for an increase of the condensation temperature. However, the precise characterization of the dynamics of a single impurity immersed in a bath of FTGP thermal modes has not been addressed yet. This is indeed the purpose of this work. In the next section, we present the FTGP model coupled with a single three-dimensional impurity, and provide details for the numerical techniques used to simulate such system. In Sec. III, we present a statistical analysis of extensive numerical simulations of the system. In particular, we find that at large times the dynamics of an impurity in a finite-temperature quantum fluid is akin to an Ornstein-Uhlenbeck process with a temperature-dependent friction coefficient, that we are able to explain. Eventually, we exploit this information to show that for the sizes of the impurities considered, their motion is consistent with a scenario where the thermal excitations behave as a gas of waves rather than a continuum liquid.

II. FINITE-TEMPERATURE MODEL

We use the Fourier truncated Gross-Pitaevskii model to describe a weakly interacting quantum fluid at finite temperature, with a repulsive impurity immersed in it [14]. The Hamiltonian of the model is given by

$$H = \int \left(\frac{\hbar^2}{2m} |\nabla \psi|^2 + \frac{g}{2} |\mathcal{P}_G[|\psi|^2]|^2 \right) d\mathbf{x} + \int V_I(|\mathbf{x} - \mathbf{q}|) \mathcal{P}_G[|\psi|^2] \, d\mathbf{x} + \frac{\mathbf{p}^2}{2M_I}, \tag{1}$$

where $\psi(\mathbf{x}, t)$ is the bosonic field, m is the mass of the constituting bosons, and $g = 4\pi a_s \hbar^2/m$ is the self-interaction coupling constant, with a_s the boson s-wave scattering length.

The bosonic field is coupled with an impurity of mass M_I, described by its classical position $\mathbf{q}(t)$ and momentum $\mathbf{p}(t) = M_I \dot{\mathbf{q}}(t)$. The impurity is modeled by a repulsive potential $V_I(|\mathbf{x} - \mathbf{q}|)$, which defines a spherical region centered in $\mathbf{q}(t)$ where the condensate is completely depleted. Note that the functional shape of the potential $V_I(|\mathbf{x} - \mathbf{q}|)$ is not important, provided that it is sufficiently repulsive to completely deplete the fluid. The relevant parameter is indeed the size of the depleted region, which in turns identifies the impurity radius a_I. The Galerkin projector $\mathcal{P}_G$ truncates the system imposing an UV cutoff in Fourier space: $\mathcal{P}_G[\hat{\psi}_\mathbf{k}] = \theta(k_{\max} - |\mathbf{k}|)\hat{\psi}_\mathbf{k}$ with $\theta(\cdot)$ the Heaviside theta function, $\hat{\psi}_\mathbf{k}$ the Fourier transform of $\psi(\mathbf{x})$ and $\mathbf{k}$ the wave vector. The time-evolution equation of the wave function and the impurity are obtained straightforwardly by varying the Hamiltonian (1):

$$i\hbar \frac{\partial \psi}{\partial t} = \mathcal{P}_G \left[-\frac{\hbar^2}{2m} \nabla^2 \psi + g \mathcal{P}_G[|\psi|^2] \psi + V_I(|\mathbf{x} - \mathbf{q}|) \psi \right], \tag{2}$$

$$M_I \frac{d\dot{\mathbf{q}}}{dt} = - \int V_I(|\mathbf{x} - \mathbf{q}|) \mathcal{P}_G[\nabla |\psi|^2] \, d\mathbf{x}. \tag{3}$$

Note that the projection of the density $|\psi|^2$ in Eq. (2) is a dealiasing step that is necessary to conserve momentum [34] in the truncated equations. This procedure slightly differs with the projected Gross-Pitaevskii model [28] as some high-momentum scattering processes are not considered in the FTGP framework.

At zero temperature and without the impurity, Eq. (2) can be linearized about the condensate ground state $\psi_0 = |\psi_0| \exp(-i\mu t/\hbar)$, fixed by the chemical potential $\mu = g|\psi_0|^2$. The excitations of the condensate propagate with the Bogoliubov dispersion relation

$$\omega_B(k) = ck \sqrt{1 + \frac{\xi^2 k^2}{2}}, \tag{4}$$

where $k = |\mathbf{k}|$, $c = \sqrt{g|\psi_0|^2/m}$ is the speed of sound, and $\xi = \sqrt{\hbar/2gm|\psi_0|^2}$ defines the healing length at zero temperature. Note that the impurity completely depletes the condensate in the region where $V_I > \mu$.

The Hamiltonian H and the number of bosons $N = \int |\psi|^2 d\mathbf{x}$ are invariants of the FTGP model. Thus, it possesses finite-temperature absolute equilibrium solutions, distributed with the probability

$$\mathbb{P}[\psi, \mathbf{q}, \dot{\mathbf{q}}] \propto e^{-\beta(H - \mu N)}. \tag{5}$$

The concept of absolute equilibria of Fourier truncated equations was first introduced in the context of the Euler equation [45,46] and directly generalizes to FTGP [34]. Such equilibria are steady solutions of the associated Liouville equation. The Liouville equation describes the microcanonical evolution of the phase-space distribution function of an ensemble of states driven by Eqs. (2) and (3). Note that a state which solves Eqs. (2) and (3) conserves the invariants N and H, and the equilibrium distribution in Eq. (5) is nothing but the probability of picking one of these states at given inverse temperature β and chemical potential μ. This is true whether the impurity is present in the system or not. The argument of the exponential in Eq. (5) is a linear combination of the invariants H and N, and β is a Lagrange multiplier identified with the inverse temperature. Given a random initial condition with energy H and number of bosons N, long time integration of Eqs. (2) and (3) will let the system evolve to an equilibrium

state belonging to the distribution (5). The temperature is not directly available as a control parameter since such dynamics is microcanonical, but it is biunivocally associated to the given conserved invariants [28].

At finite temperature, many modes are excited and interact nonlinearly. Such interactions lead to a spectral broadening of the dispersion relation, together with small corrections of the frequency. Overall, the dispersion relation can be well approximated taking into account the depletion of the condensate mode in the following manner [35]:

$$\omega_{\rm B}^{T}(k) = ck\sqrt{n_0(T) + \frac{\xi^2 k^2}{2}}, \tag{6}$$

where $n_0(T)$ is the condensate fraction. We define it as

$$n_0(T) = \frac{\langle |\int \psi\, d\mathbf{x}|^2 \rangle_T}{\langle |\int \psi\, d\mathbf{x}|^2 \rangle_{T=0}}, \tag{7}$$

namely, as the ratio between the occupation number of the zero mode at temperature T and at temperature $T = 0$. With such definition, the condensate fraction is normalized to be one at zero temperature. In this way, the depletion of the condensate due to the presence of the impurity is properly taken into account [14]. The fraction of superfluid component $n_{\rm s}(T) = \rho_{\rm s}/\bar{\rho}$ and normal fluid component $n_{\rm n}(T) = \rho_{\rm n}/\bar{\rho}$, where $\bar{\rho} = \frac{1}{L^3}\int m|\psi|^2\, d\mathbf{x}$ is the average mass density, can be computed using a linear response approach [14,47,48]. They read as, respectively,

$$n_{\rm n}(T) = \frac{\lim_{k\to 0}\chi_I(k)}{\lim_{k\to 0}\chi_C(k)}, \quad n_{\rm s}(T) = 1 - n_{\rm n}(T), \tag{8}$$

where $\chi_C(k)$ and $\chi_I(k)$ are, respectively, the compressible (longitudinal) and incompressible (transverse) coefficients of the two-point momentum correlator:

$$\langle \hat{j}_i(\mathbf{k})\hat{j}_j(-\mathbf{k})\rangle \propto \frac{k_i k_j}{k^2}\chi_C(k) + \left(\delta_{ij} - \frac{k_i k_j}{k^2}\right)\chi_I(k), \tag{9}$$

with $\hat{j}_i(\mathbf{k}, t)$ the Fourier transform of the ith component of the momentum density $j_i(\mathbf{x}, t) = \frac{i\hbar}{2}[\psi\partial_i\psi^* - \psi^*\partial_i\psi]$.

A. Numerical methods and parameters

In the numerics presented in this work, we integrate the system (2) and (3) by using a pseudospectral method with $N_{\rm res} = 128$ uniform grid points per direction of a cubic domain of size $L = 2\pi$. We further set the UV cutoff $k_{\rm max} = N_{\rm res}/3$, so that, aside from the Hamiltonian H and the number of bosons N, the truncated system (2) and (3) conserves the total momentum $\mathbf{P} = \int \frac{i\hbar}{2}(\psi\nabla\psi^* - \psi^*\nabla\psi)d\mathbf{x} + \mathbf{p}$ as well (provided that initially $\mathcal{P}_{\rm G}[\psi] = \psi$ and $\mathcal{P}_{\rm G}[V_{\rm I}] = V_{\rm I}$) [34,39]. In thermal states, the cutoff $k_{\rm max}$ plays an important role. The dimensionless parameter $\xi k_{\rm max}$ controls the amount of dispersion of the system and therefore the strength of the nonlinear interactions of the BEC gas. The smaller its value, the stronger the interaction is. Note that, as scales of the order of the healing length have to be resolved numerically, it cannot be arbitrarily small. See, for instance, Refs. [34,35] for further discussions. In this work we fix this parameter to $\xi k_{\rm max} = 2\pi/3$. Note that in our results all the lengths are expressed in units of the healing length at zero temperature ξ and the velocities in units of the speed of sound c at zero temperature. In these units, the system size is $L = 128\xi$.

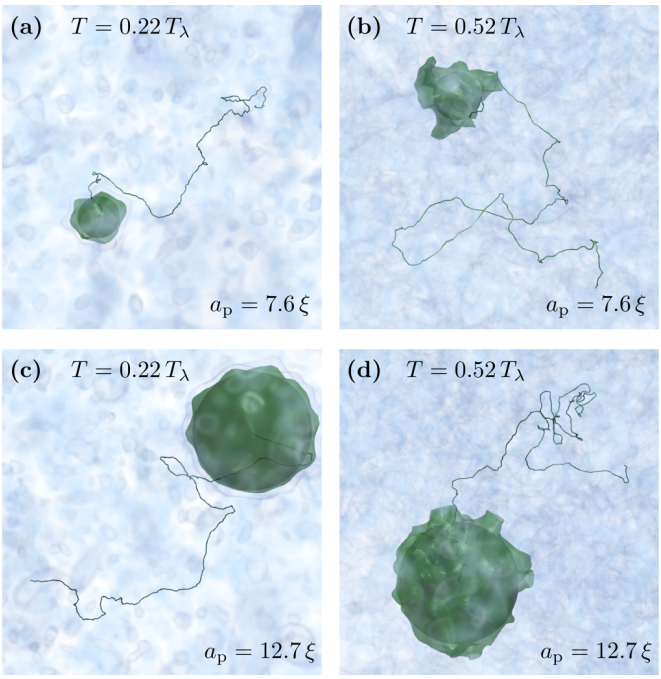


FIG. 1. Snapshots of the GP field with an impurity of size $a_{\rm I} = 7.6\xi$ at time $t = 3056\xi/c$ [(a), (b)] and an impurity of size $a_{\rm I} = 12.7\xi$ at time $t = 7130\xi/c$ [(c), (d)] at temperatures $T = 0.22\,T_\lambda$ [(a), (c)] and $T = 0.52\,T_\lambda$ [(b), (d)]. The GP sound waves are rendered in blue, the dark sphere is the impurity potential, and the green surfaces are contours of the GP density at $\rho/\bar{\rho} = 0.15$. The impurity trajectory is displayed as a solid line.

The potential used to model the impurity is a smoothed hat function $V_{\rm I}(r) = \frac{V_0}{2}(1 - \tanh[\frac{r^2-\eta_a^2}{4\Delta_a^2}])$. The impurity radius $a_{\rm I}$ is estimated at zero temperature by measuring the volume of the displaced fluid $\frac{4}{3}\pi a_{\rm I}^3 = \int(|\psi_0|^2 - |\psi_{\rm p}|^2)\, d\mathbf{x}$, where $\psi_{\rm p}$ is the steady state with one impurity. The impurity mass density is then $\rho_{\rm I} = M_{\rm I}/(\frac{4}{3}\pi a_{\rm I}^3)$. In all the simulations we fix $\mu = |\psi_0| = 1$ and for the impurity potential $V_0 = 20\mu$ and $\Delta_a = 2.5\xi$. We consider an impurity of radius $a_{\rm I} = 7.6\xi$ setting $\eta_a = 2\xi$ and an impurity of size $a_{\rm I} = 12.7\xi$ setting $\eta_a = 10\xi$.

Note that, although the shape of the impurity potential is fixed, fluctuations of the impurity surface are allowed by the model. Such fluctuations are shown in Fig. 1 (that will be commented in Sec. III) as green contours of the fluid density at a low value around the spherical potential.

We prepare separately the ground state with an impurity $\psi_{\rm p}$ (at zero temperature) and the FTGP states at finite temperature ψ_T, without the impurity. The first one is obtained by performing the imaginary-time evolution of Eq. (2), while the second one is realized with the stochastic real Ginzburg-Landau (SRGL) [14,34,35], protocol that allows to explicitly control the temperature. The SRGL method is briefly recalled below. The initial condition for the FTGP simulations is then obtained as $\psi = \psi_{\rm p} \times \psi_T$. For our analysis, we considered $\sim$22 different realizations for each of the 15 studied temperatures and for each impurity. The initial velocity of the

impurity is always set to zero and the temporal length of each realization is $\sim 9000\,\xi/c$. In all the statistical analysis presented in the following sections, we checked that including or not the data associated to the early times of the simulation does not change the results. The thermalization of the impurity will be studied explicitly in Sec. III, but this fact gives already a first indication that the impurity reaches the equilibrium with the thermal bath in the very early stages of the simulations.

We operatively define the condensation temperature T_λ as the first point of the temperature scan at which the condensate fraction $n_0(T)$ goes to zero. The normal fluid fraction $n_\mathrm{n}(T)$ and consequently the superfluid fraction $n_\mathrm{s}(T) = 1 - n_\mathrm{n}(T)$ are evaluated numerically with the following protocol [48]. At fixed temperature, we measure the angle-averaged incompressible and compressible spectra of the momentum correlator, respectively, $\chi_I^{1d}(k) \propto \langle k^2 |\mathbf{j}_I(\mathbf{k})|^2\rangle$ and $\chi_C^{1d}(k) \propto \langle k^2 |\mathbf{j}_C(\mathbf{k})|^2\rangle$. We fit the logarithm of $\chi_I^{1d}(k)/k^2$ and $\chi_C^{1d}(k)/k^2$ with a cubic polynomial in the range $3L/2\pi < k < 3k_\mathrm{max}/2$; we extrapolate the values of the fits at $k = 0$ and finally divide them to get $n_\mathrm{n}(T) = \chi_I(k=0)/\chi_C(k=0)$. Such method works well at low temperatures while it is strongly affected by numerical noise at temperatures $T \gtrsim T_\lambda$ [48]. These last points are then simply assumed to be equal to zero.

Finally, note that in this work, if not explicitly specified, all the averages are intended over realizations for a fixed temperature T. Moreover, because of isotropy, we treat each dimension of any vectorial quantity as a different realization of the same distribution.

B. Grand-canonical thermal states

We recall here the SRGL protocol used to obtain equilibrium thermal states of the truncated GP equation. We refer to Ref. [34] for further details about the method. The FTGP grand-canonical thermal states obey the (steady) Gibbs distribution which coincides with Eq. (5). A stochastic process that converges to a realization of this probability distribution is given by the following stochastic equation (in physical space):

$$\hbar\frac{\partial\psi}{\partial t} = \mathcal{P}_\mathrm{G}\left[\frac{\hbar^2}{2m}\nabla^2\psi + \mu\psi - g\mathcal{P}_\mathrm{G}[|\psi|^2]\psi + V_\mathrm{I}(|\mathbf{x}-\mathbf{q}|)\psi\right] + \sqrt{\frac{2\hbar}{\beta L^3}}\mathcal{P}_\mathrm{G}[\zeta(\mathbf{x},t)], \tag{10}$$

where $\zeta(\mathbf{x},t)$ is a complex Gaussian white noise with zero mean and delta correlated in space and time: $\langle\zeta(\mathbf{x},t)\zeta^*(\mathbf{x}',t')\rangle = \delta(\mathbf{x}-\mathbf{x}')\delta(t-t')$. In principle, such process is coupled with analogous equations for the impurity degrees of freedom [14]. Here, we do not consider them since we are interested in generating thermal states without impurities. As explained in the previous section, the impurity is added afterwards to the thermal states in order to observe its dynamics according to the evolution equations (2) and (3). In the right-hand side of Eq. (10) a deterministic term and a stochastic term compete against each other. The distribution which entails the balance between such fluctuations and dissipation is Eq. (5), i.e., the steady solution of the Fokker-Planck equation associated to Eq. (10) [34].

We define the temperature as $T = 1/k_\mathcal{N}\beta$, where $k_\mathcal{N} = L^3/\mathcal{N}$ and $\mathcal{N} = \frac{4}{3}\pi k_\mathrm{max}^3$ is the number of Fourier modes in the system. With this choice, the temperature has units of energy density and the intensive quantities remain constant in the thermodynamic limit, that is $k_\mathrm{max} \to \infty$ with L constant. Finally, in order to control the steady value of the average density $\bar\rho$, the chemical potential is also dynamically evolved with the *ad hoc* equation $\dot\mu = -\nu_\rho(\bar\rho - \bar\rho_\mathrm{t})$ during the stochastic relaxation. In this way, the system converges to the control density $\bar\rho = \bar\rho_\mathrm{t}$ that we set equal to $m|\psi_0|^2 = 1$.

We finally mention that a similar approach can be used to generate and study thermal states, which is the stochastic GP model [26]. There, the stochastic relaxation (10) is combined with the physical GP evolution (2). However, unlike the FTGP model, the stochastic GP model is dissipative and has an adjustable parameter in which the interaction between the condensate and the thermal cloud is encoded.

III. IMPURITY MOTION

We perform a series of numerical simulations of the models (2) and (3), varying the temperature and the size of the impurity. Typical impurity trajectories are displayed in Fig. 1 for two different temperatures, together with a volume rendering of the field and of the impurity. The motion of the impurity is clearly driven by a random force, due to the interaction with the thermal excitations of the condensate.

Before studying the stochastic dynamics of the impurity, we characterize some properties of the thermal states that will be used later. In Fig. 2(a) we show the condensate fraction n_0, the superfluid component n_s, and the normal fluid component n_n plotted against temperature. The lines refer to the simulations without impurity while the circles are obtained in presence of the largest impurity considered ($a_\mathrm{I} = 12.7\xi$). Almost no difference between the two cases is detected since the volume occupied by the impurity is only 0.5%. Indeed, in Ref. [14] it was shown that the condensate fraction starts to increase at high temperatures if the impurities filling fraction is larger than 4%. We can therefore safely assume that the impurity has no impact on the statistical properties of the thermal fluctuations.

From the impurity (3), we observe that the quantum fluid interacts with the impurity via a convolution between the impurity potential and the density gradient. It is thus interesting to understand the typical correlation time of density fluctuations, in particular of its gradients. In Fig. 2(b) we compute the decorrelation time τ_GP of the thermal excitations as a function of temperature. Such time is evaluated performing a FTGP evolution of thermal states without impurity and considering the time correlator of one of the components of the density gradient:

$$C_{\partial\rho}(t) = \frac{\langle\partial_i\rho(t_0)\partial_i\rho(t_0+t)\rangle}{\langle(\partial_i\rho)^2\rangle}. \tag{11}$$

The averages in Eq. (11) are performed over space and different realizations. Three examples for three different temperatures of the time evolution of this correlator are shown in the inset of Fig. 2(b). They show a damped oscillating behavior and touch zero for the first time after a time $\sim 1c/\xi$. We estimate the decorrelation time τ_GP as the time after which the correlator (11) is always less than 1%. At timescales larger than τ_GP, we expect that the interactions between the impurity

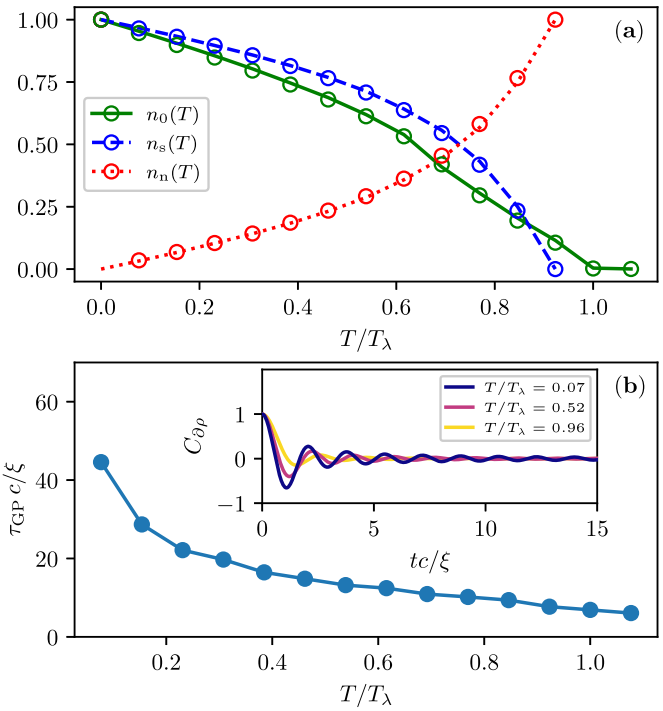


FIG. 2. (a) Temperature evolution of condensate fraction (green solid line), superfluid fraction (dashed blue line), and normal fraction (dotted red line) for simulations without impurity. The circles of corresponding colors refer to simulations in presence of an impurity of size $a_I = 12.7\xi$ and mass density $\rho_I = \bar{\rho}$. (b) Temperature evolution of the decorrelation time of the FTGP density gradients. (Inset) Time evolution of the two-point correlators of the FTGP density gradients (11) for three different temperatures.

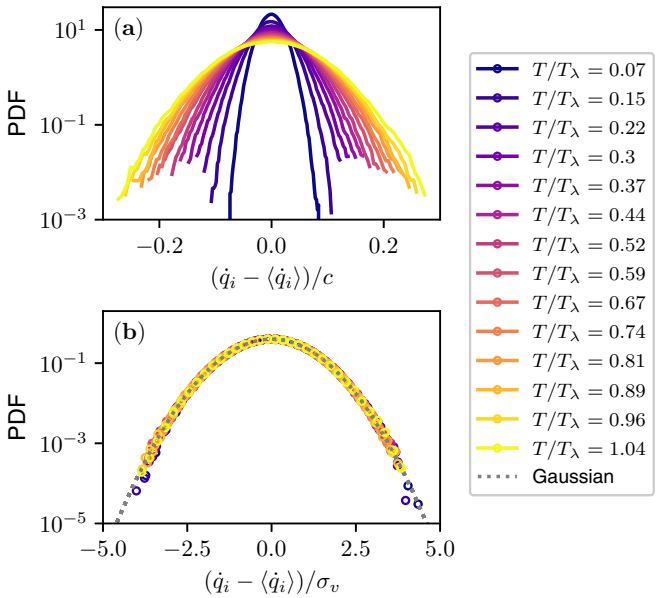


FIG. 3. PDF of the single-component velocity of an impurity of size $a_I = 7.6\xi$ and mass density $\rho_I = \bar{\rho}$, for different temperatures. (a) Velocities normalized with the speed of sound at zero temperature. (b) Velocities normalized with the standard deviation. Dotted black line is a Gaussian distribution with zero mean and unit variance.

and the thermal excitations can be considered as random and rapid. Before checking if this is the case, we verify explicitly whether the impurity reaches the thermal equilibrium with the quantum fluid.

If the number of the excitations-impurity interactions is large, the velocity of the impurity is expected to be normally distributed at the equilibrium, in accordance with the central limit theorem. Indeed, we show this in Fig. 3, where the probability density function (PDF) for the single component of the impurity velocity is displayed. Assuming ergodicity, the PDFs are computed averaging also over time, besides over realizations. Since we expect the impurity to be in thermal equilibrium with the surrounding GP fluid, the second-order moment of its velocity should relax to a constant value, that is related to the temperature via the equipartition of energy:

$$\langle \dot{q}_i^2 \rangle = \frac{k_{\mathcal{N}} T}{M_I}. \tag{12}$$

The perfect agreement between Eq. (12) and the numerical simulations is displayed in Fig. 4. It confirms that the impurity is indeed in thermal equilibrium with the thermal bath. Note that the linear scaling with temperature persists also at high temperatures, where the GP energies are not in equipartition anymore because of high nonlinear interactions. This is not a contradiction since the impurity is a classical object with a simple quadratic kinetic energy. For comparison, the deviation from equipartition of the GP energy density $e_{GP} = (H - \mu N)/L^3 + \mu^2/2g$ (without impurities) is reported in the inset of Fig. 4.

We consider now the evolution of the two-point impurity velocity correlator $C_v(t)$. If the collisions between the superfluid thermal excitations and the impurity are fast and random, we expect it to decay as

$$C_v(t) = \lim_{t\to\infty} \frac{\langle \dot{q}_i(t_0)\dot{q}_i(t_0+t)\rangle - \langle \dot{q}_i\rangle^2}{\langle \dot{q}_i^2\rangle - \langle \dot{q}_i\rangle^2} = e^{-\frac{t}{\tau_I}}, \tag{13}$$

where τ_I is the dynamical correlation time of the impurity velocity. Specifically, the behavior (13) should certainly hold

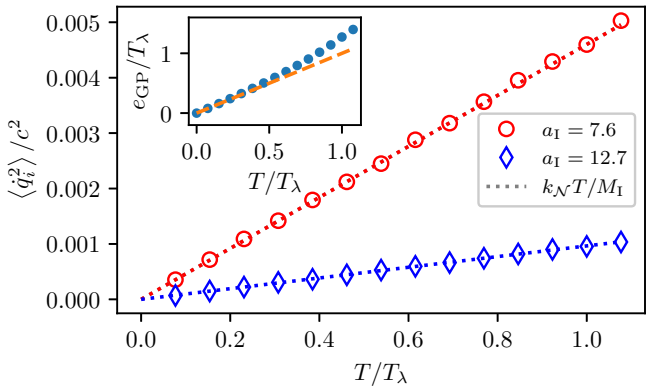


FIG. 4. Second-order moment of the single-component velocity of impurities of size $a_I = 7.6\xi$ (red circles) and $a_I = 12.7\xi$ (blue diamonds), as a function of the temperature. The mass density is $\rho_I = \bar{\rho}$ for both. (Inset) GP energy density versus temperature (blue points). Orange dashed line is the equipartition line $e_{GP} = T_\lambda$.

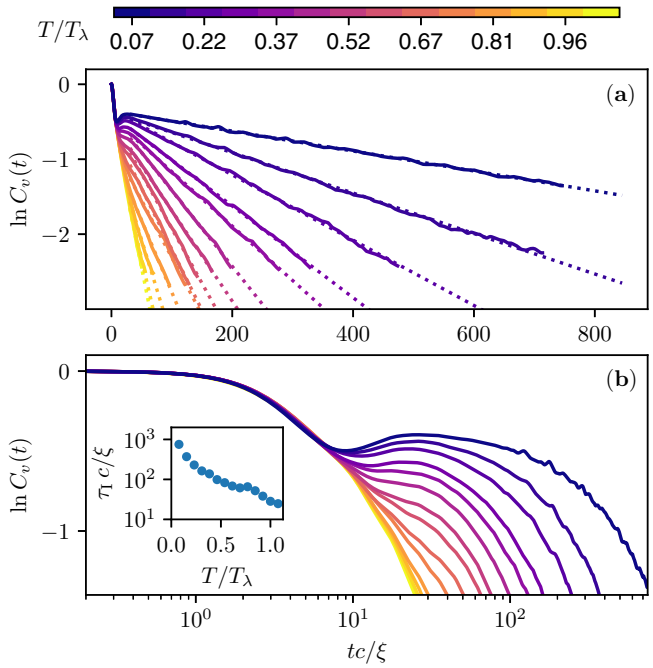


FIG. 5. Time evolution of the two-point velocity correlator for the impurity of size $a_I = 7.6\xi$ and mass density $\rho_I = \bar{\rho}$ in (a) log-lin scale and (b) log-log scale. Different colors are associated to different temperatures (same legend of Fig. 3). Dotted lines are linear fits. (Inset) Temperature evolution of the dynamical correlation time of the impurity.

at time lags larger than the decorrelation time of the GP excitations τ_{GP}, estimated in Fig. 2(b). This scenario is confirmed by the measurements of $C_v(t)$, reported in Fig. 5 for the impurity of size $a_I = 7.6\xi$. The exponential decay is evident for time lags larger than $\sim 10\xi/c$ for all the temperatures.

According to the results mentioned so far, at sufficiently large timescales the interactions between the impurity and the thermal bath can be considered to be effectively fast, random, and decorrelated. Thus, it is natural to suppose that the impurity dynamics may be described by the Ornstein-Uhlenbeck (OU) process [49]:

$$M_I \ddot{\mathbf{q}} = -\gamma \dot{\mathbf{q}} + \sqrt{\sigma^2}\zeta_r(t), \tag{14}$$

where $\zeta_r(t)$ is a (Gaussian) white noise in time, i.e., $\langle \zeta_r(t) \rangle = 0$ and $\langle \zeta_{r,i}(t_1)\zeta_{r,j}(t_2)\rangle = \delta_{ij}\delta(t_1 - t_2)$ where σ^2 is related to the diffusion coefficient. The term $-\gamma\dot{\mathbf{q}}$ is the drag force, with γ a friction coefficient that in general may depend on temperature and on the impurity size. In particular, the friction should be directly related to exponential decay timescale τ_I of the correlator (13) as $\gamma = M_I/\tau_I$. In Fig. 5 we clearly see that the correlators decay faster for higher temperatures. The values of the correlation time τ_I at different temperatures are obtained through linear fits of $\ln C_v(t)$, shown as dotted lines in Fig. 5(a). The decreasing of τ_I with temperature is then explicitly displayed in the inset of Fig. 5(b). Note that $\tau_I \gg \tau_{GP}$, consistently with the assumptions of the OU process. The physical consequence of such behavior, according to the OU picture, is that the friction γ between the impurity and the fluid is larger for larger temperatures. We will dedicate the next section to the discussion on the temperature dependence of γ.

We briefly comment on the short time-lag limit ($t \lesssim 10\xi/c$), where the measured correlator appears to decay fast and with the same slope for all the temperatures. This is particularly evident in the log-log plots in Fig. 5(b). In this regime, the assumptions necessary for an OU regime to be established are certainly not valid. Indeed, we are looking at timescales shorter than the decorrelation time of the thermal excitations τ_{GP}, so that the collisions between the excitations and the impurity cannot be considered random, rapid, and decorrelated as in the forcing $\zeta_r(t)$ in (14). It is worth noting that, for low temperatures, the velocity correlator partially recovers before the exponential decay. This unusual feature may be a consequence of a lack of decorrelation due to the small fraction of thermal excitations at low temperatures, which prevents the emergence of a diffusive regime. Such phenomenon requires further investigations.

Another important prediction that can be obtained from the OU process is that the variance of the displacement $\delta_t q_i(t) = q_i(t + t_0) - q_i(t_0)$ obeys the law

$$\langle (\delta_t q_i)^2 \rangle = \frac{\sigma^2 M_I}{\gamma^3}\left(\frac{\gamma}{M_I}t - 1 + e^{-\frac{\gamma}{M_I}t}\right). \tag{15}$$

Two regimes can be identified. At short time lags [but still large enough to consider the forcing $\zeta_r(t)$ delta correlated], the displacement is ballistic

$$\langle (\delta_t q_i)^2 \rangle \underset{t \ll M_I/\gamma}{\longrightarrow} \frac{\sigma^2}{2\gamma M_I}t^2. \tag{16}$$

Conversely, after the dynamical relaxation, a diffusive regime is established

$$\langle (\delta_t q_i)^2 \rangle \underset{t \gg M_p/\gamma}{\longrightarrow} \frac{\sigma^2}{\gamma^2}t = 2Dt, \tag{17}$$

where we have defined the diffusion constant $D = \sigma^2/2\gamma^2$.

Finally recall that, since in the OU process we also have that $\langle \dot{q}_i^2 \rangle = \sigma^2/2M_I\gamma = D\gamma/M_I$, the diffusion coefficient in Eq. (17) can be related to the equipartition of energy in thermal equilibrium (5) through the Einstein relation

$$D = \frac{k_{\mathcal{N}}T}{\gamma}. \tag{18}$$

The measurements of the average squared displacement for the impurity of size $a_I = 7.6\xi$ are shown in Fig. 6 for all the temperatures analyzed, and compared with the OU predictions. Once the squared displacement is normalized with the prefactor of the prediction (15) and assuming the Einstein relation (18) to estimate the diffusion coefficient, the separation between the ballistic regime and the diffusive one is apparent (bottom panel). The transition happens at the measured values of the dynamical correlation time $t = \tau_I$, confirming the validity of the analysis of the velocity correlator. The diffusion coefficient D is measured as the slope of the squared displacement in the diffusive regime and it is shown in the inset of Fig. 6(a). It is slightly larger than the prediction given by the Einstein relation (18). Such trend can be the signature of a memory effect due to a stochastic forcing of the fluid on the impurity which is not perfectly

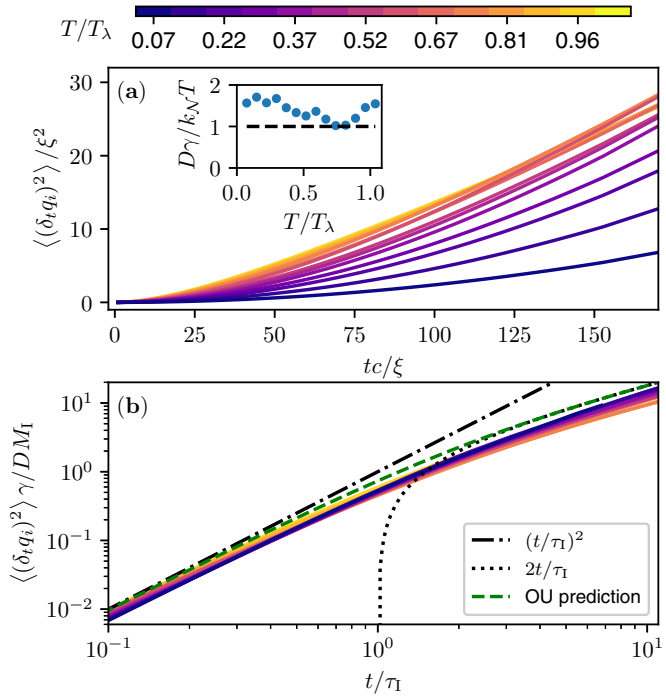


FIG. 6. Time evolution of the averaged squared displacement for the impurity of size $a_\mathrm{I} = 7.6\xi$ for different temperatures. Different colors are associated to different temperatures (same legend of Fig. 3). Dashed green line is the prediction (15), assuming the Einstein relation (18), dashed-dotted black line and dotted line are, respectively, the asymptotic equations (16) and (17). (a) lin-lin scale, times normalized with ξ/c and distances normalized with ξ. (b) log-log scale, times normalized with the correlation time τ_I and distances normalized with the prefactor of (15). (Inset) Measured diffusion coefficient as a function of temperature compared with the Einstein relation (18).

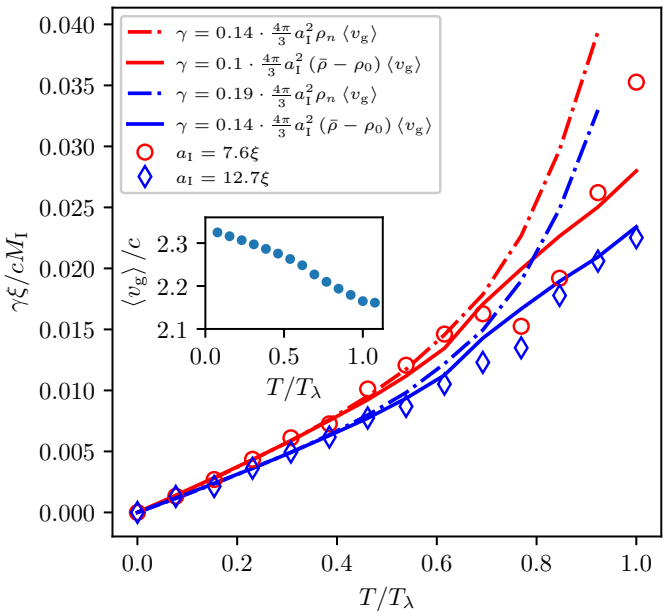


FIG. 7. Friction coefficient γ nondimensionalized by cM_I/ξ as a function of the temperature, for impurities of size $a_\mathrm{I} = 7.6\xi$ (red circles) and $a_\mathrm{I} = 12.7\xi$ (blue diamonds), with mass density $\rho_\mathrm{I} = \bar\rho$. Dashed-dotted lines are fits of the Epstein drag (20) using the normal fluid density ρ_n. Solid lines are fits of the Epstein drag using the density of noncondensed modes $\bar\rho - \rho_0$. (Inset) Average excitation velocity $\langle v_\mathrm{g}\rangle$ (21) as a function of temperature.

delta correlated. For instance, it could be traced back to the presence of coherent structures in the fluid or to the impurity surface fluctuations, due to the actual interaction between the impurity and the thermal excitations.

Friction modeling

In this section we show explicitly the behavior of the friction coefficient observed in the numerical simulations and we give a phenomenological argument to explain it. In Fig. 7, the friction γ is plotted as a function of the temperature for the two impurity sizes analyzed (red circles for the small one and blue diamonds for the large one). Each value of $\gamma = M_\mathrm{p}/\tau_\mathrm{I}$ is estimated from the measured decay time τ_I of the impurity velocity correlator, shown in the inset of Fig. 5(b).

In general terms, the friction γ depends on the interaction between the impurity and the surrounding fluid. For a classical fluid there are different regimes, depending on the value of the Knudsen number $\mathrm{Kn} = \lambda_\mathrm{mfp}/a_\mathrm{I}$, where λ_mfp is the mean-free path of the fundamental constituents of the fluid. If $\mathrm{Kn} \ll 1$, at the scale of the impurity, the fluid can be effectively considered as a continuous medium and the Navier-Stokes equations hold. As a consequence, the drag force acting on the impurity is the standard Stokes drag $\mathbf{F}_\mathrm{d} = -6\pi a_\mathrm{I}\eta\dot{\mathbf{q}}$ [50], so that the friction is related to the viscosity η as

$$\gamma = 6\pi a_\mathrm{I}\eta. \tag{19}$$

Instead, if $\mathrm{Kn} \gg 1$, the fluid behaves as a dilute gas of free molecules. In this case, the resistance of the impurity is well described by the Epstein drag [51]:

$$\mathbf{F}_\mathrm{d} = -\gamma\dot{\mathbf{q}}, \quad \gamma = \frac{4\pi}{3} C_\mathrm{d} a_\mathrm{I}^2 \rho_\mathrm{g} \langle v_\mathrm{g}\rangle = C_\mathrm{d} \frac{M_\mathrm{I}\rho_\mathrm{g}\langle v_\mathrm{g}\rangle}{a_\mathrm{I}\rho_\mathrm{I}}, \tag{20}$$

where ρ_g is the mass density of the gas and $\langle v_\mathrm{g}\rangle \gg |\dot{\mathbf{q}}|$ is the average velocity of the molecules. The prefactor C_d is a dimensionless constant that depends on the interaction between the impurity and the fluid molecules. In the case of elastic collisions of the fluid excitations (specular reflection), a simple way of understanding the formula (20) is summarized in the following [52]. If an object of mass M_I moves with velocity $\dot{\mathbf{q}}$ in an isotropic gas of free molecules, the momentum exchanged in the collision between a surface element dA and a molecule (assuming elastic collisions) is $\Delta\mathbf{p} \sim -2m_\mathrm{g}|\dot{\mathbf{q}}|\cos\theta\hat{\mathbf{n}}$, where $m_\mathrm{g} \ll M_\mathrm{I}$ is the molecule mass and θ is the angle between the object velocity and the outward normal to the surface element $\hat{\mathbf{n}}$. Assuming that the typical speed of the molecules $\langle v_\mathrm{g}\rangle$ is much larger than the object velocity, the average number of collisions in a time interval Δt is $dn_\mathrm{coll} = n_\mathrm{g}\langle v_\mathrm{g}\rangle\Delta t\, dA$, which is the number density of molecules $n_\mathrm{g} = \rho_\mathrm{g}/m_\mathrm{g}$ times the volume spanned by each molecule $\langle v_\mathrm{g}\rangle\Delta t\, dA$. The infinitesimal force arising from the momentum exchange is therefore $d\mathbf{F}_\mathrm{d} = (\Delta\mathbf{p}/\Delta t)\, dn_\mathrm{coll}$. By symmetry, if the object is spherical, the force components orthogonal to its direction of motion will cancel. Accounting for this, the net drag force results from the integration

of $|d\mathbf{F}_\mathrm{d}|\cos\theta(\dot{\mathbf{q}}/|\dot{\mathbf{q}}|)$ over half of the sphere surface. This leads precisely to Eq. (20) with $C_\mathrm{d}=1$. Considering different reflection mechanisms leads to the same equation with a different value of the prefactor C_d. For instance, in the case of full accommodation of the excitations with the impurity surface one gets $C_\mathrm{d}=(1+\pi/8)\sim 1.39$ [51].

The mean-free path $\lambda_\mathrm{mfp}(T)$ in the FTGP model has been recently estimated in Ref. [35] as the product of the group velocity of the excitations and the nonlinear interaction time (i.e., the reciprocal of the spectral broadening of the dispersion relation) at a given temperature. For $\xi k_\mathrm{max}=2\pi/3$, the value used in this work, the mean-free path λ_mfp turns out to lie between $10\,\xi$ and $50\,\xi$ at temperatures $T<0.7\,T_\lambda$, thus larger than the sizes of the impurities studied here (cf. Fig. 14 of Ref. [35]). As a consequence, we can treat the fluid as a gas of free molecules and confront the measured friction with the Epstein drag. In particular, the role of "gas molecules" in the GP fluid is played by the thermal excitations. Therefore, we can substitute the gas density ρ_g in Eq. (20) with the density of the noncondensed modes $\rho_\mathrm{g}=\bar{\rho}-\rho_0$, where $\rho_0=n_0\bar{\rho}$ or with the normal fluid density $\rho_\mathrm{g}=\rho_\mathrm{n}=n_\mathrm{n}\bar{\rho}$, computed using the momentum density correlator [48] (see Fig. 2). The velocity of the excitations $v_\mathrm{g}=\frac{\partial\omega_k}{\partial k}$ is averaged as

$$\langle v_\mathrm{g}\rangle=\frac{\sum_{|\mathbf{k}|\in S_\mathbf{k}} n_\mathbf{k}\frac{\partial\omega_k}{\partial k}}{\sum_{|\mathbf{k}|\in S_\mathbf{k}} n_\mathbf{k}}=\frac{\sum_{k=1}^{k_\mathrm{max}} k^2 n_k^{1d}\frac{\partial\omega_k}{\partial k}}{\sum_{k=1}^{k_\mathrm{max}} n_k^{1d}},\tag{21}$$

with $n_\mathbf{k}$ the occupation number of the mode $\mathbf{k}\in S_\mathbf{k}=\{1\leqslant|\mathbf{k}|\leqslant k_\mathrm{max}\}$ and $n_k^{1d}=\sum_{|\mathbf{k}|=k} n_\mathbf{k}$ its angle average.

In Fig. 7, the Epstein drag prediction (20) is compared with the numerical data. Both using the normal fluid density (dashed-dotted lines) or the density of noncondensed modes (solid lines) we get a good accordance at low temperatures, with a fitted prefactor C_d, whose values are of the order 0.1. Note that in this way we are implicitly guessing that the impurity-excitations interaction is independent of temperature. The specific values of C_d are reported in the legend of Fig. 7. They are consistent with a reasonable scenario in which thermal waves are much less efficient in transferring momentum to the impurity with respect to the standard particles reflection mechanisms [51]. We observe that C_d is slightly increasing with the impurity size (perhaps because of some variation of the impurity surface fluctuations) but it is independent of temperature. Note that the precise determination of radius dependence of C_d would require even further numerical simulations of what has been presented here.

In the inset of Fig. 7, we show the temperature dependence of the averaged excitations velocity (21), which turns out to be larger than the speed of phonons because it is dominated by high wave-number excitations. Note that the friction increment starts to diverge from the prediction at high temperatures. One reason is that the mean-free path of the GP excitations is becoming of the same order of the impurity size and thus the viscosity starts to play a role in the momentum exchange. A second cause may be that the impurity-excitations interactions are modified because of the high nonlinearity of the GP waves, leading to a temperature dependence of the constant C_d in Eq. (20). Eventually, note that a larger discordance with the measurements at high temperature is observed if the normal fluid density is used. This is probably due to a lack of accuracy in the computation of ρ_n at high temperatures, but it also suggests that it can be more reasonable to identify the density of the excitations simply with that of the noncondensed modes.

IV. DISCUSSION

In this paper we studied how the stochastic motion of an active, finite-size, and immiscible impurity immersed in a GP quantum fluid changes when the temperature is varied. We demonstrated that the interaction with the thermal excitations in the system always leads to a fast thermalization of the impurity. At time lags larger than $10\xi/c$ the correlation function of the impurity velocity shows an exponential decay, which is steeper for higher temperatures. This and the impurity squared displacement are reminiscent of an Ornstein-Uhlenbeck process.

From the measurements of the velocity correlation we extracted the temperature dependence of the friction coefficient $\gamma(T)$. The clear result is that the impurity does not experience the typical Stokes drag present in a classical fluid. Indeed, in the case of Stokes drag, the temperature dependence of the friction (19) is through the viscosity η. Since the viscosity has been shown to be slightly decreasing with temperature in the FTGP model [35], it cannot explain the trend observed in Fig. 7. The reason is that the settings studied are associated with large values of the Knudsen number, meaning that at the scale of the impurity the GP quantum fluid at finite temperature cannot be considered as a continuous liquid. On the contrary, describing phenomenologically the system as a gas of dilute thermal excitations reproduces the correct temperature increment of the friction $\gamma(T)$. Moreover, we observe a dependence of the friction with the impurity size compatible with the quadratic scaling $\gamma\propto a_\mathrm{I}^2$ predicted by the Epstein drag (20), despite some small deviations hidden in the prefactor C_d. In the case of Stokes drag, one should have observed a linear scaling $\gamma\propto a_\mathrm{I}$ that is not in agreement with our data.

We stress that the picture outlined does not apply to the particles typically used as probes in superfluid helium experiments [15,16]. Indeed, aside from being liquid helium a strongly interacting system, the typical size of those particles is four orders of magnitude larger than the healing length. Thus, in that case the Knudsen number is certainly small enough to entail the standard Stokes drag. However, a similar regime in terms of Knudsen number has been studied experimentally by using microspheres in liquid helium below 0.5 K [53]. It has been observed that the drag is determined by the ballistic scattering of quasiparticles and the temperature dependence of the friction coefficient is given by the temperature dependence of the quasiparticles density. Aside from helium, we hope that our study may be relevant for future BEC experiments, in which finite-size and immiscible impurities can be produced in the strong repulsive regime of multicomponent condensates [22], or in the study of the impurity dynamics in quantum fluids of light [19,20].

A possible follow-on of this work is the development of a self-consistent theory for the interaction between the thermal excitations and the impurity, which takes into account the dependence on the wave numbers of the colliding waves. This

could give an analytical explanation to the small value of the prefactor C_d in Eq. (20) compared to the classical Epstein drag for elastic collisions. Note that in a recent publication, the motion of a bright soliton moving in a thermal cloud of distinct atoms has been successfully modeled by using an OU dynamics [54]. In that case, the soliton is treated by using a wave function and the thermal (noncondensed) cloud as a reservoir. Although in our model the impurity is a rigid body with classical degrees of freedom, the result of [54] could inspire an analytical derivation of the OU dynamics for an impurity (14). Moreover, the characterization of the motion of a multitude of impurities in the FTGP system can be deepened, expanding the findings of Ref. [14]. Finally, the fundamental problem of vortex nucleation due to fast impurities has been thoroughly investigated at zero temperature [11–13], but few results are known in the finite-temperature regime [55,56]. In particular, the FTGP model coupled with impurities (1) would be a suitable framework to address the impurity-vortex interaction at nonzero temperature.

ACKNOWLEDGMENTS

The authors are grateful to Dr. D. Proment for fruitful discussions. The authors were supported by Agence Nationale de la Recherche through the Project No. GIANTE ANR-18-CE30-0020-01. G.K. is also supported by the EU Horizon 2020 Marie Curie project HALT and the Simons Foundation Collaboration grant Wave Turbulence (Award No. 651471). Computations were carried out on the Mésocentre SIGAMM hosted at the Observatoire de la Côte d'Azur and the French HPC Cluster OCCIGEN through the GENCI allocation A0042A10385.

[1] L. Pitaevskii and S. Stringari, *Bose-Einstein Condensation and Superfluidity*, International Series of Monographs on Physics (Oxford University Press, Oxford, 2016).

[2] M. H. Anderson, J. R. Ensher, M. R. Matthews, C. E. Wieman, and E. A. Cornell, Observation of Bose-Einstein condensation in a dilute atomic vapor, Science **269**, 198 (1995).

[3] J. Kasprzak, M. Richard, S. Kundermann, A. Baas, P. Jeambrun, J. Keeling, F. Marchetti, M. Szymańska, R. Andre, J. Staehli *et al.*, Bose-Einstein condensation of exciton polaritons, Nature (London) **443**, 409 (2006).

[4] S. Demokritov, V. Demidov, O. Dzyapko, G. Melkov, A. Serga, B. Hillebrands, and A. Slavin, Bose-Einstein condensation of quasi-equilibrium magnons at room temperature under pumping, Nature (London) **443**, 430 (2006).

[5] J. Klaers, J. Schmitt, F. Vewinger, and M. Weitz, Bose–einstein condensation of photons in an optical microcavity, Nature (London) **468**, 545 (2010).

[6] P. Kapitza, Viscosity of Liquid Helium below the λ-Point, Nature (London) **141**, 74 (1938).

[7] J. F. Allen and A. D. Misener, Flow of Liquid Helium II, Nature (London) **141**, 75 (1938).

[8] I. Carusotto and C. Ciuti, Quantum fluids of light, Rev. Mod. Phys. **85**, 299 (2013).

[9] C. Nore, M. Abid, and M. E. Brachet, Decaying kolmogorov turbulence in a model of superflow, Phys. Fluids **9**, 2644 (1997).

[10] R. J. Donnelly, *Quantized Vortices in Helium II*, Vol. 2 (Cambridge University Press, Cambridge, 1991).

[11] T. Frisch, Y. Pomeau, and S. Rica, Transition to Dissipation in a Model of Superflow, Phys. Rev. Lett. **69**, 1644 (1992).

[12] C. Nore, C. Huepe, and M. E. Brachet, Subcritical Dissipation in Three-Dimensional Superflows, Phys. Rev. Lett. **84**, 2191 (2000).

[13] T. Winiecki and C. S. Adams, Motion of an object through a quantum fluid, Europhys. Lett. **52**, 257 (2000).

[14] U. Giuriato, G. Krstulovic, and D. Proment, Clustering and phase transitions in a 2d superfluid with immiscible active impurities, J. Phys. A: Math. Theor. **52**, 305501 (2019).

[15] G. P. Bewley, D. P. Lathrop, and K. R. Sreenivasan, Superfluid helium: Visualization of quantized vortices, Nature (London) **441**, 588 (2006).

[16] M. La Mantia and L. Skrbek, Quantum turbulence visualized by particle dynamics, Phys. Rev. B **90**, 014519 (2014).

[17] N. Spethmann, F. Kindermann, S. John, C. Weber, D. Meschede, and A. Widera, Dynamics of Single Neutral Impurity Atoms Immersed in an Ultracold Gas, Phys. Rev. Lett. **109**, 235301 (2012).

[18] M. Hohmann, F. Kindermann, T. Lausch, D. Mayer, F. Schmidt, E. Lutz, and A. Widera, Individual Tracer Atoms in an Ultracold Dilute Gas, Phys. Rev. Lett. **118**, 263401 (2017).

[19] C. Michel, O. Boughdad, M. Albert, P.-É. Larré, and M. Bellec, Superfluid motion and drag-force cancellation in a fluid of light, Nat. Commun. **9**, 2108 (2018).

[20] I. Carusotto, Superfluid light in bulk nonlinear media, Proc. R. Soc. A **470**, 20140320 (2014).

[21] P. G. Kevrekidis, D. J. Frantzeskakis, and R. Carretero-González, *Emergent Nonlinear Phenomena in Bose-Einstein Condensates*, Vol. 45 (Springer, Berlin, 2008).

[22] S. Rica and D. C. Roberts, Induced interaction and crystallization of self-localized impurity fields in a bose-einstein condensate, Phys. Rev. A **80**, 013609 (2009).

[23] G. Modugno, M. Modugno, F. Riboli, G. Roati, and M. Inguscio, Two Atomic Species Superfluid, Phys. Rev. Lett. **89**, 190404 (2002).

[24] C. J. Myatt, E. A. Burt, R. W. Ghrist, E. A. Cornell, and C. E. Wieman, Production of Two Overlapping Bose-Einstein Condensates by Sympathetic Cooling, Phys. Rev. Lett. **78**, 586 (1997).

[25] S. B. Papp, J. M. Pino, and C. E. Wieman, Tunable Miscibility in a Dual-Species Bose-Einstein Condensate, Phys. Rev. Lett. **101**, 040402 (2008).

[26] N. P. Proukakis and B. Jackson, Finite-temperature models of bose–einstein condensation, J. Phys. B: At., Mol. Opt. Phys. **41**, 203002 (2008).

[27] E. Zaremba, T. Nikuni, and A. Griffin, Dynamics of trapped bose gases at finite temperatures, J. Low Temp. Phys. **116**, 277 (1999).

[28] M. J. Davis, S. A. Morgan, and K. Burnett, Simulations of Bose Fields at Finite Temperature, Phys. Rev. Lett. **87**, 160402 (2001).

[29] S. Nazarenko, M. Onorato, and D. Proment, Bose-einstein condensation and berezinskii-kosterlitz-thouless transition in the two-dimensional nonlinear schrödinger model, Phys. Rev. A **90**, 013624 (2014).

[30] C. Connaughton, C. Josserand, A. Picozzi, Y. Pomeau, and S. Rica, Condensation of Classical Nonlinear Waves, Phys. Rev. Lett. **95**, 263901 (2005).

[31] G. Krstulovic and M. Brachet, Dispersive Bottleneck Delaying Thermalization of Turbulent Bose-Einstein Condensates, Phys. Rev. Lett. **106**, 115303 (2011).

[32] N. G. Berloff and A. J. Youd, Dissipative Dynamics of Superfluid Vortices at Nonzero Temperatures, Phys. Rev. Lett. **99**, 145301 (2007).

[33] G. Krstulovic and M. Brachet, Anomalous vortex-ring velocities induced by thermally excited kelvin waves and counterflow effects in superfluids, Phys. Rev. B **83**, 132506 (2011).

[34] G. Krstulovic and M. Brachet, Energy cascade with small-scale thermalization, counterflow metastability, and anomalous velocity of vortex rings in fourier-truncated gross-pitaevskii equation, Phys. Rev. E **83**, 066311 (2011).

[35] V. Shukla, P. D. Mininni, G. Krstulovic, P. C. di Leoni, and M. E. Brachet, Quantitative estimation of effective viscosity in quantum turbulence, Phys. Rev. A **99**, 043605 (2019).

[36] V. Shukla, R. Pandit, and M. Brachet, Particles and fields in superfluids: Insights from the two-dimensional gross-pitaevskii equation, Phys. Rev. A **97**, 013627 (2018).

[37] U. Giuriato and G. Krstulovic, Interaction between active particles and quantum vortices leading to kelvin wave generation, Sci. Rep. **9**, 4839 (2019).

[38] U. Giuriato, G. Krstulovic, and S. Nazarenko, How trapped particles interact with and sample superfluid vortex excitations, Phys. Rev. Research **2**, 023149 (2020).

[39] U. Giuriato and G. Krstulovic, Quantum vortex reconnections mediated by trapped particles, Phys. Rev. B **102**, 094508 (2020).

[40] U. Giuriato and G. Krstulovic, Active and finite-size particles in decaying quantum turbulence at low temperature, Phys. Rev. Fluids **5**, 054608 (2020).

[41] N. G. Berloff and P. H. Roberts, Motion in a bose condensate: VIII. the electron bubble, J. Phys. A: Math. Gen. **34**, 81 (2000).

[42] A. Villois and H. Salman, Vortex nucleation limited mobility of free electron bubbles in the gross-pitaevskii model of a superfluid, Phys. Rev. B **97**, 094507 (2018).

[43] J. Rønning, A. Skaugen, E. Hernández-García, C. Lopez, and L. Angheluta, Classical analogies for the force acting on an impurity in a bose–einstein condensate, New J. Phys. **22**, 073018 (2020).

[44] G. E. Astrakharchik and L. P. Pitaevskii, Motion of a heavy impurity through a bose-einstein condensate, Phys. Rev. A **70**, 013608 (2004).

[45] T. Lee, On some statistical properties of hydrodynamical and magneto-hydrodynamical fields, Q. Appl. Math. **10**, 69 (1952).

[46] R. H. Kraichnan, Inertial ranges in two-dimensional turbulence, The Physics of Fluids **10**, 1417 (1967).

[47] R. Clark and G. Derrick, *Mathematical Methods in Solid State and Superfluid Theory: Scottish Universities? Summer School*, Scottish Universities‘ Summer School (Springer, New York, 1968).

[48] C. J. Foster, P. B. Blakie, and M. J. Davis, Vortex pairing in two-dimensional Bose gases, Phys. Rev. A **81**, 023623 (2010).

[49] N. G. Van Kampen, *Stochastic Processes in Physics and Chemistry*, Vol. 1 (Elsevier, Amsterdam, 1992).

[50] C. K. Batchelor and G. Batchelor, *An Introduction to Fluid Dynamics* (Cambridge University Press, Cambridge, 2000).

[51] P. S. Epstein, On the resistance experienced by spheres in their motion through gases, Phys. Rev. **23**, 710 (1924).

[52] B. de Lima Bernardo, F. Moraes, and A. Rosas, Drag force experienced by a body moving through a rarefied gas, Chin. J. Phys. **51**, 189 (2013).

[53] M. Niemetz and W. Schoepe, Stability of laminar and turbulent flow of superfluid 4he at mk temperatures around an oscillating microsphere, J. Low Temp. Phys. **135**, 447 (2004).

[54] R. G. McDonald and A. S. Bradley, Brownian motion of a matter-wave bright soliton moving through a thermal cloud of distinct atoms, Phys. Rev. A **93**, 063604 (2016).

[55] M. Leadbeater, T. Winiecki, and C. S. Adams, Effect of condensate depletion on the critical velocity for vortex nucleation in quantum fluids, J. Phys. B: At., Mol. Opt. Phys. **36**, L143 (2003).

[56] G. W. Stagg, R. W. Pattinson, C. F. Barenghi, and N. G. Parker, Critical velocity for vortex nucleation in a finite-temperature bose gas, Phys. Rev. A **93**, 023640 (2016).

6.3 *Publication*: Clustering and phase transitions in a 2D superfluid with immiscible active impurities

In this article we study numerically a system composed of a collection of immiscible impurities in the two-dimensional truncated Gross–Pitaevsii equation. Note that this is the only publication of this Thesis in which we deal with a 2D system. We recall that in this case the true condensation transition is formally forbidden by the Mermin–Wagner–Hohenberg theorem [99, 154]. Thus, the condensation transition must be considered as a finite size effect (see section 1.2.2), even if it is generated in the truncated GP framework [211].

We first consider the system at zero temperature, placing a number of light impurities in a random position. We observe that the superfluid mediated interaction between the impurities [212] sets them in motion and triggers a thermalization mechanism. Indeed, the sound waves produced by the particle dynamics interact among themselves until the fluid reaches a thermal equilbrium. Simultaneously, the short-range inter-particle interparticle interaction let them collapse into clusters, which move in a stochastic way, similarly to what observed in [78]. Eventually all the impurities collapse into a single large cluster, in thermal equilibrium with the surrounding bath of phonons. Subsequently, we generate thermal states of the system, generalizing the stochastic real Ginzburg–Landau algorithm discussed in section 6.1.1 to include also the impurity degrees of freedom. We perform a temperature scan, varying the range r_{rep} of the repulsion potential (2.58). We observe the existence of a critical temperature below which all the impurities are clustered in the equilibrium state. It turns out that this "clustering" temperature T_{cl} strongly depends on the ratio between the superfluid mediated attraction and the short-range repulsion (2.58) imposed to avoid the impurity overlap. In particular, it can be explained qualitatively as an escape problem from the potential well generated by the sum of attraction and repulsion: if the thermal fluctuations are sufficiently strong two sticked impurities are expected to split in a finite time, breaking in this way the cluster.

Besides, we observe that the presence of a large impurity cluster is responsible for an increase of the condensate fraction at large temperatures and thus an increase of the condensation temperature T_λ itself. This phenomenon does not occur if the impurities are unclustered at the condensation temperature, namely if the inter-particle repulsion is tuned to have a range r_{rep} larger than the particle radius $r_{\mathrm{rep}} > a_{\mathrm{p}}$, so that $T_{\mathrm{cl}} < T_\lambda$. Moreover such condensation shift becomes more and more important as the volume fraction Φ occupied by the impurities becomes larger. This suggests that it can be explained as a finite size effect, compatibly with what is expected in atomic BECs trapped by power-law potentials [11]. Indeed if a large object occupies a portion of the available domain, the number of active modes (and thus the energy) of the quantum fluid decreases, so that a higher temperature is required to induce the transition. Note that such effect is independent of the dimensionality of the system. For completeness, in Fig.6.3 we show that the increment of the condensate fraction at high temperatures takes place also in the three-dimensional case. Also in this case the amount of such

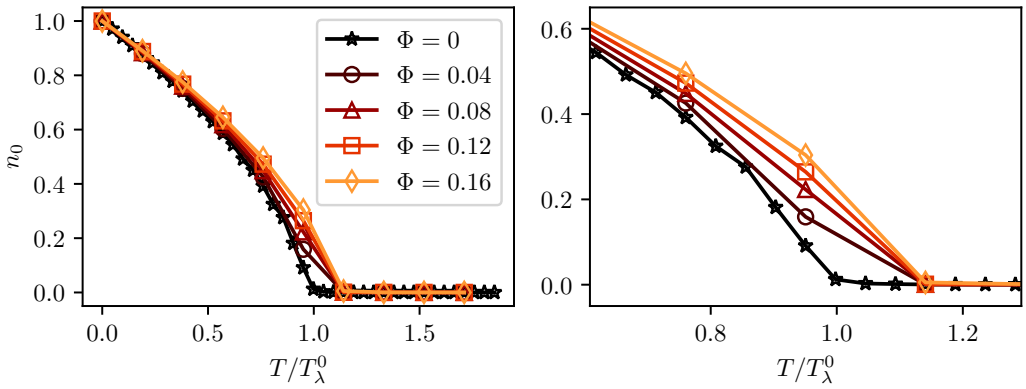


Figure 6.3. Condensate fraction as a function of temperature for different values of the filling fraction in the 3D truncated GP model with impurities. (*left*) The full temperature range analyzed. (*right*) Close-up at high temperatures. The parameters of the simulations are $N_c = 64$ collocation points per side, $L = 2\pi$, $\xi = L/N_c$ and thus $\xi k_{max} = 2\pi/3$. The parameters for the impurities and the definitions of T_λ^0 and n_0 are the same as in Figure 4 of [80].

increment is proportional to the filling fraction Φ.

Finally, the changes in the Berezinskii–Kosterlitz–Thouless (BKT) phase transition has been briefly addressed. The BKT phase transition is the well known topological phase transition of the two-dimensional XY (vector-spin) model [124, 125], whose signature is a power-law decay of the first order correlation function $g_1(r) = \int n_k e^{ik\cdot r}\, \mathrm{d}\boldsymbol{k}$ below a critical temperature T_{BKT} (in contrast to the exponential decay of the disordered phase). In the case of the 2D BEC, at sufficiently low temperature ($k_B T \ll gn$) the density fluctuations are suppressed and the effective large scale Hamiltonian is akin to the XY model, where the gradient of the phase (superfluid velocity) plays the role of the vector-spins [95]. A key role in the BKT transition is given by vortices, which are arranged in bounded vortex-antivortex pairs below T_{BKT} and in a gas of free vortices at $T > T_{BKT}$. The role of vortices in the BKT transition of the GP model has been studied for instance in [65] and [161], where the topological defects have been called "ghost vortices", since they appear and disappear continuosly in contrast to the stable objects of the zero temperature regime. In our case, we checked the existence of a power-law decay of the correlation function and measured an increase of the BKT temperature with the filling fraction of the impurity cluster. The result is thus similar to the corresponding measurement for T_λ.

OPEN ACCESS
IOP Publishing
Journal of Physics A: Mathematical and Theoretical
J. Phys. A: Math. Theor. **52** (2019) 305501 (11pp)
https://doi.org/10.1088/1751-8121/ab2607

Clustering and phase transitions in a 2D superfluid with immiscible active impurities

Umberto Giuriato[1,3], Giorgio Krstulovic[1] and Davide Proment[2]

[1] Université Côte d'Azur, Observatoire de la Côte d'Azur, CNRS, Laboratoire Lagrange, Nice, France
[2] School of Mathematics, University of East Anglia, Norwich Research Park, Norwich, NR4 7TJ, United Kingdom

E-mail: umberto.giuriato@oca.eu

Received 18 January 2019, revised 8 May 2019
Accepted for publication 31 May 2019
Published 1 July 2019

Abstract

Phase transitions of a finite-size two-dimensional superfluid of bosons in presence of active impurities are studied by using the projected Gross–Pitaevskii model. Impurities are described with classical degrees of freedom. A spontaneous clustering of impurities during the thermalization is observed. Depending on the interaction among impurities, such clusters can break due to thermal fluctuations at temperatures where the condensed fraction is still significant. The emergence of clusters is found to increase the condensation transition temperature. The condensation and the Berezinskii–Kosterlitz–Thouless transition temperatures, determined numerically, are found to strongly depend on the volume occupied by the impurities: a relative increase up to a 20% of their respective values is observed, whereas their ratio remains approximately constant.

Keywords: superfluids, Bose–Einstein condensates, clustering, phase transitions, impurities

S Supplementary material for this article is available online

(Some figures may appear in colour only in the online journal)

[3] Author to whom any correspondence should be addressed.

Original content from this work may be used under the terms of the Creative Commons Attribution 3.0 licence. Any further distribution of this work must maintain attribution to the author(s) and the title of the work, journal citation and DOI.

1. Introduction

When a fluid composed of bosons is cooled down or the number of particles is increased, the system experiences a phase transition giving rise to a macroscopic state known as Bose–Einstein condensate (BEC) [1]. Since its first experimental observation by Anderson *et al* [2], BECs have been realized in systems of very different nature such as cold atomic gases [1, 3], solid-state quasiparticles [4, 5] and light in optical micro-cavities [6]. Whereas in three spatial dimensions a condensate is stable with respect to thermal fluctuations, in two dimensions such fluctuations can destroy the long-range order of the system. This is a general result in statistical field theory known as the Mermin–Wagner–Hohenberg theorem [7, 8]: it states that a continuous symmetry cannot be spontaneously broken in dimensions lower than three, otherwise large-scale Goldstone modes would have an infinite infrared contribution to the two-point correlator. This theorem assumes the thermodynamic limit, that is the system size being infinite. However, for a finite system, condensation can be recovered, having a transition temperature T_λ that vanishes as the inverse of the logarithm of the system size.

Although condensation is formally forbidden in an infinite two-dimensional system, a peculiar phase transition of a different nature has attracted the attention of physicists and mathematicians since its independent discovery in the early 70s by Berezinskii, Kosterlitz and Thouless (BKT) [9–11]. The BKT transition is an infinite-order topological phase transition and manifests itself in systems that belong to the same universality class. By approaching the BKT transition temperature, T_{BKT}, from below, the system switches from a gas of bounded vortex-antivortex pairs to a gas of free vortices, moving from a quasi-ordered phase to a disordered one. The BKT transition has been observed in BECs made of dilute gases [12–16], exciton-polaritons [17], liquid helium films [18] and studied theoretically and numerically [19–22]; for a review on the topic, see for instance [3].

The purpose of this article is to study how the statistical mechanical properties of a two dimensional superfluid of bosons are affected by the presence of impurities. Particles and impurities have been used in superfluids since the early experiments in ^{4}He [23] mainly with detection purposes: electrons, ions and neutral impurities such as hydrogen particles and excimers have been exploited to visualize quantized vortices, to study their dynamics and the statistics of superfluid (quantum) turbulence [24–26]. More recently, the investigation of the interaction between one or more impurities and superfluids has been the main topic of experiments in cold atoms [27, 28], superfluids of light [29, 30] and polaritons in semiconductor microcavities [31]. On the theoretical side, the dynamics of impurities in a BEC has been also addressed [32], as well as the properties of ^{3}He and H impurities on thin ^{4}He films [33, 34]. In addition, Ricaand Roberts studied how a collection of impurities affects the ground-state of a BEC by using a mean field model [35]. In this last work, four phases were identified, depending on the value of the interaction couplings. In particular, if the scattering lengths between impurity fields are positive, impurities behave as localized objects, they separate from the condensate and present a hard-sphere repulsion between each other.

We investigate here impurity clustering and phase transitions occurring in a minimal model that mimics such situation: the Gross–Pitaevskii (GP) equation coupled with active immiscible impurities having classical degrees of freedom. Such model was introduced in [36] and recently used in two-dimensional numerical simulations to study impurity-impurity and impurity-vortex interactions [37, 38]. Finite-temperature BECs can be studied by using the projected GP equation, that is obtained by introducing a cut-off k_{max} in Fourier space: this regularizes the classical mean-field ultra-violet divergence. The projected GP model is an effective model to study the condensation transition in two and three dimensions [21, 39–41] and superfluid vortex dynamics at finite temperature [42–44].

2. Theoretical model and numerical results

2.1. Model for impurities in a superfluid

We generalize the projected GP model to include the dynamics of active impurities. The model is then described by the Hamiltonian

$$H = \int \left(\frac{\hbar^2}{2m} |\boldsymbol{\nabla}\psi|^2 + \frac{g}{2} |\mathcal{P}_{\mathrm{G}}[|\psi|^2]|^2 + \sum_{i=1}^{N_{\mathrm{I}}} V_{\mathrm{I}}(|\mathbf{x} - \mathbf{q}_i|) \mathcal{P}_{\mathrm{G}}[|\psi|^2] \right) \mathrm{d}\mathbf{x} + \sum_{i=1}^{N_{\mathrm{I}}} \frac{\mathbf{p}_i^2}{2M_{\mathrm{I}}} + \sum_{i<j}^{N_{\mathrm{I}}} V_{\mathrm{rep}}(|\mathbf{q}_i - \mathbf{q}_j|), \tag{1}$$

where ψ is the collective wave-function of bosons having mass m, and $g = 4\pi a_{\mathrm{s}}\hbar^2/m$ being a_{s} the s-wave scattering length of bosons interaction. N_{I} is the total number of impurities of mass M_{I}, that are described using their classical position and momentum $\mathbf{q}_i$ and $\mathbf{p}_i$, respectively. The strong repulsive potential V_{I} determines the shape of the impurities by creating a large depletion in the fluid density. V_{rep} is a repulsive potential between impurities. The Galerkin projector $\mathcal{P}_{\mathrm{G}}$ truncates the system acting in Fourier space as $\mathcal{P}_{\mathrm{G}}\hat{\psi}_{\mathbf{k}} = \theta(k_{\max} - k)\hat{\psi}_{\mathbf{k}}$ with $\theta(\cdot)$ the Heaviside function, $\hat{\psi}_{\mathbf{k}}$ the Fourier transform of $\psi(\mathbf{x})$ and $\mathbf{k}$ the wave vector. The equations of motion are directly obtained by varying (1):

$$\mathrm{i}\hbar \frac{\partial \psi}{\partial t} = \mathcal{P}_{\mathrm{G}}[-\frac{\hbar^2}{2m}\boldsymbol{\nabla}^2\psi + g\mathcal{P}_{\mathrm{G}}[|\psi|^2]\psi + \sum_{i=1}^{N_{\mathrm{I}}} V_{\mathrm{I}}(|\mathbf{x} - \mathbf{q}_i|)\psi] \tag{2}$$

$$M_{\mathrm{I}}\ddot{\mathbf{q}}_{\mathbf{i}} = -\int V_{\mathrm{I}}(|\mathbf{x} - \mathbf{q}_i|)\mathcal{P}_{\mathrm{G}}[\nabla|\psi|^2]\,\mathrm{d}\mathbf{x} - \sum_{j\neq i}^{N_{\mathrm{I}}} \nabla V_{\mathrm{rep}}(q_{ij}), \tag{3}$$

where $q_{ij} = |\mathbf{q}_i - \mathbf{q}_j|$ and we have replaced $\mathbf{p}_i = M_{\mathrm{I}}\dot{\mathbf{q}}_i$. The previous set of equations exactly conserves the Hamiltonian, the number of bosons $N = \int |\psi|^2 \mathrm{d}\mathbf{x}$ and momentum $\mathbf{P} = \int \frac{\mathrm{i}\hbar}{2}\left(\psi\boldsymbol{\nabla}\overline{\psi} - \overline{\psi}\boldsymbol{\nabla}\psi\right)\mathrm{d}\mathbf{x} + \sum_i \mathbf{p}_i$.

The impurities in the system feel an attractive force mediated by the superfluid density field [35, 37]. However, unlike the case of impurities described by classical fields [35], in the model (1) no repulsion mediated by the fluid exists. In order to mimic such a hard-sphere repulsion, we consider the Lennard–Jones-like potential $V_{\mathrm{rep}}(r) = \epsilon r_{\min}^{12}/r^{12}$, as in [37]. We fix the energy ϵ in order to set the minimum of the total interaction energy between impurities at zero temperature at a distance $r_{\min}$. Note that the specific shape of V_{rep} is not important, as long as it reproduces a hard-sphere repulsion. For the impurities potential we use a smoothed hat-potential $V_{\mathrm{I}}(r) = V_0(1 - \tanh\left[(r^2 - a_{\mathrm{I}}^2)/4\Delta l^2\right])/2$, where a_{I} sets the characteristic radius of the impurity and Δl is a smoothing parameter. Finally, let us notice that in absence of impurities and at zero temperature, equation (2) can be linearized about a uniform density state $|\psi|^2 = \rho_\infty/m$, defining the phonon (sound) velocity $c = \sqrt{g\rho_\infty/m^2}$ with dispersive effects taking place for length scales smaller than the healing length $\xi = \sqrt{\hbar^2/2g\rho_\infty}$.

We integrate the system (2) and (3) by using a pseudo-spectral code with N_{res} uniform grid points per direction of a squared domain of size $L = 2\pi$. We set $k_{\max} = N_{\mathrm{res}}/3$ so that the truncated system exactly conserves all the invariants (provided that initially $\mathcal{P}_{\mathrm{G}}\psi = \psi$ and $\mathcal{P}_{\mathrm{G}}V_{\mathrm{I}} = V_{\mathrm{I}}$) [44], $c = \rho_\infty = 1$, $V_0 = 10$ and $\epsilon = 0.006\,74$. As the healing length changes with temperature, we parametrize the solutions of (2) and (3) using its value taken at zero temperature. In thermal states, the only relevant dimensionless parameters are L/ξ, a_{I}/ξ, N_{I}, the

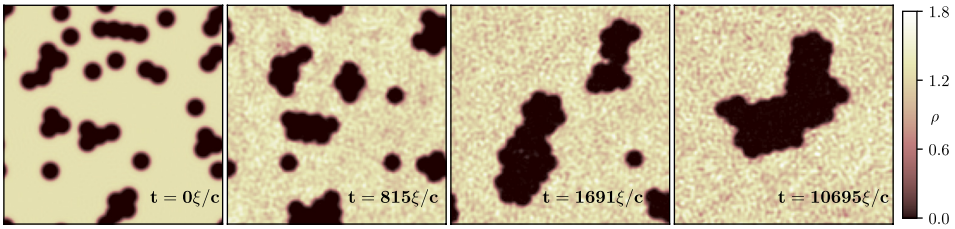


Figure 1. Snapshots of the fluid density during the GP temporal evolution of a state with 40 impurities (dark holes).

relative mass $\mathcal{M} = M_{\rm I}/\rho_\infty \pi a_{\rm I}^2$ and $\xi k_{\rm max}$. We set $L/\xi = 128$. The value of $\xi k_{\rm max}$ controls the strength of the nonlinear interactions and it is kept fixed to $\xi k_{\rm max} = 2\pi/3$. For this value, most of the excitations are phonons when the condensate fraction is large. For instance, it is compatible with the one used in [39], that is $\xi k_{\rm max} \sim 2$; such value applies to a gas of ^{87}Rb atoms.

We start by presenting a long temporal evolution of a system having 40 impurities of mass $\mathcal{M} = 0.1$, radius $a_{\rm I} = 4\xi$, initially located at random positions (avoiding overlaps) and having zero velocity. The density field of the initial condition is displayed in figure 1 ($t = 0\xi/c$). Impurities correspond to dark holes. During the time evolution, the short-range interaction among impurities mediated by the fluid let them collapse into small clusters ($t = 815\xi/c$); waves with random phases are generated, populating small length scales and starting the thermalization process. This thermal noise induces the clusters to move in a stochastic way, and to grow further ($t = 1691\xi/c$). Eventually, the system reaches thermal equilibrium where only one big cluster is observed in a bath of thermalized waves, ($t = 10\,965\xi/c$). A movie of the the evolution is available in the supplementary data (stacks.iop.org/JPhysA/52/305501/mmedia).

2.2. Grand-canonical thermal states

The evolution illustrated in figure 1 is an example of thermalization occurring in the micro-canonical ensemble, as the thermal state is achieved keeping all the invariants conserved. Such dynamical process is numerically costly and does not directly provide access to the conjugate thermodynamical variables: temperature and chemical potential (here we only consider zero momentum states). To overcome these issues, in [44] a stochastic relaxation was introduced in order to efficiently generate thermal states in the grand-canonical ensemble. We make use of this approach adapting it to the Hamiltonian (1). The stochastic dynamics is ruled by

$$\hbar \frac{\partial \hat{\psi}_{\mathbf{k}}}{\partial t} = -\frac{\partial F}{\partial \hat{\psi}^*_{\mathbf{k}}} + \sqrt{\frac{2\hbar}{\beta}}\hat{\xi}_{\mathbf{k}} \tag{4}$$

$$\frac{\partial \mathbf{q}_i}{\partial t} = -\frac{\partial F}{\partial \mathbf{q}_i} + \sqrt{\frac{2}{\beta}}\boldsymbol{\xi}^q_i, \quad M_{\rm I}\frac{\partial \dot{\mathbf{q}}_i}{\partial t} = -\frac{\partial F}{\partial \dot{\mathbf{q}}_i} + \sqrt{\frac{2M_{\rm I}}{\beta}}\boldsymbol{\xi}^{\dot{q}}_i \tag{5}$$

where $F = H - \mu N$ is the free energy of the system, μ is the chemical potential controlling the number of bosons and β is the inverse temperature; $\hat{\xi}_{\mathbf{k}}$, $\boldsymbol{\xi}^q_i$ and $\boldsymbol{\xi}^{\dot{q}}_i$ are independent Gaussian white noises of unit variance. It can be shown by using the Fokker–Planck equation associated to (4) and (5), that the stationary probability distribution is given by the Gibbs grand-canonical distribution $\mathbb{P}[\hat{\psi}_{\mathbf{k}}, \mathbf{q}_i, \dot{\mathbf{q}}_i] \propto {\rm e}^{-\beta F}$. In the micro-canonical ensemble, $\mathbb{P}[\hat{\psi}_{\mathbf{k}}, \mathbf{q}_i, \dot{\mathbf{q}}_i]$ is also the stationary solution of the Liouville equation that describes the evolution of the phase-space

distribution of the Hamiltonian system (1) [44]. It is evident from (5) that varying the impurity masses modifies only the variance of impurity momenta in the steady state. Namely, the configurations of impurities in the steady state and the statistical properties of the thermalized system are independent of impurity masses. We define the temperature as $T = 1/k_{\mathcal{N}}\beta$, with $k_{\mathcal{N}} = L^2/\mathcal{N}$ and $\mathcal{N} = \pi k_{\max}^2$ the total number of Fourier modes. With this definition T is an energy per unit of surface such that at low temperatures $F \approx TL^2$, because of equipartition. With these choices, intensive quantities remain constant when increasing the system size. In addition, we fix the total density mass $\bar{\rho} = mN/L^2 = 1$ by dynamically adjusting the chemical potential [44]. We use (4) and (5) to study the effect of impurities on the superfluid condensed fraction n_0 defined as

$$n_0 = \frac{\langle \left| \int_{\mathcal{V}'} \psi(\mathbf{x})\, \mathrm{d}\mathbf{x} \right|^2 \rangle_T}{\langle \int_{\mathcal{V}'} |\psi(\mathbf{x})|^2\, \mathrm{d}\mathbf{x} \rangle_T}, \tag{6}$$

where $\mathcal{V}'$ is the domain excluding the region occupied by the impurities and $\langle \cdot \rangle$ stands for average over realizations at temperature T[4].

2.3. Clustering of impurities

We first perform a temperature scan without impurities. The condensed fraction is shown in figure 2(a) (solid blue line). The transition temperature T_λ is the lowest temperature where the condensed fraction can be considered negligible. We estimate it in a consistent way adopting the following numerical protocol: we take the points around which $n_0^2(T)$ is close to zero and we perform a linear interpolation of it. T_λ is then determined by finding the point where the linear fit vanishes. From now on, we indicate with T_λ^0 the transition temperature in the system without impurities. Then, we perform temperature scans varying the repulsive potential parameter $r_{\min}$ with a fixed number of impurities $N_{\mathrm{I}} = 31$ having radius $a_{\mathrm{I}} = 4\xi$. The results are also shown in figure 2. In figures 2(b) and (c) snapshots of in the steady date are displayed respectively in the case of high and low repulsion among impurities. For both cases we report three different temperatures. Depending on the strength of the repulsion potential two different behaviors of n_0 can be observed, as it is clear in figure 2(a). When the repulsion among impurities is strong enough (blue markers, $r_{\min} \geqslant 11\xi$), clusters are broken already at temperatures lower than T_λ^0 (see figure 2(b)) and impurities have no appreciable effect on n_0. On the other hand, for $r_{\min} \leqslant 10.5\xi$ (red markers) impurities remain clustered and lead to an increase of the n_0 at medium-high temperatures (see figure 2(c)).

It has been shown that impurities experience a short-range attractive force, mediated by the superfluid density [35, 37]. This interaction is characterized by a potential energy, denoted here $E_{\mathrm{I}\leftrightarrow\mathrm{I}}$. We compute this energy numerically by measuring the full GP free energy of the ground state with two impurities placed at a distance Δq, without the contribution of the repulsion. The constant contribution to $E_{\mathrm{I}\leftrightarrow\mathrm{I}}$ is eventually set to zero. Impurities are then repelled because of V_{rep}, generating cluster structures as the one observed in figure 1(d). However, if thermal fluctuations are large enough, the bound among impurities can be broken. In figure 3(a) we compute the interaction energy between two impurities at zero temperature $E_{\mathrm{I}\leftrightarrow\mathrm{I}}$, as a function of their distance Δq (dotted black line). As a reference, the figure also displays the repulsive potential V_{rep} with $r_{\min} = 2a_{\mathrm{I}}$ (dotted–dashed golden line). The sum of both potentials is displayed in the same figure for different values of $r_{\min}$: for sufficiently small

[4] This definition gives the same result as $n_0 = \left(\frac{|\langle\psi\rangle_T|^2}{N}\right)\left(\frac{|\langle\psi\rangle_{T=0}|^2}{N}\right)^{-1} = \frac{|\langle\psi\rangle_T|^2}{|\langle\psi\rangle_{T=0}|^2}$. For numerical convenience we use the latter in our computations.

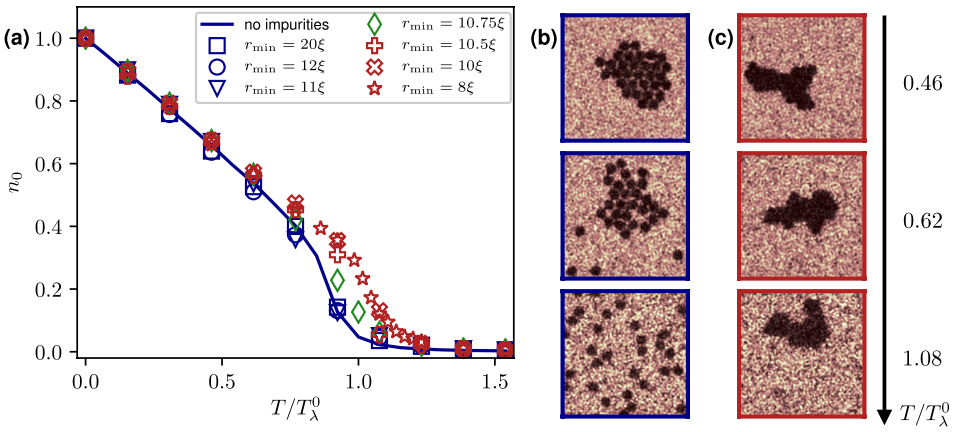


Figure 2. (a) Condensed fraction as a function of the temperature for different values of $r_{\min}$. Temperatures are expressed in units of the condensation temperature with no impurities T_λ^0. (b) Snapshots of the density field in the steady state at different temperatures in the case of high repulsion ($r_{\min} = 11\xi$) among impurities. (c) The same of (b) but for low repulsion ($r_{\min} = 8\xi$). Scans are performed with $N_{\rm I} = 31$ and $a_{\rm I} = 4\xi$.

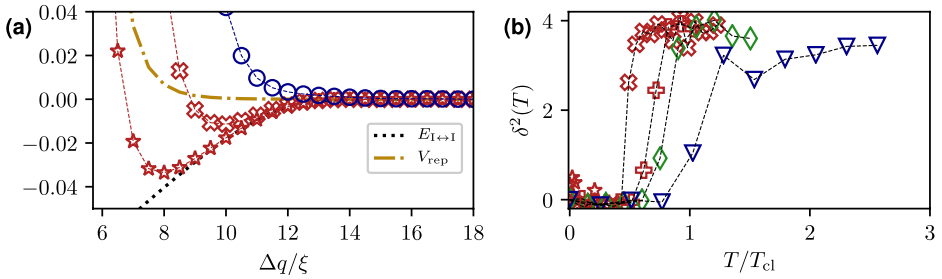


Figure 3. (a) Impurity-impurity interaction $E_{\rm I\leftrightarrow I}$ as a function of their distance $\Delta q/\xi$ (dotted black line) and repulsive potential (dotted-dashed golden line) for $r_{\min} = 8\xi$. Different markers correspond to total energy $E_{\rm I\leftrightarrow I} + V_{\rm rep}$ for different values of $r_{\min}$. (b) Relative impurity distance $\delta^2(T)$ as a function of the normalized temperature $T/T_{\rm cl}$. Scans are performed with $N_{\rm I} = 31$ and $a_{\rm I} = 4\xi$. The ratios $T_{\rm cl}/T_\lambda$ are 7.41, 2.51, 1.5, 1.02, 0.53, 0.002 for $r_{\min}$ from 8ξ to 12ξ respectively. The markers refer to the same legend as in figure 2.

values of $r_{\min}$, a potential well ΔU centered at $r_{\min}$ appears. We thus expect a pair of impurities to split in a finite time at the temperature $T_{\rm cl} \sim \Delta U/k_{\mathcal{N}}$, as in a standard escape problem from a potential well [45]. In order to quantify this clustering transition, we measure the average square distance between impurities and their center of mass

$$\delta^2(T) = \frac{\mathrm{d}^2(T) - \mathrm{d}^2(0)}{\mathrm{d}^2(0)}, \quad \text{with} \quad \mathrm{d}^2(T) = \sum_{j=1}^{N_{\rm I}} \langle |\mathbf{q}_j - \mathbf{q}_{\rm cm}|^2 \rangle \quad \text{and} \quad \mathbf{q}_{\rm cm} = \sum_{j}^{N_I} \frac{\mathbf{q}_j}{N_{\rm I}}. \tag{7}$$

Figure 3(b) displays $\delta^2(T)$ as a function of $T/T_{\rm cl}$ for different values of $r_{\min}$. A transition around $T_{\rm cl}$ is indeed observed, where discrepancies are likely due to oversimplifications made in the estimation of $T_{\rm cl}$, namely by neglecting the many-body impurity interactions and by

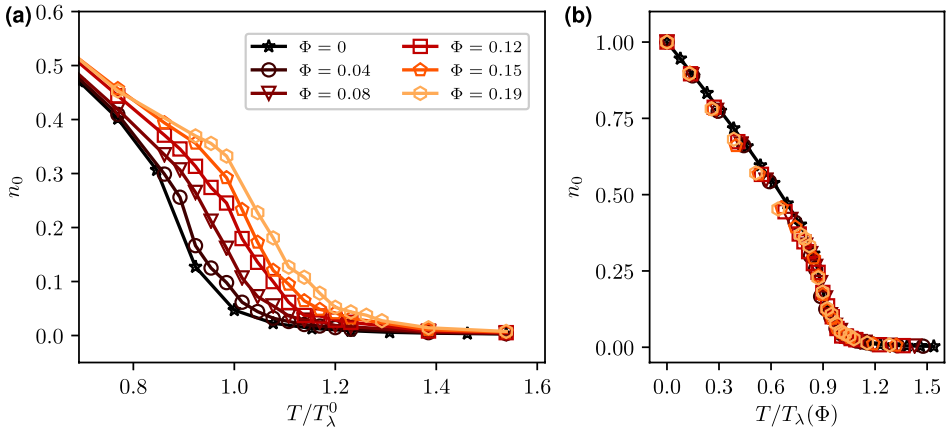


Figure 4. (a) Condensed fraction as a function of temperature for different values of the filling fraction Φ. Temperatures are expressed in units of the condensation temperature with no impurities T_λ^0. (b) Condensed fraction as a function of the temperature normalized with $T_\lambda(\Phi)$. Scans with $r_p = 4\xi$ and $r_{\min} = 2r_p = 8\xi$.

using the interaction potential obtained at $T = 0$. For weak repulsion, even if the condensate vanishes, impurities still feel the density-mediated attraction.

2.4. Condensation and BKT transition temperatures in presence of impurity clusters

Studying different values of $r_{\min}$ allowed us to show that an increasing of n_0 occurs only when the fluid depletion, due to the presence of impurities, is confined to a large connected region at all temperatures. Therefore such effect can not be simply explained by the local increase of density in regions not occupied by impurities. In the following we consider hard-sphere impurities by fixing $r_{\min} = 2a_I$. In order to quantitatively characterize the change in n_0, we study how the condensation transition changes when varying the filling fraction

$$\Phi = 1 - \frac{|\langle\psi\rangle_{T=0}|^2}{\langle|\psi|^2\rangle_{T=0}}, \tag{8}$$

which corresponds to the fraction of the total volume occupied by the impurities. In figure 4(a) the condensed fraction is shown for different values of Φ, obtained by varying the number of impurities. It is evident that the larger is the number of clustered impurities, the higher results the condensation transition temperature. We explicit the dependence of the transition temperature on the filling fraction as $T_\lambda(\Phi)$.

The condensation temperature $T_\lambda(\Phi)$ is measured for different values of Φ following the same procedure explained in the previous section. In figure 5(a) the relative increase $\Delta T_\lambda = (T_\lambda(\Phi) - T_\lambda^0)/T_\lambda^0$ is displayed. Remarkably, ΔT_λ scales linearly with Φ growing up to 20%. We have checked by varying the number of impurities, their size and the parameter $r_{\min}$ for values lower than $2a_I$, that n_0 only depends on Φ and T (data not shown). Despite the change on T_λ, the condensed fraction curves collapse as expected to a single one, once plotted versus $T/T_\lambda(\Phi)$ (see figure 4(b)).

Finally, we briefly address the role of impurities in the the BKT transition. A detailed study will be left for a further work. This phase transition manifests through a change in the behavior of the correlation function $g_1(r) = \langle\psi(0)\psi^*(\mathbf{r})\rangle$ at the BKT transition temperature $T_{\rm BKT}$. At

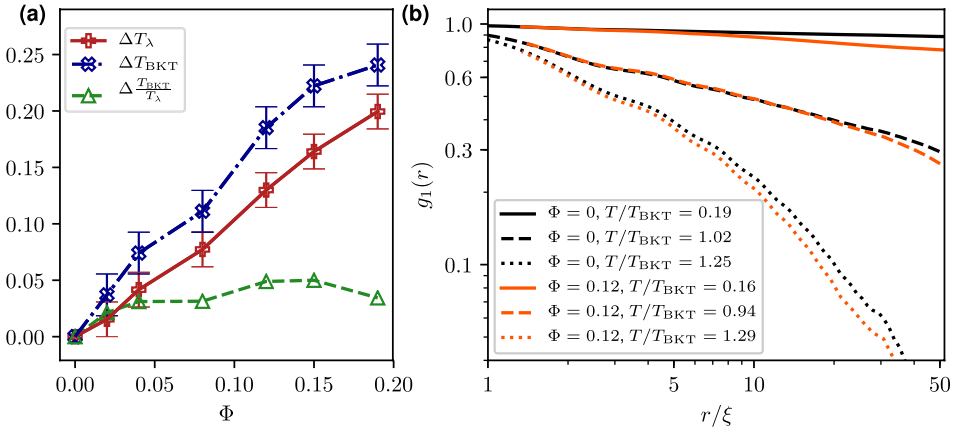


Figure 5. (a) Relative increments of T_λ and $T_{\rm BKT}$ as a function of the filling fraction Φ. The relative increment of the ratio $\frac{T_{\rm BKT}}{T_\lambda}$ is also shown. (b) Spatial correlation function $g_1(r)$ for three different temperatures (lower, close and higher than $T_{\rm BKT}$) with and without impurities.

$T < T_{\rm BKT}$, it presents a power-law decay $g_1(r) \sim r^{-\alpha}$, where α depends linearly on the temperature; at high temperatures, it exhibits the standard exponential decay of disordered systems. In figure 5(b) we show $g_1(r)$ at different temperatures (lower, close and higher than $T_{\rm BKT}$) where these two behaviors are clearly distinguishable. The BKT transition temperature can be thus determined by finding where $g_1(r)$ abruptly changes its behavior [46]. With no impurities and the parameters used in this article, the BKT transition takes place at $T_{\rm BKT} = 0.83 T_\lambda^0$. Note that because of the Mermin–Wagner–Hohenberg theorem [7, 8], the condensation critical temperature vanishes as $1/\log L$ in the thermodynamic limit, so in principle for a very large system we could have $T_\lambda^0 < T_{\rm BKT}$. We do not address such limit in this article. The presence of impurities in the system modifies the decay of $g_1(r)$ by shifting $T_{\rm BKT}$ to higher temperatures. Figure 5(a) also displays the relative increase $\Delta T_{\rm BKT} = (T_{\rm BKT}(\Phi) - T_{\rm BKT}^0)/T_{\rm BKT}^0$ of the BKT transition temperature for different filling fractions Φ. Although T_λ and $T_{\rm BKT}$ both grow up to 20% when the Φ is increased, their ratio remains almost constant. Let us remark that there are no important effects on $T_{\rm BKT}$ if impurities are not clustered.

The increase of the transition temperatures T_λ and $T_{\rm BKT}$ can be explained by a simple phenomenological argument. Large objects in the system, such as the clustered impurities, modify the fluid wave-function boundary conditions. In particular, they impose effective Dirichlet boundary condition leading to symmetries in Fourier space, decreasing the number of active modes. At a given temperature, with less active modes, the energy is smaller and thus a higher temperature is necessary to induce a transition. We stress that this result is general and does not depend on the choice of the repulsion potential $V_{\rm rep}$, as long as it is sufficiently short-range to allow the formation of a large-size cluster at all $T < T_\lambda$. Our results could apply as well to two-component BECs, with the components having different condensation temperatures and strong repulsion between them. Finally, the same effect on the condensation curve will occur in three dimensions, as it comes from a geometrical effect.

3. Discussion

In this article we studied thermal states of two-dimensional superfluids with active impurities. We demonstrated how the phase transitions are affected by the emergence of impurity clusters, opening up the possibility to raise the transition temperatures in experiments by doping superfluids with specific types of impurities. Such result rises new questions that would be interesting to address in detail. In particular, it is remarkable that the presence of impurities does not disorder the system inducing a loss of coherence. Is there a maximum value of the critical temperature that can be reached using impurities, or it will continue to increase until the impurities occupy the full domain? Could the modification of the condensation curve be rephrased as a competition between the full perimeter and the full area of the impurities? Moreover, this system presents a rich behaviour that, up our knowledge, has not yet been addressed in details. For instance, during the thermalisation dynamics, impurities cluster similarly to a diffusion-limited aggregation process [47]. Also, a complete study of the BKT transition, considering the opposite limit $T_\lambda < T_{\mathrm{BKT}}$, needs to be investigated and might devise new interesting physics.

Acknowledgments

The authors were supported by the cost-share Royal Society International Exchanges Scheme (ref. IE150527) in conjunction with CNRS. GK and DP acknowledge the Federation Doeblin for supporting DP during his sojourn in Nice. DP was supported by the UK Engineering and Physical Sciences Research Council (EPSRC) research grant EP/P023770/1. GK and UG were also supported by the ANR JCJC GIANTE ANR-18-CE30-0020-01. Computations were carried out on the Mésocentre SIGAMM hosted at the Observatoire de la Côte d'Azur. The authors acknowledge the anonymous referees for their interesting comments.

ORCID iDs

Umberto Giuriato https://orcid.org/0000-0002-0211-2458
Giorgio Krstulovic https://orcid.org/0000-0002-9934-6292
Davide Proment https://orcid.org/0000-0002-9472-0097

References

[1] Griffin A, Snoke D W and Stringari S 1996 *Bose–Einstein Condensation* (Cambridge: Cambridge University Press)
[2] Anderson M H, Ensher J R, Matthews M R, Wieman C E and Cornell E A 1995 Observation of Bose–Einstein condensation in a dilute atomic vapor *Science* **269** 198–201
[3] Hadzibabic Z and Dalibard J 2011 Two-dimensional Bose fluids: an atomic physics perspective *Riv. Nuovo Cimento* **34** 389
[4] Kasprzak J *et al* 2006 Bose–Einstein condensation of exciton polaritons *Nature* **443** 409
[5] Demokritov S O, Demidov V E, Dzyapko O, Melkov G A, Serga A A, Hillebrands B and Slavin A N 2006 Bose–Einstein condensation of quasi-equilibrium magnons at room temperature under pumping *Nature* **443** 430
[6] Klaers J, Schmitt J, Vewinger F and Weitz M 2010 Bose–Einstein condensation of photons in an optical microcavity *Nature* **468** 545
[7] Mermin N D and Wagner H 1966 Absence of ferromagnetism or antiferromagnetism in one- or two-dimensional isotropic heisenberg models *Phys. Rev. Lett.* **17** 1133–6

[8] Hohenberg P C 1967 Existence of long-range order in one and two dimensions *Phys. Rev.* **158** 383–6
[9] Kosterlitz J M and Thouless D J 1973 Ordering, metastability and phase transitions in two-dimensional systems *J. Phys. C: Solid State Phys.* **6** 1181
[10] Kosterlitz J M 1974 The critical properties of the two-dimensional xy model *J. Phys. C: Solid State Phys.* **7** 1046
[11] Berezinskii V L 1971 Destruction of long-range order in one-dimensional and two-dimensional systems having a continuous symmetry group I. classical systems *Sov. Phys.—JETP* **32** 493–500
[12] Stock S, Hadzibabic Z, Battelier B, Cheneau M and Dalibard J 2005 Observation of phase defects in quasi-two-dimensional Bose–Einstein condensates *Phys. Rev. Lett.* **95** 190403
[13] Hadzibabic Z, Krüger P, Cheneau M, Battelier B and Dalibard J 2006 Berezinskii–Kosterlitz–Thouless crossover in a trapped atomic gas *Nature* **441** 1118
[14] Krüger P, Hadzibabic Z and Dalibard J 2007 Critical point of an interacting two-dimensional atomic bose gas *Phys. Rev. Lett.* **99** 040402
[15] Schweikhard V, Tung S and Cornell E A 2007 Vortex proliferation in the Berezinskii–Kosterlitz–Thouless regime on a two-dimensional lattice of Bose–Einstein condensates *Phys. Rev. Lett.* **99** 030401
[16] Cladé P, Ryu C, Ramanathan A, Helmerson K and Phillips W D 2009 Observation of a 2d bose gas: from thermal to quasicondensate to superfluid *Phys. Rev. Lett.* **102** 170401
[17] Nitsche W H, Kim N Y, Roumpos G, Schneider C, Kamp M, Höfling S, Forchel A and Yamamoto Y 2014 Algebraic order and the Berezinskii–Kosterlitz–Thouless transition in an exciton-polariton gas *Phys. Rev.* B **90** 205430
[18] Bishop D J and Reppy J D 1978 Study of the superfluid transition in two-dimensional ^{4}He films *Phys. Rev. Lett.* **40** 1727–30
[19] Prokof'ev N, Ruebenacker O and Svistunov B 2001 Critical point of a weakly interacting two-dimensional bose gas *Phys. Rev. Lett.* **87** 270402
[20] Simula T P, Lee M D and Hutchinson D A W 2005 Transition from the Bose–Einstein condensate to the Berezinskii–Kosterlitz–Thouless phase *Phil. Mag. Lett.* **85** 395–403
[21] Nazarenko S, Onorato M and Proment D 2014 Bose–Einstein condensation and Berezinskii–Kosterlitz–Thouless transition in the two-dimensional nonlinear schrödinger model *Phys. Rev.* A **90** 013624
[22] Shukla V, Brachet M and Pandit R 2013 Turbulence in the two-dimensional fourier-truncated Gross–Pitaevskii equation *New J. Phys.* **15** 113025
[23] Donnelly R J 1991 *Quantized Vortices in Helium* II vol 2 (Cambridge: Cambridge University Press)
[24] Bewley G P, Lathrop D P and Sreenivasan K R 2006 Superfluid helium: visualization of quantized vortices *Nature* **441** 588
[25] Zmeev D E, Pakpour F, Walmsley P M, Golov A I, Guo W, McKinsey D N, Ihas G G, McClintock P V E, Fisher S N and Vinen W F 2013 Excimers he_2^* as tracers of quantum turbulence in ^{4}He in the $t = 0$ limit *Phys. Rev. Lett.* **110** 175303
[26] La Mantia M and Skrbek L 2014 Quantum turbulence visualized by particle dynamics *Phys. Rev.* B **90** 014519
[27] Spethmann N, Kindermann F, John S, Weber C, Meschede D and Widera A 2012 Dynamics of single neutral impurity atoms immersed in an ultracold gas *Phys. Rev. Lett.* **109** 235301
[28] Catani J, Lamporesi G, Naik D, Gring M, Inguscio M, Minardi F, Kantian A and Giamarchi T 2012 Quantum dynamics of impurities in a one-dimensional bose gas *Phys. Rev.* A **85** 023623
[29] Michel C, Boughdad O, Albert M, Larré P-É and Bellec M 2018 Superfluid motion and drag-force cancellation in a fluid of light *Nat. Commun.* **9** 2108
[30] Carusotto I 2014 Superfluid light in bulk nonlinear media *Proc. R. Soc.* A **470** 20140320
[31] Amo A, Lefrère J, Pigeon S, Adrados C, Ciuti C, Carusotto I, Houdré R, Giacobino E and Bramati A 2009 Superfluidity of polaritons in semiconductor microcavities *Nat. Phys.* **5** 805
[32] Klein A, Bruderer M, Clark S R and Jaksch D 2007 Dynamics, dephasing and clustering of impurity atoms in Bose–Einstein condensates *New J. Phys.* **9** 411
[33] Krotscheck E, Saarela M and Epstein J L 1988 Impurity states in liquid–helium films *Phys. Rev.* B **38** 111–28
[34] Krotscheck E and Zillich R E 2008 Hydrogen and ^{3}He atoms on ^{4}He surfaces: bound states and scattering features *Phys. Rev.* B **77** 094507
[35] Rica S and Roberts D C 2009 Induced interaction and crystallization of self-localized impurity fields in a Bose–Einstein condensate *Phys. Rev.* A **80** 013609

[36] Winiecki T and Adams C S 2000 Motion of an object through a quantum fluid *Europhys. Lett.* **52** 257
[37] Shukla V, Brachet M and Pandit R 2016 Sticking transition in a minimal model for the collisions of active particles in quantum fluids *Phys. Rev.* A **94** 041602
[38] Shukla V, Pandit R and Brachet M 2018 Particles and fields in superfluids: insights from the two-dimensional Gross–Pitaevskii equation *Phys. Rev.* A **97** 013627
[39] Davis M J, Morgan S A and Burnett K 2001 Simulations of bose fields at finite temperature *Phys. Rev. Lett.* **87** 160402
[40] Connaughton C, Josserand C, Picozzi A, Pomeau Y and Rica S 2005 Condensation of classical nonlinear waves *Phys. Rev. Lett.* **95** 263901
[41] Krstulovic G and Brachet M 2011 Dispersive bottleneck delaying thermalization of turbulent Bose–Einstein condensates *Phys. Rev. Lett.* **106** 115303
[42] Berloff N G and Youd A J 2007 Dissipative dynamics of superfluid vortices at nonzero temperatures *Phys. Rev. Lett.* **99** 145301
[43] Krstulovic G and Brachet M 2011 Anomalous vortex-ring velocities induced by thermally excited kelvin waves and counterflow effects in superfluids *Phys. Rev.* B **83** 132506
[44] Krstulovic G and Brachet M 2011 Energy cascade with small-scale thermalization, counterflow metastability, and anomalous velocity of vortex rings in fourier-truncated Gross–Pitaevskii equation *Phys. Rev.* E **83** 066311
[45] Gardiner C 2009 *Stochastic Methods: a Handbook for the Natural and Social Sciences* (*Springer Series in Synergetics*) (Berlin: Springer)
[46] Foster C J, Blakie P B and Davis M J 2010 Vortex pairing in two-dimensional bose gases *Phys. Rev.* A **81** 023623
[47] Witten T A and Sander L M 1983 Diffusion-limited aggregation *Phys. Rev.* B **27** 5686–97

Conclusions

In this Thesis we investigated systematically the dynamics of particles in superfluids, by exploiting numerical simulations of the Gross–Pitaevskii model coupled with highly repulsive moving potentials [89, 214, 242]. The main body of the results concerns the interaction between particles and superfluid vortices at very low temperature. The experimental motivation of this part of the work is the recent implementation of micron sized particles as probes in superfluid helium [28, 91, 208]. We first focused on specific settings, characterizing in detail the mutual interaction between particles and vortices. Then we explored the dynamics of particles in a complex quantum turbulence regime, in which all the mechanisms addressed before are present.

In the study about the long-range interaction between a particle and a vortex [75], we derived from the GP model an effective theory for describing the capture mechanism. This allowed us to validate the robustness of the model, besides showing a novel manner to excite monochromatic Kelvin waves along the vortex filaments. Such mechanism could inspire innovative experimental techniques for studying vortex waves in atomic Bose–Einstein condensates. The long-range effective theory exhibits a scale invariance which is qualitatively reproduced also in the reconnections of vortices mediated by trapped particles [77]. Thus, although the size of the particles that can be effectively implemented in our simulation is less than 100 vortex core sizes, this scale invariance suggests that a similar dynamics may exist also at the typical scales of superfluid helium experiments. A simple way to expand the results of this work is to consider different initial velocities of the particle in different directions. This could allow to build a cross-section for the vortex-particle collision and determine a threshold for the angle at which a particle can escape.

The simulations of vortex reconnections mediated by trapped particles [77] provided interesting insights on the momentum exchanges occurring in the system during such violent events. We showed that the main channel of momentum transfer is between the filaments and the particle (at which the reconnection takes place), that indeed gets strongly accelerated. Then, as a further support of superfluid helium experiments, we showed that the dynamics of the reconnection is almost unaffected if light particles are used to sample the vortices.

Consistently, light particles turned out to be the most suitable also for the tracking of vortex waves [79]. This direct observation from GP simulations is one of the predictions of the phenomenological model that we developed specifically to address this problem. Such effective theory stems from an analogy with the quantum mechanical description of one-dimensional crystals, in which vortex waves play the role of electron wavefunctions and particles that of atomic barriers [127]. The main difference is that the effective potential barriers due to the particles depend on the frequency of the

incoming waves, besides the inertia. The consequence of this fact is that light particles deform less the vortex wave dispersion relation, while large scale Kelvin waves can be efficiently sampled by particles of any mass. Moreover, the GP simulations and the crystal analogy agree on predicting the arising of new high frequency excitations branches in the dispersion relation, an explicit signature of the crystal behaviour of the system. Another prediction confirmed by the simulations and which has direct interest for experimental applications is the existence of a precession frequency for trapped particles, due to Magnus effect. Being such frequency proportional to the circulation, its measurement may be an indirect way of determining whether and how many vortices are piercing a particle in superfluid helium. Note that in [79], we considered only linear vortex excitations. A natural question is whether particles can be able to grasp some signatures of the energy cascade due to nonlinear interactions of Kelvin waves. At the same time, a non trivial problem is understanding if and how an array of trapped particles could affect such nonlinear interactions. One remark about the study [79] is that particles are initially set by hand at equal distances along the vortices. Although this fact is consistent with what observed in experiments, a proven theoretical explanation for such behaviour is still missing.

The effective model based on vortex line displacements coupled with point particles could be further developed in future works. Given the similarity with a crystal, additional studies might discover in superfluids the analog of phenomena typically belonging to solid state physics. For instance, tight-binding models [111] may be adapted to the vortex-particle system when particles of different masses or different sizes are considered. Considering particles randomly distributed along the vortex filament will enable vortex waves to propagate in a disorder medium and this might give rise to behaviours akin to Anderson localization [2]. More simply, allowing the point particles of the effective model to move along the vortex direction could allow to compute the momentum exchange between a particle and a packet of Kelvin waves propagating towards it. Then, it would be straightforward to compare such calculation with direct GP simulations. Finally, since the effective model is built with hydrodynamical equations, in principle it applies to vortices in classical fluids, which may be easier to generate and study in a laboratory. In this sense, it could be interesting to use classical fluids to build analogs of quantum systems.

Monitoring the dynamics of particles in a turbulent vortex tangle [76] revealed that their presence does not affect the building and the decay of a quantum turbulence regime. Even in such complex system, particles tend to remain attached to the vortex filaments most of the time, proving to be good candidates to be used as probes. The motion of particles is compatible with a classical Lagrangian dynamics over long periods [248], meaning that they can detect the Kolmogorov turbulence regime existing at scales larger than the inter-vortex distance. At smaller scales, the Magnus precession frequency is dominating the velocity spectrum, which may be responsible also for the fast decay of the acceleration correlation function. In future studies within a quantum turbulence configuration, it may be relevant to consider larger simulations and include more particles, in order to improve the statistics and maybe observe deviations from Gaussian distributions, in accordance to superfluid helium experiments [137, 197].

Moreover, the dynamics of particles coupled with a nonlocal model of quantum fluids [23, 159, 187] in a turbulent regime can be investigated. In this way, the compressibility effect would be reduced and a scenario more similar to actual superfluid helium can be achieved.

We stress that the particle model based on the GP equation exploited in this Thesis is minimal, in the sense that each particle is described just by its position and momentum, although having a finite size. Moreover, in all the settings with many particles involved, we considered only particles with the same mass and the same size. The next level of such research project is thus to add more complexity to the model. The Gross–Clark model for instance has already been used to study the dynamics of impurity fields in a superflow and their interaction with vortices [24, 232]. However, we remark that modeling particles as bubble fields limits the possibility to consider a large number of them, because of the computational cost. A longer viable solution consists in modeling particles as anisotropic potentials with a fixed ellipsoid shape, which would allow to add rotational degrees of freedom[1]. Note indeed that currently there are experimental suspects about the presence of relevant anisotropies of the particles used in superfluid helium. For example, a flickering of the light reflected by solidified hydrogen particles has been observed in experiments, which is possibly due to the (non-spherical) particle rotation. Ideally, all the problems addressed so far and presented in this manuscript could be reformulated with such more complex particles in future works. For instance, when an elongated particle attaches to a vortex or detaches from it, some angular momentum may be exchanged.

In the last part of the Thesis we included finite temperature effects to the GP model coupled with particles. In particular, we adopted the Galerkin truncation procedure, which is a well-established technique to simulate thermal modes in the GP framework [52, 128]. It turned out that the system behaves more as a gas of thermal waves than a continuous liquid [78], at least for the typical sizes of simulations and impurities that can be effectively achieved with the current computational power. In such system, the dynamics of isolated impurities is akin to an Ornstein–Uhlenbeck process. However, when many impurities are present, a clustering transition may take place [80], because of the fluid mediated attraction [212]. In presence of a cluster of impurities, we found that the critical temperatures associated to the phase transitions in the system are shifted towards higher values. This could be useful for experimental applications with atomic BECs, where active and finite-size impurities can be generated by additional condensates in the highly repulsive regime [191].

As a final remark, we stress once again that since the GP model captures naturally the hydrodynamics of quantum vortices, it is an optimal framework to study the dynamics of particles in a low temperature quantum fluid. In this sense, the results presented from chapter 3 to chapter 5 may be relevant for superfluid helium experiments, in the case where the normal component is negligible. Conversely, the GP model is not the best setting to reproduce the finite temperature effects typical of a viscous liquid on the particle dynamics, like the Stokes drag. One possibility to overcome this issue could

[1] We remark that since a superfluid is inviscid, the rotation of a spherical object has no effect on the flow.

be for instance to add explicitly a Stokes drag term in the equations for the particles, although this may generate a lack of consistency with the coupled GP equation. In this regard, using different methods to model the dynamics of particles in a finite temperature superfluid could be a better solution [179, 208], leaving the GP model in its original domain of very low temperature quantum fluids.

A Numerical Methods

In this Appendix, we provide a short description of the main numerical techniques used to achieve the results presented in the Thesis. The details related to each specific configuration studied are reported in the corresponding article, included in this manuscript.

The coupled equations (2.59) and (2.60) considered in this Thesis are respectively a PDE for the superfluid field ψ and a set of N_p ODE's, one for each particle position $\boldsymbol{q}_j$. We report them also here for clarity:

$$i\hbar\frac{\partial}{\partial t}\psi(\boldsymbol{x},t) = \left[-\frac{\hbar^2}{2m}\nabla^2 + g|\psi(\boldsymbol{x},t)|^2 - \mu + \sum_{i=1}^{N_\mathrm{p}} V_\mathrm{p}\left(|\boldsymbol{x}-\boldsymbol{q}_i(t)|\right)\right]\psi(\boldsymbol{x},t) \quad \text{(A.1)}$$

$$M_\mathrm{p}\ddot{\boldsymbol{q}}_i = -\int V_\mathrm{p}\left(\boldsymbol{x}-\boldsymbol{q}_i(t)\right)\nabla|\psi(\boldsymbol{x},t)|^2\,\mathrm{d}\boldsymbol{x} - \sum_{j\neq i}^{N_\mathrm{p}}\frac{\partial}{\partial \boldsymbol{q}_i}V^{ij}_\mathrm{rep}. \quad \text{(A.2)}$$

The field ψ is discretized with a linear span over a 3D lattice of sides L_x, L_y, L_z with respectively N_x, N_y and N_z points per side (so that the total number of collocation points is $N_\mathrm{c} = N_x \times N_y \times N_z$ and periodic boundary conditions. The length of each side is a multiple of 2π, typically simply $L_x = L_y = L_z = 2\pi$. The 2D simulations are performed in the same setting but with $N_z = 1$.

A.1 Time stepping

Calling Ψ the matrix describing the discretized superfluid field, Q the array containing all the particle positions and V the array containing all the particle velocities, the corresponding equations can be written schematically as

$$\frac{\partial\Psi}{\partial t} = \mathrm{RHS}_\Psi\left[\Psi(t),Q(t)\right], \quad \text{(A.3)}$$

$$\frac{\partial V}{\partial t} = \mathrm{RHS}_Q\left[\Psi(t),Q(t)\right], \quad \text{(A.4)}$$

$$\frac{\partial Q}{\partial t} = V(t), \quad \text{(A.5)}$$

where RHS_Ψ and RHS_Q are the discretized versions of the right hand sides of Eqs. (2.59) and (2.60), respectively. The time stepping used to solve these equations is the same for each variable Ψ, Q and V. Indeed, denoting by U a generic array, each of the

equations (A.3), (A.4), (A.5) can be written as

$$\frac{\partial U}{\partial t} = \mathrm{RHS}\left[U(t)\right], \tag{A.6}$$

where RHS is an array having the same dimensions of U. Supposing that $U(t=0)$ in the initial condition is known and being Δt the time step, we denote $t_n = n\Delta t$ with n the integer number of time steps, so that $U_n = U(t_n)$. We use a 4^{th} order Runge–Kutta scheme for the time stepping, which is of order $\mathcal{O}(\Delta t^4)$:

$$\begin{aligned}
U_{n+1} &= U_n + \frac{\Delta t}{6}\left(K_1 + 2K_2 + 2K_3 + K_4\right), && \text{(A.7)}\\
K_1 &= \mathrm{RHS}\left[U_n\right]\cdot\Delta t, && \text{(A.8)}\\
K_2 &= \mathrm{RHS}\left[U_n + \frac{K_1}{2}\right]\cdot\Delta t, && \text{(A.9)}\\
K_3 &= \mathrm{RHS}\left[U_n + \frac{K_2}{2}\right]\cdot\Delta t, && \text{(A.10)}\\
K_4 &= \mathrm{RHS}\left[U_n + K_3\right]\cdot\Delta t. && \text{(A.11)}\\
& && \text{(A.12)}
\end{aligned}$$

Note that for the realization of the thermal states using the stochastic real Ginzburg–Landau equation (see sections 6.1.1 and 6.3), just a simple Euler scheme is used for the time stepping.

A.2 Pseudo-spectral method for the superfluid field

The right-hand side of the GP equation (A.3) is composed of linear terms in Ψ and a non-linear term. In general, it can be written as

$$\frac{\partial \Psi}{\partial t} = L\left[\Psi\right] + NL\left[\Psi\right], \tag{A.13}$$

where L is a linear operator and NL is the non-linear term. In particular, the linear terms contain the multiplication of the field with the particle potential and the chemical potential, and the Laplacian of Ψ. Since the boundary conditions are periodic, the derivatives can be simply computed in Fourier space, where they are just a multiplication by wave numbers. Specifically, considering for the sake of simplicity the 1D case[1] and calling Δx the spatial mesh, the interval $[0, 2\pi]$ is splitted into N_c collocation points $x_j = j\Delta x$ with $j \in [0, N_c - 1]$. Thus, any field $f(x)$ can be expressed by its discrete Fourier series:

$$\hat{f}_N(k) = \sum_{j=-\frac{N_c}{2}}^{\frac{N_c}{2}-1} f(x_j) e^{i\frac{2\pi j}{N_c}k}, \tag{A.14}$$

[1] The generalization to more dimensions is straightforward, being the Fourier transform on each direction independent of the others.

with the wavenumber $k \in \left[-\frac{N_c}{2}, \frac{N_c}{2} - 1\right]$. The Fourier transform (A.14) requires $\mathcal{O}(N_c^2)$ operations. In the simulations, the Fast Fourier Transform (FFT) algorithm is applied, which requires only $\mathcal{O}(N_c \log_2 N_c)$ operations [182].

Once the Laplacian of Ψ has been computed in Fourier space, an inverse FFT is applied and the other terms are dealt with in physical space. In particular, the non-linear term would imply expensive convolutions in Fourier space, while it is just a multiplication in physical space. Note that the error committed by using a pseudo-spectral approach to approximate a PDE is smaller than any power of $1/N_c$.

A.3 Projection and dealiasing

Despite the great performance improvement provided by the use of a pseudo-spectral algorithm, one of its downside is given by the aliasing. For example, assuming a non-linearity of order 2, two modes k_1 and k_2 (in 1D for simplicity) would interact giving rise to a contribution to the modes $k_1 \pm k_2$. Then, because of the intrinsic periodicity of the Fourier transforms, modes such that $|k_1 \pm k_2| > N_c/2$ would be considered as low wavenumbers and affect the conservation of the invariants of the PDE. Such issue can be avoided dealiasing the system, namely reducing the Fourier space by a factor $\frac{p-1}{p+1}$, where p is the order of non-linearity [85]. In practice, a maximum wavenumber $k_{\max} = \frac{1}{p+1} N_c$ and all the modes $|\boldsymbol{k}| < k_{\max}$ are set to zero. This operation is performed by means of a Galerkin operator $\mathcal{P}_G$, which acts on a function $f(\boldsymbol{x})$ as

$$\mathcal{P}_G[f(\boldsymbol{x})] = \sum_{\boldsymbol{k}} \hat{f}(\boldsymbol{k}) e^{i\boldsymbol{k}\cdot\boldsymbol{x}} \theta_H(k_{\max} - |\boldsymbol{k}|), \tag{A.15}$$

where $\hat{f}(\boldsymbol{k})$ is the Fourier transform of f and $\theta_H(k_{\max} - |\boldsymbol{k}|) \equiv \theta_{\boldsymbol{k}}$ is the Heaviside theta. For a quadratic non-linearity, this implies a reduction by a factor $1/3$ of the Fourier space, namely only $2/3$ of the total number of modes are active. For this reason, the dealiasing procedure takes the name "2/3 rule". Since the non-linearity of the GP equation (A.13) is cubic, this would imply the use of a $2/4 = 1/2$ rule, that means losing one half of the resolution. However, a scheme has been developed specifically for the GP equation, in which the $2/3$ rule is restored even for a cubic non-linearity at the cost of performing an extra FFT [128, 131]. Such scheme is the same used in the works presented in this Thesis. Also the Leibniz rule for the derivation of a product of functions is recovered by the use of a $2/3$ dealiasing. It means that for two periodic dealiased functions $f(x) \equiv \mathcal{P}_G[f(x)]$ and $g(x) \equiv \mathcal{P}_G[g(x)]$ the following equation holds:

$$f\partial_x g + g\partial_x f = \partial_x \mathcal{P}_G[fg], \tag{A.16}$$

which in general is not true when dealiasing is not applied [128]. It can be shown that the validity of Eq. (A.16) is crucial for the conservation of momentum in GP without particles [128]. In the following, we show explicitly that this is the case also if particles are present in the system.

A.3.1 Dealiasing of the particle interaction term and momentum conservation

In this section we give an explicit demonstration of how the projection procedure with the 2/3 rule allows to conserve the total momentum of the GP-particles system (A.1), (A.2). For simplicity, we consider one single particle in $1D$ and we do not take into account the pure GP terms, which are known to conserve momentum on their own if dealiased with the 2/3 rule [128]. Therefore, the (partial) Hamiltonian of the truncated system is

$$H_{\mathrm{p}} = \int V_{\mathrm{p}}(|x - q(t)|)\mathcal{P}_{\mathrm{G}}\left[|\psi(x,t)|^2\right] \mathrm{d}x + \frac{p(t)^2}{2M_{\mathrm{p}}}, \tag{A.17}$$

where the particle potential and the superfluid field are always dealiased, i.e. $\psi \equiv \mathcal{P}_{\mathrm{G}}[\psi]$ and $V_{\mathrm{p}} = \mathcal{P}_{\mathrm{G}}\left[V_{\mathrm{p}}\right]$. Besides the restoration of the Leibniz rule (A.16), we will also need the following property of the Galerkin projector (A.15), which stems from the Parseval theorem[2] and holds for every non dealiased periodic functions $f(x)$ and $g(x)$:

$$\int \mathcal{P}_{\mathrm{G}}[f(x)]\, g(x)\, \mathrm{d}x = \int f(x)\mathcal{P}_{\mathrm{G}}[g(x)] \mathrm{d}x = \int \mathcal{P}_{\mathrm{G}}[f(x)]\, \mathcal{P}_{\mathrm{G}}[g(x)] \mathrm{d}x. \tag{A.18}$$

Moreover, another useful consequence of Parseval theorem is the validity of integration by parts

$$\int \partial_x f(x) g(x)\, \mathrm{d}x = 2\pi \sum_k ik\hat{f}(k)\hat{g}(-k) = -\int f(x)\partial_x g(x)\, \mathrm{d}x. \tag{A.19}$$

In order to compute the terms of the dynamic equation for the field stemming from the Hamiltonian (A.17), we need its variation with respect to ψ:

$$\delta H_{\mathrm{p}} = \int V_{\mathrm{p}} \left(\mathcal{P}_{\mathrm{G}}[\psi\delta\psi^*] + \mathrm{c.c}\right) \mathrm{d}x = \int \mathcal{P}_{\mathrm{G}}\left[V_{\mathrm{p}}\right] \left(\psi\delta\psi^* + \mathrm{c.c}\right) \mathrm{d}x, \tag{A.20}$$

where in the second equality we applied the property (A.18). The Hamilton equation for ψ is thus

$$i\hbar\partial_t\psi \equiv i\hbar\partial_t\mathcal{P}_{\mathrm{G}}[\psi] = \mathcal{P}_{\mathrm{G}}\left[\frac{\delta H_{\mathrm{p}}}{\delta\psi^*}\right] = \mathcal{P}_{\mathrm{G}}\left[\mathcal{P}_{\mathrm{G}}\left[V_{\mathrm{p}}\right]\psi\right] = \mathcal{P}_{\mathrm{G}}\left[V_{\mathrm{p}}\psi\right]. \tag{A.21}$$

The variation in time of the total momentum of the system $P = P_{\mathrm{GP}} + p$ (where p is the particle momentum and $P_{\mathrm{GP}} = -\frac{i\hbar}{2}\int \left(\psi^*\partial_x\psi - \psi\partial_x\psi^*\right) \mathrm{d}x$ the fluid momentum) is given by

$$\frac{\mathrm{d}P}{\mathrm{d}t} = -\frac{i\hbar}{2}\int \left(\partial_t\psi^*\partial_x\psi + \psi^*\partial_{tx}\psi - \partial_t\psi\partial_x\psi^* - \psi\partial_{tx}\psi^*\right) \mathrm{d}x + \frac{\mathrm{d}p}{\mathrm{d}t}. \tag{A.22}$$

We substitute the dynamic equation (A.21) and its complex conjugate in the first term

[2] For two functions $f(x)$ and $g(x)$, which are complex-valued on $\mathbb{R}$, square-integrable and of period 2π, Parseval theorem states that: $\frac{1}{2\pi}\int f(x)g(x)\,\mathrm{d}x = \sum_k \hat{f}(k)\hat{g}(-k)$.

of the right hand side of Eq. (A.22), which is $\frac{\mathrm{d}P_{\mathrm{GP}}}{\mathrm{d}t}$:

$$\begin{aligned}\frac{\mathrm{d}P_{\mathrm{GP}}}{\mathrm{d}t} = \quad & \tfrac{1}{2}\int \Big(\mathscr{P}_{\mathrm{G}}\left[V_{\mathrm{p}}\psi^*\right]\partial_x\psi + \psi^*\partial_x\mathscr{P}_{\mathrm{G}}\left[V_{\mathrm{p}}\psi\right] \\ & -\mathscr{P}_{\mathrm{G}}\left[V_{\mathrm{p}}\psi\right]\partial_x\psi^* - \psi\partial_x\mathscr{P}_{\mathrm{G}}\left[V_{\mathrm{p}}\psi^*\right]\Big)\,\mathrm{d}x. \end{aligned} \tag{A.23}$$

After the integration by parts (A.19), it simplifies to

$$\frac{\mathrm{d}P_{\mathrm{GP}}}{\mathrm{d}t} = \int \left(\mathscr{P}_{\mathrm{G}}\left[V_{\mathrm{p}}\psi^*\right]\partial_x\psi + \mathscr{P}_{\mathrm{G}}\left[V_{\mathrm{p}}\psi\right]\partial_x\psi^*\right)\mathrm{d}x, \tag{A.24}$$

which becomes

$$\frac{\mathrm{d}P_{\mathrm{GP}}}{\mathrm{d}t} = \int V_{\mathrm{p}}\left(\psi^*\mathscr{P}_{\mathrm{G}}\left[\partial_x\psi\right] + \psi\mathscr{P}_{\mathrm{G}}\left[\partial_x\psi^*\right]\right)\mathrm{d}x, \tag{A.25}$$

after exchanging the projectors according to (A.18)[3]. Finally, since the dealiasing is performed with the 2/3 rule, we can apply the Leibniz rule (A.16) to the term in parenthesis inside the integral, which yields:

$$\frac{\mathrm{d}P_{\mathrm{GP}}}{\mathrm{d}t} = \int V_{\mathrm{p}}\partial_x\mathscr{P}_{\mathrm{G}}\left[|\psi|^2\right]\mathrm{d}x. \tag{A.26}$$

Now we compute the contribution to the total momentum variation (A.22) coming from $\frac{\mathrm{d}p}{\mathrm{d}t}$. It is just the Hamilton equation for the particle momentum, i.e. the force due to the fluid acting on the particle:

$$\frac{\mathrm{d}p}{\mathrm{d}t} = -\frac{\partial H_{\mathrm{p}}}{\partial q} = -\int \partial_q V_{\mathrm{p}}(|x-q|)\mathscr{P}_{\mathrm{G}}\left[|\psi|^2\right]\mathrm{d}x = \int \partial_x V_{\mathrm{p}}(|x-q|)\mathscr{P}_{\mathrm{G}}\left[|\psi|^2\right]\mathrm{d}x, \tag{A.27}$$

which becomes

$$\frac{\mathrm{d}p}{\mathrm{d}t} = -\int V_{\mathrm{p}}\partial_x\mathscr{P}_{\mathrm{G}}\left[|\psi|^2\right]\mathrm{d}x, \tag{A.28}$$

after integration by parts. Comparing $\frac{\mathrm{d}P_{\mathrm{GP}}}{\mathrm{d}t}$ (A.26) with $\frac{\mathrm{d}p}{\mathrm{d}t}$ (A.28), we see that they are exactly one the opposite of the other and thus their sum vanishes. As a consequence, the contribution to the total momentum coming from the particle and its coupling with the fluid is conserved. This result, together with the momentum consevation coming from the pure GP terms [128] implies that the total momentum of the system consisting of truncated GP and a particle is also conserved. The generalization to the case with many particles is straightforward.

[3]Note that, since $\mathscr{P}_{\mathrm{G}}$ commutes with the derivative, if a function $f(x)$ is dealiased also $\partial_x f(x)$ is dealiased. In this sense, writing the projectors in Eq. (A.25) is redundant, because the field ψ and its complex conjugate are dealiased by definition.

A.4 Implementation of the particles

In this section, we give the general methods used to implement numerically the particles in Eqs. (A.1) and (A.2). The details associated to each specific problem considered can be found in the corresponding publication, reported in this manuscript.

A.4.1 Particle potential modeling

The repulsive potential V_{p} chosen to model each particle must be localized around the particle position $\boldsymbol{q}$ and being stronger than the chemical potential μ in order to deplete completely the superfluid field. The particle potential that has been used in the results reported in this Thesis is the isotropic smoothed hat function:

$$V_{\mathrm{p}}(r) = \frac{V_0}{2}\left(1 - \tanh\left[\frac{r^2 - \zeta_{\mathrm{p}}^2}{4\Delta_{\mathrm{p}}^2}\right]\right), \tag{A.29}$$

where the parameters ζ_{p} and Δ_{p} are related respectively to the boundary size and the core size of the particle. Of course this choise is somewhat arbitrary, and in fact simpler Gaussian potentials have been used elsewhere [88, 212, 214]. However, the presence of two different adjustable parameters in the potential (A.29) gives more freedom in tuning the shape of the potential. Given a set of parameter $(V_0, \zeta_{\mathrm{p}}, \Delta_{\mathrm{p}})$, the ground state ψ_{p} of the GP model containing a single particle is determined numerically using the gradient descent method (imaginary time evolution of Eq.(2.54)). Then the effective radius of the particle is estimated as

$$a_{\mathrm{p}} = \left(\frac{3V_0}{4\pi\rho_0}\right)^{\frac{1}{3}}, \tag{A.30}$$

where

$$V_0 = L^3\left(1 - \frac{\int |\psi_{\mathrm{p}}|^2 \,\mathrm{d}\boldsymbol{x}}{\int |\psi_0|^2 \,\mathrm{d}\boldsymbol{x}}\right) \tag{A.31}$$

is the total fluid volume displaced by the particle. Such evaluation assumes that the particle is a perfect hard sphere and typically the radius estimated in this way lies in the layer at the boundary of the particle where the superfluid density passes continuously from zero (at the core of the particle) to the bulk value $|\psi_0|^2$. Therefore, the larger the size of the particle is, the better its radius is defined and the estimation (A.30) is more accurate.

One issue that one has to take into account when choosing the particle potential parameters is the Gibbs effect [53]. Indeed, if the potential V_{p} is too steep at the particle boundary, unphysical ringing oscillations appear around the particle when the potential is Fourier-transformed and then transformed back in physical space (for instance to perform the truncation procedure discussed in section A.3.1). Such artifacts are imprinted to the superfluid density as well and could affect the dynamics. In all our simulations we ingeneered the particle potential parameters trying to minimize

the Gibbs effect without increasing too much the potential boundary layer Δ_{p}.

A.4.2 Repulsion potential tuning

When more than one particle is present in the system, in order to avoid an unphysical overlap of the particle potentials, the inter-particle repulsion potential V_{rep}^{ij} must be added to the system. As already discussed in section 2.3.3, in this Thesis we chose to use the repulsive part of the Lennard–Jones potential

$$V_{\mathrm{rep}}^{ij} = \gamma_{\mathrm{rep}} \mu \left(\frac{2r_{\mathrm{rep}}}{|\boldsymbol{q}_i - \boldsymbol{q}_j|} \right)^{12}, \tag{A.32}$$

where $2r_{\mathrm{rep}}$ is the range at which the repulsion starts to act (usually set equal to to the particle diameter) and γ_{rep} is an adjusting numerical pre-factor. Specifically, a protocol by which γ_{rep} can be tuned is the following. We first calculate numerically the ground state $\psi_{2\mathrm{p}}$ of the GP equation with two fixed particles (performing the imaginary time evolution of Eq. (2.59)) placed exactly at a distance $|\boldsymbol{q}_1 - \boldsymbol{q}_2| = 2r_{\mathrm{rep}}$. When the convergence is reached, we compute the right hand side of Eq. (2.55), which is the force arising from the particle-superfluid interaction acting on each particle

$$-\int V_{\mathrm{p}}\left(\boldsymbol{x} - \boldsymbol{q}_i\right) \left|\nabla \psi_{2\mathrm{p}}(\boldsymbol{x})\right|^2 \mathrm{d}\boldsymbol{x}. \tag{A.33}$$

The origin of this force is indeed due to the superfluid mediated attractive inter-particle interaction and in this configuration it has the same modulus and opposite direction for each particle. [80, 212]. We impose this force to be equal in modulus and opposite in sign to the repulsive force imposed via the ad-hoc potential (A.32)

$$-\frac{\partial V_{\mathrm{rep}}^{ij}}{\partial \boldsymbol{q}_i} = \int V_{\mathrm{p}}\left(\boldsymbol{x} - \boldsymbol{q}_i\right) \left|\nabla \psi_{2\mathrm{p}}(\boldsymbol{x})\right|^2 \mathrm{d}\boldsymbol{x}. \tag{A.34}$$

The condition (A.34) fixes the value of γ_{rep}, so that the repulsion exactly compensate the superfluid mediated attraction when $|\boldsymbol{q}_1 - \boldsymbol{q}_2| = 2r_{\mathrm{rep}}$. Given the high steepness and short range of the potential (A.32) at distances slightly smaller than $2r_{\mathrm{rep}}$ the repulsion will push the particles away as hard spheres, while at distances slightly larger than $2r_{\mathrm{rep}}$ its effect is negligible.

A.4.3 Interpolation of the superfluid force on the particle

The right hand side of the equation for the velocity of each particle (A.4) is composed of the force arising from the inter-particle repulsion (if more than one particle is present):

$$\boldsymbol{F}_i^{\mathrm{rep}} = -\sum_{j \neq i}^{N_{\mathrm{p}}} \frac{\partial V_{ij}^{\mathrm{rep}}}{\partial \boldsymbol{q}_i}, \tag{A.35}$$

and the convolution between the particle potential and the gradient of the superfluid density:

$$\boldsymbol{F}_i^{\mathrm{GP}}(\boldsymbol{q}_i) = -\int V_{\mathrm{p}}\left(|\boldsymbol{x}-\boldsymbol{q}_i|\right)\nabla|\psi(\boldsymbol{x})|^2\,\mathrm{d}\boldsymbol{x} = -\left(V_{\mathrm{p}}\star\nabla|\psi|^2\right)[\boldsymbol{q}_i]\,, \tag{A.36}$$

which have to be computed at each timestep t_{n}. The first force (A.35) can be simply evaluated, computing analytically the derivative of the repulsive potential (A.32) and substituting the known value of the particle positions at that timestep. The force (A.36) is the force arising from the superfluid-particle interaction and two steps are needed to evaluate it. The first step is the actual evaluation of the convolution and the second one is its interpolation at the particle position. The convolution can be easily computed applying the convolution theorem, namely calculating the FFT of $V_p(\boldsymbol{x})$ and $\nabla|\psi(\boldsymbol{x})|^2$, multiply them and going back to physical space. Since both the field $V_p(\boldsymbol{x})$ and $\nabla|\psi(\boldsymbol{x})|^2$ are known in the discretized grid-space, it is necessary to interpolate the convolution $\boldsymbol{f}_{\mathrm{con}}(\boldsymbol{x}) = \left(V_{\mathrm{p}}\star\nabla|\psi|^2\right)[\boldsymbol{x}_i]$ at the actual position of the particle $\boldsymbol{q}_i$. Such operation can be performed with spectral accuracy as

$$\boldsymbol{f}_{\mathrm{con}}(\boldsymbol{q}_i) = \sum_{\boldsymbol{k}}\hat{\boldsymbol{f}}_{\mathrm{con}}(\boldsymbol{k})e^{i\boldsymbol{k}\cdot\boldsymbol{q}_i}, \tag{A.37}$$

where $\hat{\boldsymbol{f}}_{\mathrm{con}}$ is the Fourier transform of $\boldsymbol{f}_{\mathrm{con}}$ (which is already known as the output of the convolution evaluation in Fourier space). The spectral interpolation (A.37) requires N_{c} operations per each component of the position and since it has to be performed for each particle, its total numerical cost (in 3D simulations) is of about $3N_{\mathrm{p}}N_{\mathrm{c}}$ operations. Such cost quickly becomes unaffordable at high resolutions and/or large number of particles. For this reason we used the spectral interpolation in all the publications presented in this manuscript, except the study of the turbulent vortex tangle [76], in which $N_{\mathrm{c}} = 512^3$ and $N_{\mathrm{p}} = 200$.

In this last case we adopted a 4^{th} B–spline (or basis-spline) interpolation algorithm, which is a polynomial method particularly accurate and practical for pseudo-spectral codes (see [226] for a more detailed description of the method and comparison with other interpolation techniques). Let us consider for simplicity only one component of the convolution vector $f = f_{\mathrm{con},x}$ and perform the interpolation of just one component of the particle position $q = q_{i,x}$. The B-spline interpolant functions B_N are piecewise polynomyal functions of degree $N-1$ defined as $B_N = B_{N-1}\star B_1$, where $B_1(x)$ is 1 for $x\in[-0.5,0.5]$ and 0 elsewhere. They are built in order to have a high level of continuity (C^{N-1}). In Fourier space, the B-spline function of order N is simply

$$\hat{B}_N(k) = \mathrm{sinc}^N(k) = \left(\frac{\sin\pi k}{\pi k}\right)^N, \tag{A.38}$$

If we indicate with $\bar{f} = (f(x_{-1}),f(x_0),f(x_1),f(x_2))$ the (vertical) array containing the values of the field f in the four grid-points about q , then the value of f at q is

approximated as

$$f(q) = \bar{f_B^T} M_4 \bar{q}, \tag{A.39}$$

where $\bar{q} = \left(1, q, q^2, q^3\right)$, the matrix M_4 is the matrix representation of the 4^{th} B-spline function, and $\bar{f_B} = \left(f^B(x_{-1}), f^B(x_0), f^B(x_1), f^B(x_2)\right)$ is the array of the coefficients of f in the B-spline basis, defined from

$$f(x) = f_B(x) \star B_4(x). \tag{A.40}$$

Such coefficients can be easily computed in Fourier space as

$$\hat{f_B}(k) = c(k)\hat{f}(k), \tag{A.41}$$

where $c(k)$ are the known constant Fourier coefficients of the inverse B-spline function $\hat{B}_4^{-1}(k)$. We can see that such method requires only the computation of an (inverse) global FFT to determine the coefficients f_B from f. Thus, independently of the number of particles, the B-spline scheme saves a factor $\sim N_{\text{p}}$ of computational cost compared to the spectral interpolation method (A.37), making it rather efficient when a large number of particles is considered. However, some issues with physical quantities at small scales arise from the B–spline interpolation, which are shown in the Appendix of Ref. [76], reported in section 5.3.

Bibliography

[1] J. F. Allen and A. D. Misener, 'Flow of Liquid Helium II', Nature **141**, 75–75 (1938) (cit. on pp. 1, 9, 11).

[2] P. W. Anderson, 'Absence of Diffusion in Certain Random Lattices', Phys. Rev. **109**, 1492–1505 (1958) (cit. on p. 198).

[3] É. L. Andronikashvili, 'INVESTIGATION OF THE THERMAL STRUCTURE OF HELIUM II BY SCATTERING OF COLD NEUTRONS', Sov. Phys. Usp. **3**, 888 (1961) (cit. on p. 14).

[4] R. J. Arms and F. R. Hama, 'Localized-Induction Concept on a Curved Vortex and Motion of an Elliptic Vortex Ring', The Physics of Fluids **8**, 553–559 (1965) (cit. on p. 45).

[5] G. E. Astrakharchik and L. P. Pitaevskii, 'Motion of a heavy impurity through a Bose-Einstein condensate', Phys. Rev. A **70**, 013608 (2004) (cit. on p. 78).

[6] K. R. Atkins, 'Ions in Liquid Helium', Phys. Rev. **116**, 1339–1343 (1959) (cit. on p. 55).

[7] T. R. Auton, 'The lift force on a spherical body in a rotational flow', Journal of Fluid Mechanics **183**, 199–218 (1987) (cit. on p. 65).

[8] T. R. Auton, J. C. R. Hunt and M. Prud'Homme, 'The force exerted on a body in inviscid unsteady non-uniform rotational flow', J. Fluid Mech. **197**, 241–257 (1988) (cit. on pp. 5, 63–65).

[9] A. W. Baggaley, C. F. Barenghi and Y. A. Sergeev, 'Quasiclassical and ultraquantum decay of superfluid turbulence', Phys. Rev. B **85**, 060501 (2012) (cit. on p. 140).

[10] A. W. Baggaley, J. Laurie and C. F. Barenghi, 'Vortex-Density Fluctuations, Energy Spectra, and Vortical Regions in Superfluid Turbulence', Phys. Rev. Lett. **109**, 205304 (2012) (cit. on p. 139).

[11] V. Bagnato and D. Kleppner, 'Bose-Einstein condensation in low-dimensional traps', Phys. Rev. A **44**, 7439–7441 (1991) (cit. on p. 184).

[12] J. Bardeen, L. N. Cooper and J. R. Schrieffer, 'Theory of Superconductivity', Phys. Rev. **108**, 1175–1204 (1957) (cit. on p. 10).

[13] C. F. Barenghi, R. J. Donnelly and W. F. Vinen, 'Friction on quantized vortices in helium II. A review', J Low Temp Phys **52**, 189–247 (1983) (cit. on p. 46).

[14] C. F. Barenghi, R. J. Donnelly and W. F. Vinen, eds., *Quantized Vortex Dynamics and Superfluid Turbulence*, Lecture Notes in Physics (Springer-Verlag, Berlin Heidelberg, 2001) (cit. on pp. 45, 46).

[15] C. F. Barenghi, D. Kivotides and Y. A. Sergeev, 'Close Approach of a Spherical Particle and a Quantised Vortex in Helium II', J Low Temp Phys **148**, 293–297 (2007) (cit. on pp. 3, 5, 65, 71–73).

[16] C. F. Barenghi, ed., *Vortices and turbulence at very low temperatures*, CISM Courses and Lectures / International Centre for Mechanical Sciences 501 (Springer, Wien, 2008) (cit. on pp. 13, 74).

[17] C. F. Barenghi, L. Skrbek and K. R. Sreenivasan, 'Introduction to quantum turbulence', PNAS **111**, 4647–4652 (2014) (cit. on pp. 139, 140).

[18] V. Barone, *Relatività. Principi e applicazioni* (Bollati Boringhieri, 2004) (cit. on p. 28).

[19] G. K. Batchelor, *An introduction to fluid dynamics*, 1. Cambridge mathematical ed., 14. print, Cambridge Mathematical Library (Cambridge Univ. Press, Cambridge, 2010) (cit. on pp. 6, 63, 64, 66, 86).

[20] J. Bec, L. Biferale, M. Cencini, A. Lanotte, S. Musacchio and F. Toschi, 'Heavy Particle Concentration in Turbulence at Dissipative and Inertial Scales', Phys. Rev. Lett. **98**, 084502 (2007) (cit. on pp. 69, 72).

[21] J. Bec, L. Biferale, A. S. Lanotte, A. Scagliarini and F. Toschi, 'Turbulent pair dispersion of inertial particles', Journal of Fluid Mechanics **645**, 497–528 (2010) (cit. on p. 69).

[22] N. G. Berloff, 'Padé approximations of solitary wave solutions of the Gross–Pitaevskii equation', J. Phys. A: Math. Gen. **37**, 1617–1632 (2004) (cit. on pp. 39, 41).

[23] N. G. Berloff and P. H. Roberts, 'Motions in a bose condensate: VI. Vortices in a nonlocal model', J. Phys. A: Math. Gen. **32**, 5611–5625 (1999) (cit. on pp. 5, 15, 199).

[24] N. G. Berloff and P. H. Roberts, 'Capture of an impurity by a vortex line in a Bose condensate', Phys. Rev. B **63**, 024510 (2000) (cit. on pp. 5, 81, 199).

[25] N. G. Berloff and P. H. Roberts, 'Motion in a Bose condensate: VIII. The electron bubble', J. Phys. A: Math. Gen. **34**, 81–91 (2000) (cit. on pp. 3, 81).

[26] N. G. Berloff and P. H. Roberts, 'Motion in a Bose condensate: IX. Crow instability of antiparallel vortex pairs', J. Phys. A: Math. Gen. **34**, 10057–10066 (2001) (cit. on p. 105).

[27] N. G. Berloff and A. J. Youd, 'Dissipative Dynamics of Superfluid Vortices at Nonzero Temperatures', Phys. Rev. Lett. **99**, 145301 (2007) (cit. on p. 167).

[28] G. P. Bewley, D. P. Lathrop and K. R. Sreenivasan, 'Visualization of quantized vortices', Nature **441**, 588–588 (2006) (cit. on pp. 4, 54, 57, 58, 197).

[29] G. P. Bewley, M. S. Paoletti, K. R. Sreenivasan and D. P. Lathrop, 'Characterization of reconnecting vortices in superfluid helium', Proc Natl Acad Sci USA **105**, 13707 (2008) (cit. on pp. 2, 48, 54, 57, 58, 105).

[30] G. P. Bewley, K. R. Sreenivasan and D. P. Lathrop, 'Particles for tracing turbulent liquid helium', Exp Fluids **44**, 887–896 (2008) (cit. on pp. 2, 54, 57).

[31] N. N. Bogolyubov, 'On the theory of superfluidity', J.Phys.(USSR) **11**, 23–32 (1947) (cit. on pp. 23, 25, 34).

[32] S. Bose, 'Plancks Gesetz und Lichtquantenhypothese', Z. Physik **26**, 178–181 (1924) (cit. on pp. 4, 10).

[33] M. U. Bruderer, 'Neutral impurities immersed in Bose–Einstein condensates', 150 (cit. on p. 3).

[34] J. Büchner, S. I. Axford, E. Marsch and V. Vasyliunas, eds., *Plasma Astrophysics And Space Physics: Proceedings of the VIIth International Conference held in Lindau, Germany, May 4–8, 1998* (Springer Netherlands, 1999) (cit. on p. 47).

[35] M. D. Bustamante and S. Nazarenko, 'Derivation of the Biot-Savart equation from the nonlinear Schrödinger equation', Phys. Rev. E **92**, 053019 (2015) (cit. on p. 45).

[36] E. Calzavarini, M. Kerscher, D. Lohse and F. Toschi, 'Dimensionality and morphology of particle and bubble clusters in turbulent flow', Journal of Fluid Mechanics **607**, 13–24 (2008) (cit. on p. 69).

[37] G. Careri, F. Scaramuzzi and J. O. Thomson, 'Heat flush and mobility of electric charges in liquid helium', Nuovo Cim **13**, 186–196 (1959) (cit. on pp. 2, 54).

[38] I. Carusotto and C. Ciuti, 'Quantum fluids of light', Rev. Mod. Phys. **85**, 299–366 (2013) (cit. on pp. 1, 9).

[39] T. V. Chagovets and S. W. Van Sciver, 'A study of thermal counterflow using particle tracking velocimetry', Physics of Fluids **23**, 107102 (2011) (cit. on p. 60).

[40] S. Choi, S. A. Morgan and K. Burnett, 'Phenomenological damping in trapped atomic Bose-Einstein condensates', Phys. Rev. A **57**, 4057–4060 (1998) (cit. on p. 169).

[41] R. C. Clark, 'Self-trapped electrons in liquid helium II', Physics Letters **16**, 42–43 (1965) (cit. on p. 80).

[42] R. C. Clark and G. H. Derrick, *Mathematical Methods in Solid State and Superfluid Theory: Scottish Universities' Summer School*, Scottish Universities' Summer School (Springer US, 1968) (cit. on pp. 169, 170).

[43] P. Clark di Leoni, P. D. Mininni and M. E. Brachet, 'Spatiotemporal detection of Kelvin waves in quantum turbulence simulations', Phys. Rev. A **92**, 063632 (2015) (cit. on p. 51).

[44] J. Classen, C.-K. Su, M. Mohazzab and H. J. Maris, 'Electrons and cavitation in liquid helium', Phys. Rev. B **57**, 3000–3010 (1998) (cit. on p. 56).

[45] S. P. Cockburn and N. P. Proukakis, 'The stochastic Gross-Pitaevskii equation and some applications', Laser Phys. **19**, 558–570 (2009) (cit. on p. 168).

[46] C. Connaughton, C. Josserand, A. Picozzi, Y. Pomeau and S. Rica, 'Condensation of Classical Nonlinear Waves', Phys. Rev. Lett. **95**, 263901 (2005) (cit. on p. 167).

[47] *Cryogenic Division Tsukuba University*, https://www.tsukuba.ac.jp/en/research/resource-facilities/cryogenic (cit. on p. 12).

[48] 'Czech Cryogenic Turbulence Facility', (cit. on p. 12).

[49] L. S. Da Rios, 'Sul moto d'un liquido indefinito con un filetto vorticoso di forma qualunque', Rend. Circ. Matem. Palermo **22**, 117–135 (1906) (cit. on pp. 42, 45).

[50] F. Dalfovo, S. Giorgini, L. P. Pitaevskii and S. Stringari, 'Theory of Bose-Einstein condensation in trapped gases', Rev. Mod. Phys. **71**, 463–512 (1999) (cit. on pp. 20, 22, 23).

[51] M. J. Davis, R. J. Ballagh and K. Burnett, 'Dynamics of thermal Bose fields in the classical limit', J. Phys. B: At. Mol. Opt. Phys. **34**, 4487–4512 (2001) (cit. on pp. 4, 164).

[52] M. J. Davis, S. A. Morgan and K. Burnett, 'Simulations of Bose Fields at Finite Temperature', Phys. Rev. Lett. **87**, 160402 (2001) (cit. on pp. 4, 7, 163, 164, 167, 199).

[53] A. Dimarogonas, *Vibration for Engineers*, 2 edition (Prentice Hall, Upper Saddle River, N.J, Jan. 1996) (cit. on p. 206).

[54] R. J. Donnelly, 'Quantized Vortices and Turbulence in Helium II', Annu. Rev. Fluid Mech. **25**, 325–371 (1993) (cit. on pp. 45, 46, 53, 66, 71).

[55] R. J. Donnelly, *Quantized Vortices in Helium II* (Cambridge University Press, Mar. 1991) (cit. on pp. 1, 42, 55).

[56] R. J. Donnelly, 'The two-fluid theory and second sound in liquid helium', Physics Today **62**, 34–39 (2009) (cit. on p. 13).

[57] G. Düring, A. Picozzi and S. Rica, 'Breakdown of weak-turbulence and nonlinear wave condensation', Physica D: Nonlinear Phenomena **238**, 1524–1549 (2009) (cit. on p. 167).

[58] A. Einstein, 'Quantentheorie des einatomigen idealen Gases', Sitzber. Kgl. Preuss. Akad. Wiss. **1**, 3–14 (1925) (cit. on pp. 4, 10).

[59] J. R. Ensher, D. S. Jin, M. R. Matthews, C. E. Wieman and E. A. Cornell, 'Bose-Einstein Condensation in a Dilute Gas: Measurement of Energy and Ground-State Occupation', Phys. Rev. Lett. **77**, 4984–4987 (1996) (cit. on pp. 20, 21).

[60] P. S. Epstein, 'On the Resistance Experienced by Spheres in their Motion through Gases', Phys. Rev. **23**, 710–733 (1924) (cit. on p. 171).

[61] G. Falkovich, K. Gaw□dzki and M. Vergassola, 'Particles and fields in fluid turbulence', Rev. Mod. Phys. **73**, 913–975 (2001) (cit. on p. 69).

[62] A. L. Fetter, 'Vortices in an Imperfect Bose Gas. I. The Condensate', Phys. Rev. **138**, A429–A437 (1965) (cit. on p. 88).

[63] R. P. Feynman, 'Chapter II Application of Quantum Mechanics to Liquid Helium', in *Progress in Low Temperature Physics*, Vol. 1, edited by C. J. Gorter (Elsevier, Jan. 1955), pp. 17–53 (cit. on pp. 12, 38, 48).

[64] E. Fonda, D. P. Meichle, N. T. Ouellette, S. Hormoz and D. P. Lathrop, 'Direct observation of Kelvin waves excited by quantized vortex reconnection', PNAS, 10.1073/pnas.1312536110 (2014) (cit. on pp. 2, 6, 51, 57, 59, 115).

[65] C. J. Foster, P. B. Blakie and M. J. Davis, 'Vortex pairing in two-dimensional Bose gases', Phys. Rev. A **81**, 023623 (2010) (cit. on pp. 169–171, 185).

[66] G. Fraser, ed., *The New Physics for the Twenty-First Century*, 2Rev Ed edition (Cambridge University Press, Cambridge, UK ; New York, Feb. 2006) (cit. on p. 12).

[67] T. Frisch, Y. Pomeau and S. Rica, 'Transition to dissipation in a model of superflow', Phys. Rev. Lett. **69**, 1644–1647 (1992) (cit. on pp. 35, 53, 76).

[68] U. Frisch and A. N. Kolmogorov, *Turbulence: The Legacy of A. N. Kolmogorov* (Cambridge University Press, Nov. 1995) (cit. on pp. 137, 139).

[69] Y. Gagne, E. J. Hopfinger and U. Frisch, 'A New Universal Scaling for Fully Developed Turbulence: The Distribution of Velocity Increments', in *New Trends in Nonlinear Dynamics and Pattern-Forming Phenomena: The Geometry of Nonequilibrium*, edited by P. Coullet and P. Huerre, NATO ASI Series (Springer US, New York, NY, 1990), pp. 315–319 (cit. on p. 139).

[70] L. Galantucci, A. W. Baggaley, N. G. Parker and C. F. Barenghi, 'Crossover from interaction to driven regimes in quantum vortex reconnections', PNAS **116**, 12204–12211 (2019) (cit. on pp. 1, 5, 49, 57).

[71] J. Gao, A. Marakov, W. Guo, B. T. Pawlowski, S. W. Van Sciver, G. G. Ihas, D. N. McKinsey and W. F. Vinen, 'Producing and imaging a thin line of He2 molecular tracers in helium-4', Review of Scientific Instruments **86**, 093904 (2015) (cit. on p. 60).

[72] I. M. Gelfand, S. V. Fomin and R. A. Silverman, *Calculus of Variations* (Courier Corporation, Jan. 2000) (cit. on p. 26).

[73] A. Ghosh and H. J. Maris, 'Observation of a New Type of Electron Bubble in Superfluid Helium', Phys. Rev. Lett. **95**, 265301 (2005) (cit. on p. 56).

[74] V. Ginzburg and L. Pitaevskii, 'On the theory of superfluidity', Sov. Phys. JETP **7**, 858–861 (1958) (cit. on p. 39).

[75] U. Giuriato and G. Krstulovic, 'Interaction between active particles and quantum vortices leading to Kelvin wave generation', Sci Rep **9**, 4839 (2019) (cit. on pp. ix, 5, 6, 41, 46, 65, 71, 85, 88, 90, 91, 105, 197).

[76] U. Giuriato and G. Krstulovic, 'Active and finite-size particles in decaying quantum turbulence at low temperature', Phys. Rev. Fluids **5**, 054608 (2020) (cit. on pp. ix, 6, 60, 74, 137, 139, 198, 208, 209).

[77] U. Giuriato and G. Krstulovic, 'Quantum vortex reconnections mediated by trapped particles', Phys. Rev. B **102**, 094508 (2020) (cit. on pp. ix, 5, 6, 48, 85, 105, 197).

[78] U. Giuriato and G. Krstulovic, 'Stochastic motion of finite-size immiscible impurities in a dilute quantum fluid at finite temperature', Phys. Rev. B **103**, 024509 (2021) (cit. on pp. ix, 7, 163, 168, 169, 171, 173, 184, 199).

[79] U. Giuriato, G. Krstulovic and S. Nazarenko, 'How trapped particles interact with and sample superfluid vortex excitations', Phys. Rev. Research **2**, 023149 (2020) (cit. on pp. ix, 6, 46, 50, 60, 66, 75, 79, 105, 115, 130–134, 141, 197, 198).

[80] U. Giuriato, G. Krstulovic and D. Proment, 'Clustering and phase transitions in a 2D superfluid with immiscible active impurities', J. Phys. A: Math. Theor. **52**, 305501 (2019) (cit. on pp. ix, 7, 22, 79, 83, 163, 168, 171, 173, 185, 199, 207).

[81] W. I. Glaberson and M. Steingart, 'Temperature Dependence of the Vortex-Core Parameter in He II', Phys. Rev. Lett. **26**, 1423–1425 (1971) (cit. on p. 44).

[82] H. Goldstein and C. P. P.
bibinitperiod J. Safko, *CLASSICAL MECHANICS* (Pearson Education, Jan. 2011) (cit. on p. 80).

[83] A. I. Golov and P. M. Walmsley, 'Homogeneous Turbulence in Superfluid 4He in the Low-Temperature Limit: Experimental Progress', J Low Temp Phys **156**, 51–70 (2009) (cit. on p. 54).

[84] A. Gordeev, T. Chagovets, F. Soukup and L. Skrbek, 'Decaying Counterflow Turbulence in He II', J Low Temp Phys **138**, 549–554 (2005) (cit. on p. 140).

[85] D. Gottlieb, j. author.)Orszag, Steven and N. S. Foundation (U.S.), *Numerical analysis of spectral methods : Theory and applications* (Philadelphia : Society for Industrial and Applied Mathematics, 1977) (cit. on p. 203).

[86] 'Grenoble Helium Infrastructures', (cit. on p. 12).

[87] A. Griffin, G. W. Stagg, N. P. Proukakis and C. F. Barenghi, 'Vortex scattering by impurities in a Bose–Einstein condensate', J. Phys. B: At. Mol. Opt. Phys. **50**, 115003 (2017) (cit. on p. 79).

[88] A. Griffin, V. Shukla, M.-E. Brachet and S. Nazarenko, 'Magnus-force model for active particles trapped on superfluid vortices', Phys. Rev. A **101**, 053601 (2020) (cit. on pp. 3, 79, 206).

[89] E. P. Gross, 'Classical theory of boson wave fields', Annals of Physics **4**, 57–74 (1958) (cit. on pp. 3, 75, 80, 197).

[90] W. Guo, S. B. Cahn, J. A. Nikkel, W. F. Vinen and D. N. McKinsey, 'Visualization Study of Counterflow in Superfluid He 4 using Metastable Helium Molecules', Phys. Rev. Lett. **105**, 045301 (2010) (cit. on p. 60).

[91] W. Guo, M. La Mantia, D. P. Lathrop and S. W. Van Sciver, 'Visualization of two-fluid flows of superfluid helium-4', Proceedings of the National Academy of Sciences **111**, 4653–4658 (2014) (cit. on pp. 2, 53, 54, 57, 60, 61, 197).

[92] W. Guo, 'Molecular Tagging Velocimetry in Superfluid Helium-4: Progress, Issues, and Future Development', J Low Temp Phys **196**, 60–72 (2019) (cit. on p. 60).

[93] W. Guo and H. J. Maris, 'Observations of the Motion of Single Electrons in Liquid Helium', J Low Temp Phys **148**, 199–206 (2007) (cit. on p. 56).

[94] 'Guo Lab Florida', (cit. on p. 12).

[95] Z. Hadzibabic and J. Dalibard, 'Two-dimensional Bose fluids: An atomic physics perspective', Nuovo Cimento Rivista Serie **34**, 389–434 (2011) (cit. on pp. 22, 185).

[96] H. E. Hall and W. F. Vinen, 'The rotation of liquid helium II II. The theory of mutual friction in uniformly rotating helium II', Proc. R. Soc. Lond. A **238**, 215–234 (1956) (cit. on pp. 2, 46, 167).

[97] W. M. Hicks and J. W. L. Glaisher, 'VII. On the steady motion and small vibrations a hollow vortex', Philosophical Transactions of the Royal Society of London **175**, 161–195 (1884) (cit. on pp. 5, 44).

[98] R. N. Hills and P. H. Roberts, 'Superfluid mechanics for a high density of vortex lines', Arch. Rational Mech. Anal. **66**, 43–71 (1977) (cit. on p. 2).

[99] P. C. Hohenberg, 'Existence of Long-Range Order in One and Two Dimensions', Phys. Rev. **158**, 383–386 (1967) (cit. on pp. 22, 184).

[100] K. Huang, *Statistical Mechanics, 2nd Edition* (Wiley, 1987) (cit. on pp. 11, 167).

[101] C. Huepe and M.-E. Brachet, 'Scaling laws for vortical nucleation solutions in a model of superflow', Physica D: Nonlinear Phenomena **140**, 126–140 (2000) (cit. on pp. 35, 53, 76).

[102] F. Hussain and K. Duraisamy, 'Mechanics of viscous vortex reconnection', Physics of Fluids **23**, 021701 (2011) (cit. on p. 47).

[103] O. C. Idowu, D. Kivotides, C. F. Barenghi and D. C. Samuels, 'Equation for Self-Consistent Superfluid Vortex Line Dynamics', Journal of Low Temperature Physics **120**, 269–280 (2000) (cit. on pp. 47, 71).

[104] D. Jin, W. Guo, W. Wei and H. J. Maris, 'Electrons in Superfluid Helium-4', J Low Temp Phys **158**, 307–316 (2010) (cit. on p. 56).

[105] J. E. Jones and S. Chapman, 'On the determination of molecular fields. —II. From the equation of state of a gas', Proceedings of the Royal Society of London. Series A, Containing Papers of a Mathematical and Physical Character **106**, 463–477 (1924) (cit. on p. 79).

[106] P. Kapitza, 'Viscosity of Liquid Helium below the λ-Point', Nature **141**, 74–74 (1938) (cit. on pp. 1, 9, 11).

[107] P. G. Kevrekidis, D. J. Frantzeskakis and R. Carretero-González, eds., *Emergent nonlinear phenomena in Bose-Einstein condensates: Theory and experiment*, Springer Series on Atomic, Optical, and Plasma Physics 45 (Springer, Berlin ; New York, 2008) (cit. on pp. 7, 82, 171).

[108] S. Kida and M. Takaoka, 'Vortex Reconnection', Annual Review of Fluid Mechanics **26**, 169–177 (1994) (cit. on p. 47).

[109] L. Kiknadze and Y. Mamaladze, 'The Magnus (Kutta-Jukovskii) Force Acting on a Sphere', arXiv:cond-mat/0604436 (2006) (cit. on pp. 6, 66).

[110] I. Kim, S. Elghobashi and W. A. Sirignano, 'On the equation for spherical-particle motion: Effect of Reynolds and acceleration numbers', Journal of Fluid Mechanics **367**, 221–253 (1998) (cit. on p. 68).

[111] C. Kittel, *Introduction to solid state physics*, 8th ed (Wiley, Hoboken, NJ, 2005) (cit. on pp. 116, 130, 131, 198).

[112] D. Kivotides, C. F. Barenghi and Y. A. Sergeev, 'Physics of solid particles in thermal counterflow', EPL **73**, 733 (2006) (cit. on p. 71).

[113] D. Kivotides, Y. A. Sergeev and C. F. Barenghi, 'Dynamics of solid particles in a tangle of superfluid vortices at low temperatures', Physics of Fluids **20**, 055105 (2008) (cit. on pp. 3, 72–74).

[114] D. Kivotides, 'Motion of a spherical solid particle in thermal counterflow turbulence', Phys. Rev. B **77**, 174508 (2008) (cit. on pp. 3, 60, 72).

[115] D. Kivotides, 'Normal-fluid velocity measurement and superfluid vortex detection in thermal counterflow turbulence', Phys. Rev. B **78**, 224501 (2008) (cit. on pp. 3, 60, 72, 74).

[116] D. Kivotides, C. F. Barenghi and Y. A. Sergeev, 'Measurement of the Normal-Fluid Velocity in Superfluids', Phys. Rev. Lett. **95**, 215302 (2005) (cit. on p. 71).

[117] D. Kivotides, C. F. Barenghi and Y. A. Sergeev, 'Numerical Calculation of the Interaction of Superfluid Vortices and a Rigid Sphere', J Low Temp Phys **144**, 121–134 (2006) (cit. on pp. 3, 72).

[118] D. Kivotides, C. F. Barenghi and Y. A. Sergeev, 'Collision of a tracer particle and a quantized vortex in superfluid helium: Self-Consistent calculations', Phys. Rev. B **75**, 212502 (2007) (cit. on pp. 73, 75).

[119] D. Kivotides, C. F. Barenghi and Y. A. Sergeev, 'Interactions between particles and quantized vortices in superfluid helium', Phys. Rev. B **77**, 014527 (2008) (cit. on pp. 3, 5, 72–74).

[120] D. Kivotides and S. L. Wilkin, 'Collisions of solid particles with vortex rings in superfluid helium', Journal of Fluid Mechanics **605**, 367–387 (2008) (cit. on p. 73).

[121] A. Kolmogorov, 'The Local Structure of Turbulence in Incompressible Viscous Fluid for Very Large Reynolds' Numbers', Akademiia Nauk SSSR Doklady **30**, 301–305 (1941) (cit. on pp. 137, 138).

[122] A. N. Kolmogorov, 'Dissipation of Energy in Locally Isotropic Turbulence', Akademiia Nauk SSSR Doklady **32**, 16 (1941) (cit. on pp. 137, 138).

[123] J. Koplik and H. Levine, 'Vortex reconnection in superfluid helium', Phys. Rev. Lett. **71**, 1375–1378 (1993) (cit. on p. 47).

[124] J. M. Kosterlitz, 'The critical properties of the two-dimensional xy model', J. Phys. C: Solid State Phys. **7**, 1046–1060 (1974) (cit. on p. 185).

[125] J. M. Kosterlitz and D. J. Thouless, 'Ordering, metastability and phase transitions in two-dimensional systems', J. Phys. C: Solid State Phys. **6**, 1181–1203 (1973) (cit. on p. 185).

[126] E. Kozik and B. Svistunov, 'Kelvin-Wave Cascade and Decay of Superfluid Turbulence', Phys. Rev. Lett. **92**, 035301 (2004) (cit. on p. 51).

[127] R. D. L. Kronig, W. G. Penney and R. H. Fowler, 'Quantum mechanics of electrons in crystal lattices', Proceedings of the Royal Society of London. Series A, Containing Papers of a Mathematical and Physical Character **130**, 499–513 (1931) (cit. on pp. 6, 116, 130, 197).

[128] G. Krstulovic, 'Galerkin-truncated dynamics of ideal fluids and superfluids: Cascades, thermalization and dissipative effects', PhD thesis (Université Pierre et Marie Curie - Paris VI, Mar. 2010) (cit. on pp. 4, 165, 199, 203–205).

[129] G. Krstulovic, 'Kelvin-wave cascade and dissipation in low-temperature superfluid vortices', Phys. Rev. E **86**, 055301 (2012) (cit. on pp. 1, 51).

[130] G. Krstulovic and M. Brachet, 'Anomalous vortex-ring velocities induced by thermally excited Kelvin waves and counterflow effects in superfluids', Phys. Rev. B **83**, 132506 (2011) (cit. on pp. 44, 168, 171).

[131] G. Krstulovic and M. Brachet, 'Energy cascade with small-scale thermalization, counterflow metastability, and anomalous velocity of vortex rings in Fourier-Truncated Gross-Pitaevskii equation', Phys. Rev. E **83**, 066311 (2011) (cit. on pp. 4, 7, 165, 167–169, 171, 203).

[132] T. S. Kuhn, *Black-Body Theory and the Quantum Discontinuity, 1894-1912* (University of Chicago Press, Jan. 1987) (cit. on p. 164).

[133] P. K. Kundu, I. M. Cohen and D. R. Dowling, *Fluid Mechanics*, 5 edizione (Academic Press, July 2011) (cit. on p. 47).

[134] P. Kuopanportti, S. Bandyopadhyay, A. Roy and D. Angom, 'Splitting of singly and doubly quantized composite vortices in two-component Bose-Einstein condensates', Phys. Rev. A **100**, 033615 (2019) (cit. on p. 82).

[135] L.D. Landau & E.M. Lifshitz, *Quantum Mechanics* () (cit. on p. 34).

[136] V. S. L'vov and S. Nazarenko, 'Weak turbulence of Kelvin waves in superfluid He', Low Temperature Physics **36**, 785–791 (2010) (cit. on pp. 51, 139).

[137] M. La Mantia and L. Skrbek, 'Quantum turbulence visualized by particle dynamics', Phys. Rev. B **90**, 014519 (2014) (cit. on pp. 2, 4, 59, 141, 198).

[138] S. H. Lamb, *Hydrodynamics* (Courier Corporation, Jan. 1945) (cit. on pp. 44, 66).

[139] L. Landau, 'Theory of the Superfluidity of Helium II', Phys. Rev. **60**, 356–358 (1941) (cit. on pp. 1, 10, 12, 53).

[140] L. D. Landau and E. M. Lifshits, *Fluid mechanics, by L.D. Landau and E.M. Lifshitz.* (Pergamon Press, London, 1959) (cit. on pp. 1, 10, 12, 14, 37, 169).

[141] J. Laurie, V. S. L'vov, S. Nazarenko and O. Rudenko, 'Interaction of Kelvin waves and nonlocality of energy transfer in superfluids', Phys. Rev. B **81**, 104526 (2010) (cit. on pp. 1, 51).

[142] K. A. Lidke, A. Wynveen, N. Baisch, C. Koay, C. F. Giese and J. W. Halley, 'Phonon Mediated Helium Atom Transmission through Superfluid Helium Four', J Low Temp Phys **140**, 429–449 (2005) (cit. on p. 172).

[143] J. A. Lipa, J. A. Nissen, D. A. Stricker, D. R. Swanson and T. C. P. Chui, 'Specific heat of liquid helium in zero gravity very near the lambda point', Phys. Rev. B **68**, 174518 (2003) (cit. on p. 11).

[144] U. Lombardo and H.-J. Schulze, 'Superfluidity in Neutron Star Matter', in *Physics of Neutron Star Interiors*, edited by D. Blaschke, A. Sedrakian and N. K. Glendenning, Lecture Notes in Physics (Springer, Berlin, Heidelberg, 2001), pp. 30–53 (cit. on pp. 9, 19).

[145] F. London, 'The λ-Phenomenon of Liquid Helium and the Bose-Einstein Degeneracy', Nature **141**, 643–644 (1938) (cit. on p. 10).

[146] *Low Temperature Physics Lancaster University*, https://www.lancaster.ac.uk/physics/research/experimental-condensed-matter/low-temperature-physics/ (cit. on p. 12).

[147] A. Marakov, J. Gao, W. Guo, S. W. Van Sciver, G. G. Ihas, D. N. McKinsey and W. F. Vinen, 'Visualization of the normal-fluid turbulence in counterflowing superfluid He 4', Phys. Rev. B **91**, 094503 (2015) (cit. on p. 60).

[148] B. Mastracci and W. Guo, 'Exploration of thermal counterflow in He II using particle tracking velocimetry', Phys. Rev. Fluids **3**, 063304 (2018) (cit. on p. 60).

[149] J. Maurer and P. Tabeling, 'Local investigation of superfluid turbulence', EPL **43**, 29 (1998) (cit. on p. 139).

[150] M. R. Maxey, 'Equation of motion for a small rigid sphere in a nonuniform flow', Phys. Fluids **26**, 883 (1983) (cit. on pp. 5, 63, 67).

[151] D. N. McKinsey, W. H. Lippincott, J. A. Nikkel and W. G. Rellergert, 'Trace Detection of Metastable Helium Molecules in Superfluid Helium by Laser-Induced Fluorescence', Phys. Rev. Lett. **95**, 111101 (2005) (cit. on p. 60).

[152] R. Mei, 'Flow due to an oscillating sphere and an expression for unsteady drag on the sphere at finite Reynolds number', Journal of Fluid Mechanics **270**, 133–174 (1994) (cit. on pp. 67, 68).

[153] K. Mendelssohn, *Quest for Absolute Zero: Meaning of Low Temperature Physics* (World University Library, 1966) (cit. on pp. 1, 11).

[154] N. D. Mermin and H. Wagner, 'Absence of Ferromagnetism or Antiferromagnetism in One- or Two-Dimensional Isotropic Heisenberg Models', Phys. Rev. Lett. **17**, 1133–1136 (1966) (cit. on pp. 22, 184).

[155] V. P. Mineev, 'The theory of the solution of two near-ideal Bose gases', Zh. Eksp. Teor. Fiz. **67**, 263–272 (1974) (cit. on p. 82).

[156] G. Modugno, M. Modugno, F. Riboli, G. Roati and M. Inguscio, 'Two Atomic Species Superfluid', Phys. Rev. Lett. **89**, 190404 (2002) (cit. on pp. 7, 82).

[157] M. Morishita, T. Kuroda, A. Sawada and T. Satoh, 'Mean free path effects in superfluid4He', J Low Temp Phys **76**, 387–415 (1989) (cit. on pp. 172, 173).

[158] K. Morris, J. Koplik and D. W. I. Rouson, 'Vortex Locking in Direct Numerical Simulations of Quantum Turbulence', Phys. Rev. Lett. **101**, 015301 (2008) (cit. on p. 139).

[159] N. P. Müller and G. Krstulovic, 'Kolmogorov and Kelvin wave cascades in a generalized model for quantum turbulence', arXiv:2007.00540 [cond-mat, physics:physics] (2020) (cit. on p. 199).

[160] C. J. Myatt, E. A. Burt, R. W. Ghrist, E. A. Cornell and C. E. Wieman, 'Production of Two Overlapping Bose-Einstein Condensates by Sympathetic Cooling', Phys. Rev. Lett. **78**, 586–589 (1997) (cit. on p. 82).

[161] S. Nazarenko, M. Onorato and D. Proment, 'Bose-Einstein condensation and Berezinskii-Kosterlitz-Thouless transition in the two-dimensional nonlinear Schr\"odinger model', Phys. Rev. A **90**, 013624 (2014) (cit. on p. 185).

[162] S. Nazarenko and R. West, 'Analytical Solution for Nonlinear Schrödinger Vortex Reconnection', Journal of Low Temperature Physics **132**, 1–10 (2003) (cit. on pp. 36, 48, 57).

[163] M. Niemetz and W. Schoepe, 'Stability of Laminar and Turbulent Flow of Superfluid 4He at mK Temperatures Around an Oscillating Microsphere', Journal of Low Temperature Physics **135**, 447–469 (2004) (cit. on p. 172).

[164] C. Nore, M. Abid and M. E. Brachet, 'Decaying Kolmogorov turbulence in a model of superflow', Physics of Fluids **9**, 2644–2669 (1997) (cit. on pp. 3, 4, 26, 36, 37, 139).

[165] C. Nore, C. Huepe and M. E. Brachet, 'Subcritical Dissipation in Three-Dimensional Superflows', Phys. Rev. Lett. **84**, 2191–2194 (2000) (cit. on p. 76).

[166] L. Onsager, 'Statistical hydrodynamics', Nuovo Cim **6**, 279–287 (1949) (cit. on p. 12).

[167] D. D. Osheroff, R. C. Richardson and D. M. Lee, 'Evidence for a New Phase of Solid He3', Phys. Rev. Lett. **28**, 885–888 (1972) (cit. on p. 10).

[168] R. E. Packard and T. M. Sanders, 'Observations on Single Vortex Lines in Rotating Superfluid Helium', Phys. Rev. A **6**, 799–807 (1972) (cit. on p. 55).

[169] M. S. Paoletti, M. E. Fisher and D. P. Lathrop, 'Reconnection dynamics for quantized vortices', Physica D: Nonlinear Phenomena, At the Boundaries of Nonlinear Physics, Fluid Mechanics and Turbulence: Where Do We Stand? Special Issue in Celebration of the 60th Birthday of K.R. Sreenivasan **239**, 1367–1377 (2010) (cit. on pp. 2, 4, 6, 48, 57, 105).

[170] M. S. Paoletti and D. P. Lathrop, 'Quantum Turbulence', Annu. Rev. Condens. Matter Phys. **2**, 213–234 (2011) (cit. on pp. 1, 12, 48, 59, 141).

[171] S. B. Papp, J. M. Pino and C. E. Wieman, 'Tunable Miscibility in a Dual-Species Bose-Einstein Condensate', Phys. Rev. Lett. **101**, 040402 (2008) (cit. on p. 82).

[172] G. Parisi, *Statistical Field Theory* (Basic Books, Jan. 1988) (cit. on p. 22).

[173] P. E. Parks and R. J. Donnelly, 'Radii of Positive and Negative Ions in Helium II', Phys. Rev. Lett. **16**, 45–48 (1966) (cit. on pp. 55, 87, 88).

[174] C. J. Pethick and H. Smith, *Bose–Einstein Condensation in Dilute Gases*, Second (Cambridge University Press, Cambridge, 2008) (cit. on pp. 1, 3, 9).

[175] L. M. Pismen, D. o. C. E. L. M. Pismen and L. M. Pismen, *Vortices in Nonlinear Fields: From Liquid Crystals to Superfluids, from Non-equilibrium Patterns to Cosmic Strings* (Clarendon Press, 1999) (cit. on p. 41).

[176] L. Pitaevskii and S. Stringari, *Bose-Einstein Condensation and Superfluidity* (Oxford University Press, Jan. 2016) (cit. on pp. 1, 3, 4, 9, 14, 16, 19, 23, 25, 33–35, 53, 169).

[177] L. P. Pitaevskii, 'Vortex lines in an imperfect Bose gas', Sov. Phys. JETP **13**, 451–454 (1961) (cit. on pp. 39, 50).

[178] J. I. Polanco and G. Krstulovic, 'Counterflow-induced inverse energy cascade in three-dimensional superfluid turbulence', arXiv:2005.10106 [cond-mat, physics:physics] (2020) (cit. on pp. 2, 72).

[179] J. I. Polanco and G. Krstulovic, 'Inhomogeneous distribution of particles in coflow and counterflow quantum turbulence', Phys. Rev. Fluids **5**, 032601 (2020) (cit. on pp. 2, 72, 200).

[180] Y. POMEAU and S. RICA, 'Vitesse limite et nucléation dans un modèle de superfluide', C. r. Acad. sci., Sér. 2, Méc. phys. chim. sci. univers sci. terre **316**, 1523–1528 (1993) (cit. on p. 53).

[181] D. R. Poole, C. F. Barenghi, Y. A. Sergeev and W. F. Vinen, 'Motion of tracer particles in He II', Phys. Rev. B **71**, 064514 (2005) (cit. on pp. 5, 63, 70, 71).

[182] W. H. Press, ed., *FORTRAN numerical recipes*, 2nd ed (Cambridge University Press, Cambridge [England] ; New York, 1996) (cit. on p. 203).

[183] N. P. Proukakis and B. Jackson, 'Finite-temperature models of Bose–Einstein condensation', J. Phys. B: At. Mol. Opt. Phys. **41**, 203002 (2008) (cit. on pp. 164, 168, 169).

[184] I. A. Pshenichnyuk, 'Static and dynamic properties of heavily doped quantum vortices', New J. Phys. **19**, 105007 (2017) (cit. on p. 82).

[185] M. Raffel, C. E. Willert, S. Wereley and J. Kompenhans, *Particle Image Velocimetry: A Practical Guide*, Second (Springer-Verlag, Berlin Heidelberg, 2007) (cit. on p. 53).

[186] F. Reif and L. Meyer, 'Study of Superfluidity in Liquid He by Ion Motion', Phys. Rev. **119**, 1164–1173 (1960) (cit. on pp. 2, 54).

[187] J. Reneuve, J. Salort and L. Chevillard, 'Structure, dynamics, and reconnection of vortices in a nonlocal model of superfluids', Phys. Rev. Fluids **3**, 114602 (2018) (cit. on pp. 5, 199).

[188] S. Rica and D. C. Roberts, 'Induced interaction and crystallization of self-localized impurity fields in a Bose-Einstein condensate', Phys. Rev. A **80**, 013609 (2009) (cit. on p. 82).

[189] L. F. Richardson, *Weather Prediction by Numerical Process*, 2 edition (Cambridge University Press, Darmstadt, Aug. 1922) (cit. on p. 138).

[190] A. Richaud, V. Penna, R. Mayol and M. Guilleumas, 'Vortices with massive cores in a binary mixture of Bose-Einstein condensates', Phys. Rev. A **101**, 013630 (2020) (cit. on p. 82).

[191] D. C. Roberts and S. Rica, 'Impurity Crystal in a Bose-Einstein Condensate', Phys. Rev. Lett. **102**, 025301 (2009) (cit. on pp. 3, 7, 82, 171, 199).

[192] P. H. Roberts, 'On vortex waves in compressible fluids. II. The condensate vortex', Proc. R. Soc. Lond. A **459**, 597–607 (2003) (cit. on pp. 1, 5, 50).

[193] J. Rogel-Salazar, 'The Gross–Pitaevskii equation and Bose–Einstein condensates', Eur. J. Phys. **34**, 247–257 (2013) (cit. on p. 23).

[194] C. Rorai, J. Skipper, R. M. Kerr and K. R. Sreenivasan, 'Approach and separation of quantised vortices with balanced cores', Journal of Fluid Mechanics **808**, 641–667 (2016) (cit. on p. 48).

[195] B. Rousset et al., 'Cryogenic turbulence test facilities at CEA/SBT', IOP Conf. Ser.: Mater. Sci. Eng. **101**, 012187 (2015) (cit. on pp. 1, 12).

[196] S. I. Rubinow and J. B. Keller, 'The transverse force on a spinning sphere moving in a viscous fluid', Journal of Fluid Mechanics **11**, 447–459 (1961) (cit. on pp. 66, 67, 69).

[197] M. S. Paoletti, R. B. Fiorito, K. R. Sreenivasan and D. P. Lathrop, 'Visualization of Superfluid Helium Flow', J. Phys. Soc. Jpn. **77**, 111007 (2008) (cit. on pp. 2, 59, 141, 198).

[198] P. G. Saffman, 'The lift on a small sphere in a slow shear flow', Journal of Fluid Mechanics **22**, 385–400 (1965) (cit. on p. 69).

[199] P. G. Saffman, *Vortex Dynamics* (Cambridge University Press, 1992) (cit. on pp. 42, 43, 45).

[200] J. P. Salazar and L. R. Collins, 'Two-Particle Dispersion in Isotropic Turbulent Flows', Annual Review of Fluid Mechanics **41**, 405–432 (2009) (cit. on p. 69).

[201] J. Salort et al., 'Turbulent velocity spectra in superfluid flows', Physics of Fluids **22**, 125102 (2010) (cit. on p. 139).

[202] B. Sawford, 'Turbulent Relative Dispersion', Annual Review of Fluid Mechanics **33**, 289–317 (2001) (cit. on p. 69).

[203] K. W. Schwarz, 'Spherical probes and quantized vortices: Hydrodynamic formalism and simple applications', Phys. Rev. A **10**, 2306–2317 (1974) (cit. on pp. 5, 72).

[204] K. W. Schwarz, 'Three-dimensional vortex dynamics in superfluid He 4 : Line-Line and line-boundary interactions', Phys. Rev. B **31**, 5782–5804 (1985) (cit. on pp. 42, 44, 46, 47).

[205] K. W. Schwarz, 'Three-dimensional vortex dynamics in superfluid ${4}\mathrm{He$: Homogeneous superfluid turbulence', Phys. Rev. B **38**, 2398–2417 (1988) (cit. on pp. 2, 5, 48).

[206] S. Serafini, M. Barbiero, M. Debortoli, S. Donadello, F. Larcher, F. Dalfovo, G. Lamporesi and G. Ferrari, 'Dynamics and Interaction of Vortex Lines in an Elongated Bose-Einstein Condensate', Phys. Rev. Lett. **115**, 170402 (2015) (cit. on p. 48).

[207] Y. A. Sergeev and C. F. Barenghi, 'Normal Fluid Eddies in the Thermal Counterflow past a Cylinder', J Low Temp Phys **156**, 268–278 (2009) (cit. on p. 57).

[208] Y. A. Sergeev and C. F. Barenghi, 'Particles-Vortex Interactions and Flow Visualization in 4He', J Low Temp Phys **157**, 429 (2009) (cit. on pp. 2, 3, 53, 56, 57, 67, 70, 74, 197, 200).

[209] Y. A. Sergeev, C. F. Barenghi and D. Kivotides, 'Motion of micron-size particles in turbulent helium II', Phys. Rev. B **74**, 184506 (2006) (cit. on pp. 5, 87, 88).

[210] Y. A. Sergeev, S. Wang, E. Meneguz and C. F. Barenghi, 'Influence of Normal Fluid Disturbances on Interactions of Solid Particles with Quantized Vortices', J Low Temp Phys **146**, 417–434 (2007) (cit. on p. 71).

[211] V. Shukla, M. Brachet and R. Pandit, 'Turbulence in the two-dimensional Fourier-Truncated Gross–Pitaevskii equation', New J. Phys. **15**, 113025 (2013) (cit. on p. 184).

[212] V. Shukla, M. Brachet and R. Pandit, 'Sticking transition in a minimal model for the collisions of active particles in quantum fluids', Phys. Rev. A **94**, 041602 (2016) (cit. on pp. 3, 7, 78, 184, 199, 206, 207).

[213] V. Shukla, P. D. Mininni, G. Krstulovic, P. C. di Leoni and M. E. Brachet, 'Quantitative estimation of effective viscosity in quantum turbulence', Phys. Rev. A **99**, 043605 (2019) (cit. on pp. 139, 165, 166, 172).

[214] V. Shukla, R. Pandit and M. Brachet, 'Particles and fields in superfluids: Insights from the two-dimensional Gross-Pitaevskii equation', Phys. Rev. A **97**, 013627 (2018) (cit. on pp. 3, 79, 197, 206).

[215] D. M. Sitton and F. Moss, 'Trapping of Negative Ions in Turbulent Superfluid Helium', Phys. Rev. Lett. **23**, 1090–1093 (1969) (cit. on p. 55).

[216] L. Skrbek and K. R. Sreenivasan, 'Developed quantum turbulence and its decay', Physics of Fluids **24**, 011301 (2012) (cit. on p. 140).

[217] K. R. Sreenivasan, 'On the universality of the Kolmogorov constant', Physics of Fluids **7**, 2778–2784 (1995) (cit. on p. 138).

[218] S. R. Stalp, L. Skrbek and R. J. Donnelly, 'Decay of Grid Turbulence in a Finite Channel', Phys. Rev. Lett. **82**, 4831–4834 (1999) (cit. on p. 140).

[219] C. Sulem and P.-L. Sulem, *The Nonlinear Schrödinger Equation: Self-Focusing and Wave Collapse*, Applied Mathematical Sciences (Springer-Verlag, New York, 1999) (cit. on p. 26).

[220] S. W. Thomson, 'XXIV. Vibrations of a columnar vortex', The London, Edinburgh, and Dublin Philosophical Magazine and Journal of Science **10**, 155–168 (1880) (cit. on pp. 1, 50).

[221] L. Tisza, 'Transport Phenomena in Helium II', Nature **141**, 913–913 (1938) (cit. on p. 10).

[222] F. Toschi and E. Bodenschatz, 'Lagrangian Properties of Particles in Turbulence', Annual Review of Fluid Mechanics **41**, 375–404 (2009) (cit. on pp. 6, 69).

[223] M. C. Tsatsos, P. E. Tavares, A. Cidrim, A. R. Fritsch, M. A. Caracanhas, F. E. A. dos Santos, C. F. Barenghi and V. S. Bagnato, 'Quantum turbulence in trapped atomic Bose–Einstein condensates', Physics Reports **622**, 1–52 (2016) (cit. on p. 21).

[224] M. A. H. Tucker and A. F. G. Wyatt, 'Four-phonon scattering in superfluid4He', J. Phys.: Condens. Matter **4**, 7745–7758 (1992) (cit. on p. 172).

[225] J. F. (W. P. L. A. UK), University of Bristol and J. F. Annett, *Superconductivity, Superfluids and Condensates* (OUP Oxford, Mar. 2004) (cit. on pp. 11, 13).

[226] M. A. T. van Hinsberg, J. H. M. Thije Boonkkamp, F. Toschi and H. J. H. Clercx, 'On the Efficiency and Accuracy of Interpolation Methods for Spectral Codes', SIAM J. Sci. Comput. **34**, B479–B498 (2012) (cit. on p. 208).

[227] E. Varga, C. F. Barenghi, Y. A. Sergeev and L. Skrbek, 'Backreaction of Tracer Particles on Vortex Tangle in Helium II Counterflow', J Low Temp Phys **183**, 215–221 (2016) (cit. on p. 74).

[228] A. Villois, D. Proment and G. Krstulovic, 'Evolution of a superfluid vortex filament tangle driven by the Gross-Pitaevskii equation', Phys. Rev. E **93**, 061103 (2016) (cit. on pp. 51, 139, 140).

[229] A. Villois, D. Proment and G. Krstulovic, 'Universal and nonuniversal aspects of vortex reconnections in superfluids', Phys. Rev. Fluids **2**, 044701 (2017) (cit. on pp. 1, 5, 36, 48, 49, 57).

[230] A. Villois, D. Proment and G. Krstulovic, 'Irreversible dynamics of vortex reconnections in quantum fluids', arXiv:2005.02048 [cond-mat, physics:nlin, physics:physics] (2020) (cit. on pp. 48, 105, 139).

[231] A. Villois and H. Salman, 'Vortex Nucleation Limited Mobility of Free Electron Bubbles in the Gross-Pitaevskii Model of a Superfluid', Phys. Rev. B **97**, 094507 (2018) (cit. on pp. 3, 81).

[232] A. Villois and H. Salman, 'Vortex nucleation limited mobility of free electron bubbles in the Gross-Pitaevskii model of a superfluid', Phys. Rev. B **97**, 094507 (2018) (cit. on p. 199).

[233] W. F. Vinen, 'Decay of superfluid turbulence at a very low temperature: The radiation of sound from a Kelvin wave on a quantized vortex', Phys. Rev. B **64**, 134520 (2001) (cit. on p. 139).

[234] W. F. Vinen, 'An Introduction to Quantum Turbulence', J Low Temp Phys **145**, 7–24 (2006) (cit. on p. 14).

[235] W. F. Vinen, 'Quantum Turbulence: Where Do We Go From Here?', in AIP Conference Proceedings, Vol. 850 (2006), pp. 169–172 (cit. on p. 60).

[236] W. F. Vinen and J. J. Niemela, 'Quantum Turbulence', Journal of Low Temperature Physics **128**, 167–231 (2002) (cit. on pp. 1, 12, 51).

[237] W. F. Vinen and D. Shoenberg, 'Mutual friction in a heat current in liquid helium II I. Experiments on steady heat currents', Proceedings of the Royal Society of London. Series A. Mathematical and Physical Sciences **240**, 114–127 (1957) (cit. on p. 140).

[238] W. F. Vinen and D. Shoenberg, 'The detection of single quanta of circulation in liquid helium II', Proceedings of the Royal Society of London. Series A. Mathematical and Physical Sciences **260**, 218–236 (1961) (cit. on p. 12).

[239] P. M. Walmsley and A. I. Golov, 'Quantum and Quasiclassical Types of Superfluid Turbulence', Phys. Rev. Lett. **100**, 245301 (2008) (cit. on p. 140).

[240] G. A. Williams and R. E. Packard, 'Photographs of Quantized Vortex Lines in Rotating He II', Phys. Rev. Lett. **33**, 280–283 (1974) (cit. on p. 55).

[241] R. L. Williams, 'Ionic Mobilities in Argon and Helium Liquids', Can. J. Phys. **35**, 134–146 (1957) (cit. on p. 54).

[242] T. Winiecki and C. S. Adams, 'Motion of an object through a quantum fluid', Europhys. Lett. **52**, 257–263 (2000) (cit. on pp. 3, 77, 78, 197).

[243] T. Winiecki, B. Jackson, J. F. McCann and C. S. Adams, 'Vortex shedding and drag in dilute Bose-Einstein condensates', J. Phys. B: At. Mol. Opt. Phys. **33**, 4069–4078 (2000) (cit. on p. 76).

[244] T. Winiecki, J. F. McCann and C. S. Adams, 'Vortex structures in dilute quantum fluids', Europhys. Lett. **48**, 475–481 (1999) (cit. on pp. 76–78).

[245] T. Winiecki, J. F. McCann and C. S. Adams, 'Pressure Drag in Linear and Nonlinear Quantum Fluids', Phys. Rev. Lett. **82**, 5186–5189 (1999) (cit. on pp. 3, 35, 53, 76).

[246] N. Yadav, V. Vadakkumbatt, H. J. Maris and A. Ghosh, 'Exploding and Imaging of Electron Bubbles in Liquid Helium', J Low Temp Phys **187**, 618–626 (2017) (cit. on p. 56).

[247] E. J. Yarmchuk, M. J. V. Gordon and R. E. Packard, 'Observation of Stationary Vortex Arrays in Rotating Superfluid Helium', Phys. Rev. Lett. **43**, 214–217 (1979) (cit. on p. 55).

[248] P. K. Yeung and S. B. Pope, 'Lagrangian statistics from direct numerical simulations of isotropic turbulence', Journal of Fluid Mechanics **207**, 531–586 (1989) (cit. on pp. 6, 141, 198).

[249] T. Zhang, D. Celik and S. W. Van Sciver, 'Tracer Particles for Application to PIV Studies of Liquid Helium', Journal of Low Temperature Physics **134**, 985–1000 (2004) (cit. on p. 56).

[250] T. Zhang and S. W. Van Sciver, 'The motion of micron-sized particles in He II counterflow as observed by the PIV technique', J Low Temp Phys **138**, 865–870 (2005) (cit. on pp. 56, 59, 60, 74).

[251] T. Zhang and S. W. Van Sciver, 'Large-scale turbulent flow around a cylinder in counterflow superfluid 4 He (He (II))', Nature Physics **1**, 36–38 (2005) (cit. on pp. 56, 57).

[252] D. E. Zmeev, F. Pakpour, P. M. Walmsley, A. I. Golov, W. Guo, D. N. McKinsey, G. G. Ihas, P. V. E. McClintock, S. N. Fisher and W. F. Vinen, 'Excimers He 2 * as Tracers of Quantum Turbulence in He 4 in the T = 0 Limit', Phys. Rev. Lett. **110**, 175303 (2013) (cit. on p. 60).

[253] S. Zuccher, M. Caliari, A. W. Baggaley and C. F. Barenghi, 'Quantum vortex reconnections', Physics of Fluids **24**, 125108 (2012) (cit. on p. 48).